Anales de Mecánica de la Fractura

Conferência Ibérica de Fractura e Integridade Estrutural 2010

17, 18 e 19 de Março de 2010

Faculdade de Engenharia da Universidade do Porto, Portugal

XXVII Encuentro del Grupo Español de Fractura / 12as. Jornadas de Fractura da SPM

Conferencia Ibérica de Fractura e Integridad Estructural 2010

17, 18 y 19 de Marzo de 2010

Facultad de Ingeniería de la Universidad de Oporto, Portugal

XXVII Encuentro del Grupo Español de Fractura / 12as. Jornadas de Fractura da SPM

Vol. I

Editado por la Secretaría del Grupo Español de Fractura

I.S.S.N.: 0213-3725

Depósito Legal:

Impressão: RioGráfica

E-book: www.engebook.com

CIFIE 2010
March 17-19, 2010

organized by
Sociedade Portuguesa de Materiais – SPM and Grupo Español de Fractura GEF

Faculdade de Engenharia da Universidade do Porto - FEUP, Portugal,

Sponsors

walter+bai ag

Zwick / Roell

FUNDAÇÃO
LUSO-AMERICANA

FCT
Fundação para a Ciência e a Tecnologia
MINISTÉRIO DA CIÊNCIA, TECNOLOGIA E ENSINO SUPERIOR

U.PORTO

ORGANIZING COMMITTEE

Portuguese members

- José António Martins Ferreira (Universidade de Coimbra)
- Manuel J. M. de Freitas (IST, Lisbon)
- Maria Manuela Bastos Oliveira (INETI, Lisbon)
- Paulo M. S. Tavares de Castro (FEUP), *chair*
- Pedro P. Camanho (FEUP)

Spanish members

- Antonio Martín Meizoso (CEIT-Universidad de Navarra, San Sebastián)
- Gustavo V. Guinea (Dpto. Ciencia de Materiales, ETSI Caminos, Canales y Puertos, Universidad Politécnica de Madrid), *coordinator of Spanish participation*
- Javier Belzunce (Universidad de Oviedo, Gijón)
- José Fernández Sáez (Universidad Carlos III de Madrid, Madrid)
- Marc Anglada (Universidad Politécnica de Cataluña, Barcelona)

Honorary, non executive members of the Organizing Committee

- Carlos A. G. Moura Branco (IST, Lisbon)
- Manuel Elices (UPM, Madrid)
- Manuel Fuentes (CEIT-UN, San Sebastian)

LOCAL ORGANIZING COMMITTEE

- Daniel F. C. Peixoto
- Maria Fernanda Fonseca
- Miguel A. Bessa
- Miguel A. V. de Figueiredo
- Paulo M. S. T. de Castro
- Pedro M. G. P. Moreira
- Pedro P. Camanho
- Valentin Richter-Trummer

SCIENTIFIC COMMITTEE

INVITED KEYNOTE SPEAKERS

- Eann A Patterson, Editor of the journal *Fracture and Fatigue of Engineering Materials and Structures*, Chair and Professor of Mechanical Engineering, Michigan State University, USA
- Ky Dang Van, Formerly Research Director at the Laboratoire de Mécanique, École Polytechnique, Paris, France, (until September 2008)
- Michael Windisch, Fracture Mechanics and Damage Tolerance Depart. TEA, MT Aerospace AG, Augsburg, Germany
- Nikos Stergiopulos, Director, Laboratory of Hemodynamics and Cardiovascular Technology, Bâtiment AI, 1015 Lausanne, Switzerland

FOREWORD

Spain and Portugal have an established tradition of periodical scientific meetings on the area of fracture, fatigue and structural integrity. The Spanish Conferences on Fracture are organized by the Grupo Español de Fractura and are held every year, whereas the Portuguese Conferences on Fracture are held every two years in the context of the Sociedade Portuguesa de Materiais – SPM.

The last edition of the Portuguese Conference on Fracture (11st) took place in the Caparica campus of the Universidade Nova de Lisboa on February 13-15, 2008. At the same year the XXV Encuentro del Grupo Español de Fractura was held on March 5-7 at the Parador de Siguenza. During those conferences the idea of a joint event to be held in 2010 following the wake of past joint Spanish-Portuguese conferences (Braga, 1987, Mérida, 1993 and Luso, 1996) was discussed. The agreement was achieved on October 2008, when it was decided to hold a joint Iberian Conference on Fracture the 17-19 March 2010 at the campus of Faculdade de Engenharia da Universidade do Porto - FEUP, in Porto, Portugal

Portugal is a country associated to developments in Fracture research since the seventies and eighties of last century. Among examples of related events in Portugal, the early 5th European Conference on Fracture, organized in 1984 in the context of the European Group on Fracture (predecessor of ESIS), the 6th International Conference Biaxial/Multiaxial Fatigue and Fracture, 2001, the 1st International Conference on Engineering Failure Analysis ICEFA-1, 2004, or a considerable number of more recent events of the European Mechanics Society (EUROMECH) may be mentioned.

After an initial period in the seventies, dedicated to the creation and promotion of a critical mass of researchers, when Portuguese students had scholarships to obtain doctorates abroad, particularly in the UK and France, the more recent decades witnessed the steady development of the research capacity in Portugal. A clear sign of the increasing internationalization of the R&D activities in Portugal is the growth of international publications and participation in EU projects, or the frequent stays in Portuguese universities of post-doctoral researchers and visiting professors through programmes such as the EU ‘Marie Curie’, the US Fulbright Commission or the NATO post-doctoral scholarships, among others. Fatigue and fracture research in Portugal was the object of a special issue of the journal Fatigue and Fracture of Engineering Materials 2 and Structures - vol.27, Sept. 2004 - with Professor Paulo M. S. T. de Castro acting as guest editor.

Both for Spain and Portugal, the published proceedings of these series of meetings constitute important archives of the work performed; in Spain they have taken the form of a series, *Anales de Mecánica de la Fractura*, already with 26 issues. Perusal of these publications shows a wealth of research on all aspects of the field, from experimental work and numerical modelling on a variety of structures and materials, to case studies and reports of real engineering applications in many different fields as aeronautical, mechanical, civil, railways, process engineering, etc.; as elsewhere, recent years witnessed growing interest in biomedical applications.

The Iberian Conference on Fracture and Structural Integrity 2010 - Conferência Ibérica de Fractura e Integridade Estrutural, CIFIE'2010 - has brought together researchers and professionals of the two countries that during three days have shared their knowledge and experience in fields like Analytical and numerical methods; Case studies of fracture, fatigue and durability; Durability of structures; Experimental techniques; Fatigue of materials and structures; Deformation and Fracture of materials (metallic alloys, ceramics, composites, polymeric and bio) and Interaction with the environment.

In addition, CIFIE'2010 has counted with the participation of four relevant keynote speakers, Prof. Ky Dang Van, formerly Research Director at the Laboratoire de Mecanique at the École Polytechnique (Paris, France), Prof. Eann A. Patterson, Chair of Mechanical Engineering at Michigan State University (U.S.A) and Editor of the Journal of Strain Analysis for Engineering Design and the International Journal of Fatigue and Fracture of Engineering Materials and Structures, Prof. Nikos Stergiopulos, Director at the Hemodynamics and Cardiovascular Technology Laboratory at the École Polytechnique Féderale de Lausanne (Switzerland) and Mr. Michael Windisch, Head of Fracture Mechanics Department at MT Aerospace AG (Augsburg, Germany).

The organizers want to thank Faculdade de Engenharia da Universidade do Porto for their unconditional support as well as logistical help, the companies INSTRON, WALTER+BAI, SEM - MTS - RUMUL, ZWICK ROELL and the institutions Fundação para a Ciência e Tecnologia, Portugal, Fundação Luso Americana, Portugal, and Universidade do Porto for their financial support without which CIFIE'2010 conference would not have been possible. They also want to thank all the participants, most specially the keynote speakers who have generously given their time and talent to this event, and all the people involved in the organization of the conference and in the preparation of the XXVII volume of *Anales de Mecánica de la Fractura* for their continued support and help.

It is hoped that this event might contribute to create closer links among the Spanish and Portuguese scientific and technical communities interested in these areas, and that further joint conferences such as this will be held in the future, with the next future joint event taking place in Spain.

Paulo M. S. T. de Castro
Universidade do Porto

Gustavo V. Guinea
Universidad Politécnica de Madrid

INDEX

KEY NOTE LECTURES

BIOMATERIALS AND BIOLOGICAL MATERIALS

CASES

COMPOSITES, COATINGS

CONCRETE, CEMENT

EXPERIMENTAL METHODS

FATIGUE

FRACTURE

NUMERICAL AND PROBABILISTIC METHODS

POLYMERS

RESIDUAL STRESS, PEENING, SHAPE

WELDING

Authors' affiliations – institutions

Aalborg University, Denmark

California Institute of Technology, Pasadena, CA, USA

Centro de Engenharia Mecânica da Universidade de Coimbra – CEMUC, Portugal

Centro de Estudios e Investigaciones Técnicas de Gipuzkoa – CEIT, San Sebastián, España

Centro de Información Técnica de Aplicaciones del Vidrio - CITAV, Madrid, España

Centro de Ingeniería y Desarrollo Industrial - CIDESI, Querétaro, México

Centro Federal de Educação Tecnológica de Minas Gerais - CEFET-MG, Departamento de Engenharia Civil, Belo Horizonte, Minas Gerais, Brasil

Centro Nacional de Investigaciones Metalúrgicas – CENIM, Consejo Superior de Investigaciones Cientificas - CSIC, Departamento de Corrosión y Protección, España

Centro Tecnológico de Componentes - CTC, Santander, España

Consejo de Seguridad Nuclear – CSN, Madrid, España

Dublin City University, Research Institute for Networks and Communications Engineering, Ireland

École Polytechnique Federale de Lausanne – EPFL, Interfaculty Institute of Bioengeering, Suisse

École Polytechnique, Laboratoire de Mécanique des Solides, Paris, France

Essilor Portugal, Portugal

Estado Maior da Força Aérea, Direcção de Engenharia e Programas da Força Aérea Portuguesa, Amadora, Portugal

European Space Agency – ESA, European Space Research and Technology Centre - ESTEC, Noordwijk, the Netherlands

Fraunhofer Institut für Werkstoffmechanik - IWM, Freiburg, Deutschland

Friedrich Miescher Institute for Biomedical Research, Basel, Switzerland

Fundación Instituto Madrileño de Estudios Avanzados – IMDEA, Materiales, Madrid, España

Fundación Instituto Tecnológico de Materiales - ITMA, Centro Tecnológico del Acero y Materiales Metálicos, Avilés, España

Harbin Engineering University, China

Hospital Universitario Puerta de Hierro-Majadahonda, Servicio de Cirugía Cardiaca, Majadahonda, España

INESCO Ingenieros SL, Centro de Desarrollo Tecnológico de la Universidad de Cantabria – CDTUC, Santander, España

Instituto Andaluz de Tecnología, Sevilla, España

Instituto Ciencias de la Construcción Eduardo Torroja - IETcc, Consejo Superior de Investigaciones Cientificas - CSIC, Madrid, España

Instituto de Cerámica y Vidrio, Consejo Superior de Investigaciones Científicas – CSIC, Madrid, España

Instituto de Ciencia de Materiales de Madrid – ICMM, Consejo Superior de Investigaciones Científicas – CSIC, Madrid, España

Instituto de Ciência e Engenharia de Materiais e Superfícies – ICEMS, Portugal

Instituto de Engenharia Mecânica - IDMEC, Porto, Portugal

Instituto de Engenharia Mecânica e Gestão Industrial - INEGI, Porto, Portugal

Instituto Politécnico de Bragança, ESTG, Bragança, Portugal

Instituto Politécnico de Coimbra, Departamento de Engenharia Mecânica, CEMUC, Portugal

Instituto Politécnico de Leiria, Centro para o Desenvolvimento Rápido e Sustentado do Produto – CDRsp, Portugal

Instituto Politécnico de Setúbal, Escola Superior de Tecnologia de Setúbal, Departamento de Engenharia Mecânica, Portugal

Instituto Politécnico de Tomar, Departamento de Engenharia Mecânica, Abrantes, Portugal

Instituto Superior de Engenharia de Lisboa, Departamento de Engenharia Mecânica, Portugal

Instituto Superior de Engenharia do Porto, Portugal

Instituto Superior de Entre Douro e Vouga, Santa Maria da Feira, Portugal

Instituto Tecnológico de Morelia, Morelia Michoacán, México

Laboratoire de Mécanique de Lille, Université de Lille 1, UMR CNRS 8107, Villeneuve d'Ascq, France

Marinha Portuguesa, Direcção de Navios, Departamento de Estudos, Alfeite, Portugal

Michigan State University, Department of Mechanical Engineering, USA

Microtest SA, Madrid, España

Mondragon Unibertsitatea, Department of Mechanical Engineering and Industrial Manufacturing, Mondragón, España

MT Aerospace AG, Department TEA, Augsburg, Deutschland

National Aeronautics and Space Administration - NASA, Langley Research Center, VA, USA

OMS Automation Services, Setúbal, Portugal

Politecnico di Torino, Dipartimento di Ingegneria Strutturale e Geotecnica - DISTR, Italia

Unilever R&D

Universidad Carlos III de Madrid, España

Universidad de Alcalá, Alcalá de Henares, Madrid, España

Universidad de Antíoquia, Medellín, Colombia

Universidad de Barcelona, España

Universidad de Burgos, Escuela Politécnica Superior, España

Universidad de Cantabria, Santander, España

Universidad de Castilla-La Mancha, Ciudad Real, España

Universidad de Jaén, España

Universidad de Málaga, España

Universidad de Navarra, San Sebastián, España

Universidad de Oviedo, Escuela Politécnica Superior de Ingeniería de Gijón, España

Universidad de Salamanca, España

Universidad de Santiago de Chile - USACH, Facultad de Ingeniería, Chile

Universidad de Sevilla, España

Universidad Michoacana de San Nicolás de Hidalgo, Morelia Michoacán, México

Universidad Politécnica de Madrid, España

Universidad Politécnica de Valencia, España

Universidad Rey Juan Carlos, Móstoles, España

Universidad Simón Bolívar, Caracas, Venezuela

Universidade da Beira Interior – UBI, Covilhã, Portugal

Universidade da Coruña, España

Universidade de Aveiro, Portugal

Universidade de Coimbra, Faculdade de Ciências e Tecnologia - FCTUC, Portugal

Universidade de Trás-os-Montes e Alto Douro – UTAD, Vila Real, Portugal

Universidade do Porto, Faculdade de Engenharia, Portugal

Universidade Lusófona do Porto, Portugal

Universidade Nova de Lisboa, Faculdade de Ciências e Tecnologia, Caparica, Portugal

Universidade Técnica de Lisboa - UTL, Instituto Superior Técnico - IST, Portugal

Università di Firenze, Italia

Università di Modena e Reggio Emilia, Italia

Universitat de Girona, España

Universitat Politècnica de Catalunya, España

Universitatea "Politehnica" Bucuresti, Department of Strength of Materials, Romania

Université d'Artois, France

Université de Mascara, Laboratoire LPQ3M BP 763, Algeria

Université de Sidi Bel Abbes, Department of Mechanical Engineering, Algeria

Université des Sciences et Technologies de Lille - USTL, Laboratoire de Mécanique de Lille - LML, Villeneuve d'Ascq, France

Université Lille Nord de France, Lille, France

University of Oxford, United Kingdom

University of Portsmouth, United Kingdom

Virginia Polytechnic Institute and State University - Virginia Tech, Blacksburg, VA, USA

Authors' affiliations – countries

Algeria
Brasil
Chile
China
Colombia
Denmark
France
Germany
Ireland
Italy
México
Portugal
Romania
Spain
Switzerland
The Netherlands
United Kingdom
United States of America
Venezuela

Key note lectures

QUANTIFYING THE EFFECTS OF PLASTICITY ON CRACK STRESS FIELDS

E. A. Patterson [1]

[1] Department of Mechanical Engineering, Michigan State University,
2555 Engineering Building, East Lansing, USA.
E-mail: eann@egr.msu.edu

ABSTRACT

The presence of plastic zones at the tip and along the flanks of cracks has been recognized for a long time; however there has been controversy about their influence on crack propagation because of the difficulty in quantifying their impact on the stress/strain fields around the crack. In the last decade, there have been substantial advances in full-field measurement techniques which have allowed strains around a propagating crack to be monitored. An overview of three such techniques is provided and illustrated through their use in both fundamental studies and applications in the aerospace industry. Post-processing algorithms have been developed to compute stress intensity factors from displacement data obtained from digital image correlation using the surface texture of the material around the crack tip which offers the potential to monitor behavior in engineering components. A similar approach has been taken with thermoelastic stress analysis; however in recent experiments the phase difference between the applied load cycle and local temperature changes has been used to quantitatively identify the size and shape of the plastic zone at the crack tip. This novel approach has been used to study the interaction of the crack tip with the plastic zone during overload events. Photoelasticity has been used for sometime to evaluate stress intensity factors however in recent work it has been used to qualitatively examine the mechanisms associated with plasticity-induced shielding of crack tips; and to develop a new model that allows the associated forces to be characterized quantitatively. Together, these techniques from experimental mechanics allow a deeper understanding to be obtained of crack propagation mechanisms in complex applications such as the fracture of wing-skin panels and fatigue failure from cold-worked holes.

KEY WORDS: plasticity, crack propagation, digital image correlation, thermoelastic stress analysis, photoelasticity.

1. INTRODUCTION

Experimental mechanics has been deployed for many years in the study of fracture and fatigue phenomena. Photoelasticity was used more than seventy-five years ago to study the stresses around a crack [1]. About fifty years ago it was being utilized to study dislocations [2, 3] and to determine crack tip stress intensity factors [4, 5]. In this early work, photoelastic fringe orders were determined at single points on the apogee of fringe loops, this was later extended to acquiring data along a selected line, usually perpendicular to the crack path [6] and subsequently to the multi-point over-deterministic method (MPODM) [7] in which a set of stress field equations, typically either Westergaard's [8] or of the Muskhelishvili type [9], is fitted to a large array of experimental data points. Other techniques of experimental mechanics have been developed along similar paths including reflection photoelasticity [10], moiré interferometry [11], holographic interferometry [12] and thermoelasticity [13]. Sanford [14] and more recently Patterson and Olden [15] have provided reviews of the use of optical methods of strain analysis for determining stress intensity factors.

In the 1990s thermoelastic stress analysis became a viable technique for quantitative monitoring of the elastic stress field around the tips of fatigue cracks as a consequence of the development of staring array cameras [16]. In parallel, digital image correlation began to be used for the analysis of cracks [17]. Digital image correlation differs from the thermoelasticity or photoelasticity in that the primary data obtained are displacement fields to which a Muskhelishvili-type description can be fitted [18, 19]. Thermoelastic stress analysis and digital image correlation can be used on any material with only a small level of surface preparation making them attractive options for investigating the structural integrity of engineering components [20-23].

Since they are founded in linear elastic fracture mechanics, all of the techniques described above for determining the stress intensity factors involve the evaluation of the elastic stress, strains or displacements around a crack tip. With the exception of thermoelastic stress analysis, all the measurement techniques are valid for the assessment of plastic deformations but this has received very little attention although there were some very early investigations [24]. Perhaps, as a consequence the influence of the plastic zone around the crack tip and along the flanks on fatigue behavior, sometimes known as 'plasticity-induced closure', is poorly understood [25]. Plasticity-induced closure is one of a number of crack closure mechanisms; and crack closure remains controversial because there are

some fundamental aspects that not completely understood [26]. The purpose of this paper is to illustrate how the techniques of experimental fracture mechanics can be extended to provide information on the influence of the plastic zone in both fundamental studies and more application-orientated work.

2. PHOTOELASTICITY

Photoelasticity is based on the temporary birefringence of transparent materials subject to strain which, when viewed in polarized light causes them to generate fringe patterns that are proportional to the difference in the induced principal strains. The effect is integrated along the light path and so James et al. [27] used thin polycarbonate specimens to obtain the stress intensity factor during cyclic fatigue loading using the MPODM approach. They observed that in the presence of plasticity along the crack flank, the stress intensity factor in the unloaded portion of the fatigue cycle was elevated compared to the nominal value. They demonstrated that the elevated values arose due to the presence of residual stresses around the crack tip when the fatigue load had been removed. Subsequently, they modeled contact of the fracture surface during the fatigue cycle and estimated the magnitude of the flank contact load as a function of the fatigue cycle [28]. This work has been substantially extended by Christopher et al. [25] who considered the effect of the plastic zone around the crack on the surrounding elastic stress field. This involved considering the shape of the plastic field, its origins and its cyclic variation during fatigue loading which led Christopher et al. [29] to define a new set of stress intensity factors: K_F which characterizes the stress field driving the crack and in the absence of closure is equal to the conventional mode I stress intensity actor K_I; K_S which characterizes the interfacial shear stress established between the elastic and plastic zones along the crack flank as a consequence of compatibility of displacements; and K_R which characterises the direct stress retarding the crack growth parallel to the plane of the crack. This model was verified for a number of simple cases using photoelastic data from saw-cuts in brittle and ductile materials as well as from a fatigue crack. In recent work this model [30] has been used to examine the mechanism by which overloads affect the fatigue crack behaviour, in particular K_F increased by about 20%, K_S by 100% and K_R was unchanged by a 120% overload for a single cycle.

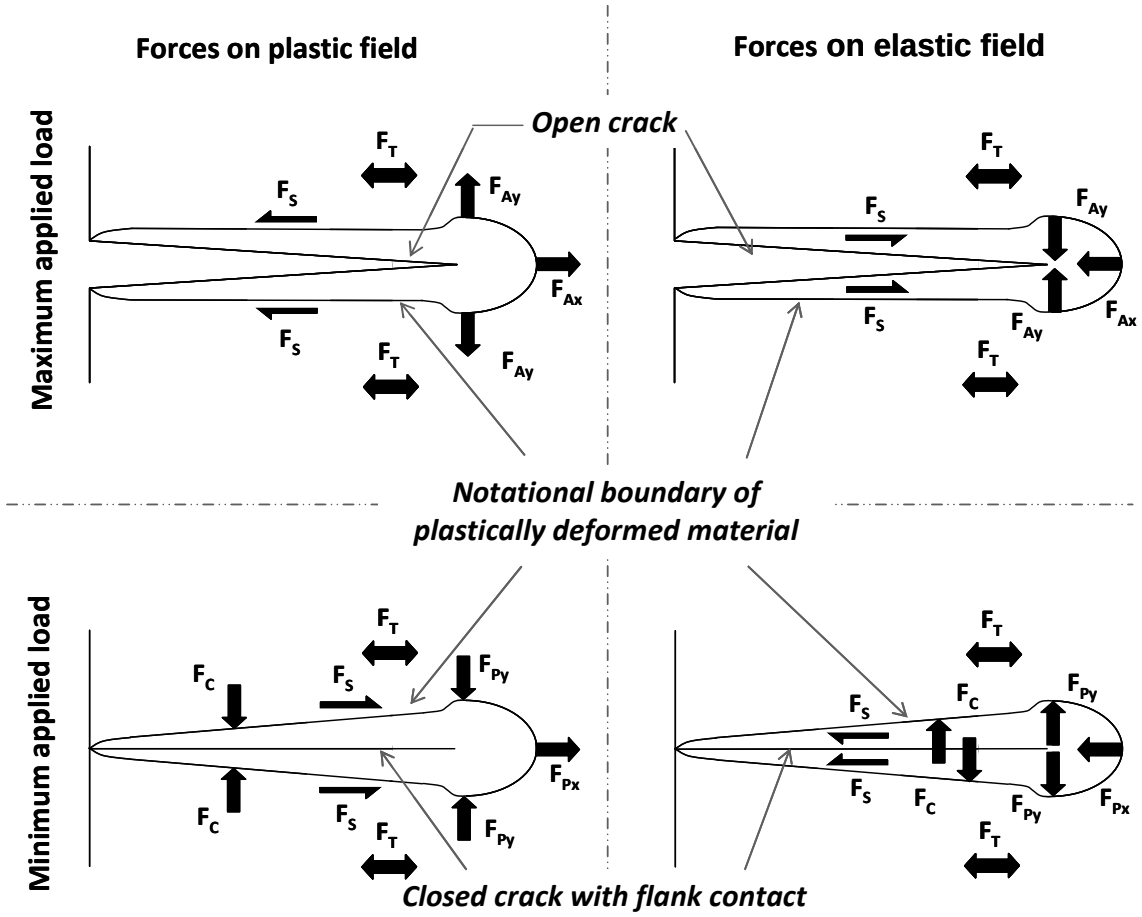

Figure 1. Schematic illustrating forces acting at the interface between the crack plastic zone and the surrounding elastic material for the maximum applied load (top) and the minimum applied load (bottom) during a fatigue cycle with the forces acting on the plastic zone shown (left) and the equal and opposite forces acting on the elastic field (right) (from [25])

3. THERMOELASTICITY

In thermoelastic stress analysis a very sensitive infra-red detector is used to monitor the change in the surface temperature of a component with applied load. In adiabatic, cyclic loading the amplitude of the surface temperature at a point is directly proportional to the amplitude of the sum of the principal stresses at the same point. The potential of thermoelastic stress analysis to provide data on the influence of the plastic zone around the crack was recognized early in the development of the technique [31]; however only recently has a comprehensive demonstration been provided [23] of the equivalence of thermoelastic data to that obtained from compliance analysis based on strain gauge measurements [32]. Unfortunately, since thermoelastic stress analysis provides the sum of the principal stresses it does not allow the evaluation of all of the stress intensity factors in the new model of Christopher et al. [25]; however an alternative feature of thermoelastic stress analysis has been utilized to investigate the effects of plasticity. In the thermoelastic effect, the induced strain and resultant temperature should be exactly out-of-phase (180°) with one another, so that a tensile strain causes a temperature drop and a compressive strain causes a temperature rise in adiabatic, elastic conditions. When plasticity is induced the resultant heat generation will cause a shift in the phase which can be detected by modern infrared cameras. Diaz at al. [33] have demonstrated that by employing a map of the phase differences between the applied load and surface temperatures it is possible to identify the plastic zone ahead of the crack, locate the crack tip and observe the extent of the crack flank contact. In recent work, Patki and Patterson [34] have shown that a quantitative measurement of the crack tip plastic zone can be obtained from such a phase map and correlated with fatigue crack behavior during overloads. They found that after an overload: the plastic zone size was larger, ΔK_I smaller and the growth rate slower and that these changes were proportional to the applied overloads; then as the crack tip emerged from the enlarged plastic zone: the plastic zone radius decreased, ΔK_I increased and the growth rate increased to values approximately equal to the pre-event values. They were able to correlate this behavior to Wheeler's model [35] for overloads.

4. DIGITAL IMAGE CORRELATION

In digital image correlation features on the surface of the component are tracked during the deformation and, or displacement of the component for small, overlapping facets within the image. In conventional analysis a speckle pattern is sprayed onto the object or component surface, however Lopez-Crespo et al. [36] have been able to obtain stress intensity factors using the metallic surface texture as the pattern. Work is in progress to exploit this capability to estimate the extent of the plastic zone and to compute the stress intensity factors defined by Christopher et al. [29]. However, in recent work, Du et al. [37] have demonstrated the use of digital image correlation on a large scale structures (approximately 5m × 1.5m) to track the development of the plastic zone size and the stress intensity factor for 10 minutes during a fracture test until just before complete rupture of the aircraft panel. They found that the structural assemblage of ribs, stringers and hole reinforcements in the panel acted as an energy sink allowing the skin to sustain very high levels of strain and correspondingly high values of the stress intensity factor that were substantially larger than the material fracture toughness.

5. DISCUSSION AND CONCLUSIONS

Three techniques of experimental mechanics have been highlighted, their basic principles outlined and recent progress in their application to quantifying the effects of plasticity on crack stress fields described. In general, optical methods of stress and strain measurement have been used for measuring elastic stress or strain fields. This is probably because not many applications demand information on plastic strains and because it is easier to interpret data when the material is homogeneous, isotropic and elastic. The later is certainly true for photoelastic and thermoelastic stress analysis. In addition, the field of structural integrity and structural prognosis is built upon linear elastic fracture mechanics with substantial less attention paid to elastic-plastic fracture mechanics.

Photoelasticity has provided substantial insights into the interaction of the plastic zone around a crack and the surrounding elastic stress field. However, transmission photoelasticity requires a transparent material which limits its applicability and interest, while reflection photoelasticity offers substantially less resolution, especially close to the crack. However, the insights obtained from transmission photoelasticity are helping to drive the development of thermoelastic stress analysis and digital image correlation in these areas. This is significant because both of these techniques offer the prospect of routine use in service applications either independently or in tandem [38]. These new developments include the concept of: (a) assessing the extent of plasticity in terms of size and shape of the plastic zone along the crack flank and around the crack tip; (b) measuring stress, strains or displacements in the surrounding elastic field where the data can be interpreted with confidence; (c) using the measured data to evaluate or characterize the forces acting at the interface between the elastic and plastic zones; and from which (d) the forces on the crack tip can be deduced. The growth of the crack is not a static or pseudo-static process so measurements have to be made throughout the load cycle if an accurate picture of the effects of the plasticity on the crack stress field is to be formed and its consequence understood in terms of the structural

prognosis. Some work remains to be done but most of the pieces of this jigsaw are now in place.

ACKNOWLEDGEMENTS

The author acknowledges the organizing committee of the CIFIE 2010 for their generous invitation to present this paper at the conference. The opinions expressed in this paper are those of the author however any new insights presented have arisen through discussions with collaborators who the author would like to acknowledge: David Backman of the Canadian National Research Council's Institute for Aerospace Research, Richard Burguete of Airbus UK, Colin Christopher of the University of Plymouth, Francisco Diaz of the Universidad de Jaén, Neil James of the University of Plymouth and Philip Withers of the University of Manchester.

REFERENCES

[1] Holister, S.C., Experimental study of stress at crack in compression member, *American Concrete Institute – Journal*, 5(4):361-365, 1934.

[2] Zandman, F., Mesures photoelastiques des deformations elastiques et plastiques fragmentations cristallines dans les metuax, *Revue de Metallurgie*, 53(8):638-644, 1957.

[3] Nye, J.F., Spence, R.D., Sprackling, M.T., Photoelastic study of dislocations arrangements in crystals, *Philosophical Magazine*, 2(18):772-772, 1957.

[4] Irwin, G.R., Discussion of the paper: The Dynamic Stress Distribution Surrounding a Running Crack - Photoelastic Analysis, *Proc. Soc. Exp. Stress Anal*., 16, pp. 93-96, 1958.

[5] Erdogan, F., Tuncel, O., Paris, P.C., Experimental investigation of crack tip stress intensity factors in plates under cylindrical bending, *ASME Papers*: 62-MET-5, 1962.

[6] Schoedl, M.A., Smith, C.W., Local stress near dead surface flaws under cylindrical bending fields, *ASTM STP 536*, pp. 45-63, 1973.

[7] Sanford, R.J., Dally, J.W., A general method for determining mixed mode stress intensity factors from isochromatic fringe patterns, *Engng. Fract. Mech*., 11, pp. 621-683, 1979.

[8] Westergaard, H.M., Bearing pressures and cracks, *ASME Transactions, J. Applied Mechanics*, 6(2):A49-A53, 1971.

[9] Muskhelishvili, N.I., *Some basic problems of the mathematical theory of elasticity*. P. Noordhoff, Groningen, 1953.

[10] Gerberich, W., Stress distribution about slowly growing crack determined by photoelastic-coating method, *Experimental Mechanics*, 2(12):359-365, 1962.

[11] Miyamoto, H., Shirota, Y., Kashima, K., Determination of stress intensity factors using moiré method, *ASM*, 2:1084-1088, 1976.

[12] Duddedar, T.D., O'Regan, R., Measurement of the strain field near a crack tip in polymethylmethacrylate by holographic interoferometry, *Experimental Mechanics*, 11(2):49-56, 1971.

[13] Stanley, P., Chan, W.K., Determination of stress intensity factors and crack-tip velocities from thermoelastic infra-red emissions, *IMechE Conference Publications*, 1:105-114, 1986.

[14] Sanford, R.J., Determining fracture parameters with full-field optical methods, *Experimental Mechanics*, 29(3):241-247, 1989.

[15] Patterson, E.A., Olden, E.J., Optical analysis of crack tip stress fields: a comparative study, *Fatigue and Fracture of Engineering Materials and Structures*, 27(7):623-636, 2004.

[16] Tomlinson, R.A., Olden, E.J., Thermoelasticity for the analysis of crack tip stress fields – a review, *Strain*, 35(2):49-55, 1999.

[17] McNeill, S.R., Peters, W.H., Sutton, M.A., Estimation of stress intensity factor by digital image correlation, *Engineering Fracture Mechanics*, 28(1):101-112, 1987.

[18] Yoneyama, S., Morimoto, Y. and Takashi, M., Automatic evaluation of mixed-mode stress intensity factors utilizing digital image correlation, *Strain*, **42**, 21-29, 2006.

[19] Roux, S., Hild, F., Stress intensity factor measurements from digital image correlation: post-processing and integrated approaches, *I.J. Fracture*, 140:141-157, 2006.

[20] Lopez-Crespo, P., Burguete, R.L., Patterson, E.A., Shterenlikht, A., Withers, P.J., Yates, J.R., Study of a crack at a fastener hole by digital image correlation, *Experimental Mechanics*, 49(4):551-559, 2009.

[21] Yusof, F., Withers, P.J., Real-time acquisition of fatigue crack images for monitoring crack-tip stress intensity variations with fatigue cycles, *J.*

Strain Analysis for Engineering Design, 44(2):149-158, 2009.

[22] Honda, T., Sasaki, T., Yamaguchi, A., Yoshihisa, E., Detection of fatigue crack initiated at weld toe and evaluation of stress intensity factor range by means of thermoelastic stress analysis, *Trans. JSME, Part A*, 73(11):1280-1287, 2007.

[23] Diaz, F.A., Patterson, E.A., Yates, J.R., Assessment of effective stress intensity factors using thermoelastic stress analysis, *J. Strain Analysis for Engineering Design*, 44(7):621-631, 2009.

[24] Underwood, J.H., Kendall, D.P., Measurement of microscopic plastic-strain distributions in region of crack tip, *Experimental Mechanics*, 9(7): 296-304, 1969.

[25] Christopher, C.J., James, M.N., Patterson, E.A., Tee, K.F., Towards a new model of crack tip stress fields, *I.J. Fracture*, 148(4):361-371, 2007.

[26] James, M.N., Some unresolved issues with fatigue crack closure – measurement, mechanism and interpretation problems. *Proc. of the Ninth International Conference on Fracture, Sydney*, eds. B L Karihaloo et al., (1997), 5: 2403-2414.

[27] James, M.N., Pacey, M.N., Wei, L-W., Patterson, E.A., Characterisation of plasticity-induced closure: crack flank contact force versus plastic enclave, *Engineering Fracture Mechanics*, 70(17):2473-2487, 2003.

[28] Pacey, M.N., James, M.N., Patterson, E.A., A new photoelastic model for studying fatigue crack closure, *Experimental Mechanics*, 45(1):42-52, 2005.

[29] Christopher, C.J., James, M.N., Patterson, E.A., Tee, K.F., A quantitative evaluation of fatigue crack shielding forces using photoelasticity, *Engng. Fract. Mechanics*, 75(14):4190-4199, 2008.

[30] Colombo, C., Patterson, E.A., Vergani, L., Photoelastic analysis of crack tip shielding after an overload, *Proc. Int. Conf. on Crack Paths (CP2009)*, 23-25 September 2009, Vicenza, Italy, paper no. 025, 2009.

[31] Leaity, G.P., Smith, R.A., The use of SPATE to measure residual stresses and fatigue crack growth, *Fatigue and Fracture of Engineering Materials and Structures*, 12(4):271-282, 1989.

[32] Stoychev, S., Kujawski, D., Methods for crack opening load and crack shielding determination: a review, *Fatigue and Fracture of Engineering Materials and Structures*, 28:1053-1067, 2003.

[33] Patterson, E.A., Diaz, F.A., Yates, J.R., Observations on photo-emission and the process zone of a fatigue crack, *J. Testing & Evaluation*, 3(6) paper id JAI13222 (2006).

[34] Patki, A., Patterson, E.A., Thermoelastic stress analysis of fatigue cracks subject to overloads, *Fatigue and Fracture of Engineering Materials and Structures* (submitted).

[35] Wheeler O.E., Spectrum loading and crack growth, *J. Basic Engineering*, **D94(1)**, 181-186, 1972.

[36] Lopez-Crespo, P., Shterenlikht, A., Patterson, E.A., Withers, P.J., and Yates, J.R., The stress intensity of mixed mode cracks determined by digital image correlation, *J. Strain Analysis for Engineering Design*, 43(8):769-780, 2008.

[37] Du, Y, Diaz Garrido, F.A., Burguete, R.L., Patterson, E.A., The application of digital image correlation during a fracture test on an aircraft panel, *Proc. SEM Conf. Exptl. & Appl. Mech*., Albuquerque, NM., 2009.

[38] Backman, D., Cowal, C., Patterson, E.A., Analysis of the effects of cold expansion of holes using thermoelasticity and image correlation, *Fatigue and Fracture of Engineering Materials and Structures*, submitted.

ON A UNIFIED FATIGUE MODELLING FOR STRUCTURAL ANALYSIS BASED ON THE SHAKEDOWN CONCEPT

K. Dang Van

MECAMIX, X-TECH
Ecole Polytechnique, 91128 Palaiseau, France

ABSTRACT

Fatigue analysis of structures requires nowadays specific numerical tools able to take account of complex multiaxial loadings generated by the use of FEM structural calculations. Traditionally fatigue is studied in different ways depending on the fatigue regime and the field of interest: fatigue limit analysis, life prediction in high or low cycle fatigue, thermal fatigue… The application of the shakedown theory to the analysis of the fatigue problems permits to present a unified theoretical background to both high and low cycle fatigue. This point of view allows interpreting all types of industrial problems of fatigue in an efficient manner. The description of the stabilised mechanical state after shakedown at macroscopic and mesoscopic scales gives access to engineering values which will drive the fatigue damage of the structure. The formulations are intrinsic and suffer no ambiguities. Some examples of fatigue analysis for different industrial areas are presented.

KEY WORDS: Fatigue, shakedown.

1. INTRODUCTION

One of the main goals in structural design is to avoid rupture due to fatigue. During a long period, and still now, engineers used simple stress approaches. Uniaxial criteria like S-N curves, Goodmann-Haigh diagrams, Kt- Kf concept are sufficient when the stresses are derived by using analytical elastic approaches like beam theory. The generalization of FEM calculations make possible to characterise with more accuracy the stress and strain state near the hot spots of mechanical structures. They are most of the time complex: numerous mechanical components experience in service multiaxial repeated varying stresses where two or more principal stresses fluctuate with time (i.e. they vary with time but they may also rotate like in the rolling contact fatigue). Multiaxial fatigue criteria are then needed in order to make fatigue calculations. Early multiaxial fatigue criteria are derived by using equivalent stress or strain based on static yield theories obtained by replacing the static von Mises or Tresca stress by an "amplitude" of von Mises or Tresca stress. These approaches often qualified as empirical may be non conservative for out of phase loading paths.

In order to introduce more physical explanations, different authors (Findley, Mc Diarmid …) propose the critical plane approach which emerges from observations that cracks initiate on some preferred planes which undergo plastic deformation. Persistent slip bands are induced by shear stress and normal stress assists the cracking. Application of critical plane approaches to structures presents however some difficulties which prevent their wide diffusion.

More recently, some authors propose energy based multiaxial fatigue life prediction approach including elastic energy (a variation of "positive" elastic energy is associated with a variation of plastic energy) in order to study high cycle multiaxial fatigue taking account of stress state and mean stresses.

In the sixties a special interest occurred in studying low cycle fatigue. Due to Manson and Coffin work, models based on strain amplitude and plastic strain amplitude became popular. Application of Manson Coffin type approaches necessitates inelastic analysis. This is at the origin in the eighties of extensive researches on constitutive equations which are necessary to perform elastoplastic structural calculations (Mroz, Chaboche, Dafalias, Ohno…).

In order to study low cycle fatigue problems involving high temperature cycles, generalisation of methods based the inelastic strain range used as damage parameter (strain range partitioning methods, Manson's universal slopes…and many other methods) were proposed. However, applications of these methods (based on uniaxial tests) on industrial structures are difficult because the strains are generally complex and multiaxial. Moreover, beside the fact that they can be difficult to calculate, they are not sufficiently predictive since inelastic strain range is not sufficient for characterizing the strain loading path. Energy based model already mentioned is a promising alternative.

Nowadays engineers have at their disposal a wide range of proposals. However the current fatigue structural computational methods are not as developed as expected and evaluation of fatigue resistance of structures is still a difficult task. The diversity of proposed approaches is so great that design engineers

meet many difficulties to have a clear idea of the fatigue calculations which have to be done. Some questions remain not very clearly explained: why cycles are necessary to cause fatigue, why fatigue resistance is much lower than static resistance. This paper aims to suggest some new avenues in order to answer to these questions. Furthermore, the adopted point of view permits to present a unified theoretical background to high and low cycle fatigue and allows interpreting different types of fatigue industrial problems in an efficient manner.

2. THE NEED OF A MULTISCALE APPROACH

Phenomena which cause fatigue failure differ from those which can be observed in static failures. It can be caused by a presence of a crack or a defect which concentrates the stresses: in that case, it is traditional to consider that it is mainly a problem of propagation after a short period of incubation. However, in the absence of such defects, an initiation period is necessary for the formation of the first detectable cracks which will lead to the final breakage. This period can take a great part of the fatigue life, particularly in the high cycle fatigue regime. In this regime, even if no plastic strain is detected at the engineering scale, one can observe plastic slip bands localized in some grains. Since the first observations by Gough, many other scientists have studied the microstructural changes in fatigue, and particularly the mechanisms of the formation of persistent slip bands and the associated intrusion extrusion phenomena. As noted by these authors, the characteristic feature of the cyclic deformation is an inhomogeneous distribution of the plastic strain in the material. This is particularly true when the applied load is low corresponding to the high cycle fatigue. It is then difficult to derive computational methods which can be employed by engineers for the prediction of the fatigue resistance of mechanical structures by using macroscopic parameters. Before the initiation of a crack, the observable behaviour of the material does not show in many cases any deviation from elasticity. Though not detectable at the macroscopic scale, it is precisely the evolution of the irreversible processes (broadening of the persistent slip bands) which take place at the level of the metallic grains which leads to the initiation of the first cracks. The introduction of the grain scale is thus suitable to model correctly and to capture the main features of mechanisms of plastic deformation which are not detectable at the macroscopic scale when the specimen is submitted to low or moderate cyclic loads.

In discussing fatigue phenomena we shall distinguish three scales:

- The microscopic scale of dislocations
- The mesoscopic scale of grains
- The macroscopic scale representing phenomena at the scale of engineers

In a simplified analysis one can say that fatigue phenomena start generally with appearance of slip bands in grains which broaden progressively during the first cycles. The number of grains where slip bands develop increases with the applied load.

In the high-cycle fatigue regime (HCF), the material seems to be purely elastic; in general no inelastic behaviour (plastic or viscous) is detected and as a consequence, the use of stress or strain at this engineering scale is equivalent. In practice stress is often preferred to strain. However at the mesoscopic level, plasticity occurs in certain number of grains and generates heterogeneous plastic strain. Only some crystals undergo plastic slip corresponding to a heterogeneous distribution of micro cracks. The initiation of the first visible crack, at the macroscopic scale represents a large part of the fatigue life.

The low-cycle fatigue regime (LCF) implies significant macroscopic strains conducting to irreversible deformations. At the mesoscopic level, the metal grains are subjected to plastic deformation in a more homogeneous manner. The first micro cracks in the persistent slip bands appear quite early in the life of the structure. The strain and the plastic strain are no more related to the stress through a simple relation but depend closely on the loading path. For instance it is well known that two similar stress states may correspond to two completely different plastic strain histories. The use of stress parameters or strain parameters is then not equivalent. Furthermore, a small increase of stress may induce large strain variation, and therefore strain parameter is preferred.

In both LCF and HCF, damage phenomena occur in the grains. The use of mesoscopic fields is therefore more appropriate for studying fatigue. The macroscopic fields (stress Σ, strain E, plastic strain E^p…) are related to the mesoscopic fields (stress σ, strain σ, plastic strain ε^p…). This dependence is complex and exact relations can be found for instance in [1]; however intuitively the first quantities are approximately the mean value of the latter. The macroscopic fields are therefore supposed constant in a small volume, surrounding the point under consideration. In the theories of polycrystalline aggregates, this volume is called “representative volume element” or RVE. For instance the mesoscopic stress σ and the macroscopic stress Σ are related by the following (exact) formula:

$$\sigma = A\,\Sigma + \rho \qquad (1)$$

ρ is the local residual stress and A is the elastic stress localization tensor. A is the identity tensor if the local and the macroscopic elastic moduli are similar. This relation shows that Σ is not adequate for characterizing phenomena which occur at the grain scale since *the local stress σ in the grain is not proportional to Σ.* The additive term ρ, function of the plastic strain, is closely related to the loading path. Therefore fatigue criteria using maximum stress (or some combination of maximum stress) are only valid for the loading paths for

which they are derived by correlating experimental results. They should be extended to take account of multiaxial loadings, and as a consequence their use for practical design is difficult, and sometime non conservative. However, this way to proceed is very often used even if it is not theoretically valid.
To illustrate this relation, one can consider the Lin Taylor model which supposes that the total macroscopic and mesoscopic strain are equal, $E = \varepsilon$.
Thus, $\varepsilon^e + \varepsilon^p = E^e + E^p$ and if l and L are respectively the mesoscopic and the macroscopic compliance of the material, one obtains

$$\sigma = lL^{-1}.\ \Sigma + l.(E^p - \varepsilon^p)$$

expression which is similar to (1) . lL^{-1} corresponds to the localisation tensor A and is equal to the identity tensor if l = L. We shall make this assumption in the following.
$l.(E^p - \varepsilon^p)$ corresponds to the local residual stress ρ, characterizing the difference between the local stress σ and the mean stress in the V.E.R Σ. Thus ρ is due to the heterogeneity of plastic strain, difference between the local plastic strain ε^p and its mean value E^p. ρ decreases, if this difference diminishes and the gap between mesoscopic and macroscopic parameters vanishes. This situation occurs when plastic deformation is important.
The evaluation of the local mesoscopic fields from the macroscopic ones is in general a difficult task because *the material is locally heterogeneous and has to be considered as a structure when submitted to complex loading histories*. Depending on the loading characteristics one can accept reasonable simplifying assumptions which will permit a solution to the problem. The multiscale approaches in fatigue that we promote are precisely based on the use of mesoscopic parameters instead of engineering macroscopic quantities. All the variables of equation (1) depend of time t except when the asymptotic cyclic state is purely elastic, i.e. when elastic shake down occurs. *In order to derive a unified theory of fatigue, we shall suppose that the elastic shakedown occurs at the level of the microstructure as well as at the macroscopic one.*

3. RECALL OF SOME ELASTIC SHAKEDOWN RESULTS AND APPLICATIONS.

In the proposed modelling, the concept of shakedown is essential. Recalling of some mathematical results is necessary. Let us start with the famous Melan-Koiter theorem which gives a sufficient condition for elastic shakedown for a structure made of elastic perfectly plastic material ($J_2(\Sigma)<k^2$). It can be stated as follows:
"If there exist a time θ and a fixed self equilibrated stress field R(x) and a safety coefficient m>1 such that for any point x of the structure and t> θ, $J_2[m(\Sigma_{el}(x,t)+R(x)]<k^2$, the structure will shakedown elastically."
Σ_{el} is the stress response of the structure submitted to the same external loading, but under the assumption that the material has a pure elastic behaviour. In this famous paper, Koiter [2] draws our attention on the fact that the original formulation and demonstration of the theorem by Melan [3] is not correct, since this author does not say anything about the dissipated energy which can be infinite even if the plastic strain (and as a consequence the residual stress) is bounded. It is clear that infinite dissipated energy has no physical meaning, so that Koiter added that *"if the total amount of plastic work is accepted as suitable criterion for assessing the overall deformation, boundedness of the overall deformation may be proved if the structure has a safety structure m>1 with respect to shakedown."* Thus, bounded dissipated energy, bounded plastic strain and existence of stabilized residual stress are different related aspects of elastic shakedown.
The Melan Koiter theorem is recently extended to generalized strain hardening material (which include all classical strain hardening behaviours) by Q.S. Nguyen [4]. In these cases, the (intensive and extensive) strain hardening parameters must be bounded too and are independent of time for t> θ.
However, the previous theorems are difficult to apply, since the residual stress field must be self equilibrated, a condition which is difficult to fulfil. Another proposal due to Mandel et al. [5] makes it possible to overcome this difficulty in the case of strain hardening material. The plasticity criterion can be written $J_2[(\Sigma - \alpha)]<k^2(P_{eq})$. α the kinematic hardening parameter is the centre of the current convex of plasticity and $k(P_{eq})$ is its radius. Generally k increases with the equivalent plastic strain P_{eq} until some maximum value k* and then decreases. (k* can be interpreted as the onset of ductile fracture). Since $\Sigma = \Sigma_{el} + R$, one obtains:

$$J_2[(\Sigma_{el}(x,t) - Z(x,t)]<k^2$$

where $Z = \alpha - R$. Z *is not necessarily self equilibrated*, since α has not to fulfil this condition.
For cyclic loadings, α and R are function of time t; however Z(x,t) must be inside or on the convex, the centre of which is $\Sigma_{el}(x,t)$. With an adequate choice of coordinates, this convex is a hypersphere in the deviatoric space. The trajectory of $\Sigma_{el}(x,t)$ is known at any point x of the structure because it is the solution of an elastic problem. Shakedown may occur only if for t> θ the intersection of these convex is not empty, as shown on figure 1. The limit of the possibility of shakedown occurs when the intersection domain (ABC of figure 1) is reduced to a point, for a value corresponding to the maximum of $k^2(E^p_{eq}) = k^{*2}$. The dissipated energy density required for reaching this limit state corresponds to the local bound for possible shakedown. Beyond this bound, failure will occur.

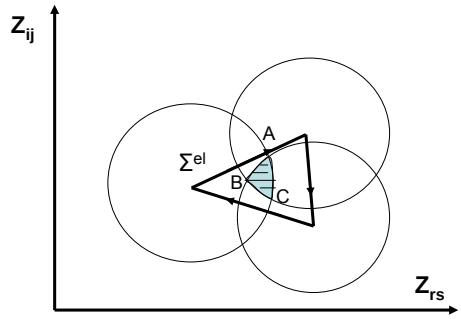

Figure 1- Illustration of trajectory of plasticity convex at shakedown in the Z space

In our fatigue model we suppose that *fatigue corresponds to the limit of elastic shakedown possibility of the material* of the structure. This hypothesis implies that fatigue will not occur if elastic shakedown happens at both scales, macroscopic and mesoscopic scales. The local plastic dissipation, which must be bounded, corresponds to fatigue initiation energy. The number of cycles necessary to dissipate this energy corresponds to the initiation period. In the following we shall suppose moreover that this limit depends of the hydrostatic tension occurring during the loading cycle. This hypothesis is not in contradiction with classical concepts used in plasticity theories which suppose that plastic slip is independent of hydrostatic pressure, because we consider *the limit of possibility of shake down* which may depend on the hydrostatic pressure. Let us recall that Rice-Tracey [6] or Gurson's criteria [7] for ductile fracture depend on shear, but also on hydrostatic tension.
From a theoretical point of view, this fatigue modelling permits to answer to a fundamental question: what is the difference between monotonic loading rupture and fatigue and why cycling is necessary to obtain fatigue failure.

4. HIGH CYCLE FATIGUE

In high cycle fatigue the loadings are usually not very important, and the structure is globally elastic. Therefore, the fatigue failure initiates only in some grains. It is difficult to evaluate directly the plastic strains and the dissipated energy in the grains that will fail. It is more judicious to proceed indirectly by an inverse way: since the fatigue limit corresponds to the shake down limit, one can evaluate the local stress at the stabilized state if these grains are at (or near) the fatigue limit. Starting from the knowledge of $\Sigma(x,t)$ at a point x of the structure, we derive the local stress σ by constructing the smallest hypersphere containing $\Sigma(x,t)$, the centre of which corresponds to $\Sigma^* = \alpha^* - \rho^* \approx \rho^*$, because it can be shown that $|\alpha^*|/|\rho^*| << 1$. Thus we have an estimation of the local stress tensor $\sigma(t) = \Sigma(t) + \rho(t)$ in grains which may fail by fatigue.
Different fatigue criteria can be formulated based on the stabilized stress tensor.

- for instance a linear combination of the shear and the concomitant hydrostatic pressure p, $\tau + ap < b$. (Dang Van);
-Papadopoulos criterion, $k^* + ap_{max} < b$ can be interpreted in the same way: the radius of the elastic domain at the limit of possible elastic shakedown depends on the maximum hydrostatic tension in the loading cycle.
The different computation steps for the application of the first criterion are the following:
-First evaluate the mesoscopic stress $\sigma(x,t)$ tensor knowing the macroscopic stress cycle $\Sigma(x,t)$; this can be done under the assumption of elastic shakedown near the fatigue limit by constructing the smallest hypersphere surrounding the macroscopic loading path. Different algorithms can be used, see for instance [ ].
- Second, one must consider the plane on which the set $(\tau(t), p(t))$ is "maximum" relative to the criterion. This computation can be done as follows:
The maximum local shear stress at any time t is given by $\tau(t) = \text{Tresca}(\sigma(t)) = \max|\sigma_I(t) - \sigma_J(t)|$
The stresses $\sigma_I(t)$, $\sigma_J(t)$ are the principal stresses at time t.
-The quantity that quantifies the danger of fatigue occurrence is defined by $d = \max[\tau(t)/(b - ap(t))]$, d is calculated over a period, and the maximum is to be taken over the cycle.
Determination of the parameters a and b can be easily done with classical fatigue tests. The knowledge of two independent fatigue limits (at least) are needed, for instance the rotating bending f and alternated torsion fatigue limit t. Then a and b are given by:
$a = 3(t - f/\sqrt{3})/f$, $b = t$.

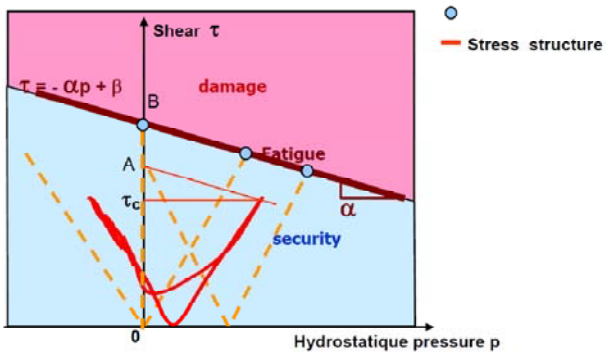

Figure 2- Illustration of the main steps for the application of Dang Van's criterion

5. LOW CYCLE FATIGUE

In this regime, because the mascroscopic plastic strain may be important, so that the differences between macroscopic and mesoscopic quantities become less and less marked. To characterize damage phenomena which occur in the grains, any macroscopic parameter could be chosen. However, the stress is not a good choice because a small variation of stress may induce a large variation of strain and dissipated energy. The deformation is more appropriate, particularly the plastic strain. This parameter becomes popular thanks to the

works of Manson and Coffin who propose to use the plastic strain amplitude to correlate the life duration of their test specimens submitted to tension compression loadings. However we propose to choose the dissipated energy because it is a scalar parameter with a clear physical meaning, easy to compute in multiaxial situations (particularly in presence of thermomechanical loadings), and which leads to good predictions on structures. Let us notice, that for general cyclic loading paths, there is (on the contrary to uniaxial loadings mentioned previously) no evident relation between the amplitude of plastic strain and dissipated energy, and therefore the choice between dissipated energy and plastic strain amplitude as fatigue parameter is not neutral.

6. APPLICATIONS TO HIGH CYCLE FATIGUE

Three applications will be done which permits to present some aspects and advantages of the proposed theory. However, it is noteworthy that many other examples exist which are not discuss in this presentation. In particular the application of the previous criterion to the prediction of fatigue induced by contact between solids is studied in the following reference [9].

6.1. Fatigue limit of notched specimens

The high-cycle fatigue design of structures in the presence of stress concentrations areas (holes, notches, indentations…) is still difficult and the way to take account of these defects is particularly important. In the current industry approaches, it is carried out by semi-empirical corrections requiring a large number of tests and which domain of validity must be carefully delimited. The most common approach is based on the concept of stress concentration factor K_t, defined as the ratio of the maximum stress at the notch evaluated under the assumption of a purely elastic behavior and the nominal stress. However, the fatigue limit of a notched specimen is different from that of the smooth specimen divided by k_t, which led engineers to introduce the concept of fatigue strength reduction factor k_f. This coefficient is however not general. In the presence of residual stresses, the correction factor previously determined for a particular load, a particular material, will be no longer valid for another load or another material. Various proposals of empirical corrections exist; they require tests database which are used to carefully delimit the validity range of the proposed factors. Another way to take account of the effects of stress concentration is the use of theories of critical distances based on elastic stresses. Depending on the specific form of these theories, the relevant stresses for fatigue analysis are estimated at a certain distance from the notch (point method) or averaged along a line (line method) or along an area (area method). However, these approaches are inefficient in case of multiaxial loadings. In the following we demonstrate the efficiency of the proposed modelling for the prediction of the fatigue limit of notched specimens by calculations associated with an adequate choice of the representative volume element (RVE).

Let us recall that in the proposed approach, it is supposed that fatigue will not occur if elastic shakedown is possible at both macroscopic and mesoscopic scales. This hypothesis implies that the stresses are near the fatigue limit (but below this limit) and that *the macroscopic stress Σ in the RVE becomes purely elastic after a certain number of cycles.* Therefore it exists a stabilized residual stress R (due to plastic deformation near the notch) so that $\Sigma(t) = \Sigma_e l(t) + R$ is a pure elastic stress state. The mesoscopic stress is then given by:

$$\Sigma(t) = \Sigma_e l(t) + R + \rho$$

In order to check the validity of this proposal, elastic-plastic simulations are performed and calibrated with tests on smooth and notched specimens made of 42CrMo4 steel (Re=928 MPa, Rm=1024 MPa) subjected to tension-compression with or without mean value, to rotating bending and to alternated torsion. (Details of specimen tested and elastoplastic calculations and corresponding results are given in [10]). The obtained fatigue limits are the following, where S_a is half the stress amplitude and S_m is the mean stress of the same nature:

- Tension, k_t=1, S_a = 508 MPa, S_m = 0
- Tension, k_t=1, S_a = 467 MPa, S_m = 400 MPa
- Tension, k_t=2, S_a = 252 MPa, S_m = 500 MPa
- Tension, kt=3, S_a = 220 MPa, S_m = 0
- Tension, k_t=3, S_a = 165 MPa, S_m = 500 MPa
- Torsion, k_t=1, S_a = 320 MPa, S_m = 0
- Bending, k_t=1, S_a = 540 MPa
- Bending, k_t=2, S_a = 267 MPa
- Bending, k_t=3, S_a = 180 MPa

The methodology used to check the validity of the proposed theory is based on the following features:

1. cyclic elastic-plastic finite element simulations to calculate the stabilized mechanical state with different meshing refinements;
2. use of the Dang Van fatigue limit criterion associated with a material representative volume (critical volume);
3. use of an optimisation process coupling simulations and experiments to determine the critical volume. This volume is determined as the one which permit to obtain the best correlation between calculated fatigue limits and experimental ones for all the tests.

The obtained results represented on figure 3 show that a critical layer of 100 microns is suitable.

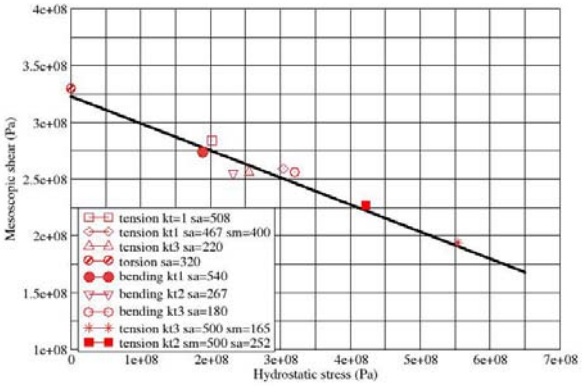

Figure 3: Fatigue limit of notched specimens tested with a critical layer (VER) of 100 microns

6.2 Fatigue strength of crankshaft

In this example, it is shown that the proposed fatigue modelling permits comprehensive design to prevent the occurrence of fatigue failure on an automotive engine component, the crankshaft. Crankshafts are designed for «infinite» life and the validation procedures use full load bench tests during hundreds of hours. This component is made of nodular cast iron or forged steel. The critical areas, filets between bearing and flanges, are reinforced by pressure rolling or thermal treatment such as induction quenching or nitriding.

For the fatigue assessment of a component with local reinforcements, a comprehensive approach is necessary. In the case of pressure rolled crankshaft, this means:

- simulation of the pressure rolling operation to calculate the local plastic stress and strain, *i.e.* the initial residual stress field.
- simulation of the residual stress evolution to a steady state under the service loading
- a fatigue strength calculation taking into account this history.

An example is given for a forged steel crankshaft, with a bearing diameter of 50 mm, and a filet radius of 1.35 mm and of depth 0.5 mm. The pressure rolling is performed with a roller 1.35 mm in radius, and an applied force of 9000 N.

Simulation of pressure rolling: Pressure rolling is modelled with a direct stationary method [11]. The main feature of the method is that the analysis of the rolling is performed in a (r, θ, z) axis system tied to the moving load applied by the roller. In steady stage regime, and for a constant angular rate ω of the roller, the physical values no longer depend on time but on their angular position in the direction of rolling.

After the first iteration, the mechanical fields are reinitialized upstream of the load, and this double loop (projection - initialisation) is repeated until the yield criterion is satisfied and the stationarity condition [ε^p (upstream, z) = ε^p (down stream, z)] is met. This method directly yields the stabilized mechanical state after repeated rolling. This procedure is preferred to the usual finite element method, with incremental translation of the load, which requires large computer memory and very lengthy calculations.

In the present case, the residual stresses are calculated. High values of residual stresses are induced by this mechanical treatment, about –400 MPa in the three directions on 1.5 mm depth. This is the consequence of the high contact pressure, which generates a strong triaxial loading, with a high hydrostatic pressure, and a relatively minor deviatoric effect.

The calculated values are in a reasonable agreement with X-Ray measurements of the residual stresses, at the surface.

Relaxation of residual stresses: The state of the residual stress after the rolling operation will evolve under the effect of the service loading. To reach this new state, one must find the elastically shakedown state which gives a stabilized residual stress field. This calculation can be done, using the simplified method of inelastic analysis of structures proposed by Zarka [12]. In our case, if we consider the service loading to be a simple alternated bending moment corresponding to the fatigue limit level, we observe only a limited relaxation of the residual stresses.

Fatigue strength under service loading: One usually considers that fatigue improvement by pressure rolling of forged steel can be essentially attributed to residual stresses. Therefore the fatigue assessment of the component is done with the Dang Van approach, using the fatigue data of the material without treatment. The pressure rolling and service history through the stabilized residual stress field is taken into account in the loading path.

The efficiency of the approach is illustrated in figure 4, which shows the load path at the critical point for the fatigue limit level found experimentally under alternate bending. The material data necessary for those calculations are E and ν, a kinematics hardening law derived from a cyclic strain curve and two fatigue limits for the Dang Van diagram.

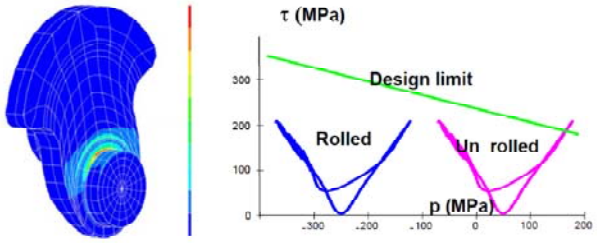

Figure 4: Loading path at the critical locus of the crankshaft.

6.3- High Cycle Fatigue assessment of welded structures: a structural approach

The third example is devoted to present a new way to check the high fatigue resistance of welded structures which find its roots in the proposed fatigue modelling .

Current practice in welded structure design is based on the use S-N curves, hot spot principal stress or structural principal stress limited to specific geometries. However, they are difficult to handle on complex shape components and for multiaxial loadings, which is the

case in most of industrial structures. To overcome this difficulty, we come back to the structural approach with a clear definition of the design stress that can be transposed to multiaxial structural problems.
The classical introduction of the design stress is based on the extrapolation of far field stresses with unclear rules. In order to clarify the description of this design stress we propose an approach deriving from an analogy with the concepts, which are at the origin of the Fracture Mechanics. Actually, it is known that the mechanical state in the highly damaged crack tip zone, called by H.D. Bui [13, 14] the process zone, is inaccessible by the usual continuum solid mechanics. In this zone, the material is neither really continuous nor homogeneous and the local strains are not small. Nevertheless, the stress solution obtained from linear homogeneous and isotropic elasticity in small strains allows the correct description of the mechanical state outside of the process zone. Although it is erroneous at the vicinity of the crack tip, it makes sense in terms of an asymptotic solution that allows the correct control and the interpretation of the phenomena produced in the process zone. Likewise, we will look for a way to build the asymptotic solution that allows the correct control and interpretation of the phenomena produced in the critical zone of the weld. For that purpose we adopt an approach with meshing rules taking into account the local rigidity due to the weld instead of the local geometry of the weld itself (as it is the case in Fracture Mechanics, where the actual geometry of the crack tip is not taken into account) that is a very hazardous data. Therefore, the fatigue design can be based on a structural stress calculation from a finite element shell analysis.

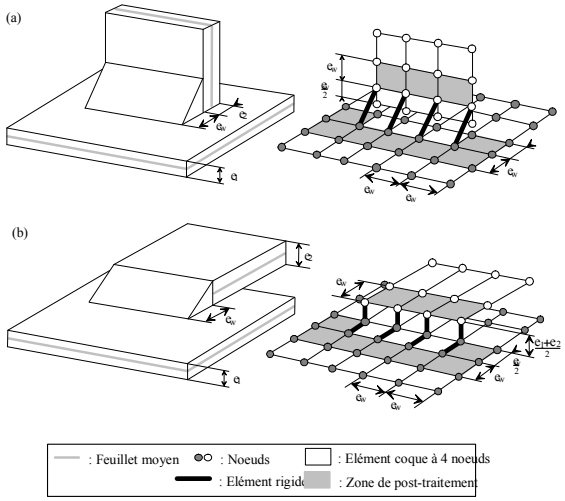

Figure 5. Thin shell modelling (a) for fillet weld; (b) for overlap welded joint.

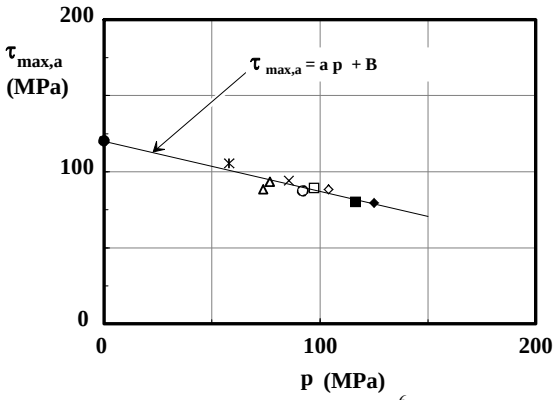

Figure 6. Mean fatigue strength at 10^6 cycles [15].

On this basis design rules were established for welded structures [15] with a structural stress, the asymptotic solution, which gives access to the fatigue strength through a unique S-N line where S is a local equivalent stress defined from τ and p at the Hot Spot : $\tau_0=\tau$-ap, as described hereafter.
This implies the notion of elastic shakedown at all scales, the shakedown at the mesoscopic scale, in the sense of Dang Van criterion can exist only if the elastic shakedown occurs at the structural scale.
From a large data base the Dang Van criterion for welded steel structure is:

$\tau_a = a\ p + b$, as shown in Figure 6.

Figure 7 summarizes the application of the local approach to predict thefatigue resistance of an engine sub-frame made of a metal sheets joined by continuous welds submitted to out of phase multiaxial loading. For an easier interpretation by the design office, the calculated value of the criterion displayed graphically is the quantity $Cd = (\tau_a - (a\ p + b))/\tau_a$. The failure happens at the predicted locus and fatigue strength can be evaluated.

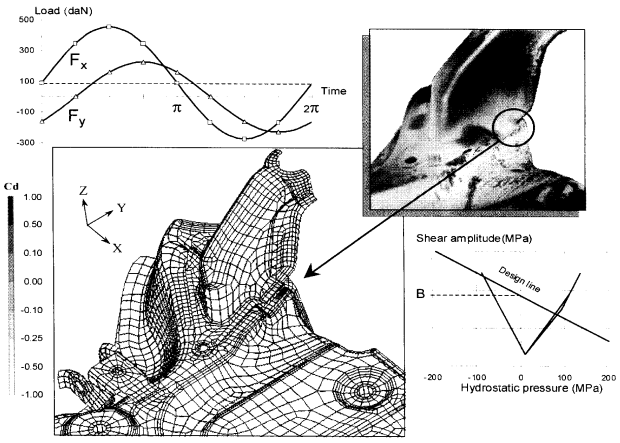

Figure 7. Application to engine sub-frame undergoing multiaxial out of phase loading (Courtesy of PSA Peugeot Citroën)

7 THERMO MECHANICAL LOW CYCLE FATIGUE APPLICATION

The difficulty of the thermo mechanical damage simulation comes from the complex steps of the analysis. The modelling of the limit conditions, the choice of the constitutive equations of the material, the numerical strategy, the damage driving force identification and finally the fatigue criterion condition the success of such simulations.
Based on these observations, to be appropriate to the industrial context, thermo mechanical modelling should respect several constraints:
- the necessity to represent the behavior of the material in the structure by simple constitutive equations. Thus, one should favor the representation of the mechanical behavior without coupling with damage. From experience most of the time this coupling is not necessary and does not improve the accuracy of the prediction on structure. Usually it is not necessary to describe the evolution of the structure cycle by cycle and particularly the early stage of the life of the structure. Therefore the identification of the parameters of the constitutive equations can be done on the steady state cycles obtained from material testing.
- the implementation in a finite element code using a numerical integration algorithm for the constitutive law stable and robust enough to authorize large integration steps. Reasonable hypothesis should be introduced in the analysis: the thermal analysis is independent of the mechanical behaviour, the mechanical analysis is not coupled with damage, and the fatigue analysis is based on a stabilised cyclic behaviour of the structure. Thus the objective of the thermo mechanical calculations is to obtain this stabilised fatigue cycle.
A cast iron exhaust manifold of a diesel engine, computed by PSA Peugeot Citroën, illustrates our proposal. Cylinder heads are also calculated by this approach.
The fatigue assessment and the validation are made on a standard durability cycle with a classical engine testing device. The equivalent damage history consists in a succession of full load at 4000 rpm and light load at the same regime. The transient period from full to light load and light to full load takes 30 s and the total cycle takes approximately 700 s. The external surface of manifold is monitored by regular visual inspection to detect crack apparition.
The aim of the thermal computations is the prediction of the temperature field distribution on the manifold from engine data, exhaust gas temperature and mass flow rate, which can already be estimated in the early phases of the project. The thermal computation is performed in two steps. A steady state temperature field distribution is first determined and afterwards the transient response is computed under some assumptions concerning the evolution of the boundary conditions and the evolution of thermal exchange coefficients.
In order to perform mechanical analysis, the constitutive law to characterise the material from ambient to 800°C is needed. At 20°C it presents elastoplastic behaviour, above 700 °C an almost purely viscous one. The fact that one has to deal with a simple unifying law over the whole temperature range is dictated both by the F.E. transient analysis and the short development time constraint. This conducts to the choice of an elasto viscoplastic (EVP) material model. A reasonably representative model of the high temperature EVP behaviour of the material is achieved with a visco elastoplastic constitutive law with six temperature depending coefficients. An important point is to take care of the representativeness of the characterisation tests in the sense of aging and stabilisation of the behaviour corresponding to long-term service conditions.

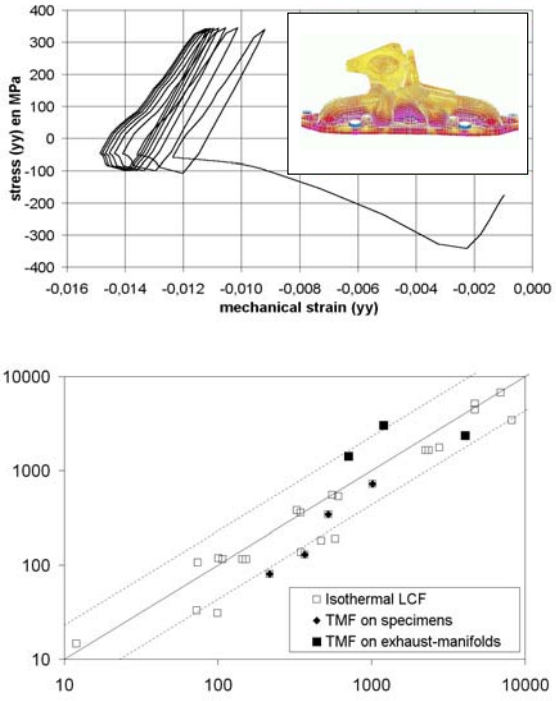

Figure 8: Thermo mechanical calculation and stabilization and predicted life versus experimental fatigue life on tested specimens and on exhaust manifolds.

The FE analysis has been performed in two steps: first the manifold has been screwed on the cylinder head and second a series of thermal cycles have been computed. The imposed temperature distribution was a result of the previous transient thermal calculations. The number of cycles is chosen in order to obtain a stable cycle for the mechanical fields. The results has been analysed in term of dissipated energy per cycle, as indicated in Figure 8.
The final objective is to evaluate the fatigue strength, or the lifetime of the structure, from the stabilised response of this structure. Charkaluk and Constantinescu [16] observe that the dissipated energy per cycle at steady state

$$W = \int_{cycle} \sigma : \dot{\varepsilon}^{p} \, dt$$

can be representative of the fatigue behavior of a material.
The interest of the dissipated energy per cycle comes from three main points:

- this energetic quantity can be easily generalized to multiaxial situation
- its determination is dependant of the temperature because it integrates the whole loading path and therefore allows calculations with anisothermal loading.
- W_S is representative of the cyclic behavior of materials.

The fatigue criterion can be simply expressed by a relationship:

$$W = c\, N^{\beta}$$

The predictivity of the calculation is satisfactory as indicated by numerous comparative results between experiments and calculation on figure 3.
To take into account the fact that the dissipated energy is based only on the deviatoric part of the stress tensor, it is proposed to introduce the instantaneous hydrostatic pressure in the criterion in order to improve the predictivity of the previous relation when high triaxiality is present [17, 18]

$$(W + \alpha\, p_{maxs}) = c\, N^{\beta}.$$

8 CONCLUSIONS

From theoretical point of view, fundamental questions have still not been answered satisfactorily: what is the difference between monotonic loading rupture and fatigue and why cycling is necessary to obtain fatigue failure. Although many progresses has been done in understanding of physical phenomena, many difficulties still exist to achieve an interdisciplinary consensus in the way to model fatigue crack initiation. Depending on the discipline, points of view are often different. An engineering mechanical approach is presented. In this proposal, fatigue is induced by build up of plastic deformations due to cycling, in a heterogeneous way in the high cycle regime, and in a more homogeneous way in low cycle fatigue. The fatigue resistance in this modelling, corresponds to the limit of the possibility of the material with which the structure is made of to shakedown. This hypothesis implies that the total acceptable plastic work is bounded and consequently the build up of plastic strain and residual stress must be beyond some limit state. Residual stresses correspond to store energy, so that the admissible store energy is bounded too. Thus the shakedown theory gives a general framework to the fatigue analysis, as well as for low cycle fatigue than for high cycle fatigue. Many applications to industrial structures submitted to complex multiaxial loadings are already successfully done, particularly in the automotive industry. The adaptability of this approach should be highlighted, whatever the situation , thermo mechanical loading, contact, residual stresses effect, assemblies … a common view is adopted, the fatigue criterion is easy to handle in an industrial context and does not need many informations. As far as the HCF criterion takes into account the multiaxiality of the stress tensor, no adjustable parameters nor corrective coefficients are necessary whatever the situation including contact problems. For LCF criterion the energy description of the damaging parameter allows to solve any problem including the difficult one of visco plasticity behaviour under anisothermal transient loading.

REFERENCES

[1] H.D.Bui, K. Dang Van,C. Stolz, Relations entre grandeurs microscopiques et macroscopiques, C.R.A.S., Tome 292, Série 2, 1981, pp.1155-1158

[2] Koiter,W.T. (1960), General Theorems for Elastic-Plastic Solids, In Progress in Solid Mechanics, eds. Sneddon, J.N. and Hill, R., 1, North-Holland, Amsterdam, pp. 165-221

[3] Melan, E. (1938), Zur Plastizität des räumlichen Kontinuums, Ing. Arch., 9, 116.

[4] Nguyen, Q. S., (2000), Stability and Nonlinear Solid Mechanics, J. Wiley & Sons

[5] Mandel J., Halphen B., Zarka, J.(1977), Adaptation d'une structure Elastoplastique à Ecrouissage Cinématique, Mech. Res. Comm.,(4), p. 309-314.

[6] Rice J.R., Tracey, D.M., 1969, On the ductile Enlargement of Voids in Triaxial Stress Fields JMPS, Vol.17, pp.201-217.

[7] Gurson, A.L., 1977, Continum Theory of Ductile Rupture by Void Nucleation and Growth: Part I-Yield Criteria and Flow Rules for Porous Ductile Media, ASME J. of Engineering Materials and Technology, Vol 99, pp. 2-15.

[8] Dang Van, K., Fatigue Analysis by the Multiscale Approach, High Cycle Metal Fatigue, From Theory to Applications, C.I.S.M. Courses and Lectures N° 392, Ed. Ky Dang Van & Ioannis V. Papadopoulos, Springer 1999 pp.57-88,

[9] Dang Van, K., Maitournam, H.M., Rolling contact in railways: modelling, simulation and damage prediction, Fatigue Fract. Engng. Mater. Struct., Vol. 26, 2003, pp. 939-948.

[10] Maitournam H.M., Dang Van K., Flavenot J.F., Fatigue design of notched components with stress gradients and cyclic plasticity, 12th International Spring Meeting, Paris, May 20-22, 2008, JIP 2008

[11] K. Dang Van, M.H. Maitournam, Steady-State Flow in Classical Elastoplasticity: Application to Rolling and SlidingContact, J. Mech.Phys.Solids, 41, 11, 1993, 1691-1710.

[12] J. Zarka, Direct analysis of elastic-plastic structures with overlay materials during cyclic loading, Int.J. Meth. In Eng., Vol.15, p.225.

[13] Bui, H.D. Problèmes généraux de croissance de fissure. Partie I, approche de l'endommagement.

Revue française de Mécanique, Vol. 4, (1983), pp. 3-7

[14] Bui, H.D., Dang Van, K. Some recently developed aspects of Fracture Mechanics. Nuclear Engineering and Design, Vol. 105, (1987), pp. 3-12

[15] Fayard, J.L., Bignonnet, A., Dang Van, K., Fatigue Design Criterion for Welded Structures, Fatigue Fract. Engng. Mat.struct. 19 (1996), pp.723-729.

[16] E. Charkaluk and A. Constantinescu. Energetic approach in thermomechanical fatigue for silicon molybdenum cast-iron. Materials at High Temperatures, 17, (3), 2000, pp. 373-380.

[17] A. Constantinescu, K. Dang Van, H.M. Maitournam, A unified approach for high and low cycle fatigue based on shakedown concepts, Fat. Fract. Engng. Mat. Struct., 26, (2003) pp.1-8.

[18] S. Amiable, A. Constantinescu, S. Chapuliot, A. Fissolo. Prédiction de durée de vie des structures sous chargement de fatigue thermique. 17ème congrès de Mécanique, Troyes sept. 2005

FRACTURE MECHANICS APPLICATIONS FOR SPACE STRUCTURES WITHIN ESA PROGRAMS

M.Windisch

MT Aerospace AG
Franz Josef Strauß Str. 5, 86153 Augsburg
E-Mail: Michael.Windisch@mt-aerospace.de

ABSTRACT

This paper gives a short overview about the current practie of fracture mechanics methods for critical space structures as for example pressure vessels and propellant tanks. The currently applied fracture control procedures are more or less linked to the basic principles evaluated within past US space programs and reference is given to these. Special emphasis is given to non-linera fracture mechanics methods, which are applied at MT Aerospce since 20 years within European space programs as ARIANE 5 and ATV.

KEY WORDS: fracture mechanics, space applications, ESACRACK, ARIANE 5, ATV, SINTAP, damage mechanics.

1. INTRODUCTION

The development of fracture mechanics concepts and applications were strongly linked to aerospace development starting already with the Apollo program. The basic principles were first evaluated on the basis of LEFM at those days and have been continously improved up today, where non-linear methods are applied for high loaded structures where small scale yielding conditions are violated.

These improved methods as for example 3D crack simulation (j-integral) and damage mechanics material modelling allow the fracture analysis, where in the past structural tests had to be performed with large effort. In addition these methods have supported the analysis and understanding of bi-axiality and constraint effects. These effects explain the differences between the fracture behaviour of laboratory specimens and full scale structures.

2. FRACTURE MECHANICS HISTORY IN SPACE APPLICATIONS

First fundamental fracture control concepts have been evaluated which were later further specified for the space shuttle program [1,2,3,4]. These concepts include not only static fracture prediction but all aspects of the interdisciplinary nature of failure prediction as for example

- static loading (crack initiation and instability)
- cyclic loading (crack growth prediction)
- sustained loading (stress corrosion cracking and hydrogen embrittlement)
- material selection aspects

The further development of these concepts was related to a number of failure cases, which revealed the necessity of improved methods especially with the manned space programs, where failure always is linked with the loss of human life.

3. FRACTURE CONTROL

Although different space programs show slightly different approaches in fracture control principles, the main methodology is comparable. The different space programs apply own fracture control requirements. The latest ESA requirements applicable for ESA payloads and satellites can be found in [5]. The following different fracture control approaches mainly apply according to the following definitions:

Safe life: It must be demonstrated, that a crack does not become critical after application of 4 times the dimension life spectrum and always applies to single load path structures. A crack growth analysis is required.

Fail safe: Fail safe applies to multiple load path structures, where it can be demonstrated, that the loss of one load path does not lead to the failure of the remaining load paths. Limit load capability and a fatigue analysis of the remaining load paths after load redistribution is required.

Contained: A specific requirement mainly coming from the space shuttle program requires, that all potential structure elements with mass larger than g, which might be released by fatigue etc. must be contained to protect the environment from a possible impact.

LBB: For pressure vessels with non hazardous media it may be sufficient in specific cases, that a growth of an initial surface crack up to penetration will not lead to the burst of the tank but to the release of pressure by leak only.

4. GENERAL REQUIREMENTS

The damage tolerance assesment is strongly linked to the general requirements and safety factors. The yield

and ultimate load safety factors for pressurized structures are defined for structural tanks as the booster cases and the large main and upper stae cryogenic tanks and for small and high pressurant tanks as follows.

Table 1: Safety Factors

Structure	Yield	Ultimate
Structural Tanks	1.10	1.25
Propellant and High Pressurant Tanks	1.25	1.50

The minimum required burst pressure = ultimate factor x operational pressure. The same procedure applies for proof testing applying the yield safety factor. The highly mass optimized tank structures therefore at hot spots show stresses close to yield stress during proof testing and close to ultimate stress at ultimate load conditions.

The material allowables, used for the assessment, are statistical evaluated minimum properties (A-values). In the case of fracture toughess, where either large scatter is observed or only limitd tests have been performed, a knock down factor of 70% is applied on mean values, as statistics are not applicable.

A further important requirement applies for defects, which are observed during the series production. These, in most programs, have to be demonstrated against ultimate load condition.

Therefore the following two limiting cases occur in spacecraft damage tolerance assessment:

1. At hot spots local yielding may occur during proof testing. Therefore the required NDI detection limit has to be evaluated with non-linear prediction methods.
2. If a possible defects is observed (pore line in welds, inclusion in large forgings etc.), which is recharacterized as a crack, and treated with fracture mechanics, stresses for ultimate load conditions (beyond yield stress limit) have to be applied for the justification again requiring non-linear methods.

4. CURRENT PRACTICE IN EUROPEAN SPACE PROGRAMS

The application of fracture mechanics in the past US programs was limited to LEFM conditions. In those cases where the applicability of LEFM was violated, assessment was made by testing. Autofrettage of composite overwrapped pressure vessels (COPV) is a typical example. During Autofrettage large plasticity occurs and failure prediction based on LEFM does not apply.

The development of the ARIANE 5 launcher and the ATV (Automated Transfer Vehicle) spacecraft was initiated with high challenges in mass saving. The result of these goals show highly optimized structures with stresses during operational conditions close to or even at yield stress level. LEFM is applied for all low loaded structures and structural parts. ESACRACK with the module NASGRO from the US space program is applied as standard software for those parts.

Apart these, non-linear methods as R6, SINTAP, FITNET are applied [6,7,8] or even damage mechanics simulations have been used to analyze complex structural conditions [9,10,11,12]. Some examples are given in the next sections.

4.1. ARIANE 5 Booster Case Weld Interface

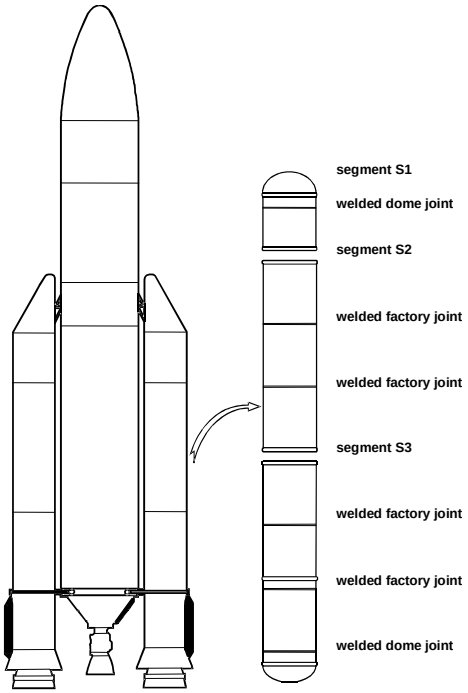

Figure 1: Schematic Illustration of ARIANE 5 Inter-Segment Connections replaced by Welds

The ARIANE 5 booster cases are made from the high strength low alloy steel 48 CrMoNiV 4 10 (D6AC) with martensitic microstructure. The relatively high carbon content (0.45 - 0.5 %) leads to high strength. The generic version consists of 8 shear bolt cnnections, which connect the 7 cylinders and two domes. The Figure 1 shows thos connections, which now have been replaced by EB welds. The EB welding is applied by one nominal weld and two cosmetic passes at the inner and outer surface, resulting in complex microstructural zones as indicated in Figure 2 and Table 2.

These different zones have all be characterized by tensile and fracture toughness tests to identify the most critical zone. In those cases, where the material zone is too small for specimen manufacturing, the material was produced by simulation of the relevant temperature vs. time cycles with a Gleeble 2000 machine

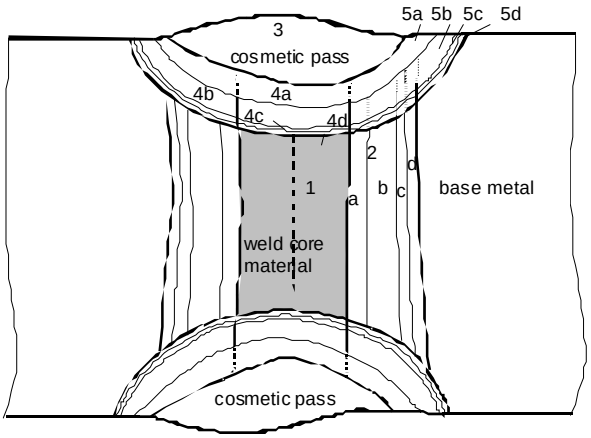

Figure 2: Definition of Microstructural Zones

Table 2: Defintion of Microstructural Zones

1	Core Weld Metal (CWM), width ≈ 3.2 mm
2	HAZ caused by the core weld: 2a = Coarse-Grained HAZ (CGHAZ), width ≈ 0.5 mm 2b = Fine-Grained HAZ (FGHAZ), width ≈ 1.65 mm 2c = Inter-critically reheated HAZ (ICHAZ), width ≈ 0.25 mm 2d = Sub-critically reheated HAZ (SCHAZ), width ≈ 0.25 mm
3	Cosmetic Pass Weld Metal (CPWM)
4	Reheated Core Weld Metal (RCWM): 4a = completely transformed CWM with austenite grain growth Globular CWM (GCWM), width ≈ 0.5 mm 4b = completely transformed CWM without austenite grain growth 4c = partially transformed (inter-critically reheated) CWM 4d = (high) Tempered CWM (TCWM), width ≈ 0.15 mm
5	HAZ caused by the cosmetic pass: 5a,b,c,d (equivalent. to 2a,b,c,d)

The before mentioned high carbon content is also responsible for brittle zones in the weld microstructure. The cleavage fracture modelling was performed on basis of the RKR model [13].

First the critical fracture stress was evaluated with the numerical simulation of notched round tensile tests as shown in Figure 3 and Figure 4. In the next step fracture toughness tests with SE(B) specimens were simulated to determine the critical distance x_c as shown in Figure 5. These two parameters are necessary for the RKR damage model. The advantage of the model is already demonstrated in Figure 5. The two specimens with different a/W ratio give different fracture toughness values but can both well be predicted with the RKR model. The well known geometry influence of fracture toughness testing is avoided with the RKR model.

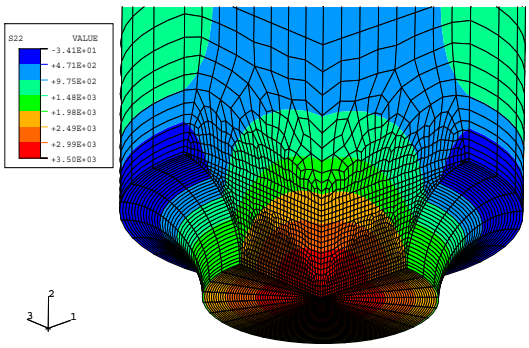

Figure 3: Axial stress in notched tensile specimen

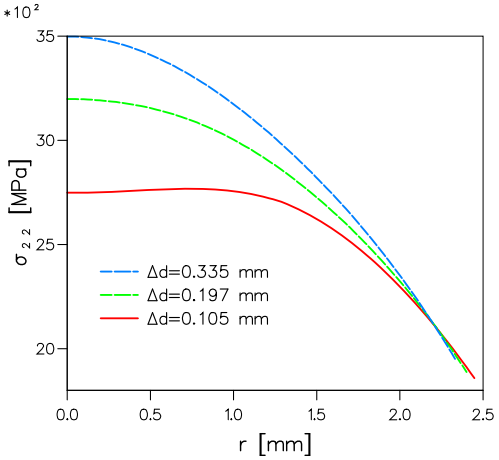

Figure 4: Axial stress distribution in the notched tensile specimen for three displacements at and below fracture

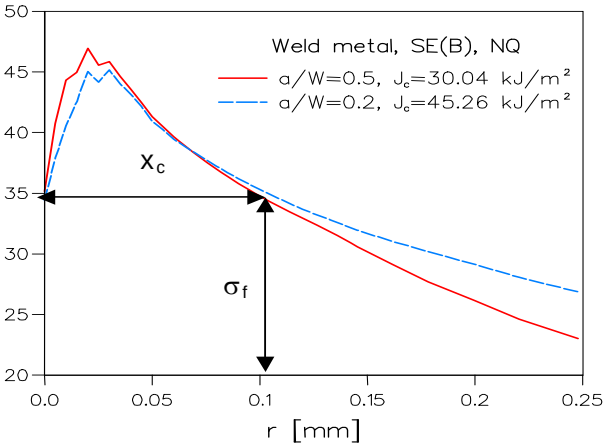

Figure 5: Evaluation of the Critical Distance x_c by the Numerical Simulation of SE(B) Specimens

Once the RKR model was qualified by the described procedure, any further specimen test or the final structural configuration could be investigated as shown in Figure 6 for SCT specimens.

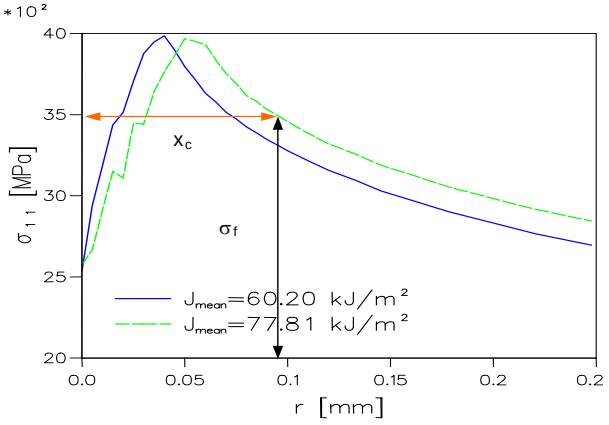

Figure 6: Stress Distribution at the Crack Tip for SCT Specimens

In addition to the local approach (RKR model), a two parameter fracture mechanics concept was applied to ductile material zones. A relation between the constraint

of different specimen or component geometries and the critical J-integral can be evaluated as shown in Figure 7.

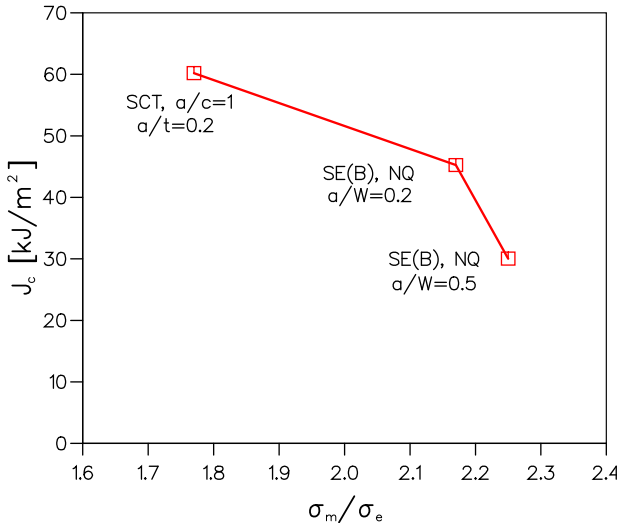

Figure 7: J-integral at failure for different specimens as a function of constraint

These two fracture prediction approaches then have been successfully applied to the sub-scale pressure vessel testing. Burst tests have been performed with several vessels (Figure 8) with surface and embedded cracks resulting from non-optimized welding at this stage of the program (Figure 9).

Figure 8: Sub-Scale Pressure Vessel after Burst Test

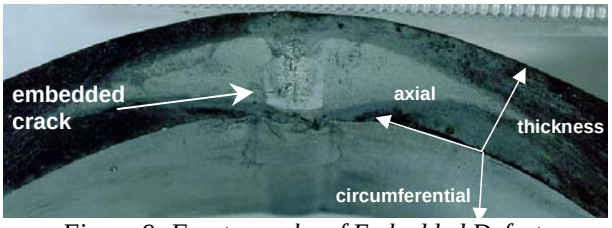

Figure 9: Fractography of Embedded Defect

The crack profiles were extended over different material zones and therefore both concepts (RKR and j-integral) were applied. The good agreement with the test results is shown in Table 3. In the case of the embedded deefect the larger difference between prediction and test results is explained by the complex geometry of the crack which was not completely modelled in the FE mesh.

Table 3: Experimental and Numerical Results of Burst Test Analysis

	Pressure at Burst	**Numerical Prediction**	
		J_c Concept	**RKR Model**
Vessel 1 *	93 MPa	81 MPa	78 MPa
Vessel 2 #	100 MPa	90 MPa	95 MPa
* embedded defect, # surface defect			

4.2 Ductile Fracture Simulation in AA 2219 Material at Cryogenc Conditions

The large cryogenic hydrogen and oxigen tanks of the ARIANE 5 main stage and upper stage are made of AA2219 aluminum alloy. The alloy shows high ductile fracture behaviour and failure prediction was performed with the Gurson damage model [14] for different material conditions, including welds. The Figure 10 shows the numerical simulation of a SE(B) specimen test results. The prediction of the void volume fraction allows the accurate prediction of crack initiation.

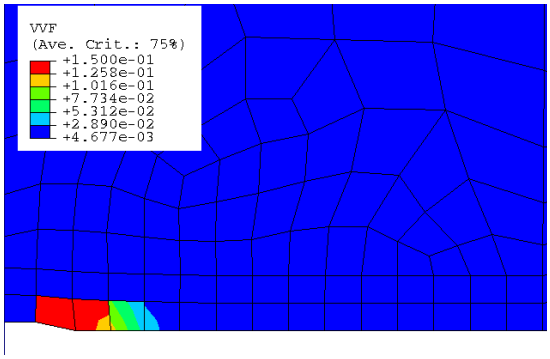

Figure 10: Numerical Simulation of the Void Volume Fraction in the SE(B) Specimen

The Figure 11 shows the good agreement between the numerical simulation and the test results.

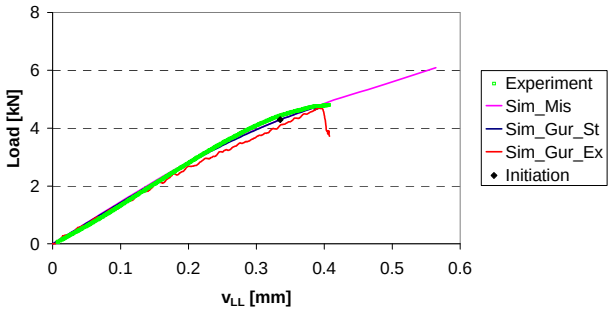

Figure 11: Load Displacement Behaviour of the SE(B) Specimen at -196 °C

Based on these results and large experience gained with the material and damage modeling, the fracture toughness of different crack configurations could be predicted as shown in Figure 12. The fracture toughness is shown versus triaxiality (mean normal stress / von Mises stress) for different surface crack configurations and the SE(B) specimen, thus identifying the conservatism of the standard specimen and further potential for structural assessment.

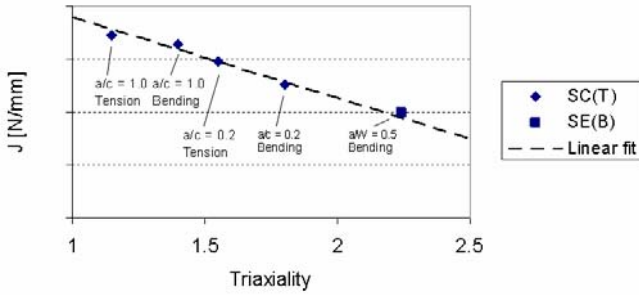

Figure 12: Relation between critical fracture toughness and stress triaxiality for the AA2219 Forging material at -196°C

4.3 Crack Initiation in AA2219 TIG Welds at Local Imperfections

The Gurson damage modelling has been further applied for the crack initiation at the fusion line of AA2219 TIG welds. The test result is shown in Figure 13, the numertrical simulation in Figure 14.

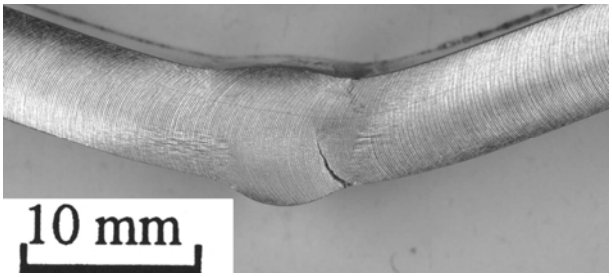

Figure 13: Bending Test of AA 2219 TIG Weld

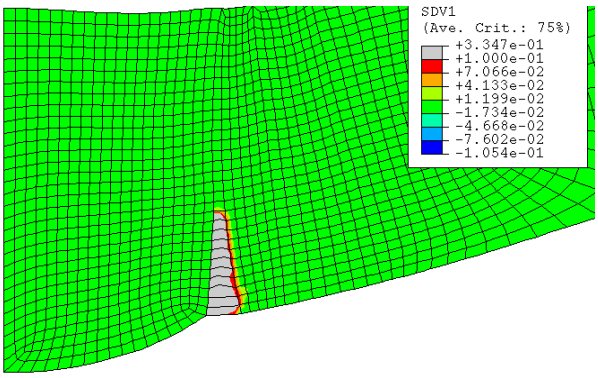

Figure 14: Damage Zone at the Fusion Line During Global Load Drop (Void Volume Fraction)

This kind of simulation allows the accurate prediction of local imperfections of TIG welds, where the assessment of local stress hot spots either by the application of notch factors or standard stress based FE analysis would give over-conservative results.

4.3 COPV BEHAVIOUR DURING AUTOFRETTAGE

High pressure vessels for spacecraft applications are in most cases made of metallic liners (titanium, INCONEL, stainless steels, aluminum) with composite overwrap. Autofrettage is performed to plastify the liner and result in compression stresses after unloading. The liner therefore shows high plastic strain and failure prediction has to be performed with non-linear methods.

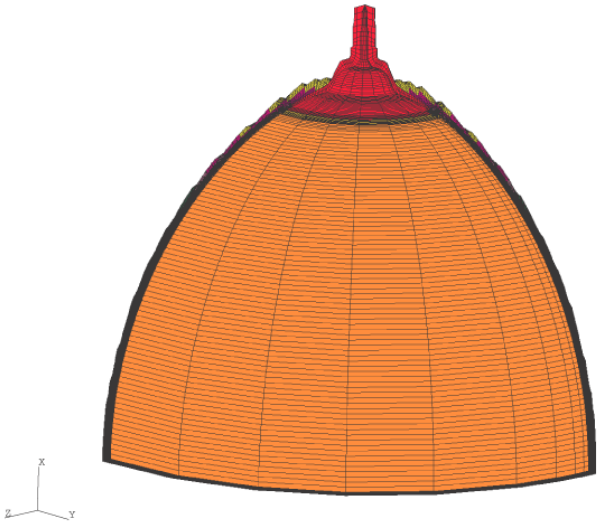

Figure 15:_ FE Mesh of theCOPV

Figure 16 shows details of the FE mesh of a COPV where a surface crack was investigated at the polar weld. Local weld imperfections were observed resulting in high local plasticity.

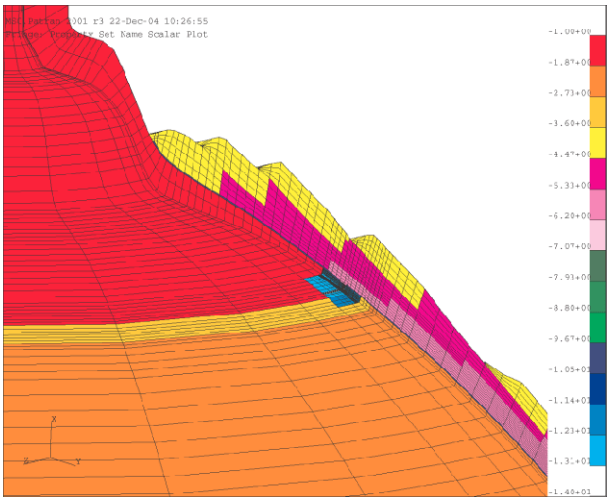

Figure 16: FE Mesh of the COPV with local Surface Crack

In this case even the application of non-linear based methods as SINTAP failed, as the analytical equations apply only for pure metallic crack cases. The COPV

however is shielded by the composite overwrap leading to displacement control even at plastified hot spots. This is demonstrated in Figure 17, where the j-integral prediction is shown versus pressure. The j-integral pressure relation remains linear over the complete pressure range although plastic strain up to 5 % appears. In a second step again Gurson simulation showed that no crack initiation occurred for a crack size, which is close to the inspection limits of the NDI.

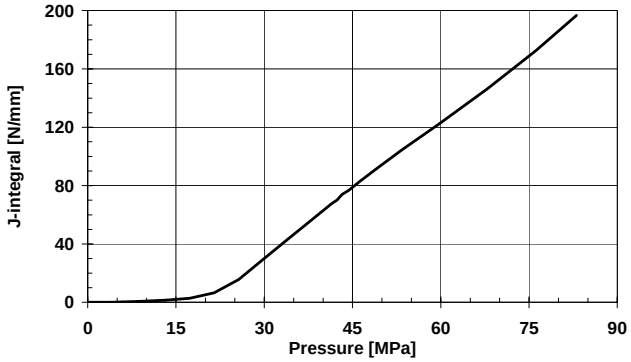

Figure 17: J-integral Dependence from COPV Inner Pressure

6. SUMMARY

The presented examples show the high potential of modern fracture mechanics methods based on damage mechanics modelling. Many phenomena as geometry dependence of fracture behaviour can now be explained and even quantified with those methods. It must however be pointed out that large experience is needed as these methods are highly sensitive both in parameter evaluation and numerical modelling. The here presented simulations have all been performed at FH-IWM Freiburg and I want especially thank D.Siegele, I.Varfolomeyev, D.Memhard, D.Sun and many others for their support.

Analytical prediction methods have not been referenced in this paper but may be found with detailed description and comparison with test results in [9,11].

5. REFERFENCES

NASA documents can be found at http://ntrs.nasa.gov/, ECSS standards can de downloaded from http://www.ecss.nl/.

[1] NASA-SP-8040
Fracture Control of Metallic Pressure Vessels

[2] NASA-CR-3957:
A Review of Fracture Mechanics Life Technology

[3] NASA 731-0005-83:
General Fracture Control Plan for Payloads using the Space Transportation System

[4] NASA-CR-4628:
Significant Issues in Proof Testing: A Critical Appraisal

[5] ECSS-E-ST-32-01C:
Space Engineering: Fracture Control

[6] Koçak et. al. (editors) 'FITNET Fitness-for-Service (FFS) – Procedure (Volume I) & Annex (Volume II)' Revision Mk8, January 2008,

[7] IWM-VERB, Version 8.0, Fraunhofer-Institut für Werkstoffmechanik, 2008

[8] Berger, C., J.G.Blauel, B.Pyttel and L.Hodulak, 'FKM Guideline – Fracture Mechanics Proof of Strength for Engineering Components', 2nd revised edition, 2004, VDMA Verlag GmbH, ISBN 3-8163-0496-6

[9] Windisch, M., Eisenmann, A., Albinger, J., Varfolomeyev, I., Memhard, D. Siegele,D.: Application of Analytical (SINTAP) and Damage Mechanics Based Numerical Simulation for the Assessment of (Plastically) Hot Spots in the ARIANE 5 Main Stage Tank Bulkheads, European Conference on Spacecraft Structures, Materials & Mechanical Testing 2005, Noordwijk, ESA SP-581

[10] Windisch, M., Clormann, U., Grunmach, G., Burget, W. ,Sun, D-Z.: Damage Tolerance Verification Concept of the Ariane 5 Booster Welding Interface, European Conference on Spacecraft Structures, Materials and Mechanical Testing, 2000 Noordwijk, ESASP-468, 2001., p.499

[11] Varfolomeyev, I., Hodulak, L., Siegele, D., Windisch, M.: Validation of the FITNET Analysis Procedure for the Assessment of ARIANE 5 Thin-Walled Components, Proceedings of FITNET 2006, International Conference on Fitness-for-Service, 17-19 May 2006, Amsterdam, The Netherlands

[12] Windisch, M., Sun, D-Z., Memhard, D., Siegele, D.: Defect Tolerance Assessment of ARIANE 5 Structures on the Basis of Damage Mechanics Material Modelling, Engineering Fracture Mechanics (2008)

[13] Ritchie, R.O., Knott, J.F., Rice, J.R., On the relationship between critical tensile stress and fracture toughness in mild steel, J. Mech. Phys. Solids, 21,1973, 395-410

[14] Gurson, A.L., Continuum Theory of Ductile Rupture by Void Nucleation and Growth: Part I – Yield Criteria and Flow Rules for Porous Ductile Media, J. Eng. Mater. Technology 99 (1977), 2-15

ELASTIN ANISOTROPY IN VASCULAR STRAIN ENERGY FUNCTIONS

R. Rezakhaniha[1], E. Fonck[1], C. Genoud[2], N. Stergiopulos[1]

[1] Interfaculty Institute of Bioengeering,
Ecole Polytechnique Federale de Lausanne,
Station 15, 1015 Lausanne, Switzerland
E-mail: nikolaos.stergiopulos@epfl.ch

[2] Friedrich Miescher Institute for Biomedical Research,
Basel, Switzerland

ABSTRACT

Vascular wall shows nonlinear anisotropic mechanical properties. The identification of a strain energy function (SEF) is the preferred method to describe its complex nonlinear elastic properties. None of the currently proposed constituent-based models succeeded in describing accurately results of multi-dimensional mechanical tests. We hypothesized that shortcomings of current models are partly due to unaccounted anisotropic properties of elastin. We performed inflation-extension tests on common carotid of rabbits before and after enzymatic degradation of elastin and applied constituent-based SEFs, with an isotropic and an anisotropic elastin part, on the experimental data. We used transmission electron microscopy (TEM) and serial block-face scanning electron microscopy (SBFSEM) to examine the arterial elastin structure. Our results show that constituent-based models with an anisotropic elastin part, characterize more accurately arterial biomechanics than models with an isotropic elastin. Furthermore, there is structural evidence behind the elastin anisotropy in arteries based on electron microscopy techniques.

KEY WORDS: elastin, anisotropy, rabbit, structural strain energy functions, electron microscopy.

1. INTRODUCTION

The vessel wall exhibits relatively strong nonlinear properties and undergoes wide range of deformations. These characteristics make the identification of a strain energy function (SEF), the preferred method to describe the complex nonlinear elastic properties of the vascular tissue. None of the currently proposed structural models succeeded in describing accurately and simultaneously both the pressure-radius (P-r_o) and pressure-longitudinal force (P-F_z) curves. We hypothesized that the shortcomings of current models are partly due to unaccounted anisotropic properties of elastin.

2. METHODS

2.1. Experimental Setup

A set of experimental data was obtained from inflation-extension tests on two groups of carotid arteries of rabbits in the totally passive state: a control group and an elastase treated group, as described by Fonck et al. [1]. This data (pressure-diameter, longitudinal force-pressure and zero-stress-state geometry) provided for a complete biaxial mechanical characterization of rabbit carotid artery in the presence and absence of elastin. The data was served as the basis for validating the applicability of the new biomechanical model of the vascular wall.

2.2. Transmission Electron Microscopy (TEM)

In order to look at the ultra-structure of the arterial elastin, an intact artery has been fixed at its in vivo longitudinal stretch (λ_z=1.4) and its mean physiological pressure (70 mmHg). The artery has been prepared for TEM and stained with palladium to enhance the elastin contrast. Circumferential and longitudinal sections have been acquired to give more detailed information on the elastin structure.

2.3. Serial Block-faced Scanning Electron Microscopy (SBF-SEM)

We used the same blocks prepared for the TEM. Image stacks were obtained using Serial block-face scanning electron microscopy SBFSEM developed by Denk and Horstmann [2] (Denk and Horstmann 2004). Images were done on three different sites in media at the accelerating voltage of 3.5keV and in the low vacuum mode (0.35 Torr). The section thickness was 50 nm and the obtained images were 2048x2048 pixels with 8.9 nm per pixel.

2.4. Theoretical Considerations

Our proposed SEF is based on the Zulliger et al.'s model [3]. The Zulliger et al.'s model consists of an isotopic part accounting for elastin fibres ψ_{elast} and an anisotropic part representing collagen fibers ψ_{coll}:

$$\psi = f_{elast}\ \psi_{elast} + f_{coll}\ \psi_{coll} \quad (1)$$

where f_{elast} and f_{coll} are fractions of elastin and collagen in the tissue.
We introduce an anisotropic SEF for elastin by considering a family of fibers in the circumferential direction embedded in a neo-Hookean matrix:

$$\Psi_{elast} = c^{i}_{elast}\,(I_1 - 3) + c^{a}_{elast}\,(I_4^{"} + \frac{2}{\sqrt{I_4^{"}}} - 3) \quad (2)$$

Where

$$I_4^{"} = e_\theta . C . e_\theta = \lambda_\theta^2 \quad (3)$$

λ_f is the stretch in the main elastin fiber direction, C is the right Cauchy-Green deformation tensor and e_f indicate the unit vector in the direction of fibers .C^{i}_{elast} represents the modulus for the isotropic elastin component and C^{a}_{elast} is an elastic constant for the anisotropic part of elastin. To test the model, experimental P-r_o and P-F_z curves of both artery groups were fitted simultaneously and the quality of fit was assessed.

3. RESULTS

When only P-r_o curves are fitted, both the anisotropic and the isotropic models gave excellent results. However, the original Zulliger et al.'s model with an isotropic part was not able to fit well both the P-r_o and P-F_z experimental data based on control arteries simultaneously (Figure 1). Further, when we applied the original model on elastase treated arteries, considering only the collagen part of the original model and in the absence of elastin, we obtained a good fit on both P-r_o and P-F_z sets of data, suggesting that the collagen part of the SEF is well enough defined to account for the role of collagen fibers in the absence of elastin (Figure 2). Finally, when the anisotropic model was applied to the entire set of data (control and elastase-treated), we obtained a much better fit as compared to the original isotropic mode.

The results from imaging show that elastin exists not only in the form of elastic lamellae (EL) but also elastic fibers are present in the interlaminal space (Figure 3). In circumferential sections, interlaminal elastin fibers (IEFs), normally seem to make a link between smooth muscle cells (SMCs) and the lamellae and are mostly in the same alignment with smooth muscle cells (Figure 3.b). In the longitudinal sections, we could mostly observe only the cross sections of the elastin fibers in the gap between SMCs and ELs. This suggests that elastin fibers are aligned with long axis of SMCs and therefore mostly oriented in circumferential direction. The results are in accordance with a recent work by O'Connell et al [4].

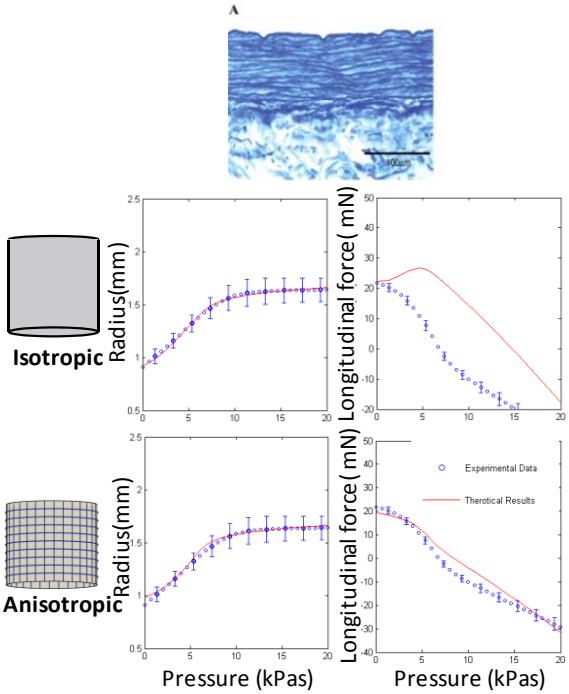

Figure 1. The isotropic and anisotropic models applied on the experimental data of intact arteries

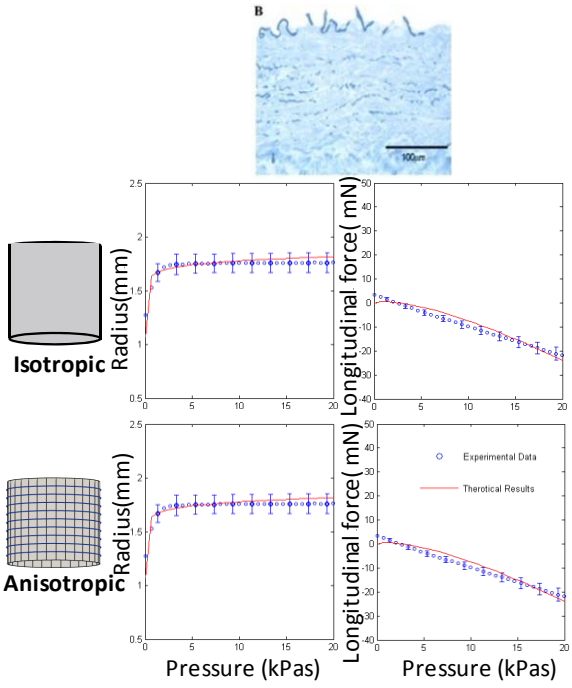

Figure 2. The isotropic and anisotropic models applied on the experimental data of elastase treated arterie

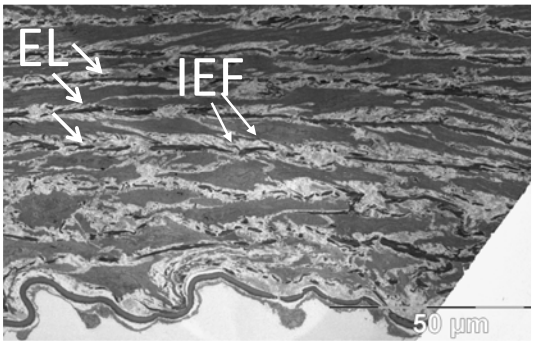

3.a

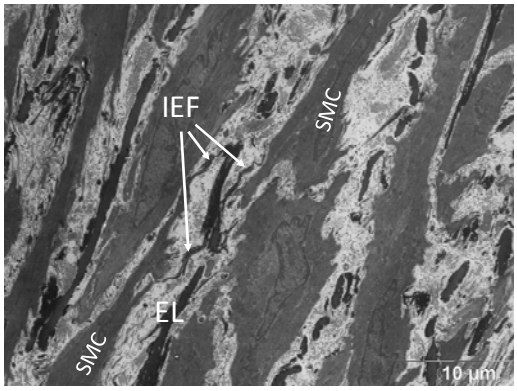

3.b

Figure 3. Cross section of a rabbit common carotid artery as seen by the transfer electron microscopy. IEF: interlaminal elastic fibers, El: elastic lamella , SMC: smooth muscle cell

4. CONCLUSION

We conclude that shortcomings of the isotropic model in fitting both the P-r_o and P-F_z experimental data lies in the identification of the SEF for elastin and that the SEF for the collagen component in Zulliger et al. is sufficient to give a 3D description of the arterial wall in the absence of elastin. The proposed anisotropic description of elastin seems to be in accordance with the ultrastructure of arterial elastin and provides a better characterization for the biomechanical response of the arterial wall, as compared to the isotropic model.

ACKNOWLEDGEMENTS

The authors acknowledge Dr. Graham Knott and Stephanie Rosset at EPFL's SV Electron microscopy facilities for the assistance with specimen preparation and imaging, Alessandra Griffa and J.C. Sarria at EPFL's BIOP facilities for their assistance in image analysis. This work was supported by the Swiss National Science Foundation (Grant No. 325230-125445).

REFERENCES

[1] Fonck, E., Prod'hom, G., Roy, S., Augsburger, L., Rufenacht, D., and Stergiopulos, N., 2007, "Effect Of Elastin Degredation on carotid wall mechanics as assessed by a constituent-based biomechanical model " American Journal of Physiology - Heart and Circulatory Physiology, 292(6), pp. H2754-H2763.

[2] Denk, W., and Horstmann, H., 2004, "Serial block-face scanning electron microscopy to reconstruct three-dimensional tissue nanostructure," PLoS Biol, 2(11), p. e329.

[3] Zulliger, M. A., Stergiopulos, N., and Rachev, A., 2004, "A constitutive formulation of arterial mechanics including vascular smooth muscle tone," Am J Physiol Heart Circ Physiol, 287(3 56-3), pp. H1335-1343.

[4] O'Connell, M. K., Murthy, S., Phan, S., Xu, C., Buchanan, J., Spilker, R., Dalman, R. L., Zarins, C. K., Denk, W., and Taylor, C. A., 2008, "The three-dimensional micro- and nanostructure of the aortic medial lamellar unit measured using 3D confocal and electron microscopy imaging," Matrix Biol., 27(3), pp. 171-181.

Biomaterials and Biological Materials

INFLUENCIA DE LA EDAD Y LOS ANEURISMAS EN LA ROTURA DE LA PARED DE LA AORTA ASCEDENTE

J.M. Atienza[1], F.J. Rojo[1], E. Claes[1], C. M. García-Herrera[2], C. García-Montero[3], R.L. Burgos[3], G.V. Guinea[1]

1 Departamento de Ciencia de Materiales, E.T.S.I. de Caminos, Canales y Puertos, Universidad Politécnica de Madrid. c/ Prof. Aranguren s/n, 28040, Madrid, España.

2 Departamento de Ingeniería Mecánica, Universidad de Santiago de Chile, USACH, Av. Bernardo O'Higgins 3363, Santiago de Chile, Chile

3 Servicio de Cirugía Cardiaca del Hospital Universitario Puerta de Hierro-Majadahonda, c/ Manuel de Falla, 1. 28222 - Majadahonda, España.

RESUMEN

Para mejorar los criterios de diagnóstico y prevención de las enfermedades cardiovasculares resulta fundamental conocer las propiedades mecánicas de la pared arterial. Este trabajo estudia el comportamiento mecánico y la rotura de la aorta torácica ascendente humana, tanto para individuos sanos como en pacientes aneurismáticos. Se estudia, asimismo, la influencia de la edad en las propiedades mecánicas. Se ha evaluado el comportamiento mecánico hasta rotura de la aorta torácica ascendente de 23 donantes sanos cuyas edades varían desde los 15 a los 65 años, y de 14 pacientes aneurismáticos, con edades entre 40 y 87 años. Se han realizado ensayos de tracción tanto en dirección longitudinal como circunferencial para evaluar la anisotropía de la pared arterial. Los resultados muestran que la influencia de la edad en las propiedades mecánicas de la pared arterial es significativa, tanto para los individuos sanos como para los enfermos. No se encuentran diferencias significativas entre el comportamiento en rotura de las sanas y las aneurismáticas cuando se comparan pacientes de las mismas edades. En cambio, la zona de trabajo fisiológico de las aortas enfermas se sitúa en la parte más rígida de su respuesta mecánica, perdiendo parte de su función amortiguadora de las ondas de presión generadas por el corazón.

ABSTRACT

Mechanical properties of aortic wall, both healthy and pathological, are needed in order to develop and improve diagnostic and interventional criteria, and for the development of mechanical models to assess arterial integrity. This study focuses on the mechanical behaviour and rupture conditions of the human ascending aorta and its relationship with age and pathologies. Fresh ascending aortic specimens harvested from 23 healthy donors and 14 with aneurysm were tensile tested *in vitro* under physiological conditions. Tensile strength, stretch at failure and elbow stress were measured. Results showed that age causes a major reduction in the mechanical parameters of healthy ascending aortic tissue, and that no significant differences are found between the mechanical strength of aneurysmal aortic specimens and the corresponding age-matched control group. The mean physiological wall stress acting on pathologic aortas were far from rupture, with factors of safety (defined as the ratio of tensile strength to the mean wall stress) larger than six. In contrast, the physiological operation of pathologic vessels lays in the stiff part of the response curve, losing part of its function of damping the pressure waves from the heart.

PALABRAS CLAVE: Ensayos de Tracción, Aorta Humana, Aneurisma, Envejecimiento.

1. INTRODUCCIÓN

La aorta es el paradigma de las grandes arterias, cuya función no es únicamente servir como conductos para el torrente sanguíneo, sino que además deben modular su pulsatilidad mediante su respuesta mecánica. El deterioro de las propiedades mecánicas de la aorta afecta a la función cardiaca y está relacionado con las enfermedades cardiovasculares. Un mejor conocimiento de la respuesta mecánica de la aorta y su conexión con las diferentes patologías resulta fundamental para prevenir accidentes cardiovasculares, así como para desarrollar tratamientos más efectivos.

El aneurisma de aorta es una enfermedad cardiovascular frecuente, caracterizada por la dilatación de la pared arterial que en los casos más extremos puede llegar a romperse. Aunque algunos de los pacientes pueden presentar síntomas vagos de la enfermedad -como dolores de espalda o en el abdomen- la mayoría de los casos son asintomáticos hasta la rotura del aneurisma, lo que supone un gran riesgo para la vida del paciente.

La cirugía para eliminar la zona dilatada es una operación comprometida, con un 5 % de mortalidad, cuya indicación se realiza cuando el riesgo de rotura del aneurisma supera al de la operación quirúrgica. Los criterios de evaluación utilizados hoy en día son estadísticos y se basan casi exclusivamente en el tamaño del aneurisma, que se considera operable cuando el diámetro de la aorta supera los 5.5 cm. Sin embargo, no

es infrecuente la rotura de aneurismas de menor diámetro.

Aunque se admite que el tamaño del aneurisma no es probablemente el único determinante del riesgo de rotura no existen estudios suficientes para incluir otros parámetros que mejoren el criterio de diagnóstico y ayuden a la toma de decisiones clínicas.

En realidad, la rotura de un aneurisma ocurre cuando las tensiones mecánicas que actúan en esa zona superan la resistencia de la pared arterial. Los criterios actuales, basados en el tamaño -bien sea los que sólo tienen en cuenta el diámetro absoluto, o aquellos que añaden otros factores como la superficie corporal (BSA: body surface area)- no tienen en cuenta el comportamiento mecánico de la pared arterial.

Por eso, en los últimos años se está realizando un importante esfuerzo para entender el comportamiento mecánico de la pared aórtica y cómo éste se ve afectado por las diferentes patologías vasculares. A pesar de ello, los datos experimentales publicados sobre la resistencia mecánica de la aorta humana siguen siendo limitados y a veces controvertidos. Se suele aceptar que la aorta sana es más resistente que la enferma e incluso algunos estudios han mostrado que detrás del aneurisma hay un deterioro mecánico muy fuerte, con una pérdida de más de un 30% en resistencia [1]. Sin embargo, otros estudios han mostrado un comportamiento similar en aortas sanas y patológicas [2].

Para ser capaces de interpretar correctamente esos resultados, es imprescindible entender la influencia de factores no patológicos como la edad, el sexo o la altura de los individuos. En particular resulta clave poder separar las consecuencias propias del envejecimiento del efecto provocado por el desarrollo de las diferentes enfermedades, ya que ambos procesos están muy relacionados con la respuesta mecánica de los tejidos blandos.

En el presente trabajo se ha evaluado el comportamiento mecánico hasta rotura de la aorta torácica ascendente de 23 donantes sanos cuyas edades varían desde los 15 a los 65 años, y de 14 pacientes con aneurismas con edades entre los 40 y 87 años. Se han realizado ensayos de tracción tanto en dirección longitudinal como circunferencial, caracterizando el comportamiento anisótropo de la pared arterial.

Los resultados muestran que la influencia de la edad en las propiedades mecánicas de rotura (tensiones y deformaciones máximas) es muy significativa, por lo que es imprescindible tenerla en cuenta a la hora de evaluar el riesgo de rotura. No se han encontrado diferencias significativas en la resistencia de la pared arterial de muestras aneurismáticas y muestras sanas de la misma edad, si bien las primeras responden con más rigidez en la zona de trabajo fisiólogica, perjudicando la función amortiguadora del vaso.

2. MATERIAL

Los ensayos de este trabajo se han realizado sobre segmentos de aorta torácica ascendente humana obtenidos con la colaboración del Servicio de Cirugía Cardiaca del Hospital Puerta de Hierro de Madrid. En todos los casos las muestras se extrajeron de acuerdo con los protocolos establecidos por el Comité de Ética de dicho hospital.

Las muestras de tejido arterial sano se han obtenido de personas que han sufrido algún accidente o han muerto por causas que no tienen relación con aspectos cardiovasculares. En concreto, los segmentos estudiados se obtuvieron de cadáveres de donantes para trasplante cardiaco y pulmonar.

Erbel y Eggebrecht [3] definen dos parámetros para diferenciar el tamaño normal de la aorta: la edad y el área de la superficie corporal o BSA. Éste último parámetro se estima con la talla y el peso de la persona. En las Tablas 1 y 2 se muestran los datos de los donantes sanos. Para este estudio los vasos se han dividido en dos grupos dependiendo de la edad: Grupo 0A (<35 años, 9 muestras), Grupo 0B (>35 años, 14 muestras).

Tabla 1. Datos de las muestras del grupo 0A: vasos sanos menores de 35 años

Sexo [F o M]	Edad [años]	BSA [m^2]
M	16	1.88
M	18	1.98
M	20	2.05
M	20	1.54
M	25	2.12
M	29	1.99
F	31	1.78
M	32	1.95
M	35	1.82

Tabla 2. Datos de las muestras del grupo 0B: vasos sanos mayores de 35 años

Sexo [F o M]	Edad [años]	BSA [m^2]
M	36	1.67
F	44	1.67
M	45	1.97
F	45	1.60
F	46	1.66
F	48	1.44
M	49	1.93
F	50	1.78
M	50	1.81
M	52	1.82
M	57	2.06
M	57	1.68
M	62	
F	64	

Las muestras de tejido arterial patológico se han obtenido de pacientes que sufrieron una intervención de aneurisma en el Hospital Puerta de Hierro. De acuerdo a los protocolos aprobados por el Comité de Ética de dicho Hospital, todos los pacientes dieron un informe de consentimiento previo a la operación. En la Tabla 3 se recogen los datos de los pacientes aneurismáticos, en total 14 pacientes entre 44 y 87 años.

Tabla 3. Datos de los vasos del grupo I: pacientes aneurismáticos

Sexo [F o M]	Edad [años]	BSA [m^2]
M	44	1.95
F	45	1.95
M	51	1.68
M	51	1.94
M	53	1.80
F	57	1.71
M	58	1.97
M	60	1.83
M	62	1.94
M	65	1.90
M	71	2.12
M	75	2.15
M	81	1.99
F	87	

3. TRABAJO EXPERIMENTAL

3.1. Probetas

Para caracterizar el comportamiento mecánico de los tejidos se realizaron ensayos de tracción uniaxial sobre probetas extraídas de los segmentos arteriales (Fig. 1). Las probetas se diseñaron en forma de hueso para evitar las roturas en la zona de mordazas. El espesor de las probetas venía dado por la pared de la arteria, y osciló entre los 1.6 y 2.3 mm.

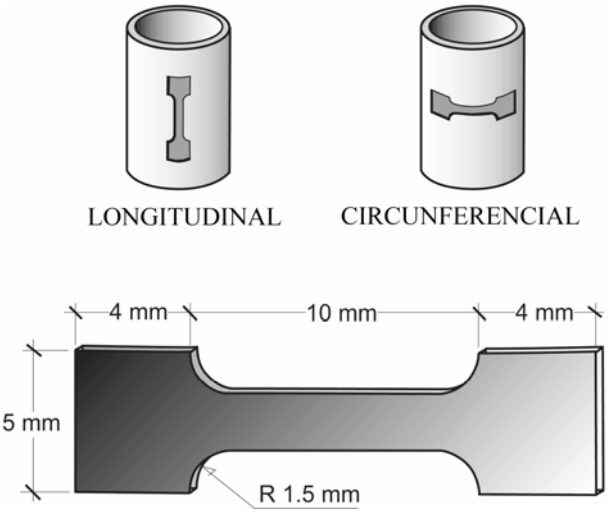

Figura 1. Orientación y dimensiones de las probetas.

Para caracterizar el comportamiento anisótropo se obtuvieron al menos tres probetas en cada una de las dos direcciones principales de los vasos (circunferencial y longitudinal). En la Figura 1 se muestran las direcciones seleccionadas.

3.2. Dispositivo experimental

Los ensayos se realizaron en el interior de una célula de polimetilmetacrilato transparente que permitía la visualización del vaso y la medida de sus dimensiones por métodos ópticos mediante un video extensómetro Keyence LS-7500 de 0.001mm de precisión. Las arterias se ensayaron sumergidas en suero fisiológico (PBS), cuya temperatura se mantuvo estable a 37 ºC con precisión de ±1ºC mediante un baño termostático (Unitronic 6320200). La temperatura del vaso se medía mediante un termopar tipo K situado en sus proximidades (< 5mm). Las arterias se fijaron por sus extremos a las mordazas de una máquina de ensayos mecánicos Instron 5866.

La precisión en la medida del alargamiento axial, medido a través del transductor incorporado a la máquina de ensayos, era de 0.001mm. El dispositivo experimental es descrito con más precisión en [4]. La velocidad de solicitación durante todo el ensayo fue 0.03 mm/s (velocidad de deformación aproximada de 15%/min). Los ensayos se realizaron en estado pasivo, sin que existiera activación eléctrica o química de las células presentes en la pared vascular.

3.3. Obtención de la tensión y deformación de rotura

La tensión de Cauchy se calculó a partir de la carga instantánea (P) dividida por el área transversal real (P/a). El alargamiento (λ) se obtuvo dividiendo la longitud instantánea (l) por la longitud inicial (L). La deformación (ε) se obtuvo restando 1 al alargamiento. El área transversal real se ha calculado utilizando la condición de incompresibilidad, propia de los tejidos blandos, que conduce a la relación $a=A/\lambda$, donde A es el área transversal inicial.

Para simplificar el análisis y la comparación de las curvas tensión-alargamiento, de cada una de ellas se obtuvieron tres parámetros que resumen el comportamiento mecánico de la arteria: la deformación máxima (ε_{max}) y la tensión real máxima (σ_{max}), correspondientes a la rotura de cada probeta, y la tensión en el punto del codo (σ_e), definido por el brusco cambio en la rigidez del material (Fig. 2).

Se consideró que la rotura de la probeta se producía cuando una de las capas que forman la pared de la arteria rompe, lo que se ve reflejado en una disminución repentina de la carga registrada en el ensayo. La tensión de codo se determinó a partir de la primera derivada de la tensión con respecto al alargamiento, tal y como se describe en el Apéndice.

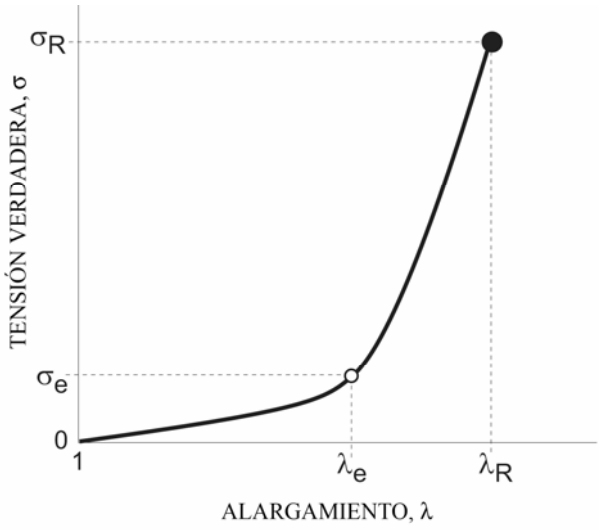

Figura 2. Curva tensión-alargamiento de una arteria y parámetros mecánicos.

A partir de los ensayos para cada dirección se obtuvieron el valor medio de resistencia, deformación máxima y tensión en el codo y el error cuadrático (definido como la desviación típica de la muestra dividida entre la raíz cuadrada del número de probetas) para cada uno de los pacientes estudiados.

4. RESULTADOS Y DISCUSIÓN

4.1. Resistencia y deformación de rotura de la pared arterial

En la Figura 3 se muestra la tensión de rotura para los dos grupos de donantes sanos y el grupo de pacientes aneurismáticos. Para evaluar la anisotropía de la pared arterial se han mostrado los resultados tanto para la dirección longitudinal como para la circunferencial

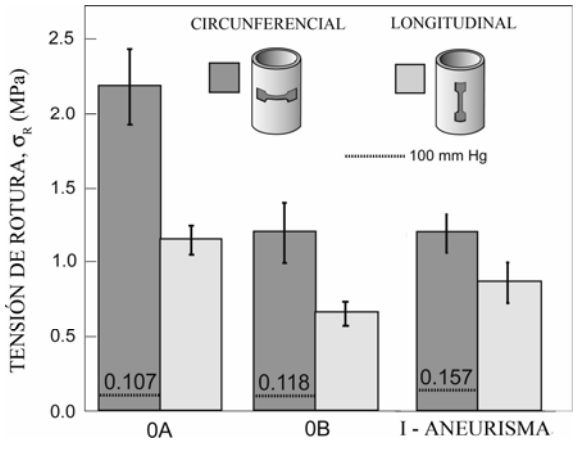

Figura 3. Tensión de rotura de rotura (media y error cuadrático) en direcciones circunferencial y longitudinal para los vasos sanos jóvenes (0A), sanos mayores (0B) y aneurismáticos.

En el caso de los vasos sanos se observa una importante anisotropía para los pacientes más jóvenes, siendo la dirección circunferencial mucho más resistente que la longitudinal. Estas diferencias se reducen con la edad, si bien tanto para los vasos sanos mayores como para los aneurismáticos la dirección circunferencial sigue siendo más resistente.

Se observa que la tensión de rotura se reduce drásticamente con la edad en la dirección circunferencial al igual que ocurre en la dirección longitudinal.
Los valores presentados concuerdan con las observaciones de Okamoto et al. [5] para aorta ascendente aneurismática humana, comprobándose que las tensiones últimas en los vasos sanos son comparables a las de vasos enfermos de edad similar.

Los valores obtenidos por Vorp et al. [6] y Raghavan et al. [7] también se encuentran en el rango de los obtenidos en este estudio. Sin embargo, nuestro trabajo muestra que no se puede afirmar que la causa de la reducción de la resistencia se deba solamente a la enfermedad, ya que la edad juega un papel muy importante.

Para cuantificar adecuadamente el riesgo de rotura de cada vaso, las tensiones de rotura obtenidas deben compararse con las tensiones circunferenciales concretas a las que está sometida la arteria en condiciones de trabajo fisiológico. Dichas tensiones pueden evaluarse aproximadamente utilizando la aproximación de pared delgada, a partir de la presión interior (aproximadamente 100 mmHg), el diámetro y el espesor de la arteria. Los valores calculados para los vasos estudiados se muestras como líneas de puntos en la Figura 3. En ella se comprueba que la tensión de trabajo de la pared arterial se encuentra lejos de la rotura en todos los casos, si bien el factor de seguridad se reduce con la edad y también con la patología.

En cuanto a la deformación de rotura, en la Figura 4 se muestra su valor en direcciones circunferencial y longitudinal en función de la edad de los vasos. Se observa que la deformación de rotura disminuye también con la edad. De nuevo, la edad parece tener una influencia mucho más determinante que la patología.

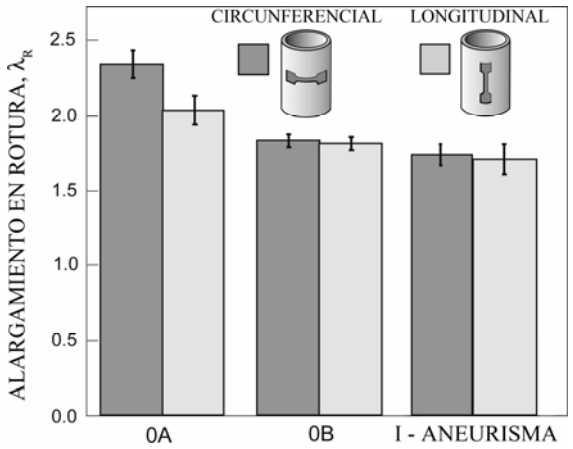

Figura 4. Deformación de rotura (media y error cuadrático) en direcciones circunferencial y longitudinal para los vasos sanos jóvenes (0A), sanos mayores (0B) y aneurismáticos).

4.2. Tensiones en el codo: condiciones de trabajo de la aorta ascendente

La determinación de la tensión de rotura tiene un interés incuestionable para evaluar el riesgo de rotura de la pared arterial. No obstante, los resultados mostrados en este trabajo demuestran que tanto los vasos sanos como enfermos trabajan lejos de esa rotura.
La degeneración o dilatación de la pared arterial fruto de un aneurisma es un proceso continuo generado, entre otros factores, por el efecto permanente de las tensiones alternadas debido a la circulación sanguínea. Desde esta perspectiva, la respuesta mecánica de la aorta durante su trabajo bajo cargas fisiológicas, y su variación con la edad y las patologías es de gran interés para la investigación cardiovascular.

Las curvas tensión-alargamiento de la pared arterial presentan dos zonas bien delimitadas: una inicial muy deformable, y otra mucho más rígida. Las fibras de elastina son las principales responsables del comportamiento mecánico en la primera zona flexible, mientras que el progresivo alineamiento y puesta en carga de las fibras de colágeno son las que marcan el comportamiento en la zona rígida. La zona de transición o punto de codo está bastante bien marcado y se puede hallar sin dificultad utilizando el método expuesto en el Apéndice.

En la Figura 5 se muestran las tensiones de codo en dirección circunferencial, tanto para los vasos sanos como para los enfermos junto a las presiones de trabajo fisiológico de las arterias calculadas con la aproximación de pared delgada. Se puede observar que las tensiones de codo decrecen de forma importante con la edad.

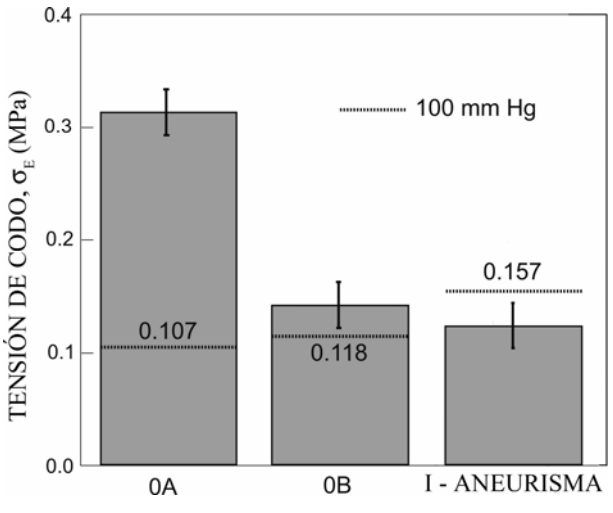

Figura 5. Tensión de codo (media y error cuadrático) en direcciones circunferencial y longitudinal para los vasos sanos jóvenes (0A), sanos mayores (0B) y aneurismáticos).

Los valores correspondientes a las tensión del codo de arterias patológicas no son estadísticamente diferentes de los sanos cuando se comparan edades similares. Sin embargo, cuando entra en consideración la tensión de la pared arterial debida a la presión fisiológica se ve que las arterias sanas trabajan por debajo de su presión de codo, es decir, en la zona flexible de su respuesta mecánica. En el caso de las enfermas, éstas trabajan claramente por encima de su presión de codo, en la zona más rígida de la curva tensión-alargamiento, por lo que pierden parte de su función de amortiguamiento. Esta pérdida de flexibilidad hace que la carga que deben soportar las fibras de colágeno sea mayor y provoca una pérdida de fibras elásticas, aumentando el diámetro arterial y con ello aún más la tensión de trabajo de la pared, favoreciendo así de forma indirecta el riesgo de rotura.

5. CONCLUSIONES

En este estudio se ha caracterizado la tensión y deformación de rotura de la aorta torácica ascendente de vasos sanos y aneurismáticos. Los resultados han puesto de manifiesto que:

- Las propiedades mecánicas en rotura (tensión y deformación máxima) de la aorta ascendente disminuyen significativamente con la edad.

- El material de la aorta ascendente presenta una importante anisotropía en los pacientes jóvenes: la tensión y deformación de rotura son mayores en la dirección circunferencial. Estas diferencias se reducen con la edad.

- No parece que la pared arterial de las aortas aneurismáticas presente menos resistencia que las sanas de la misma edad. No obstante, las aortas aneurismáticas trabajan en la zona más rígida de su respuesta mecánica, lo que puede influir de forma indirecta en el riesgo de rotura, al provocar la pérdida de fibras elásticas y sobrecargar las fibras de colágeno.

AGRADECIMIENTOS

Los autores desean agradecer al Ministerio de Educación y Ciencia la financiación a través del proyecto MAT2009-10258, a la Comunidad de Madrid a través del programa MADR.IB-CM/S-SAL/0312/2006, a la Fundación Agustín de Betancourt y a Conicyt (Chile) por la financiación recibida a través de becas de investigación.

REFERENCIAS

[1] Vorp DA. *Biomechanics of abdominal aortic aneurysm*. Journal of Biomechanics 40(9), pp. 1887-1902. 2007.
[2] Iliopoulos DC, Kritharis EP, Giagini AT, et al. *Ascending thoracic aortic aneurysms are associated with compositional remodeling and vessel stiffening but not weakening in age-matched subjects*. Journal of Thoracic and Cardiovascular Surgery 137(1), pp. 101-109. 2009.
[3] Erbel R, Eggebrecht H. *Dimensions and the risk of dissection*. Heart 92(1), pp. 137-142. 2006.

[4] Guinea GV, Atienza JM, Elices M, et al. *Thermomechanical behavior of human carotid arteries in the passive state*. American Journal of Physiology-Heart and Circulatory Physiology 288(6), pp. H2940-H2945. 2005.
[5] Okamoto RJ, Wagenseil JE, DeLong WR, et al. *Mechanical properties of dilated human ascending aorta*. Annals of Biomedical Engineering 30(5), pp. 624-635. 2002.
[6] Vorp DA, Schiro BJ, Ehrlich MP, et al. *Effect of aneurysm on the tensile strength and biomechanical behavior of the ascending thoracic aorta*. Annals of Thoracic Surgery 75(4), pp. 1210-1214. 2003.
[7] Raghavan ML, Vorp DA, Federle MP, et al. *Wall stress distribution on three-dimensionally reconstructed models of human abdominal aortic aneurysm*. Journal of Vascular Surgery 31(4), pp. 760-769. 2000.

APÉNDICE: Determinación de la tensión de codo a partir de la curva tensión-alargamiento de una arteria.

Este Apéndice explica el método seguido para obtener las coordenadas del punto de transición (codo) a partir de la curva tensión-alargamiento de una arteria (Fig. A1).

El procedimiento se basa en obtener la primera derivada de la curva tensión - alargamiento (Fig. A2), que en nuestro caso se obtuvo numéricamente para cada ensayo utilizando el software "Kaleidagraph". En dicha curva, la zona de transición se identifica fácilmente como una zona cuasilineal previa al escalón horizontal superior.
El punto de codo se define como el punto medio de esta zona de transición, tal y como se muestra en la Figura A2, obteniéndose de esta forma tanto la tensión de codo como la deformación de codo.

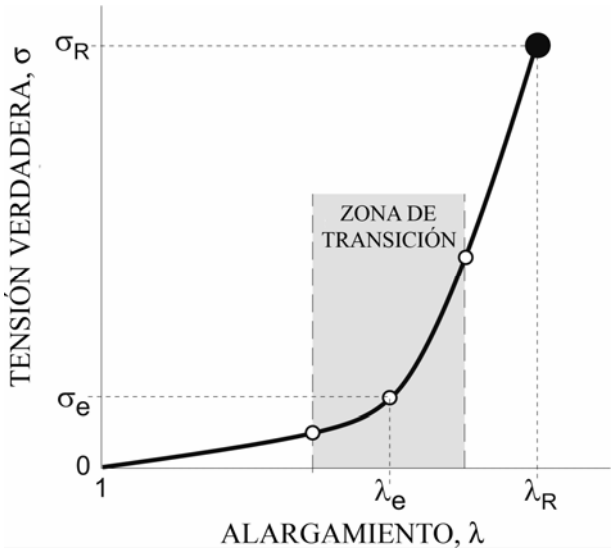

Figura A1. Curva tensión-alargamiento de la pared arterial.

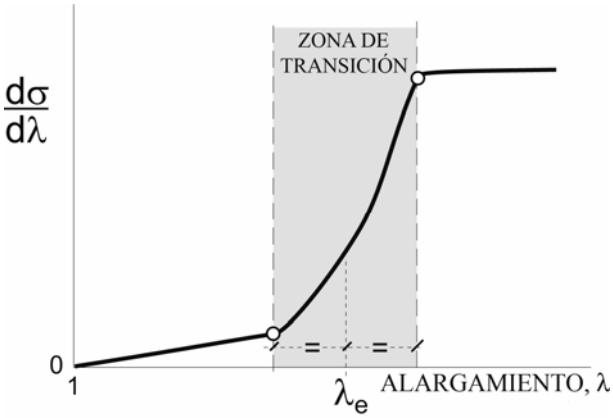

Figura A2. Primera derivada de la curva tensión-alargamiento de la pared arterial

MODE II FRACTURE OF CORTICAL BONE TISSUE

N. Dourado[1], M.F.S.F. de Moura[2], J.J.L. Morais[3]

[1] CITAB/UTAD, Departamento de Engenharias, Quinta de Prados, 5001-801
Vila Real, Portugal.
E-mail: nunodou@gmail.com
[2] Faculdade de Engenharia da Universidade do Porto,
Departamento de Engenharia Mecânica,
Rua Dr. Roberto Frias, 4200-465 Porto, Portugal
E-mail: mfmoura@fe.up.pt
[3] CITAB/UTAD, Departamento de Engenharias, Quinta de Prados, 5001-801
Vila Real, Portugal.
E-mail: jmorais@utad.pt

ABSTRACT

In this work a numerical study has been performed to verify the adequacy of the End Notched Flexure (ENF) test to determine the fracture toughness under mode II loading of cortical bovine bone tissue. In this work a detailed numerical analysis using the finite element method and a cohesive damage model was performed in order to optimize the specimen geometry when applied to bone fracture characterization under mode II loading. A data reduction scheme based on specimen compliance and crack equivalent concept was used to overcome the difficulties inherent to crack monitoring during its growth. It was verified that a judicious selection of the geometry allows a rigorous estimation of toughness in mode II.

KEY WORDS: bone, fracture, mode II loading, ENF test

1. INTRODUCTION

Fracture of healthy bone tissue needs to be understood in order to predict and reduce fractures due to aging, exercise, over-use and disease. Fracture tests using bovine bone are frequently performed since it provides longer specimens relative to the human case. Although the fracture properties are not equal [1, 2], the fracture behavior of bovine bone is similar to the human, which justifies its use in experimental tests. This particularity can be used to identify new test methods using bovine bone.

The majority of the works about fracture characterization of bone tissue are dedicated to mode I loading. Effectively, the mode II fracture characterization is much less studied owing to the difficulties inherent to tests execution. Only a few works were performed dedicated to mode II fracture characterization of bone. Norman et al. [3] proposed the compact shear test for mode II fracture characterization of human bone. However, this test presents some disadvantages related to small variation of compliance (C) as a function of pre-crack length (a_0) which difficult the establishment of the compliance calibration C=f(a), mixed-mode crack growth instead of pure-mode II, and unstable propagation which means that only crack initiation fracture toughness is available.

In order to overcome these drawbacks, the applicability of the End Notched Flexure test (ENF) to mode II fracture characterization of bone is numerically assessed in this work. This test is especially adequate for mode II fracture characterization due to its simplicity and the possibility to use the beam theory to measure the fracture energy. However, it also presents some limitations related to spurious influence on the fracture process zone (FPZ) of the central loading. In this study, the specimen geometric conditions to be fulfilled in order to provide accurate measurements of bone toughness under mode II loading are identified.

2. DATA REDUCTION SCHEME

The classical data reduction schemes used to determine the fracture energy in mode II are usually based on the specimen compliance calibration or on the beam theory. In both cases, a rigorous measurement of crack length during its growth is a fundamental task. However, in the ENF test (Figure 1) the crack tends to close during its growth which difficult the identification of its tip. Moreover, in bone a non-negligible fracture process zone (FPZ) in the vicinity of the crack tip, characterized by the development of toughening mechanisms, exists which also contribute to the above referred difficulty.

To overcome these drawbacks an alternative data reduction scheme based on specimen compliance and crack equivalent concept is proposed in the following.

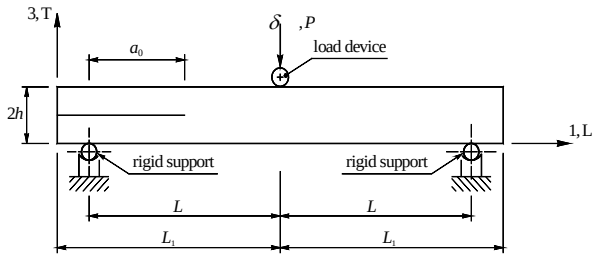

Figure 1. ENF test (L=32.5 , L_1=35 and h=4 mm).

Using the Timoshenko beam theory, the specimen compliance is given by [4],

$$C = \frac{3a^3 + 2L^3}{8Bh^3E_{\mathrm{L}}} + \frac{3L}{10BhG_{\mathrm{LT}}} \tag{1}$$

In the early stages of loading, the initial values of compliance C_0 and crack length a_0 can be used to estimate a corrected flexural modulus E_{f} ,

$$E_{\mathrm{f}} = \frac{3a_0^3 + 2L^3}{8Bh^3}\left(C_0 - \frac{3L}{10BhG_{\mathrm{LT}}}\right)^{-1} \tag{2}$$

This procedure is quite effective since material variability among different specimens leads to non-negligible scatter on the elastic modulus. The beam theory (equation (1)) does not include root rotation effects and stress concentrations at the crack-tip. Following this approach, the longitudinal modulus is not a measured property but an estimated parameter thus including the above referred effects. During crack growth the current compliance C is used to estimate an equivalent crack length a_{e} through equations (1-2),

$$a_{\mathrm{e}} = \left[\frac{C_{\mathrm{c}}}{C_{0\mathrm{c}}}a_0^3 + \frac{2}{3}\left(\frac{C_{\mathrm{c}}}{C_{0\mathrm{c}}} - 1\right)L^3\right]^{1/3} \tag{3}$$

where

$$C_{\mathrm{c}} = C - \frac{3L}{10BhG_{\mathrm{LT}}} \;;\; C_{0\mathrm{c}} = C_0 - \frac{3L}{10BhG_{\mathrm{LT}}} \tag{4}$$

Using equation (1), G_{II}=f(a_{e}) can be obtained as

$$G_{\mathrm{II}} = \frac{9P^2a_{\mathrm{e}}^2}{16B^2h^3E_{\mathrm{f}}} \tag{5}$$

In summary, this method is based on the equivalent crack concept and does not require crack length monitoring during its growth. A resistance curve (R-curve) can be easily obtained only from the load-displacement curve.

3. NUMERICAL ANALYSIS

The numerical analyses were performed using a cohesive damage mode (Figure 2), allowing both crack initiation and growth [4]. A bilinear relationship is established between stresses (σ) and relative displacements (δ) at the integration points of the interface finite elements. These elements are designated as cohesive elements in the following discussion. A quadratic stress criterion and a linear energetic criterion were used to simulate damage initiation and growth under mixed-mode loading.

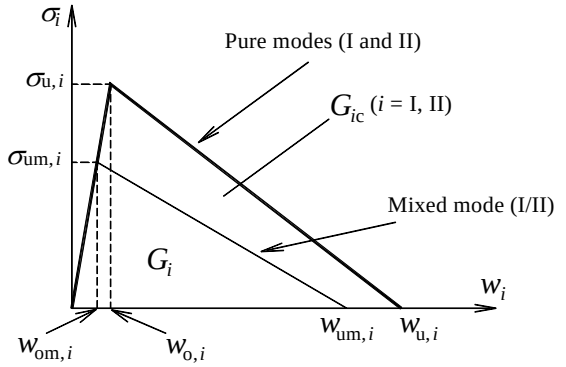

Figure 2. Sketch of the pure (I or II) and mixed (I/II) bilinear cohesive model.

A two-dimensional analysis was implemented in ABAQUS® software using isoparametric plane stress eight-node solid elements (Figure 3). Cohesive elements were disposed at the specimens' half-height along direction x, allowing the simulation of damage initiation and growth. At the pre-crack length the cohesive elements were considered "opened" which means that they only transmit normal compressive stresses, avoiding spurious interpenetrations. Loading and supporting devices were simulated as rigid bodies and contact conditions assumed to prevent interpenetration. Small increments ($0.1\%\times\delta$ – see Figure 1) were considered to provide stable crack growth. A non-linear geometrical analysis was carried out.

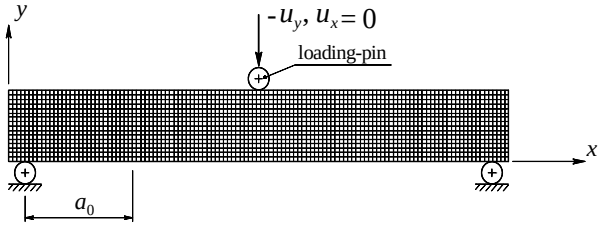

Figure 3. Mesh used in the ENF specimen simulation.

4. RESULTS

The maximum specimen length that can be obtained from the bovine femur is about 70 mm. On the other hand, the crack tip during its propagation must be maintained far from the loading point, since the compressive effects tend to affect decisively the measured toughness. In fact, during self-similar crack propagation the fracture process zone (FPZ) at the crack tip must be maintained distant of the central loading point since the compressive effects lead to a spurious toughness enhance. In this context, an important role can be played by the toughness (G_{IIc}) and local strength ($\sigma_{u,II}$) under mode II loading. Effectively, high values of G_{IIc} and/or low values of $\sigma_{u,II}$ contribute to increase the size of the FPZ (the descending branch of the triangle in Figure 2 increases) thus aggravating the limitations of the application of the ENF test to fracture characterization of bone under mode II loading. In addition the pre-crack length also influences this behavior. Consequently, three crack lengths (a_0 = 15, 18 and 20 mm), three local typical shear strengths ($\sigma_{u,II}$ = 35, 40 and 50 MPa) and four characteristic mode II toughness values (G_{IIc} = 4, 5, 6 and 7 N/mm) were considered in a parametric study. It must be noted that the used cohesive parameters can be considered pessimistic concerning the performance of the ENF test. In fact, Turner et al. [5] present values ranging between 50.4 MPa and 51.6 MPa for human bone strength, which has inferior properties than bovine. On the other hand, Feng [6] evaluated the G_{IIc} of bovine bone as being equal to 2.43±0.836 N/mm. This means that more favorable conditions (higher strengths and lower fracture energies) are expected to exist in the experiments.

Numerous simulations were carried out to verify which combination of studied parameters could provide accurate estimates of G_{IIc}. This verification was executed comparing the measured G_{IIc} with the introduced value in the cohesive model. Considering normalized strain energy (Figure 4) the efficacy of the proposed geometry is assessed when the ratio (G_{II} /G_{IIc}) points to the unity at the plateau of the *R*-curve. Moreover, the self-similar crack growth condition was verified by means of the cohesive zone length (l_{FPZ}). This parameter must maintain constant for some extent in order to satisfy the required conditions of self-similar crack growth (Figure 4).

It was verified that a judicious selection of the specimen dimensions allows a rigorous estimate of toughness in mode II loading. In fact, considering a_0=20 mm reasonable plateaus are obtained for all the examined values of G_{IIc} when $\sigma_{u,II}$ = 50 MPa. It should be noted that this is an underestimated local shear strength value [5].

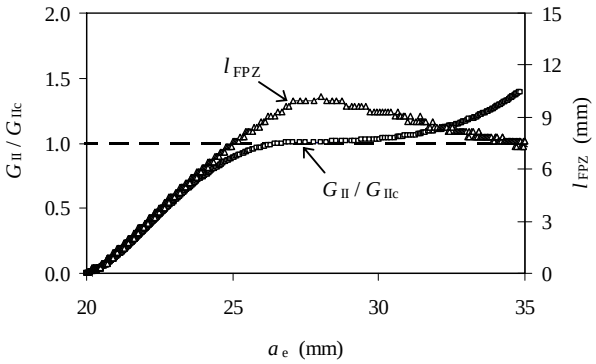

G_{IIc} = 5 N/mm; a_0 = 20 mm; $\sigma_{u,II}$ =50 MPa

Figure 4. R-curve and the corresponding cohesive zone length.

This means that higher real values would provide shorter FPZs that do interact with the central loading region for longer crack lengths. Even for the highest toughness value considered (G_{IIc} = 7 N/mm) a short plateau can be identified (Figure 5). This means that the ENF test can be applied to bone fracture characterization under mode II loading since the real conditions would be more favorable than the ones used in Figure 5.

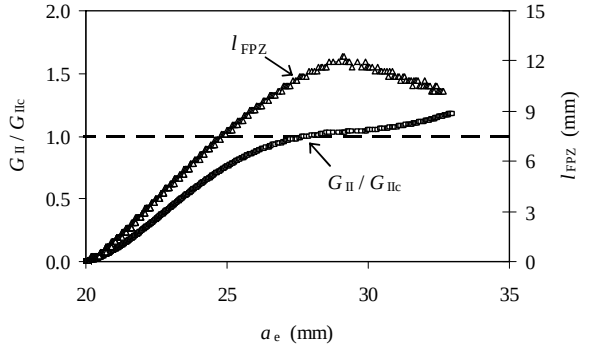

G_{IIc} = 7 N/mm; a_0 = 20 mm; $\sigma_{u,II}$ =50 MPa.

Figure 5. R-curve and the corresponding cohesive zone length.

5. CONCLUSIONS

The ENF test was analyzed numerically in order to verify its applicability to characterize the bovine bone fracture under mode II loading. A data reduction scheme based on specimen compliance and crack equivalent concept was used to overcome the difficulties inherent to crack monitoring during its growth. A cohesive damage model was used to simulate damage initiation and propagation, thus assessing the influence of several parameters on the measured G_{IIc} and the efficacy of the proposed data reduction scheme. The effects of initial crack length, local strength and toughness were analyzed in order to verify their

influence on the measured G_{IIc} relatively to the inputted value.

The present study allows to identify the limiting aspects of the ENF test and to optimize the geometry leading to a correct estimation of the properties of bovine bone under mode II loading. The critical aspect of the ENF test is related to the eventual spurious effect of the central loading point on the measured G_{IIc}. However, the presented work showed that with careful geometry selection, good estimations of G_{IIc} can be provided by the ENF test.

ACKNOWLEDGEMENTS

The authors thank the Portuguese Foundation for Science and Technology for supporting the work here presented, through the research project PTDC/EME-PME/71273/2006.

REFERENCES

[1] Vashishth, D., Behiri, J. C., Bonfield, W., "Crack growth resistance in cortical bone. Concept of microcrack toughening", *Journal of Biomechanics*, 30:763-769, 1997.

[2] Catanese III, J., Iverson, E.P., Ng, R.K., Keaveny, T.M. Heterogeinity of mechanical properties of demineralized bone. *Journal of Biomechanics*, 32, 1365-1369, 1999.

[3] Norman T.L., Nivargikar V., Burr D.B. "Resistance to crack growth in human cortical bone is greater in shear than in tension", *Journal of Biomechanics*, 29:1023-31, 1996.

[4] de Moura, M. F. S. F., Silva, M. A. L., de Morais, A.B., Morais, J.J.L. "Equivalent crack based mode II fracture characterization of wood". *Engineering Fracture Mechanics* 73, 978-993, 2006.

[5] Turner, C. H., Wang, T., Burr, D. B. "Shear strength and fatigue properties of human cortical bone determined from pure shear tests". *Calcified Tissue International* 69, 373-378, 2001.

[6] Feng, Z., Rho, J., Han, S., Ziv, I. "Orientation and loading condition dependence of fracture toughness in cortical bone". *Materials Science and Engineering C* 11, 41–46, 2000.

EFECTO DE LA LONGITUD DE ONDA DE LA RADIACIÓN UV SOBRE LA SEDA DE ARAÑA

G. B. Perea , J. Pérez-Rigueiro, G. R. Plaza, G. V. Guinea, M. Elices

Departamento de Ciencia de Materiales, E.T.S. de Ingenieros de Caminos,
Canales y Puertos, Universidad Politécnica de Madrid, C/ Profesor Aranguren s/n,
28040 Madrid, España.
E-mail: bperea@mater.upm.es

RESUMEN

En el presente trabajo se continúa el análisis de la influencia de la radiación UV sobre las propiedades mecánicas de las fibras de seda de araña. Para ello se ha empleado la seda producida por la glándula ampollácea mayor de la especie *Argiope trifasciata* y se ha estudiado el comportamiento en tracción simple de fibras de seda sometidas a diferentes tiempos de irradiación con luz UV de longitudes de onda de 254, 312 y 365 nm. Se ha encontrado que la radiación ultravioleta disminuye la tensión de rotura y la deformación de rotura modificando, en algunos casos, el aspecto general de las curvas tensión-deformación. Además se ha hecho uso de la radiación UV de longitud de onda de 254 nm para introducir daño en las fibras con objeto de realizar un análisis fractográfico sistemático. El estudio se complementa con la evaluación del efecto producido por la irradiación en el fenómeno de supercontracción.

ABSTRACT

The present work continues the analysis on the influence of UV radiation on the mechanical properties of spider silk fibers. Major ampullate gland silk (MAS) fibers were collected from *Argiope trifasciata* spiders, and tensile tested after irradiation. Wavelengths of 254, 312 and 365 nm were used. It has been found that exposure to UV radiation reduces the tensile strength and the deformation at breaking of the fibers, modifying in some cases the shape of the stress-strain curve. In addition, radiation with a wavelength of 254 nm was used to induce damage in the fibers in order to perform a systematic fractographic analysis. The study is complemented with the evaluation of the effect exerted by UV irradiation on the supercontraction of spider silk.

PALABRAS CLAVE: Seda de araña, fractografía, microestructura.

1. INTRODUCCIÓN

Las fibras de seda de araña constituyen un material enormemente atractivo. Su elevada resistencia y deformabilidad les permite almacenar gran cantidad de energía mecánica, que pueden después disipar, de modo que son especialmente apropiadas para absorber impactos [1], [2]. La combinación en un solo material de una elevada resistencia mecánica y una gran deformación de rotura implica un elevado trabajo hasta rotura. Esta combinación es difícil de alcanzar en los materiales artificiales ya que las mejoras en la resistencia mecánica suelen implicar una disminución de la deformación de rotura y viceversa [3].

De todas las sedas producidas por las arañas, la más resistente es la producida en la glándula ampollácea mayor o seda MAS. Las excelentes propiedades de la seda MAS son necesarias para cumplir su función en la construcción de la estructura de las telas y como hilo de seguridad que mantiene a la araña unida a la superficie sobre la que se desplaza. Este atractivo ha hecho que se hayan dedicado importantes esfuerzos a intentar producir fibras de proteínas inspiradas en la seda de araña mediante Ingeniería Genética [4]. Pese a los esfuerzos realizados, las fibras bioinspiradas no han llegado aún a igualar las propiedades de la seda producida por las propias arañas. En efecto, las técnicas de Ingeniería Genética actualmente sólo pueden producir de manera eficiente proteínas con pesos moleculares que son cinco veces menores que los de las proteínas naturales [5], [6]. Existe, por este motivo, un gran interés en establecer la relación entre el peso molecular de las proteínas que constituyen la seda de araña y las propiedades mecánicas que ésta presenta.

Con el fin de establecer esta relación, en el presente trabajo se continúa haciendo uso de la radiación UV de varias longitudes de onda [7], [8], aprovechando que el principal efecto de la luz ultravioleta es la rotura de enlaces covalentes [9]. Hay que indicar, sin embargo, que la rotura de los enlaces covalentes no implica necesariamente una disminución del peso molecular de las proteínas [10], sino que podría dar lugar a entrecruzamientos. La aparición de entrecruzamientos (enlaces covalentes entre proteínas) conduciría a un aumento del peso molecular. La irradiación UV es por tanto un medio para caracterizar la modificación de las propiedades mecánicas de la seda de araña en función

de la variación del tamaño de las proteínas que la conforman.

Para caracterizar la influencia de la radiación UV sobre las propiedades mecánicas de la seda de araña, se han sometido las fibras a diferentes tiempos de irradiación y se han obtenido sus curvas fuerza-desplazamiento para poder caracterizar su variación con el tiempo de exposición. Además se ha extendido el análisis para incluir el efecto de la radiación UV sobre la supercontracción de las fibras [11], [12]. En último lugar y con el fin de identificar los mecanismos de daño de las fibras de seda de araña irradiadas con luz UV se ha realizado un análisis fractográfico sistemático de muestras con diferentes niveles de alineamiento molecular.

2. PROCEDIMIENTO EXPERIMENTAL

En este estudio se ha utilizado la seda de araña MAS, hilo producido por la glándula ampollácea mayor de la especie *Argiope trifasciata*. La seda se ha obtenido mediante la técnica de hilado forzoso en una máquina de tracción [13]. Brevemente, el procedimiento de hilado comienza con la inmovilización de la araña en una bolsa de plástico que se fija con alfileres sobre una superficie de poliestireno expandido. La bolsa se perfora para permitir el acceso a las hilanderas, de las que se obtiene el primer tramo de seda. La araña inmovilizada se sitúa sobre la base de una máquina universal de ensayos Instron 4411. Posteriormente se une el tramo inicial de seda a un trozo de poliestireno expandido acoplado a un imán. Este imán se fija a una célula de carga inductiva HBM Q-11 que permite medir la fuerza con la que se extrae el hilo en cada momento. La célula de carga se encuentra situada en la mordaza móvil de la máquina de tracción, mientras que la araña inmovilizada se coloca en la base de la máquina. El proceso de extracción del hilo se lleva a cabo desplazando la mordaza móvil a velocidad constante mientras que la araña permanece fija en la base de la máquina. Se ha obtenido seda a dos velocidades de hilado: 50 mm/min y 500 mm/min. Con este método de extracción de hilo se obtiene aproximadamente 1 metro de fibra. La técnica de hilado forzoso en máquina de tracción tiene la ventaja de que las fibras obtenidas presentan la menor variabilidad observada en los distintos procesos de hilado permitiendo identificar el efecto de la radiación UV mediante la comparación de los resultados obtenidos a partir de muestras irradiadas y de muestras control sin irradiar.

Para determinar la influencia de la radiación UV en las propiedades mecánicas de la seda de araña y su relación con los diferentes estados de alineamiento molecular hemos hecho uso del proceso de supercontracción. La inmersión de las fibras de seda MAS en agua, sin impedir su acortamiento, produce una serie de cambios en sus propiedades; a este fenómeno se le conoce como supercontracción y se caracteriza por una disminución de más del 50 % de la longitud inicial de fibras. A las fibras sometidas al proceso de supercontracción se las denomina fibras MS [14] y corresponden al estado de máximo enrollamiento (o equivalentemente de mínimo alineamiento) de las proteínas de la seda. Por el contrario, las fibras obtenidas mediante hilado forzoso, denominadas fibras FS, se encuentran en el estado de máximo alineamiento de sus proteínas.

Para la irradiación de las muestras se utilizan dos lámparas ultravioleta modelo Vilmer Lourmat 215 LC de 15 W de potencia. Una de ellas puede emitir a 254 nm y 365 nm y la otra emite a 312 nm.

Para poder determinar los cambios en las propiedades mecánicas de la seda de araña tras el proceso de irradiación se han realizado ensayos mecánicos de tracción simple. A partir de ellos se han determinado las curvas fuerza-desplazamiento del material utilizado. Una vez obtenidas estas curvas y mediante la medida de la sección transversal de la seda en el microscopio electrónico de barrido se han determinado las curvas tensión ingenieril-deformación ingenieril. Para realizar los ensayos mecánicos se ha utilizado la máquina Instron 4411 en la que se ha sustituido la mordaza inferior de por una balanza de precisión modelo PRECISA XT 220 A con una resolución de 0.1mg (1μN) [14]. Todos los ensayos mecánicos se han hecho en condiciones nominales de 25ºC y 35% de humedad relativa.

Las superficies de fractura se obtuvieron a partir de los extremos del hilo que quedan después de realizar el ensayo de tracción. Las muestras fueron recubiertas con grafito para aumentar su resistencia frente al haz electrónico, permitiendo su observación en el microscopio electrónico de barrido sin dañar la seda. Una vez depositado el grafito se metalizan las muestras con oro durante 4 minutos. Posteriormente fueron observadas y fotografiadas en un microscopio electrónico de barrido JEOL 6300. Las condiciones típicas de observación han sido un voltaje de 10kV y una intensidad de 6.10^{-10} A, aunque estos parámetros se han variado dependiendo de la necesidad de observación de cada muestra. Las imágenes se han obtenido con aumentos entre x10000 y x15000.

3. RESULTADOS Y DISCUSIÓN

En la figura 1 se muestran las curvas tensión-deformación ingenieriles obtenidas para las fibras FS obtenidas mediante hilado forzoso sometidas a diferentes tiempos de irradiación con luz UV de longitud de onda de 254 nm.

En primer lugar, se observa una flexibilización del material, además de una disminución de la tensión y deformación de rotura a medida que aumenta el tiempo de irradiación de las muestras.

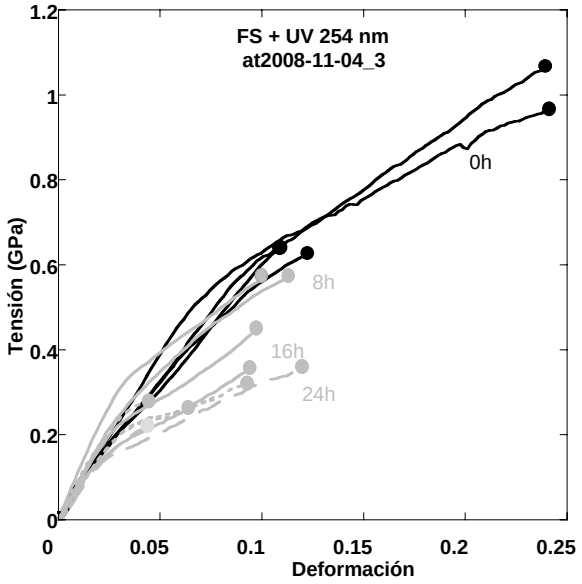

Figura 1. Curvas tensión ingenieril–deformación ingenieril de fibras FS sometidas a diferentes tiempos de irradiación con luz ultravioleta de 254nm.

La figura 2 muestra el efecto de la radiación UV de λ=254 nm sobre las propiedades mecánicas de muestras sometidas al proceso de máxima supercontracción (fibras MS) e irradiadas a tiempos variables.

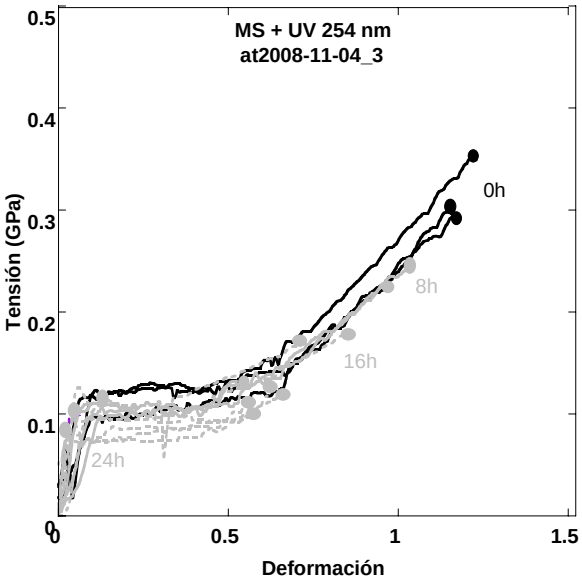

Figura 2. Curvas tensión ingenieril–deformación ingenieril de fibras MS sometidas a diferentes tiempos de irradiación con luz ultravioleta de 254nm.

A diferencia de los que ocurría en las fibras FS, en las fibras MS irradiadas con luz UV de 254 nm no se observa flexibilización apreciable del material. Al igual que en el caso anterior se observa una disminución de la tensión y de la deformación de rotura a medida que aumenta el tiempo de irradiación.

En la figura 3 se muestran las curvas tensión deformación ingenieriles para muestras de seda irradiadas con luz UV de 254 nm y posteriormente supercontraídas.

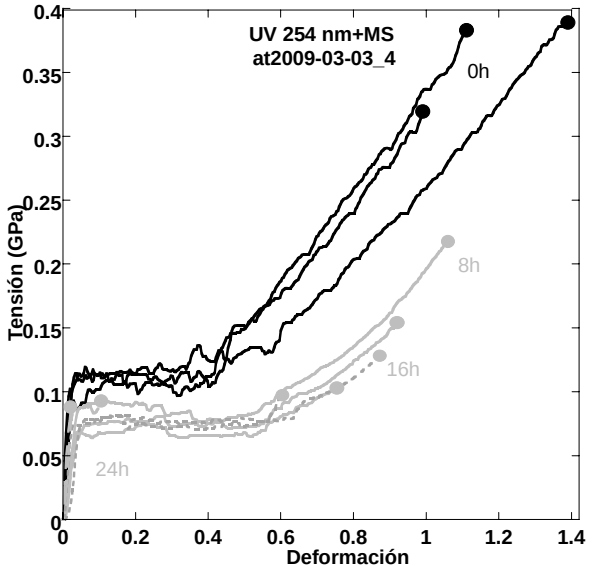

Figura 3. Curva tensión ingenieril-deformación ingenieril de fibras FS sometidas a diferentes tiempos de irradiación con luz ultravioleta de 254nm y luego supercontraídas.

En este caso se aprecia una disminución significativa de la tensión de la meseta (región entre el límite elástico y el comienzo de la rama de endurecimiento en la que la tensión es prácticamente constante) a medida que aumenta el tiempo de irradiación. Además, al igual que ocurría en las muestras FS y MS sometidas a diferentes tiempos de irradiación con luz UV, se aprecia una disminución de la tensión de rotura y de la deformación de rotura a medida que aumenta el tiempo de irradiación.

En la figura 4 se representan nuevamente las curvas de las muestras sometidas a irradiación y posterior supercontracción. En este caso, y a diferencia de la figura 3, se representa en el eje de abscisas el valor de L/L_0 donde L es la longitud instantánea de la fibra y L_0 la longitud en el estado FS. Esta representación tiene la ventaja de que permite tener en cuenta la posible influencia de la radiación UV en la longitud de supercontracción. En efecto, el primer valor del eje x para cada curva es una medida de la longitud que se ha supercontraído el hilo. De esta manera es fácil apreciar que en el proceso de supercontracción de las muestras FS irradiadas, a medida que aumenta el tiempo de exposición a la luz UV, las fibras se supercontraen menos.

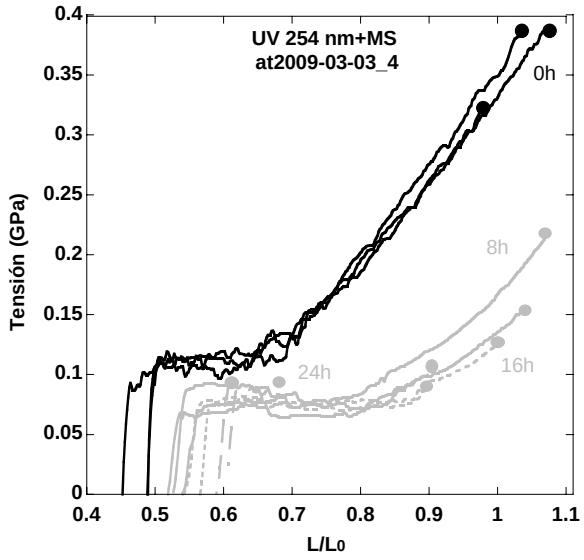

Figura 4. Curva tensión ingenieril-longitud (L/L_0) de hilos sometidos a diferentes tiempos de irradiación con luz ultravioleta de 254nm y luego supercontraídos.

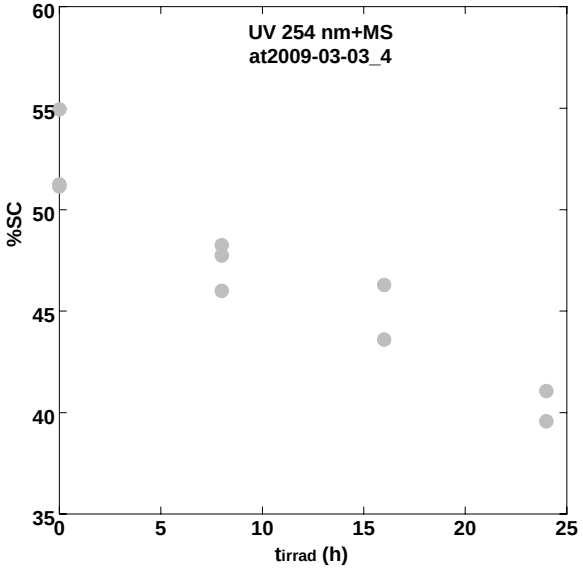

Figura 5. Porcentaje de supercontracción frente al tiempo de irradiación (t_{irrad}) de hilos FS sometidos a diferentes tiempos de irradiación con luz ultravioleta de 254nm y luego supercontraídos.

La longitud de supercontracción, que llamaremos L_{MS}, es la longitud de las fibras irradiadas y supercontraidas al comienzo del ensayo, es decir cuando la tensión es cero. En la gráfica se ve que, a medida que aumenta el tiempo de exposición a la radiación UV de las muestras de seda, la longitud de supercontracción es mayor y por tanto las muestras se supercontraen menos. Dicha menor contracción al incrementarse el tiempo de exposición a la radiación UV de las muestras de seda se pone de manifiesto más claramente si se representa gráficamente el porcentaje de supercontracción (%SC) frente al tiempo de irradiación (Figura 5). El porcentaje de supercontracción se define de la siguiente forma:

$$\%SC = 100 \times \frac{L_0 - L_{MS}}{L_0} \qquad (1)$$

Siendo L_0 la longitud inicial de la muestra en el estado de alineamiento FS y L_{MS} la longitud de la muestra supercontraída.

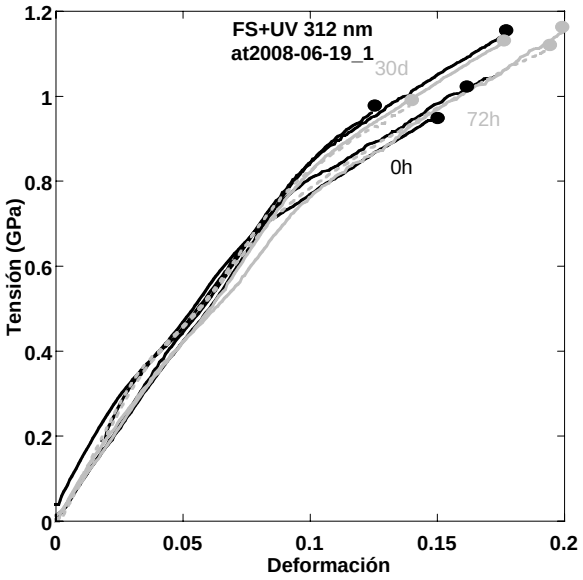

Figura 6. Curva tensión ingenieril–deformación ingenieril de fibras FS sometidas a diferentes tiempos de irradiación con luz ultravioleta de 312nm.

La radiación UV de 312 nm (Figura 6) y 365 nm (Figura 7) no producen ningún efecto sobre las propiedades mecánicas de la seda de araña.

Como se ha mostrado, la radiación UV de longitud de onda de 254 nm es la única de las utilizadas en este trabajo que modifica las propiedades mecánicas de la seda de araña. En particular se ha comprobado que la irradiación a esa longitud de onda provoca una disminución en los valores de tensión y deformación de rotura junto con una flexibilización de las fibras FS. En las muestras MS sometidas a diferentes tiempos de irradiación con luz UV también se aprecia la disminución de las tensiones y deformaciones de rotura al aumentar el tiempo de irradiación, no modificándose el aspecto general de la curva. En las muestras irradiadas y luego supercontraídas la disminución de la tensión de la meseta es acusada produciéndose también una disminución en el porcentaje de supercontracción al aumentar el tiempo de irradiación.

Los resultados obtenidos no permiten discernir si los efectos asociados con la irradiación UV son el resultado de un acortamiento de las cadenas o, por el contrario, de la formación de entrecruzamientos entre las cadenas, ya que es posible justificar los resultados macroscópicos bajo ambas condiciones. Si bien, cada una implica unos

micromecanismos de deformación y rotura radicalmente diferentes. La distinción entre ambos posibles fenómenos deberá realizarse mediante el empleo de técnicas bioquímicas.

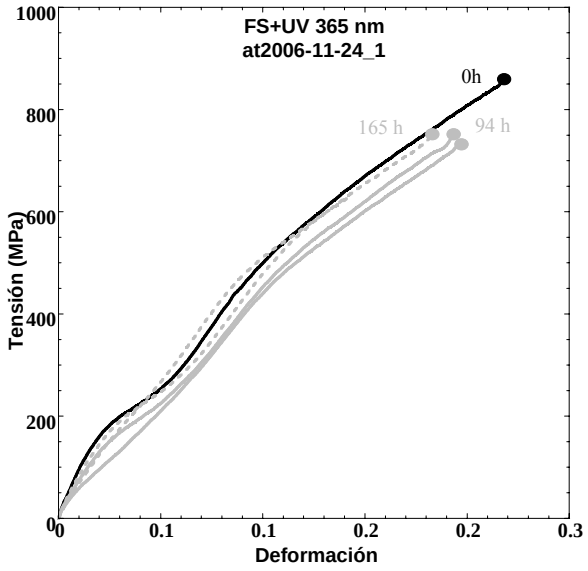

Figura 7. Curva tensión ingenieril–deformación ingenieril de fibras FS sometidas a diferentes tiempos de irradiación con luz ultravioleta de 365 nm.

Debido a que la radiación UV de longitudes de onda de 312nm y 365nm no produce ningún efecto sobre las propiedades mecánicas de la seda de araña, el análisis fractográfico se ha restringido a muestras irradiadas con luz UV de 254 nm (Figuras 8 y 9).

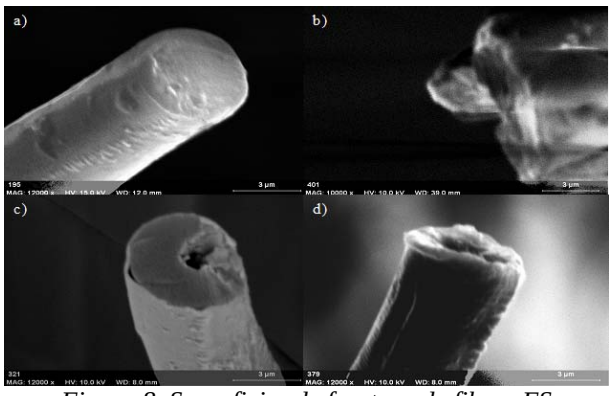

Figura 8. Superficies de fractura de fibras FS irradiadas, expuestas a tiempos de irradiación de a) 0h, b) 8h, c) 16h y d) 24h.

En general podemos decir que en las superficies de fractura obtenidas se observa una ausencia de un mecanismo claro de disipación de energía durante la rotura, independientemente de que el material haya sido sometido a un proceso de supercontracción y del tiempo de exposición a la radiación de éste. Podemos decir que el comportamiento en fractura de la seda de araña es localmente frágil. Además se observa que, a medida que aumenta el tiempo de exposición a la radiación UV, las superficies de fractura presentan una topografía más rugosa, al menos en las muestras FS.

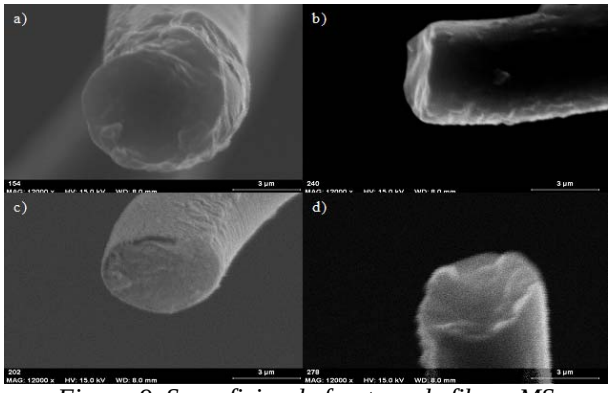

Figura 9. Superficies de fractura de fibras MS irradiadas, expuestas a tiempos de irradiación de a) 0h, b) 8h, c) 16h y d) 24h.

4. CONCLUSIONES

En las curvas obtenidas se observa que la radiación UV de longitudes de onda de 312 y 365 nm no produce ningún efecto sobre las propiedades mecánicas de la seda de araña. Sin embargo, la radiación UV de longitud de onda de 254 nm modifica considerablemente sus propiedades mecánicas. Se produce una disminución en los valores de tensión y deformación de rotura junto con una flexibilización del material en la condición FS a medida que aumenta el tiempo de exposición a la radiación. Por otra parte, se observa que en las fibras supercontraídas y luego irradiadas se produce un acortamiento de la meseta. Además se aprecia un importante efecto en el fenómeno de la supercontracción, observándose que las fibras se supercontraen menos a medida que aumenta el tiempo de irradiación.

En las fractografías no se observa un mecanismo claro de disipación de energía durante la rotura, definiéndose por tanto el comportamiento en fractura de la seda de araña como localmente frágil. Además, a medida que aumenta el tiempo de exposición a la radiación UV las superficies de fractura presentan una topografía más irregular y rugosa.

AGRADECIMIENTOS

Las arañas han sido mantenidas en cautividad por Óscar Campos. El trabajo ha sido financiado por el Ministerio de Educación y Ciencia (España) a través del proyecto CIT-420000-2008-30, por el Ministerio de Ciencia e Innovación (España) a través del proyecto MAT2009-10258 y por la Comunidad de Madrid (España) a través del programa MADR.IB-CM/S-SAL/0312/2006.

REFERENCIAS

[1] Kaplan, D.L., Lombardi, S.J., Muller, W.S y Fossey, S.A., Silks, Biomaterials, Byrom, D. (Ed.), Stockton Press, New York, pag. 1-53, 1991.

[2] Elices, M., Pérez-Rigueiro, J., Plaza, G. and Guinea, G.V. , Recovery in spider silk fibers, J. Appl. Polym. Sci. 92, 3537-3541, 2004.

[3] Elices M., Guinea G.V., Plaza G., Pérez-Rigueiro J., *Argiope trifasciata Spider Silk Fibers*, Journal of Materials, núm. Febrero, 2005.

[4] Izquierdo Rojo M., *Ingeniería Genética*, Ediciones Pirámide, Madrid, 1993.

[5] Viney C., Silk Fibers: Origins, Nature and Consequences of Structure en Structural Biologicial Materials, Elices M. (Ed.), Pergamon Materials Science, Amsterdam, pag. 293-334, 2000.

[6] Mello, C. M., Senecal, K., Yeung, B., Vouros, P. y Kaplan, D., Initial characterization of Nephila clavipes dragline protein en Silk Polymers. Materials Science and Biotechnology Kaplan D., Adams W.W., Farmer B., Viney C. (Eds.), ACS Symposium Series 544, pag. 67-79, 1994.

[7] Pérez Rigueiro J., Elices M., Plaza G. R. y Guinea G.V., *El efecto de la irradiación ultravioleta sobre la seda de araña,* Anales de Mecánica de la Fractura pag. 593-598, 2006.

[8] Rueda J., Pérez Rigueiro J., Elices M. y Guinea G.V., *Influencia de la radiación UV en el comportamiento a fractura del hilo de arama*, Anales de Mecánica de la Fractura pag. 343-348, 2002.

[9] Stryer, L., *Bioquímica*, Editorial Reverté, Barcelona, pag. 15-42, 1990.

[10] Becker, M.A. y Tuross, N., Initial degradative changes found in B. mori silk fibroin en Silk Polymers. Materials Science and Biotechnology Kaplan D., Adams W.W., Farmer B., Viney C. (Eds.), ACS Symposium Series 544, pag. 253-269, 1994.

[11] Work, R.W., Dimensions, birefringences, and force-elongation behaviour of major and minor ampullate silk fibers from orb-web-spinning spiders.The effect of wetting on these properties, Textile Res. J., 47, pag. 650-662, 1977.

[12] Gosline, J.M., Denny, M. y DeMont, M.E., Spider silk as rubber, Nature, 309, pag. 551-552, 1984.

[13] Pérez Rigueiro, J., Elices, M., Plaza, G., Real, J. I., Guinea, The effect of spinning forces on spider silk or propierties, The Journal of Experimental Biology 208, pag. 2633-2639, 2005.

[14] Guinea, G.V., Elices, M., Pérez-Rigueiro, J., Plaza, G.R., Stretching of supercontracted fibers: a link between spinning and the variability of spider silk, J. Exp. Biol., 208, pag. 25-30, 2005.

MODE I FRACTURE OF CORTICAL BONE TISSUE

F.A.M. Pereira[1], N. Dourado[1], J.J.L. Morais[1], M.F.S.F. de Moura [2], J.M.C. Xavier[1], M.I.R. Dias[3], J.M.T. Azevedo[4]

[1] CITAB/UTAD, Departamento de Engenharias, Quinta de Prados, 5001-801
Vila Real, Portugal
E-mail: nunodou@gmail.com
[2] Faculdade de Engenharia da Universidade do Porto, Departamento de Engenharia Mecânica e Gestão Industrial, Rua Dr. Roberto Frias, 4200-465 Porto, Portugal
E-mail: mfmoura@fe.up.pt
[3] UTAD, Departamento de Ciências Veterinárias, Quinta de Prados, 5001-801
Vila Real, Portugal
[4] CECAV/UTAD, Departamento de Zootecnia, Quinta de Prados, 5001-801
Vila Real, Portugal

ABSTRACT

The objective of this work is to analyse the adequacy of the Double Cantilever Beam (DCB) test to determine the fracture toughness under pure mode I loading of cortical bone tissue. A data reduction scheme based on specimen compliance and crack equivalent concept is used to overcome the difficulties inherent to crack monitoring during its growth. The data reduction scheme provides a complete resistance curve, which is fundamental to estimate the fracture energy. The obtained results demonstrate the efficacy of the DCB test and the proposed data reduction scheme on the bone fracture characterization under mode I loading.

KEY WORDS: bone, fracture, mode I loading, DCB test

1. INTRODUCTION

The development of accurate testing methods to evaluate bone toughness is fundamental, since it provides an essential tool to predict the age-related bone fracture risks and associated bone diseases [1-3]. The compact tension test [1] and the single-edge notched specimen under three point bending [4] are frequently used in bone fracture characterization under mode I loading. The difficulties associated to get specimens with the required size lead to the employment of the single-layer compact sandwich specimen [3]. In this specimen a bone coupon was sandwiched between two holders of polymethylmethacrylate.

In order to overcome the difficulties associated to the definition of a suitable test, the objective of this work is to analyze the adequacy of the Double Cantilever Beam (DCB) test to determine the fracture toughness under pure mode I loading of cortical bovine bone tissue (Figures 1 and 2). This test is particularly adequate for mode I fracture characterization due to its simplicity and the possibility to use the beam theory to measure the fracture energy. However, the classical data reduction schemes used for the DCB, are usually based on crack length (a) monitoring during its growth, which was observed to be very difficult to perform with accuracy in this quasi-britlle material (Figure 3). To overcome this drawback, a data reduction scheme [5] based on specimen compliance (C) and crack equivalent concept was used. The method is based on the beam theory to establish the $C = f(a)$ relationship. The equivalent crack length (a_e) is estimated from the current compliance measured during the experimental test. The Irwin-Kies equation is used to compute the toughness (G_{Ic}) as a function of a_e. This procedure provides the complete R-curve estimate, which is fundamental to get the fracture energy.

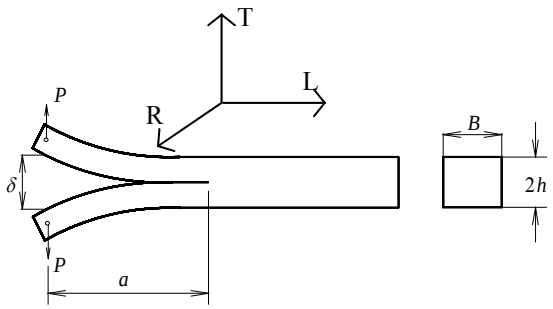

Figure 1. DCB test (a = 20, B=2 and h=3.5 mm).

2. DATA REDUCTION SCHEME

The developed data reduction scheme is known as Compliance Based Beam Method (CBBM) since it uses the Timoshenko beam theory to establish the relationship [5]

$$C = \frac{8a^3}{E_L B h^3} + \frac{12a}{5BhG_{LT}} \quad (1)$$

where E_L is the longitudinal elastic modulus and G_{LT} the shear modulus in the TL plane (Figure 1). This equation can be used to estimate the equivalent crack length as a function of the current compliance C computed directly from the measured load-displacement (P-δ curve, i.e. $a_e = f(C)$). The solution of this equation is obtained using the Matlab® software. Following this procedure the effect of the FPZ is taken into account, since its presence affects the current compliance. The combination of Eqs. (1) and Irwin-Kies's

$$G_I = \frac{P^2}{2B}\frac{dC}{da} \quad (2)$$

leads to

$$G_I = \frac{6P^2}{B^2 h}\left(\frac{2a_e^2}{E_L h^2} + \frac{1}{5G_{LT}}\right) \quad (3)$$

Using this method a complete R-curve is determined without the direct measurement of a_e.

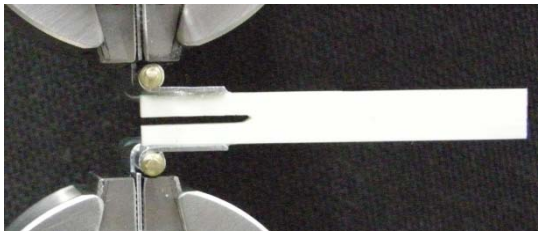

Figure 2. DCB test setup.

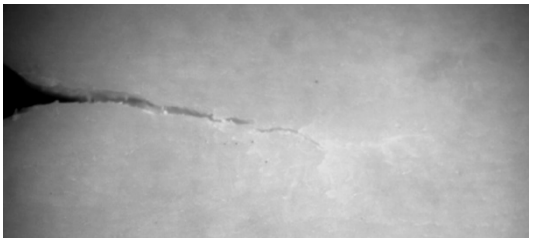

Figure 3. Crack-tip detail in bone under loading.

3. EXPERIMENTAL TESTS

A total number of nine DCB specimens with a length of 60 mm were machined using a milling machine to get the nominal dimensions (Figure 1): $B = 2$, $h = 3.5$ and $a_0 = 20$ (dimensions in mm). The initial crack length a_0 was introduced in two steps. First, a notch (1 mm thick) was machined using a circular saw. Then, a pre-crack (depth: 0.5 – 1.0 mm) was created just before the fracture tests, by tapping a sharp razor blade into the notch. The specimens were orientated with the initial crack in the TL propagation system (where T is the normal to the crack plane and L is the crack propagation direction, Figure 1) and the nominal crack-growth direction along the proximal–distal direction of the femur. The specimens were kept moist at all steps of the machining process with physiological saline. Moreover, they were wrapped in gauze soaked in physiological saline, and frozen at -20ºC for storage.

A servo-electrical material testing system (MicroTester INSTRON 5848) was used to undergo fracture tests under displacement control and normal environmental conditions (65% RH at 20°C). A 2 kN load-cell was installed and the displacement rate of the actuator was set to 0.5 mm/min. The acquisition frequency was set to 5Hz. The loading was applied to the specimen through a couple of piano hinges (Figure 2), thus inducing a pure mode I loading. Piano hinges were bonded to the specimen using a fast curing epoxy adhesive. Figure 3 shows the difficulty associated to the direct crack-length (a) measurement during damage progression.

4. EXPERIMENTAL RESULTS

Figures 4 and 5 present the typical P-δ and the corresponding R-curve, obtained using the proposed data reduction scheme. The P-δ curve shows a pronounced non-linear behaviour near the peak load. This trend is explained by the existence of a pronounced fracture process zone (FPZ) constituted by micro-cracking and crack-branching (Figure 3).

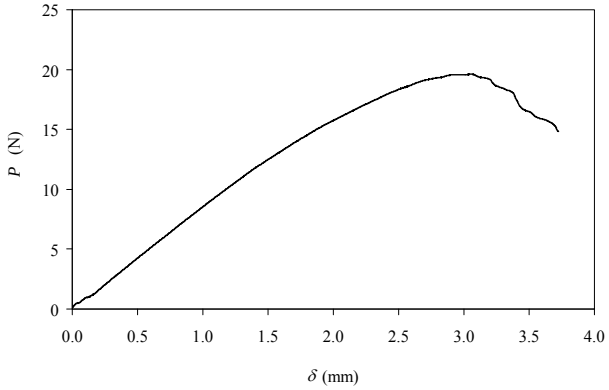

Figure 4. Typical P-δ curve of bone (mode I).

The consequence of this softening process is a ductile behaviour which is reflected on the referred non-linear profile of the P-δ curve. Consequently, the respective R-curve (Figure 5) shows a large

ascending branch (approximately 3 mm of a_e) till the plateau value defining the material fracture energy (G_{Ic}) is attained (i.e., approximately 2.0 N/mm in Figure 5). The extensive ascending branch corresponds to the FPZ development up to its critical size, from which the self-similar crack growth takes place, leading to conditions for an appropriate measurement of the material fracture energy. Table 1 presents a summary of the elastic modulus and fracture energy obtained for nine tested specimens. The coefficient of variation is acceptable for this type of material. Effectively, bone is a natural material exhibiting a high variability in its properties.

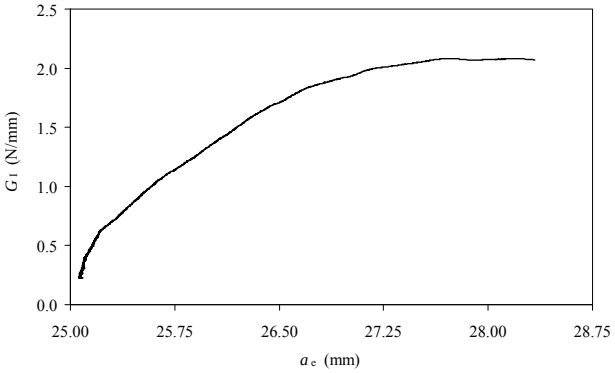

Figure 5. R-curve of bone under mode I.

Table 1. Fracture test results of cortical bone.

	Experimental	
Specimen	E_L (GPa)	G_{Ic} (N/mm)
1	19.498	1.606
2	16.659	1.690
3	17.323	2.224
4	17.984	2.133
5	22.375	1.524
6	19.857	2.050
7	21.098	1.715
8	21.364	2.367
9	23.311	1.893
Average	19.94	1.91
Cov (%)	11.53%	15.53%

5. CONCLUSIONS

In this work fracture of cortical bone tissue from young bovine femur under mode I loading was analysed. The double cantilever beam test was used with success, which constitutes an important result owing to significant advantages that this test presents relatively to other fracture tests for mode I fracture characterization. In addition, a new data reduction scheme based on the specimen compliance and crack equivalent concept was applied. The compliance based beam model does not depend on crack measurements during its growth and allows the attainment of the entire *Resistance*-curve (*R*-curve), thus leading to the clear identification of fracture energy. The experimental tests were performed on bone specimens, considering the TL propagation system. The *R*-curves obtained using the proposed data reduction scheme, clearly show that a plateau value defining the fracture energy of cortical bone under mode I loading is easily obtained.

The principal achievements of this work put into evidence the applicability of the double cantilever beam test applying the described data reduction method to determine the fracture energy of bone under mode I loading.

ACKNOWLEDGEMENTS

The authors thank the Portuguese Foundation for Science and Technology for supporting the work here presented, through the research project PTDC/EME-PME/71273/2006.

REFERENCES

[1] Norman TL, Vashishth D, Burr DB. Fracture toughness of human bone under tension. J Biomech 1995, 28(3): 309-320.

[2] Vashishth D, Tanner KE, Bonfield W. Contribution, development and morphology of microcracking in cortical bone during crack propagation. J Biomech 2000, 33: 1169-1174..

[3] Wang X, Agrawal CM. Fracture toughness of bone using a compact sandwich specimen: effects of sampling sites and crack orientation. J Biomed Mater Res 1996, 33: 13-21.

[4] Phelps JB, Hubbard GB, Wang X, Agrawal CM. Microstructural heterogeneity and the fracture toughness of bone. J Biomed Mater Res 2000, 51: 735-741.

[5] de Moura MFSF, Morais J, Dourado N. A new data reduction scheme for mode I wood fracture characterization using the double cantilever beam test. Eng Fract Mech 2008, 75:3852-65.

CONTACT DAMAGE IN ARTIFICIALLY AGED 3Y-TZP

Z de Armas Sancho, A Mestra, E Jiménez-Piqué and M Anglada

Centro de Integridad Estructural y Fiabilidad de los Materiales, CIEFMA
Dpto de Ciencia de los Materiales e Ingeniería Metalúrgica
Universitat Politècnica de Catalunya, UPC
Av. Diagonal 647, 08028 Barcelona, Spain
zamirfim@ yahoo.es

ABSTRACT

Tetragonal zirconia polycrystals doped with 3% mol of yttria (3Y-TZP) are increasingly employed as implants in the human body, because they are biocompatible and have relatively high strength and fracture toughness. These properties are related to the small submicrometer grain size and to the operation of a toughening mechanism around cracks which is referred to as phase transformation toughening. Another important feature of 3Y-TZP is the phenomenon of low temperature degradation (LTD) that takes place in contact with water at temperatures in an interval around 250 ºC. Water activates t-m transformation at the surface and progresses inside the body producing a t-m surface transformed layer. As a result, roughness and microcracking are produced in the surface. In a first stage, for short times of ageing, this layer is responsible for degradation of surface mechanical properties; at a later stage, after long degradation times, it induces a strong reduction in the bulk strength.
In this paper we present a study of the mechanical behaviour of hydrothermal degraded 3Y-TZP under monotonic and cyclic spherical indentation. The investigation is focused mainly on analyzing the mechanical response of the material under spherical indentation in terms of the degraded layer. Plastic deformation and cracking induced by spherical contact loading are studied under increasing loads in hydrothermally degraded and in as sintered specimens. The contact hardness and elastic modulus of the degraded layer are extracted from nanoindentation using continuous stiffness measurements. It is found that permanent damage induced in degraded specimens is always larger than in as sintered specimens. Critical loads to induce ring cracking in degraded specimens are lower than in as sintered specimens.

KEY WORDS: Contact Fatigue, Strength Degradation, Zirconia.

1. INTRODUCTION

Tetragonal zirconia polycrystals doped with 3% mol of yttria (3Y-TZP) are increasingly employed as implants in the human body because of their biocompatibility and relatively high strength and fracture toughness (1000 MPa, 5 $MPam^{1/2}$) [1]. The reason for these relatively high mechanical properties is a small grain size and a phase transformation toughening mechanism based on the stress-assisted tetragonal to monoclinic (t-m) transformation around the crack tip, which is accompanied by an increase in volume of about 4% [2]. This transformation leads to the development of localised compressive stresses around the crack flanks inducing in this way a drop in the crack tip stress intensity factor.

Another important feature of 3Y-TZP is the phenomenon referred to as low temperature degradation (LTD) that takes place when the material is exposed to water. Water activates the t-m transformation at the surface, which progresses into the bulk producing a monoclinic surface layer [3]. As a result, the surface roughness is increased and micro-cracking appears inside this layer. Initially, only the mechanical properties of the surface are degraded, with lower hardness and elastic modulus than the interior [4]. But, at later stages, a strong reduction in the bulk strength is also observed. LTD is easily detected after a few hours of degradation at temperatures around 250 C, but it has been also observed on femoral heads of 3Y-TZP of hip-joint replacements several years after implantation [5].

In the present work, we have studied damage under spherical contact fatigue in 3Y-TZP previously degraded by exposure to LTD for different periods of time. The results are compared with the behaviour of the non-degraded as sintered material.

Hertzian indentation is a method very extended for studying contact mechanics in brittle materials [6]. This methodology allows evaluating the damage and deformation produced by the contact of a sphere with a solid surface. One advantage is that it allows observing the evolution of the damage mechanisms through a progressive transition from the initial elasticity regime until the development of full plastic regime. This is not possible with an indent with a sharp tip since plastic deformation takes place from the beginning of the contact with the surface. In addition, there are analytical expressions for the elastic problem of a solid under Hertzian contact loading.

In ceramic materials, the contact of a sphere with the surface induces two main types of damage [7]. One occurs in low fracture toughness ceramics and is the

appearance of a circular crack near the radius of contact of the sphere with the surface, which eventually extends into the bulk in the form of a cone. This type of damage was reported by Hertz as early as in 1881 (cone cracking).

Another type of damage may occur in tough ceramics and consists in the appearance of a "cuasi-plastic" damage zone below the contact area which is characterized by the formation of microcracks [8].

Numerous studies are reported about contact fatigue in ceramics [9-11]. In the present work, the fatigue by spherical contact in 3Y-TZP has been studied for several times of LTD. Due to the loads and to the indenter radius, the damage zone studied includes both the transformed layer formed during degradation, as well as the non-affected tetragonal bulk.

2. MATERIALS AND METHODS

The starting material was commercial TZ-3YSB-E powder (Tosoh, Japan), with an average crystallite size of 27 nm. About 40 g of powder was placed in a cylindrical polymeric mould in an ultrasonic bath for 15 minutes in order to homogenize the powder. Then, the closed mould was cold isostatically press under a 200 MPa applied pressure during 3 minutes. The produced green bodies were sintered at 1450 ºC for 2 hours with heating and cooling ramps of 3 ºC/min.

The cylinders were cut into 2 mm thick discs, which were ground with a diamond disc of 68 µm average particle size, and finally they were polished up to colloidal silica finish (30 nm) in order to have mirror-like appearance. The density was measured by Archimedes method and it was found to be 6.01 g/cm^3 which is 99% of the theoretical density.

Hydrothermal ageing was performed in an autoclave maintaining a steam atmosphere at a temperature of 131 ºC and at pressure of 2 bars for different times (10, 30 and 60 hours). The specimens degraded for these times will be referred to as D10, D30 and D60 respectively, while the non-degraded as sintered specimens will be referred to as "AS".

The microstructure and damage were observed by optical microscopy, confocal laser microscopy and scanning electron microscopy (SEM). The monoclinic phase content was analysed by micro-Raman spectroscopy and atomic force microscopy (AFM).

2.1 Monotonic Spherical Indentation

Several types of monotonic tests were carried out. Contact hardness and elastic modulus were determined by nanoindentation with a Berkovich tip up to 2 µm depth. The Berkovich tip was calibrated against a standard fused silica. Nanoindentation tests were performed with a MTS Nanoindenter XP with a continuous stiffness measurement (CSM) module, which allows continuous measurement of contact stiffness (S) and load (P) as a function of penetration depth (h). Indentations were made to a maximum load of 500 mN to a maximum penetration depth of about 1600 nm, and under a constant deformation velocity of 0.05 s^{-1}. Nine indentations were made as 3x3 matrices on each material and the results were presented with standard deviation. The values of hardness (H) and Young's modulus (E) were calculated as a function of penetration depth using the method of Oliver and Pharr [12]. In this method, the contact depth is estimated from the load-displacement data using:

$$h_c = h_{\max} - e\frac{P_{\max}}{S} \quad (1)$$

Where, $P_{\max}$ is the peak indentation load and e is a constant which depends on the indenter geometry [13] and S is the contact stiffness. Empirical studies have shown that e ˜ 0.75 for a Berkovich indenter. From the measurements of load and displacement data, the projected contact area, *A*, of the indentation impression is estimated by evaluating indenter shape function at the contact depth, h_c; that is $A=f(h_c)$. The shape function, $f(d)$, relates the cross-sectional area of the indenter to the distance, *d*, from its tip.

Once the contact area is determined from the load displacement data, the hardness, *H*, and effective elastic modulus, E_{eff}, were calculated as follows.

$$H = \frac{P_{\max}}{A} \quad (2)$$

$$E_{eff} = \frac{1}{b}\frac{\sqrt{p}}{2}\frac{S}{\sqrt{A}} \quad (3)$$

Where ß is equal to 1.034 for a Berkovich tip. This technique provides data with continuous measurement of the hardness and elastic modulus as a function of depth.

Nanoindentation with a spherical tip of radius R=25.75µm was also used to record the elastic and plastic regimes of deformation. For a spherical indenter of radius R, in the elastic regime there is a linear relation between the average contact pressure p_0 and the indentation strain, *a/R* [6]:

$$p_0 = \left(\frac{3E}{4pk}\right)\cdot\frac{a}{R} \quad (4)$$

where p_0 is defined as a function of the applied load *F* and the contact radius *a*:

$$p_0 = \frac{F}{p\,a^2} \quad (5)$$

and k is a constant which depends on the elastic properties of the indenter and the material:

$$k = \frac{9E}{16}\left(\frac{1-n^2}{E} + \frac{1-n'^2}{E'}\right) \quad (6)$$

The contact radius is related to the depth of the circle of contact by:

$$a \approx \sqrt{2Rh_c} \quad (7)$$

Here, E, ν and E´, ν´ are elastic modulus and Poisson's ratio of the material and indenter, respectively.

The average indentation pressure was measured against a/R and according to equation (4) in the elastic regime and a straight line should result. At higher pressures plastic deformation takes place, but still it is interesting to plot p_0 against a/R since by the empirical Meyer's law it can be demonstrated that the curve obtained is independent of the radius of the sphere. Macroscopic tests with a sphere of larger radius were focused on obtaining the indentation stress - strain curves and the critical load for damage appearance. The tests were performed in a universal testing machine (Instron Model 8511), using cemented tungsten carbide spheres of radius R =1.25 mm, in a range of loads between 500 and 3000 N. The load was increased in steps of 100 N. It was applied at a speed of 20 N/s using a 50 N preload in laboratory air environment and with a relative humidity of 20 - 45%. For each degradation condition, three samples were tested.

After unloading, each specimen was examined in the optical microscope to detect permanent deformation and surface cracks. If damage was detected, further closer observation was performed with a confocal laser microscope. In the monotonic contact tests, the criterion used to define the critical load for cracking was the appearance of a well developed ring crack around the residual imprint. When such crack was detected, the specimen was cut into two halves perpendicular to the surface and carefully polished in order to reveal any progression of the surface ring crack into the bulk to form a cone crack.

2.2. Cyclic loading spherical indentation tests

Fatigue tests were performed under the same conditions as in monotonic loading for a range of cycles between 10 and 10^6. All fatigue tests were performed with a sinusoidal waveform of 15 Hz and R=0.1. According to the critical loads obtained for cracking in the monotonic tests, three load levels were chosen for fatigue characterization (500, 750 and 1000 N).

3. RESULTS AND DISCUSSION

3.1. Change in microstructure by degradation

The effect of degradation is to induce monoclinic phase in a surface layer. Although its concentration is not constant along the depth direction, as a first approximation, this layer will be considered as it had constant monoclinic concentration, that is, it shall be treated as a "coating" with well defined mechanical properties.

After long degradation times (more than 10 hours), the concentration of monoclinic phase is practically constant into the depth direction until there is a relatively sharp drop. Table 2 gives the main characteristics of the degraded layers.

Table 1. *Berkovich nanoindentation elastic modulus and hardness of AS and degraded layers.*

	Thickness of degraded layer (μm)	Elastic Modulus (GPa)	Hardness (GPa)
AS	-	220	16
D10	~ 2	-	15
D30	6.3	-	13
D60	12	170	11

Because of the existence of micro-cracks in this degraded layer [5], its elastic modulus is smaller than for the inner bulk material. That is, being the degradation layer more compliant, it will take up more deformation than AS.

3.2. Monotonic Spherical Contact Loading

Figure 1 shows the penetration curves up to a load of 600mN obtained from instrumented indentation with a spherical tip.

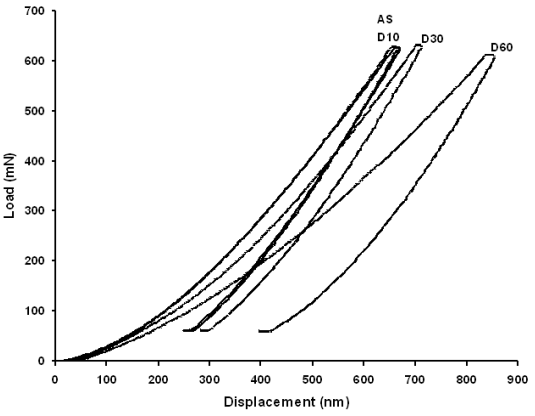

Figure 1: Load vs. displacement, instrumented nanoindentation

It can be appreciated that for specimens degraded for more than 10 hours the total and inelastic displacements are larger. This is in line with a thicker degraded layer produced during longer degradation times as well as with the fact the degraded layer is more compliant and has a lower strength than the "substrate" (AS material).

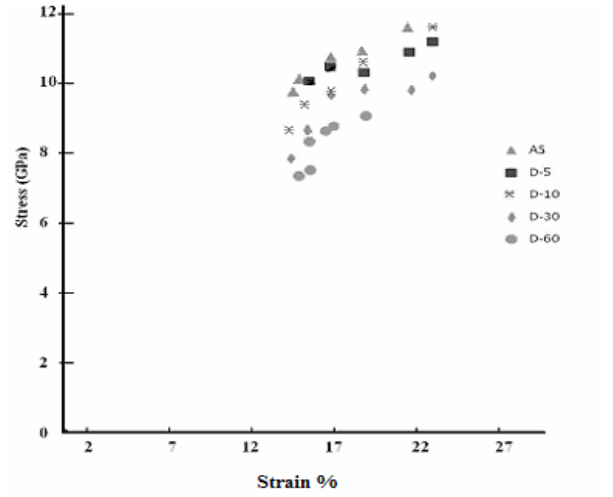

Figure 2. Mean pressure versus strain in spherical indentation tests.

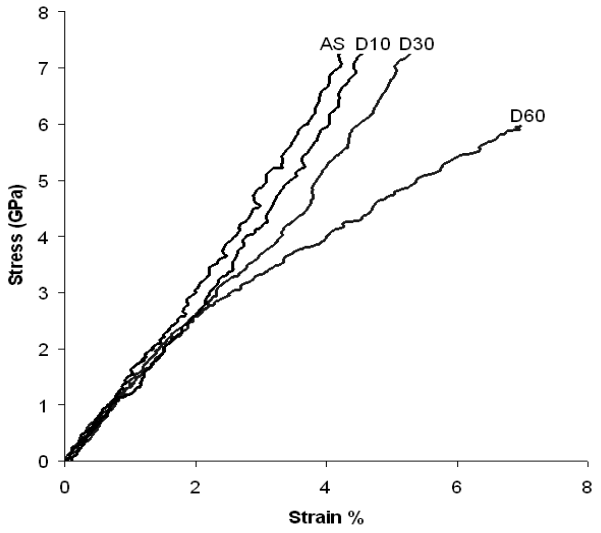

Figure 3. Stress vs. strain in nanoindentation test

Figure 2 shows the curves of mean pressure p_0 against indentation strain obtained by using the ball of 1.2 mm diameter in the specimens in the servo-hydraulic testing machine at high loads. It can be appreciated that the stress necessary to induce a given plastic strain in degraded specimens is smaller than in AS.

In degraded specimens, the effective elastic modulus of degraded layer + substrate measured by nanoindentation depends on the time of degradation and the depth of penetration. When the nanoindentation main elastic contribution comes from the degraded layer, the value of the elastic modulus for the degraded layer was found to be equal to about 170 GPa. However, it is obvious that in our macroscopic spherical indentation tests the elastic contribution of the "substrate" is very large because of the small thickness of the degraded layer in comparison with the contact radius. Because only residual deformation was measured in our macroscopic experiments, all experimental points are in the plastic regime. In order to measure the elastic and transition regime we use instrumented indentation with the contact area measured from the contact stiffness (see figure 3). Here it is very clear the proportionality between pressure and strain is lost at smaller pressures for the degraded specimens.

The elastic modulus for AS calculated from figure 3 (230 GPa), is close to the value of 220 GPa reported by Berkovich nanoindentation. The elastic modulus measured for D60 was 182 GPa, that is, lower than for AS. It is clear from the results shown in figure 3 that D60 exhibits a deviation from the elastic behaviour earlier than the rest of the samples.

The first damage observed is the residual deformation circular imprint and subsequently the formation of circular cracks around the first. As the load level was increased, the circular crack progresses towards the interior of the material in the form of a cone crack, as can be seen in figure 4.

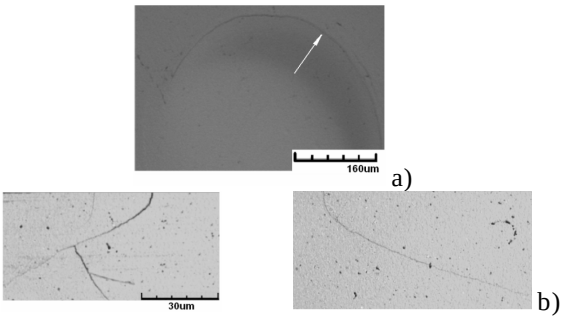

Figure 4. a) ring cracks on the top surface; b) cone cracks in the cross section.

The critical load P_c and the critical pressure p_{oc} for the appearance of the circular cracks in each one of the degradation stages of the material are given in table 2. These values correspond to the minimum monotonic load able to produce a complete circular crack around the residual imprint.

Table 2. Critical loads for the appearance of circular cracks in monotonic and cyclic contact loading

Sample	P_c (mont) (N)	p_{0c} (GPa)	Pfc (cyclic) (N)
D60	1500	8.88	750
D30	1800	9.95	900
D10	2300	10.6	1150
AS	3000	12.2	1500

3.3. Cyclic Spherical Contact Damage

The results of the contact fatigue tests for the three levels of maximum load tested are represented in figure 4 where it can be seen the number of cycles imposed at

each level together with information about the appearance of damage in form of a circular crack. The figure reveals that the material is always sensitive to fatigue. Clearly the critical amplitude for crack damage appears at loads lower than Pc (load for cracking under

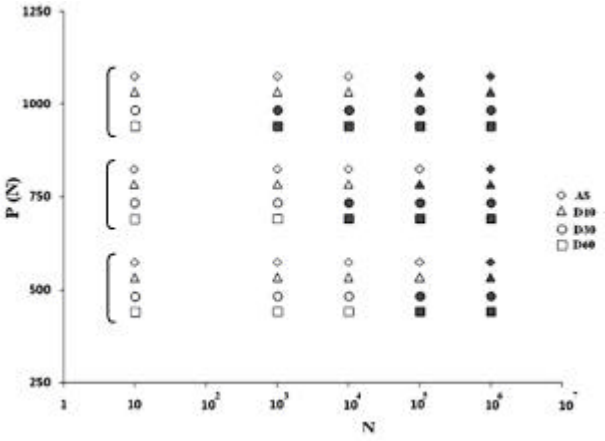

Figure 4. Load versus numbers of cycles. No critical damage is shown by open symbols whereas the presence of circular cracks is shown by closed symbols.

monotonic loading), and it diminishes as we increase the number of cycles. It can be also observed than the number of cycles needed for the appearance of damage depends on the duration of hydrothermal ageing. The degraded materials D30 and D60 offer a much lower resistance to contact loading. The non-degraded material does not reveal damage until a number of cycles of at least two orders of magnitude higher than for the degraded specimens.

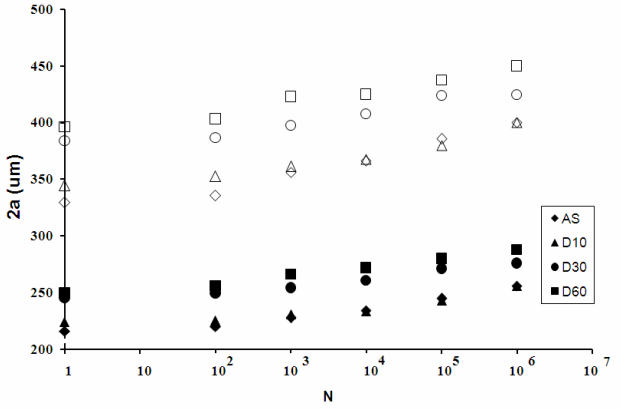

Figure 5. Residual spherical imprint diameter vs. number of cycles for two load levels: 1000N (open symbols) and 500N (closed symbols).

In figure 5, the diameter of the residual plastic imprint is plotted in terms of the number of cycles for the different cyclic loads and specimen conditions. For a given load level, the diameter of the residual imprint increases with the number of cycles. In addition, longer degradation times induce larger residual deformation for a fixed number of cycles.

Figure 6 displays the appearance of the residual imprint on the surface in terms of number of cycles and time of degradation. After the first 10^4 cycles, the residual imprint is clearly developed for all conditions. For larger number of cycles, two regions are observed: one rough annular region and the centre which is smoother.
The central part of the imprint is subjected to high normal pressure while just outside the contact radius is where there is the higher tensile stress and where the normal stress becomes zero. For AS at the surface near the contact radius, the maximum Hertz tensile stress is much lower than the yield point as well as for inducing either transformation or cracking. However, in the aged condition, the yield strength of the degraded layer is much lower than for the "substrate". Here from figure 3 it can be noticed that yielding for D60 takes place at stresses which are about 1/3 of the yield strength of AS. This has been also shown by Adrian e al [13] who showed that the system substrate+degraded layer could have a bend strength as low as 25% after (150 hours of ageing). However these stresses are higher than the maximum tensile elastic stress near the contact radius.

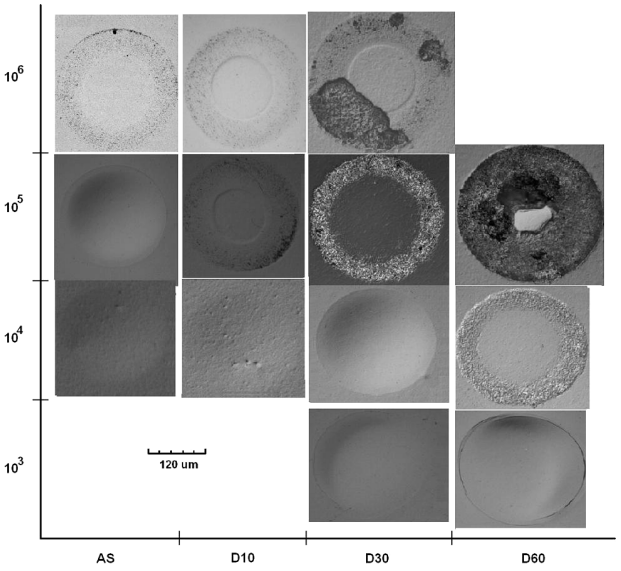

Figure 6. Evolution of the residual spherical imprint radius and damage with increasing number of cycles and time of degradation for a load amplitude of 500 N.

In the degraded layer there are microcracks which can be the nucleus for the generation of the ring crack. This is the reason for the earlier appearance of ring cracks in degraded specimens. This effect is stronger for specimens degraded for longer times. In this case not only there are many nuclei on the surface, but also in the depth direction, so that the extension of the ring crack into the depth will be easier.

For degraded specimens the first damage mechanism that takes place after the generation of the circular crack is the pull out of grains in an annular region close to the contact radius. Later there is superficial chipping in this region. Finally, a mechanism of fracture by layers appears that progresses inside the material.

For AS, the mechanisms of pull - out and micro-chipping take place for a number of cycles higher that 10^5 cycles, as it is observed in figure 7. In this material the susceptibility to damage will be marked by the transformation t - m that takes place during the process of cyclic indentation, since there is not initial micro-cracked region.

Micro-Raman spectroscopy analysis was carried out on AS specimens after 10^5 and 10^6 cycles of loading at a maximum load of 500 N (see, Table 3). Outside the contact zone no monoclinic phase was detected.

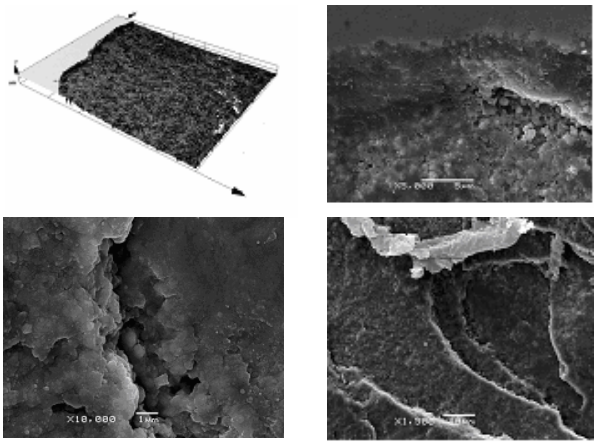

Figure 7. Damage for D30: a) Circular crack border. b) Pull out in the surface near de circular crack. c) Detail of circular crack; d) Final failure.

Table 3. Micro-Raman analysis on imprint of AS after contact fatigue with a maximum load of 500 N.

Cycles	Zones (residual imprint)	Monoclinic phase (volume %)
10^5	Center	7
	Border	12
10^6	Centre	13
	Border	20

4. CONCLUSIONS

The behaviour of 3Y-TZP under spherical indentation and contact fatigue has been studied in specimens subjected to LTD for different times of up to 60 hours. The main conclusions are:

1. The effect of degradation is clearly revealed by instrumented indentation and the degraded layer has lower hardness and elastic modulus than the substrate reaching yield strengths of about 25% after 60 hours of degradation.
2. The permanent deformation induced in degraded specimens is always larger than in the as sintered material.
3. The critical loads to induce ring cracking in degraded material are lower than in the as sintered material.
4. The damage induced by contact fatigue is larger in the specimens degraded for longer times, so that the degraded layer plays an important role in the failure related contact response of 3Y-TZP.

ACKNOWLEDGEMENTS

Financial support from Spanish "Ministerio de Ciencia e Innovación" under the project MAT 2008-03398 is greatly acknowledged. Z. de Armas acknowledges a scholarship from the Alßan Programme of the EU.

REFERENCES

[1] **Helmer J D, Driskell T D** *"Research on bioceramics" Symposium on Used of Ceramics as surgical Implants Clemson,* **South Carolina: Clemson University (1969).**

[2] **Poter D L, Heuer A H**. *"Mechanics of toughening partially stabilized zirconia (PSZ)"* **J. Am. Ceram Soc 60:183-184 (1977)**

[3] **Kobayashi K Kuwajima H, and Masaki T** *"Phase change and mechanical properties of ZrO2-Y2O3 solid electrolyte after ageing"* **Solid State Ion 3(4) 489-493 (1980)**

[4] **Gaillard Y, Jiménez E P, Soldera F, Mucklich F, Anglada M** *"Quantification of hydrothermal degradation in zirconia by nanoindentation"* **Acta Materialia Volume 56 Issue 16 Pages 4206-4216**

[5] **J. Chevalier, L. Gremillard and S Deville, "***Low temperature degradation of Zirconia and implications for Biomedical Implants"*. **Annu. Rev. Mater. Res. 37, 1-32 (2007)**

[6] **Lawn, B.R.** *"Indentation of ceramics with spheres: a century after Hertz."***J. Am. Ceram. Soc. 81.8 (1998): 1977-1994.**

[7] **Rhee, Y.-W., Kim, H.-W., Deng, Y., and Lawn, B.R**. *"Brittle fracture versus quasi plasticity in ceramics: a simple predictive index."* **J. Am. Ceram. Soc. 48.3 (2001): 561-565.**

[8] **Lawn, B.R., Padture, N.P., Cai, H., and Giberteau, F**. *"Making ceramics "ductile"."* **Science 263 (1994): 1114-1116.**

[9] **Kim, D.K., Jung, Y.-G., Peterson, I.M., and Lawn, B.R**. *"Cyclic fatigue of intrinsically brittle ceramics in contact with spheres."* **Acta mater. 47.18 (1999): 4711-4725**.

[10] **Lee, K.S., Jung, Y.-G., Peterson, I.M., Lawn, B.R., Kim, D.K., and Lee, S.K**. *"Model for cyclic fatigue of quasi-plastic ceramics in contact with spheres."***J. Am. Ceram. Soc. 83.9 (2000): 2255-2262**.

[11] **J. Zhou, J. Mah, P. Shrotriya, C, mercer, W. O. Soboyejo. "***Contact damage in an yttria stabilized zirconia: Implications for biomedical applications"*. **J. Mater Sci: Mater Med (2007) 18:71 – 78**

[12] **W. C. Oliver and G. M. Pharr: "***Measurement of hardness and elastic modulus by instrumented indentation: Advances in understanding and refinements to methodology***". J. Mater. Res. 19, 3 (2004).**

[13] **A. Feder, M. Anglada.** *"Low-Temperature Ageing Degradation of 2.5 Y-TZP Heat-Treated at 1650°C,"* **J. Eur. Ceram. Soc., 25, 3117–24**

DEVELOPMENT OF STRENGTHENING SOLUTIONS FOR DOWEL-TYPE WOOD CONNECTIONS

C.L. Santos[1], A.M.P. de Jesus[2,3], J.J.L. Morais[1], E.R.M.A. Queirós[2], A.M.V. Lima[2]

[1] CITAB/Engineering Department, School of Sciences and Technology
University of Trás-os-Montes and Alto Douro, Quinta de Prados, 5001-801 Vila Real
E-mail: clsantos@utad.pt; jmorais@utad.pt

[2] Engineering Department, School of Sciences and Technology
University of Trás-os-Montes and Alto Douro, Quinta de Prados, 5001-801 Vila Real, Portugal
E-mail: ajesus@utad.pt; edgarruben@hotmail.com; alima@utad.pt

[3] UCVE, IDMEC – Pólo FEUP, Rua Dr. Roberto Frias, 4200-465 Porto, Portugal

ABSTRACT

This paper presents a study concerning the development of reinforcing techniques for dowel-type wood connections. One of the proposed techniques is based on the application of CFRP laminates (glued with epoxy resin) in the areas surrounding the holes of the wood members. The other technique is based on the application of steel inserts, glued to the holes of the timber members. In this latter technique two distinct commercial epoxy adhesives are investigated. Both techniques are demonstrated for the maritime pine wood. The experimental program included embedding tests, carried out according to the EN 383/1993 standard, with and without reinforcement, and covering parallel and perpendicular-to-grain quasi-static loading. The proposed experimental program allowed the evaluation of the embedding strength and foundation modulus. The analysis of this information showed the improved performance of the strengthening solutions. Also, it is important to emphasize that the reinforcement based on CFRP laminates eliminated fragile failure modes in the wood members.

KEY WORDS: Dowel-type connections, Maritime Pine Wood, Reinforcing solutions, CFRP, Metallic Inserts.

1. INTRODUCTION

Joints are often the weakest points in timber structures. The loss of perfect continuity in the structure, which is caused by the presence of joints, will result in a reduction of the global strength. This implies an increase in dimensions of the assembled elements. About 80% of structural failures have their origin on connections [1]. The dowel-type connections are the main fastening technique used worldwide in timber structures. The singularity of wood joints is not only attributed to a combination of different materials, such as wood and steel, but also due to the highly anisotropic behaviour of wood. Fundamental to an efficient utilisation of dowel-type joints is the understanding of their mechanical behaviour under load (e.g. load-slip behaviour, stress distributions, ultimate strength and failure modes). The mechanical behaviour of wood joints is a complex problem governed by a number of geometric, material and loading parameters (e.g. wood species, fastener diameter, end distances, edge distances, spacing, number of fasteners, fastener/hole clearances, friction and loading configuration).
According to the actual worldwide design rules [2,3], the calculation of mechanical timber joints is based upon the Johansen's yield model (YM) [4]. It only predicts the ultimate loads associated to ductile failure modes; brittle failure modes (e.g. shearing out, splitting perpendicular to grain) are not foreseen [5]. Since the YM does not allow the modelling of fragile failure modes, design codes suggest empiric minimum dimensions for joints (e.g. hole-member end distances) in order to avoid the fragile failure modes, which are undesirable for structures in service.

The reinforcement of dowel-type joints, aiming the improvement of the mechanical performance including the reduction of fragile failures, is a challenging research topic. Several reinforcing techniques have been proposed to improve the stiffness, strength and ductility characteristics of the joints (e.g. resin injected dowels, expanded tube joints, shear plate connectors, glued composites such as FGRP) [6-8].
A new reinforcing solution, based on bonded metallic inserts has been proposed for high performance composites materials [9,10]. This paper proposes the extension of this technique to dowel-type wood joints. Based on an experimental work, authors demonstrate the potential of this reinforcing technique. Embedding tests were carried out on unreinforced and reinforced series, according the procedures of the EN383/1993 standard [11]. The embedding tests were carried out on maritime pine wood (*Pinus pinaster* Ait. species) according both the parallel (longitudinal) and

perpendicular (radial) to grain directions, allowing the comparison of the embedding strength and foundation modulus.
Additionally, this paper assess an alternative reinforcing technique based on the application of Carbon Fibre Reinforced Plastic (CFRP) in the form of laminates glued with epoxy resin to the sides of wood members, surrounding the holes for insertion of the dowels. The performance of this reinforcement is demonstrates also using embedding tests according to the EN 383/1993 standard [11], along the longitudinal and radial directions of wood.

2. EXPERIMENTAL PROGRAM

A reinforcing technique consisting on the application of metallic inserts into the holes of the wood members being joined, using a structural adhesive is proposed in this work. Also, another reinforcing technique based on the application of CFRP laminates is investigated in this work. It is expected that these techniques contribute to the stress concentration reduction in wood, in the vicinity of the holes, beneficiating the strength of the connection.
An experimental program is proposed in this paper to demonstrate the efficiency of the reinforcing techniques for dowel-type connections. In particular, series of compressive embedding tests are carried out, according the EN 383/1993 standard procedures [11], in both longitudinal and radial directions. Two alternative structural adhesives were investigated in the reinforced solution based on metallic inserts. For the reinforced solution based on CFRP laminates only an adhesive is used.
The reinforcing techniques investigated in the paper are illustrated in Figure 1. The metallic inserts, used in one the proposed reinforcing technique, were introduced on pre-drilled holes carried out on the wood members, one at each side of the member. The insert is glued to wood using an epoxy resin. Figure 2 represents the geometry and dimensions of the metallic inserts. The performance of the strengthening solution is dependent on the efficiency of the adhesive. In this paper, two alternative adhesives were tested, namely the ARALDIDE® 2011 and the HILTI® RE500.
The CFRP laminates used as an alternative reinforcing technique were specifically manufactured for this investigation. It consisted on a bidirectional laminate in order to allow good performance in both radial and longitudinal wood directions. The laminate resulted from the superposition of 10 alternate lamellas of unidirectional SEAL Texipreg® HS160 RM, according to the sequence $[(0/90)_2/0]_S$. Epoxy resin was used to impregnate the lamellas. Each lamella has a thickness of 0.15mm, which gives a laminate of about 1.5 mm thick. 84x50 mm^2 CFRP laminates were glued centred in the wood members. Wood members were previously machined to accommodate the laminate in order to preserve to thickness of the member of 30 mm. Holes for dowels were drilled after curing the adhesive, using drills with high hardness tungsten finishing, to avoid damaging the CFRP laminates.
In order to assess the performance of the proposed reinforcing techniques, embedding tests of wood member of Maritime Pine (*Pinus pinaster* Ait.) were carried out, according the EN 383/1993 standard. Both parallel- (longitudinal) and perpendicular-to-grain (radial) compressive embedding tests were carried out, as illustrated in Figure 3. The nominal diameter of the dowel (*d*) was chosen equal to 14 mm and the member's thickness (*t)* equal to 30 mm. The dimensions of the members are proportional to the diameter of the dowel (see Figure 3) as proposed in the EN 383/1993 standard. Eight series of tests were prepared as described on Table 1: six reinforced series (R) and two unreinforced series (NR). Half of the series were tested under radial compression (RC) and the other half under longitudinal compression (LC). Regarding the series reinforced with metallic inserts, half were obtained using the HILTI® RE500 adhesive (A) and the other half using the ARALDITE® 2011 adhesive (B). The CFRP laminates were glued to the wood members using the Sikadur® 30 epoxy-based resin. Table 1 refers the density values of each series. The average density values range from 550.1 kg/m^3 to 646.7 kg/m^3. The displacement rates were 0.3 mm/min for the LC series and 1.0 mm/min for the RC series. The wood used in the tests was air dried until approximately a moisture content of 12%.
Tests were performed on an INSTRON® machine, model 1125, rated to 100kN, under crosshead displacement control. One linear variable differential transducer (LVDT) was used to measure the relative displacement between the dowel and the base plate (see Figure 3). The LVDT used in the experimental program is from the Applied Measurements® with reference AML/EU ± 10-S10 (measurement range of ±10mm). The data was acquired by means of a SPIDER® 8-30 system. Respecting the EN 383/1993 standard, a loading-unloading-reloading procedure was adopted: firstly specimens were loaded until 40% of the maximum estimated load (Fest), and the crosshead position held during 30s; after this stage, specimens are unloaded until $0.1F_{est}$ and the crosshead position again maintained along more 30s; finally, specimens are reloaded until failure.

Figure 1. Specimens reinforced with metallic inserts (left) and CFRP laminates (right).

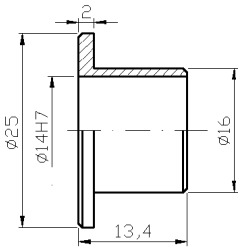

Figure 2. Geometry and dimensions of the metallic insert (dimensions in mm).

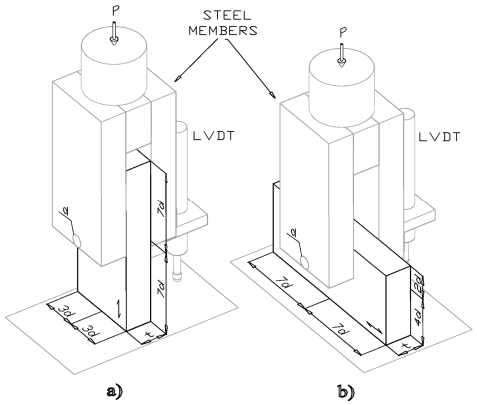

Figure 3. Schematic representation of the embedding tests according the EN383/1993 standard: a) longitudinal compression; b) radial compression.

Table 1. Summary of the test series

Series	N.º of Speci-mens	Density		
		Mean	Std. Dev.	Coef. of Var.
		Kg/m^3		%
LC_NR[(1)]	24	570.1	38.3	6.7
LC_R_A[(2)]	12	626.8	31.0	4.9
LC_R_B[(3)]	11	633.6	32.1	5.1
LC_R_CFRP[(4)]	15	595.9	48.47	8.1
RC_NR[(1)]	24	550.1	49.0	8.9
RC_R_A[(2)]	12	615.4	29.5	4.8
RC_R_B[(3)]	12	646.7	37.0	5.7
RC_R_CFRP[(4)]	15	581 .7	48.4	8.32

(1) : wood member not reinforced
(2) : wood member reinforced with glued metallic inserts - HILTI® RE500 adhesive
(3) : wood member reinforced with glued metallic inserts - ARALDITE® 2011 adhesive
(4) : wood member reinforced with CFRP laminates

3. RESULTS AND DISCUSSION

Figure 4 illustrates the load-displacement curves obtained for the four embedding test series, carried out according the longitudinal direction. Figure 5 illustrates the load-displacement curves obtained for the four embedding test series, carried out according the radial direction. Displacements in the graphs were measured using an LVDT, as illustrated in Figure 3. The LVDT gives the displacement between the end of the dowel and the base of the testing machine. Regarding the longitudinal compression tests, unreinforced series and reinforced series with metallic inserts, exhibit a maximum load plateau, which defines the ultimate load (see Figure 6a)). Typically, after some amount of deformation, at almost constant load, fragile failures occur, with a sudden load drop. For these test series, the failure load is defined as the absolute maximum load. The longitudinal test series reinforced with glued CFRP laminates, exhibits a yield plateau, after which an irregular increasing load is verified. This increasing strength is due to the beneficial effect of the CFRP laminates, which postpones the fragile failure modes. For this latter series, the failure load was considered as the load prior the first load drop at the initial yield plateau. The analysis of the load-displacement curves from the embedding tests in the radial direction shows that for the unreinforced series there is a smooth transition from the elastic to inelastic behaviours. Also, there is a monotonic load increase after yielding. In this case, the ultimate failure load was defined as the load at 0.05d permanent displacement (see Figure 6b)), where d is the dowel diameter. All the reinforced series shows a yield plateau before the load starts to increase again. This yield plateau is more pronounced for the series reinforced with glued CFRP laminates. For these reinforced test series, the failure load was defined as the first load peak appearing at the yield plateau.

Using the failure loads it was possible to establish the embedding strength, f_h, for all test series using the following formula:

$$f_h = \frac{F_{\max}}{d \cdot t} \tag{1}$$

where: F_{max} is the failure load, d is the diameter of the dowel and t is the thickness of the wood member.

Despite the embedding tests were carried out according the EN383/1993 standard, which proposes a loading path consisting on an initial load until 40% of the maximum estimated load, followed by an unloading until 10% of the maximum estimated load and a final reloading until failure, an initial stiffness was evaluated neglecting the unloading/reloading paths. The load-displacement curves (Figures 4 and 5) were edited to remove the unloading/reloading hysteresis. An initial elastic stiffness (k_1) was evaluated using the linear regression analysis applied to the linear range of the load-displacement curves, as illustrated in Figure 6. Another stiffness value (k_2) was defined for the embedding tests in the radial direction, after yielding, as defined in Figure 6b). The previous referred stiffness parameters can be normalised, dividing their values by the projected area of the hole, resulting the foundation modulus (K_i):

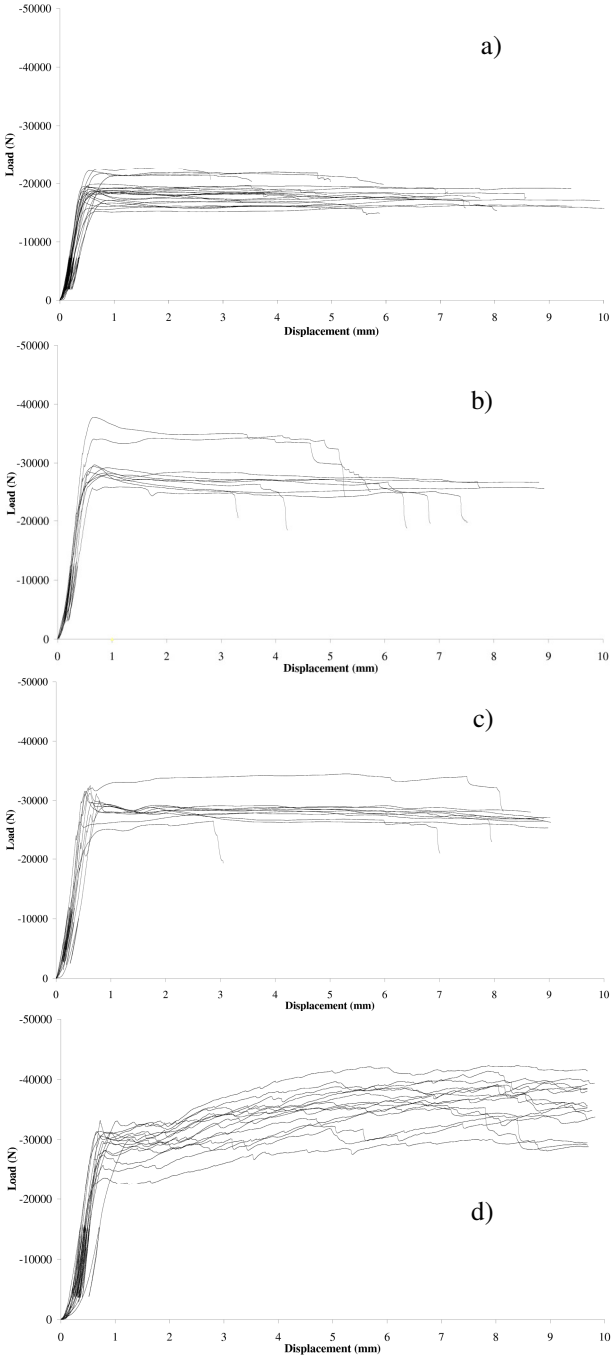

Figure 4. Experimental load-displacement curves obtained for the test series: (a) LC_NR series; (b) LC_R_A series; (c) LC_R_B series; (d) LC_R_CFRP series.

$$K_i = \frac{k_i}{d \cdot t} \tag{2}$$

where: K_i is the foundation modulus, k_i the stiffness, d is the diameter of the dowel and t if the thickness of the member.

Figures 7 and 9 illustrate the evolution of the embedding strength with the wood density, since the latter property is often used to explain variations of mechanical propertied of wood, within the same species and among species. The analysis of the figures reveals a significant gain in the embedding strengths when the reinforcements are used, even if density differences are taken into account. The correlation between the embedding strength and density is significant for both unreinforced series. For some reinforced series this trend is also observed, but there are some reinforced tested series for which no correlation between the embedding strength and density is verified.

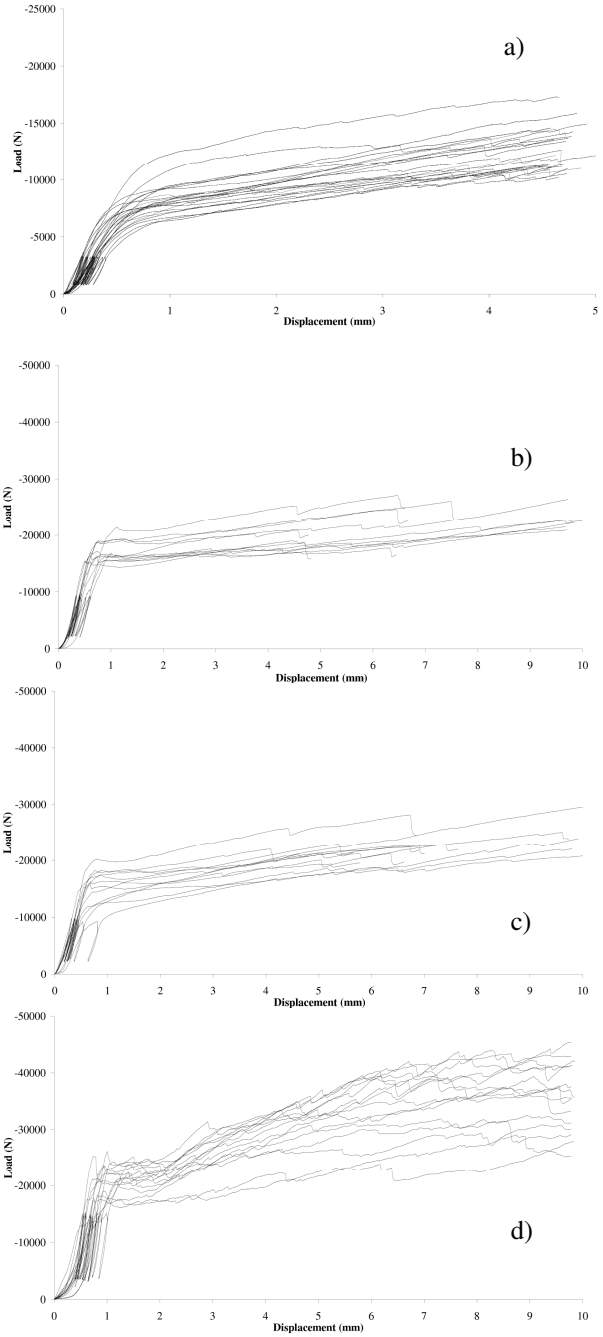

Figure 5. Experimental load-displacement curves obtained for the test series: (a) RC_NR series; (b) RC_R_A series; (c) RC_R_B series; (d) RC_R_ CFRP series.

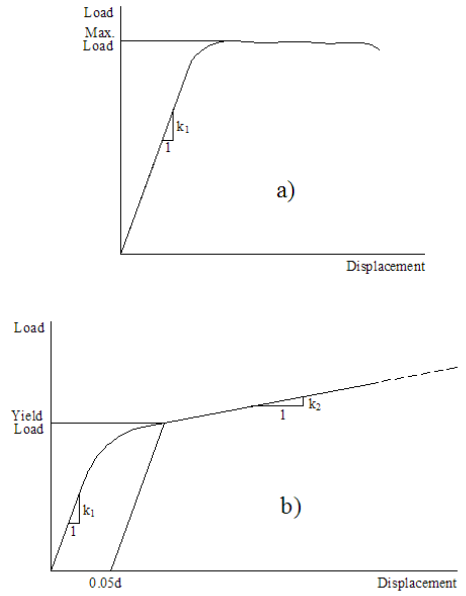

Figure 6. Typical load-displacement behaviours: a) longitudinal compression; b) radial compression.

Table 2 summarizes the average values of the embedding strength for all the testing series. It is clear a higher gain in the embedding strength for tests carried out in the radial compression. In radial direction, the use of CRFP laminates results in significant higher embedding strength when compared with the unreinforced solutions or even with the reinforced solutions with metallic inserts. However, for the longitudinal compression tests, both reinforcing techniques produce similar results. Concerning the reinforcement with metallic inserts, the use of HILTI® RE500 adhesive resulted higher embedding strength properties for the radial compression tests; for longitudinal compression tests, the use of ARALDITE® 2011 adhesive resulted in slightly higher embedding strength.

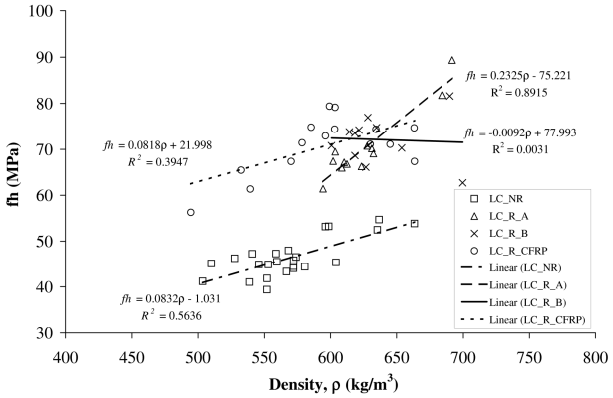

Figure 7. Evolution of the embedding strength with density for unreinforced and reinforced wood member in longitudinal compression tests.

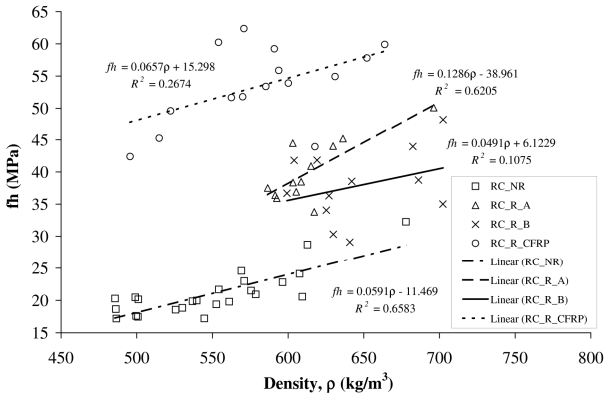

Figure 8. Evolution of the embedding strength with density for unreinforced and reinforced wood members in radial compression tests.

Average foundation moduli (K_1, K_2) are presented in Table 2 for each test series. For this parameter no general correlation was verified with density, therefore respective graphs were omitted. An increase in K_1 is observed for all reinforced solutions. Regarding K_2, only the CFRP laminates had a beneficial effect.

Table 2. Summary of the test results.

Series	f_h				K_1				K_2			
	Mean	St. Dev.	COV	Gain	Mean	St. Dev.	COV	Gain	Mean	St. Dev.	COV	Gain
	MPa		%	%	N/mm^3		%	%	N/mm^3		%	%
LC_NR	46.4	4.2	9.1	-	113.3	23.5	20.7	-	-	-	-	-
LC_R_A	70.5	7.6	10.8	51.9	164.6	36.0	21.8	45.3	-	-	-	-
LC_R_B	72.1	5.2	7.2	55.5	152.4	38.4	25.2	34.5	-	-	-	-
LC_R_CFRP	72.8	6.5	8.9	56.9	146.4	28.6	19.5	29.2				
RC_NR	21.1	3.6	0.2	-	37.2	8.8	23.7	-	3.1	0.7	22.6	-
RC_R_A	40.2	4.8	12.0	90.4	74.8	20.1	26.9	100.9	2.0	0.8	42.9	-36.6
RC_R_B	37.9	5.5	14.6	79.5	67.1	16.3	24.3	80.5	2.8	0.9	30.5	-8.7
RC_R_CFRP	53.5	6.1	11.5	153.6	97.6	31.3	32.1	162.4	4.6	1.3	29.0	48.4

The proposed reinforcing solutions have more significant effect on K_I, for radial compression, rather then for longitudinal compression embedding tests. For radial compression tests, the use of CFRP laminates resulted in the higher foundation modulus. Concerning the reinforcement with metallic inserts, the use of HILTI® RE500 adhesive always produced higher foundation modulus, for both radial and parallel-to-grain compression tests.

The use of CFRP laminates to reinforce dowel-type connections produced significant increases in both foundation modulus and embedding strength. Additionally, it fully eliminates the fragile failure modes, which are yet observed for some specimens reinforced with metallic inserts. However if costs are taken into account, the use of glue metallic inserts becomes more attractive, since CFRP laminates are generally expensive.

4. CONCLUSIONS

Two alternative reinforcing solutions for dowel-type wood connections were proposed and compared their mechanical performance under monotonic loading. The first solution consisted on the application of metallic inserts into the holes of the wood members to be joined, using an epoxy adhesive. The second solution consisted on gluing CFRP laminates on both sides of wood members.

The efficiency of the proposed reinforcements was demonstrated through an experimental program consisting on embedding tests, carried out according the EN 383/1993 standard. Both the embedding strength and elastic foundation modulus (K_I) increased for the reinforced solutions. The proposed strengthening techniques are more effective for the radial loading, which corresponds to the weakest direction. Two alternative epoxy adhesives were tested with the metallic inserts, namely the ARALDITE® 2011 and the HILTI® RE500. The HILTI® RE500 adhesive demonstrated to be the most efficient to join the steel insert to wood.

The use of CFRP laminates demonstrated to be more efficient than the use of glued metallic inserts. It resulted in higher embedding strength and elastic foundation modulus. The ductility of the joint is also beneficiated since the fragile failure modes are eliminated. The cost is the one drawback of the CFRP solution as well as its possible anaesthetic impact on wooden structures.

REFERENCES

[1] Itany, R.Y. and Faherty, K.F., (1984). "Structural wood research, state-of-the-art and research needs," Proceedings of the Workshop, Milwaukee, WI, Oct. 5-6, 1983. ASCE, New York, 210 pp.

[2] Soltis, L.A., Wilkinson, T.L., (1987). "Bolted-Connection Design," General Technical Report FPL-GTR-54, Forest Products Laboratory – USDA, Madison, WI, USA.

[3] European Committee for Standardization, (2004). "EN 1995-1-1 Design of timber structures. Part 1-1: General rules and rules for buildings," CEN-TC250, Brussels.

[4] Johansen, K.W., (1949) "Theory of timber connections." International Association for Bridge and Structural Engineering: IABSE Journal 9: 249 - 262.

[5] Patton-Mallory, M., Pellicane, P.J., Smith, F.W., (1997). "Modelling bolted connections in wood: review." Journal of Structural Engineering 123(8): 1054-1062.

[6] Rodd, P.D., Leijten, A.J.M., (2003). "High-performance dowel-type joints for timber structures." Progress in Structural Engineering and Materials 5: 77-99.

[7] Davis, T.J., Claisse, P.A., (2001). "Resin-injected dowel joints in glulam and structural timber composites." Construction and Building Materials 15: 157-67.

[8] Claisse, P.A., Davis, T.J., (1998). "High performance jointing systems for timber." Construction and Building Materials 12: 415-425.

[9] Camanho, P.P., Tavares, C.M.L, Oliveira, R., Marques, A.T., Ferreira, A.J.M., (2005). "Increasing the efficiency of composite single-shear lap joints using bonded inserts." Composites Part B - Engineering 36: 372-383.

[10] Camanho, P.P., Lambert, M., (2006). "A design methodology for mechanically fastened joints in laminated composite materials." Composites Science and Technology 66(15): 3004-3020.

[11] European Committee for Standardization, (1993). "EN383: Timber Structures. Test Methods. Determination of Embedding Strength and Foundation Values for Dowel Type Fasteners." European Standard, Brussels.

INFLUENCE OF SINTERING CONDITIONS ON THE MICROSTRUCTURAL AND MECHANICAL PROPERTIES OF POROUS Ti c.p. FOR BIOMEDICAL APPLICATIONS

Y. Torres [1], J. Pavón [2], I. Nieto [1], J. A. Rodriguez [1]

[1] Department of Mechanical and Materials Engineering, University of Seville, Avda. Camino de los Descubrimientos, s/n, 41092 Seville, Spain
E-mail: ytorres@us.es

[2] BIOMAT Group, Bioengineering Program, University of Antioquia, Calle 67, No. 53-108, Medellín, Colombia
E-mail: jjpavon@udea.edu.co

ABSTRACT

Among all biomaterials used for bone replacement, it is recognized that both commercially pure titanium (Ti c.p.) and Ti_6Al_4V alloy are the materials that show the best *in vivo* performance due to their excellent balance between mechanical, physical-chemical and biofunctional properties. However, one of the most important disadvantages of them is their higher stiffness with respect to the bone which produces the *stress shielding* phenomenon, promoting the bone resorption around the implant with an associated risk of failure. In this work is investigated the influence of the main powder metallurgy processing parameters, compaction pressure and sintering temperature, in the porosity, stiffness and yield strength of porous commercially pure titanium (Ti c.p.) samples manufactured for reducing the stress shielding phenomenon. The results have shown that lower values of both compaction pressure and sintering temperature implies lower values of samples stiffness, as logical consequence of the higher porosity. The spherical levels of pores as well as the free mean pathway between them were increased for higher values of both compaction pressure and sintering temperature. The better stiffness results, by comparison with cortical bone, were obtained for 38.5 MPa and a sintering temperature of 1000°C. These conditions also corresponded to the better balance with respect to desired yield strength and the expectable higher fatigue resistance due to more spherical pores.

KEY WORDS: Biomaterials, Porous Titanium, Powder Metallurgy, Stress Shielding.

1. INTRODUCTION

Bone properties degradation associated to both traumas and diseases, and its replacement, is currently one of the most important public health problem. This bone damage is evident by the density reduction since the 30 years old, which implies a strength reduction up to 40% that could be increased by both the cyclic load degradation and the surface wear of joints. Of all biomaterials used for bone replacement, it is recognized that both commercially pure titanium (Ti c.p.) and Ti_6Al_4V alloy are the materials that show the best *in vivo* behaviour due to their excellent balance between mechanical, physical-chemical and biofunctional properties. However, they have three disadvantages which, in many cases, compromises the implants and prosthesis liability: 1) the stiffness of titanium is higher than the bone one which produces the *stress shielding* phenomenon, promoting the bone resorption around the implant; 2) despite its high osteointegration capability, titanium is surrounded by a fibrous tissue because of its bioinert behaviour which is related with many loosening events and 3) it is required more studies about its liability from damage prevention criteria, because this is the only admissible criteria for biomaterials design. Regarding the stress shielding problem, there are some works and developments of both biocomposites and porous titanium implants that still not reach the suitable equilibrium between mechanical and biofunctional properties [1-4]. Several previous works have shown that is possible to match the stiffness of cortical bone by using different techniques to fabricate porous titanium samples [5-15]. However, there is a lack of studies about the real effect of this porosity on other important mechanical properties, i.e. mechanical strength and fatigue life, and also about the relationships between both the porosity and microstructure with the mechanical properties.

In this work is investigated the influence of main sintering conditions, compaction pressure and temperature, on both microstructural and mechanical properties of porous Ti c.p. samples. The powder metallurgy process used to manufacture the samples consisted of a conventional process of compaction followed by sintering of Grade 4 Ti c.p. samples. This work was developed in the framework of a project in which the aim is to evaluate the improvement of the equilibrium between biofunctional and mechanical properties of porous titanium implants designed to improve osteointegration, to reduce stress shielding and to prevent the damage.

2. EXPERIMENTAL PROCEDURE

2.1 Samples processing

The powder was previously fabricated by a hydrogenation/dehydrogenation process. The particle size distribution, according to the supplier SE-JONG Materials Co. Ltd., Corea, showed a mean size of 23.3 μm with a chemical composition equivalent to Grade 4 Ti c.p. ASTM F67-00. In order to obtain porosities between 30% and 50%, to ensure the desired stiffness [4,16-17], the compaction pressures used were 38.5, 89.7, 147.4 and 211,5 MPa (from the compressibility curve of the titanium powder), and the sintered temperatures were 1000, 1100, 1200 and 1300°C for 2 h. The powder mass used to obtain the cylindrical samples (diameter of the 12 mm) was of 5.14 g. The compaction step was carried out by using an Instron 5505 universal machine to apply the pressure needed for the desired porosity, followed by a MALICET ET BLIN U-30 universal machine in order to remove the samples from the matrix. The compaction loading rate was 600 kgf/s, the dwelling time was 2 min and the unloading time was 15 s for decreasing load up to 15 kgf. The sintering process was performed in a CARBOLYTE STF 15/75/450 ceramic furnace with a horizontal tube using high vacuum ($5x10^{-4}$ mbar).

2.2 Density, porosity and microstructural characterization

Density and porosity (total and interconnected) measurement was carried out by using Arquimedes method with distilled water impregnation due to its experimental simplicity and reasonable reliability (ASTM C373-88). The porosity was also assessed by image analysis using an optical microscope NIKON EPIPHOT coupled with a camera JENOPTIK PROGRES C3, and a properly analysis software (IMAGE-PRO PLUS 6.2). This analysis was performed only in the middle part of the cylinders because it presents theoretically the most homogeneous pores distribution. Before the image analysis, the sectioned part was properly prepared by a sequence of conventional steps (resin mounting, grinding and polishing) followed by a mechano-chemical polishing with magnesium oxide and hydrogen peroxide. The porosity parameters estimated by this method were the convexity (convex perimeter/pore perimeter), form factor ($F_f = 4\pi A/PE^2$, where A is the pore area and PE is the experimental perimeter of the pore), mean free path between the pores, the porosity itself, maximum and mean area of pores, grade of contiguity of the pores, equivalent diameter, elongation factor and pores density. Conventional optical microscopy (OM) and scanning electron microscopy (SEM) were also used for the basic observation of the microstructural features of the samples.

2.3 Mechanical testing

For mechanical compression testing, smaller cylinders were machined from the central part (more homogeneous) of the original sintered cylinders, following the recommendations of the Standard ASTM E9-89a (height/diameter = 0.8). The tests were carried out with a universal electromechanical Instron machine 5505 by applying a strain rate of 0.005 (mm/mm·min). All tests were considered finished for a strain of 50% and, afterwards, it was estimated both Young modulus, E, and yield strength, σ_y. The Young modulus estimation from the compression stress-strain curves was corrected with the testing machine stiffness (87.9 kN/mm). The dynamic Young modulus measurement using the ultrasound technique was performed with a KRAUTKRAMER USM 35 equipment, which was used to estimate both longitudinal and transverse propagation velocity of acoustic waves. For each case it was used the properly probe PANAMETRICS and a suitable ultrasonic couplant fluid. Once the acoustic wave velocities and densities are measured, the dynamic Young modulus calculation is made by using a proper mathematical expression. Finally, the Young modulus of porous samples were also estimated by a calculation made from both porosity and pores form factor measurements, using the model proposed by Nielsen [18].

3. RESULTS AND DISCUSSION

3.1 Samples processing

Fig. 1 shows an example of the sample aspect after the sintering process for compaction pressure and sintering temperature of 38.5 MPa and 1300°C, respectively.

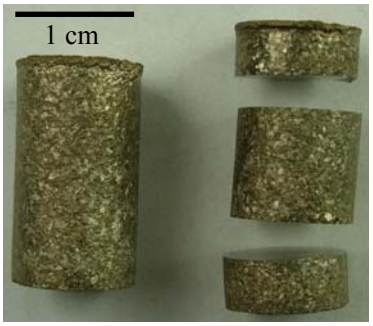

Fig. 1. Porous Ti c.p. PM material (38,5 MPa and 1300 ºC) and machined in three pieces.

None of the sintered samples showed any phenomena of oxidation and contamination of titanium, which is a clear indicator of the role played by the vacuum during sintering. Also, as it was mentioned previously, all characterization and mechanical testing was focused in the central part of the cylinders because of its porosity uniformity.

3.2 Density, porosity and microstructural characterization

Fig. 2 shows the dependence of both total and interconnected porosity, in terms of both compaction pressure and sintering temperature.

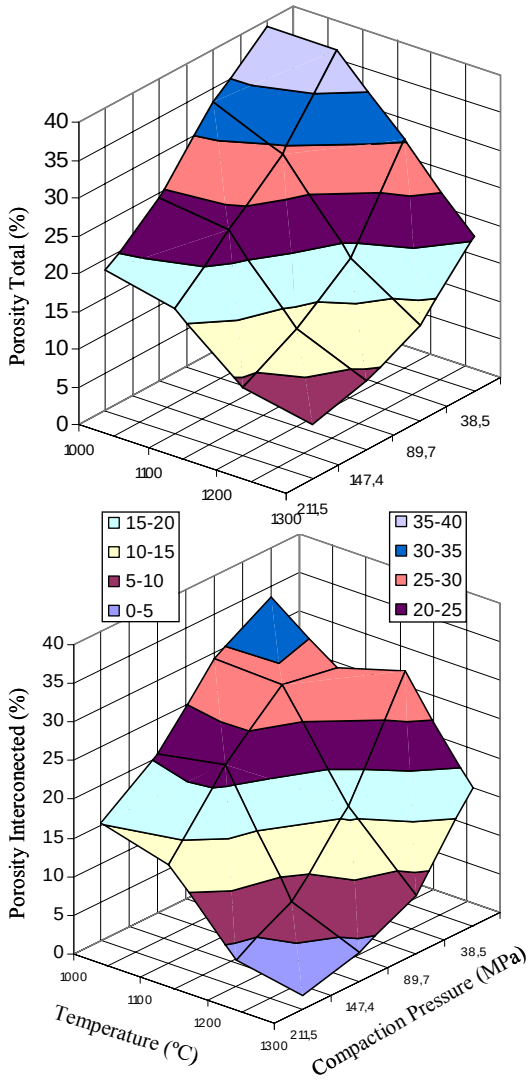

Fig. 2. Porosity behaviour as a function of both compaction pressure and sintering temperature.

As it was expected, the lower values of total porosity, and higher density, were obtained for the higher values of both compaction pressure and sintering temperature. Regarding the total porosity range guide to reach the desired stiffness, according to previous works (30% and 50%), this was obtained for compaction pressure values between 35.8 MPa and 89.7 MPa and sintering temperatures between 1000°C and 1200°C as can be clearly observed in the figure 2. From this it can be inferred that for a total porosity range of 30% to 40% and a sintering temperature range of 1000°C to 1200°C, it can be used a compaction pressure range of 38.5 MPa to 89.7 MPa, with higher porosity values for both lower compaction pressure and sintering temperature. With respect to interconnected porosity behaviour, it presents the same trend as the total porosity. However, in this case there is not a defined desired range because it will depend on the elastic properties of the material to be used as filler compound (bioactive glass, high-density polyethylene, etc.). In fact, this kind of porosity should be most properly controlled to be only at the surface in order to promote the bone ingrowth, considering the risk of reducing both mechanical strength and fatigue resistance.

In Fig.3 it is summarised the behaviour of the pores morphology parameters in terms of both compaction pressure and sintering temperature. From these results it can be noticed, as it was expected, that the most important parameters, form factor (F_f) and free-mean path or distance between pores (λ), increased for higher values of both compaction pressure and sintering temperature. As a logical consequence, porosity was reduced (higher stiffness) especially by compaction pressure effects, as sintering temperature has stronger influence in F_f. However, the most important feature of the pore morphology behaviour is the different trend of both F_f and λ parameters for lower and higher compaction pressure: it is observed that for a fixed low compaction pressure (38.5 MPa) an increasing sintering temperature has a stronger effect in both F_f and λ, with a small porosity reduction, than for a fixed higher compaction pressure (211.5 MPa). This trend implies that, in order to improve both mechanical and fatigue resistance with a small effect in the desired porosity (stiffness), it advisable to work with small sintering temperature increments for the lowest compaction pressure which is consistent with the stronger effect in F_f due to an increasing sintering temperature. Sintering temperature increments for highest compaction pressure produce largest pores due to coalescence of the smallest ones present at lowest temperatures.

3.3 Mechanical testing

The compression stress-strain curves of the samples for the different processing conditions are depicted in Fig.4. From this figure it is verified that an increment in sintering temperature, for a fixed compaction pressure, implies higher values of both Young modulus and yield strength. However, it is interesting to remark the different sensitivity to sintering temperature depending on the compaction pressure level: it is clear that both E and σ_y are more sintering temperature sensible for the lowest compaction pressure which is clearly consistent with the higher sintering temperature sensitivity observed previously for porosity parameters (F_f and λ). This result indicates that F_f and λ not only can affect plastic properties (yield and mechanical strength, and fatigue resistance) but also the elastic properties of the titanium porous sample. Therefore, this has to be considered in order to improve the mechanical properties of porous titanium without any important effect on the stiffness of the sample.

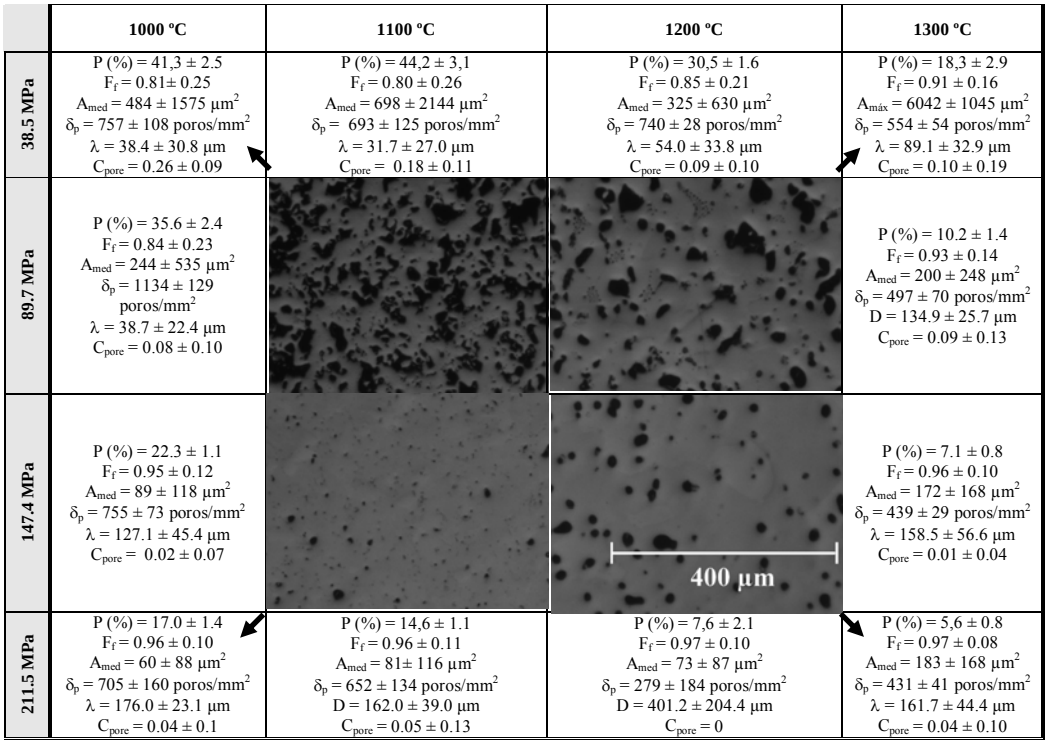

Fig. 3. Effects of the temperature and compaction pressure in characteristic of the pores.

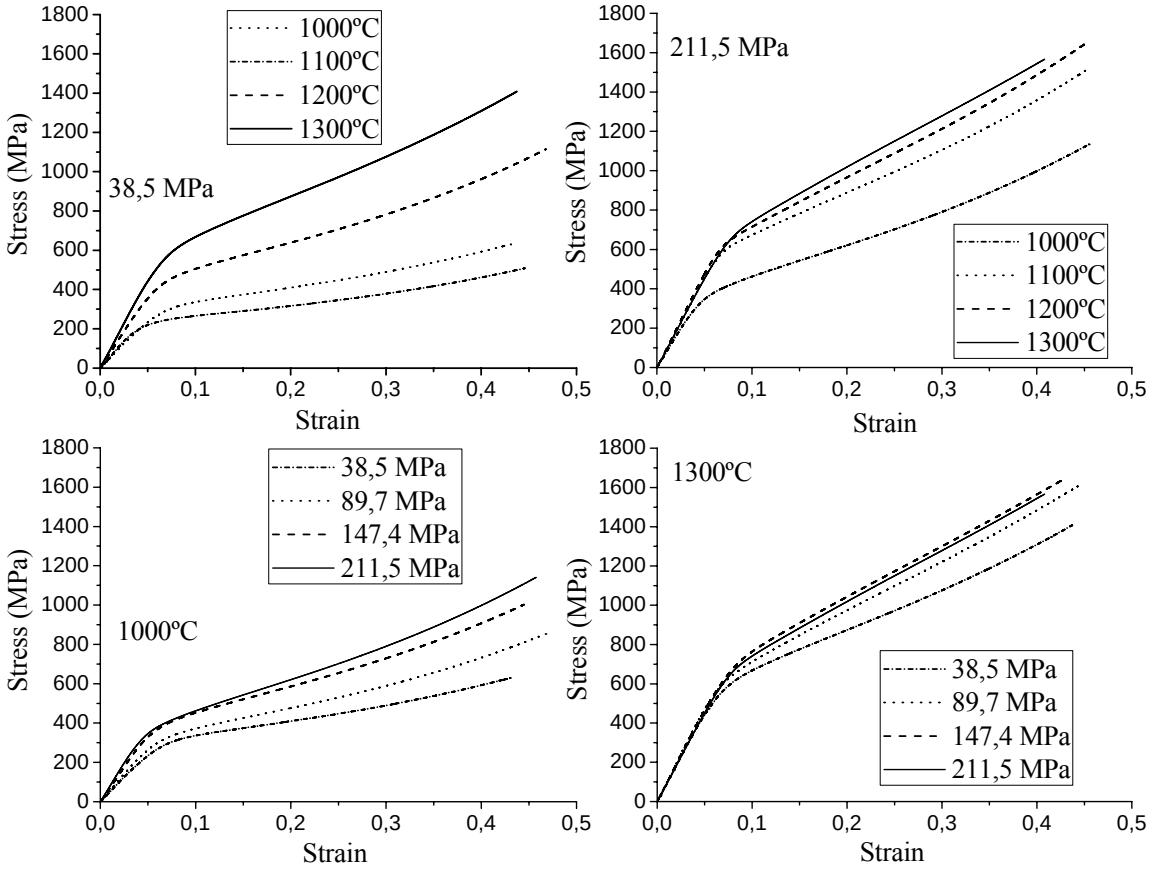

Fig. 4. Compression stress-strain curves of the samples for the different processing conditions.

Note, from the same figure, that compaction pressure increment for lowest and highest sintering temperatures show the same E and σ_y sensitivity: they are more sensible for compaction pressure increments at the lowest sintering temperature. Regarding the searched stiffness value for cortical bone replacement ($E_{CB} \approx 20$ GPa).

Fig. 5 shows that the better results (20 to 25 GPa) were obtained for the lowest compaction pressure (35.8 MPa) with sintering temperatures of 1000 and 1100°C, corresponding to the highest porosity (~ 40 %). In this figure are also included the trends obtained by other authors and it is noticed that their results fix reasonably well with those obtained in this work. Finally, it should be mentioned that yield strength values, corresponding to the better stiffness results, were always higher than the cortical bone one.

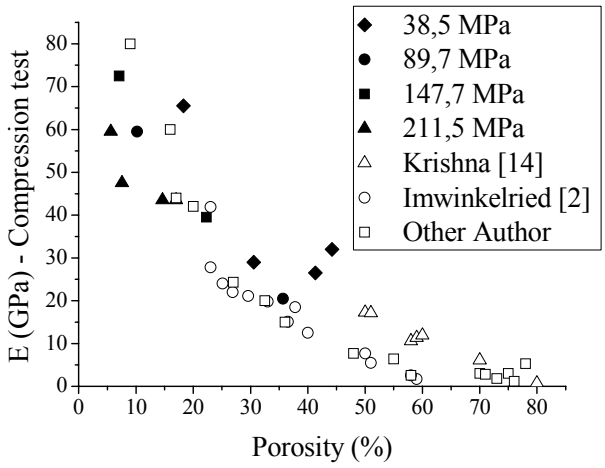

Fig. 5. Behavious of Young modulus by compression test in terms of total porosity. Relation between the compression young modulus and porosity.

From Fig. 5 it is noticed the influence of using the stiffness correction of testing machine in Young modulus evaluation: corrected values are higher for same porosity. However, these values remain lower than those obtained with the ultrasound technique as can be observed and discussed later.

The Young modulus measurements obtained by ultrasound technique (dynamic Young modulus) showed a higher values trend than those estimated from the compression stress-strain curves (see Figs. 5 and 6). However, for the lowest Young modulus values the results are more similar. These differences could be explained due to normal uncertainties of the compression test measurement and also because of the higher well known reliability of the ultrasound technique.

The theoretical curves which are inlcuded in Fig. 6 coorrespond to mathematical expressions that relate Young moudlus with porosity: Gibson and Ashby [19] is used for compression test estimation and Pabts-Gregorova [20] and Knudsen are for ultrasound data. Note that ultrasound thecnique measurements of this work are in well concordance with theretical estimations...

In Fig. 6 is presented the dynamic Young modulus behavior in terms of compaction pressure, sintering temperature and porosity. As in the case of the compression test measurement, the better stiffness results correspond to both lowest compaction pressure and sintering temperature (35.8 MPa and 1000°C - 1100°C) with a porosity of approximately 40 %. Note that the relation between measurements, compression test and ultrasound, and porosity are in well concordance with those reported in previous works [2,14, 20]: 20 MPa to 25 MPa for 50% of porosity. Despite the better stiffness results obtained in this work were for lowest sintering temperature, this does not imply any detriment of mechanical strength as could be expected from the literature. In fact, the authors are currently developing a new work in which they are using lower compaction pressure (13 MPa) and even loosing sintering, with such a good results as 50% porosity and 14,3 GPa for 1000ºC, and 45% porosity and 21,7 GPa for 1200 ºC.

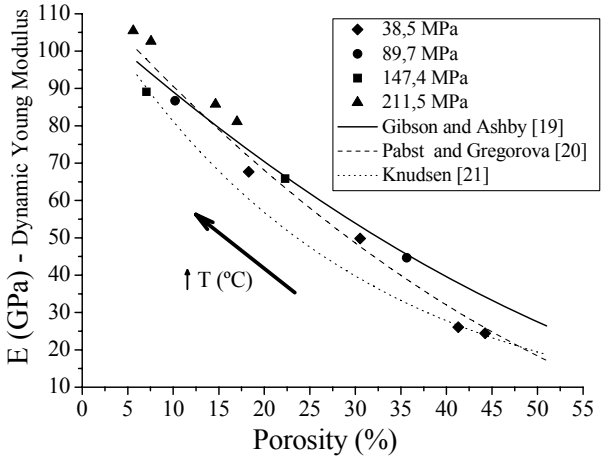

Fig. 6. Relation between the dynamic Young modulus and porosity.

Similar stiffness values for lower porosity could be explained due to some measurement uncertainties in the previous works (all compression test measurements in this work were corrected with the testing machine stiffness) and also because the ultrasound technique study was carefully and detailed carried out. In fact, the reliability and certainty of the ultrasound measurements were contrasted and validated by comparison with well known and accepted pore-elasticity model like Nielsen one [18]: Fig. 7 presents the adjust between the both Young modulus experimental measurements and the calculation by using the Nielsen model including porosity parameter experimentally determined. Nielsen model is given by the following expression:

$$E_p = E_{Ti}\frac{\left(1-\frac{P}{100}\right)^2}{1+\left(\frac{1}{F_f}-1\right)\left(\frac{P}{100}\right)} \qquad (1)$$

where E_{Ti} is the Young modulus of Ti porous free, P is the total porosity and F_f is form factor of the porous sample. From Fig. 7 it is evident that Young modulus measurements from ultrasound technique present the best fix with respect to calculations from Nielsen

model, for the complete range of both compaction pressure and sintering temperature. On the other hand, measurements obtained from compression test, in this work and also in some previous study, show an important deviation for highest Young modulus values.

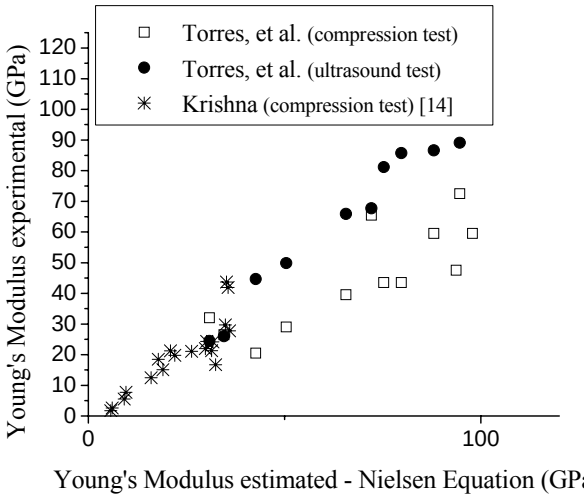

Fig. 7. Comparison of Young modulus measurement by different methods with the calculation by estimated Nielsen equation.

4. CONCLUSIONS

According to the results of the study about the influence of conventional powder metallurgy conditions in both microstructural and mechanical properties of porous Ti for bone replacement, the following salient findings can be drawn:

1. The better stiffness results of porous Grade 4 Ti cp porous samples for cortical bone replacement (20 to 25 GPa against to aprox. 20 GPa of bone) were obtained for the lowest values of both compaction pressure and sintering temperature (38.5 MPa and 1000°C -1100°C), with a porosity of approximately 40 %. These results correspond to the central part of cylindrical samples initialled fabricated, due to its highest porosity uniformity.
2. The main porosity parameters, form factor and mean free path, presented a highest sensitivity to sintering temperature increments for a lowest compaction pressure. This trend was consistent with the behavior exhibited by both Young modulus and yield strength from compression tests: highest sensitivity for sintering temperature increments at lowest compaction pressures as well as for compaction pressure increments for lowest sintering temperatures. The knowledge of this sensitivity could be determinant in order to improve both mechanical strength and fatigue life with a low influence in the porosity and, therefore, in the stiffness of the samples.
3. Ultrasound technique used for dynamic Young modulus estimation of porous Ti samples has shown to be a suitable tool for the study of this kind of materials. This was reasonably verified by comparison of the measurements obtained by this technique with the values calculated from a theoretical model like Nielsen one, which include porosity parameters experimentally determined.

ACKNOWLEDGMENTS

The authors wish to thank to the laboratory technicians J. Pinto and the student J.M. Recio for carrying out the microstructure characterization and mechanical testing.

REFERENCES

[1] Gerard, D. A. and Koss, D. A., International Journal of Fatigue, 13 (2): p. 345-352, 1991.
[2] Imwinkelried, T., Journal of Biomedical Materials Research - Part A, 81 (4): p. 964-970, 2007.
[3] Yue, S., et al., Journal of Biomedical Materials Research, 18 (9): p. 1043-1058, 1984.
[4] Oh, I. H., et al., Scripta Materialia, 49 (12): p. 1197-1202, 2003.
[5] Ryan, G., et al., Biomaterials, 27(13): p. 2651-2670, 2006.
[6] Dunand, D. C., Advanced Engineering Materials, 6(6): p. 369-376, 2004..
[7] Asaoka, K., et al., Journal of Biomedical Materials Research, 19(6): p. 699-713, 1985.
[8] Spoerke, E. D., et al., Journal of Biomedical Materials Research - Part A, 84(2): p. 402-412, 2008.
[9] Dewidar, M. M. and Lim, J. K., Journal of Alloys and Compounds, 454(1-2): p. 442-446, 2008.
[10] Wenjuan, N., Chenguang, B., GuiBao, Q, Qiang, W., Materials Science and Engineering: A, 506(1-2): p. 148-151, 2009.
[11] An, Y. B., et al., Materials Letters, 59(17): p. 2178-2182, 2005.
[12] Orrù R., Licheri, R., Locci A.M., Cincotti, A., Cao, G., Materials Science and Engineering: R: Reports, 63(4-6): p 127-287, 2009.
[13] Traini, T., et al., Dental Materials, 24(11): p. 1525-1533, 2008.
[14] Krishna B.V., Bose, B., Bandyopadhyay, A., Acta Biomaterialia, 3: p. 997–1006, 2007.
[15] Ryan, G. E., et al., Biomaterials, 29(27): p. 3625-3635 2008.
[16] Wang, J. F., et al., Journal of Materials Processing Technology, 197(1-3): p. 428-433, 2008.
[17] Spoerke, E. D., Murray, N. G., Li, H. L., Brinson, L. C., Dunand, D. C. and Stupp, S. I., Acta Biomaterialia, 1(5): p. 523-533, 2005.
[18] Nielsen LF., J Am Ceram Soc.,. 67(2): p. 93–8,1984.
[19] Gibson, L.J. and Ashby, M.F., Cellular Solids: Structure and Properties, second edition, Cambridge University Press, 1997.
[20] Pabst, W. and Gregorová, E., J. Mater. Sci., 39: p. 3501, 2004.
[21] Knudsen, F.P., J. Am. Ceram. Soc., 44: p. 376, 1959.

Cases

RISK OF FAILURE INDICES APPLIED TO SELECTION OF MATERIAL FOR PIPELINES

M. V. Biezma, J. R. San Cristóbal, R. Martínez
Degradation and Corrosion Research Group. E.T.S. Naútica. University of Cantabria
Germán Gamazo s/n. 39904 Santander. Spain
E-mail: biezmav@unican.es

ABSTRACT

The use of pipelines is, to some extent, the most economical way to transport hydrocarbons. Pipelines deteriorate over time, and in particular, an important failure or damage mode in pipelines is corrosion. Corrosion defects, in axial and longitudinal directions, diminishes the original thickness of the pipeline producing a remaining strength lower than the original. In some cases, the pressure of failure can be reached. Pipeline managers require assessments of integrity and safety in order to make appropriate decisions. The selection of materials for petrochemical pipelines is a laborious and difficult task. However, at the time to make the decision about the material to select for this application, the risk of failure of these materials, which work under aggressive environments, has not been considered. The unexpected failures can cause important losses, not only economic but also environmental and social.
The aim of this paper is to show different indices related with the risk of failure. These risk measures are evaluated and used as criteria in the selection of a specific material for a petrochemical API 5L pipelines.

KEY WORDS: Pipelines, Risk of Failure, Material Selection.

1. INTRODUCTION

The exploration, exploitation and transportation of crude oil and gas in petrochemical industry produce impact potentially negative, to personal, environment, with important economic repercussion. Millions of barrels crude oil has been dumped to selvage zones, rivers, lakes and oceans. The repercussion of that sometimes will be appears some years after produced the accident. Occidental Europe imports 97% of its needs from Africa and Medium Orient. USA, Russian, Canada, Mexico and Venezuela for example, have reserves at thousands of kilometers from the centres of consumption deposits.

In petrochemical activity is necessary to devote attention to the pipeline material selection, since the there are a lot of variables that can affect their useful life. One of the mayor problems is linked with corrosion phenomenon. Corrosion defects, in axial and longitudinal directions, diminishes the original thickness of the pipeline producing a remaining strength lower than the original. In some cases, the pressure of failure can be reached. Pipeline managers require assessments of integrity and safety in order to make appropriate decisions. The selection of materials for petrochemical pipelines is a laborious and difficult task. However, at the time to make the decision about the material to select for this application, the risk of failure of these materials, which work under aggressive environments, has not been considered.

There are four fundamental aspects to the correct operation of a piping system: security, supply continuous, economic efficiency and compliance with laws and international regulations. Despite the continuous improvements implemented in the aspect of safety, specifically in the monitoring and inspection processes, accidents and cracks in gas pipelines and oil pipelines continue to occur, either due to different variables in relation to material in nature, inadequate materials selection, manufacturing process, design, and a lack of inspection and maintenance [1]. In this case the decision maker has to consider several conflicting objectives, as social, economic, technological, environmental etc.

In this paper, we focus in materials selection taking into account the risk of failure under aggressive environments, in particular the selection of API 5L steel pipelines used in petrochemical industry.

2. MATERIAL SELECTION IN THE PETROCHENMICAL INDUSTRY

Pipelines, like other structures in nature, deteriorate over time. This natural deterioration in a metallic pipeline usually occurs as a result of the damaging effects by the surrounding environment. Corrosion is recognized as one of the most important degradation mechanisms that affect the long-term reliability and integrity of metallic underground and submerged pipelines. The environment in contact with a pipelines used in transportation of crude oil and gas has a very important amount of H_2S, a very corrosive acid gas

soluble in water, whose origin is in the own fuel or produced by metabolism of SRB Sulphate Reduced Bacteria. Thus, it is necessary a correct inspection and maintenance of the pipe and its protections, with the purpose of preventing leakage or escapes, due to unexpected failure with the corresponding environmental impact.

To ensure the reliability of pipelines, many research efforts have been devoted to predicting pipeline failure using deterministically and probabilistically tools. Pipeline operators throughout the world are confronted with the expensive and risky task of operating aged pipelines because of corrosion and its potential damaging effects. Furthermore, growing uncertainty adds to the problem.

The major effect of corrosion is the loss of metal cross-section. This results in a reduction of pipeline carrying capacity and safety. However, for a pipeline containing active corrosion defects, the major concern of a pipeline operator is the need to have a simple technique which can be used to evaluate the pipeline's current reliability. The problem then is to determine how the sizes of corrosion defects affect the integrity of a buried pipeline and pipeline with anticorrosive measurements, protective barrier and cathodic protection, since is very important to assess of remaining life of a pressurised pipeline containing active corrosion defects, [2-5].

There are different methods to estimate the remaining strength of corroded pipeline with internal active corrosion defects. The most employed are ASME B31G, [6], RSTRENG, PCORRC, DNV RP F-101, and SHELL-92.

The steels employed in petrochemical pipeline are API 5L, *American Petroleum Institute,* with different grades, attending the mechanical strength, consequence of their chemical composition [7-8]. Throughout last years has been increase their weldability due to low carbon equivalent value, but with higher mechanical strength, due to presence of different chemical elements. The Table 1 presents the yield strength and mechanical strength of different grades API 5L steels, and Table 2 present the chemical composition (%wt) of API 5L x100.

Table 1. Mechanical properties of API 5L steels

Grade	Yield Strength (MPa)	Mechanical strength (MPa)
X42	289	413
X56	386	489
X60	413	517
X65	448	530
X70	482	565
X80	551	620
X100	690	760

Table 2. Chemical composition of API 5L X100

C	Mn	Ni	Cu	Mo	Nb	Ti
0.06	1.96	0.39	0.17	0.11	0.04	0.01

3. APPLICATION

For analytical purposes we have considered three different materials to be employed in 10 kilometres of a crude oil transport pipeline. Table 3 shows the estimated costs of the three alternatives and the six possible scenarios which can occur depending on the probability of failure. The cost of failure refers to the different types of costs which may surge as a consequence of a failure, say , repairs, downtime, new materials, whereas the cost of no failure refers only to the cost of the material. Material A is the material with a greater probability of failure (0.60). The cost of no failure for this material is the lower (25,000), whereas the cost of failure is the highest (75,000). Material B is an "intermediate" material between the most expensive one (Material C) and the cheapest (Material A). Finally, Material C is the material with the lowest probability of failure (0.10) and the lowest cost of failure (40,000). Figure 1 shows the decision tree corresponding to the three decision alternatives at the time to select a material.

Table 3. Materials to Select, Probability of Failure and Associated Costs.

Material	Outcome	Probability	Costs (€)
A	Failure	0.60	75,000
	No Failure	0.40	25,000
B	Failure	0.20	60,000
	No Failure	0.80	30,000
C	Failure	0.10	40,000
	No Failure	0.90	50,000

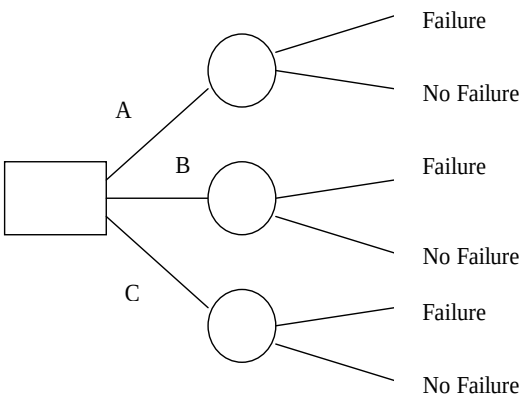

Figure 1. Decision Tree.

The three possible indices [9] that may be used as attributes in the decision process are: the Expected Cost, the Best Cost of each alternative, and the Standard Deviation of the Cost. Table 4 shows the values of these three risk indices calculated from the data of Table 3 for the three different materials

Table 4. Risk indices for the different materials

Material	Expected Cost	Best Cost	Standard Deviation
A	45,000	25,000	35.36
B	36,000	-	21.21
C	49,000	-	7.07

Once we have calculated the different risk indices, the next step is to select the material in accordance to the criteria. Each one of the three different criteria implies a different material to select. Following the Expected Cost criteria, the material to select is Material B, whereas the Best Cost criteria imply to select material A and attending the Standard Deviation criteria imply to select material C.

Table 5. Material to select depending on the criteria

Criteria	Material to select
Expected Cost	B
Best Cost	A
Standard deviation	C

4. CONCLUSIONS

The selection of materials for a given application is a challenging and difficult task, in particular in the selection of materials under high risk of failure, like petrochemical pipeline, due to the high corrosion activity inside pipeline. The unexpected failures can cause important losses, not only economic but also environmental and social. In this case the decision maker has to consider several conflicting objectives, as social, economic, technological, environmental etc.

In this paper, we focus in materials selection taking into account the risk of failure under aggressive environments. We have considered three different risk indices, the Expected Cost, the Best Cost of each alternative, and the Standard Deviation of the Cost. We show how different measures imply different selection of materials.

REFERENCES

[1] U. S. Office of Pipeline Safety. *Accident Summary Statistics by Year*, U. S. Department of Transportation, 2006.

[2] Benjamín, A.C., Freire, J.L.F., Vieira, R.D., Diniz, J. L., de Andrade, E. Q. *"Burst Test on Pipeline Containing Interaction Corrosion Defects"*, 24 th International Conference on Offshore Mechanics and Artic Engineering (OMAE), Halkidiki, Greece, June, 2005.

[3] Shu-Xin, L., Shu-Rong, Y., Hai-Long, Z., Jian-Hua, L., *Predicting Corrosion Remaining Life of Underground Pipelines with a Mechanically-Based Probabilistic Model*. Journal of Petroleum Science and Engineering 65, pag. 162–166, 2009.

[4] Cosham, A., Hopkins, P., McDonald, M.A., *Best Practice for the Assessment of Defects in Pipelines Corrosion*. Engineering Failure Analysis, 14, pag. 1245-1265, 2007.

[5] Kiefner, J.F., Vieth, P.H., *Evaluating Pipe Conclusion: PC Program Speeds New Criterion for Evaluating Corroded Pipe*. Oil & Gas Journal, 88, pag. 91-93, 1990.

[6] ASME B31G -1991. *Manual for Determining the Remaining Strength of Corroded Pipeline.* Ameritas Society for Mechanical Engineers, New York, 1991.

[7] American Petroleum Institute. *Summary of Technical Differences between API 5L (43rd ed.) and ISO 3183" (2nd ed.) / API 5L (44th ed.).* August 2008

[8] Terada, Y., Yamashita, M., Hara, T., Tamehiro, H., Ayukawa, N. *Development of API X100 UOE Line Pipe*. Nipon Steel Technical Report No. 72, 1997.

[9] M.A. Matos, *Decision under Risk as a Multicriteria Problem.* European Journal of Operations Research 18, pag. 1516-1529, 2007.

ESTUDO DE ANÁLISE DE FALHA DE UM CABO DE AÇO PRÉ-ESFORÇADO DE UMA PONTE SUSPENSA

C. M. Branco[1], A. Sousa e Brito[1], T. L. M. Morgado[2]

[1] ICEMS-IST-UTL – Instituto de Ciência e Engenharia de Materiais e Superfícies
Departamento de Engenharia Mecânica - Instituto Superior Técnico
Av. Rovisco Pais
Lisboa, Portugal

Email: cmbranco@dem.ist.utl.pt
Email: aasousabrito@gmail.com

[2] ICEMS-IST-UTL – Instituto de Ciência e Engenharia de Materiais e Superfícies
Departamento de Engenharia Mecânica - Politécnico de Tomar
Rua 17 de Agosto de 1808
Abrantes, Portugal

E-mail: tmorgado@ipt.pt

RESUMO

Neste artigo apresenta-se o resultado do estudo das causas de dano ocorrido num dos cabos pré-esforçados de aço de uma ponte suspensa. O estudo iniciou-se com a caracterização química, mecânica e microestrutural do material. O comportamento à fadiga foi estudado através de ensaios de fadiga realizados em condições o mais similares às condições ambientais a que os cabos estavam sujeitos (com e sem contacto com água). Complementou-se este estudo com análise fractográfica por microscopia electrónica de varrimento (MEV), de provetes ensaiados e de amostras obtidas directamente dos cabos danificados. Verificou-se que as superfícies de fractura dos varões constituintes dos cabos apresentavam dois modos de falha: fractura frágil em mais de 50% dos varões e fractura dúctil "taça e cone" nos restantes. Os resultados dos ensaios de fadiga conjuntamente com o estudo fractográfico permitiram concluir que a principal causa de falha, que originou o colapso da ponte, foi a corrosão sob tensão.

PALAVRAS CHAVE: ponte suspensa, aço de alto teor de carbono, curvas S-N, modos de falha, corrosão sob tensão.

ABSTRACT

This paper presents results of a failure analysis study to characterize the damage phenomenon that occurred in prestressed steel cables of a suspension bridge. This study includes: material characterization using chemical, microestrutural and hardness analysis; fractographic analysis by scanning electron microscopy (SEM); mechanical tests of the material in static tension; fatigue tests (S-N curves) and fractographic analysis of fatigue fracture surfaces. The fatigue tests were carried out in laboratory air only and in the laboratory air also but after previous exposure in tap water to simulate the working environment of the cables. Fractured surfaces of the rods were of brittle failure type and also of cup-and cone type. Due to the characteristics of the work environment (close to a river) stress corrosion was also observed and it is likely that hydrogen and oxygen embrittlement was obtained.
Results from fatigue tests and fractographic study allow to the conclusion that the main cause of cable failure, which led to a collapse of the bridge, was stress corrosion cracking (SCC).

KEY WORDS: suspension bridge, high carbon steel, stress corrosion cracking, fatigue life curves, fracture analysis

1. INTRODUCÃO

O presente trabalho respeita ao estudo das causas de ruína de um cabo de suspensão de um dos lados de uma ponte, que atravessa um dos rios mais importantes do norte do país.

O cabo era constituído por 84 varões, distribuídos por 12 enrolamentos de 6+1 varões. A parte acidentada do

mesmo (sujeita a este estudo) correspondia ao interior da ancoragem, tendo o comprimento de 1950 mm.

Exceptuando-se cinco varões centrais dos enrolamentos, que não sofreram fractura, pois apresentavam-se com o comprimento original, todos os restantes apresentavam fracturas distribuídas de modos distintos, identificados macroscopicamente:

- 21 varões, correspondendo integralmente à totalidade dos varões de três cordões de enrolamento, apresentavam superfícies de fractura dúctil, tipo "cone e taça", sitas perto do início da ancoragem (entre 100 e 250 mm);
- 45 varões (ou sejam mais de 50%), fracturados a distância entre 600 e 900 mm do início da ancoragem e apresentando elevado estado de corrosão (fig.1), exibiam fractura de tipo frágil alguns dos quais com extremidades em "ponta de lança", desenvolvendo-se longitudinalmente em comprimentos variáveis, atingindo por vezes 50 mm (fig.2);
- os poucos varões remanescente fracturados a distância idênticas ao do caso anterior, mas apresentando superfícies de fractura de difícil identificação macroscópica devido a elevado grau de corrosão.

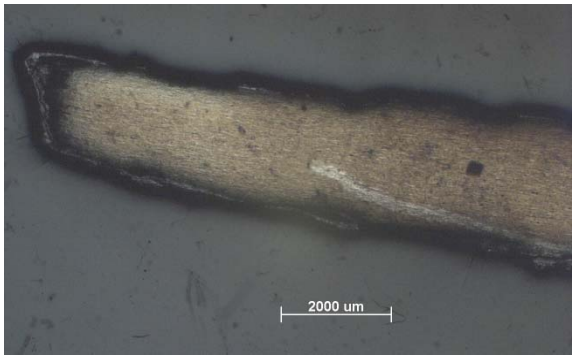

Figura 1. Observação a baixa ampliação de um dos varões fracturados, verificando-se efeito de forte corrosão superficial muito irregular.

Figura 2. Superfície de fractura de um varão fracturado segundo fácies de tipo frágil, em "ponta de lança" com elevado grau de corrosão, destacando-se a cavidade assinalada pela seta.

2. CARACTERIZAÇÃO QUIMICA, MECÂNICA E MICROESTRUTURAL DO MATERIAL

A composição química do material consta da tabela 1, verificando tratar-se de um aço de alto teor em carbono (0,91%) de alta resistência e baixa ductilidade. Trata-se de um aço hipereutectóide (% C> 0,8%) ao manganês.

Tabela 1. Composição química do material

ELEMENTO	[%]
Carbono (C)	0.91
Manganês (Mn)	0.59
Fósforo (P)	0.02
Enxofre (S)	0.06
Silicio (Si)	0.39
Cobre (Cu)	0.12
Níquel (Ni)	0.07
Crómio (Cr)	0.06
Molibdénio (Mo)	0.06 (L.Q.)

Os ensaios de tracção foram realizados em provetes cilíndricos segundo a norma E8 [1] com diâmetro de 6mm e comprimento de deformação L_0= 20mm.

Ensaios mecânicos de tracção e durometria apresentaram valores de tensão de rotura 1865 a 1932 MPa e valores de dureza 556 HV2, mostrando tratar-se de um aço duro e resistente [2]. O aço revelou-se do tipo frágil pois obtiveram-se valores do alongamento de rotura de 0,19.

A observação microestrutural de amostras obtidas em diversos varões e locais apresentavam sistematicamente microestrutura muito fina, alinhada longitudinalmente, com presença de inclusões não metálicas, tendo só com ampliações possíveis no microscópio electrónico de varrimento, sido identificadas zonas de *perlite fina* (fig. 3 a) e b)).

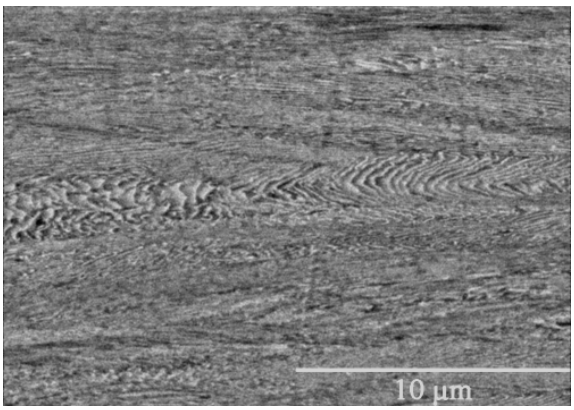

a)

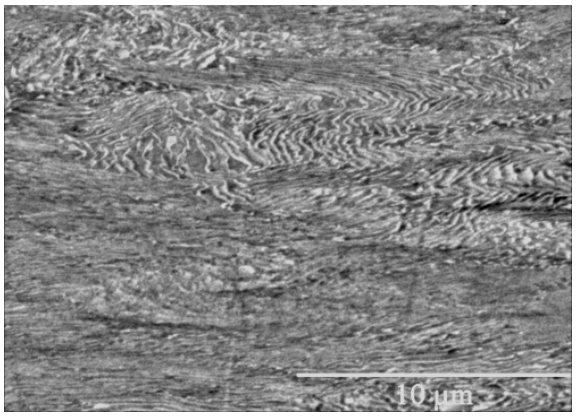

b)

Figura 3. Microestruturas obtidas por MEV identificando estrutura alinhada e perlite fina.

3. ENSAIOS DE FADIGA

Os ensaios de fadiga foram realizados em duas séries: uma série foi realizada apenas ao ar e a outra série foi realizada também ao ar mas com provetes submetidos a corrosão prévia em condições descritas a seguir.

3.1. Ensaios prévios de corrosão

Foram realizados previamente ensaios de corrosão numa amostra de doze provetes (fios) retirados da zona de estudo. Estes provetes foram imersos em água corrente com um caudal de 3 l/min num tempo de ensaio contínuo de 264 h (11 dias). Mediu-se o diâmetro dos fios antes e depois do banho assim como o peso. Neste ensaio fez-se uma avaliação dos efeitos das picagens e da dissolução causada pela água corrente. Destes ensaios concluiu-se que os provetes apresentavam um efeito significativo das picadas e da dissolução e oxidação causado pela acção da corrosão.

3.2. Ensaios de fadiga ao ar em provetes com e sem corrosão prévia

Foram ensaiados 10 provetes sem corrosão prévia e outros dez com corrosão prévia. O ciclo de fadiga aplicado consistiu numa onda sinusoidal a amplitude de tensão constante em tracção com R= 0,5 e frequência entre 5 e 16 Hz consoante o valor da carga.

Escolheu-se uma onda de carga com R= 0,5 para simular o efeito de uma pré-carga de tracção a que tirantes deste tipo estão normalmente sujeitos, no qual o ciclo de tensões é do tipo repetido consistindo numa solicitação alternada dinâmica, sobreposta a uma carga média de tracção devido ao peso próprio e (ou) pré-esforço e aos efeitos ambientais.

Os ensaios de fadiga foram realizados até à rotura ou até se atingir $6x10^6$ ciclos sem partir, consoante o que ocorrer primeiro, consistindo este valor de número de ciclos com o critério de vida infinita.

Os ensaios de fadiga obtidos nos provetes sem corrosão prévia, deram um elevado nível de dispersão de tal modo que não foi possível obter uma correlação válida entre a tensão máxima, σ_{max}, e o número de ciclos de rotura, N_r.

Para os provetes que foram ensaiados com corrosão prévia as condições de ensaio são mais uniformes, e a melhor correlação é obtida para a curva apresentada na Fig. 4, cuja equação é dada pela expressão (1):

$$\sigma_{max} = 3621 N_r^{0,0822} \quad (1)$$

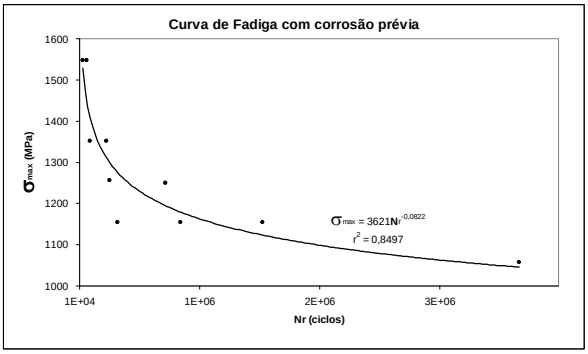

Figura 4. Curva de fadiga obtida dos provetes com corrosão prévia.

4. ANÁLISE FRACTOGRÁFICA

A análise fractográfica foi efectuada por microscopia electrónica de varrimento (MEV). Os exames foram dificultados pelo elevado grau de corrosão que grande parte das superfícies de fractura apresentavam.

Seguiu-se o mesmo critério das observações macroscópicas referidas em 1. Deste modo observaram-se:

- provetes com ***fracturas dúctil*** (tipo ***cone e taça***) nitidamente identificáveis a pequenas ampliações, apresentando fracturas secundárias geralmente radiais a partir duma zona central (Fig. 5 a)); maiores ampliações dessas zonas centrais permitiram a identificação de morfologias típicas deste modo de fractura, designada "***por coalescência de cavidades***" [3] (Fig 5 b)).

- provetes com fractura tipo "ponta de lança" foram observados ao longo das superfícies longitudinais de fractura e nos casos possíveis nas superfícies transversais que ligam as primeiras ao varão integral (Fig. 6 a) e b)); a presença de intensa corrosão (Fig. 6 b)) tornou difícil a observação, impedindo uma perfeita visualização das superfícies originais de fractura, mas permitindo

por vezes evidenciar uma descoesão no interior do fio estirado (Fig. 6 c)), denunciando uma possível separação de superfícies segundo trajectos longitudinais de baixa resistência; entre os múltiplos factores que poderiam promover este modo de fractura contam-se os factores ambientais que provocam corrosão sob tensão e fragilização por hidrogénio; as extremidades dessas pontas de lança também apresentam aspecto irregular e serrilhado confirmando as ilações tiradas (Fig. 6 d)).

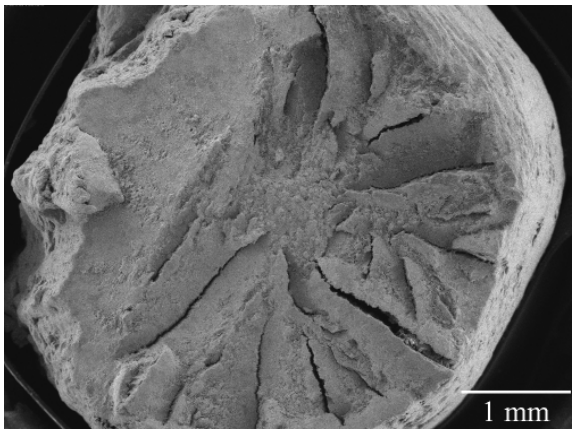

a)

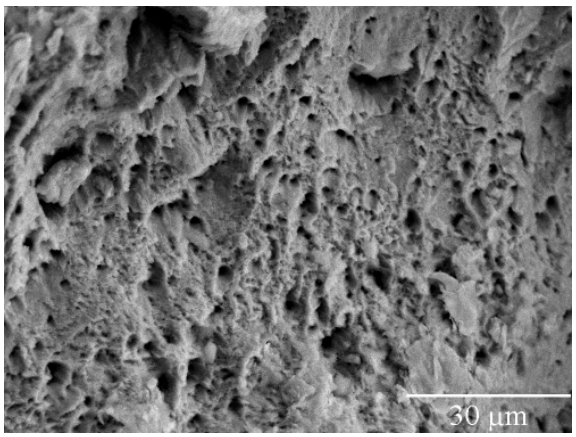

b)

Figura 5. Observação por MEV a) superfície fracturadas de modo dúctil b) zona central da amostra apresentado morfologia de fractura por coalescência de cavidades.

a)

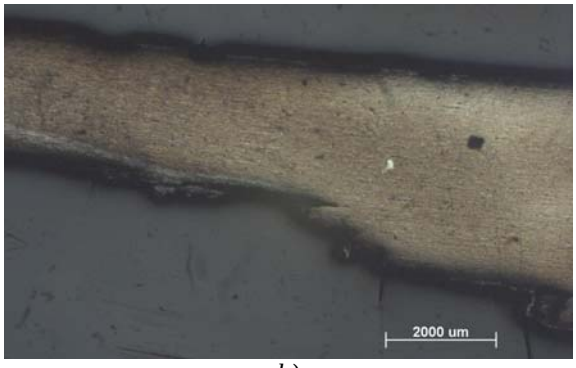

b)

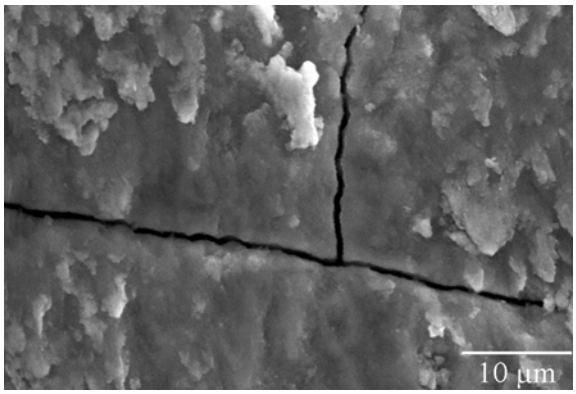

c)

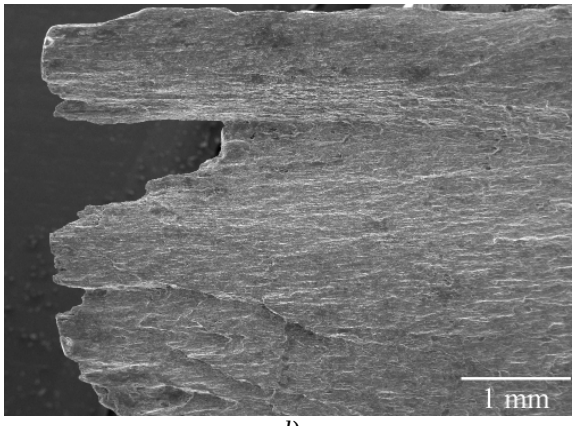

d)

Figura 6. Observações a diversas ampliações de provetes fracturados em "ponta de lança".

5. CONCLUSÕES

Através da análise microestrutural não foram detectadas diferenças sensíveis entre as microestruturas intrínsecas apresentadas por amostras tiradas de varões fracturados por diferentes mecanismos. Igualmente, não foi detectada evidência de contribuição de defeitos microestruturais originais, quer devidos ao material em si, quer ao processamento, como possíveis responsáveis pela ruína do cabo, que deverá então ser atribuída às condições mecânicas e ambientais durante o serviço do órgão.

Para as duas situações analisadas nos ensaios de fadiga (com ou sem corrosão prévia) verificou-se uma grande dependência entre a vida de fadiga e a tensão máxima do ciclo de fadiga i.e. uma pequena variação da tensão máxima causa uma grande variação da vida de fadiga.

Da análise fractográfica permite-se concluir que a fractura do cabo processou-se segundo duas fases sequenciais: na primeira os varões foram sendo atacados por corrosão sob tensão, que afectando de modo grave mais de 50 % dos varões, levou-os progressivamente à fractura; quando o número de varões remanescentes deixou de satisfazer aos esforços aplicados, os mesmos romperam-se quase instantaneamente, por fractura dúctil.

6. RERERÊNCIAS

[1] ASTM E8M-04, *Standard Test Methods for Tension Testing of Metallic Materials [Metric]*, Developed by Subcommittee: E28.04, Book of Standards Volume: 03.01, West Conshohocken, USA.

[2] C M. Branco e A. Sousa e Brito, *Estudo Microestrutural, Fractográfico e de Comportamento Mecânico (tracção e fadiga) dos fios de pré-esforço dos tirantes da ponte José Luciano de Castro, Penacova*, DEM - CEMUL/UTL, Lisboa, 2007.

[3] Hull Derek, *Fractography* Cambridge University Press, 1999.

FRACTURA DEL VIDRIO TEMPLADO EN MUROS CORTINA

Francisco Capel and J Pablo Calvo.
Instituto de Cerámica y Vidrio. Consejo Superior de Investigaciones Científicas.
C/ Kelsen, nº 5. 28049 Madrid.
Centro de Información Técnica de Aplicaciones del Vidrio

RESUMEN

El vidrio templado soporta cualquier tipo de tensiones mecánicas cuando está colocado en su lugar de uso. Sin embargo, presenta problemas intrínsecos de rotura debido a incluiones incluidas en la masa fundida y que se forman durante el proceso de fabricación. Una de las clásicas razones de rotura catastrófica diferida en el tiempo que se producen en el vidrio templado es debida a partículas de sulfuro de níquel. La fase α de la variedad hexagonal de sulfuro de níquel de alta temperatura, con estructura niquelina, transforma a la fase β (millerita) de la variedad romboédrica, estable a la temperatura de 380 ºC. Esta transformación va acompañada de una expansión de volumen del 2.8 % que es suficiente para nuclear microgrietas las cuales se propagan en la zona de tensiones a tracción provocando la rotura del vidrio. En el presente trabajo se hace una revisión de la fractura inducida por partículas de sulfuro de níquel y una colección de vidrios rotos conteniendo dichas partículas son analizadas usando microscopía electrónica de barrido (MEB). la fractura de los vidrios se explica basándose en las propiedades de las partículas de sulfuro de níquel. Se presenta también una posible explicación del mecanismo de formación de las partículas.

PALABRAS CLAVE: Fractura, vidrio templado, sulfuro de níquel

ABSTRACT

The tempered glass supports any type of mechanical stress when it is located outside of its place of use. However, it presents an intrinsic problem of breakage due to mass inclusions formed during the manufacturing process. One of the classic reasons delayed catastrophic ruptures in tempered glass is due to nickel sulphide particles. The α-phase, of the hexagonal array of nickel sulfide, high temperature, with niquelina structure, transforms to β-phase (millerite) variety stable at a temperature of 380 ºC. This transformation is accompanied by a volumetric expansion of about 2.8 % that is sufficient to nucleate microcracks which, in tempered glass, propagate in the internal tensile stress field with destruction of the body.
In the present paper is a brief review of the nickel sulphide induce fracture in tempered glass and a collected several pieces of broken glass cullet containing stones in them and analyzed them using SEM. The phenomenon of fracture is explained by the properties of nickel sulphide particles. A tentative explanation is given of the mechanism by which these particles are formed.

KEY WORDS: fracture, tempered glass, nickel sulphide.

1. INTRODUCIÓN

El vidrio templado puede romper por defectos superficiales, tales como fisuras, arañazos, golpes en los bordes, que actúan como centros de concentración de tensiones; desigual enfriamiento durante el templado que genera tensiones diferentes en el vidrio o cualquier causa externa que supere su resistencia mecánica. Otra forma de rotura del vidrio templado es debida a las inclusiones de sulfuro de níquel cuando se sitúa en la zona de tracción del mismo por transformación de fase que conlleva un aumento de volumen, generándose, por tanto, una concentración de tensiones cerca de dicha inclusión (1).

Las grandes sociedades vidrieras empezaron a inquietarse por este tema y estudiaron un método basado en un tratamiento térmico para tratar de eliminar o aminorar el problema, el denominado *Heat Soak Test* (2). El proceso consiste en calentar el vidrio a una temperatura de unos 280 ± 10ºC, mantenerlo durante dos horas y enfriarlo lentamente. Con este proceso se reduce bastante la incidencia de la fractura de los vidrios por inclusiones de NiS ya que el cambio de fase se produce antes de que los vidrios se instalen en el edificio. Sin embargo este proceso no es efectivo 100 % y no todas las empresas pueden costear este ensayo.

En el presente trabajo se presenta una revisión de las distintas opiniones que existen sobre el tema y posteriormente el análisis de la naturaleza y morfología de las partículas de una serie de casos en donde se han producido fractura espontánea en cuerpos de vidrio templado.

Las inclusiones de NiS, generalmente esféricas o elípticas, presentan expansión de volumen por cambio de fase en el enfriamiento. Esta expansión de volumen es suficiente para nuclear microcristales los cuales, en el vidrio templado, generan un campo de tensiones internas, alrededor de la partícula, suficiente para romper el vidrio. Estas fracturas presentan la

particularidad de producirse al cabo de cierto tiempo, en algunos casos bastante largo, después de templarse.

Este fenómeno fue detectado por primera vez por Ballantyne (4), el cual identificó la naturaleza de las inclusiones y encontró que la posición de la partícula dentro del vidrio es importante. Si la inclusión se encuentra en el centro de la hoja, es decir en una zona de tracción, un pequeño aumento de la tensión puede provocar la ruptura; por el contrario si la inclusión se encuentra en la zona de compresión no hay peligro de rotura a no ser que una deformación mecánica externa modifique el estado de tensiones.

Según el diagrama de fases establecido por Wagner (6) En el campo Ni_3S_2-Ni_7S_6 existe un punto de transición a 397 ºC correspondiente a la transformación $\alpha \rightarrow \beta$ Ni_7S_6 y en el dominio Ni_7S_6-NiS hay dos puntos de transformación:

$$\text{a } 400\ ºC:\ \alpha \rightarrow \beta\ Ni_7S_6$$
$$\text{a } 379\ ºC:\ \alpha \rightarrow \beta\ NiS$$

Más allá del campo del NiS se sitúa una zona de solución sólida $Ni_{(1-x)}S$, y el punto de transformación de la fase $\alpha \rightarrow \beta$ $Ni_{(1-x)}S$ está situado a 282 ºC.

La transformación de la fase α de la variedad hexagonal de sulfuro de níquel de alta temperatura, con estructura *niquelina,* a la fase β con el nombre de *milerita (*65 wt% Ni - 34wt% S), que es la forma romboédrica estable a baja temperatura se produce lentamente y con un fuerte aumento de volumen, del orden de un 2.8 %. La temperatura precisa de la transformación depende fuertemente de la estequiometría. El paso de la variedad β existente en el vidrio recocido a la α se produce rápidamente a 720 ºC durante el templado. Sin embargo, la reversibilidad de α a β es lenta, desarrollándose por debajo de los 400 ºC. Al ser una función del tiempo y la temperatura es por lo que dicha reversibilidad puede tardar años en producirse.

Dado que la fractura por sulfuro de níquel se produce en la actualidad con cierta regularidad, existe la necesidad de localizar NiS en acristalamientos antes de romperse.

En Brisbane, un equipo de la Universidad de Queensland y de Resolve Engineering han encontrado un camino para detectar dicho compuesto. Se trata del conocido proceso photoglass (8). J. C. Barry y col (9) han estudiado mediante *Scanning Electron Microscopy (SEM) y Energy Dispersive X-ray Spetroscopy (EDS)* una serie de partículas de NiS extraídas por este método y clasificadas en dos grupos: unas que denominan *clásicas* y otras *atípicas* que presentan una forma ovalada y una textura más suave. Concluyeron que la composición de todas las inclusiones con color amarillo-oro eran de sulfuro de níquel con un rango de composiciones de $Ni_{52}S_{48}$ a $Ni_{48}S_{52}$ y son peligrosas y provocan fractura en el vidrio. Según los autores del trabajo, la diferencia significativa entre inclusiones pasivas y peligrosas está en la diferencia de composición sino en la diferencia del tipo de material en los poros internos. Las inclusiones pasivas tienen carbón en el interior de sus poros, mientras que las peligrosas tienen Na_2O.

El sulfuro de níquel se forma en la mezcla vitrificable, antes de la fusión por la acción del sulfato de sodio, de un compuesto de níquel y de un medio reductor. El producto formado funde por debajo de 1000 ºC.

El aporte de azufre en el vidrio viene dado por el sulfato de sodio, calcio o bario que se usan como afinantes. La cantidad de azufre proveniente de la combustión es despreciable.

La introducción de níquel viene dada por los dispositivos construidos con aceros inoxidables y refractarios, como son las cajas de agua, bulloneras, quemadores, agitadores, etc. Algunas materias primas se someten a una acción mecánica en aparatos constituidos por aleaciones de níquel; también puede venir el níquel como contaminación de las mismas. El fuel puede contener hasta 100 ppm de níquel y de vanadio.

Los reductores son numerosos en la fabricación del vidrio: carbono mediante la adición voluntaria de carbon, coke, fuel en las mezclas vitrificables; metales en el calcín, cajas de agua, utensilios; atmósferas debidas a productos no quemados que producen CO; sulfuros.

Swain (13,14) estudia la microfisuración que provoca la transformación de fase de inclusiones en vidrios templados térmicamente y los compara con los análisis de mecánica de fractura. Estima que la presión hidrostática resultante de la transformación de fase $\sigma \rightarrow \beta$ del NiS es de 834 MPa para una inclusión completamente pura y totalmente transformada.

Teniendo en cuenta las tensiones generadas por los diferentes coeficientes de dilatación entre el vidrio y el sulfuro de níquel que son del orden de -219 MPa, la presión hidrostática resultante dentro de la esfera transformada es de 615 MPa.

Las observaciones de vidrios templados con inclusiones de NiS que se han fracturado espontáneamente revelan que la fractura se inicia a partir de inclusiones superiores a 110 μm de diámetro localizadas en el campo de tensiones a tracción en la mitad del vidrio plano. Inclusiones comprendidas entre 80 y 110 μm fueron responsables en algunos casos de fracturas espontáneas, mientras que por debajo de 80 μm no eran peligrosas y el campo de tensiones estaba comprendido entre 50 y 60 MPa (13,14).

2. PROCESO EXPERIMENTAL

2.1.-Observación visual y mediante microscopía óptica de luz reflejada.

Una serie de vidrios templados que han sido fracturados en distintos lugares de la geografía española han sido analizados con objeto de conocer la composición de las partículas metálicas causantes de la rotura. Antes de separar la zona de vidrio fracturado en donde se encuentra la bolita de sulfuro de níquel, observable a simple vista, se ha procedido a fotografiar dicha zona, tal y como se puede apreciar en la Fig. 1.

La morfología de la fractura que presentan los vidrios rotos por inclusiones de sulfuro de níquel es muy típica: alrededor de la inclusión metálica se forma una especie de ocho, también denominado alas de mariposa. A partir de dicha zona se generan una serie de figuras fragmentadas, típicas del vidrio templado.

Fig.1.-Observación visual de la partícula de NiS en el vidrio fracturado

Una amplia zona en donde se encuentra la inclusión metálica se separa cuidadosamente del resto del acristalamiento fracturado mediante láminas de plástico adheridas a ambos lados de la hoja de vidrio. Cuando los vidrios son monolíticos es difícil que los fragmentos se mantengan unidos y de ahí la dificultad de obtener muestras de estudio. No sucede lo mismo cuando se trata de vidrios laminares en donde es posible rescatar la zona que contiene la inclusión metálica. En este caso es necesario introducir los vidrios que contienen la inclusión en alcohol con objeto de liberar al vidrio laminar de la hoja de polivinil butiral. Ambos trozos de vidrio que contienen la bolita de NiS, se han observado mediante microscopía óptica de luz reflejada. En uno de los trozos se encuentra la inclusión metálica propiamente dicha y en el otro contiene la huella de dicha partícula, denominada *cuna*.

En la Fig. 2 se pueden apreciar la partícula metálica en el centro de la sección transversal del vidrio. A partir de la misma hay una pequeña zona de fractura y a cntinuación una amplia zona lisa que corresponde a la zona de *smooth mirror* de la superficie de fractura que se forma alrededor de la inclusión metálica debido a las grandes tensiones a tracción a que está sometido el vidrio en el centro provocadas por el proceso de templado térmico. A partir de dicha zona "espejada" aparece la zona de *hackel*, no representada en la figura, correspondiente a la región de fractura propiamente dicha.

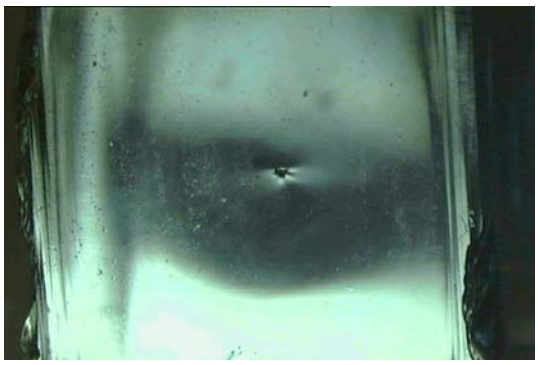

Fig.2.-Observación MOR de la partícula de NiS en el vidrio.

En la Fig.3 se representa la partícula de NiS y la fractura que genera a su alrededor. Como se puede observar en la figura la inclusión metálica presenta una forma esférica cuya superficie tiene un aspecto rugoso, es de color amarillo oro tal y como se ha referenciado en la literatura (6)

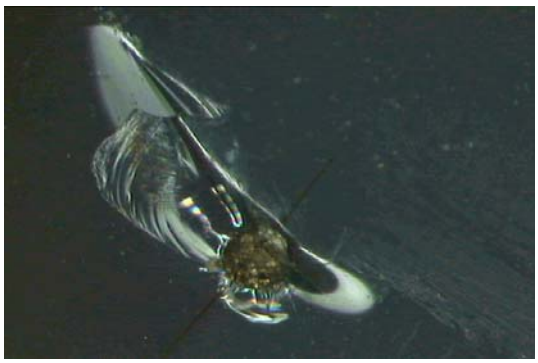

Fig.3.-Observación MOR de la partícula de NiS en el vidrio

2.-Observación por MEB-EDX

Mediante microscopía electrónica de barrido (MEB) equipado con un espectroscopio de energías dispersivas (EDX) se ha podido analizar dichas inclusiones, confirmando la existencia de NiS y otros elementos que contiene la inclusión.

En la Fig. 4 se presentan la morfología la bola de NiS. Como se puede observar presenta un aspecto rugoso y algunas de las zonas de la superficie están muy deterioradas.

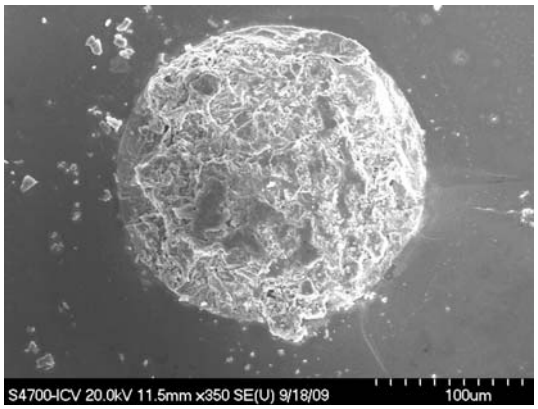

Fig. 4.-Aspecto que presenta la bola de NiS, observada por microscopía electronica de barrido (MEB)

Del análisis mediante MEB-EDX de una de las partículas, Fig.5 y Tabla 1, se deduce que la naturaleza de la inclusión es de sulfuro de níquel. No obstante hay zonas que están enriquecidas en Ni, es decir como si no se hubiese completado totalmente la formación de NiS. En algunas de las zonas analizadas se detecta la presencia de hierro y de níquel metálico. También se ha detectado la presencia de vidrio encima de la partícula.

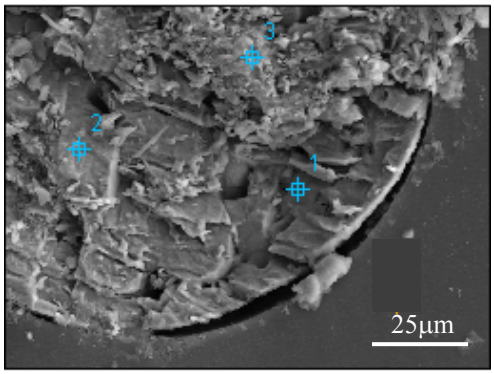

Fig. 5.-Análisis mediante MEB-EDX de una partícula de NiS.

Tabla I

	Na_2O	SiO_2	SO_3	CaO	Fe_2O_3	NiO
1		25.31	3.32	0.49	0.92	69.96
2		3.78	58.98		0.26	36.98
3	3.48	8.05	20.58		1.03	66.86

CONCLUSIONES

Una de las causas principales de fractura de los vidrios templados térmicamente es debida a las inclusiones metálicas de NiS que se generan durante la fusión.

El análisis por MOLR nos muestra la inclusión en el centro del vidrio, es decir, la zona sometida a tracción, causa fundamental para que rompa el vidrio.

El análisis por MEB-EDX indica la existencia dentro de la partícula de NiS de zonas más enriquecidas en Ni. También se ha detectado la presencia de hierro y níquel metálico dentro de la partícula metálica que podrían ser los agentes nucleantes de la formación del NiS.

Bibliografía:

[1] BAO Yiwang, Mr. YANG Jianjun, Mr SHL Xinyong, Another cause for spontaneous breakage of tempered glass-silicon particles in tensile zone. Glass Performance Days 2007. 7001-703.

[2] European Norms: EN 14179-1-2 2005. Title of Standard, Glass in Building, Heat-soaked thermally-toughened soda lime silicate safety glass.

[4] J.E.R. Ballantyne, CSIRO, División of Building Researh, Melvourne, Australia, Report 061-5 (1961),

[6] R. Wagner, Glastechn. Ver. **50** (1977) Nr. 11, S. 296-300)

[8] T. Ford, International Conference on Building Envelope Systems and Technology. University of Bath, April 1977.

[9] An electron microscopic study of nickel sulfhide inclusions in toughened glass. Journal of Material Science **36** (2001) 3721-3730).

[13] Swain M.V. Nickel sulphide inclusions in glass: an example of microcracking induced by a volumetric expanding a phase change. J. Mat Science, 1981; 16: 151-158.

[14] Swain M.V. A fracture mechanism description of the microcracking about NiS inclusions in glass. J. Non Crystalline Solids, 1980; 38-39: 451-456.

ANÁLISIS DE FALLO DEL TUBO DE DRENAJE DE UN SOBRECALENTADOR

S. Cicero[1], R. Lacalle[1,2], R. Cicero[1], J. García[1,2]

[1] Universidad de Cantabria, ETS Ingenieros de Caminos, Canales y Puertos
Departamento de Ciencia e Ingeniería del Terreno y de los Materiales
Av/Los Castros s/n, 39005, Santander, Cantabria, Spain
ciceros@unican.es

[2] INESCO Ingenieros SL, Centro de Desarrollo Tecnológico de la
Universidad de Cantabria (CDTUC), Fase A, Mod. 203, Av/ Los Castros s/n, 39005, Santander, Cantabria, Spain

RESUMEN

Este trabajo presenta el análisis de fallo del tubo de drenaje de un sobrecalentador utilizado en el generador de vapor de un vertedero, con el cual se obtiene energía a partir del biogas producido por los restos orgánicos. El estudio comprende análisis químicos y microestructurales junto con medidas de microdurezas e inspecciones visuales y por microscopía SEM.

Se detectaron incrementos significativos de dureza en la sección de rotura, sugiriendo que dicha sección se localiza en la Zona Afectada Térmicamente (ZAT) de una soldadura situada en sus proximidades. Como mecanismo principal del fallo se ha identificado la fatiga del material, asistida por procesos de corrosión. Las diferentes áreas encontradas en la superficie de fractura sugieren que dicha fatiga fue causada por las operaciones de mantenimiento del sobrecalentador, que consistían básicamente en el golpeteo de un tubo colector que une el tubo de drenaje con el sobrecalentador. Finalmente, no se encontraron evidencias de condiciones anómalas de operación que pudieran haber favorecido el fallo, como pudieran ser la existencia de sobrepresiones o el trabajo del tubo a temperaturas anormalmente elevadas.

ABSTRACT

This paper analyses the failure of a steam generator superheater drain tube used in a dump to obtain energy from the biogas produced by organic waste. The analysis comprises chemical and microstructure analyses, together with microhardness measurements and visual and SEM inspection.

Significant increases in hardness in the failure section were detected, suggesting that the failure section is located in the heat affected zone of a nearby weld. Fatigue has been identified as the major cause of the final failure, assisted by corrosion processes. The different areas found on the fracture surface suggest that fatigue processes were caused by the maintenance operation consisting of hitting the collector tube to which the drain tube is joined. Finally, no evidence has been found in relation to any other anomalous operating conditions, such as overpressure or unexpected high temperatures.

PALABRAS CLAVE: Fatiga, corrosión, picaduras, microdurezas, Zona Afectada Térmicamente.

1. INTRODUCCIÓN

Tras un año en servicio, el tubo de drenaje de un sobrecalentador utilizado en el generador de vapor de un vertedero experimentó un fallo inesperado. El generador (de 10.5 MW de potencia) permite aprovechar el biogás generado por los restos orgánicos y tiene un conjunto de calentadores, recalentadores y sobrecalentadores con distintas funciones, tal y como se recoge [1,2]. Los sobrecalentadores conducen vapor seco, pero en determinadas circunstancias (transitorios del generador) puede llegar a transportar vapor de agua, por lo que se requieren tubos de drenaje que evacuen dicho vapor.

En este trabajo se analiza el fallo de uno de los tubos de drenaje, combinando inspección visual de la superficie de fractura, análisis tensional cualitativo, análisis químico, medidas de microdurezas, análisis microestructural y análisis SEM.

2. MATERIAL, GEOMETRÍA Y CONDICIONES DE TRABAJO.

El tubo está fabricado en acero St 35.8 según la DIN 17175 [3] para tubos sin soldadura utilizados a altas temperaturas. Las tablas 1 y 2 recogen, respectivamente, la composición química y las propiedades mecánicas de la especificación.

Tabla 1.Composición química del acero St 35.8 [3]

C	Si	Mn	P	S
≤0.17	0.10- 0.35	0.40 -0.80	<0.040	<0.040

Tabla 2. Propiedades mecánicas del acero St 35.8 [3]

σ_{yRT} (MPa)	$\sigma_{y400ºC}$ (MPa)	σ_u (MPa)
235	110	360-480

El diámetro exterior del tubo es de 24 mm y el espesor es de 5 mm.

La temperatura y la presión en el tubo son 420 ºC y 44 bar, respectivamente. De igual forma, el sobrecalentador requiere operaciones de mantenimiento continuas para eliminar posibles depósitos. Para ello, los colectores que unen los tubos de drenaje los sobrecalentadores se golpean, provocando cargas dinámicas variables (cortantes y flexión alterna) en los tubos de drenaje. El proceso queda recogido en la Figura 1, que proporciona una descripción cualitativa de la posición de la sección de rotura. Puede observarse que dicha sección se encuentra próxima a la conexión entre el tubo de drenaje y el colector, junto a una soldadura transversal. La distancia exacta a dicha soldadura no era conocida, puesto que solo fue proporcionada para el análisis la parte inferior del tubo.

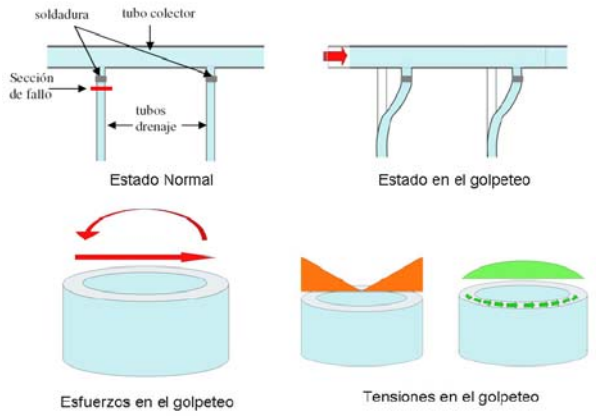

Figura 1. Condiciones de trabajo durante el golpeteo de mantenimiento.

3. ANÁLISIS QUÍMICO, MICRODUREZAS Y MICROESTRUCTURAS.

La composición química del material del tubo se determinó mediante espectrometría de emisión óptica, mostrándose los resultados en la Tabla 3, en la cual se observa que no hay desviaciones con respecto a la especificación del material [3].

Las medidas de microdurezas (HV1) se realizaron en dos localizaciones: una próxima a la sección de rotura (10 mm) y otra alejada de la misma (100 mm). El objetivo fue determinar si existían zonas de material con propiedades mecánicas diferenciadas. Un esquema del proceso se muestra en la Figura 2, mientras que los resultados se recogen en la Tabla 4. Se observa que no hay diferencias significativas entre las dos localizaciones analizadas.

Tabla 3. Composición química del tubo de drenaje.

Zona	C	Si	Mn	P	S
Cerca (10 mm) Sección de rotura	0.11	0.26	0.58	<0.010	<0.010
Lejos (100 mm) Sección de rotura	0.10	0.26	0.57	<0.010	<0.010

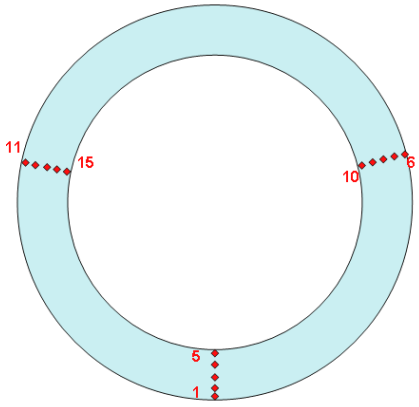

Figura 2. Localización de las medidas de microdurezas.

Tabla 4. Resultados de microdurezas (HV1).

	HV1 a 10 mm de sección de rotura	HV1 a 100 mm de sección de rotura
1	142.8	159.5
2	141.0	143.6
3	139.4	142.2
4	139.9	159.6
5	138.6	147.6
6	159.0	142.1
7	149.3	154.2
8	146.1	160.1
9	132.5	150.0
10	141.1	154.5
11	158.8	139.9
12	159.1	146.9
13	146.9	150.2
14	144.0	140.0
15	142.4	142.3

De igual modo, se realizaron medidas de microdurezas en la dirección longitudinal del tubo, desde la sección de rotura y en sentido descendente (ver Figura 1), con el objetivo de comprobar si la dicha sección se encontraba en la Zona Afectada Térmicamente (ZAT) de la soldadura situada sobre ella. Los resultados (Tabla 5) confirman este hecho.

Table 5. Microdurezas (HV1) en dirección longitudinal

	Distancia a la sección de rotura (mm)	**HV1**
1	0.5	208.8
2	1	179.6
3	2	163.7
4	3	151.0
5	8	139.3
6	12	140.5
7	16	142.5
8	20	137.0

El análisis microestructural se realizó, análogamente, en dos localizaciones: una próxima a la rotura (10 mm) y otra alejada de la misma (100 mm). Para ello se atacaron muestras con nital (2% de HNO_3). Los resultados (Figura 3) muestran estructuras ferrítico-perlíticas muy similares, en concordancia con los resultados de durezas. Se realizaron análisis similares que descartaron la posibilidad de decarburaciones asociadas a temperaturas de trabajo anormalmente elevadas.

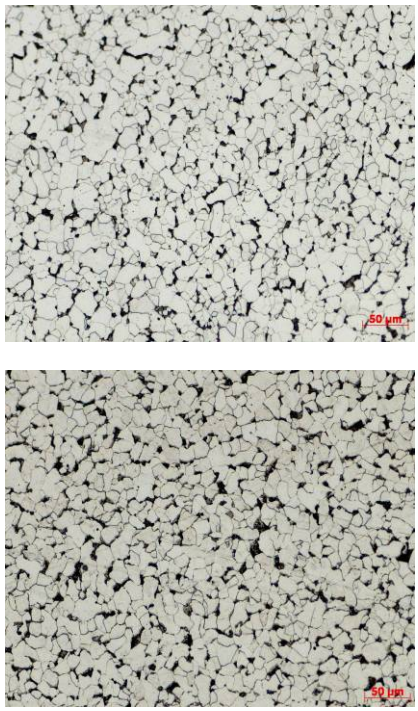

Figura 3. Microestructuras en el tubo de drenaje: a) a 10 mm de la rotura; b) a 100 mm de la rotura.

4. ANÁLISIS DE LA SUPERFICIE DE FRACTURA

La Figura 4 muestra la sección de rotura, en la cual se distinguen 4 zonas: las zonas A y C son planas, mientras que las zonas B y D tienen una pendiente aproximada de 45º. Este tipo de superficies ha sido analizado en [4], sin que se justificase su particular morfología. La explicación al respecto es la siguiente (ver Figura 1): las zonas A y C se encuentran sometidas fundamentalmente a tensiones normales de flexión (con tensiones cortantes pequeñas), mientras que las zonas B y D están sometidas a tensiones cortantes elevadas y tensiones normales bajas (nulas en la fibra neutra de la sección), lo cual produce la propagación de fisuras a 45º. Además se observa que la Zona A presenta mayor oxidación, lo que sugiere que fue la primera en experimentar los procesos de fisuración.

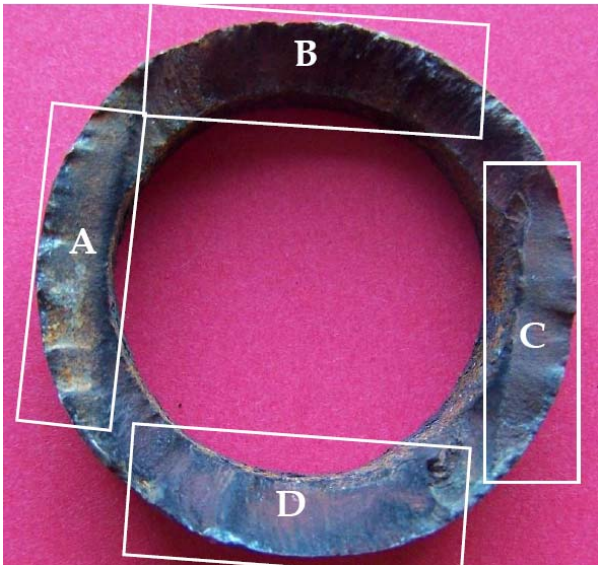

Figura 4. Localización de las diferentes zonas de la superficie de fractura (en recepción) .

La superficie de fractura fue decapada con objeto de eliminar la capa de óxido y las impurezas existentes en la misma. Tras el decapado se realizó otra inspecció visual. En la Zona A (Figura 5) se observaron marcas de trinquete o "*ratchet marks*", indicando la existencia de múltiples puntos de iniciación de fatiga [5], por lo que este fenómeno aparece como una de las causas del fallo; en las Zonas B y D (Figura 6) se observaron playas de fatiga asociadas a la propagación de fisuras (confirmando a la fatiga como proceso clave del fallo analizado); finalmente, en la Zona C (Figura 7) se vuelven a observar "*ratchet marks*", así como dos zonas rugosas en su transición a las Zonas B y D, que parecen ser los ligamentos remanentes existentes en el instante previo al fallo final.

Figura 5. Macro de la Zona A, mostrando las marcas de trinquete asociadas a múltiples puntos de iniciación de la fatiga.

Figura 6. Macro de la Zona B, mostrando las playas de fatiga asociadas a un proceso de propagación de fisuras.

Figura 7. Macro de la Zona C, mostrando las marcas de trinquete y los dos ligamentos remanentes.

Se realizaron macrografías adicionales en las superficies interior y exterior del tubo, observándose en ambos casos multitud de picaduras y pérdidas localizadas de metal (Figura 8).

Figura 8. Picaduras encontradas en la superficie exterior del tubo.

Tras la inspección visual se realizó un análisis SEM de la superficie de fractura. La Figura 9 muestra uno de los puntos de iniciación de fisuras asociados a las marcas de trinquete observadas en la Zona A. Se puede observar que la iniciación va asociada a un defecto superficial producido por la corrosión que ha podido actuar como concentrador de tensiones. Un interacción similar entre fatiga y picaduras por corrosión ha sido recogida, por ejemplo, en [6].

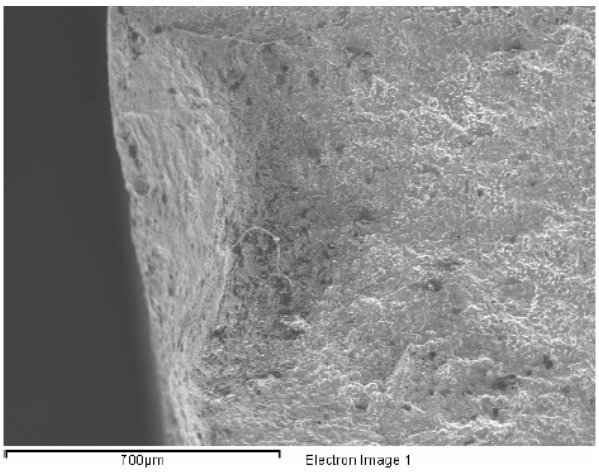

Figura 9. Punto de iniciación de fatiga en la zona A.

La Figura 10 muestra marcas de fatiga encontradas tanto en la Zona B como en la D. Estas marcas, con evidente concavidad, están asociadas a un proceso de propagación de fisuras.

En la Zona C, el análisis SEM revela mecanismos muy similares a los observados en la Zona A (reafirmando lo observado en la inspección visual). La Figura 11 muestra un punto de iniciación de fatiga asociado a una picadura.

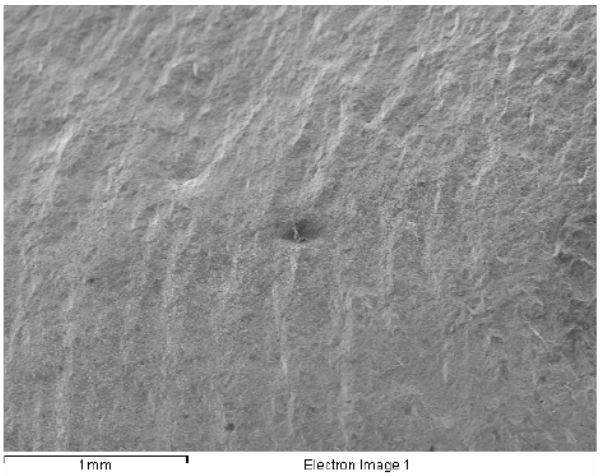

Figura 10. Marcas de fatiga observadas en la Zona D.

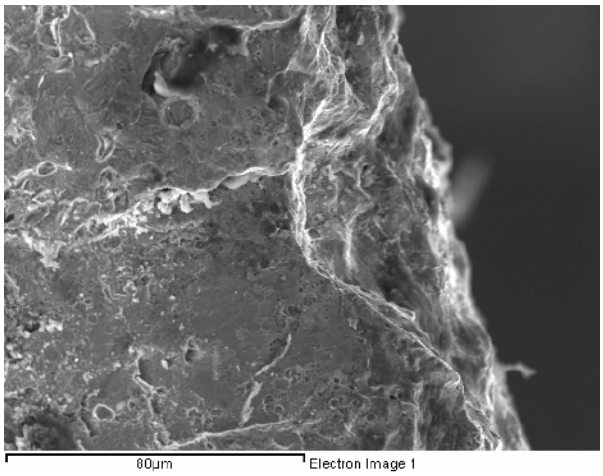

Figura 11. Punto de iniciación de fatiga observado en la Zona C.

De igual forma, cabe destacar que tanto en la Zona A como en la Zona C se observaron pequeñas áreas con propagación intergranular (Figura 12), lo cual sugiere la existencia de interacciones entre la fatiga y procesos de corrosión.

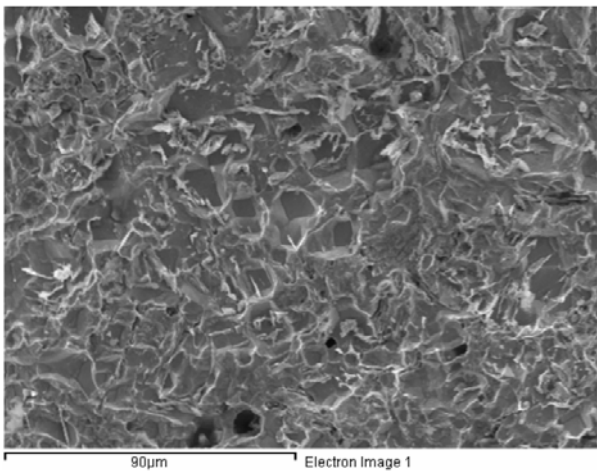

Figura 12. Indicios de propagación intergranular observados en las Zonas A y C.

Finalmente, la Figura 13 muestra los microhuecos observados en los ligamentos remanentes mencionados con anterioridad, lo cual indica que el fallo final del tubo se produjo por colapso plástico de la sección remanente.

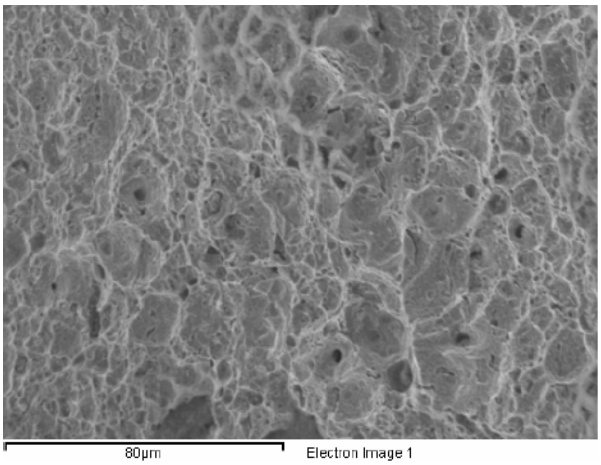

Figura 13. Microhuecos observados en los ligamentos remanentes.

5. ANÁLISIS DE LOS RESULTADOS

Los resultados recogidos anteriormente permiten afirmar que se ha producido una iniciación de fisuras en las Zonas A y C como consecuencia del efecto combinado de las tensiones ocasionadas por el golpeteo de mantenimiento de los tubos de drenaje (que provoca vibraciones y cargas variables en los mismos) y por la corrosión superficial detectada tanto en la superficie interior como en la exterior del tubo (que provoca la aparición de picaduras y pérdidas de material que actúan como concentradores de tensiones y como puntos de iniciación de la fatiga). La corrosión, que en condiciones normales de operación no tiene por qué producirse, puede haber sido ocasionada por la presencia inesperada de cantidades excesivas de vapor de agua.

Sin embargo, parece que la iniciación primaria ocurrió en la Zona A (más oxidada en recepción) y que la propagación se produjo a lo largo de las Zonas B y D desde la Zona A hasta la C. La concavidad observada en las marcas de fatiga (Figura 10) ha sido justificada en [5,7] como una combinación de flexión alterna con tensiones bajas y concentraciones de tensiones medias/severas (en este caso, causadas por los defectos superficiales y por la presencia de una soldadura en las proximidades).

De forma simultánea, una fisura menor propagó por la Zona C en dirección opuesta. En ambos casos, las evidencias de cierta componente intergranular en la propagación sugieren que la fatiga estuvo asistida por procesos corrosivos.

Finalmente, ambas fisuras alcanzaron los ligamentos remanentes (encontrados en la transición entre la Zona C y las Zonas B y D) y se produjo el fallo final por colapso plástico.

El golpeteo del tubo colector justifica, de igual modo, tanto el proceso de fatiga que ocasiona el fallo como la morfología de la superficie de fractura. Además, se puede afirmar que no ha habido ningún tipo de sobrepresión en relación con el fallo, dado que un hecho de este tipo hubiese producido fisuras de tipo longitudinal.

La localización de la sección de fallo queda justificada por el hecho de que se encuentra en el interior de la ZAT de una soldadura próxima, lo cual produce incrementos tanto de la dureza del material como de la fragilidad del mismo.

6. CONCLUSIONES

Del análisis realizado a lo largo de este trabajo, se puede concluir que el fallo del tubo de drenaje fue causado por un proceso de fatiga que ocurre de forma simultánea en dos extremos de la sección transversal del mismo y que se ve favorecido por procesos corrosivos tanto en la fase de iniciación como en la de propagación. Dado que la corrosión no debería haberse producido en condiciones normales, las razones de este fenómeno requieren más investigación al respecto con el objetivo de evitar fallos futuros.

La secuencia del proceso se ha explicado en el anterior apartado y se puede resumir del siguiente modo: se produjo un proceso simultáneo de fatiga en dos extremos de la sección de rotura (zonas A y C) provocó la propagación de dos fisuras en sentidos opuestos. La fisura con origen en la Zona A propagó a lo largo de la mayor parte de las sección (a través de las Zonas B y D) y alcanzó, junto con la fisura con origen en C, lo ligamento remanentes. El fallo final se produjo por colapso plástico de los mismos.

La singularidad de la forma de la sección de rotura (plana en las Zonas A y C y a 45º en las Zonas B y D) ha sido justificada por medio del tipo de tensiones dominantes que actúan en cada una de ellas: tensión-compresión en las primeras y cortantes en las segundas. Además, la localización de la sección de rotura se ha puesto en relación con el hecho de que se encuentra en la ZAT de una soldadura existente en el tubo de drenaje.

Finalmente, los análisis metalográficos y químicos revelan que el fallo no ha estado relacionado con deficiencias del material o con condiciones de operación anormales (ej. temperaturas por encima de las de diseño que causen decarburación, sobrepresiones, etc).

7. REFERENCIAS

[1] Annaratone, D., *Steam Generators Description and Design*, Springer, 2008.

[2] Ganapathy, V., *Industrial Boilers and Heat Recovery Steam Generators: Design, Applications, and Calculations*, CRC Press, New York, 2003.

[3] DIN 17175-79 Standard: *Seamless steel tubes for elevated temperatures*, 1979.

[4] Park, M., "Fatigue failure of a hydraulic filter head", *Engineering Failure Analysis* 2002; 9: 435–450.

[5] Sachs, N.W., "Understanding the surfaces features of fatigue fractures: how they describe the failure Cause and the failure history", *Journal of Failure Analysis and Prevention* 2005; 5 (2): 11-15.

[6] Bulloch , J.H., Callagy, A.G., Scully, S., Greene, A., "A failure analysis and remnant life assessment of boiler evaporator tubes in two 250 MW boilers", *Engineering Failure Analysis* 2009; 16: 775–793

[7] ASM Handbook, Vol. 11, *Failure Analysis and Prevention*, 2002

ANÁLISIS DEL FALLO POR FRACTURA FRÁGIL DE UNA TURBINA PELTON

D. Ferreño, J.A. Álvarez, E. Ruiz, D. Méndez

Departamento de Ciencia e Ingeniería del Terreno y de los Materiales
E.T.S de Ingenieros de Caminos, Canales y Puertos. Universidad de Cantabria
Avenida de los Castros s/n 39005 Santander

E-mail: ferrenod@unican.es

RESUMEN

En este trabajo, se analiza la rotura experimentada por una turbina Pelton de grandes dimensiones, fabricada en acero ASTM CA-6NM, tras recibir un tratamiento térmico de temple y revenido. Esta investigación inicial se ha centrado en varios aspectos. En primer lugar, se ha comprobado que el proceso de fabricación satisface los requerimientos establecidos en la especificación técnica. Seguidamente se ha estudiado la homogeneidad del componente para lo cual se ha analizado en diferentes regiones su composición química, se ha estudiado su naturaleza metalográfica y se ha caracterizado su respuesta mecánica por medio de ensayos de dureza Vickers. El estudio fractográfico efectuado ha permitido identificar los mecanismos de rotura predominantes así como la defectología presente en la superficie de fractura. El alcance de este trabajo debe completarse con un estudio detallado mediante simulación numérica del proceso de tratamiento térmico así como de su interacción con los defectos localizados en el componente.

PALABRAS CLAVE: Turbina Pelton, análisis de fallo, acero ASTM CA-6NM

ABSTRACT

In this work, the fracture of a Pelton turbine with big dimensions, manufactured in ASTM CA-6NM steel, after receiving a quenching plus tempering heat treatment, is analysed. This incipient research was focused on several aspects. First, it was checked the fulfilment of the specification during the fabrication of the component. Next, the homogeneity of the part was suited; for this purpose, several regions in the broken turbine were selected, and the chemical composition was analysed. Moreover, the metallographic nature, the mechanical behaviour through Vickers tests was also determined. The fractographical study allowed at identifying the predominant fracture mechanisms and the defects present in the fracture surface. The scope of this work must be completed with a detailed numerical simulation of the heat treatment process and its interaction with the defects found on the broken component.

KEYWORDS: Pelton turbine, failure analysis, ASTM CA-6NM steel

1. INTRODUCCIÓN

La turbina Pelton (Figura 1), inventada por Lester Allan Pelton en 1879, representa uno de los tipos más eficientes de turbina hidráulica. Consiste en una rueda (denominada rodete o rotor) dotada de cucharas (palas o álabes) en su periferia, las cuales están especialmente fabricadas para convertir la energía hidráulica del chorro de agua que incide sobre las cucharas en energía mecánica, para posteriormente convertirla en energía eléctrica con un generador.

Las turbinas Pelton están diseñadas para explotar grandes saltos hidráulicos de bajo caudal. Las centrales hidroeléctricas dotadas de este tipo de turbina cuentan, la mayoría de las veces, con una larga tubería llamada galería de presión para trasportar al fluido desde grandes alturas, a veces de hasta más de doscientos metros. Al final de la galería de presión se suministra el agua a la turbina por medio de una o varias válvulas de aguja, también llamadas inyectores, los cuales tienen forma de tobera para aumentar la velocidad del flujo que incide sobre las cucharas.

Los álabes de la turbina pueden estar fundidos con la misma rueda o unidos individualmente por medio de bulones o pernos, siendo ésta la forma más común de fabricación, ya que facilita su construcción y mantenimiento. Sin embargo, se funden en una sola pieza rueda y álabes cuando la rueda tiene un gran velocidad específica: con este proceso de fabricación se

logra mayor rigidez, solidez uniformidad y montaje rápido.

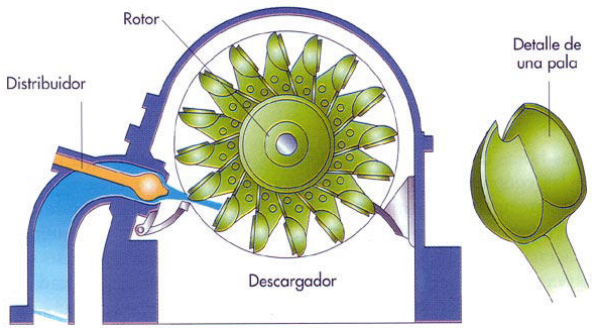

***Figura 1**. Esquema de la disposición y funcionamiento de una turbina Pelton*

Como puede intuirse a partir de lo dicho, el proceso de selección de materiales para la fabricación de turbinas Pelton debe ser especialmente cuidadoso, puesto que durante su vida en servicio debe resistir solicitaciones como la fatiga, la corrosión y la erosión. El acero o la fundición de grafito laminar, resisten perfectamente estas condiciones cuando son moderadas. Cuando las condiciones trabajo son más exigentes, se recurre al acero aleado con níquel, en el orden de 0.7 a 1%, y con un 0.3% de molibdeno. Para condiciones muy severas, con aguas corrosivas, se emplean aceros inoxidables martensíticos aleados al Ni y Mo, como el CA-6NM.

En este trabajo se analiza el proceso de rotura de una turbina Pelton de grandes dimensiones, fabricada en una sola pieza de acero ASTM CA-6NM. Tras recibir un tratamiento térmico de temple y revenido. La Figuar 2 permite apreciar una imagen de la superficie de fractura de este componente.

***Figura 2**. Fotografía mostrando la rotura de la turbina Pelton*

2.- MATERIAL Y TRATAMIENTO TÉRMICO

De acuerdo con la especificación técnica suministrada por el fabricante, la turbina Pelton aquí analizada está fabricada en un solo bloque de acero GX4CrNi13-4+QT, de acuerdo con la norma europea EN10283. Este acero se corresponde con el ASTM CA-6NM. La Tabla 1 recoge la composición química establecida en la especificación del material:

Tabla 1: Composición del material (% en peso) de acuerdo con la especificación ASTM

C_{max}	Cr	Ni	Mo
0.06	11.5-14.0	3.5-4.5	0.40-1.00

Asimismo, en la Tabla 2 re presentan algunos valores típicos de las propiedades mecánicas.

Tabla 2: Propiedades mecánicas típicas del acero ASTM CA-6NM

Límite elástico (MPa)	Resistencia a tracción (MPa)	Elongación (%)
550	755	15

Como se aprecia en la especificación europea, el material debe recibir un tratamiento térmico de temple y revenido.

3. DESPIECE DEL COMPONENTE

Tras recibir uno de los grandes bloques que se muestran en la Figura 2, se procedió a su despiece, extrayendo una serie de cupones de diferentes regiones de la pieza. La Figura 3 permite apreciar, sobre la superficie de fractura, las zonas de extracción de cupones. Se ha procurado tomar muestras repartidas por el contorno y por el interior de la pieza, a fin de detectar posibles heterogeneidades.

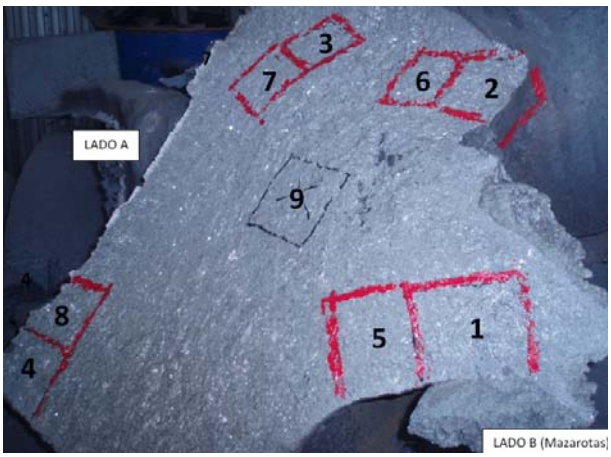

***Figura 2**. Fotografía mostrando la rotura de la turbina Pelton*

4. COMPOSICIÓN QUÍMICA

Se dispone de varias fuentes de información relativas a la composición química del material constitutivo de la turbina Pelton aquí analizada; en primer lugar, el

propietario ha suministrado el informe de la composición química durante la colada, cuyos resultados se reproducen en la Tabla 3 donde, además, se han incluido los valores recomendados. Como puede apreciarse, todos los elementos químicos satisfacen los límites impuestos por la especificación.

Tabla 3. Composición química (% en peso) según especificación, valores recomendados y en colada

Elemento	Mínimo	Ideal	Máximo	Colada
C	0.02	0.05	0.05	0.031
Si	0.00	0.70	1.00	0.417
Mn	0.80	0.90	1.50	0.845
P	0.00	0.00	0.03	0.0107
S	0.00	0.00	0.01	0.004
Cr	12.00	13.00	13.50	12.343
Ni	3.50	4.50	5.00	4.061
Mo	0.00	0.00	0.70	0.631
V	0.00	0.00	0.20	0.043
Cu	0.00	0.00	0.30	0.168

Por otra parte, en el contexto de esta investigación se han realizado análisis químicos (técnica EDAX, espectroscopía de energía dispersiva por rayos X) en las regiones 1, 2, 3, 4 y 9 de la pieza. Los principales resultados se recogen en la Tablas 4-8.

A pesar de que se trata de una técnica semi-cuantitativa, de forma que los resultados deben ser considerados con cierta cautela, se han detectado algunos patrones repetitivos. En concreto, en varios de los análisis los resultados han revelado una ligera pobreza en Mn y un ligero exceso de Mo.

Tabla 4. Composición química (% en peso) en la región 1 de la turbina

Elemento	Promedio	Desviación
Si	0.53	0.17
Cr	12.89	0.15
Mn	0.72	0.32
Fe	79.90	0.14
Ni	4.29	0.11
Mo	1.66	0.25

Tabla 5. Composición química (% en peso) en la región 2 de la turbina

Elemento	Promedio	Desviación
Si	0.55	0.06
Cr	13.18	0.36
Mn	0.73	0.13
Fe	79.91	0.66
Ni	4.24	0.37
Mo	1.41	0.12

Tabla 6. Composición química (% en peso) en la región 3 de la turbina

Elemento	Promedio	Desviación
Si	0.43	0.14
Cr	12.98	0.11
Mn	0.94	0.36
Fe	80.68	0.91
Ni	3.88	0.65
Mo	1.08	0.31

Tabla 7. Composición química (% en peso) en la región 4 de la turbina

Elemento	Promedio	Desviación
Si	0.48	0.03
Cr	12.49	0.34
Mn	0.78	0.32
Fe	80.54	0.35
Ni	4.37	0.28
Mo	1.34	0.13

Tabla 8. Composición química (% en peso) en la región 9 de la turbina

Elemento	Promedio	Desviación
Si	0.53	0.12
Cr	13.01	0.35
Mn	0.62	0.13
Fe	79.49	0.28
Ni	4.54	0.11
Mo	1.80	0.33

4. ESTUDIO FRACTOGRÁFICO

En esta sección se recogen algunas imágenes ilustrativas del estudio fractográfico efectuado, las cuales se comentan brevemente a continuación:

- La Figura 3 ofrece una de las imágenes tomadas sobre la muestra 1, en la que puede apreciarse un elemento no identificado. La composición química del mismo revela que se trata de una alúmina.
- La Figura 4 permite apreciar una región parcialmente fundida, de pequeñas dimensiones, localizada en la muestra 2. También se han localizado ejemplos de fusiones parciales en otras zonas aunque siempre de pequeña entidad, esperables en una pieza de grandes dimensiones.
- La Figura 5 permite apreciar los mecanismos dúctiles (microhuecos) responsables de la propagación de fisura en la zona 4.
- Por el contrario, en la región central (zona 9) se observa una presencia mayor de mecanismos frágiles (decohesiones intragranulares) acompañada, en ocasiones (véase la Figura 6) por pequeños desgarros de fusión parcial.

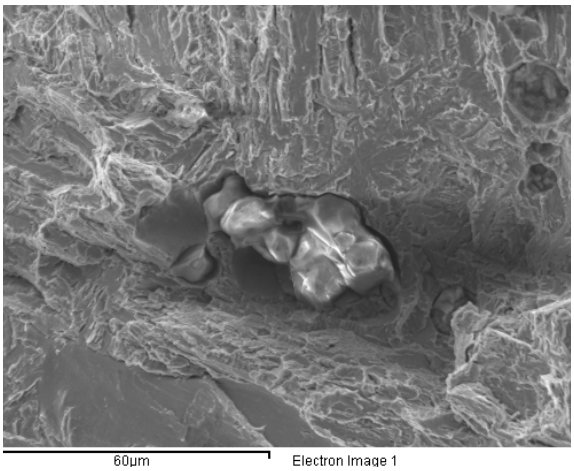

***Figura 3**. Alúmina detectada en la región 1*

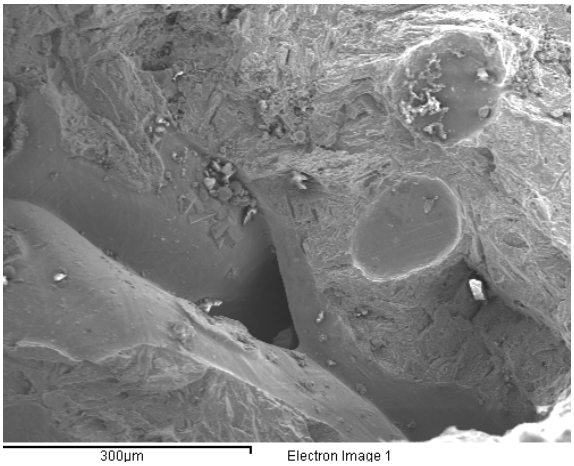

***Figura 4**. Fusión parcial detectada en la muestra 2*

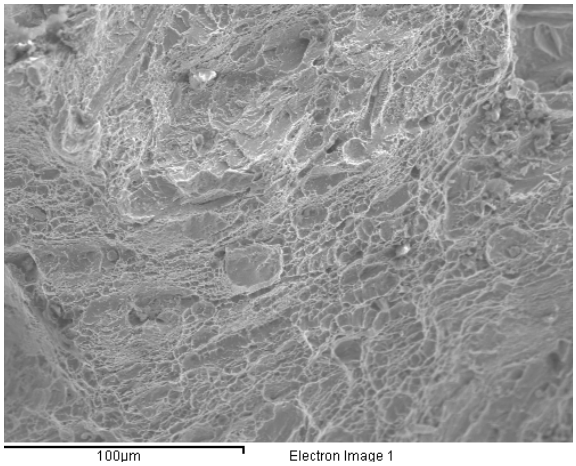

***Figura 5**. Mecanismos dúctiles de propagación en la región 4*

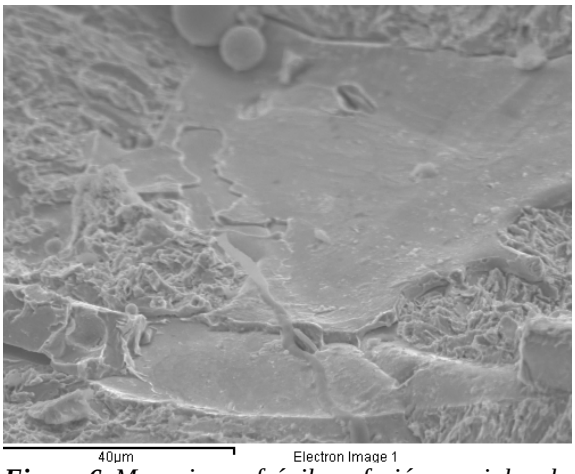

***Figura 6**. Mecanismos frágiles y fusión parcial en la región 9*

5. ESTUDIO METALOGRÁFICO

Se he efectuado un estudio metalográfico sobre cada una de las cinco muestras tras pulido hasta calidad de espejo y diferentes ataques (vilella, karlin, HNO_3+HCl+H_2O). Como se aprecia en las imágenes que se adjuntan, la microestructura está constituida predominantemente por martensita revenida con presencia ocasional de ferrita. A modo de ejemplo, la Figura 7 permite apreciar una de las micrografías obtenidas sobre la muestra 4.

Este estudio se ha desarrollado sobre todas las muestras, cuantificando mediante análisis de imágenes la cantidad de ferrita. La Figure 8 muestra una imagen correspondiente a la cuantificación. El resultado del estudio permite afirmar que no se han detectado diferencias apreciables en cuanto al contenido de ferrita entre las diferentes regiones.

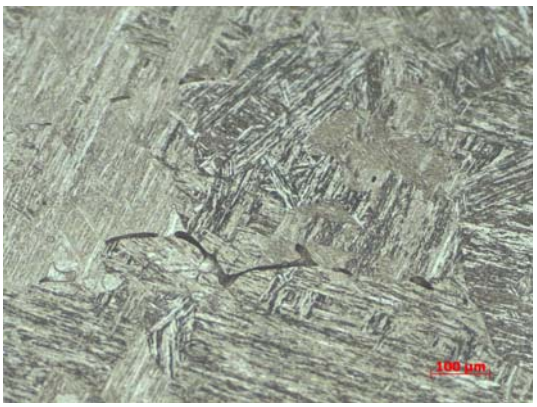

***Figura 7.** Ejemplo de la distribución de fases en la muestra 4*

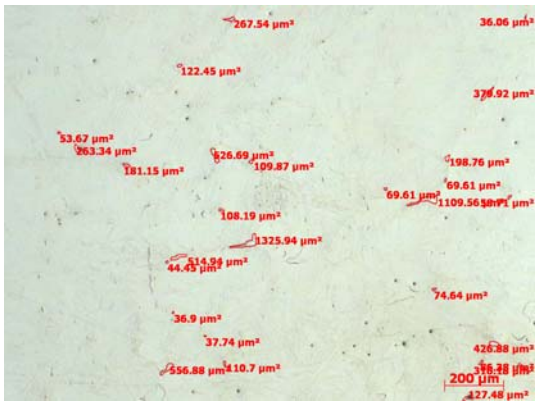

Figura 8. *Cuantificación de ferrita (ejemplo) sobre la muestra 1*

6. PROPIEDADES MECÁNICAS

Se han efectuado varios ensayos de caracterización de las propiedades mecánicas y en fractura. En la Tabla 9 se presentan los principales resultados del ensayo de tracción; comparando con los valores de la Tabla 2 se puede comprobar la idoneidad mecánica del material.

Tabla 9: Resultados del ensayo de tracción

Límite elástico (MPa)	Resistencia a tracción (MPa)	Elongación (%)	Reducción área (%)
640	840	16.5	33

Por otra parte, se han efectuado tres ensayos de impacto Charpy, a una temperatura de 0ºC; los valores de energía absorbida son de 95, 98 y 100, esto es, se trata de una respuesta tenaz y homogénea, lo que invita a pensar que a dicha temperatura el material se encuentra en la región upper shelf.

Se ha efectuado, asimismo, un ensayo de dureza Brinell, ofreciendo el resultado de 262 HB.

A fin de detectar posibles heterogeneidades en la muestra se ha desarrollado una campaña de ensayos de dureza Vickers en diferentes regiones. La Figura 9 permite apreciar los valores obtenidos indicando en cada caso el valor medio y la desviación estándar (en cada región se han realizado 25 ensayos con cargas de 200 g durante 20 s). Los valores obtenidos concuerdan razonablemente con lo esperable en una microestructura de martensita revenida, propia de este material con el tratamiento térmico de temple y revenido.

Como puede apreciarse en la Figura 9, son las zonas 2 y 4 las que se encuentran en el contorno de la pieza, en contacto con su superficie exterior. Por otra parte, las durezas en las zonas 1, 3 y 9, ofrecen valores más moderados y se encuentran en el interior de la pieza. No obstante debe tenerse en consideración el valor de las incertidumbres obtenidas (desviación estándar, indicada en la propia figura). En este sentido, puede descartarse la existencia de comportamiento mecánicos diferentes en función de la región sobre la pieza.

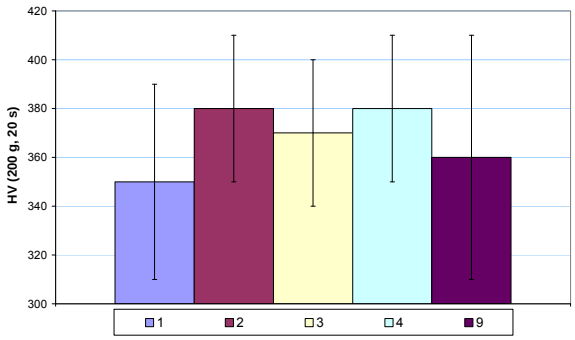

Figura 9*. Resultados de dureza Vickers en diferentes regiones*

Como se ha indicado anteriormente, el estudio metalográfico evidencia la existencia de dos fases claramente diferenciadas, una poco abundante (ferrita) y otra con una presencia mucho mayor (martensita revenida). Para una correcta identificación de las mismas se ha efectuado una campaña de microdurezas con cargas reducidas (20 g, 20 s) seleccionando cuidadosamente el punto de aplicación del indentador.

La Figura 10 permite apreciar un ejemplo de una de las microdurezas llevadas a cabo sobre una de las islas de ferrita δ localizadas. Debe indicarse que, en todos los casos, las islas de ferrita presentan reducidas dimensiones por lo que ha resultado imposible realizar las microdurezas en condiciones idóneas (esto es, garantizando que la distancia entre la huella y el contorno de la isla de ferrita sea de, al menos, tres veces el tamaño de la propia huella; este hecho se pone claramente de manifiesto en el caso del ejemplo mostrado en la Figura 10). Por ello, presumiblemente los valores de dureza en la ferrita obtenidos experimentalmente, serán más elevados que los que indica la bibliografía.

A modo de ejemplo, los resultados obtenidos para la muestra 1 -dureza media junto con la desviación estándar correspondiente, para cada fase- se ofrecen en la Figura 11. En todos los casos se observa una diferencia apreciable de dureza entre fases siendo los valores de la martensita revenida adecuados para esta fase mientras que los de la ferrita resultan elevados respecto de los valores habituales; este hecho puede tener su explicación en las consideraciones expuestas en el párrafo anterior, relativas a la representatividad de los resultados.

Otro aspecto relevante procede del hecho de que los resultados obtenidos son similares, con independencia de la región en la cual se hayan efectuado los ensayos.

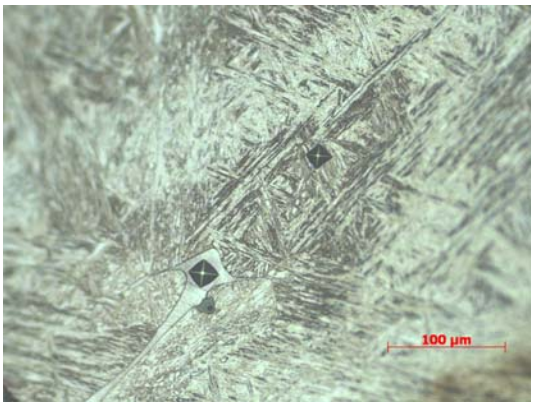

***Figura 10**. Ejemplo de microdureza sobre una isla de ferrita*

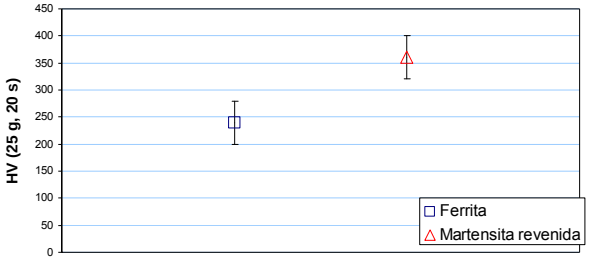

***Figura 11**. Resultados de los ensayos de microdureza Vickers sobre cara una de las fases, muestra 1*

7. DEFECTOLOGÍA

El estudio metalográfico y fractográfico ha permitido apreciar una serie de defectos interiores, de pequeña entidad, en las piezas analizadas. En el Apartado 4 se señaló la existencia de regiones con fusión incompleta, que pueden actuar como precursoras de una rotura frágil ante estados tensionales existentes en la pieza. Queda por averiguar y cuantificar la entidad de las tensiones térmicas residuales en la pieza tras haber recibido un tratamiento térmico de temple y doble revenido.

Por otra parte, de ha apreciado la existencia de fisuras en el interior de alguno de los cupones analizados. La Figura 12 ofrece, a modo de ejemplo, una de las fisuras localizadas en la muestra 9. En la misma pyuede apreciarse la nucleación de la grieta en la intercara entre la matriz y la banda de ferrita δ. Una discontinuidad de esta naturaleza puede desencadenar un fallo frágil en presencia de un estado tensional desfavorable. Dicho estado tensional podría estar originado por las tensiones residuales generadas por el tratamiento térmico.

8. CONCLUSIONES Y TRABAJO FUTURO

En atención a los razonamientos recogidos en este trabajo, pueden establecerse las siguientes conclusiones:

- Existe una ligera diferencia de comportamiento mecánico entre las diferentes zonas analizadas de la pieza (como ha mostrado el estudio de dureza efectuado), si bien, dichas diferencias quedan recogidas dentro de las incertidumbres experimentales. Por dicho motivo, la pieza puede considerarse como homogénea desde el punto de vista mecánico.

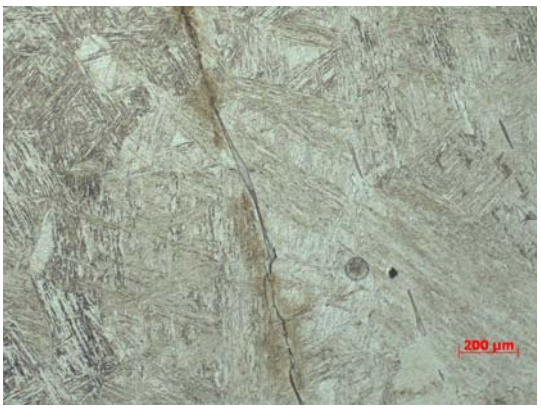

***Figura 12**. Fisura localizada en el interior de la muestra 9*

- La rotura de la pieza parece tener su origen en la zona central de la misma en la que se aprecian pequeñas fisuras emergentes. No obstante estas también están presentes en alguna de los cupones periféricos. No se puede ser concluyente respecto a las causas de las mismas.
- Queda por determinar el papel que las tensiones residuales pueden haber desempeñado en el proceso de rotura. Asimismo, se desconoce el comportamiento en fractura del material en función de la región de análisis.
- El tipo de propagación observado es mixto con zonas caracterizadas por la presencia de roturas transgranulares, y otras con predominio de microhuecos.
- El acero analizado presenta una microestructura de tipo duplex con presencia de ferrita y martensita revenida. Una primera observación muestra un predominio de la segunda con pequeños porcentajes de la primera; si bien se precisa un estudio mas profundo para obtener una distribución real de ambas. No se han detectado variaciones en la distribución de las fases presentes en función de la ubicación en la pieza.

REFERENCIAS

[1] Kubiak J. Urquiza G. Rodríguez J.A. González G. Rosales I. Castillo G. Nebradt J. Failure Analysis of the 150 MW gas turbine blades. Engineering Failure Analysis 16 (2009) 1794-1804.

[2] Gysel W. Gerber E. Trautwein A. CA6NM: New Developments Based on 20 Years' Experience. Stainless Steel Castings, ASTM STP 756, 1982, PP. 403-435.

ANÁLISIS DE FISURACIÓN EN COMPENSADORES DE DILATACIÓN DE LA RED DE AGUA SANITARIA DE UN HOSPITAL

R. Lacalle[1, 2], S. Cicero[1], R. Cicero[1], y J. García[1, 2]

[1]Departamento de Ciencia e Ingeniería del Terreno y de los Materiales
E.T.S de Ingenieros de Caminos, Canales y Puertos. Universidad de Cantabria
Avenida de los Castros s/n 39005 Santander

[2]INESCO INGENIEROS S.L.
Centro de Desarrollo Tecnológico de la Universidad de Cantabria, Mod. 9, Fase B
Avenida de los Castros s/n 39005 Santander

E-mail: lacaller@unican.es

RESUMEN

En este trabajo se analiza la fisuración sufrida por buena parte de los compensadores de dilatación instalados en el sistema de agua caliente sanitaria de un hospital. Estos componentes, que fallaron pocos meses después de su puesta en servicio, constan de una manguera metálica interior y un trenzado de hilo metálico exterior que aporta rigidez al conjunto. El fallo se produjo por la aparición de múltiples fisuras longitudinales en la manguera metálica interior.

Para tratar de determinar la causa de la fisuración se realizaron diversos exámenes visuales, un análisis mediante microscopía electrónica de barrido (SEM) y un análisis mediante elementos finitos de las condiciones de trabajo de los componentes. Tras estas tareas, se concluyó que una incorrecta colocación de los compensadores podría ser la causa más probable del fallo.

PALABRAS CLAVE: Análisis de fallo, compensadores de dilatación, simulación elementos finitos

ABSTRACT

In this paper the cracking process in most of the expansion compensators installed in sanitary hot water system of a hospital is analysed. These components, which failed just few months after their assembly, are made up of an internal metal hose and an external wire metal braid. The failure occurred in the internal hose, as a consequence of the apparition of multiple cracking.

In order to investigate the reason for the cracking, several visual examinations, a SEM analysis and some Finite Element Simulations were performed. The final conclusion of this work was that an inaccurate assembly of the compensators could be the most possible cause of the failure.

KEYWORDS: Failure Analysis, Expansion Compensators, Finite Element Simulation

1. INTRODUCCIÓN

El agua sanitaria de grandes instalaciones como hoteles u hospitales es habitualmente calentado en una sala de calderas y desde allí, por presión, se distribuye a todos los puntos del complejo. Las líneas de tuberías que realizan el transporte desde las calderas hasta el lugar de consumo, presentan, a menudo, grandes longitudes, haciendo necesaria la introducción de elementos capaces de compensar las dilataciones debidas a las fluctuaciones de temperaturas en la red, que de otra forma podrían comprometer la integridad de las tuberías constituyentes del sistema.

En este trabajo, se analiza la fisuración acontecida en buena parte del centenar de compensadores de dilatación instalados en el sistema de agua caliente sanitaria de un hospital. Estos fallos, además de implicar cuantiosos daños económicos asociados a la sustitución de los elementos fisurados, conllevan la anulación de la línea afectada lo que se traduce en cierres temporales de quirófanos o plantas del hospital.

Para buscar la causa del fallo de estos elementos se realizaron inspecciones visuales de los compensadores, análisis químicos del material constituyente de los

mismos, observaciones mediante microscopía electrónica de barrido (SEM) y finalmente simulaciones mediante elementos finitos teniendo en cuenta las condiciones de trabajo de los sistemas de tuberías.

2. DESCRIPCIÓN DEL COMPONENTE

Con el objeto de minimizar las tensiones de tipo térmico en tuberías, es común colocar elementos capaces de asumir gran parte de los movimientos asociados a fenómenos de índole térmica, reduciendo notablemente los esfuerzos a asumir por el sistema [1]. En el caso analizado, y dada escasa rigidez de los tramos rectos de tubería, constituidos por polipropileno, es necesario recurrir a una solución capaz de asumir, sin apenas introducir esfuerzos, todo el movimiento de las tuberías. Por ello, en el caso analizado, se optó por recurrir a elementos de gran flexibilidad [2] como el que se muestra en la Figura 1. Tal y como puede verse en el esquema de la Figura 2 [2], estos compensadores están formados por una manguera metálica interior capaz de asumir grandes movimientos, y que tiene la misión fundamental de garantizar la estanqueidad del conjunto, además de por un trenzado exterior de hilo metálico. Este trenzado, sin mermar en exceso la capacidad de movimientos, aporta la rigidez necesaria para permitir hacer frente a solicitaciones de tipo presión interior.

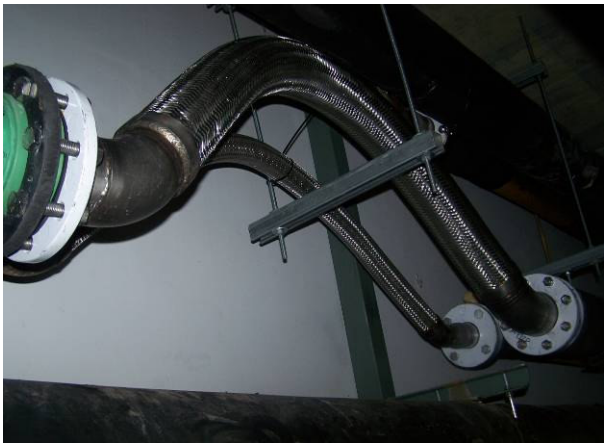

Figura 1. Tipología de los compensadores de dilatación analizados

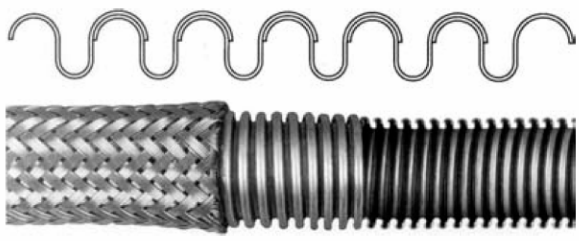

Figura 2. Esquema de los compensadores de dilatación

El material constituyente tanto de la manguera metálica interior como de los hilos del trenzado exterior es, según la especificación del producto [2], un acero inoxidable 1.4541 (semejante a un AISI 321).

Por su parte, la presión interior de trabajo de los sistemas de tuberías de agua sanitaria se sitúa en 0.85 MPa, siendo la temperatura habitual 60 ºC. Periódicamente, y para combatir posibles brotes de legionella, se somete a todos los sistemas a un hipercalentamiento hasta una temperatura de 75ºC.

Cabe mencionar también que, el cerca del centenar de compensadores de dilatación instalados en el hospital analizado, presentan, como es lógico, diferentes diámetros en función de las dimensiones de la línea de tubería a la que pertenezcan. Este extremo puede ser observado en la imagen de la Figura 1, donde se muestran dos compensadores de dilatación con dos diferentes diámetros.

3. DESCRIPCIÓN DEL FALLO

Pocos meses después de su instalación, buena parte de los compensadores de dilatación colocados en el sistema de agua sanitaria de un hospital comenzaron a presentar fugas motivadas por la aparición de múltiples fisuras en la manguera metálica interior. Las fisuras presentan en todos los casos la tipología mostrada en la Figura 3. Este fallo, que afectó de forma fundamental a aquellas líneas de mayor diámetro de tubería (100 mm), se localizó, por otra parte, en la zona del extradós de los componentes, coincidiendo con la región de máxima curvatura de los compensadores de dilatación (Figura 1).

Figura 3. Tipología de las fisuras de la manguera metálica interior

Observando la Figura 3, queda de manifiesto que la disposición preferente de las grietas es de tipo longitudinal, según el avance de la tubería, localizadas además en las zonas de valle de la manguera metálica. Esta disposición de las fisuras, apunta a la presión interior como solicitación causante del fallo (tensiones

de presión interior del orden del doble en dirección circunferencial que en dirección axial), descartando fenómenos de otra naturaleza, como por ejemplo fatiga térmica, ya que en tal caso, las fisuras deberían aparecer con orientación circunferencial. No obstante, para los compensadores de dilatación de 100 mm de diámetro, por ejemplo, la especificación del fabricante indica que las máximas presiones de trabajo se sitúan en torno a 8 MPa, muy lejos de las presiones reales sufridas por el componente.

4. ANÁLISIS MEDIANTE SEM

Para tratar de verificar si el fallo podría venir motivado por causas imputables al material, se llevó a cabo un análisis mediante microscopía electrónica de barrido (SEM). En este análisis se realizó una observación detallada de las superficies de varias fisuras en busca de alguna evidencia de fenómenos de corrosión [3-5]. Además, se practicó un microanálisis por SEM del material de la manguera metálica interior de uno de los compensadores fisurados con la intención de comprobar si realmente se correspondía con el material indicado por las especificaciones del producto [2].

La Figura 4 muestra una imagen SEM de una de las superficies de fisura, donde, como en el resto de las observaciones realizadas, no se detecto ninguna evidencia de la presencia de corrosión en cualquiera de sus formas. Por su parte, la Tabla 1 resume los resultados del microanálisis por SEM efectuado sobre material de una manguera metálica interior. Se comprueba que los valores concuerdan, dentro de las incertidumbres propias de la técnica, con los esperados para un acero inoxidable 1.4541 [6], como indicaba la especificación del producto.

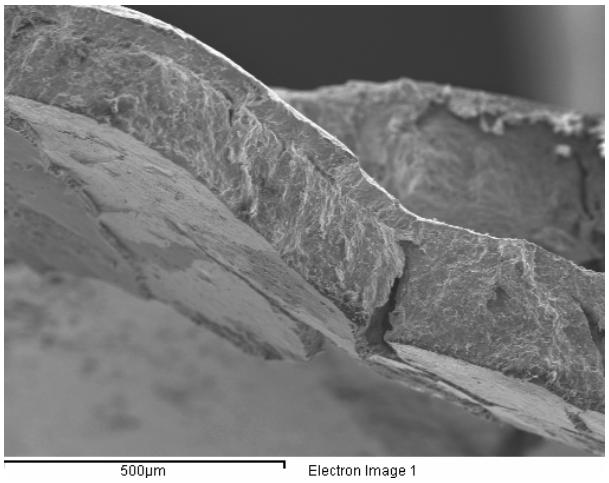

Figura 4. Tipología de los compensadores de dilatación analizados

Tabla 1. Composición química de una muestra de manguera metálica y comparación con valores de referencia [6] (resultados en % en peso).

	Fe	Cr	Ni	Mn	Si
Muestra	69.0	18.5	9.5	2.2	0.7
1.4541	68.0	18.0	11.0	2.0	1.0

5. SIMULACIÓN MEDIANTE ELEMENTOS FINITOS

Los compensadores de dilatación siguen el esquema geométrico de la Figura 5, donde la longitud entre apoyos "A" varía en función de los movimientos de éstos. Durante un periodo de operación normal del sistema de agua sanitaria (Presión = 0.85 MPa, Temperatura = 60ºC), se midió la distancia entre apoyos "A" en un compensador de fácil acceso, resultando ser igual a 1130 mm. Teniendo en cuenta que la longitud de tramo recto de tubería entre compensadores es de 20 metros y dado que el coeficiente de dilatación térmica lineal del polipropileno constituyente de estos tramos de tubería es aproximadamente 0.15 mm/m·ºC, en situación de hipercalentamiento (75ºC), es de esperar una reducción de la distancia "A" de unos 45 mm, con lo que la longitud "A" en situación de hipercalentamiento para el compensador medido sería aproximadamente de 1085 mm (Figura 6). Dado que la longitud de los compensadores de dilatación, "L" puede considerarse constante (despreciando pequeñas dilataciones térmicas), las variaciones de la longitud "A" implican a su vez drásticas variaciones en el radio de curvatura del componente "R". Así, atendiendo a simples consideraciones geométricas, el radio de curvatura "R" puede deducirse a partir de los datos conocidos de "L" y de "A" siguiendo las expresiones (1) a (3).

$$A = 2\cdot R\cdot\cos\left(\frac{\pi}{4}\right) + \left(L - \frac{\pi}{2}R\right)\cdot\cos\left(\frac{\pi}{4}\right) \quad (1)$$

$$A = R\cdot\cos\left(\frac{\pi}{4}\right)\cdot\left(2 - \frac{\pi}{2}\right) + L\cdot\cos\left(\frac{\pi}{4}\right) \quad (2)$$

$$R = \frac{\frac{A}{\cos(\pi/4)} - L}{2 - \frac{\pi}{2}} \quad (3)$$

Según (3), el radio de curvatura en la situación medida sería de aproximadamente 230 mm, mientras que para la situación de hipercalentamiento, con un acercamiento entre apoyos de 45 mm, el radio de curvatura sería tan sólo de 80 mm. Este cambio, modifica necesariamente el comportamiento estructural del componente. Para conocer el estado tensional en ambos supuestos, se simularon los dos escenarios mediante el método de los Elementos Finitos empleando el código ANSYS [7]. Además, y a modo de referencia, se simuló también el

comportamiento de un tramo recto de compensador. En dicha simulación, de carácter elastoplástica, se consideró, de acuerdo con [8], un límite elástico igual a 250 MPa, una tensión de rotura de 500 MPa, y un alargamiento bajo carga máxima del 15%.

En todos los casos fue considerada una presión interior igual a 0.85 MPa (presión de trabajo). Para los propósitos de la simulación, la geometría fue simplificada de acuerdo al esquema de la Figura 7. La contribución del trenzado metálico exterior para resistir presiones fue simulada considerando un elemento de rigidez infinita en dirección radial. Esta simplificación conduce a unas situaciones de mayor rigidez que las reales (más capacidad para soportar presiones interiores), de tal manera, que las tensiones obtenidas en la simulación podrán ser consideradas como límites inferiores de las presentes en el sistema.

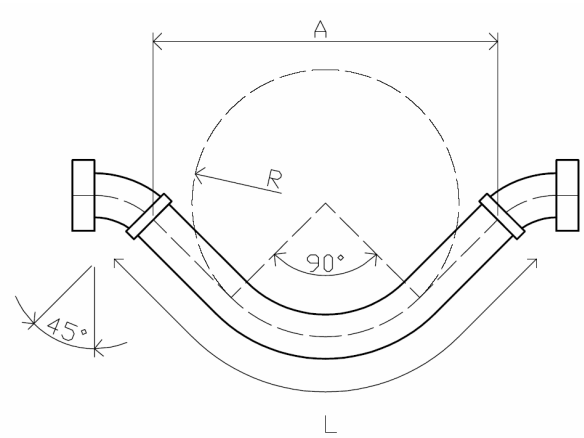

Figura 5. Esquema geométrico de un compensador de dilatación.

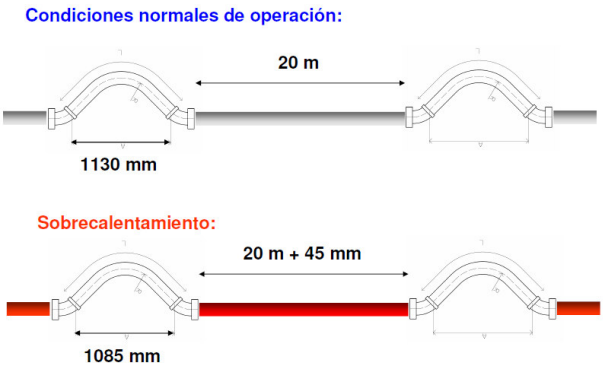

Figura 6. Esquema de los desplazamientos en el sistema para condiciones normales de operación y condiciones de sobrecalentamiento.

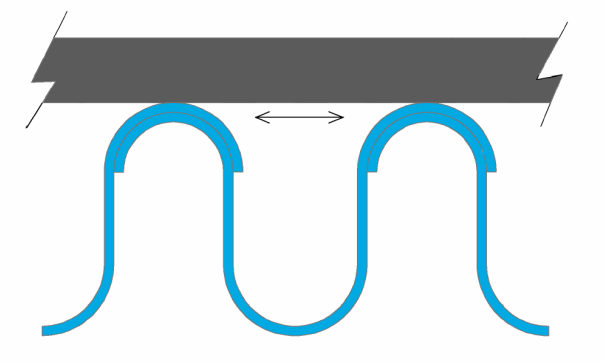

Figura 7. Simplificación estructural empleada en los modelos de elementos finitos.

Las Figuras 8, 9 y 10 muestran los resultados de las simulaciones para tramo recto en condiciones normales de operación, para el tramo de máxima curvatura en condiciones normales de operación y para tramo de máxima curvatura en condiciones de hipercalentamiento. En concreto se puede observar, en un paso de espira de la manguera interior, la magnitud de las tensiones según la orientación circunferencial, es decir, las concomitantes con las fisuras longitudinales presentes en los compensadores de dilatación. Se comprueba que, para la situación de hipercalentamiento (Figura 10), las tensiones en la zona de valle del extradós, son del orden de la resistencia a tracción del material, justificándose de esta forma la fisuración de los componentes. Este notable aumento tensional se explica fundamentalmente debido a que, a medida que se distorsiona la forma original del componente, el trenzado es incapaz de ejercer su misión rigidizadora, mermándose la capacidad del sistema para resistir presiones interiores. Además, el alto grado de deformaciones contribuye a la plastificación de ciertas regiones en el componente.

Se observa además en las Figuras 8, 9 y 10, que las máximas tensiones de tracción se sitúan precisamente en los valles, mientras que en los picos las tensiones llegar a ser incluso de compresión, justificándose de este modo que las fisuras en los componentes reales se alojen únicamente en los valles, deteniéndose al alcanzar los picos.

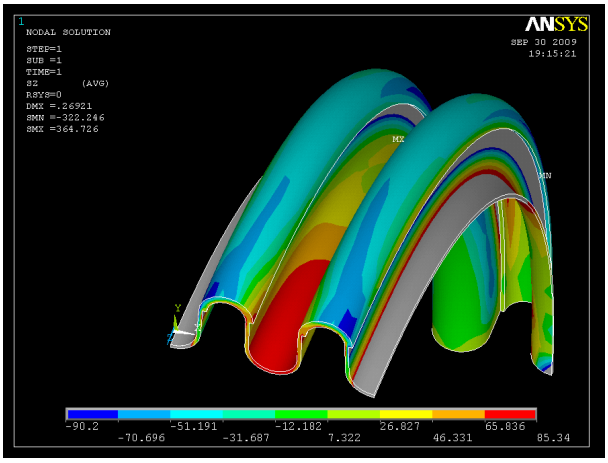

Figura 8. Simulación de tramo recto para condiciones normales de operación. Tensiones máximas en valle = 85 MPa.

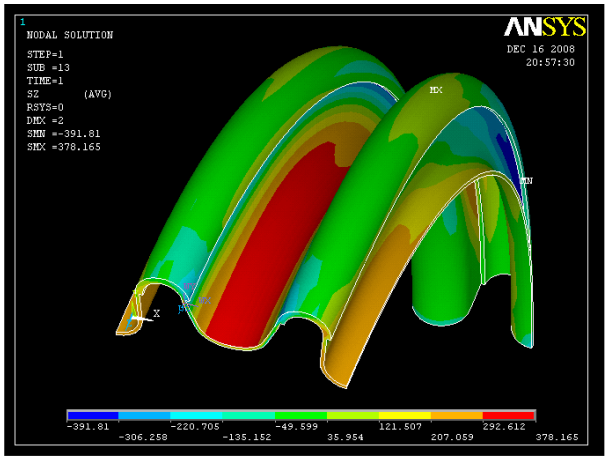

Figura 9. Simulación de zona de máxima curvatura para condiciones normales de operación (A=1130 mm, R=230 mm). Tensiones máximas en valle = 378 MPa.

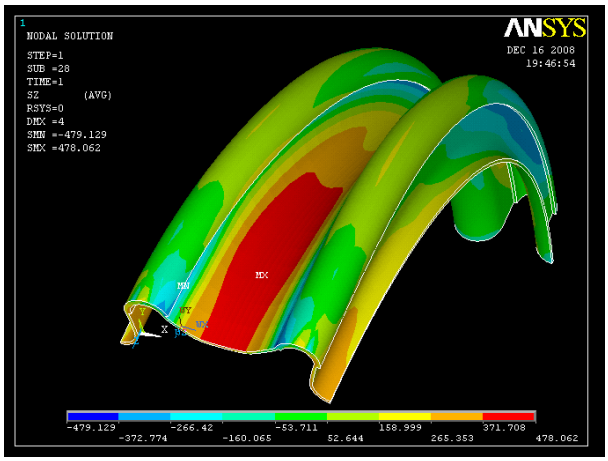

Figura 10. Simulación de zona de máxima curvatura para condiciones de hipercalentamiento (A=1085 mm, R=80 mm). Tensiones máximas en valle = 478 MPa.

6. CONCLUSIONES

En este trabajo ha sido analizado el fallo de compensadores de dilatación de los sistemas de tuberías de agua sanitaria de un hospital. En base a las tareas realizadas, pueden extraerse las siguientes conclusiones:

- De acuerdo con los análisis químicos realizados, el material constituyente de las mangueras metálicas interiores no presenta ninguna anomalía en su composición.

- Tras el análisis mediante microscopía electrónica de barrido (SEM), no se han detectado evidencias de la participación de procesos de corrosión en la fisuración de los componentes.

- El análisis mediante elementos finitos de los compensadores de dilatación, revela que, para las condiciones en que se encuentran montados algunos de los dilatadores, las tensiones alcanzan valores muy elevados (cercanas al límite resistente del material), lo que sin duda compromete la integridad del componente. La causa de estos altos niveles tensionales es el reducido radio de curvatura, que implica que el trenzado exterior no ejerza de forma efectiva su misión de auxilio a la manguera metálica para resistir presiones internas, al tiempo que dicha curvatura provoca por sí sola elevadas plastificaciones.

En base a estas conclusiones, un inapropiado montaje se presenta como la hipótesis más probable del fallo. Este extremo se ve reforzado por el hecho de que, con independencia de su diámetro todos los compensadores presentan la misma longitud y distancia entre apoyos (Figura 1), cuando desde un punto de vista estructural, compensadores con diámetros más grandes requieren de distancias entre apoyos más elevadas.

De esta manera, se recomienda que los compensadores sean colocados con distancias entre apoyos tales que, bajo las condiciones de funcionamiento más severas (hipercalentamiento) se garanticen tensiones en las zonas más solicitadas por debajo de los límites resistentes del material.

REFERENCIAS

[1] Cicero, S., Lacalle, R., Cicero, R., “Assessment of Local Thin Areas in a Marine Pipeline by Using the FITNET FFS Corrosion Module”, International Journal of Pressure Vessels and Piping (86), 2009, pp 329-334.

[2] BOA SUPRA helically corrugated stainless steel hose, BOA AG, Expansion Joints, Metal Hoses, Metal Bellows.

[3] ASM International, Fractography, ASM Handbook, Volume 12, 1987.

[4] ASM International, Failure Analysis and Prevention, ASM Handbook, Volume 11, 2002.

[5] C. R. Gagg, P.R. Lewis, "Environmentally assisted product failure – Synopsis and case study compendium", Engineering Failure Analysis, Volume 15, Issue 5, July 2008, Pages 505-520.

[6] D. Peckner and I. M. Bernstein, Handbook of Stainless Steels, McGraw-Hill Book Company, New York, NY, (1977).

[7] ANSYS Inc., 2008, Release 11.0.

[8] Matweb, Material Property Data, http://www.matweb.com/.

ANÁLISE DO COMPORTAMENTO ESTRUTURAL E À FADIGA DE ANTEPARAS DE LANCHAS RÁPIDAS EM ALUMÍNIO

[1, a] Pedro Catarino, [1, b, 3] Rui F. Martins, [2, c] Paulo Silva

[1]Faculdade de Ciências e Tecnologia, Universidade Nova de Lisboa
UNIDEMI, Departamento de Engenharia Mecânica e Industrial, *Campus* de Caparica, 2829-516 Caparica, Portugal
Email:[a] pmmcatarino@hotmail.com, [b] rfspm@fct.unl.pt

[2] Marinha Portuguesa, Direcção de Navios, Departamento de Estudos
Base Naval de Lisboa, 2800-001 Alfeite, Portugal
Email: [c] pires.silva@marinha.pt

[3] ICEMS/IST, Av. Rovisco Pais, 1, 1049-001 Lisbon - Portugal

RESUMO

O presente artigo tem como principal objectivo apresentar a análise realizada ao comportamento estrutural e à fadiga de painéis reforçados unidireccionalmente em ligas de alumínio das séries 5000 e 6000 (anteparas), quando submetidos ao efeito de *slamming* e de alagamento de compartimentos estanques adjacentes. O estudo do comportamento estrutural das anteparas foi realizado utilizando o Método dos Elementos Finitos (MEF), tendo sido modeladas as estruturas como projectada e como fabricada, de modo a verificar-se a contribuição das imperfeições resultantes do fabrico das anteparas nas tensões estruturais induzidas pelos carregamentos impostos. Para a realização da análise à fadiga, a antepara foi instrumentada com um extensómetro e o espectro de extensões foi obtido em navegação, por intermédio de uma ponte extensométrica da HBM, durante 25 minutos. A matriz de *rainflow* do espectro de tensões recolhido foi construída e, com base numa Curva S-N de ligas de alumínio, foi feita a previsão de vida à fadiga da antepara em estudo.

PALAVRAS-CHAVE: Anteparas, *Slamming*, Extensometria, Previsão de Vida à Fadiga, MEF.

ABSTRACT

The main purpose of this article is to present the analysis of structural behaviour and fatigue of unidirectional reinforced panels in aluminium alloys 5000 and 6000 (bulkheads), when subjected to the effect of slamming and flooding of watertight adjacent compartments. The study of the structural behaviour of the bulkhead was performed using the Finite Element Method (FEM) and have been modelled the structures as designed and as constructed, in order to assess the contribution of imperfections resulting from the manufacture of the bulkhead in the stresses induced by structural loads. To perform the fatigue analysis, the bulkhead was instrumented with a strain gage and the strain range was obtained during a 25 minute navigation through a HBM extensometer bridge. The rainflow matrix of the strain spectrum acquired has been made and, based on a SN curve, the fatigue life prediction of the bulkhead under study was made.

KEY WORDS: Bulkheads, Slamming, Fatigue Life Prediction, Finite Element Analysis (FEA).

1. INTRODUÇÃO

As embarcações em estudo podem-se considerar lanchas rápidas em alumínio com 14,5 metros de comprimento total, deslocamento máximo de 18 toneladas, 4,3 metros de boca (largura máxima do navio), com capacidade para atingirem uma velocidade máxima de 25 nós [1].

A sua estrutura, em liga de alumínio, foi dimensionada de forma a possibilitar a operação em mar de força 8 (altura significativa de onda de 9 a 14 m) e ventos de força 10 (48 a 55 nós).

Figura 1. Embarcação em Estudo

As anteparas em estudo (Figura 2) são painéis verticais reforçados unidireccionalmente, construídos em ligas de alumínio de construção naval, que dividem em compartimentos o espaço interno do casco da

embarcação, conferindo-lhe estanquicidade, protecção contra incêndio e contribuindo para manter a forma e aumentar a resistência do casco de toda a embarcação.

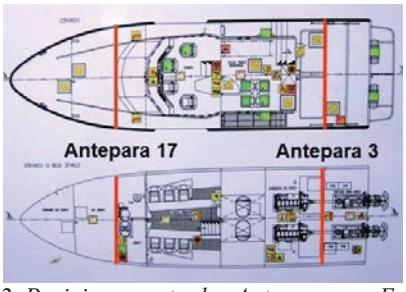

Figura 2. Posicionamento das Anteparas em Estudo na Embarcação Estudada

A chapa das anteparas têm 5 mm de espessura e os reforços (perfis em L), possuem 3 mm de espessura, tendo sido soldados perpendicularmente ao plano da chapa da Antepara com um espaçamento de 250 mm. A liga de alumínio utilizada no fabrico das chapas das Antepara é a liga 5083-H111 (Al-Mg) (uma liga não tratável termicamente), enquanto que os reforços são construídos na liga 6086-T6 (Al-Mg-Si), que é tratável termicamente. Ambas as ligas são conhecidas pelo seu bom desempenho em ambientes marítimos. Na Tabela 1 e 2 estão as principais propriedades mecânicas das ligas 5083-H111 e 6082-T6, respectivamente.

Tabela 1. Propriedades Mecânicas da liga 5083-H111 utilizada na chapa das Anteparas [2]

Tensão de Cedência [MPa]	Tensão de Rotura [MPa]	Extensão de Ruptura [%]
190	300	16

Tabela 2. Propriedades Mecânicas da liga 6082-T6 utilizada nos reforços das Anteparas [2]

Tensão de Cedência [MPa]	Tensão de Rotura [MPa]	Extensão de Ruptura [%]
260	310	10

As anteparas foram projectadas para suportar principalmente a pressão hidrostática resultante do hipotético alagamento dos compartimentos estanques adjacentes, assim como as solicitações de compressão, devidas ao efeito de *Slamming* (carregamento no plano), que é o resultado vibratório da estrutura no primeiro modo de vibração natural causado pelo impacto hidrodinâmico da proa aquando da reentrada na água, induzindo forças elevadas, de alta frequência, semelhantes a impulsos [3]. O valor de carregamento devido ao efeito de *Slammin,* utilizado no estudo do comportamento estrutural das Anteparas teve por base um estudo [4] onde se considerou um navio com deslocamento de 90 toneladas, 22 nós de velocidade máxima e altura significativa de onda igual a 10 m, tendo sido calculada uma pressão máxima de impacto igual a 150 kPa. As embarcações em estudo têm um deslocamento de 18 toneladas, uma velocidade superior a 25 nós, e o cálculo de [4] foi revisto no trabalho [5], de acordo com a formulação inclusa em [6], tendo-se chegado a valores próximos de 150 kPa.

No que diz respeito ao valor de pressão hidrostática a que Anteparas poderão estar sujeitas, este vem na forma:

$$P_{h,máx} = \rho g h\,[Pa] \qquad (1)$$

Onde ρ é a massa volúmica da água salgada a 25ºC ($1025\ kg/m^3$), g corresponde à aceleração da gravidade e h à altura da coluna de água aplicada à antepara.
Foi considerada também uma outra formulação, de acordo com as regras da Lloyds [6], que dá um valor de pressão constante superior em cerca de 20% do valor médio da formulação (1), na seguinte forma:

$$P_K = 7.2 \times h\ [kN/m^2] \qquad (2)$$

2. MODELAÇÃO 3D DAS ANTEPARAS COMO PROJECTADAS E COMO FABRICADAS E ANÁLISE PELO MEF

O estudo do comportamento mecânico e estrutural das Anteparas pode-se aproximar ao estudo de placas finas reforçadas, uma vez que são elementos estruturais planos, em que a espessura tem uma dimensão muito pequena quando comparada com as outras dimensões (Modelo de Placa de Kirchhoff).

Optou-se por iniciar o estudo das Anteparas analisando o comportamento de placas sujeitas a diferentes condições de carregamento e condições de fronteira, validando os resultados obtidos por via numérica, (CosmosWorks®, Ansys®) por comparação com os resultados obtidos através de expressões analíticas (Soluções de Navier e Levy), validando o uso do *software* para o estudo do comportamento estrutural das Anteparas em estudo.

O processo de fabrico das Anteparas, principalmente a soldadura dos reforços à chapa, induz deformações quer na chapa, quer nos reforços, que têm de ser atenuadas *à posteriori* através de processos térmicos e físicos como a "martelagem" ou "traccionamento". De modo a obter-se a contribuição e influência das deformações induzidas pelo processo de fabrico das Anteparas reforçadas, assim como dos reforços estruturais, na distribuição de tensões e no comportamento mecânico das estruturas analisadas, optou-se por fazer a modelação de várias configurações de anteparas (Figura 3). Os valores das deformadas permanentes existentes nas anteparas após a aplicação dos processos de atenuamento foram retirados de [5], tendo sido obtidos por medição, *in situ,* de 45 pontos, correspondentes a 4 cotas analisadas por antepara. Na Figura 3 estão representadas as várias configurações de Anteparas que foram modeladas.

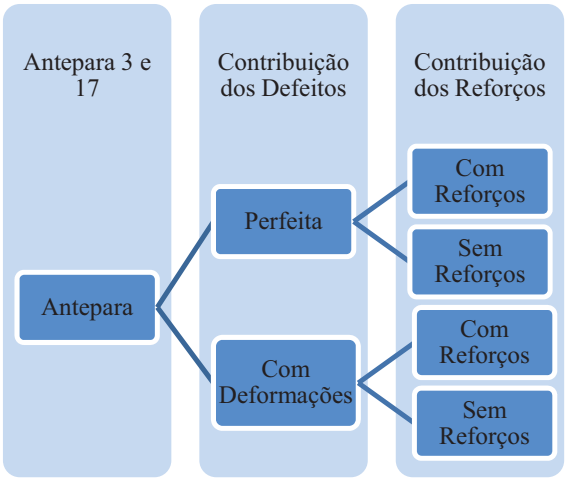

Figura 3. Configurações das Anteparas modeladas

Como exemplo, na Figura 4 está representado o alçado principal e a planta da Antepara 3 com deformações, onde se pode verificar a posição dos reforços e as deformações modeladas.

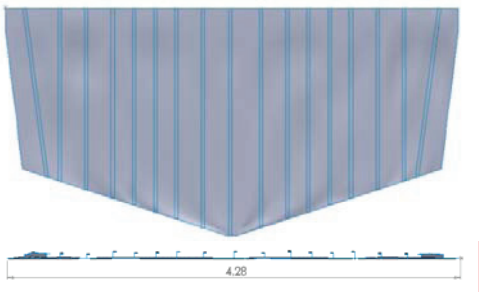

Figura 4. Modelação da Antepara 3 como fabricada. Dimensão em metros

As condições de fronteira que foram aplicadas a ambas as Anteparas e que melhor representam o cenário real, ainda que com diferenças evidentes em relação às condições de serviço, são o encastramento no topo da Antepara, correspondendo à ligação da Antepara ao convés do navio e a condição de simplesmente apoiada nas restantes faces, correspondendo à ligação da Antepara com o casco do navio. O tipo de elemento finito utilizado em todas as análises realizadas foi o elemento bidimensional xy (placa/casca) SHELL93.

Foram simuladas duas situações distintas em termos de carregamentos: o carregamento de compressão no plano devido ao efeito de *Slamming*, a que correspondeu a aplicação de uma pressão de 150 kPa; combinado com a aplicação de pressão lateral hidrostática, devida ao hipotético alagamento total de um compartimento estanque adjacente.
Foram escolhidos cinco pontos considerados representativos do comportamento estrutural de cada configuração de Antepara (Figura 5), onde foram determinados os valores de tensão de *Von Mises* induzidos pelos carregamentos actuantes.

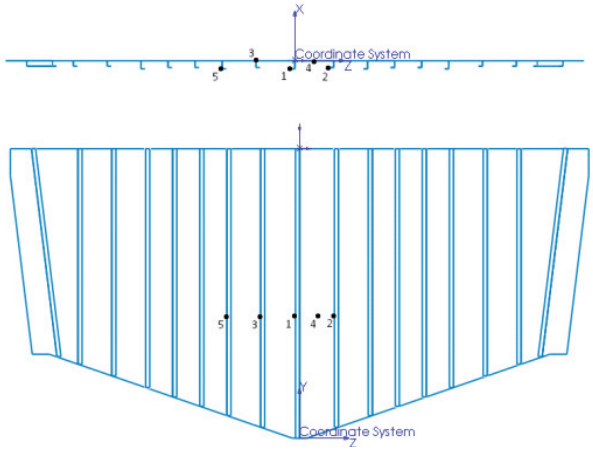

Pontos Representativos:

1. Ponto de valor de tensão máxima (no reforço);
2. Ponto no reforço adjacente ao reforço central;
3. Ponto no reforço adjacente ao central na união com a placa;
4. Ponto da placa entre reforços;
5. Ponto num reforço, não central, não adjacente ao reforço central.

Figura 5. Antepara 3: Alçado Principal e em planta, contendo a posição dos pontos representativos

Como exemplo, na Figura 6 está representado o gráfico de tensões obtido em Ansys para a Antepara 3, real, com carregamento combinado (no plano e pressão lateral hidrostática).

Da análise dos resultados obtidos para os diferentes casos de estudo (Tabela 3 e 4), conclui-se que, para a situação de carregamento exclusivamente no plano, os reforços sofrem pouca solicitação, pelo que a tensão máxima é induzida na chapa da Antepara. Verifica-se que a existência de defeitos iniciais tem pouca influência nos valores de tensão induzidos e que o efeito dos defeitos é anulado com a introdução dos reforços. Para a situação de pressão lateral hidrostática, verifica-se que o valor de tensão máxima, não considerando as tensões induzidas junto à fronteira encastrada, é obtido no reforço principal/central devido à condição de vão máximo, à maior altura do perfil em questão e, consequentemente à maior distância ao eixo neutro da Antepara à fibra externa, sendo, em geral, muito próximas das tensões de cedência da liga de alumínio utilizada (200 MPa), enquanto que as tensões na chapa da Antepara não excedem os 35 MPa.

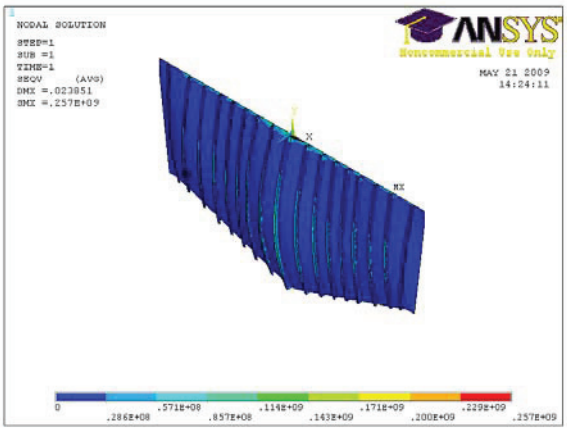

Figura 6. Antepara 3 real com carregamento combinado no plano e pressão lateral hidrostática

Tabela 3. Antepara 3. Valores de Tensão de V.Mises

	Antepara 3 como fabricada	
	Carregamento no Plano	Carregamento Combinado
Tensão a meio vão (ponto 4, Fig.5) [MPa]	0,177	24
Tensão máxima no reforço principal (ponto 1, Fig.5) [MPa]	0,078	199

Tabela 4. Antepara 17. Valores de Tensão de V.Mises

	Antepara 17 como fabricada	
	Carregamento no Plano	Carregamento Combinado
Tensão a meio vão (ponto 4, Fig.5) [MPa]	0,128	12
Tensão máxima no reforço principal (ponto 1, Fig.5) [MPa]	0,1	143

3. RECOLHA E ANÁLISE DE ESPECTROS DE EXTENSÃO

Tendo sido obtidos os valores de tensões induzidos nas anteparas perfeitas e imperfeitas em estudo (Tabelas 3 e 4), para os carregamentos estáticos anteriormente referidos, recorreu-se à aplicação de extensómetros na chapa da Antepara 17, com o objectivo de se obterem os valores de extensão reais, de natureza dinâmica, existentes na Antepara.

Realizaram-se primeiramente ensaios de natureza estática e dinâmica, que tiveram lugar na Divisão de Laboratórios e Qualidade (DLQ) do Arsenal do Alfeite (AA), de modo a possibilitar um primeiro contacto com o uso dos instrumentos de medição (ponte extensométrica), com as técnicas de colagem, etc., e de modo a se validarem as técnicas de extensometria utilizadas. Em todos os ensaios realizados utilizou-se o esquema de ¼ de ponte, com um extensómetro activo, e três resistências de 120 Ω, que veio também a ser o esquema utilizado durante a recolha do espectro de extensões induzido na Antepara. Durante o ensaio dinâmico de validação em laboratório foi estudada a resposta dos extensómetros colados sobre uma viga encastrada de alumínio em função da variação da velocidade imposta (10 aos 80 mm/s) e da frequência de oscilação (dos 10 aos 20 Hz) (Figura 7), tendo sido verificado que a frequência máxima de leitura exacta e precisa pelo equipamento utilizado era de 5 Hz.

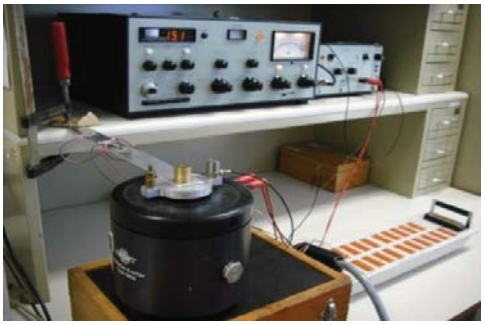

Figura 7. Montagem experimental do ensaio dinâmico

Com o objectivo de se obterem as tensões induzidas em navegação, foi colado um extensómetro uniaxial na chapa da Antepara 17, num local escolhido tanto pela observação (MEF) da distribuição de tensões máximas derivadas do carregamento no plano (*Slamming*), como pela disponibilidade de espaço a bordo da embarcação. O local escolhido para a colagem do extensómetro foi a meio da Antepara, num ponto próximo do reforço principal com altura máxima e próximo da base desta. Efectuaram-se os processos típicos referentes a tratamentos de superfície e colagem do extensómetro e foi instalado a bordo todo o equipamento necessário às medições (Fig.8).

Figura 8. Extensómetro colado na Antepara e equipamento instalado a bordo

As provas de mar realizaram-se no Mar da Palha (Estuário do Tejo). A velocidade da embarcação durante

a prova foi de 24 nós, podendo-se considerar constante, e a altura significativa das ondas foi de aproximadamente 30 cm. A prova teve uma duração de aproximadamente 25 minutos e uma frequência de aquisição de dados de 5Hz. Com os dados obtidos foi efectuado um gráfico Extensão vs. Tempo, como ilustrado na Figura 9.

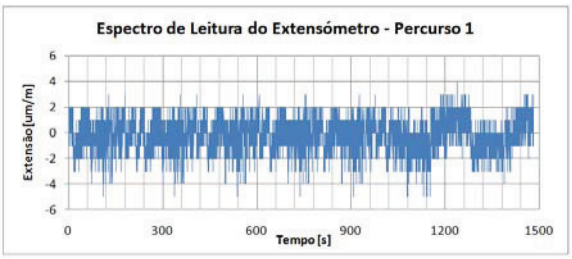

Figura 9. Espectro de leitura

O valor de extensão mínima registada foi de -5µm/m a que corresponde uma tensão de compressão induzida na Antepara 17 de aproximadamente 0.35 MPa (3).

$$\sigma = \varepsilon \times E = 5 \cdot 10^{-6} \times 71 \cdot 10^{9} = 0.355 \text{ MPa} \quad (3)$$

O valor de tensão de *Von Mises* que se obteve através do MEF, para a Antepara 17 e na zona de localização do extensómetro, quando simulado o efeito de *Slamming* foi de 0.15 MPa, isto é, um valor 57% inferior ao valor obtido experimentalmente. As possíveis causas para a diferença registada poderão ser:

- A velocidade de aplicação da carga real, por implusos, é diferente da carga estática simulada pelo MEF;
- As condições de fronteira consideradas no modelo numérico não correspondem exactamente às existentes no navio;
- A geometria da antepara real não é exactamente igual à modelada, uma vez que, próximo da zona onde foi colocado o extensómetro existe agora uma porta de passagem entre compartimentos adjacentes;
- Poderão ainda existir erros associados à colagem e leitura dos valores provenientes do extensómetro aplicado, uma vez que os valores de extensão medidos são de muito pequeno valor, quase no início da escala de medição da ponte extensométrica, podendo facilmente incorporar ruído no sinal eléctrico.

4. ANÁLISE À FADIGA

Tendo em consideração o espectro de carga real obtido (Fig.9), fez-se a estimativa de vida à fadiga da Antepara 17 com o auxílio do *software* de MEF SolidWorks/CosmosWorks.

Com base no espectro de extensões, ou bloco de carregamento, adquirido, obteve-se a matriz de *rainflow* correspondente, com a gama de tensão, tensão média e número de ciclos por cada evento, como ilustrado no histograma apresentado na Figura 10.

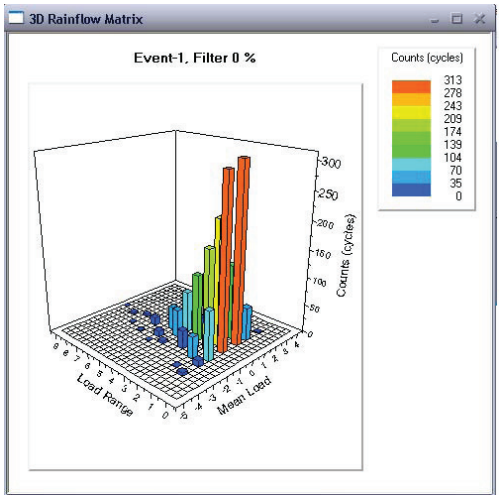

Figura 10. Histograma da matriz de Rainflow obtida

O alumínio utilizado nas chapas das Anteparas (5083-H111) e o alumínio utilizado nos reforços (6082-T6) têm uma tensão de rotura de 300 e 310 MPa, respectivamente, motivo pelo qual se utilizou na análise de vida à fadiga a curva S-N correspondente a alumínios com tensão de rotura superior a 260 MPa, como ilustrado na Figura 11, a qual foi retirada da referência bibliográfica [7].

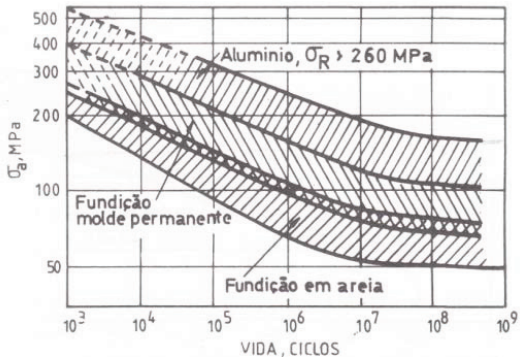

Figura 10. Curvas S-N [8]

Uma vez que a tensão média correspondente ao espectro de carga real é, em alguns ciclos, diferente de zero (Fig.10), foi utilizado o critério de dimensionamento de Soderberg para fazer a correcção da tensão limite de fadiga (4):

$$\sigma_a = \sigma_{f0}\left(1 - \frac{\sigma_m}{\sigma_c}\right) \quad (4)$$

onde:

- σ_{f0} - Tensão limite de fadiga para uma tensão média igual a zero;

- σ_c - Tensão de cedência;
- σ_R - Tensão de rotura.

Os factores de redução para a tensão admissível de fadiga, σ_{fadm} (5), considerados foram:

- k1 = 0.72 (coeficiente representativo do efeito de acabamento superficial laminado[7]);
- k2 = 1 - coeficiente representativo do factor dimensão;
- k3 = 0.868 - coeficiente representativo de uma fiabilidade de 95%;
- k4 = 1 - coeficiente representativo para tipo de solicitação;
- k5 = 1 - coeficiente representativo do efeito da temperatura;

ficando:

$$\sigma_{fadm} = k1 \cdot k2 \cdot k3 \cdot k4 \cdot k5 \cdot \sigma_f = 0.72 \cdot 1 \cdot 0.868 \cdot 1 \cdot 1 \cdot \sigma_f = 0.625 \cdot \sigma_f \quad (5)$$

Os resultados em termos de vida à fadiga em número de blocos de carregamento e dano por bloco foram:

- Dano para o espectro introduzido = 1,8E-6
- Vida à fadiga = 5,362E5 blocos

Conclui-se que, para uma utilização típica da embarcação em estudo, de aproximadamente 400 horas de navegação por ano, e para o espectro de carga introduzido, a vida à fadiga da Antepara corresponde a 220000 horas de navegação, o que se pode considerar vida infinita para o tipo de utilização referida.

5. CONCLUSÕES

Verificou-se através da modelação 3D das Anteparas 3 e 17 das embarcações que para o caso de carregamento devido ao *Slamming,* carregamento exclusivamente no plano, os reforços sofrem pouca solicitação. A tensão máxima é induzida na chapa da Antepara e equivalente à pressão de carregamento. A distribuição de tensões é equivalente na Antepara com reforços e na Antepara sem reforços. Porém o deslocamento máximo diminui substancialmente com a introdução dos reforços (até 95%).

Para a situação de hipotético alagamento de compartimentos estanques, a tensão máxima é induzida no reforço central principal com aproximadamente 200 MPa. Isto deve-se à condição de vão máximo e maior altura dos reforços principais e consequente de maior distância relativa ao eixo neutro da Antepara. As tensões induzidas na chapa das Anteparas não excedem os 35MPa.

Os defeitos iniciais têm pouca influência para qualquer das situações de carregamento no plano e pressão lateral. O efeito dos defeitos é anulado com a introdução dos reforços.

A comparação de tensões induzidas entre as Anteparas perfeitas e com defeitos iniciais levou à conclusão que as tensões induzidas nas Anteparas com defeitos iniciais são em geral, e para alguns pontos, inferiores às tensões induzidas nas Anteparas perfeitas (até 15%), possivelmente devido aos efeitos de membrana e de inércia induzida pela chapa com geometria semelhante à de chapa corrugada.

Realizaram-se provas de mar com a intenção de adquirir o espectro de extensões em serviço e fazer uma estimativa de vida à fadiga da Antepara 17. As provas tiveram lugar com condições de mar favoráveis à navegação e, para as extensões recolhidas, a vida à fadiga da Antepara 17 obtida através do *Software* SolidWorks/CosmosWorks foi de aproximadamente 220000 horas de navegação, que se pode considerar vida infinita para um espectro de utilização média da embarcação de 400 horas por ano.

REFERÊNCIAS

[1] *Revista da Armada*, Janeiro de 2008

[2] Matias, C., Silva, P.P., Martins, R.F. (2008), "On the analysis of structural details in lightweight aluminium crafts. Ways of improving structural reliability by applying "safe life" vs. "fail safe" principles." PCF 2008, 11th Portuguese Conference on Fracture, pp. 431-443, Monte de Caparica, Portugal

[3] The Naval Architect, Feature 7, Setembro 2008

[4] Silva, P.P. Mateus, A., Witz, J., Pereira, C., (2004), "Performance Enhancement of Structural Details in Aluminum Crafts", PRADS2004 9th International Symposium on Practical Design of Ships and Other Floating Structures, pp. 790-797, Lübeck-Travemünde, Germany

[5] Matos, J., Silva, Paulo, Martins, R.F., Mateus, A.R.. "Influence of Production Defects in the Structural Resistance of Reinforced Panels in Aluminium Crafts", IRF'2009-3rd International Conference on Integrity, Reliability and Failure, Oporto, 2009

[6] Rules and Regulations for Classification of Special ServiceCraft, Lloyd's Register of Shipping, 1999, London

[7] Branco, C. Moura; Fernandes, A. Augusto; Castro, Paulo, Fadiga de Estruturas Soldadas, 2ª Edição, 1999

PREVISÃO DE VIDA À FADIGA DE UM COMPONENTE FERROVIÁRIO BASEADA NAS FUNÇÕES DA DISTRIBUIÇÃO CUMULATIVA NORMAL ESTANDARDIZADA DA TENSÃO EQUIVALENTE

T. L. Morgado [1], C. M. Branco[2], V. Infante[2]

[1] ICEMS - IST – UTL Instituto de Ciência e Engenharia de Materiais e Superfícies
Departamento de Engenharia Mecânica do Instituto Politécnico de Tomar
Escola Superior de Tecnologia de Abrantes
Rua 17 de Agosto de 1808, 2200-370 Abrantes, Portugal
E-mail: tmorgado@ipt.pt

[2] ICEMS - IST – UTL Instituto de Ciência e Engenharia de Materiais e Superfícies
Departamento de Engenharia Mecânica,
Instituto Superior Técnico da Universidade Técnica de Lisboa,
Av. Rovisco Pais, 1049-001 Lisboa, Portugal
E-mail: cmbranco@dem.ist.utl.pt
E-mail: virginia.infante@ist.utl.pt

RESUMO

Neste artigo é apresentada uma metodologia de cálculo para obtenção da previsão de vida à fadiga tendo em conta as curvas S-N para fiabilidades de 50% e 90%, e as funções da distribuição cumulativa normal estandardizada da tensão equivalente de um componente ferroviário. Este componente, denominado engate, é de aço vazado obtido por fundição em areia com a especificação ASTM A148 90-60, e é usado nos comboios de mercadorias. Esta peça tem como principal função o acoplamento do primeiro vagão à locomotiva e o acoplamento dos diferentes vagões entre si. Esta peça ferroviária está sujeita a carregamentos de amplitudes variáveis e apresenta problemas de fissuração prematura.
Para a realização deste trabalho foram obtidos dados em serviço, usando rosetas extensométricas, numa viagem de rotina com os vagões carregados. Foram determinadas as zonas mais críticas do componente e calculadas as respectivas vidas à fadiga. A metodologia também foi testada na zona nominal, sendo apresentado o resultado da previsão de vida à fadiga nessa zona.

PALAVRAS-CHAVE: componente ferroviário, carregamentos de amplitude variável, previsão de vida à fadiga, função distribuição cumulativa normal estandardizada.

ABSTRACT

This article is presented a methodology for calculate fatigue life prediction taking into account the S-N curves for 50% and 90% reliabilities and the standardized equivalent stress–time histories of a railway component. This component, called railway coupling, is obtained by steel casting with ASTM specification A148 90-60, and is used on freight trains. The principal function of this component is the coupling between the first wagon and locomotive and between the different wagons. This railway structural piece is subject to varying amplitudes uploads and premature cracking problems. Data were obtained using strain gauges rosettes in service, in a load wagons routine travel. Fatigue life predictions, in years, were calculated for the determinate critical zones. The present methodology was tested on nominal zone and the result of fatigue life prediction was calculated.

KEY WORDS: railway component, variable amplitude loading, fatigue life prediction, standardized load-time histories.

1. INTRODUÇÃO

As estruturas ferroviárias estão sujeitas a problemas de fadiga que podem originar ruína. Com a excepção dos carris de caminho de ferro em que um dos principais mecanismos de dano é a fretagem e a fadiga de rolamento, nos restantes componentes estruturais o principal aspecto a ter em conta no projecto é definitivamente a fadiga estrutural.

A fadiga estrutural, que origina frequentemente fissuração nas zonas críticas é causada pelas cargas dinâmicas que se exercem na estrutura induzidas por

vários efeitos que têm maior ou menor importância consoante o tipo de órgãos ou componente estrutural.
Em contraste com o caso do projecto estático baseado nas tensões de cedência ou de rotura do material, ou seja nas tensões admissíveis, o projecto à fadiga baseia-se nas curvas S-N para uma amplitude de carga constante, ou nas curvas de vida à fadiga para cargas de amplitude variável.

A vida à fadiga deverá ser determinada pelas condições de carregamento em serviço, através do "espectro" de cargas ou tensões obtidas em serviço nas zonas críticas do componente.

No estudo da influência dos carregamentos na vida de fadiga (número de ciclos de fadiga), observa-se que no caso de carregamento de amplitude variável, a vida à fadiga depende da distribuição de frequência acumulada ("forma do espectro"), e pode ser várias ordens mais elevadas do que a verificada em carregamentos de amplitude constante [1, 2]. A importância do "espectro de carga" foi reconhecida por Ernest Gaβner, em 1938, ao formular o procedimento para a simulação do carregamento a amplitude variável, para estruturas aeronaúticas. Pela década de 60 (século vinte), com o surgimento das máquinas de ensaio servo hidráulicas, o histórico programa "eight-block-programme test" pode ser substituído pelo processo de carga versus tempo mais realístico, recorrendo à função de distribuição de frequência cumulativa Gaussiana. Os diagramas cargas versus tempo dependem das aplicações particulares e das funções dos componentes, nos últimos 65 anos têm sido desenvolvidas diferentes aplicações relacionadas com o espectro padrão [3], e continuam-se a desenvolver.

Neste trabalho é desenvolvida uma metodologia de cálculo para obtenção da previsão de vida à fadiga tendo em conta as funções da distribuição cumulativa normal estandardizada da tensão equivalente de um componente ferroviário e as curvas S-N para fiabilidades de 50% e 90%. Este componente, denominado engate, é de aço vazado obtido por fundição em areia com a especificação ASTM A148 90-60, e é usado para ligar o primeiro vagão do comboio à locomotiva e às diferentes carruagens entre si.

2. CURVAS S-N

A derivação das curvas de projecto para diferentes probabilidades de sobrevivência adoptadas é obtida através da análise estatística dos resultados experimentais (duração de vida) para vários níveis de tensão a amplitude constante. Para cada nível de tensão pode definir-se uma função densidade de probabilidade da duração à fadiga. A curva de projecto é obtida unindo os pontos correspondentes a uma determinada probabilidade de sobrevivência. Os modelos matemáticos que têm sido propostos para descrever a dispersão da duração à fadiga são diversos [4, 5].

Com base nesta metodologia é possível determinar a tensão admissível para uma determinada duração prevista, assumindo uma determinada probabilidade de sobrevivência.

A norma ASTM E739-91 (2004) [6] sugere um procedimento para tratamento estatísticos de dados que deverá ser tido em conta na construção das curvas de projecto. Este procedimento foi seguido e na Figura 1 encontra-se esquematizado em linguagem natural, o algoritmo de cálculo para a obtenção da curva S-N para uma determinada probabilidade de falha.

Obtenção da curva S-N para uma determinada probabilidade de falha

1. Inicio do programa:
2. Ler vector da variável dependente
Ler vector da variável independente
3. Determinar
- classes de variáveis independentes
- a média de cada classe
- o desvio padrão de cada classe
- valores da função probabilidade de falha de cada classe

4. Construir
- gráfico log (variável independente) versus log (valor da função probabilidade)

5. Determinar
- por regressão linear dos pontos obtidos no gráfico, os parâmetros da recta y=mx+b

6. Com os parâmetros obtidos, construir a curva S-N para valores de N [10^4 , 10^7]
7. Fim do Programa

Figura 1 Algoritmo em código natural usado na obtenção da curva S-N para uma determinada probabilidade de falha.

A descrição estatística do comportamento à fadiga com as correspondentes probabilidade de sobrevivência e dispersão, é importante para considerações de segurança. A banda de dispersão valores associada às curvas S-N é assumida como uma distribuição normal Gaussiana em escalas logaritmicas. Um dos parâmetros característicos de uma banda de dispersão é o índice de intervalo de dispersão T_σ, obtido pela expressão (1), para probabilidade de sobrevivência de 10% e 90% [7]. O factor de segurança j, depende do valor da probabilidade de falha e do índice de intervalo de dispersão T e é expresso pela relação (2).

$$T_\sigma = \frac{\sigma(P_s = 10\%)}{\sigma(P_s = 90\%)} \tag{1}$$

$$j = \left(\frac{1}{T}\right)\exp\left(\frac{\left(2{,}36\sqrt{\left|\lg\left(1-P_s\right)\right|}\right)-1}{2{,}56}\right) \tag{2}$$

Os dados usados na obtenção das curvas S-N foram obtidos dos ensaios de fadiga em 12 provetes de geometria cilíndrica, maquinados segundo a norma ASTM E8M-04 [8]. A secção resistente dos provetes tem um diâmetro ∅=10,7 mm e um comprimento de referência L_0= 25 mm. Os provetes foram ensaiados à tracção com ciclos de amplitude de tensão alternada

constante para uma razão de tensões de R=0,05. A frequência de ciclos de carga utilizada nos ensaios foi de 8-10Hz. O critério de fim de ensaio utilizado foi a rotura ou uma vida superior ou igual a 6.000.000 de ciclos.
Estes ensaios foram realizados na servo-hidraúlica DARTEC M1000/RK do Laboratório de Ensaios Mecânicos do DEM do IST.

Na Figura 2 encontram-se representadas as curvas S-N para probabilidades de falha considerando a distribuição log-normal onde as dispersões e os factores de segurança para as fiabilidades de 90% são respectivamente, T_σ ($P_{s=90\%}$)= 1:1,29 e j_σ ($P_{s=90\%}$)= 2,19.

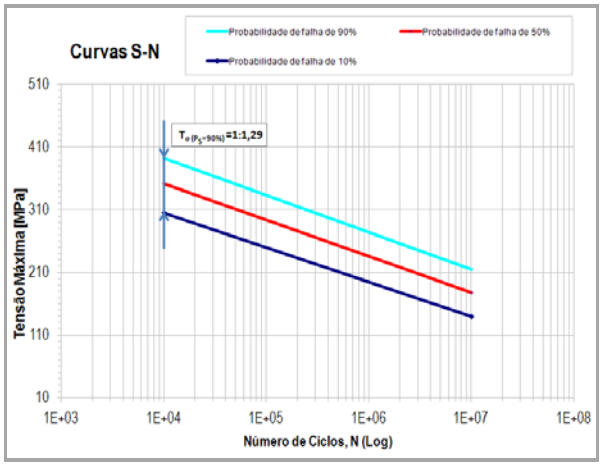

Figura 2 Curvas de projecto com as respectivas dispersões para fiabilidade de 90%.

3. FUNÇÃO DA DISTRIBUIÇÃO CUMULATIVA NORMAL ESTANDARDIZADA DAS TENSÕES EQUIVALENTES

O diagrama de frequência cumulativa das tensões corresponde a probabilidade cumulativa das tensões em termos de escalões de tensões versus número de ciclos. A curva destes diagramas é portanto uma função contínua.

As recomendações do IIW [9] sugerem ainda que o cálculo de dano deva ter em conta 20 escalões de tensões para um número de ciclos de vida esperados, superior a 10^8; e para um número de ciclos inferior, 8 a 10 escalões de tensões sejam suficientes. O espectro pode ser caracterizado através de uma tabela de escalões discretos.

No entanto, a análise estatística de dados sugere diferentes regras empíricas que deverão ser tidas em conta na determinação da quantidade de classes e amplitude destas, para grandes amostras. Esta metodologia foi a seguida, no âmbito deste trabalho.

Assim foi desenvolvido um procedimento empírico, tendo em conta os diferentes espectros obtidos em serviço através de extensometria eléctrica, do engate que liga a locomotiva ao primeiro vagão, no percurso Sines-Ermidas [10], para a determinação da amplitude das classes e construção dos histogramas.

O método de contagem de ciclos recomendado pelo IIW [9] é o método Rainflow e foi o utilizado no âmbito deste artigo. No entanto, é de salientar que os autores realizaram estudos comparativos dos diferentes métodos de contagem de ciclos propostos e descritos na literatura e verificou que para grandes amostras, os métodos de contagem como o método de gamas no sentido ascendentes e no sentido descendente e o método de Rainflow tendem para o mesmo valor [11, 12].

Tendo-se chegado à conclusão que as funções distribuição cumulativas eram do tipo Gaussiana ou seja obedece à lei (3). As variáveis s, $\overline{\sigma}_{eq}$ e L, representam respectivamente o desvio padrão, a tensão equivalente média e o tamanho da amostra.

$$P(\xi \geq \sigma_{eq}) = \frac{1}{s\sqrt{2\pi}} \int_{\sigma_{eq}}^{\infty} \exp\left[-\frac{1}{2}\left(\frac{\xi - \overline{\sigma}_{eq}}{s} \right)^2 \right] d\xi \quad (3)$$

Na Figura 3 encontra-se esquematizado em linguagem natural, o procedimento de cálculo para a obtenção da distribuição cumulativa estandardizada utilizado.

Obtenção da função da distribuição cumulativa normal estandardizada

1. Inicio do programa:
2. Ler vector da variável classes de tensões
3. Determinar
   - a média de cada classe
   - a frequência absoluta simples de cada classe
   - a frequência relativa simples de cada classe
   - a frequência absoluta relativa de cada classe
   - a média da amostra
   - o desvio padrão da amostra
   - valores da função distributiva cumulativa normal estandardizada
4. Construção do diagrama da função distribuição cumulativa normal estandardizada das tensões
5. Fim do Programa

Figura 3 Algoritmo em código natural usado na obtenção da função da distribuição normal estandardizada.

Os resultados dos diagramas da função cumulativa normal estandardizada das tensões obtidas em serviço das rosetas 1, 6 e 7 [10] estão apresentados nas Figuras 4, 5 e 6 respectivamente. Nestes diagramas teve-se em conta a regra de Sturges. As rosetas 1 e 6 foram escolhidas por apresentarem valores de tensão mais críticos e a roseta 7 foi escolhida para comparação por se encontrar na zona nominal. Constata-se que a frequência acumulada para as rosetas 1, 6 e 7 apresenta valores até 7E+01, 9E+3 e 9E+5, respectivamente.

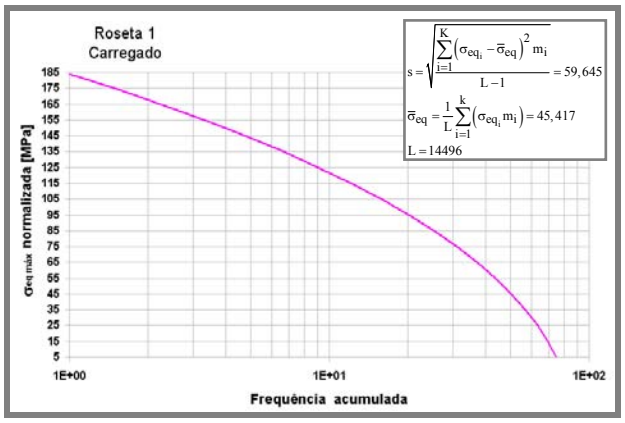

Figura 4 Função da Distribuição Cumulativa Normal Estandardizada da tensão equivalente da roseta 1 no percurso Sines-Ermidas.

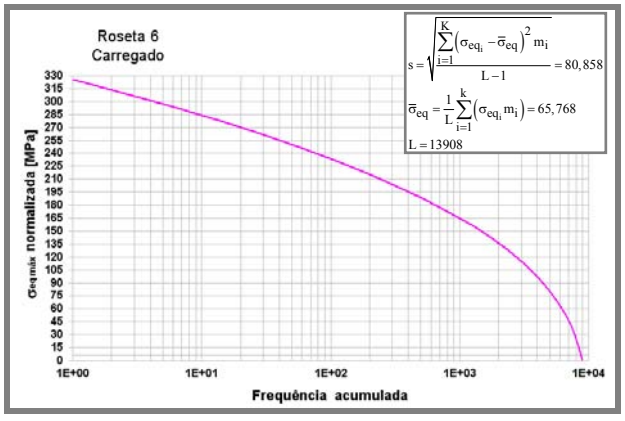

Figura 5 Função da Distribuição Cumulativa Normal Estandardizada da tensão equivalente da roseta 6 no percurso Sines-Ermidas.

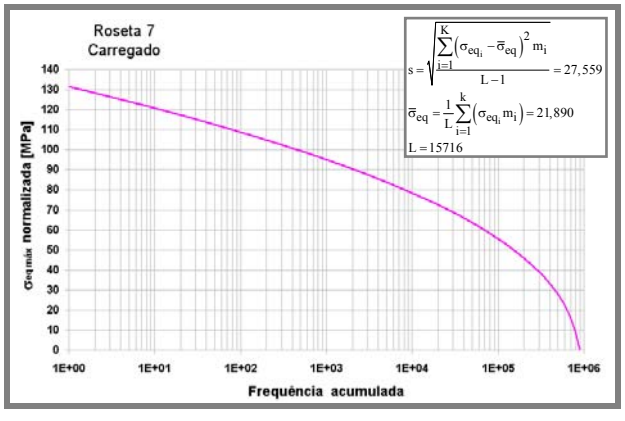

Figura 6 Função da Distribuição Cumulativa Normal Estandardizada da tensão equivalente da roseta 7 no percurso Sines-Ermida.

4. PREVISÃO DE VIDA À FADIGA

Na programação da rotina de cálculo de dano do componente ferroviário em causa, considerou-se o modelo linear de acumulação de dano com a regra de Miner. Entrou-se em conta com as tensões máximas equivalentes obtidas em serviço e com as curvas S-N obtidas para as fiabilidades de 50% e 90%.
Ou seja, com os dados das funções de distribuição cumulativa Gaussiana, é obtido o dano real para as diferentes fiabilidades através das curvas de vida à fadiga, recorrendo às equações (4) e (5) [13]. Onde o somatório das frequências absolutas simples do número de ciclos é dado pelo parâmetro $\overline{N}_{exp}$; L_s é o somatório da variável estandardizada na distribuição Gaussiana; n_i é o número de ciclos por classes no histograma e N_i é o número de ciclos correspondentes a cada tensão por classes do histograma nas curvas S-N.

$$D_{real}=\frac{D_{esp}}{L_s}\overline{N}_{exp} \tag{4}$$

$$D_{esp}=\sum_{i=1}^{n}\frac{n_i}{N_i} \tag{5}$$

5. RESULTADOS

No cálculo da previsão da vida de fadiga deste componente ferroviário teve-se em conta o número de viagens por ano que em média os componentes em causa realizam.

Na Figura 7 são apresentados os resultados da metodologia proposta, onde se constata que:

- A roseta 7, sendo uma roseta nominal é de esperar que apresente uma vida infinita, como se verifica.
- As rosetas mais críticas, rosetas 1 e 6, para fiabilidades de 90% apresentam valores de previsão de vida abaixo de um ano.
- Para fiabilidades de 50%, a previsão de vida é de cerca de 5 anos para a roseta 1 e de cerca de 3 anos para a roseta 6.

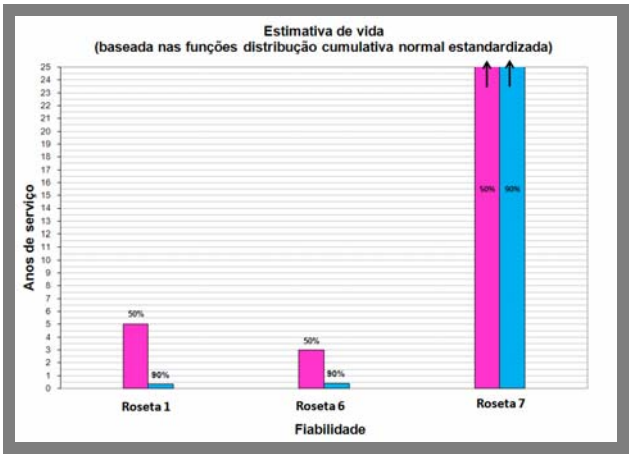

Figura 7Previsão de vida tendo em conta as funções da Distribuição Cumulativa Normal Estandardizada das tensões equivalentes das rosetas 1, 6 e 7 no percurso Sines-Ermida.

6. CONCLUSÕES

Durante o trabalho de pesquisa realizada aos componentes retirados de serviço, as zonas de fissuração prematura coincidiram com as zonas de maior concentração de tensões, ou seja entre a cabeça do engate e o corpo do engate (zona da colagem da roseta 1 e roseta 6); também se verificou que em determinados componentes a fissuração prematura também aparecia no seu interior; e constatou que não houve surgimento de fissuração prematura na zona designada por nominal (zona de colagem da 7).
Do que foi analisado neste artigo, conclui-se que a metodologia de cálculo aqui apresentada prevê fissuração prematura de acordo com o que sucede na vida útil de serviço destes componentes, tanto para as zonas críticas como para a zona nominal.

7. REFERENCES

[1] Sonsino C. M., "Fatigue design and testing of components", 6as Jornadas de Fractura - Porto 1998, Livro das comunicações, Divisão de Fractura da Sociedade Portuguesa de Materiais, 3-46.

[2] C. Berger, K.-G. Eulitz, P. Heuler, K.-L. Kotte , H. Naundorf, W. Schuetz, C.M. Sonsino, A. Wimmer, H. Zenner, "Betriebsfestigkeit in Germany - an overview", International Journal of Fatigue, 24 (2002) 603–625.

[3] Heuler P., Klaütschke H. "Generation and use of standardized load spectra and load–time histories". International Journal of Fatigue 2005;27(8):974–90.

[4] Shu-Ho Dai, Ming-O Wang, "Reliability Analysis in Engineering Applications", Van Nostrand Reinhold, New York, 1992. ISBN: ISBN 0-442-00842-2.

[5] Nakasawa Hajime, "Statistical S-N Testing Method with 14 Specimens: JSME Standard Method for determination of S-N Curves", In Statistical Research on Fatigue and Fracture, ed. Tsuneshichi Tanaka, London, New York: Elsevier Applied Science, (1987) 59-69.

[6] ASTM E739-91(2004), "Standard Practice for Statistical Analysis of Linear or Linearized Stress-Life (S-N) and Strain-Life (e-N) Fatigue Data", Developed by Subcommittee E08.04, Book of Standards Volume: 03.01, West Conshohocken, USA.

[7] Sonsino C. M., "Course of SN-curves especially in the high-cycle fatigue regime regard to component design and safety", Int. J. Fatigue (2007), doi:10.1016/j.ijfatigue.2006.11.015.

[8] ASTM E8M-04, "Standard Test Methods for Tension Testing of Metallic Materials [Metric]", Developed by Subcommittee: E28.04, Book of Standards Volume: 03.01, West Conshohoken, USA.

[9] Hobbacher A., "Fatigue design of welded joints and components. Recommendations of IIW Joint Working Group XIII-XV", XIII-1539-96/XV-845-96, Abington Publishing.

[10] Morgado T. L., "Integridade estrutural de um componente ferroviário", Tese de Doutoramento, IST-UTL Lisboa, 2009.

[11] Morgado T. L., Branco C. M., Infante V., "Local Elastic deformations in the railway couplings used for coal transport", 9as Jornadas de Fractura - Setúbal 2004, Livro das comunicações, Divisão de Fractura da Sociedade Portuguesa de Materiais, 475-494.

[12] Morgado T. L., "Estudo da influência do factor de concentração de tensões no cálculo do dano das rabetas dos vagões de transporte de carvão", Relatório científico para as provas públicas de Professor Adjunto do Departamento de Engenharia Mecânica do Instituto Politécnico de Tomar, Setembro de 2003.

[13] Radaj D., Sonsino C. M., Frickle W., "Fatigue assessment of welded joints by local approaches", Woodhead Publishing Limited, second edition, Cambridge, England, 2006. ISBN-13: 978-1-84569-188-2.

UTILIZATION OF DURABILITY CRITERION TO DEVELOP AUTOMOTIVE COMPONENTS

L. C. H. Ricardo

Assistant Professor in Structural Mechanics Division of Structural Mechanics
Department of Civil Engineering Aalborg University Sohngårdsholmsvej 57,
Aalborg, Denmark, 9000
E-mail: lchr@civil.aau.dk

ABSTRACT

Today the automotive companies must reduce the time to development of new products with improvement in performance, durability and low cost reductions where possible. To achieve this goal the carmakers need to improve the design criterion of car systems like body, chassis and suspension components. This paper will present a review of the techniques used in the automotive industry regarding durability before mentioned systems. The paper will present the procedures to obtain the spectrum loading to use in finite element analysis and the validation in laboratory and proving grounds.

KEY WORDS: automotive applications, design criterion, durability, proving ground, finite element method

1. INTRODUCTION

The heart of the design process is the set of analysis tools that the designer employs. The use of the finite element analysis is shown in Figure 1.Scale model testing using simulated service loads should normally be considered in the early stages of the design process. [1].

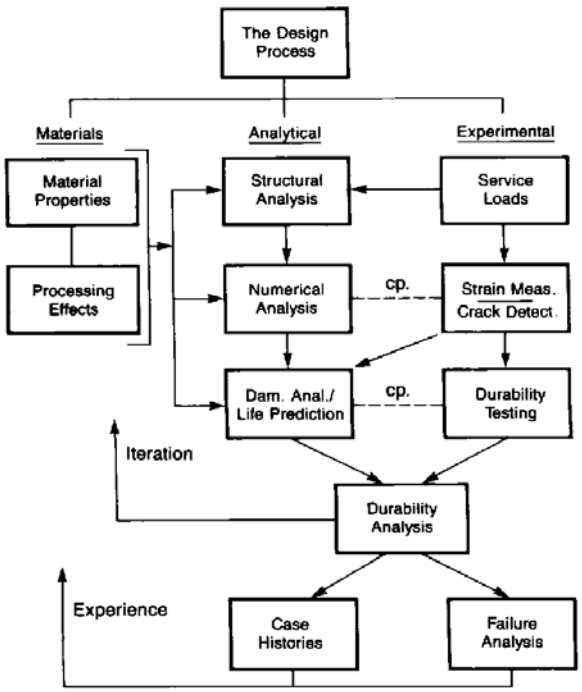

Figure 1 Design Process

The engineering procedures used in the automotive industry to promote structural integrity in cars and trucks are continuously evolving.

Significant changes are still taking place in instrumentation, analysis procedures and methods of handling and analyzing data. As long as these techniques continue to evolve, engineers will have the opportunity to utilize these new resources to make improvements in their fatigue design procedures.
To plan a product, the engineering department may need to have a survey completed to determine the needs of the customer. In each area it is possible to determine the range of expected usage. The usage pattern of many products primarily results from, the different applications of the product as well as the customer who is using it.

2. DURABILITY PROCEDURES

Carboni et. al [2] present a methodology to the development of truck wheels where these components are given special attention, because the fatigue design criterion must guarantee an appropriate structural integrity during service life. In fatigue assessment of wheels, the commonly accepted procedure by manufacturers is to pass two durability tests, namely the ‘‘radial fatigue test’’ and the ‘‘cornering fatigue test’’ [3–4]. These tests are conventionally defined and are based on simple load conditions not representing the real in-service behavior of components.

Another widely used type of test is based on standardised load spectra (grouped under the name ‘‘CARLOS’’: CAR LOading Spectra) consisting of a preset sequence of lateral and vertical forces obtained by extrapolation of loads measured directly on components during typical (straight driving, braking, cornering, parking,. .) both on-road and off-road.

In the special case of truck wheels, LBF (Germany) has developed ‘‘Eurocycle’’ [5,6], an accelerated test spectrum able to represent, in a 65 km route, 2032 km of typical exercise of truck wheels on European roads. Load spectra are applied to the real component, during fatigue tests, by a special Biaxial Test Facility [6,7].

The manner in which a product interacts with the environment during its use produces forces on hence it is necessary to characterize their magnitude, frequency, rate of change, etc.

To evaluate the durability of a product for any specific configuration, usage area and type customer, and the designer must obtain and evaluate loading information by numerical and experimental techniques (Ricardo & Andrade [8]. In service, the vehicle components are in most cases subjected to variable loads. The structure represents more or less complicated elastic systems; time-varying operational loads can excite their natural modes. Therefore, the response, which is in the form of a stress-time history at a point of the structure that is far enough from the point of load introduction, may show differences with regard to amplitudes as well as to frequencies compared with the corresponding load-time history. This means that a stress-time history contains both the effects of external loadings and the response of the structure to these loadings.
Grubisic [9] introduces a way to determine the load spectrum of design showing some procedures normally used in these situations. To determine the loadings that will be in used estimating life of automotive components some conditions are required:

1) measurements done with a vehicle prepared with sensors to run in mixed routes (off-road, city and both)
2) measurements done with a vehicle prepared with sensors to run by different drivers in the same routes
3) measurements done with a vehicle prepared with sensors uses by different drivers in different routes.
Figure 2 shows the parameters used to specify the loading spectrum.

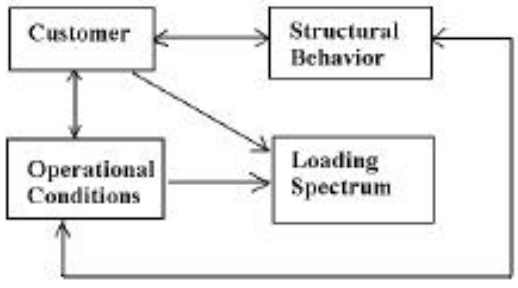

Figure 2 Parameters of Loading Spectrum

The utilization of the Power Spectral Density (PSD) analysis are obtained from the acceleration signals as part of the test program; design a structure or component considering just static loads and knowing that service loads are dynamic is wrong, because the regular fatigue criteria like Goodman [10] and Gerber [11] are based on the static loads and do not consider the effects of damage from natural frequencies in the structure.
Knowledge of natural frequencies is an important information on the dynamic behavior of the structure since it lets the experimental team to know if the assumptions used in the design are correct or not.
In the literature there are some works that cover this subject; Morril et al. [12] introduce a methodology to work with random vibration in an automotive structure. Lin et al. [13] present a method performance estimation to be used during the experimental development. This method is based on a response frequency analysis, where the number of natural frequencies obtained is limited to provide the input to compute damage in each natural frequency, by applying the Miner method [14].

Ricardo [15] presents an example of development of an automotive component considering finite element method, variable amplitude loading and Miner method.
In this paper a battery tray of a car is shown; that is instrumented with accelerometers as shown in Figure 3 (channels 1 to 6) with current battery tray and support; and the strain gages in Figure 4 (channels 7 to 11) shown the proposal of battery tray in hard points to input the data in the battery tray CAE model to check the structural behavior. The acquisition data were in several roads tests that meaning the major service loads and the frequencies of work were obtained. The frequencies of work are compared with numerical frequencies obtained from the CAE model in a modal analysis. Some measurements are shown in Figures 5 and 6. The validation of best proposal will be in a proving ground with accelerated durability test during 12,000 Km

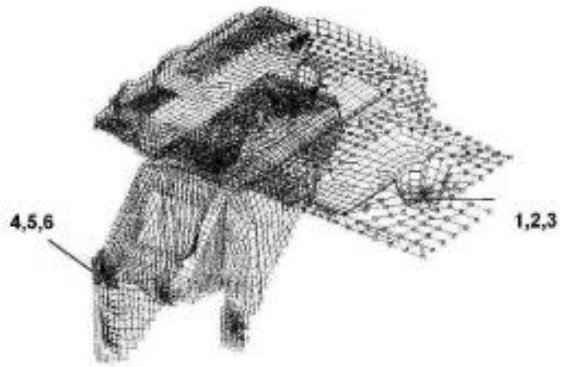

Figure 3 Position of Accelerometers

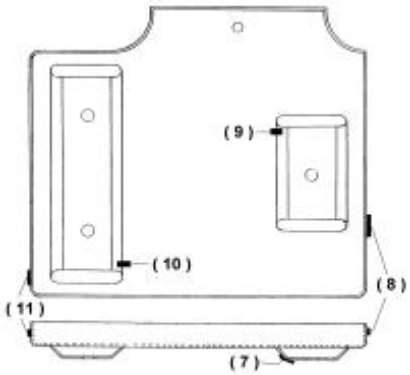

Figure 4 Position of Strain-Gages

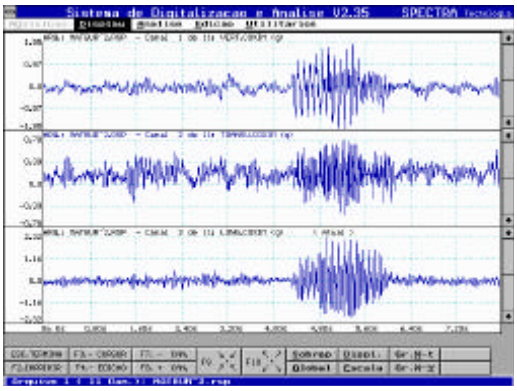

Figure 5 Acceleration at Battery Tray

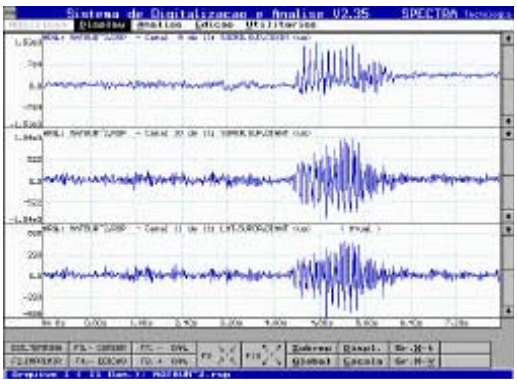

Figure 6 Strain at Battery Support

Figure 7 Damage Matrix

Table 1 shows the results, the damage accumulative analysis, and their correlation with the durability criterion and Figure 7 gives an example of damage matrix utilized to estimate the life of structure.

Table 1: Results of damage accumulation

damage in percents	cycles to failure	equivalent distance (Km)	criterion of durability (120 Km)
0.001255	7.97 E+4	399	OK
0.000003	3.33 E+7	1.66E+5	OK
0.000183	5.46 E+5	2732	OK
0.000152	6.58 E+5	3300	OK
0.000001	1.0E+ 8	5.0E+5	OK

Khalil & Topper [16] present a paper that cover the crack propagation in steels with application in automotive area. The paper determines the crack opening stress intensity factors in a aluminum alloy 2024-T351 and a SAE 1045 under variable amplitude loadings.

The average crack-opening stresses were within between 6 and 13 percent of the average calculated crack-opening stresses. The fatigue life predictions based on the modeled crack-opening stresses and the fatigue notch model were in good agreement with the experimentally determined fatigue data. In the interest of simplifying the use of crack-opening stress in design, the average crack-opening stress was correlated with the frequency of occurrence of the cycle reducing the crack-opening stress to the average level.

The use of a crack-opening stress level corresponding to the cycle causing a reduction to a crack-opening stress

reached once per 200 cycles gave a conservative estimate of fatigue life for the soft metals 2024-T351 aluminum alloy and 1045 annealed steel, while for the 1045 quenched and tempered steel the cycle causing a reduction to a crack-opening stress reaching once per 10 cycles gave a conservative life estimate.

In Ricardo [17], it is presented weld seam simulations in additional suspension components are prsented. Specifically, several types of weld seams in shock absorbers structures are modeled. HYPERMESH [18] and ABAQUS [19] are used as pre-postprocessor and solver, respectively, to perform the numerical modeling. Figure 8 show a case example and a detail thereof. The design criterion used in the FE models is fatigue failure or stresses exceeding 70% of the yield strength under bending about any axis. Physical tests were conducted to validate the numerical results, and close correlation between the numerical and experimental data was found. Both manufacturing and stress level considerations were examined, and the best option of weld seam detail was selected. To reproduce the weld seam configuration with a high level of confidence, some parts that might normally be modeled with shell elements were instead modeled with solids elements, specifically, ABAQUS type C3D10, seen in Figure 9 with present an example of post-processor of the analysis. Table 2 presents performance of some models.

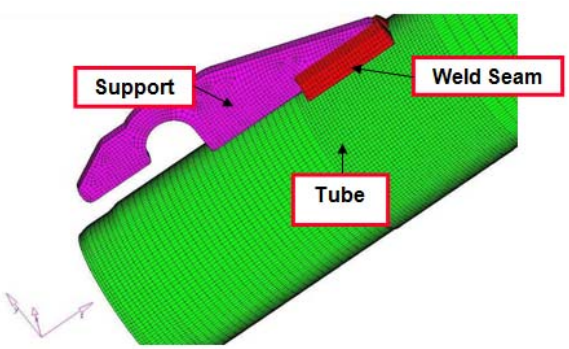

Figure 8 - Example weld seam FE model.

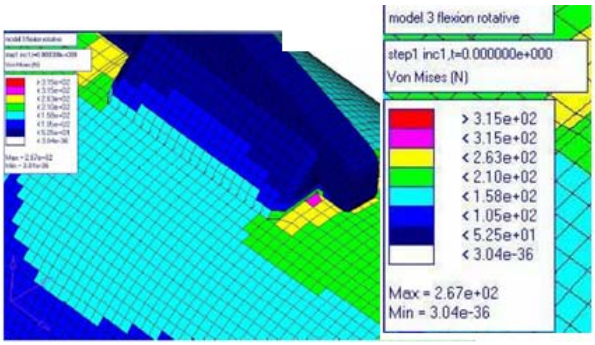

Figure 9 - Model 3 of weld seam.

Table 2 - Summary of Results

Model	case	Tube (thickness) mm	Support	Stress (Tube) MPa
1	1	2.25	Fixed	355
	2	2.25	Free	307
	3	2.25	Fixed	352
2	4	2.25	Free	267
	5	2.25	Fixed	416
3	6	2.25	Free	347
	7	2.5	Fixed	318

3. CONCLUSIONS

The present paper shows some procedures to developing components in automotive applications considering durability criteria. The customers are requesting products with more confidence level regarding structural integrity, low cost and high performance. The car will be continue to be a very useful way of transportation very useful and the trucks will continue to transport the products for long and short distances. These issues become the Research Engineering area to develop new design criteria and change the current one.

4. RERERENCES

[1] SAE, "*Fatigue Design Handbook*", USA,1988

[2] Carbonia, M.; Berettaa, S. & A. Finzi, Defects and in-service fatigue life of truck wheels, *Engineering Failure Analysis*, 10, 2003,pp. 45–57

[3] *ISO 3006* Road vehicles—passenger car wheels—fatigue testing methods, vol. 2. Switzerland, 1976

[4] Wright DH. *Testing automotive materials and components*. SAE Publication; 1993.

[5] Grubisic V, Fischer G. Procedure for optimal lightweight design and durability testing of wheels. *Int. J Vehicle Design*, 1984

[6] Grubisic V, Fischer G. Automotive wheels, methods and procedure optimal design and testing. *SAE Technical Paper 830135*,1983

[7] Grubisic V, Fischer G, Heinritz M. Design optimisation of forged wheel hubs for commercial vehicles. *SAE Technical Paper 841706*, 1984

[8] Ricardo, L. C. H. & Andrade, A.P.H.; *"The use*

of Fatigue to Design Structures Under Variable Loading", "In : Miller, K.J.; Brown, M.W. & Rios, E.R. (Eds.). *ECF12 Fracture from Defects***,** Emas Publishing, Sheffield, England, September, Vol. I: Fatigue, pp. 289-296; 1998.

[9] Grubisic, V. "Determination of Load Spectra for Design and Testing", *Int. J. of Vehicle Design*, Vol. 15, Nº1/2, UK, 1994

[10] Goodman, J**.** *Mechanics Applied to Engineering*, Longmans, Green & Co., London, England, 1899

[11] Gerber, W. "Bestimmung der Zulossigen Spannungen in Eisen Constructionen", *Z. Bayer Arch. Ing. Ver*. , Vol.6, Alemanha, 1874

[12] Morril, J H. ; Achatz, T. & Khosrovaneh, A. " An Application for Fatigue Damage Analysis Using Power Spectral Density from Road Durability Events", *SAE Paper 980689*, USA, 1998

[13] Lin, J.S.; John, C.M. St; and Luft, P. "The Use of Frequency Domain Vibration Methods for Automotive Component Durability ", *SAE paper 960971*, USA,1996

[14] Miner, M. A. "Cumulative Damage in Fatigue**",** *Journal. of Applied Mechanics*, ASME, Vol.12, USA, 1945 p. A159-A164.

[15] Ricardo L.C.H; Andrade, A. P. H. & Topper T.H. "Experimental Procedure to Estimate the Fatigue Life of a Component under Variable Amplitude Loading", (2002) In: Blom, A.F (Ed.). *Fatigue 2002***,** Emas Publishing, Stockholm, Sweden, Vol. 4, pp.2293-2300.

[16] M. Khalil ,T.H. Topper Prediction and correlation of the average crack-opening stress with service load cycles, *International Journal of Fatigu*e ,25,2003, pp. 661–670

[17] Ricardo, L.C.H.; "Simulation of Weld Seam in Suspension Components", SAE Brazil Congress, 2007 *SAE Paper 2007-01-2534*, November 28-30, Sao Paulo, Brazil

[18] Altair, *Hypermesh* version 7.0,USA, 2005

[19] *Abaqus version 6.1*, USA, 2004

FAILURE ANALYSIS OF HIGH-PERFORMANCE SURFACES USED FOR TRANSVERSAL STABILITY OF SHIPS (BILGE KEELS)

[1, a] Hugo Rodrigues, [1, b, 3] Rui F. Martins, [2, c] L. Leal das Neves, [2, d] Paulo Silva

[1]Faculdade de Ciências e Tecnologia, Universidade Nova de Lisboa
UNIDEMI, Departamento de Engenharia Mecânica e Industrial
Campus de Caparica, 2829-516 Caparica, Portugal
Email:[a] hugo_rodrigues@live.com.pt, [b] rfspm@fct.unl.pt

[2] Portuguese Navy, Directorate of Ships, Studies Department
Naval Base of Lisbon, 2800-001 Alfeite, Portugal
Email: [c] leal.neves@marinha.pt , [d] pires.silva@marinha.pt

[3] ICEMS/IST, Av. Rovisco Pais, 1, 1049-001 Lisbon - Portugal

ABSTRACT

During a scheduled maintenance program of a ship, several cracks were detected in the internal structure of bilge keels, as well as on the connection of these to the hull. The cracks encountered compromised the watertight integrity of the hull and, in the long run, could jeopardize its integrity.
This paper presents a failure analysis of the structural damages detected, in order to identify the causes of failure and propose improvements that could avoid them. Several stress concentration areas were identified, which coincided with the critical areas where there have been found the structural failures. It was confirmed the reinforcements (stiffeners) influence in the increased levels of stress in the welded joints of the bilge keels to the hull.
Alternative design geometries for the bilge keel internal structure are presented as well as it is shown that the application of brackets or a bulb flat on the connection of the bilge keels to the hull can reduce the high level of tensile stresses that are induced in the structure.
The fatigue analysis according to the *Germanischer Lloyd* Classification Society is applied to the new structural internal geometry and is presented on this paper.

KEY WORDS: Bilge Keels, Structural Failures, Failure Analysis, Improved Design Arrangement, Finite Element Analysis.

1. INTRODUCTION

The hydrodynamic resistance of a ship to roll motion can be increased through passive and/or active stabilizers. Encased in the passive roll stabilizers are the bilge keels under study, which, in addition to attenuate the roll motion, present a low manufacturing cost, compared with the cost associated with the manufacture of active stability systems.

In essence, bilge keels are hull appendices, applied approximately at half length of the ship, on both sides of the hull, which transform the vessel's motion kinetic energy into fluid motion, especially under the form of vortex shedding [1]. Their efficiency depends on their location, size and shape [1]. The bilge keels studied and presented in this article have a triangular, or "V", arrangement as shown in Figure 1.

The bilge keel in study is built in D36 steel, characterized by the chemical composition and mechanical properties referred in Table 1 and 2 [2], respectively. The steel, furnished in the normalized condition, possesses good weldability and low harden effect after welding, due to the low probability of martensitic transformation during cooling [2].

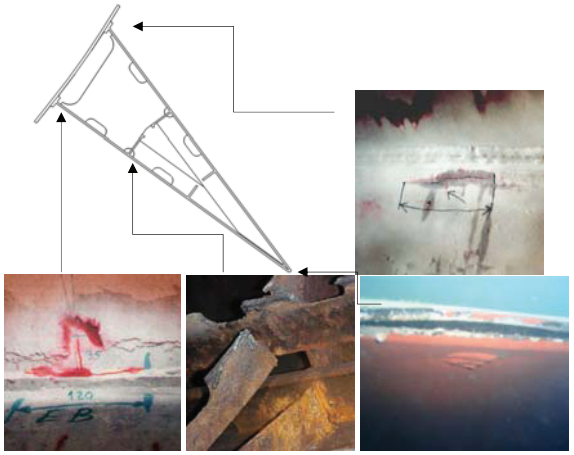

Figure 1. Cross section view of the bilge keel with a "V" arrangement studied. Examples of cracks detected.

.Table 1. Chemical composition of D36 naval steel grade type [2].

C [%]	Si[%]	Mn [%]	P [%]	S [%]	Al [%]
0.18	0.5	≥0.7	0.035	0.035	≥0.02

Table 2. Mechanical Properties of D36 naval steel grade type used in the bilge keels manufacture [2].

Yield Strength [MPa]	Tensile Strength [MPa]	Elongation [%]
≥355	490-620	≥21

The connection to the hull is performed through a doubler plate (Figure 2), where a full welding penetration without any intermittent fillet welds is imposed. The doubler plate connection to the hull is often encountered in marine structures, not only due to its easiness in production, because it provides a faster and easier way to perform the alignment of the bilge keel over the hull structure, but also represents an excellent configuration to avoid multi-axial stress states at the connection to the hull [1].

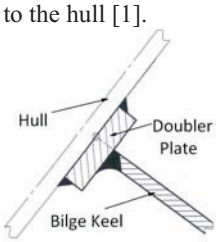

Figure 2. Doubler connection detail of the bilge keel to the hull.

In case of an accident or catastrophic failure, the bilge keel will partly, or entirely, detach from the ship's hull structure without causing structural damages that could compromise the hull plating water tightness.

2. FAILURE REGISTER

2.1. Cracks in the Bilge Keel Connection to Hull

Several cracks were detected by visual and dye penetrant inspection up to 150mm long, mainly in the welded connection between the bilge keel plating and the doubler plate (Fig.1), but also in much smaller number and size, on the doubler connection to the ships' hull plating.

2.2. Fractures in the Internal Structure of Bilge Keel

After a close inspection at the internal structure of the bilge keel, multiple fractures, originated from fatigue cracks, were recorded. These occurred at the intersection between the longitudinal and transverse reinforcements of the bilge keels, leading to the complete separation of the link between them (Fig.1).

2.3. Fractures in the Bilge Keels Plating Edge

At the bilge keels plating edge multiple fractures were recorded, resulting in the loss of the bilge keel watertightness and the separation of the welded connection/joint between the two plates that define the external surface used for the transversal stability of ships (Fig.1).

2.4. Structural Failures Location

Both the cracks in the bilge keel internal reinforcements and the cracks at the plating edge occurred along the entire length of the bilge keel.
The remaining cracks (Figure 3, points marked) were located in the middle plane of the internal reinforcements of the hull (bulkheads /frames) and, in some cases, also in the alignment with the middle plane of the bilge keel internal reinforcements (Figure 3).

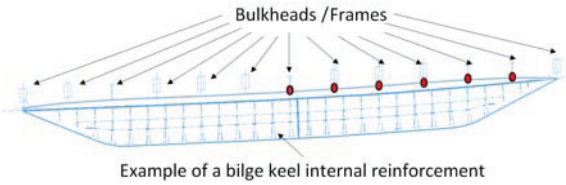

Figure 3. External overview of the bilge keel. Recorded location of cracks (marked points).

3. DESIGN LOAD, P_{BK}

While one can often adequately predict heave, pitch, sway, yaw and even surge, roll motions of a ship are still remarkably difficult to predict, since roll is the motion that is very dependent upon viscous effects of the fluid on the surfaces used for transversal stability of a ship [3]. Nevertheless, design principles from the *Germanischer Lloyd* Classification Society were used [4], in order to determine the maximum load applied on the bilge keels, P_{BK} (fig.4) (1)

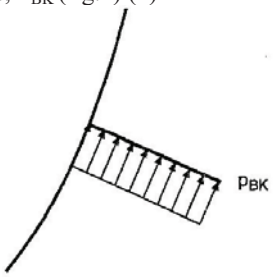

Figure 4. Design load, uniformly distributed across the bilge keel span.

Equation 1 is valid for ships with a length ***L*** between 50m and 200 m, measured in the corresponding waterline and for bilge keels located between 0.4***L*** and 0.6***L***.

$$P_{BK} = \frac{52000 \times d}{(L+240)^{1.1}} \times \gamma_{fdyn} \left[kN/m^2\right] \quad (1)$$

Where, *d*, represents the density fluid value, involving the bilge keels (of 1.025, for saltwater at 25ºC), ***L*** the distance measured from bow to stern, on the waterline

(109m, for the case in study), and γ_{fdyn} the partial safety factor representative of permanent and cyclic loads acting on the undamaged structure in normal operational conditions (considered a value of 2). Accordingly, a design load (P_{BK}) of approximately 170kPa, was calculated.

Since the waterline length of the ship, where the bilge keels under study are installed, is 109m, the domain of validity for the design load is satisfied; regarding the second parameter on the range of validity of the equation, between 0.4***L*** and 0.6***L***, the design load is only valid for approximately 70% of the length of the bilge keels under study, as shown in Figure 5. Although the region where the application of the design load is valid does not include the entire length of the bilge keel, it covers some of the registered structural failures (Fig. 5), not invalidating the calculated value of the design load and its implementation in subsequent studies.

Figure 5. Valid domain for the design load, overlapped with the location of the recorded cracks.

4. BILGE KEEL GEOMETRY MODELING AND ANALYSIS BY FINITE ELEMENT METHOD (FEM)

4.1. Nonlinear FEM Analysis of a Bilge Keel Section

A bilge keel section with 200 mm long was modeled, in order to perform an analysis of the induced stress and deflection on the structure due to the design load. The model shown in Figure 6 includes the internal structural arrangement of the bilge keel and a hull section of 400x500mm length with a 3m curvature radius.

The three-dimensional model was uniformly loaded with 170kPa in the upper face of the bilge keel plating, corresponding to the design load (P_{BK}). The edges of the hull were fixed, in order to simulate the boundary conditions present in the real structure (Figure 6).

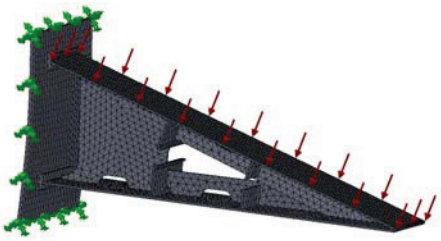

Figure 6. Three-dimensional model of the bilge keel section modeled, which includes the internal structural arrangement, the finite element mesh, the design load and the boundary conditions.

When submitted to an uniaxial tensile test, some mechanical properties of the D36 steel used in the bilge keel construction (Table 1 and 2) are characterised by its true Stress–Strain curve, as shown in Figure 7 [5]. The calculated coefficient and exponent of the Ramberg-Osgood Law, K and n, were 879.2 MPa and 0.1634, respectively, and the stress-strain curve was considered in the definition of the FE material model.

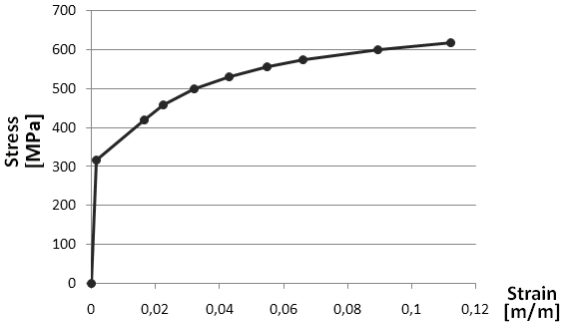

Figure 7. True Stress-Strain curve for the D36 naval steel [5].

The regions identified as hot spots were numbered (Figure 8), having been registered their corresponding *Von Mises* stress values (Table 3).

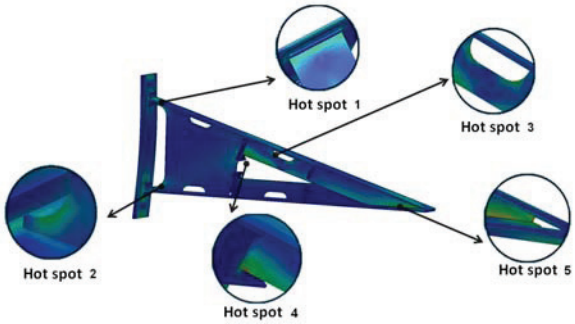

Figure 8. Bilge keel hot spots location.

Table 3. Maximum Von Mises stress values located in the hot spots for the nonlinear Finite Element Analysis (FEA) performed.

Total of Nodes	Total of elements	Hot Spot 1	Hot Spot 2	Hot Spot 3	Hot Spot 4	Hot Spot 5
50680	24702	229 MPa	317 MPa	336 MPa	364 MPa	359 MPa

The data presented in Table 3 shows high levels of stress concentration located in the hot spots, inducing local plastic deformations, but also yield strength safety factors close to one, which leads to the nucleation and propagation of low-cyclic fatigue cracks.

With reference to the yield strength value of the structural steel in which the bilge keel is made of (355MPa), the hot spots numbers 4 and 5 entered the plastic regime, concurring with the location of the register structural failures (Figure 1).

4.2. Study of the Influence of the Hull Reinforcements' Alignment with the Internal Structure of the Bilge Keel

Having been identified as hot spot 1, the stress concentration at the bilge keel to the hull connection (Figure 8), and having been detected a pattern in the location of the structural failures, namely the registration of cracks in the alignment of the hull internal reinforcements, an analysis of the position influence of the bulkhead/frames in the induced stress values in the connection between the bilge keel and the hull was carried out.

As shown in Figure 9, it was found that the presence of the hull's internal reinforcements (bulkheads or frames) resulted in an increase of the maximum stress value present in the connection between the bilge keel and the hull, since the maximum induced stress of 230 MPa increased to approximately 260 MPa (+13%). In addition, there was also a maximum stress concentration in the region closest to the alignment of the reinforcements.

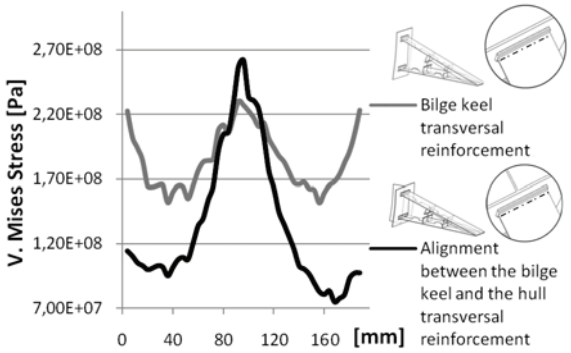

Figure 9. Influence of the alignment between the bilge keel and the hull transversal reinforcement.

5. ALTERNATIVE GEOMETRIES

Taking into account the results from the FEM analyses, new geometries were designed and analysed in order to propose a viable substitute for the bilge keel internal structure and its connection to the hull.

5.1. New Internal Bilge Keel Geometry

With the objective of maintaining unchanged, as much as possible, the hydrodynamic characteristics of the bilge keel, in particular those related to its energy dissipation and drag coefficient, only the internal geometry of the bilge keel was redesigned, maintaining the thicknesses of the components, so that the rigidity of the structure was kept unchanged. The new developed internal geometries are shown in Table 4.

Several details were included in the new internal arrangements in order to minimize the stress concentrations (Figure 9) and, concomitantly, facilitate its production. An example representative of these details is the application of a steel bulb with 15mm in diameter in the bilge keel plating edge (Figure 10).

Table 4. Alternative internal geometries

Reference	Description	Illustration
Geometry nr: 1	Model containing only one solid and continuous transversal stiffener.	
Geometry nr: 2	Model containing one transversal and longitudinal stiffener, with smooth cuts in the intersection between them.	
Geometry nr: 3	Model containing only one transversal stiffener with two sections, with soft cut contours.	
Geometry nr: 4	Model containing one transversal and longitudinal stiffener, with smooth cuts in the intersection between them and with two sections with soft cut contours	
Geometry nr: 5	Model containing only one transversal stiffener, with multiple circular cuts sections and stress concentration reliever holes.	
Geometry nr: 6	Model containing one transversal and longitudinal stiffener, with smooth cuts in the intersection between them, and with multiple circular cuts sections and stress concentration relievers holes.	

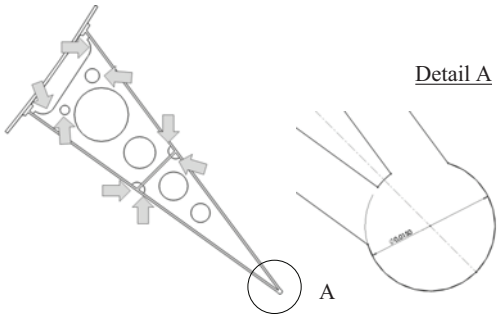

Figure 10. Stress concentration relievers.

All the tridimensional models of the new bilge keel internal arrangements were uniformly loaded with 170kPa, corresponding to the design load. Also the same boundary conditions as shown in Fig.6 were applied, in order to compare the results with those obtained for the current model.

Table 5 presents a summary of the results obtained from the FEA, pointing out the main features of the new geometries regarding the maximum *Von Mises* stresses induced in the structure, the number of existing hot spots, the maximum deflection value obtained and the mass of the new bilge keel's internal geometries developed.

Table 5. Results obtained from the FEA of the new internal bilge keel geometries.

	Mass (kg)	Nr.of hot spots	Maximum Deflection (mm)	Von Mises Stress (MPa)
Current Geometry	41,34	5	3.8	364 MPa
Geometry 1	39,44	3	≈3.3	249 MPa
Geometry 2	40,90	3		255 MPa
Geometry 3	37,77	6		246 MPa
Geometry 4	39,27	6		260 MPa
Geometry 5	37,84	3		230 MPa
Geometry 6	39,33	3		248 MPa

The analysis showed a significant reduction in the stress level (a minimum reduction of 28% and a maximum reduction of 37%). Of all the analysed geometries, geometry number 5 presents the best alternative to the existing geometry, because it's definitely the geometry that showed the lowest level of maximum induced stress, 230MPa, together with the smallest number of hot spots and a lower mass. Notwithstanding, alternative geometries which include longitudinal reinforcements, namely geometries number 6, 2 and 4 (Table 4), in this order, should be considered in case bilge keel longitudinal strength needs to be enhanced. These solutions also revealed a lower maximum induced stress than the current geometry (Table 5).

5.2. Improved Design to Reduce the Stress in the Bilge Keel Connection to the Hull

Having been registered several cracks in the bilge keel connection to the hull, two alternative solutions have been designed, so as to reduce the maximum induced stress value to the connections under study (Figure 11), in order to eliminate the structural failures found.

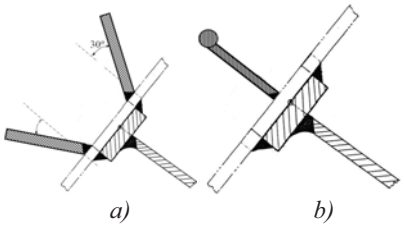

a) *b)*

Figure 11. Cross section view of the bilge keel connection to the hull with a) brackets. b) bulb flat

The proposed solutions consisted in the application of brackets inside the hull (Figure 11a), or a bulb flat along the bilge keel connection (Figure 11b). A two-dimensional FEA was performed simulating the doubler plate discontinuity and the presence of the brackets (Figure 12) or the bulb flat. Accordingly with Figure 12 and with the data presented in Table 6, both proposed solutions could be considered to reduce the stresses induced in the doubler plate connection to the ship's hull, ensuring the water tightness of the hull.

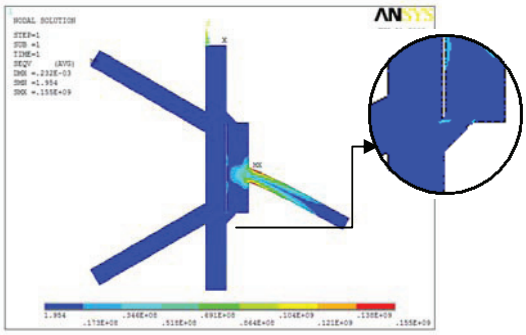

Figure 12. Two-dimensional FEA of the bilge keel connection to the brackets

Table 6. Stresses present in the bilge keel upper plating, with the implementation of brackets and bulb flat.

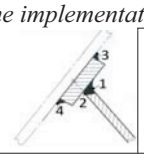	Stress in Point 1 [MPa]	Stress in Point 2 [MPa]	Stress in Point 3 [MPa]	Stress in Point 4 [MPa]
Current model	157	149	29	50,6
Application of brackets	155	154	4,8	3,9
Application of bulb plate	122	134	29,7	27,3

6. FATIGUE ANALYSIS

A fatigue strength assessment of the redesigned doubler plate connection to the ship's hull (Figure 13) has been made assuming the inexistence of the doubler plate and in accordance with the fatigue design curves included in *Germanischer Lloyd* Rules [4], which state that for structures submitted to cyclic loads resulting from waves or engines [4] and for infinite life, eq.2 must be fulfilled.

$$\Delta\sigma_{Rc} \cdot f_n \geq \Delta\sigma \cdot \left(fa \cdot F_{dyn}\right) \qquad (2)$$

where $\Delta\sigma_{Rc}$ is the corrected fatigue strength reference value, f_n is the correction factor considering the allowable number of load cycles and the type of spectrum applied and $\Delta\sigma(f_a.F_{dyn})$ is the stress range due to the dynamic loads applied in the assessed structure.

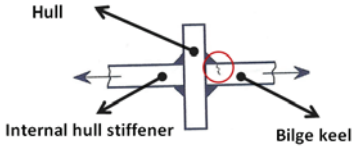

Figure 13. Simplification of bilge keel to the hull connection with internal stiffeners (bulb flat).

The S-N curves (Figure 14) for the welded detail represented in Figure 13, relative to two standard classes of Spectra A and B [4], were corrected through the application of a factor, f_n, [4], where Spectrum A represents the denominated straight-line spectrum, which is a typical stress range spectrum of seaway-induced stress ranges [4] and Spectrum B represents a parabolic spectrum, which represents a Normal function density of probability type of stress range. The fatigue curves presented in Figure 14 are representative of the fatigue resistance of medium/high strength structural steels used in shipbuilding [4].

Once known the maximum stress value present at the cruciform joint (155 MPa, Table 6) it was assumed a local stress of 170 MPa (Figure 14) due to the weld toe stress concentration factor (Figure 13) for the stress variation present in structure due to dynamic loads, $\Delta\sigma$ ($f_a.F_{dyn}$). The fatigue life prediction can be observed in Figure 14. For the spectra B or A, which reflect the service conditions of the ship, the estimated lifetime is approximately 16 years and infinite lifetime, respectively. The cycle conversion was carried out once known that $5x10^7$ fatigue life cycles in a class A spectrum, is equivalent to a lifetime of 25 years with 230 days per year of service at sea [4].

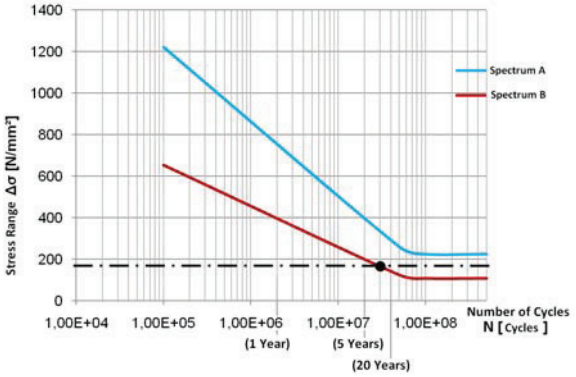

Figure 14. Fatigue life prediction for spectra A and B

7. CONCLUSIONS

This paper refers to an analysis performed to the structural failures found in bilge keels, with the objective of presenting structural solutions to solve them.

It was confirmed, through the analyses carried out by FEM that the location of the internal failures in the bilge keels coincides with high stress concentration regions. It was verified the existence of stress levels close to the material yield strength and, consequently, some areas were identified where local plasticity can occur.

The alignment between the bilge keel's internal structure and the hull transversal reinforcements results in an increased and more concentrated stress level along the hull-bilge keel connection, when compared to the stress level induced by the presence of the bilge keel transversal reinforcement only.

A 2D FEA performed to the doubler plate and the bilge keel, and between the doubler plate and the hull allowed to determine the maximum *Von Mises* stress present in the welded joint due to the stress concentration introduced by the welded detail, fact which is in accordance with the failure observed. The application of brackets or a bulb flat allowed to reduce the maximum stress induced to 155MPa between the doubler plate and the bilge keel.

In order to propose a new solution capable of preventing the structural failures identified in the internal bilge keel structure, six alternatives geometries to the internal structure of bilge keel were designed and analysed, maintaining unchanged the hydrodynamic characteristics of the bilge keel. The best solution found (geometry nr.5, Table 4) contains 3 hot spots regions and a maximum *Von Mises* stress of 230MPa, corresponding to a reduction of 37% in the stress induced levels when compared to the current geometry. Notwithstanding alternative geometries which include longitudinal reinforcements, namely geometries number 6, 2 and 4 (Table 4), in this order, should be considered in case bilge keel longitudinal strength needs to be enhanced. These solutions also revealed a lower maximum induced stress than the current geometry (Table 5).

Finally, a fatigue life assessment analysis to the bilge keel welded connection to the hull resulted in an infinite lifetime for a Spectrum A type. Adopting a more conservative approach, the fatigue lifetime for a class B spectrum estimated a fatigue lifetime of 16 years.

REFERENCES

[1] *ON THE STRUCTURAL DESIGN OF BILGE KEELS.* Mateus, António F. Hamburg, Germany : 2006. 25th International Conference on Offshore Mechanics and Arctic Enginneering.

[2] *Det Norske Veritas, Offshore Standard DNV-OS-B101, Metallic Materials*, April 2009.

[3] *Grant, David James. Full Scale Investigation of Bilge Keel Effectiveness at Forward Speed.* April 28, 2008.

[4] *Lloyd, Germanischer. Rules for Classification and Construction, III Naval Ship Tecnology.* : Germanischer Lloyd, 2004.

[5] *Zhang, Guihua. Development of Numerical Approaches to Predict Ductile and Cleavage Fracture of Structural Materials.* University of Akron, December 2007.

FATIGUE LIFE TIME PREDICTION OF POAF EPSILON TB-30 AIRCRAFT - PART I: IMPLEMENTATION OF DIFERENT CYCLE COUNTING METHODS TO PREDICT THE ACCUMULATED DAMAGE

B. A. S. Serrano [1], V. I. M. N. Infante[2], B. S. D. Marado[3]

[1] Direcção de Engenharia e Programas da Força Aérea Portuguesa,
Estado Maior da Força Aérea
Av. Leite de Vasconcelos
2614-506 Amadora
E-mail: baserrano@emfa.pt

[2] Área Científica de Projecto Mecânico e Materiais Estruturais,
Instituto Superior Técnico
Av. Rovisco Pais, 1
1049-001 Lisboa
E-mail: virginia.infante@ist.utl.pt

[3] Direcção de Engenharia e Programas da Força Aérea Portuguesa,
Estado Maior da Força Aérea
Av. Leite de Vasconcelos
2614-506 Amadora
E-mail: bsmarado@emfa.pt

ABSTRACT

The prediction of fatigue lifetime can be calculated by analyzing the accumulated damage of the aircraft structure through Miner's rule and vertical acceleration spectra.
Two different cycle counting methods were used to analyze the vertical acceleration signal which was recorded during 72 flight hours. The first method was the rainflow counting method and the second one the level cross counting method, which is the method similar to the one used by the Portuguese Air Force (PoAF).
The results of these two counting methods were compared with the spectrum used by Epsilon manufacturer. Once the spectra were obtained, the damage was also calculated using two methods: the method that considers the influence of the mean stress and the method in which the damage is calculated according to the trapezoid rule. At the end all the spectra were used to calculate the damage through these two methods.
The main conclusion was that the operation of the PoAF Epsilon aircraft is more severe than the reference used by the manufacturer, and consequently the lifetime predicted for the aircraft should be 12 % lower than the life defined by the manufacturer.

KEY WORDS: fatigue, spectrum, damage, vertical acceleration, cycle counting methods

1. INTRODUCTION

In order to predict the fatigue lifetime of the aircraft, the manufacturer of Epsilon carried out a real scale fatigue test at the Centre d'Essais Aeronautique de Toulouse (CEAT). During these tests the manufacturer realized that the aircraft lifetime is determined by the fracture of the second bulkhead beam, which occurred after 89458 simulated flight hours (FH) [1]. In this test the manufacturer used a spectrum that was considered characteristic of the typical aircraft operation.
In order to define the secured fatigue lifetime of operation for the PoAF, one of the squadron's aircraft was previously instrumented to measure and record vertical acceleration and local stress in critical areas. The objective of this study was analyse the collected data through two different counting methods and two different ways of assessing the damage.
Finally, the objective is to compare the PoAF damage with the manufacturer's damage in order to predict the lifetime of PoAF aircraft, because the spectrum of vertical acceleration of the manufacturer is different from the PoAF one.

2. FATIGUE CONCEPTS

According to ASTM [2] the fatigue phenomenon is related to dynamics solicitations, which structurally and permanently changes the material in a specific location where cracks will appear. The process involves 4 phases: the nucleation of the crack, the microscopic growing of the crack, the propagation phase, and finally the rupture (fracture) of the material.

2.1 Parameters that influence fatigue

There are several parameters that influence the fatigue behaviour of the material:

- The surface finishing of an aircraft component influences the fatigue behavior. Better surface finishing increases fatigue resistance of materials and the crack initiation is more difficult.
- The dimensions of the component are important because bigger components mean bigger volume and area, so more surface imperfections could occur, thus originating cracks.
- The mean stress increases the ultimate fatigue strength in S-N curve. The Soderberg and Goodman expression are used to count the influence of the mean stress. In this paper it was used the Goodman law according to expression (1), [3].

$$\frac{\sigma_a}{\sigma_{f0}} + \frac{\sigma_m}{\sigma_r} = 1 \qquad (1)$$

- Usually, fatigue crack begins in areas with a high stress concentration factor, because the fatigue strength in these areas is lower.
- The environment of operations influences the fatigue behaviour in a significant way. If the component operates in a wetland area containing salt water, besides the dynamics loadings the component will be attacked by a chemical process which degrades the material (stress corrosion) causing superficial cracks. Another important environment factor is the temperature, which can cause thermal stress in the material.

2.2 Aircraft dynamics solicitation

The structure of an aircraft in his typical operation has to resist to different dynamics loadings that change during the flight. There are 4 phases in an aircraft flight with different loadings: the taxiing, in which the aircraft is on the ground, the take-off, the mission and finally the landing. In this paper the information available is related to 50 flights, which means approximately 72 flight hours. Those numbers were chosen because they can illustrate the basic training of a student pilot.

3. CYCLE COUNTING METHODS

The counting methods are used to count the number of cycles of vertical acceleration signals during flights in order to predict the accumulated damage of the structure. Two different kinds of cycle counting methods exists [4,5,6]: methods that use one single parameter and methods that use two parameters. In this paper the methods used were the level cross counting method and the rainflow method. The first one is a single parameter method that counts the number of times the signal crosses specific levels (see figure 1), the method is similar to the one used by the PoAF to count cycles in this aircraft so it is referred as FAP Counting (CFAP).

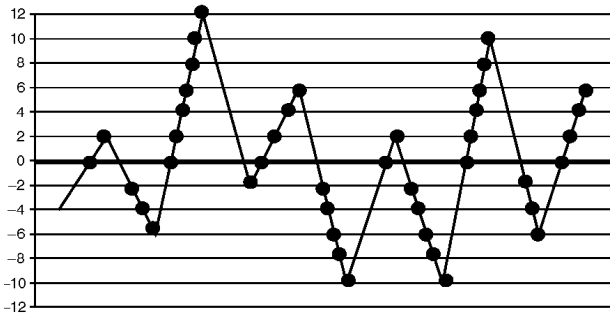

Figure 1 -Level cross counting method

The second one is also quite commonly used in fatigue studies. The computational implementation of this method begins with the analyses of the signal, and then the highest or the lowest peak is chosen.
The new signal will start at this peak and then the distances between the 3 sequential points are analyzed according to figure 2. In this paper this method is refereed as Rainflow Counting (CRAINFLOW).

- If $\Delta S_1 > \Delta S_2$ the cycle is not count;
- If $\Delta S_1 \leq \Delta S_2$ it is count one cycle. The maximum, minimum and mean values of the cycle are calculated;

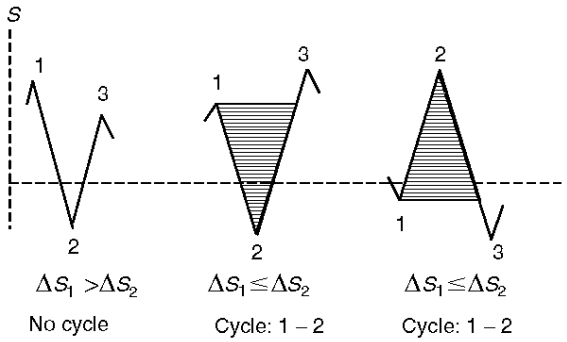

Figure 2 - Computational implementation of the rainflow method

The results of these two different methods that were implemented computationally were compared to the spectrum that the manufacturer used to predict the lifetime of the Epsilon aircraft.
However, to make the comparison with the manufacturer spectrum possible, the spectra that were obtained with each method had to be reorganized.
After that it was used a transfer function determined experimentally by [7] to know the stress magnitude for each cycle based. Before the implementation of both counting methods the signal of the vertical acceleration was analyzed by a range factor to avoid noise or undesirable variations, [8]. The influence of the range factor means a different number of cycles that could be counted. So it was necessary to study the influence of the range factor in the determination of the spectra.

4. DAMAGE CALCULATION

The lifetime of a component is defined taking into account its cycles of operation and the S-N curve that characterizes the material's resistance to fatigue, however in cases of variable amplitude loading the S-N curves can not be used directly.
Therefore, there are several methods to associate the variable amplitude loadings to the component lifetime by calculating the accumulated damage. The main methods are: the linear law of cumulative damage, the hypothesis of non-linear damage and the continuous mechanics damage [9]. The simplest and most used is the first method, the law of Palmgren and Miner.
Once the number of cycles was calculated it was possible to determine the damage that these cycles induced in the structure. In this paper the Miner's rule was used according to expression (2). Where n is the number of cycles that were counted at a specific stress and N_r is the number of cycles which could be sustained by the material for previous stress until the material failed through fatigue. Consequently, in order to know N_r it was necessary to determine de S-N curve of the material Alloy 2024-T351, and so axial tension tests and axial fatigue tests were performed. The first one was done to determine the material properties and to guess the first stress to use in the fatigue tests.

$$D = \sum \frac{n}{N_r} \leq 1 \tag{2}$$

4.1 FAP DAMAGE (DFAP)

This methods was implemented according to [10] to the spectrum that comes from CRAINFLOW, CFAP and the manufacturer. To implement this method the following steps were followed:

- Determination by the S-N curve the number of cycles that the material can withstand before a fracture at maximum stress occurs;
- With the expression (2) by making a variable change and using the trapezium rule the total damage can be calculated by the expression (3).

$$D = \int \frac{dN}{N_r} = 2.3 \int_0^5 \frac{N}{N_r} dy = \frac{2.3 \times 0.25}{2} \sum_{i=o}^{19} \left(\frac{10^{0.25i}}{N_r} + \frac{10^{0.25(i+1)}}{N_r} \right) \tag{3}$$

4.2 MEAN STRESS DAMAGE (DTM)

This method was called Mean Stress Damage (DTM) and uses the spectra provided by the manufacturer, CRAINFLOW and CFAP in order to make possible the comparison.
The determination of the accumulate damage it was done by using expression (4) which comes from the Goodman expression but only depends on σ_{max} (maximum stress), σ_{f0} (limit fatigue stress), R (stress ratio) and σ_r (fracture stress):

$$\frac{\sigma_a}{\sigma_{f0}} + \frac{\sigma_m}{\sigma_r} = 1 \Rightarrow \sigma_{\max} \left[\frac{1-R}{2\sigma_{f0}} + \frac{1+R}{2\sigma_r} \right] = 1 \tag{4}$$

This new expression is very useful because the counted cycles didn't have the same value of R that was used in the experimental test so that it's necessary consider this difference.
The value of R is calculated using σ_{max} and σ_m (mean stress) values. After the application of expressions (3) and using the S-N curve a new value of N_r is calculated. Now the damage can be obtained using the Miner rule, where the n takes the value of the number of cycles with the same magnitude.

5. EXPERIMENTAL TESTS TO DETERMINE THE PROPERTIES OF ALLOY 2024 T-351

To determine the properties of Alloy 2024-T351 specific specimens were created to use in the test machines according to ASTM 466-96 [11].

5.1 Tension test

The tension test was done in 2 specimens with the INSTRON machine model 3369 at Instituto Superior Técnico (IST), whose maximum load capacity is 50 KN. The results obtained are shown in table 1.

Table 1- Tension tests data

	Specimen		
	1	2	Average
E [GPa]	75.15	80.56	77.85
σ_{yield} [MPa]	381.11	395.63	388.37
σ_{UTS} [MPa]	462.24	476.38	469.31

According to FAA [12] the properties obtained in this paper are slightly bigger (for the Young module there is a discrepancy of 7.5 % and for the Yielding stress of 16 %). This test was important because, besides the determination of the properties of the materials in the direction of lamination, it tells the average stress that should be used in fatigue tests.

5.2 Fatigue test

To characterize the material behaviour due to fatigue loading 8 specimens were used, 2 for each stress magnitude. The tests were performed in INSTRON machine model 1342 of the Instituto Politécnico de Setúbal whose capacity of load is 250 KN. The results are shown in figure 3. These tests were performed with stress ration of R=0 and K_t=0 (stress concentration factor).

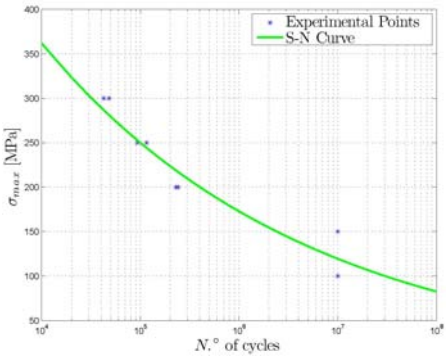

Figure 3- S-N curve of the Alloy 2024-T351 (laminated direction)

6. COMPUTATIONAL RESULTS

6.1 Results of the counting methods

The counting methods were implemented computationally using the MATLAB® programme. As stated at the beginning, different ranges were used to prepare the signal for each counting method. The results obtained with the CRAINFLOW and CFAP for the range values of 0, 0.3, 0.5, 0.7 and 1.2 are shown in figure 4,5,6,7 and 8.

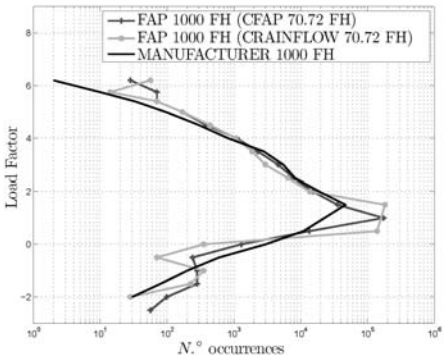

Figure 4 - CFAP and CRAINFLOW spectra (range=0)

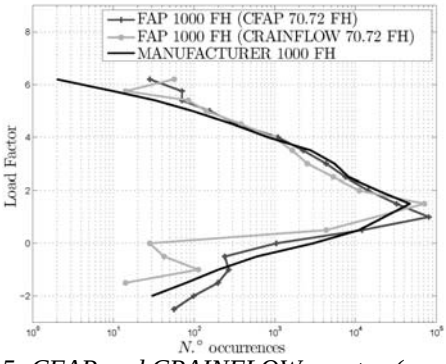

Figure 5- CFAP and CRAINFLOW spectra (range=0.3)

6.2 Results of the damage calculation

Once the spectra of the PoAF squadron were obtained, the damage was calculated by 2 different methods: the DFAP and DTM. Results are shown in figures 9 and 10.

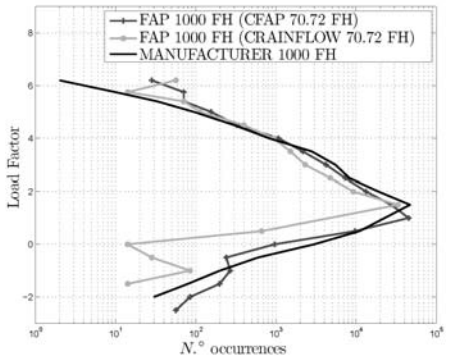

Figure 6 -CFAP and CRAINFLOW spectra (range=0.5)

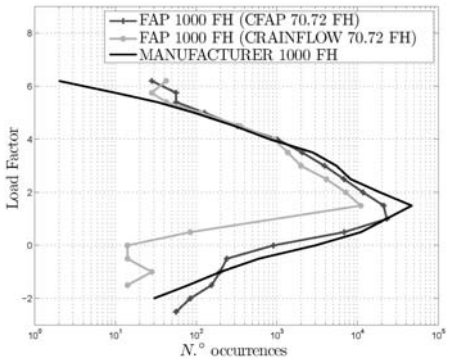

Figure 7 -CFAP and CRAINFLOW spectra (range=0.7)

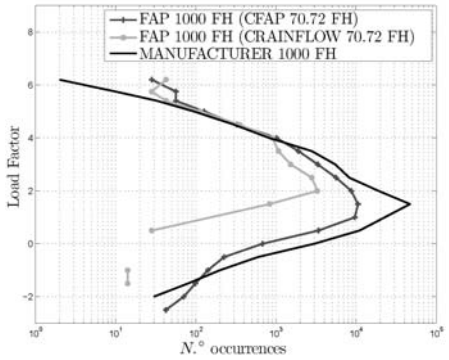

Figure 8 -CFAP and CRAINFLOW spectra (range=1.2)

7. ANALYSES AND DISCUSSION OF THE RESULTS

7.1 Counting methods

By the analysis of figures 4 to 8 the values of range used to obtain a reasonable PoAF spectrum are: 0 and 0.3.

For these values the results obtained with the rainflow counting method (CRAINFLOW) are very similar to the results that are obtained with the level cross counting method (CFAP). When the range value increases, the CRAINFLOW method is more affected than the CFAP. According to figure 8 the cycles of lowest magnitude are not accounted, so the occurrences are lowest for vertical acceleration events smaller than 2, because when the highest values of range are being used the smallest values of vertical acceleration are not taken in consideration.

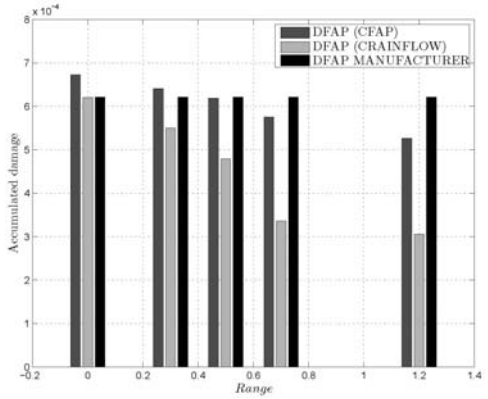

Figure 9- Damage calculated with the DFAP

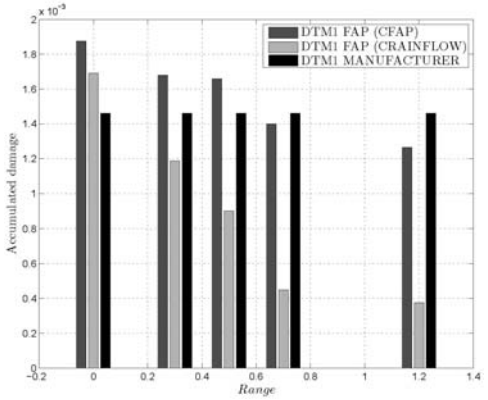

Figure 10 - Damage calculated with the DTM

Table 2-Final results for the TVF obtained from the accumulated damage

Method	range	Spectra	TVF $_{PoAF}$ [FH]	TVF $_{PoAF}$ Final [FH][1]	Difference [%][2]
DFAP	0	CFAP	82666	27553	7.60
DFAP	0.3	CFAP	86786	28928	2.99
DTM	0	CFAP	69628	23208	22.17
DTM	0.3	CFAP	77773	25923	13.06
DTM	0.5	CFAP	78706	26236	12.02
DTM	0	CRAINFLOW	77240	25745	13.7
Average			78799	**26266**	**11.92**

In fact, if at the beginning a level of omission for vertical acceleration values was defined, the small values of vertical acceleration could be rejected without any problem. But in this paper an omission level was not used.

On the analysis of severity it was assumed the hypothesis that higher occurrences of higher load factors can cause more damage than a smaller number of occurrences of lower load factors. According to this hypothesis the PoAF spectra are more severe than the manufacturer, since the number of occurrences for higher values of load factors is slightly higher than the manufacturer; this is clearly visible in figure 4 and 5.

7.2 Damage calculation

From the results obtained in the counting methods is expected that the damage of the PoAF spectrum will be slightly higher than the manufacturer. In order to compare the damage value that was obtained with the different methods, the results were represented in figures 9 and 10.
From the analysis of figure 9 it is for the CFAP with range values of 0 and 0.3 that the PoAF damage is higher than the manufacturer damage. As was stated at the beginning of this chapter the PoAF damage will be slightly bigger that the manufacturer's, so that the CRAINFLOW spectrum cannot be used to calculate the fatigue lifetime of the aircraft because in all cases the value of the damage is not higher than the manufacturer.

When the damage is calculated with the DTM (figure 10) the spectrum obtained with the CRAINFLOW method for a range of 0 can be used to analyse the fatigue lifetime of the aircraft. Because the damage in that case is slightly higher than the damage calculated with the spectrum of the manufacturer. The spectrum obtained with the CFAP for a range of 0 to 0.5 can also be used to predict the fatigue lifetime. For a range values higher than 0.5 the CFAP and the CRAINFLOW cannot be used because the damage is smaller than the manufacturer's.

7.3 Prediction of Epsilon aircraft lifetime

The manufacturer of the Epsilon aircraft due to a real test done at the CEAT realized that the fatigue life of the aircraft (TVF) was 89458 FH. However it was use a safety factor (CS) of 3 that establish the 29819 FH for the TVF [1].
In this paper the TVF of the Epsilon aircraft was calculated based on the damage values of the methods that provided values of damage slightly bigger than the manufacturer (figures 9 and 10). For example, in the CFAP spectrum for range 0.3 was obtained a D_{PoAF} = 6.405 x 10^{-4} and a $D_{Manufacturer}$ = 6.2136 x10^{-4}. The calculation method used was the following:

$$\begin{cases} D_{\text{Manufacturer 1000 FH}} = 6.2136 \times 10^{-4} \\ TVF = 89458 \text{ FH} \end{cases}$$

$$D_{\text{Manufacturer 89458 FH}} = D_{\text{Manufacturer 1000 FH}} \times 89{,}458$$
$$= 0.055586$$

[1] It was used a safety factor (CS) of 3 defined by the manufacturer [1]
2 Relative difference compared to the damage given by the manufacturer spectrum

For the manufacture the ruin of the structure does not happen when the damage is 1, as the Miner's law says, but when the accumulated damage is 0.055586. So it's assumed that the structure of the Portuguese aircraft will fail when the accumulated damage $D_{PoAF \setminus TVF \setminus FH}$ reaches the value of 0.055586. So assuming that the total accumulated damage for the failure of the manufacture it's the same for the Portuguese aircraft it's possible to predict the fatigue life for the Portuguese aircraft:

$$\begin{cases} D_{\text{PoAF } 1000\,\text{FH}} = 6.405\times10^{-4} \\ TVF_{PoAF} = ?\,\text{FH} \end{cases}$$

$$D_{\text{PoAF TVF FH}} = D_{\text{PoAF 1000 FH}} \times \frac{TVF_{PoAF}}{1000}$$

$$TVF_{PoAF} = 86786$$

The manufacturer to determine the TVF, which should be taken as a reference by the operators of Epsilon, was used a safety factor of 3. The final TVF considered more reasonable, obtained with the method illustrated above, are shown in table 2. The TVF determined by the manufacturer was 29800 FH.
According to table 2 the fatigue life time of PoAF aircraft should be 11.92 % less than the life time predicted by the manufacturer. For instance this fact it's in conformity with figure 4 where the PoAF spectrum are severe than the spectra type used by the manufacturer.

8. SUMMARY

After this work the main conclusions are:

- According to the counting methods the results obtained with the rainflow counting method (CRAINFLOW) and the crossing level counting method (CFAP) are very similar;
- The best spectrum to predict the fatigue life of a structure are the spectrum obtained by CRAINFLOW and the CFAP methods for smaller values of range (0 or 0.3);
- The damage values obtained with the DTM method are higher than the results of the DFAP, consequence of the nature of the process;
- The load spectrum of Portuguese Epsilon aircraft is more severe that the spectrum adopted as a reference by the manufacturer. Therefore the fatigue life time of the Portuguese Epsilon TB-30 should be 26000 FH, 12% less than the fatigue life time that was determinate by the manufacturer.

9. RECOMMENDATIONS

In this work the prediction of the fatigue life time was based on the damage accumulation and the Miner's rule. In the future this study should be done assuming the propagation of the crack. This new study will give the adequate inspection periodicity of the critical zone and it will also predict the fatigue life using a different method.

ACKNOWLEDGEMENTS

Finally the authors are very grateful to Portuguese Air Force Department of Engineering, to Air Force Academy and Instituto Superior Técnico.
The views expressed in this paper are those of the authors and do not necessarily reflect those of the Portuguese Air Force.

REFERENCES

[1] CEAT, *Epsilon - Documents de Synthese suite a la campagne D'Essai de Fatigue. SOCATA*, Groupe Aeroespatiale, 1996.

[2] ASTM, *Standard terminology - relating to fatigue and fracture testing*. ASTM E 1823 - 96 (Reapproved 2002), 2004.

[3] Bannantine Julie A. Comer Jess J., *Handrock James L. Fundamentals of Metal Fatigue Analysis*. Prentice Hall, first edition, 1989.

[4] Pan Jwo Hathaway Richard B. Barkey Mark E Lee, Yung-Li, *Fatigue Testing and Analysis. Elsevier*, 2005.

[5] J. B. de Jonge, *Counting Methods for the Analysis of Load Time Histories*. National Aerospace Laboratory (NLR), N.A.

[6] ASTM, *Standard practices for cycle counting in fatigue analysis*. ASTM E 1049 - 85, 2004.

[7] Marco Milharadas, Relatório do Tirocínio EngAer. 2003.

[8] W. J. Vink, NLR *Contract Report CR 97253 L. National Aerospace Laboratory* (NLR), N.A.

[9] Jr. K. Sobczyk, B.F. Spencer, *Random Fatigue: From Data to Theory.Academic Press*, INC, 1992.

[10] João Pedro Silva, *Relatório do Tirocínio EngAer 2002/3*. Abril 2003.

[11] ASTM, *Conducting force controlled constant amplitude axial fatigue tests of metallic materials*. ASTM E 466-96, 2004.

[12] John Bakuckas Richard C. Rice, Jana L. Jackson and Steven Thompson, *Metallic Materials Properties Development and Standardization (MMPDS).* Federal Aviation Administration, January 2003.

PRE-VALIDATION OF WELDED JOINTS IN A BIKE FRAME

P. Machado[1], R.A. Cláudio[1], A. Valido[1], R. Duarte[2], O. Martins[2]

[1]Departamento de Engenharia Mecânica,
Escola Superior de Tecnologia de Setúbal/Instituto Politécnico de Setúbal
Campus do IPS, Estefanilha, 2910-761 Setúbal, Portugal
E-mails: pmachado@est.ips.pt; rclaudio@est.ips.pt; avalido@est.ips.pt

[2]OMS, Automation Services,
Parque Industrial da Mitrena, L18
2910-738 Setúbal, Portugal
E-mails: rui.Duarte@o-m-s.net; orlando.martins@o-m-s.net

ABSTRACT

In many industrial situations, it is necessary to prove that a certain product meets quality requirements even if it is not yet produced. For the present case, is it necessary to verify that an automated weld procedure for bike frames, different from the conventional, meets the structural strength requirements imposed by an international standard. However, due to the extent of automation required, it is impossible to produce at least one bike frame in order to test it. For preliminary validation proposes and to optimize welding parameters, it was proposed to perform tests on specimens.
This work presents a procedure to verify if the welded joints meet the requirements of EN14766 standard in terms of fatigue strength, by testing specimens. The bike frame geometry was analysed using the finite element method with the loads and constrains defined by EN14766 standard. From this model it was possible to indentify which joins were critically loaded and their respective acting loads. A special griping device was designed for a single axis servo-hydraulic testing machine in order to apply normal loads and bending moments similar to the ones calculated. Several H shaped welded specimens were fatigue tested and the results shown that this automated welding procedure is able to meet EN14766 standard requirements in terms of fatigue resistance.

KEY WORDS: Fatigue testing, EN14766, Weld, Finite Element Method.

1 INTRODUCTION

Usually one of the most important constrains in production is the time necessary to develop and implement a production line with capacity to assure the final quality of the product. Nowadays all these steps take a long time, considering the automation level used, but it will be rewarded in production time. If the production procedures are not well defined or detailed, this can lead to the reprogramming of the entire production line or dimensioning of the entire project.

In the particular case of welded joints, all the procedure must be optimized, ensuring that the quality and mechanical resistance requirements, imposed by law or by the client, are granted. When we are talking about a larger production volume, another issue is the time to make a weld. In a bike frame, where there are about fifteen welding joints, all seconds are precious! When there is a production target of 1.000.000 frames. Only 1 second more on each weld will make the production target to delay 23 months (considering only one production line).

The bike frame welding is usually made using the TIG process but in this case it was used the MIG process that have been robotized to improve the quality. So that this process can be accepted by the client it is necessary to fulfil the client's requirements. The static mechanical resistance will be ensured by traction tests to shaped H specimens. Thought this analysis it was possible to optimize the welding process under static loading, however, this is not sufficient to ensure that the bike frame can support dynamic loads without fatigue damage.

Norm EN14766 [1] defines dynamic tests to be performed on a bike frame. These consider the simulation of three different loading cases (pedalling, horizontal load and vertical load, figures 1, 2 and 3 respectively) to apply on the bike frame.

The production costs of a bike frame for fatigue testing are tremendous considering that all the robots for automated production must be programmed. Programming a welding procedure for a specimen is much less time and cost consuming. The specimen also allows changing quite easily welding setup that will give new characteristics to the welded joint, allowing optimisation.

According to the norm EN14766, [1] three different fatigue tests are required to the bike frame that can be simulated in specimens. Each represents a different situation that the bike suffers during its circulation. The first one (figure 1) simulates the pedalling loads. It is composed by two forces of 1200N, applied on each pedal alternately. These forces are applied on a device that simulates the pedal position, and made a 7,5º angle with the vertical when the bike is observed from the front. In each cycle there are two applied forces, one on each pedal. This difference happens because of the chain positioning that supports some of the load transmitted to the bike framed by the pedal forces.
In the second test a horizontal load is applied to the bike's fork (that can be considered rigid), maintaining the rear wheel support fixed, as shown in figure 2.
In the third test (figure 3) a vertical load is applied to the bike frame using a device that represents the cyclist seat. Each one of these tests has a total of 50000 cycles, making a total of 150000 cycles to the bike frame. At the end of all tests the bike frame should not present any traces of fatigue cracks.

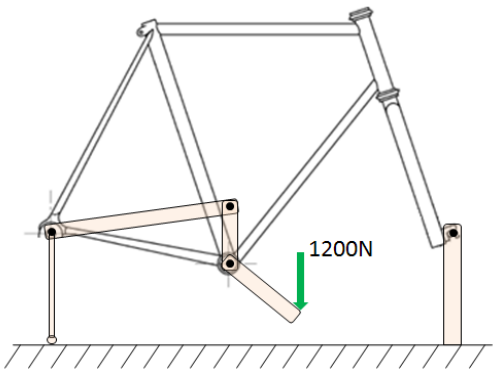

Figure 1. Test 1 (Pedalling).

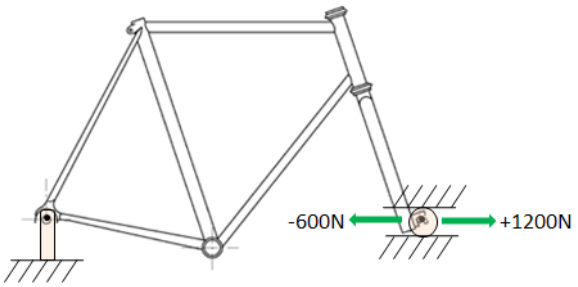

Figure 2. Test 2 (Horizontal Load).

The objective of this work is to validate a welding procedure verifying that it ensures the norm EN14766, [1] requirements. At this time is economically impossible to build a bike frame, the validation of the process will be made by specimen's testing. The specimens used are H shaped and welded using the same parameters to weld the bike frame and will be submitted to similar loads to those calculated in the bike frame, resulted by the tests previously defined. The similar loads will be obtained by the finite element method using the software Cosmos M [6], analysing the tests defined in norm EN14766, [1].

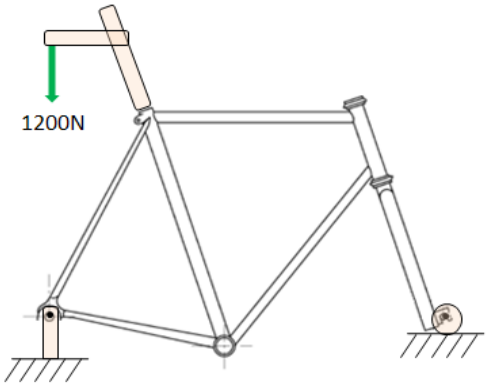

Figure 3. Test 3 (Vertical Load).

2 FINITE ELEMENT MODEL

The bike frame analysis was preformed by the finite element method using the finite element code CosmosM [6]. The structural discretization was throughout three-dimensional two-node beam elements (beam 3d CosmosM element) with six degrees-of-freedom per node: three displacements, u, v and w, respectively in x, y and z directions, and three rotations, Θ_x, Θ_y, and Θ_z, respectively about x, y and z axis.
Figure 4 represents the 12 degrees-of-freedom of the beam element as well as the local coordinate system.

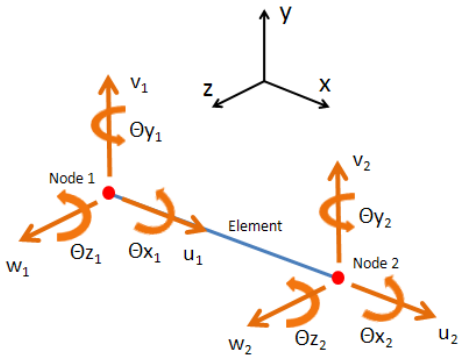

Figure 4. 3d Beam Element.

The bike frame was discretized by 149 beam elements. The linear parts of the frame were discretized by only one element each. For the discretization of the curve parts of the frame it was used several elements in order to fit the geometry to be as close as possible to the real one.

In order to determine which one of the joints, identified in figure 5, is the critical one, it was used the Miner rule that allows to calculate the damage that each section suffer when it is subjected to combined loads [2, 3 and 4].

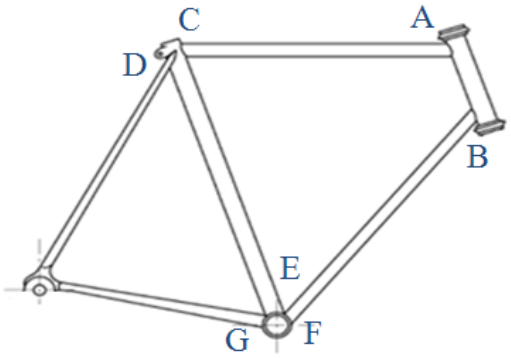

Figure 5. Welded joints analyzed.

To estimate the number of cycles that would lead to failure, it was used the Basquin's Law with general Al6061T6 properties [5].

$$N = \left(\frac{\sigma_a}{a} \right)^{1/b} \tag{2}$$

where σ_a is the equivalent alternated stress to the structural element in analysis.
The constants a and b are calculated as:

$$a = \frac{(0{,}9 S_{ut})^2}{S_e} \tag{3}$$

$$b = -\frac{1}{3} \log\left(\frac{0{,}9 S_{ut}}{S_e} \right) \tag{4}$$

where S_e is the Fatigue Strength and S_{ut} is the Ultimate Tensile Strength.
We may note that the objective is to calculate which section is the critical one and not the component's life.
The equivalent alternated stress was calculated using the values of the alternated and medium stress in the following Goodmans's equation:

$$\sigma_{eq.alt} = \frac{\sigma_{alt}}{1 - \frac{\sigma_{med}}{\sigma_{yield}}} \tag{5}$$

where $\sigma_{eq.alt}$ is the equivalent alternated stress, σ_{alt} is the alternated stress, σ_{med} is the medium stress and σ_{yield} is the yield stress of the material.

The values of Medium Stress, Equivalent Alternated Stress and Maximum Stress as well as the damaged, obtained for each one of the joints of figure 5, corresponding to the different tests, are presented in table 1. The sum of all the damage in each joint is also represented.

According to table 1, the critical section is the section named G, identified in figure 5, because it has a higher damage value. The critical section is located in the lower right arm of the back wheel (figure 6). This section will provide the loads to apply on the testing specimens. From the three different tests defined by the norm EN14766, [1], the one that contributes more to the damage in this section is the test 1 that simulates the pedalling forces. For an easier perception is possible to see a detail from the critical section in figure 6.

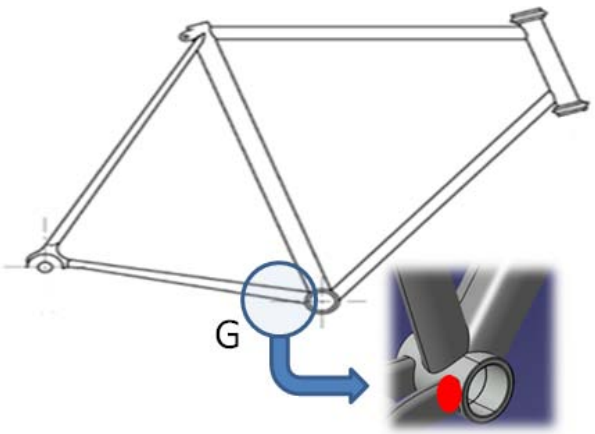

Figure 6. Critical section.

There are other sections that are critically loaded such as section E and A that present values of damage close to damage values of the section G, 0,10 and 0,07% respectively.

Table 1. FE Analysis results.

	Section	A	B	C	D	E	F	G
Test 1	Medium Stress [MPa]	22.68	25.11	9.54	17.62	41.48	13.73	43.88
	Eq. Alt. Stress [MPa]	24.90	27.86	9.92	18.92	49.53	14.51	53.00
	Damage	0.0000	0.0000	0.0000	0.0000	0.0010	0.0000	0.0017
Test 2	Medium Stress [MPa]	39.68	7.41	16.53	0.40	29.92	27.87	13.21
	Eq. Alt. Stress [MPa]	46.99	7.63	17.68	0.40	33.89	31.29	13.93
	Damage	0.0006	0.0000	0.0000	0.0000	0.0000	0.0000	0.0000
Test 3	Medium Stress [MPa]	5.79	1.87	1.97	9.94	4.17	2.80	6.72
	Eq. Alt. Stress [MPa]	5.92	1.88	1.99	10.34	4.24	2.84	6.90
	Damage	0.0000	0.0000	0.0000	0.0000	0.0000	0.0000	0.0000
Total Damage [%]		0.07	0.00	0.00	0.00	0.10	0.00	0.17

3 SPECIMENS

The H shaped specimens used in the fatigue testes, are represented in figure 7.

Figure 7. H shaped welded specimens.

These specimens were obtained by a robotized MIG welding process, which will be used on the bike frame construction. As it can be seen in figure 8, the specimens are made with three aluminium tubes with two circular welds. Initially some specimens were statically tested in order to optimize the welding parameters, including time, with the requested mechanical strength.

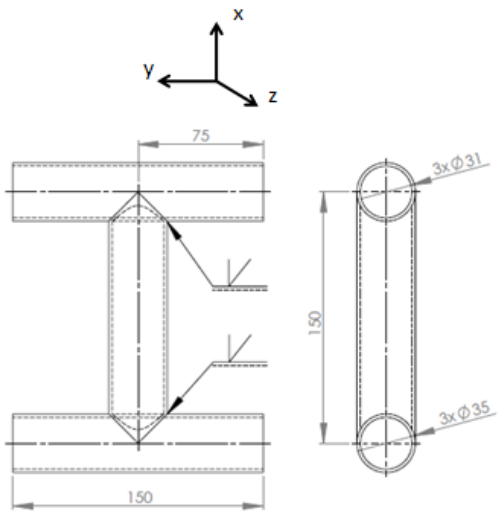

Figure 8. H shaped welded specimen.

The material used on the specimens is the Aluminium alloy AL 6061. The specimens suffered a heat treatment (T6) after welding, which cycle is represented in figure 9.

4 LOADS TO APPLY ON THE SPECIMEN

After the finite element method study, the loads to apply to the specimens were calculated. For this it was considered that the testing machine used to perform the fatigue tests is uniaxial and does not allow the application of shear loads.

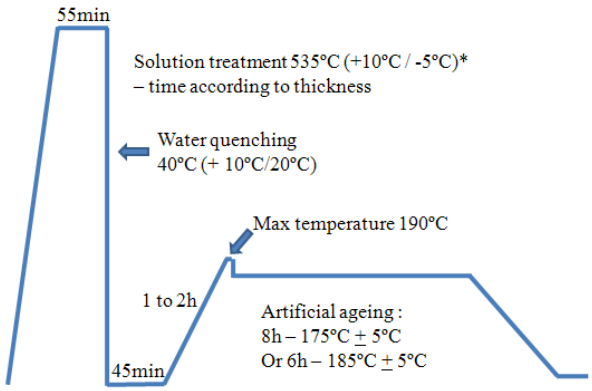

Figure 9. Heat Treatment T6 for Al6061 alloy.

The normal load to be applied to the specimen was calculated by:

$$N_{spec} = \frac{\sigma_{Neq}}{A_t} \tag{6}$$

where A_t is the resistent area of the specimen and σ_{Neq} is a Von Mises equivalent stress given by:

$$\sigma_{Neq} = \sqrt{\sigma_{Fr} + 3.(\tau_{Vt} + \tau_{Vs} + \tau_{Tr})} \tag{7}$$

where σ_{Fr} is the stress due to the normal load Fr, τ_{Vt} is the stress due to shear force in Y direction, Vt, τ_{Vs} is the shear stress due to shear force in Z direction, Vs, and τ_{Tr} is the shear stress due to torque, Tr.

The values fo these stress components were obtained througtout the finite element analysis of the bike frame.

To obtain the bending moments about y and z axis, the normal load (N_{spec}) was applied and the specimens were misaligned in directions z and y, respectively (axis reference in figure 8). The misalignement values Y and Z were calculated so that the same stress values due to bending moments obtained by finite element analysis for the critical section were introduced on the specimens:

$$Y = \frac{\sigma_{Mz}.I_t}{N_{spec}.r_t} \tag{8}$$

$$Z = \frac{\sigma_{My}.I_t}{N_{spec}.r_t} \tag{9}$$

where I_t and r_t are, respectively, the second moment of area and the outside radious of the tube cross-section used on the specimens.

In table 2 are presented the normal load values and the misalignement values to apply on the specimens for each one of the fatigue tests to be done.

Table 2. Loads to be applied on fatigue tests.

	Test 1	Test 2	Test 3
Fmax [KN]	6.71	3.80	1.92
Fmin [KN]	0.67	-1.90	0.19
Fmed [KN]	3.69	0.95	1.06
Falt [KN]	3.02	2.85	0.86
Y [mm]	-5.75	-5.77	3.99
Z [mm]	-11.26	3.31	4.56

For the tests were load ratio was R=0, it was considered R=0.1, to avoid problems with any possible mechanism clearance in the testing machine.

In order to ensure that the norm EN14766, [1], requirements are fulfilled, the specimens has to resist 50000 cycles for each one of the tests without any failure or visual evidence of fatigue cracks.

5 FATIGUE TESTS

The fatigue tests were made on a servo-hydraulic machine Instron 1342 (figure 10) equipped with a load cell +/-250KN and a digital controller Instron Fastrack 8800. This machine has only one actuation axis and can apply dynamic loads to the specimens.

Figure 10. Servo-hydraulic testing machine.

It was necessary to build a clamping system (figure 11, table 3) to the fatigue tests so that it could be possible to aplly axial loads and bendings at the same time with similar stress values to the ones obtained in the critical section from the bike frame analysis. The bending moments are created by the normal load and by the misalingnemt of the specimens in directions yy and zz.

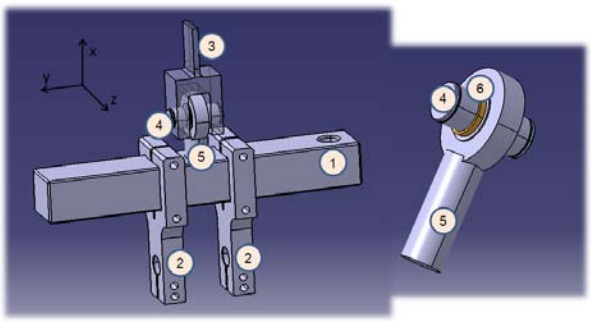

Figure 11. Clamping system.

In figure 12 it is possible to see a specimen already in test using the clamping system, with some visible misalignment in zz direction to create bending in yy direction.

Table 3. Clamping system parts.

Nº	Description	Amount
1	Clamp	2
2	Specimen support	4
3	Machine coupling	2
4	Pin	2
5	M36 Rod End	2
6	Spacing Ring	4

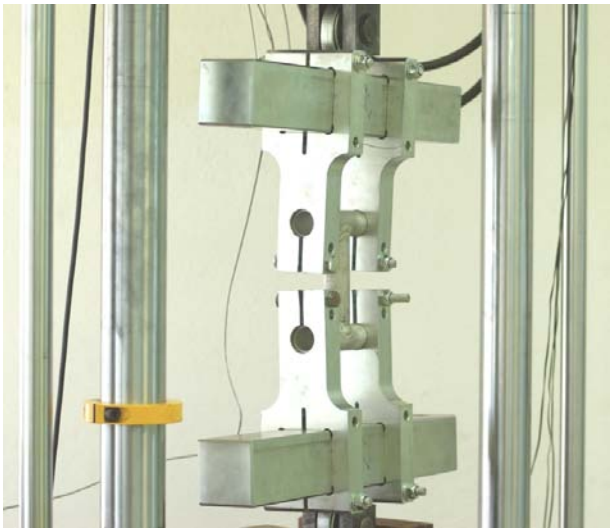

Figure 12. Testing specimen mounted in the testing machine.

6 RESULTS

During the fatigue tests, the specimens were observed several times in order to identify the possible fatigue cracks. Afterwards the specimens were observed with a binocular magnifying glass, in a microscope that allowed a detailed analysis of the specimen's surface, and a liquid penetrant test (figure 13) according [1]. Any cracks were found during and after the fatigue test.

Figure 13. Liquid Penetrant Testing.

7 CONCLUSIONS

The resulting loads and stresses, from the three different tests defined in norm EN14766, were calculated using the finite element method. By this analysis it was possible to identify the critical section of the bike frame that is located in the lower right arm of the back wheel.

Several tests were made in H shaped specimens that represent the welding process used in the bike frame production. The loads applied by a testing machine in the specimens were determined to reproduce the stress field applied in the bike frame. In both specimens that were tested, no one had any evidence of fatigue or fatigue cracks after the 150000 cycles (50000 test 1 + 50000 test 2 + 50000 test 3).

The procedure used to test a specimen instead of an entire bike frame is correct, although some calculations are needed on the bike frame and some special devices such as clamping systems must be developed so that the fatigue tests can be successfully made. This procedure is justifiable when is necessary to make a previous evaluation about a welding process or when is necessary to approve a procedure. It is much more economical than build the entire bike frame and test it.

Based on this procedure, the specimen's test, in spite of being a good indicator of the fatigue resistance, does not dismiss the full bike frame test according to the norm EN14766. The welding fatigue resistance is dependent on weld geometry and quality, and that cannot be always assured, specially in difficult access joints.

8 REFERENCES

[1] - Norm NF EN 14766, AFNOR - Association Française de Normalisation, 2006

[2] - "Mechanical Engineering Design", Joseph E. Shigley, Charles R. Mischke, McGrawHill 6th Edition, 2003

[3] - "Fadiga de Estruturas Soldadas", C.Moura Branco, A. Augusto Fernandes, Paulo M. S. Tavares de Castro**,** Calouste Gulbenkian Foundation**,** 1st Edition, August 1986

[4] - "Mecânica dos Materiais", Carlos A. G. de Moura Branco, Calouste Gulbenkian Foundation, 4th Edition, 2006

[5] - Online Material Information Resource www.matweb.com, used in 12 July 2009

[6] – COSMOSM, User Guide Volume1, Version 2.95, Structural Research and Analysis Corporation

STRESS INTENSITY FACTOR CALIBRATION FOR A LONGITUDINAL CRACK IN A FUSELAGE BARREL

S.M.O. Tavares[1] , P.M.S.T. de Castro[1]

[1] Faculdade de Engenharia da Universidade do Porto and IDMEC-Porto
Rua Dr. Roberto Frias, 4200-465 Porto, Portugal
E-mail: {sergio.tavares;ptcastro}@fe.up.pt

ABSTRACT

Aircraft structures require minimum weight configurations with high strength in order to support all operation stresses with high reliability. Framework construction is the base of these airframes where cross sectional shapes are bolted, welded, bonded, pinned, riveted or machined into a rigid assembly. The vertical and horizontal cross-members are arranged to withstand all structural loads and the skin to support the pressure gradient. This type of fuselage has been in use for about 80 years; it is very strong and of relatively light weight when used with high specific strength materials. Due to the impossibility of producing defect free structures and to avoid damages during all life cycle, these structures require to be damage tolerant in order to be trustworthy. Damage tolerance is a concept predominantly applied in the primary structural parts of civil airframes in order to tolerate a defect that can be detected and repaired in the next maintenance check.
The two most frequently types of structural damages in a fuselage are the longitudinal cracks due the pressurization cycles and the circumferential cracks due the bending and torsion of the fuselage.
In this article, the stress intensity factor, quantifying the intensity of the stress field around a crack tip for a longitudinal crack under the pressurization load, is studied.
For this purpose, a barrel composed by two frames was chosen, with the longitudinal stiffeners and with the geometry usually found in civil airframes. A central crack, between the two frames, was simulated in a finite element model composed by solid elements. The stress intensity factor for different crack lengths, until the crack tips reach the frame were calculated using linear elastic fracture mechanics assumptions and the modified virtual crack closure technique. In addition, the stress intensity factors along the skin thickness were determined. The variation of the SIFs values along the thickness is non symmetric due the bulging effect, which it is illustrated in this article.

KEY WORDS: Airframes, damage tolerant, linear fracture mechanics, modified VCCT, stress intensity factor.

1. INTRODUCTION

The fuselage is the main structure in the aircraft that holds crew, passengers and cargo. An aircraft fuselage structure must be capable of withstanding many types of loads and stresses, and at the same time with low weight.
Truss, monocoque, and the semi-monocoque solutions are found for the design of this structure. Truss or framework types of construction have wood, steel or aluminum tube, or other cross sectional shapes which may be bolted, welded, bonded, pinned, riveted or machined into a rigid assembly[1]. The vertical and diagonal cross-members are arranged to withstand both tension and compression loads. This type of fuselage has been in use for about 80 years. It is very strong and of relatively light weight. The truss assembly is usually covered with a fabric skin. The fabric skin is usually doped and painted which makes it taught and airtight, and adds to its strength. Although cloth fabric is not considered a primary structural member, some aircraft are covered with a glass cloth or mat consisting of impregnated glass fiber reinforced with epoxy or other resins, which is sometimes part of the primary structure.
Both the monocoque and semi-monocoque fuselage structures use their skin as an integral structural or load carrying member. Monocoque (single shell) structure is a thin walled tube or shell which may have rings, bulk-heads or formers installed within. It can carry loads effectively, particularly when the tubes are of small diameter. The stresses in the monocoque fuselage are transmitted primarily by the strength of the skin. As its diameter increases to form the internal cavity necessary for a fuselage, the weight-to- strength ratio becomes more efficient, and longitudinal stiffeners or stringers are added to it. This progression leads to a semi-monocoque fuselage, which depends primarily on bulkheads, frames and formers for vertical strength, and

[1] This structural design was also used in automotive engineering, as in the iconic Maserati Birdcage of the sixties.

longerons and stringers for longitudinal strength. Semi-monocoque is the most popular type of structure used in aircraft design today, [1]. It is composed of a long tube shape with different reinforcements in order to sustain and reinforce the structure.

The principal source of the stresses in this structure is the internal pressure in high altitude caused by difference of cabin pressurization and reduction of the outside pressure with increase in altitude, but the structure is subjected to other loads, as bending, torsion, thermal loads, etc.. In this article, the effect of internal pressure when the fuselage presents a crack was analyzed. The traditional aircraft fuselage is composed of the skin consisting of a cylindrical shell typically 1-3 mm thick, circular frames and axial longerons (or stringers), and normally these components are manufactured with an aluminum alloy and are connected by rivets. As an example, a fuselage configuration of the Fokker 100 is presented in Figure 1. Figure 2 shows the cross-sectional properties of the substructure reported in [3], representative of a generic frame and longerons design. It was intended to carry out a SIF calculation of a representative section of a cracked fuselage. Since the intention was to test a methodology and numerical procedure, and not to calculate solutions for a given aircraft model, an equivalent geometry based in the data in the report [3] was used as modeled a representative case.

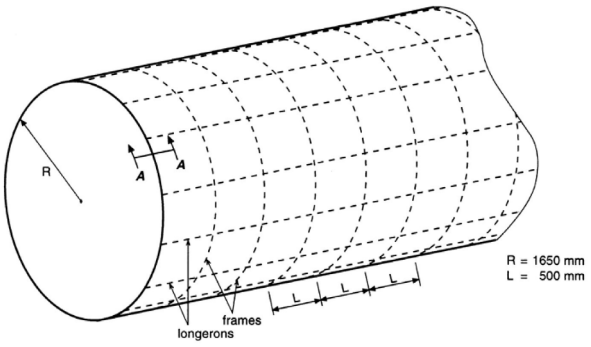

Figure 1. Aircraft fuselage configuration of Fokker 100, [2].

Detailed dimension of the frame and longeron used in the finite element mesh are shown in Figure 3.

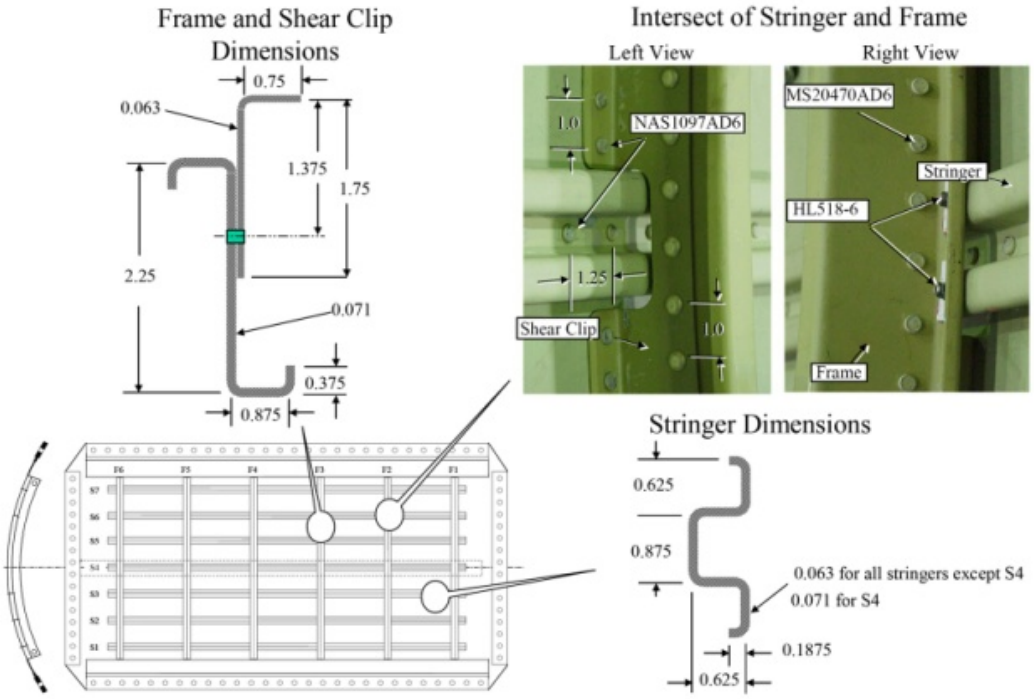

Figure 2. Dimensions of frame, stringer and intersect of stringer and frame, [3].

A part of this fuselage with two frames with 500 mm spacing and 28 longerons, representing half of this fuselage, will be used for SIF calculations. Figure 4 shows a schematic representation of the modeled geometry. The SIFs are calculated for the situation consisting of a single crack in the center of the two frames and parallel to the longerons. An infinite number of crack locations and configurations could be modeled; however the chosen case for the present study represents a typical one and is one of the worst cases. Only half of the fuselage (180°) was modeled. This option makes it possible to use this model for future calculations considering other loading scenarios and simulates the real case with better precision than a smaller part as in Figure 2.

Bending and torsional moments, vertical shear and pressure loads are examples of loads on the fuselage during its service. Internally, the passenger floor, the cargo floor and structure weight promote bending, torsional and vertical shear stresses in the structure. In addition, the wings create significant stresses in fuselage, [4]. The internal pressure is carried primarily

by the skin, rather than by the internal framework, hence it is considered the principal load and cause of loss of fuselage integrity, in the presence of some crack or other damage, [5]. The SIF calculation presented in the following section takes into account the effect of the internal pressure only. Other effects are not easily quantified due the dependency to the location in the overall fuselage.

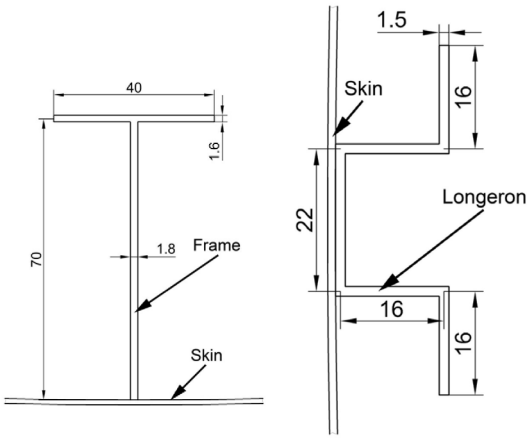

Figure 3. Longeron and frame geometries and dimensions used in the finite element model.

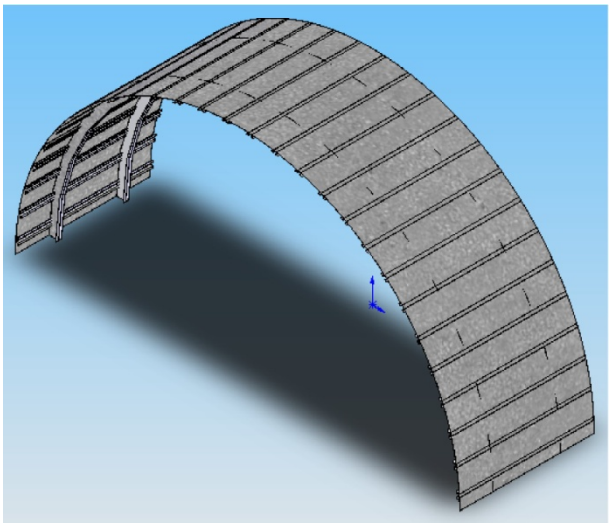

Figure 4. Fuselage frame, representation of modeled geometry.

2. FINITE ELEMENT MODEL

With the geometry presented in Figure 4, a mesh was constructed in order to perform stress field calculation using finite element models. To model this fuselage solid instead of shell elements were used. This option aims at more flexible model, usable for thermo-mechanical analysis. Two elements along the thickness were used in the skin; with the possibility evaluate stress along the skin thickness. In the other components only one element along thickness was used.

The mesh was performed with FEMAP software because it provides powerful tools for meshing geometry, as well as for applying loads and boundary conditions, [6]. Firstly 1/28th of the complete model was modeled using this software, Figure 5. Afterwards, the complete mesh was produced with a radial copy of this part. The following step was the application of the boundary conditions. As symmetry exists in the plane xz or y = 0, the nodes in this plane were restricted in the y direction. In addition, the model was restricted in the z direction in the plane z = 0 and in the x direction in the x =0 line. These are secondary restrictions, however they allow the elimination of large displacements in the x and z directions and reduce the model size. Figure 6 shows schematically the complete mesh and the boundary conditions (in orange).

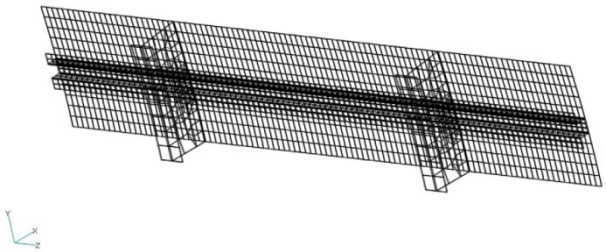

Figure 5. Mesh of 1/28th of the FE model.

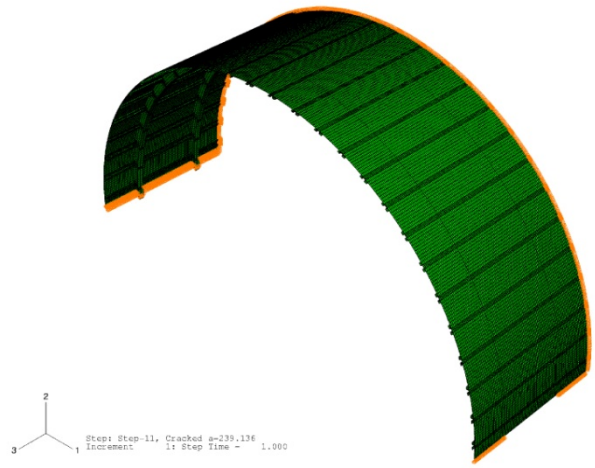

Figure 6. Complete mesh with boundary conditions.

The internal pressure is applied in all the internal faces. For this study the value 0.1 kPa is considered. This value is achieved at altitudes above 12000 m. The most common values are 0.05-0.06 kPa, but this value depends on the gradient between the internal pressure and external pressure.

In recent commercial airplanes the internal pressure is increased for a better comfort of the passengers during the flight.

Figure 7 shows the mesh with the internal pressure applied in the internal element faces of the fuselage. A central crack between the two frames was modeled.

A total of 10 different crack lengths were modeled for evaluation of stress intensity factors and calibration of this structure. The global model was composed by 11 steps and was processed in the finite element package ABAQUS, [7], with parabolic solid element C3D20 that is a 20-node quadratic brick with 27 integration points. Solid elements with 8 nodes reduce substantially the

model size however they cannot simulate the curvature of the skin and large differences in stress fields were found. The properties of this model are summarized in Table 1. The model was computed in dual Core workstation with Intel Xeon 3060 Conroe 2.4GHz processor and 4Gb of RAM memory. The model was completed after 63759 seconds (about 18 hours).

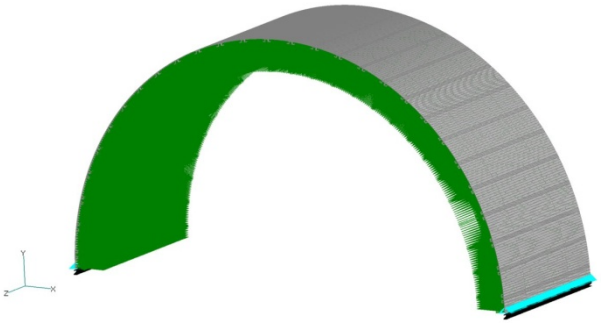

Figure 7. Complete mesh with internal pressure and symmetrical boundary conditions.

Table 1. FE model variables.

Number of Elements	136528
Number of Nodes	796251
Number of equations	2388753
Floating point operations per interactions	4.21E+12

3. RESULTS

Figure 8 shows a result of the von Mises stress field and the amplified deformed shape promoted by the pressurization of the cabin, for the complete frame without cracks. The full representation is obtained by the symmetry conditions of the plane xz or in ABAQUS coordinate system, *1-3*.

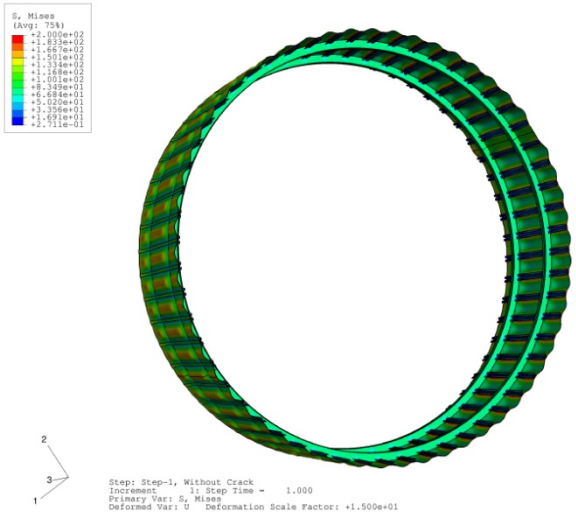

Figure 8. Von Mises stress field and deformed shape of the complete frame, displacement scale factor 15×.

Figure 9 presents a detail of the deformed shape with a scale factor of 30×. The shape of the skin between the frames and longerons is typically entitled as pillow effect.

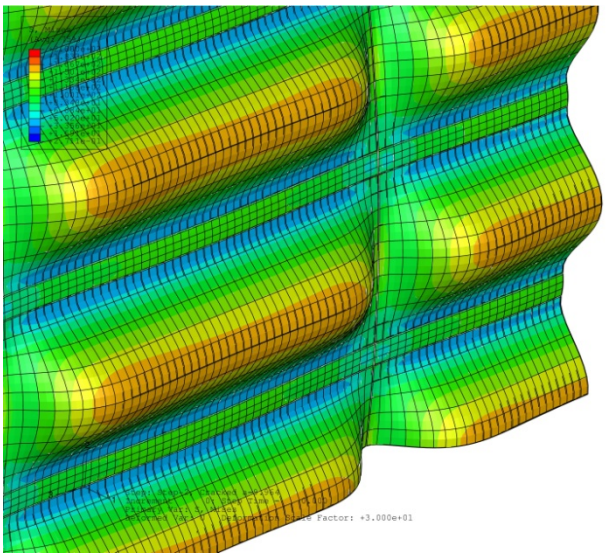

Figure 9. Von Mises stress field and deformed shape detail, displacement scale factor 30×.

3.1. Stress intensity factors

Stress intensity factors for different crack lengths were determined through the virtual crack closure technique (VCCT) in a modified version.

The virtual crack closure technique is based in the energy release rate. This energy can be calculated by variation strain energy release rate when an extension of crack length (Δa) is imposed:

$$G = \frac{\partial U}{\partial a} \approx \frac{U_{a+\Delta a}}{\Delta a} \tag{1}$$

A modified version of the VCCT proposed by Krueger in 2002, [8], presupposes that if the nodal displacements are measured, near the crack before and after grow the crack length to $a+\Delta a$ (an infinitesimal increment), for nodes equidistant to the crack tip, the nodal displacements are identical. This assumption allows computing the energy release rate (G) using only one finite element analysis for each crack length. For 3D parabolic finite elements, the determination of the energy release rate with the modified virtual crack closure technique can be determined using the nodal loads and nodal displacements; however it requires considering the different weights of the nodes in the middle and in the corner of the element. As example, for a parabolic element with 20 elements, the mode I, considering the notation presented in Figure 10, the equation used to determine the energy release rate for the node at the crack surface (node 3) is:

$$G_I = -\frac{1}{2\Delta a \cdot \Delta b}\left[F_{z_3}\left(u_{z_{1^*}} - u_{z_1}\right) + F_{z_4}\left(u_{z_{2^*}} - u_{z_2}\right) + \frac{1}{2}F_{z_6}\left(u_{z_{5^*}} - u_{z_5}\right)\right] \tag{2}$$

where F_z is the nodal force in the z direction, u_z is the displacement in z direction and Δa and Δb are the element dimensions. For the nodes positioned in the middle of the element, in this case node 6 and 12, and the corner nodes 9 and 15 similar equations can be used

to determine the energy release rate at the respective positions.

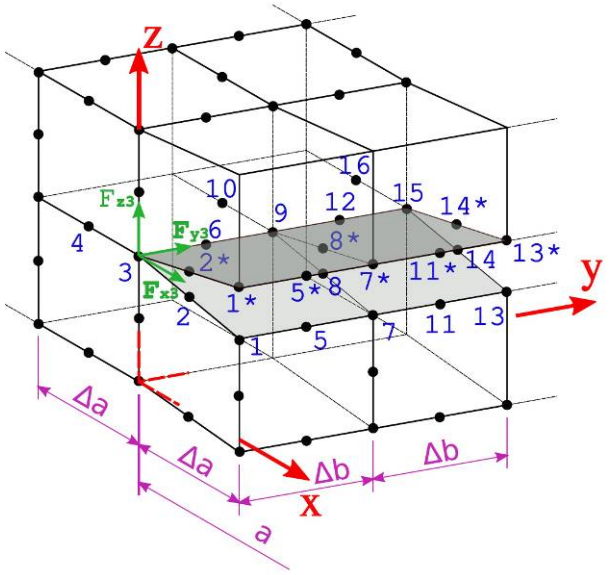

Figure 10. Modified VCCT, annotation for a generic finite element.

The stress field around the crack is presented in Figure 11 for two distinct crack lengths. For the smaller crack length the stress field adopts the usual shape of a crack in an infinite plate. For the crack with length of 239 mm, Figure 11 b), the stress field is affected by the frame reducing the stress intensity and slowing down the crack propagation.

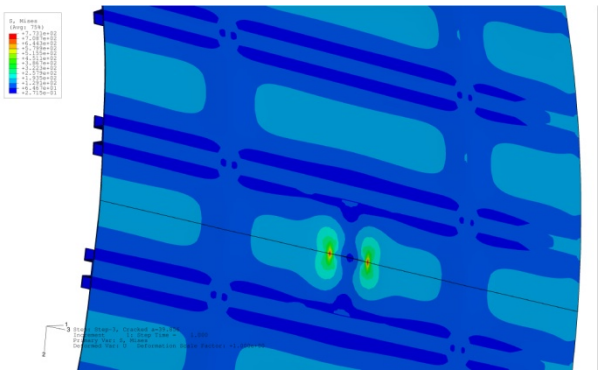

a) a=39.9 mm

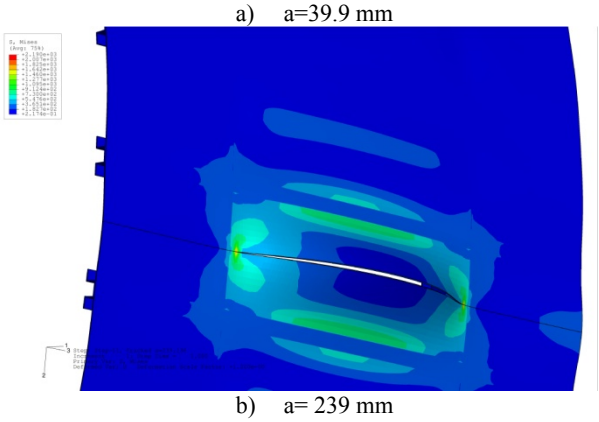

b) a= 239 mm

Figure 11. Stress field around the crack for two crack lenghts.

The skin thickness of the barrel was simulated using two elements with three nodes per face; therefore SIFs for 5 points along the skin thickness were determined.
The values estimated for the different thickness are compiled in Figure 12, for the case of an internal pressure of 100kPa.

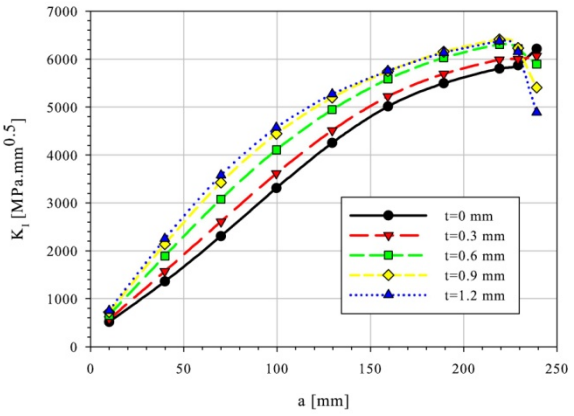

Figure 12. SIFs values for a centred crack fuselage frame.

The SIFs can be made non-dimensional using the equivalent tangential stress or hoop stress (σ_t) generated by the applied pressure and not taking into accout the reinforcement elements as the frames and longerons. This equivalent σ_t stress can be related with internal pressure in a thin-walled pressure vessel:

$$\sigma_t = \frac{pR}{t} \tag{3}$$

where R is the radius of the cylinder (1650 mm) and t is the shell thickness (1.2 mm). Applying these values the tangential stresses are 137.5 MPa.
Figure 13 presents the non dimensional stress intensity factors, with the $\sigma_t\sqrt{\pi a}$ value, in a three dimensional mode.

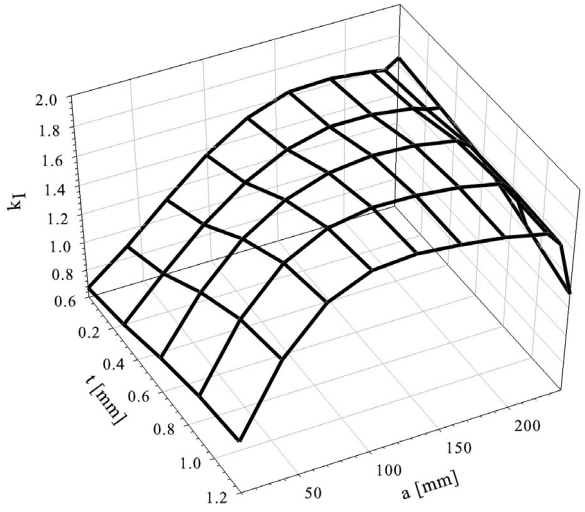

Figure 13. Non dimensional SIFs values for a centred crack fuselage frame.

Bulging is an important problem in the structure subject to internal pressure. This effect take out the symmetry of the stress intensity factors along the thickness as is noticeable in Figures 12 and 13.
Several cross sections for three different crack lengths are presented in Figure 14, where the deformation of the skin is shown at the center of the crack in order to visualize this result and for a better understand of the effects in a crack.

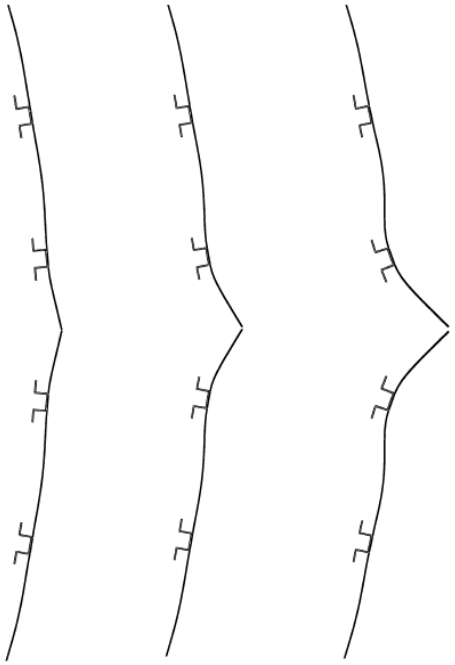

Figure 14. Bulging effect for three different crack lengths (a=59.855 mm; a=129.532 mm; a=239.136 m respectively).

4. CONCLUSIONS

Lightweight structures for air transportation exploit damage tolerant design philosophies in order to increase the service life of the structural parts with high reliability.
In this article, a 3D finite element mesh corresponding a barrel composed by two frames of one representative fuselage was done.
The internal pressure is one of the main loads that the fuselage needs to hold. The compression and decompression cycles are usually used as reference for the fatigue life of the fuselage.
A central crack growth in this finite element model was modeled and the stress intensity factors were determined using the modified virtual crack closure technique. The application modified VCCT and the 3D model, allowed to determine the variation of SIFs along the skin thickness and the influence of the bulging effect in the SIFs.
The consequence of the bulging effect may be noteworthy for a crack in the middle and parallel of two longerons. The effect of the frames in the obstruction of the crack growth was visible in the last crack lengths.
This mesh allows the application of multiple loads and crack orientations in order to study the stiffness of the structure in the presence of different damages.

ACKNOWLEDGEMENTS

DaToN Project, EU FP6 contract AST3-CT-2004-516053 and FCT fellowships SFRH /BD/ 35143/2007 are acknowledged.

REFERENCES

[1] P. Katz, *Stresses and strains on aircraft* www.navair.navy.mil/safety/documents/Stress_Strain.doc , 1997.

[2] H.J. ten Hoeve, L. Schra, A.L.P.J. Michielsen, and H. Vlieger, "Residual strength test on stiffened panels with multiple-site damage", Technical report, NLR CR 96792 L, DOT/FAA/AR-98/53, National Aerospace Laboratory NLR, The Netherlands, February 1999.

[3] John Bakuckas, "Full-scale testing and analysis of fuselage structure containing multiple cracks" Technical report, DOT/FAA/AR-01/46, Federal Aviation Administration (FAA), William J. Hughes Technical Center, Airport and Aircraft Safety, Research and Development Division, Atlantic City International Airport, 2002.

[4] L. Boni and D. Fanteria, "Finite-element-based assessment of analytical methods for the design of fuselage frames", *Proceedings of the Institution of Mechanical Engineers Part G-Journal of Aerospace Engineering*, 220(G5), pp. 387-398, 2006.

[5] P. E. O'Donoghue and J. Ju, "Experimental/numerical techniques for aircraft fuselage structures containing damage", in *15th European Conference of Fracture, Advanced Fracture Mechanics for Life and Safety Assessment*, Stockholm, Sweden, 2004. European Structural Integrity Society (ESIS).

[6] FEMAP - Finite element modeling and postprocessing - Version 9.2 - Users manual. UGS Corp., 2006.

[7] ABAQUS user's manual, Version 6.6. 2006.

[8] R. Krueger, "The virtual crack closure technique: History, approach and applications", NASA Technical Report, NASA/CR-2002-211628, ICASE Report No. 2002-10, 2002.

Composites, coatings

THIN OPTICAL FILMS FRACTURE: BEHAVIOR WITH INCREASING TEMPERATURE

C. Baptista[1,2*], A. Dantas[2], C. Matos[2], V. Belchior[2], R. Martins[1], E. Fortunato[1]

[1] Materials Science Department, CENIMAT/I3N,
Faculty of Sciences and Technology of New University of Lisbon,
Campus de Caparica, 2829-516 Caparica, Portugal
[2] Essilor Portugal, Rua do Pino Verde 2, 2635-096, Rio de Mouro Portugal
[*] Presenting author

Abstract

Thin films and multilayered structures are increasingly employed in all sectors of modern industry. For example on an optical spectacle lens, multilayered are coated for various functions such as scratch resistance, anti-reflection, etc [1].

Coatings are needed on polymer ophthalmic lenses to enhance both the mechanical durability of the relatively soft plastic surface and the optical performance of the lens. High value ophthalmic spectacle lenses are coated with a multilayer system consisting of a primer coating, abrasion resistant hard coating and a multilayer AR coating stack [2]. The next figure shows the constitution of a coated spectacle lens:

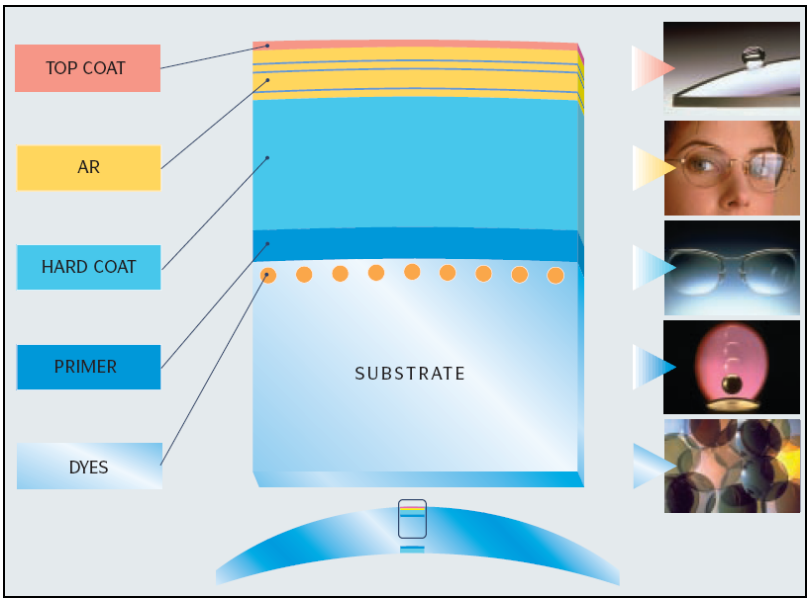

Figure 1 – A coated plastic lens is a complex system [3].

The optimization of coating performance continues to be a considerable technical challenge for the manufacturer of coated ophthalmic spectacle lenses.

This work presents a thin film testing temperature behavior performed inside a SEM system (FEI Quanta 400FEG / SEM), equipped with a heating system under high vacuum conditions. This study aims to simulate the use of ophthalmic lenses by the client, particularly in situations of sun exposure and heat set.

The SEM software allowed to obtain several movies *"in situ"* where it is possible to observe the evolution and behavior of the different thin films with increasing temperature.

The study involved dip-coating of ophthalmic lenses into a sol of controlled chemical composition (primer and hard coats) and electron beam deposition of Zirconia and Quartz interchangeably (AR coat). Allyl diglycol carbonate (CR-39™) was used as substrate because this is the most widely used thermosetting plastic material in ophthalmic companies [2,4,5].

Fractures in thin films propagate from small flaws in these. If this films were completely perfect and uniforms (almost impossible) they don´t peel or fracture. This way, and that the tests were controlled, there have been deliberate laser failures in order to observe the fractures associated.

The results show that the effect of temperature begins to become evident from the 40 º C (temperature perfectly fair in sunlight). These fractures are associated with the primer coat thermal expansion. This layer is relatively soft and elastic and is designed to buffer stress forces between the hard coat and substrate [2]. The hard coat cannot follow the expansion of the primer coat and eventually fracture.

Since temperatures above 70 º C major fractures are observed in the primer coat. The next figure shows the thin optical film microcracks evolution with the increasing temperature:

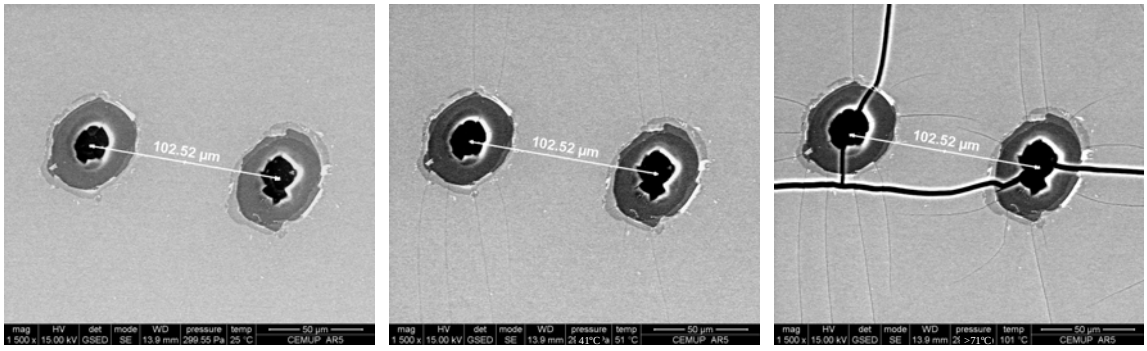

Figure 2 – Thin optical films evolution behavior with temperature.

Future works are being done using different substrate materials and thin film interface adhesion conditions.

Keywords: Thin films; SEM; Temperature; Ophthalmic.

Acknowledgement: The authors acknowledge the Portuguese Science Foundation (FCT) and Essilor Portugal for the financial support to the project SFRH/BDE/15656/2007 and CEMUP (Materials Centre of Porto University).

References:

[1] – Zhong Chen, Zhenghao Gan, Fracture toughnes measurement of thin films on compliant substrate using controlled buckling test, Thin Solid Films 515 (2007) 3305-3309

[2] – Frank Samson, Ophthalmic lens coatings, Surfaces and Coatings Technology 81 (1996) 70-86

[3] – Essilor, Coatings, Ophthalmic Optics Files (1997)

[4] – Essilor, Ophthalmic Optics Files – Lens Materials

[5] – D.R. Gunasegaram, I.M. Bidhendi, N.J. McCaffrey, Modelling the casting process of plastic ophthalmic lenses, International Journal of Machine Tools & Manufacture 40 (2000) 623-639

RESISTANCE CURVES IN THE TENSILE AND COMPRESSIVE LONGITUDINAL FAILURE OF COMPOSITES

Pedro P. Camanho[1], Giuseppe Catalanotti[1] ,Carlos G. Dávila[2], Claudio S. Lopes[1], Miguel A. Bessa[1], José C. Xavier[3]

[1]DEMec, Faculdade de Engenharia, Universidade do Porto,
Rua Dr. Roberto Frias, 4200-465 Porto, Portugal-
E-mail: pcamanho@fe.up.pt

[2]NASA Langley Research Center, Hampon VA, USA

[3]Universidade de Trás-os-Montes e Alto Douro, Portugal

ABSTRACT

This paper presents a new methodology to measure the crack resistance curves associated with fiber-dominated failure modes in polymer-matrix composites. These crack resistance curves not only characterize the fracture toughness of the material, but are also the basis for the identification of the parameters of the softening laws used in the analytical and numerical simulation of fracture in composite materials. The method proposed is based on the identification of the crack tip location by the use of Digital Image Correlation and the calculation of the J-integral directly from the test data using a simple expression derived for cross-ply composite laminates. It is shown that the results obtained using the proposed methodology yield crack resistance curves similar to those obtained using FEM-based methods in compact tension carbon-epoxy specimens. However, it is also shown that the Digital Image Correlation based technique can be used to extract crack resistance curves in compact compression tests for which FEM-based techniques are inadequate.

KEY WORDS: Intralaminar fracture toughness; composite laminates; digital image correlation.

1. INTRODUCTION

Despite the significant advances in the analysis models for the prediction of fracture in composite materials, such as advanced failure criteria and associated damage models, sophisticated kinematic representations of fracture mechanisms, and cohesive elements to deal with delamination, the accurate prediction of intralaminar fracture mechanisms, acting at the ply level, still presents several challenges.

The majority of existing models to predict intralaminar fracture of polymer-based composite materials reinforced by carbon fibers are based on softening constitutive models [1]. The shape of the softening law, e.g., linear, exponential or other, is generally assumed to be inconsequential for the prediction of fracture. While this assumption is valid under small-scale bridging conditions, the shape of the cohesive law plays a fundamental role in the prediction of fracture under large-scale bridging conditions, where the process zone length may be large relative to other length scales in the problem [2]. When crack propagation includes different energy dissipation mechanisms that act over different length scales, the nature of these mechanisms must be accounted for in the cohesive law.

Several failure mechanisms including fiber tensile fracture, fiber-matrix pull-out and matrix cracking are present when a crack propagates in a plane perpendicular to the fiber direction. To account for these different failure mechanisms, the authors have proposed in a previous paper a combined linear-exponential softening law for fiber tensile fracture [3], and demonstrated that a simple linear softening law is unable to predict the load-displacement relation obtained in a cross-ply Compact Tension (CT) test specimen, while a bi-linear softening law provides an accurate prediction [4].

The definition of the parameters used in the softening law related to the fiber kinking failure mechanisms is based on the experimental determination of the crack resistance curve (R-curve) of the Compact Compression (CC) test specimen. However, the CC test specimen presents several problems that are yet to be resolved: the tractions that are transferred along a kink band render the numerical calculation of the J-integral using the Finite Element Method (FEM) inaccurate [5]. In addition, the experimental determination of the exact location of the tip of a kink band is difficult.

Therefore, the objective of this paper is to address these problems by using an alternative method that is based on the use of the Digital Image Correlation (DIC) technique. An automatic algorithm that post-process the data obtained from the DIC system is used to detect the crack tip location and to establish the R-curve from the surface measurements of the displacement field.

2. CONFIGURATION OF THE TEST SPECIMENS

The material used is the carbon-fiber reinforced epoxy IM7-8552 provided by Hexcel composites. The material properties of IM7-8552, measured in a previous investigation [6], are shown in Tables 1 and 2.

Table 1. Elastic properties of IM7-85522

E_{1T} (GPa)	E_{1C} (GPa)	E_2 (GPa)	G_{12} (GPa)	υ_{12}
171.4	150	9.1	5.3	0.3

where E_1 and E_2 are respectively the ply longitudinal and transverse modulus, G_{12} is the ply shear modulus, and υ_{12} is the ply major Poisson ratio.

Table 2. Strengths of IM7-85522 (MPa)

X_T	X_C	Y_T	Y_T	S_L
2326	1200	62	200	92

where X_T and X_C are respectively the ply longitudinal tensile and compressive strength, Y_T and Y_C are respectively the ply transverse tensile and compressive strengths, and S_L is the ply shear strength.

The pre-impregnated plies were laid-up in an $[90/0]_{8s}$ configuration and cured according to Hexcel's specifications. The resulting plates were cut using a diamond-coated disk to their nominal overall dimensions. The specimens were finally machined to their final geometry, shown in Figure 1. The holes for the load introduction points were cut using tungsten – carbide drills and by clamping the specimens between to sacrificial carbon-epoxy plates. This procedure prevents the test specimens from delamination at the entrance and exit of the drill.

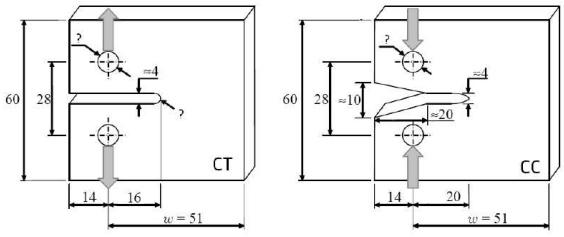

(a) CT specimen (b) CC specimen

Figure 1. Geometry of the CT and CC test specimens (after Pinho [5]).

3. IDENTIFICATION OF THE CRACK TIP LOCATION

The accurate measurement of the crack location is performed by post-processing the information obtained by the DIC system. The function K(P) proposed by Grégoire [7], which identifies a discontinuity inside a pattern, was modified to enable the identification of crack tips in carbon-epoxy CT and CC test specimens, and implemented in a MATLAB code which provides the following information:

- K(P)=0 - no discontinuity (bulk material).
- K(P)=-1 - discontinuity (crack).
- K(P)=1 - crack tip.

Figure 2 shows the result of the application of the MATLAB algorithm during the crack propagation stage of a CT specimen. The exact location of the crack tip is identified and quantified by the location where K(P)=1. This procedure obviates the need for the visual identification of the crack tip, which is prone to human errors especially in the case of the CC test specimen.

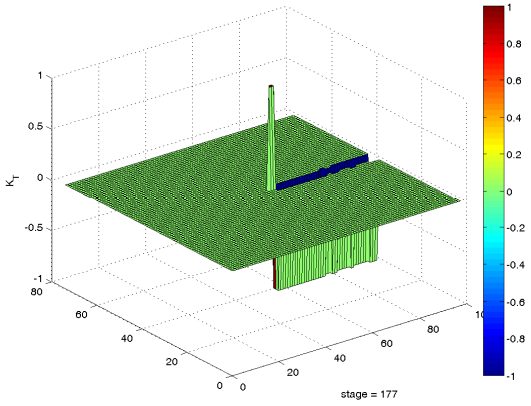

Figure 2. Identification of the crack tip location in a CT test specimen.

4. EXPERIMENTAL DETERMINATION OF THE J-INTEGRAL

We propose a new method to evaluate the J-integral and to measure the crack resistance curve based on the surface displacement and strain fields obtained from a Digital Image Correlation (DIC) system.

The digital image correlation ARAMIS software developed by GOM (http://www.gom.com/) was used in this work. This measurement system is equipped with an 8-bit Baumer Optronic FWX20 camera (resolution of 1624x1236 pixels, pixel size of 4.4µm and sensor format of 1/1.8") coupled with a Schneider-Kreuznach Componar-S 50mm f/2.8 lenses. Using DIC, several matrices containing the in-plane displacement and strain fields are obtained; these fields are the basis for the calculation of the J-integral.

For the cross-ply laminate used here, and assuming that there is no bending of the specimen, the J-integral can be defined using classical lamination theory as:

$$J = \frac{t}{2}\int_{\Omega_0}\left(\{\bar{\sigma}\}\{\varepsilon\}^T n_1 - 2\left\{\frac{\partial u}{\partial x_1}\right\}^T [\bar{\sigma}]\{n\}\right) \mathrm{d}s \quad (1)$$

where the stress tensor, collected in $\{\sigma\}$, is averaged through-the-thickness of the laminate and *t* corresponds to the laminate thickness.

The contour selected to calculate the J-integral from the DIC system is shown in Figure 3.

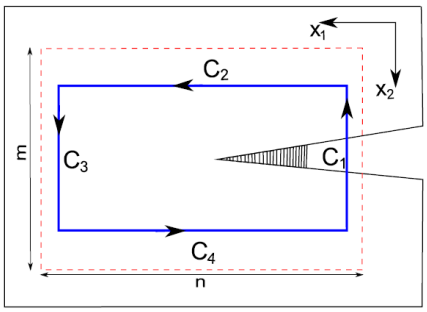

Figure 3. Contour used to calculate the J-integral

4.1. Calculation of the stresses.

The stresses are computed from the homogenized stiffness matrix as: $\{\sigma\} = [\bar{C}]\{\varepsilon\}$where $\{\varepsilon\}$ is the strain matrix calculated at a given position by the DIC.

4.2. Calculation of dx_1, dx_2, and ds.

The differentials dx_1 and dx_2 are taken as the differences between the centers of adjoining macro-pixel windows, measured along the corresponding axes. The differential ds is the Euclidian norm of dx_1 and dx_2.

4.3. Calculation of $\{n\}$

This vector is directly defined by the simple contour sub-divisions shown in Figure 3, taking the following forms: $\{1,0,0\}^T$ on C_3, $\{0,1,0\}^T$ on C_4, $\{-1,0,0\}^T$ on C_1, and $\{0,-1,0\}^T$ on C_2.

4.4. Calculation of $\left\{\frac{\partial u}{\partial x_1}\right\}$

This vector is calculated using the central difference method applied in three adjoining macro-pixels.

Having calculated all the terms required in equation (1), the J-integral is computed from the summation of all discrete contributions of each macro-pixel, which are calculated using equation (1) with the relevant terms calculated as explained in the previous points. This methodology was implemented in a MATLAB program that enables the automatic generation of the R-curve by assigning to each crack length the corresponding value of the J-integral.

5. COMPACT TENSION TESTS

The CT test was conducted using an MTS 312.31 testing machine with a load capacity of 250 kN. The tests were performed using a load cell of 100 kN and the speed of the machine used in the displacement controlled test was 2mm/min. Figure 4 shows the set-up used during the CT tests. The test specimen was previously sprayed with a white ink to generate a random distribution of points, as required by the DIC system.

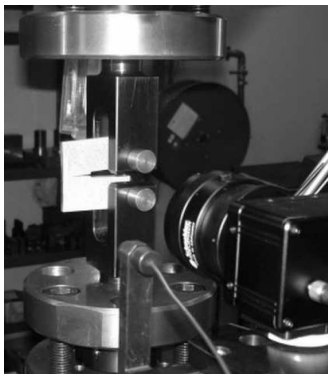

Figure 4. Compact tension test specimen and DIC system.

Figure 5 shows the R-curves measured from the FEM post-processing of the test results obtained by the method proposed by Pinho et al. [4] and those obtained by processing of the displacement and strain fields measured by the DIC system. Figure 4 shows a good correlation between the two techniques.

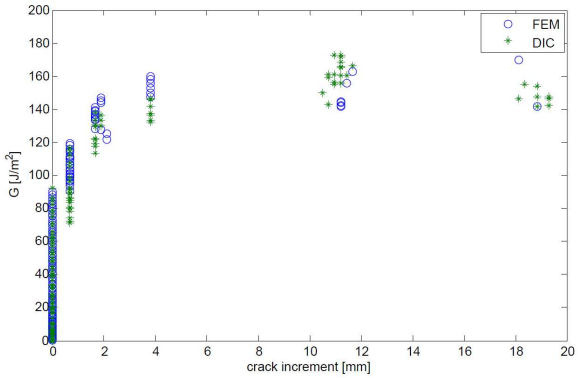

Figure 5. R-curves extracted from a CT specimen using FEM and DIC.

The results show an initial fracture toughness of 92J/m^2 that steadily increases up to 146J/m^2 for a crack increment of 4mm. This R-curve results from fiber bridging, as shown in Figure 6.

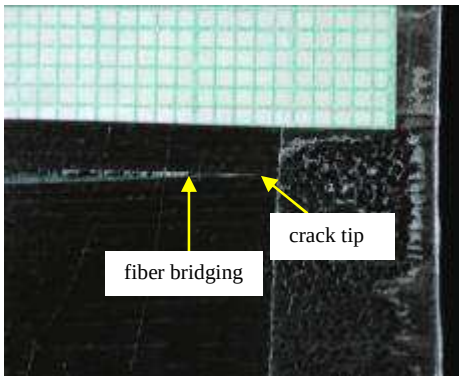

Figure 6. CT test specimen showing fiber bridging.

6. COMPACT COMPRESSION TESTS

The CC tests were conducted with the same test machine and speed as those used in the CT tests. As previously explained, the FEM-based calculation of the J-integral is not appropriate to the calculation of the R-curve because it does not account for the contact and load transfer across the kink band. Figure 7 shows that the FEM-based and DIC-based R-curves differ approximately by a factor of two. The FEM-based solution yield unrealistically high values of the fracture toughness that could be result in an unreliable softening law for the fiber kinking failure mode.

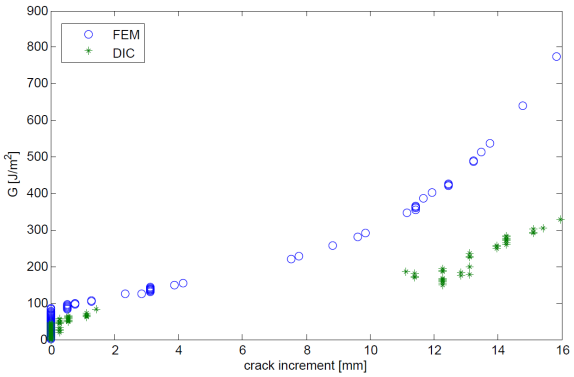

Figure 7. R-curves extracted from a CC specimen using FEM and DIC.

It is worth noticing that the initiation values of the fracture toughness are also different: 80J/m^2 for the DIC-based solution and 100J/m^2 for the FEM-based solution. In addition, the algorithm developed to detect the exact location of the tip of the kink band was unable to yield reliable results for kink bands lengths comprised between 2mm and 11mm. The reason for this uncertainty is the presence of a delamination associated with the propagation of the kink band, which pollutes the data in the vicinity of the tip of the kink band.

Figure 8 shows the propagation of the kink band from the initial notch and illustrates the difficulty in detecting the exact location of the tip of the kink band by visual inspection alone. Figure 8 also shows the delamination that accompanies the propagation of the kink band.

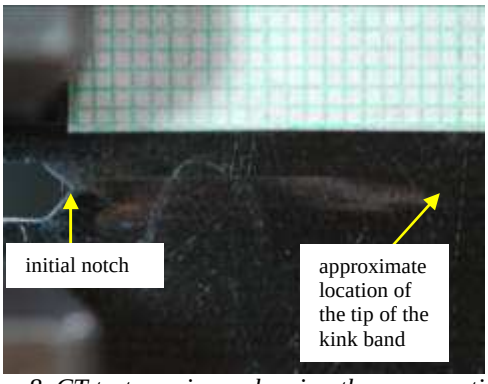

Figure 8. CT test specimen showing the propagation of a kink band.

7. CONCLUSIONS

The displacement and strain fields obtained using DIC during the CT and CC tests of composite laminates may serve as the basis for the rigorous determination of the location of the crack or kink band tips and for the automatic computation of the J-integral. The models develop for these purposes were implemented in a MATLAB code that obviates the need of any complex pre-and post-processing, either based on FEM or standard data reduction methods. In addition, the proposed methodology can be used to generate R-curves for CC tests. Some difficulties encountered in the identification of the tip of the kink-band in the presence of delamination still need to be addressed.

The carbon-epoxy material system used, IM7-8552, shows an R-curve for fiber dominated failure modes under tensile loads, where the fracture toughness raises from 92J/m^2 to 146J/m^2. An even more pronounced R-curve was obtained for fiber dominated failure modes under compressive loads, where the fracture toughness ranges from 80J/m^2 to approximately 300J/m^2 for high lengths of the kink band.

ACKNOWLEDGEMENTS

The second author acknowledges the financial support of the European Commission under Contract No. MRTN-CT-2005-019198.

REFERENCES

[1] Lapczyk, I. and Hurtado, J.A., "Progressive damage modeling in fiber-reinforced materials", *Composites Part A*, 38, pp. 2333-2341, 2007.

[2] Sørensen, B.F. and Jacobsen T.K. (1998) "Large-scale bridging in composites: R-curves and bridging laws", *Composites Part A*, 29, pp. 1443-1451, 1998.

[3] Maimí P., Camanho P.P., Mayugo J.A., and Dávila C.G., A continuum damage model for composite

laminates: Part I - Constitutive model. *Mechanics of Materials*, 39, pp. 897-908, 2007.

[4] Dávila, C.G., Rose, C.A., and Camanho, P.P., "R-curve toughening in the longitudinal fracture of composites and associated cohesive law", *International Journal of Fracture*, 158, pp. 211-223, 2009.

[5] Pinho, S.T., Robinson P., and Iannucci L., "Fracture toughness of the tensile and compressive fibre failure modes in laminated composites", *Composites Science and Technology*, 66, pp. 2069-2079, 2006.

[6] Camanho, P.P., Maimí, P., and Dávila, C.G., "Prediction of size effects in notched laminates using continuum damage mechanics", *Composites Science and Technology*, 67, pp. 2715-2727, 2007.

[7] Grégoire, D., *Initiation, propagation, arrêt et redémarrage de fissures sous impact*, PhD Thesis, LaMCoS - INSA de Lyon, 2008.

TAPER ANGLE OPTIMIZATION OF SCARF REPAIRS IN CARBON-EPOXY LAMINATES

R.D.S.G. Campilho [1,2], A.M.G. Pinto [3], M.F.S.F. de Moura [2], I.R. Mendes [3], M.D. Banea [2], L.F.M. da Silva [2]

[1] Instituto de Engenharia Mecânica e Gestão Industrial,
Campus da FEUP, Rua Dr. Roberto Frias, nº 400, 4200-465 Porto, Portugal.
E-mail: raulcampilho@hotmail.com

[2] Departamento de Engenharia Mecânica, Faculdade de Engenharia da Universidade do Porto,
Rua Dr. Roberto Frias, 4200-465 Porto, Portugal.

[3] Instituto Superior de Engenharia do Porto
Rua Dr. António Bernardino de Almeida, 431, 4200-072 Porto, Portugal.

ABSTRACT

The increasing use of Carbon-Fibre Reinforced Plastic (CFRP) laminates in high responsibility applications introduces an issue regarding their handling after damage. The availability of efficient repair methods is essential to restore the strength of the structure. The availability of accurate predictive tools for the repairs behaviour is also essential for the reduction of costs and time associated to extensive tests. This work reports on a numerical study of the tensile behaviour of three-dimensional (3D) adhesively-bonded scarf repairs in CFRP structures, using a ductile adhesive. The Finite Element (FE) analysis was performed in ABAQUS® and Cohesive Zone Models (CZM's) was used for the simulation of damage in the adhesive layer. A parametric study was performed on two geometric parameters. The use of over-laminating plies covering the repaired region at the outer or both repair surfaces was also tested as an attempt to increase the repairs efficiency. The results allowed the proposal of design principles for repairing CFRP structures.

KEY WORDS: Carbon-Epoxy; Cohesive Zone Models; Composite; Finite Element Analysis; Repair.

1. INTRODUCTION

CFRP components are being more and more used in structures demanding a high performance because of their superior characteristics (such as high strength, high stiffness, long fatigue life and low density). However, CFRP materials usually show a high sensitivity to temperature, moisture and impacts. Thus, repair strategies should always be considered over replacement [1]. Adhesively-bonded repairs are an option, but these typically do not restore the initial strength and stiffness of the components without a significant weight penalty. Thus, a substantial amount of research has been carried out recently on efficient repair techniques and adhesives technology [2]. Several studies are available for the repair of composite panels [3], including FE works describing predictive techniques for the repairs strength [2]. Unlike the single-strap solution, scarf repairs do not cause a substantial bending of the components, which reduces peel stresses [4]. Moreover, shear stress distributions along the bond length are practically uniform due to the tapering effect at the scarf edges [5]. The outcome of this optimization of stresses is a higher efficiency [6] and the substantial or full strength recovery typically achieved by this method usually makes scarf repairs as permanent [7]. Scarf repairs are also flush with the damaged structure, preventing aerodynamic disturbance. Despite all of these advantages, scarf repairs are more difficult to execute, which reflects on higher costs. In addition, they require a large repair area, since relatively small angles are necessary to restore the strength of components [7, 8]. This repair is fabricated by machining a tapered cavity to remove the damaged material. A conical patch is then adhesively-bonded to the structure [5, 9].

In tension, experimental and FE studies show an exponentially increasing strength of scarf assemblies (joints or repairs) with the reduction of the scarf angle (α), due to the corresponding increase of bond area [7, 8]. On the failure modes, the literature reports that values below $\alpha \approx 2^{\circ}$ lead to cross-sectional failures of the laminates outside the repaired region, while bigger values typically yield failures of the adhesive bond [5, 9]. Odi and Friend [10] compared the stress distributions between three FE approaches to simulate stepped and $\alpha = 3^{\circ}$ CFRP scarf repairs under tension, using equivalent orthotropic elastic properties for the CFRP components. For the scarf repairs, shear stresses in the adhesive were nearly constant, leading to a high efficiency, as the adhesive failed simultaneously at the entire bond length. 3D ply-level analyses of composite repairs have recently become feasible, as a result of the advancement of desktop computers. In recent years, fairly accurate predictions were achieved on the static strength of adhesively-bonded repairs using CZM's coupled with FE simulations [11, 12]. This technique, which accounts

for the progressive damage evolution, is particularly meaningful for scarf repairs due to the difference between damage initiation and failure loads [13]. The work of Campilho et al. [5] validates with experiments a trapezoidal CZM applied to tensile loaded Two-Dimensional (2D) scarf repairs on CFRP laminates, for values of α between 2º and 45º. To account for the experimental fractures, the cohesive failure of the adhesive layer and composite interlaminar and intralaminar (in the transverse and fibre directions) failures were considered. The corresponding cohesive laws were estimated by inverse modelling. The accurate predictions validated the proposed technique.

This study reports on the tensile behaviour of 3D scarf repairs in CFRP structures, using a ductile adhesive (Araldite® 2015). Since the proposed numerical methodology was already validated with experiments in previous works, giving accurate estimations [11, 12], this research is restricted to a purely numerical optimization of the repairs that will allow the definition of principles for repairing. Traditionally, the design of scarf repairs is based on 2D models, as a simplification of the 3D geometry [14]. The primary motivation for this work stems from the known inconsistencies between the 2D approximations and the 3D repair [3]. In fact, with the 2D simplification, stresses along the scarf bond are regarded as constant in the width direction of the repairs, thus neglecting the concentrations at the scarf edges near the longitudinal mid-plane of the 3D repair [7]. Moreover, the 2D simplified geometry does not capture the typical 3D stress effects of these repairs that may result on a premature catastrophic failure at or near the interfaces between the composite and the adhesive layer [15]. The FE analysis was performed in ABAQUS® and used CZM's for the simulation of damage in the adhesive layer. Trapezoidal cohesive laws in each pure mode were used to account for the ductility of the adhesive. A parametric study was performed on the repair width (b) and α. The use of over-laminating plies covering the repaired region at the outer or both repair surfaces was also tested to increase the repairs efficiency. The results obtained allowed the establishment of design principles for repairing.

2. NUMERICAL ANALYSIS

The cohesive fracture of an adhesive layer of Araldite® 2015 with thickness (t_A) of 0.2 mm was simulated with a mixed-mode (I+II+III) CZM, whose detailed description can be found in the work of Campilho et al. [16]. A trapezoidal law between stresses and relative displacements between homologous points of the cohesive elements with zero thickness was considered, to account for the adhesive ductility [5, 11, 12]. The formulation allows a mixed-mode behaviour, in which damage onset is predicted using a quadratic stress criterion and failure with a linear energetic criterion. In the FE models, crack propagation with cohesive elements was only considered for the cohesive failure of the adhesive bond. A stress-based criterion was assumed for the tensile failure of the composite parts. For the 0º plies, oriented with the load, the experimentally determined strength from unidirectional specimens was considered (1280±177 MPa, the average value was used for the prediction of failure). For the 90º plies, i.e., experiencing a matrix failure, typical values from the literature were used (≈40 MPa) [5]. In the numerical models, failure was predicted as the load of patch debonding onset [17], guaranteeing that neither the laminate nor the patch attained the mentioned strengths. The prospect of interlaminar and intralaminar failures near the scarf was not considered, despite the chance of this occurrence [5], owing to slightly smaller cohesive properties for these propagations compared with the properties of most structural adhesives. This procedure was adopted due to the modelling difficulties and additional computational time required to simulate these localized fractures, which do not influence by a significant amount the global characteristics of 3D repairs such as the ones proposed in this work. Under this simplification hypothesis, the predictions should be interpreted in relative terms between the different tested solutions, allowing the establishment of design principles for these repairs, instead of being viewed as precise quantitative predictions. The adhesive layer was introduced in the numerical models by the trapezoidal CZM, with experimentally defined properties for the specific value of t_A used in the repairs. The cohesive laws of the adhesive layer in pure-modes I and II were estimated in a previous work by the authors [5] by DCB (mode I) and ENF (mode II) tests with the same value of t_A, using an inverse technique. The pure mode III cohesive law was considered equal to the pure mode II one. A detailed description of the cohesive model, inverse determination of the cohesive parameters and respective discussion, and finally the properties of a t_A=0.2 mm adhesive layer of Araldite® 2015 can be found in the aforementioned work by the authors [5].

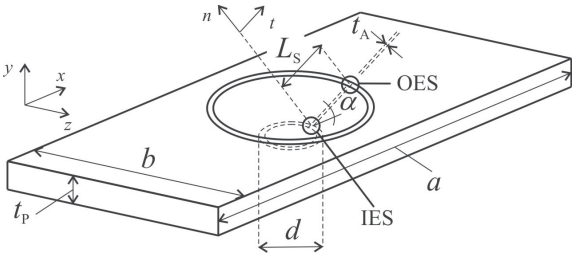

Figure 1. Scarf repair geometry.

Figure 1 shows the scarf repair geometry and characteristic dimensions. The Outer Edge of the Scarf (OES) and Inner Edge of the Scarf (IES) loci are also defined. The following dimensions were considered for the FE analysis: a=200 mm, b=50 and 80 mm, t_P=2.4 mm, d=10 mm, t_A=0.2 mm and α=10, 15, 25 and 45º (for the repairs with b=50 mm) or α=5, 10, 15, 25 and 45º (for the repairs with b=80 mm). The minimum values of α were imposed by the respective values of b. Sixteen plies and $[0_2,90_2,0_2,90_2]_S$ lay-up laminates and

patches were used in this analysis (0.15 mm ply unit thickness).

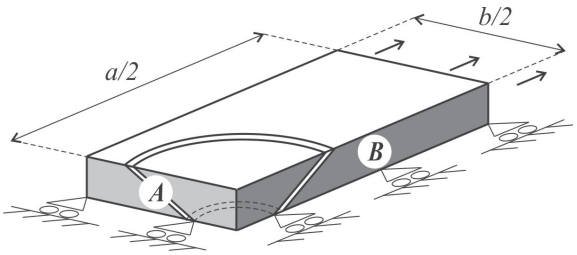

Figure 2. FE idealization with symmetry conditions.

Figure 2 represents the numerical idealization of the scarf repair tensile test. Only ¼ of the laminate was modelled, by the use of symmetry conditions at the mid-transversal (***A***) and mid-longitudinal (***B***) planes. The scarf repairs were simulated in ABAQUS® with 3D models. The cohesive elements, used to simulate a cohesive failure of the adhesive layer, were introduced in the numerical models along the scarf. A geometrical non-linear analysis was performed, using 8-node hexahedral and 6-node pentahedral solid finite elements available in ABAQUS®. Figure 3 shows the mesh at the repaired region for the α=15º repair (b=50 mm). The mesh is particularly refined at the scarf region, with forty elements along L_S, to ensure a bigger refinement at the loci of stress concentrations [7, 8].

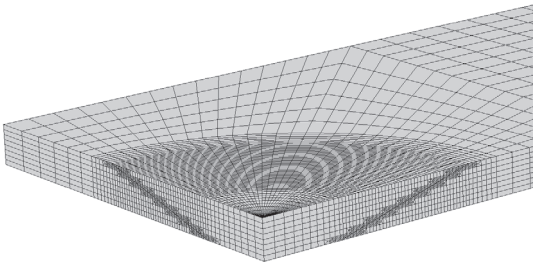

Figure 3. Detail of the mesh at the repaired region.

Thirty elements were considered for ¼ of the patch in the radial direction. At the scarf region, each group of two equally oriented and adjacent plies was modelled with five solid elements. Mesh coarsening was applied to reduce the number of elements outside this region. The laminate and patch were modelled as elastic orthotropic, considering the properties of reference [18].

3. STRENGTH OF THE STANDARD SCARF REPAIRS

Figure 4 shows the load-displacement (P-δ) curves for the different values of α, considering b=50 mm. The values of P and δ are the direct output of the simulations, i.e., considering half-width and half-length of the repairs. The original curves were shifted (Δ=0, 0.05, 0.10 and 0.15 mm) for an easier visualization. An identical stiffness of the repairs and increasing values of P were found with the decrease of α [7, 8].

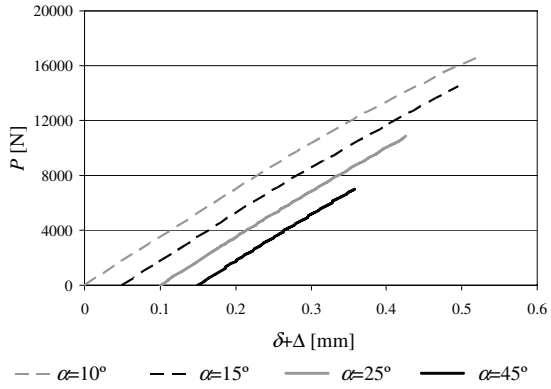

Figure 4. FE P-δ curves for different values of α.

The stiffness reduction near the peak load is due to softening of the adhesive layer, in anticipation of patch debonding. Fracture of the repairs was identical for all the values of α, with a simultaneous fracture of the adhesive at the entire bond near plane ***B*** after localized damage at the IES and OES, propagating swiftly in the radial direction of the scarf up to approximately 45º of plane ***B***. An example of this fracture is presented in Fig. 5 for a α=15º repair (b=50 mm).

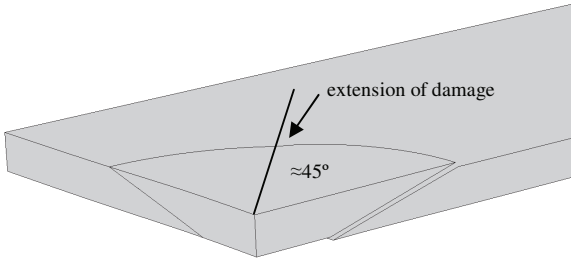

Figure 5. FE failure for a α=15º repair (b=50 mm).

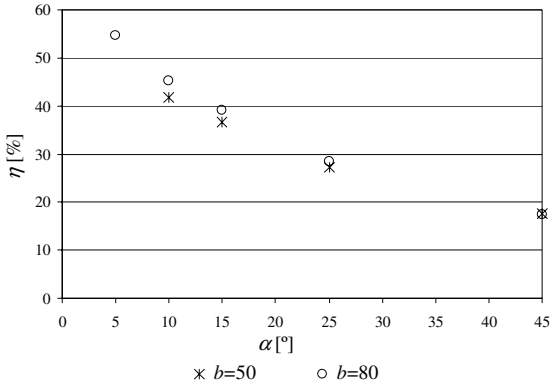

Figure 6. η as a function of α for the repairs with b=50 and 80 mm.

Figure 6 plots the efficiency of the repairs (η) as a function of α for the repairs with b=50 and 80 mm. η is the quotient between the patch debonding onset load and the unnotched composite strength. The failure load was determined by tensile tests on three undamaged specimens with b=15 mm and the same lay-up and thickness of the damaged laminates, giving an average value of failure stress and deviation of 655±134 MPa. For the calculations of η, the average value was considered in the estimation of the failure load for the b=50 and 80 mm undamaged laminates, using the respective cross-sectional areas. In all of the repairs, including in the study of Section 4, it was checked that the failure strength of the 0º and 90º plies was not attained prior to patch debonding onset. The exponential increase of η with the reduction of α is related to the corresponding increase of the bond area [7, 8]. The values of η are slightly bigger for the repairs with b=80 mm, with an increasing difference to the b=50 mm repairs as α diminishes, due to a larger influence of the laminate resistant area at the symmetry plane ***A*** on the global characteristics of the repairs for b=80 mm, since the repair dimensions are similar for a given value of α. The best results are always granted by the smallest value of α, i.e., α=10º for b=50 mm (η≈42%) and α=5º for b=80 mm (η≈55%).

4. STRENGTH OF THE SCARF REPAIRS WITH OVER-LAMINATING PLIES

An alternative to the use of very small values of α, required to fully restore the structure strength, consists on the application of external doublers (or over-laminating plies) adhesively-bonded at the repaired region to protect the patch tips and to provide a larger cross-sectional area at the repaired region, thus increasing the strength of the repairs [19]. These plies are generally very thin and designed to follow the parent structure contour as closely as possible. Although the most efficient solution is to bond over-laminating plies on both the laminate faces [20], a more practical solution consists on their application only on the outer face of the repair (upper surface in Fig. 1) [21]. This choice can also be imposed by accessibility difficulties to the inner face of the composite structure, or be rendered unfeasible for sandwich laminates with composite faces. In the present work, an optimization study was carried out on the influence of using over-laminating plies on the value of η, considering reinforcement only at the outer face of the repair (single reinforcement) and at both faces (double reinforcement). The over-laminate consisted of two plies of circular shape: a 0º ply adjacent to repair surface, covered by a 90º ply. Figure 7 shows the geometry for double reinforcement. Two overlaps with the damaged structure at the outer face (e) were tested for the single reinforcement: 2.5 and 5 mm. For the double reinforcement, only e=5 mm was considered. Bigger values were not considered, to guarantee a minimum clearance with the repair edges for the smallest values of α (for each value of b).

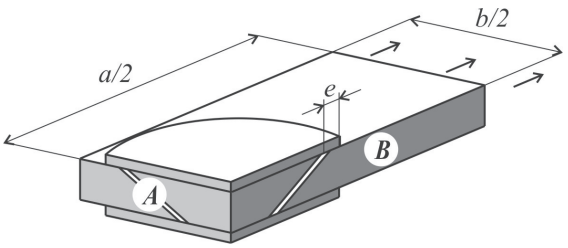

Figure 7. FE idealization of the scarf repair with double reinforcement.

Identical dimensions were considered for the reinforcements on both faces for fabrication simplification purposes and maximum effect of the over-laminates, although the inner face of the repairs may be over-reinforced [20]. Fracture for the different tested solutions depended on the type of reinforcement (single or double) and value of α. For the single reinforcement and bigger values of α, the asymmetry of loading induced by the over-laminating plies led to a slight transverse deflection of the laminate that caused premature crack initiation near plane ***B*** at the IES (unreinforced region). This damage then propagated towards the OES and to the overlap region, simultaneously to radial growth of damage towards plane ***A***. Figure 8 (a) shows damage initiation at the IES for a α=45º repair with b=50 mm and e=2.5 mm.

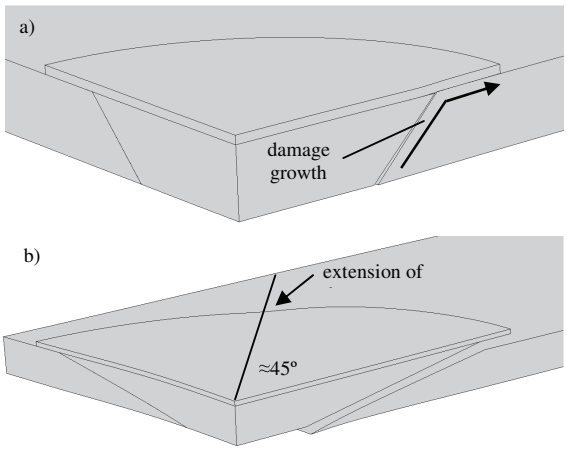

Figure 8. FE failure initiation for a α=45º repair (a) and failure for a α=10º repair (b) (e=2.5 mm, b=50 mm and reinforcement on the outer face).

For the smaller values of α, fracture was simultaneous over the entire bond and overlap region. Although the transverse deflection of the repairs still subsisted, the bigger taper length in the laminate and patch allowed a slight bending of the scarf tips, enough to avoid a premature fracture at the IES. Figure 8 (b) relates to a α=10º repair with b=50 mm and e=2.5 mm.

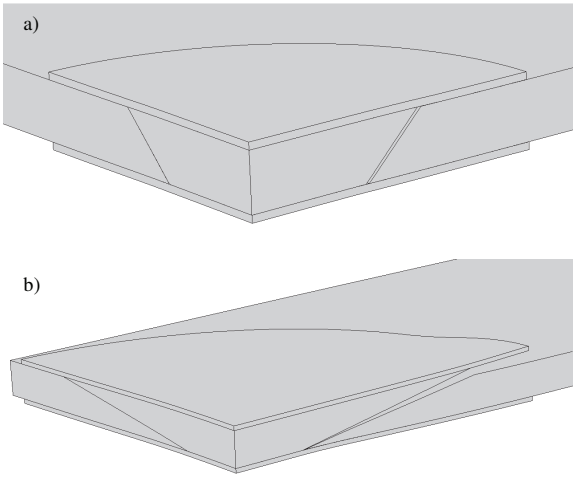

Figure 9. FE failure initiation for a α=45º repair (a) and failure for a α=10º repair (b) (e=2.5 mm, b=50 mm and double reinforcement).

The asymmetry of load induced by the over-laminating plies is prevented using double reinforcement. Thus, for the bigger values of α the entire scarf bond failed simultaneously near plane ***B***, whilst the overlapping plies were kept under load (Fig. 9 a). Increasing further the load causes the detachment of the over-laminate at the outer face, followed by the one at the inner face, both from plane ***B*** towards plane ***A***. For the smaller values of α, the overlap area between the reinforcement plies and the laminate is much larger for the inner plies than for the outer plies, which results on failure along the scarf bond and at the outer over-laminate, whilst the inner one is kept intact (Fig. 9 b). Figure 10 and Fig. 11 plot the values of η as a function of α for the repairs with single and double reinforcement, respectively.

Figure 10 globally shows the exponential trends formerly mentioned, with an increasing difference in the value of η between the *b*=50 and 80 mm repairs with the reduction of α, whose cause was already discussed. The value of *e* showed a large impact on η, with bigger values being recommended on account of higher repair efficiency. This is due to the larger shear resistant area between the laminate and over-laminating plies. The highest efficiency for the *b*=50 mm and 80 mm repairs (single reinforcement) was attained with the α=10º repair (η≈49%) and the α=5º repair (η≈62%), respectively. These results confirm a non-negligible improvement to the standard scarf repair (up to 20%). The results of Fig. 11 (double reinforcement) also evidence an increasing difference of η with the reduction of α between the *b*=50 and 80 mm repairs. The improvement of η was substantial, with the highest values for the *b*=50 and 80 mm repairs being found for the α=10º repair (η≈58%) and the α=5º repair (η≈72%), respectively. These correspond to improvements to the unreinforced repair between 30 and 60%.

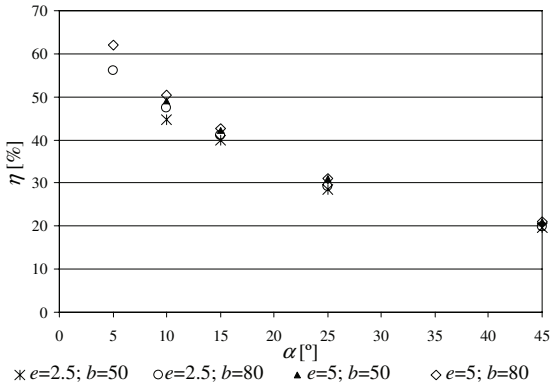

Figure 10. η as a function of α for the repairs with single reinforcement (dimensions in mm).

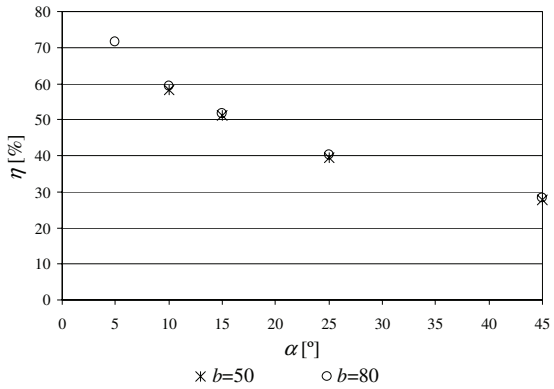

Figure 11. η as a function of α for the repairs with double reinforcement (dimensions in mm).

5. CONCLUDING REMARKS

In this work, a numerical analysis was performed on the tensile behaviour of three-dimensional scarf repairs in carbon-epoxy structures, using a ductile adhesive (Araldite® 2015). The Finite Element analysis was performed in ABAQUS® and used Cohesive Zone Models for the simulation of damage onset and growth in the adhesive layer. Trapezoidal cohesive laws in each pure mode were used to account for the ductility of the adhesive. Validation of the Finite Element methodology used was performed in previous works, which assures the legitimacy of the results. A parametric study was performed on the scarf angle, considering two values of width for the laminates to be repaired. The strength improvement increased exponentially with the reduction of the scarf angle, which implies that small angles are always recommended. The use of over-laminating plies at the outer or both of the repair faces was tested as an attempt to increase the repairs efficiency, which for scarf repairs without over-laminate was close to 50% of the unnotched laminates strength, for the smallest scarf angle. Results showed that efficiencies of approximately

70% of the undamaged strength could be attained by the use of over-laminating plies on both the laminate faces, with maximum improvements from the scarf repairs without over-laminate between approximately 20 and 60%, depending on the scarf angle. Reinforcing only at the outer face of the repair, which may be the only feasible option due to accessing or disassembly difficulties, is also recommended, despite a smaller restitution of strength. Efficiencies above 70% could be achieved using smaller scarf angles than the ones tested, which would imply a larger width of the laminates to be repaired. This work allowed the establishment of principles to design scarf repairs. However, the presented quantitative predictions should be considered valid only for the specific set of conditions selected for the analysis, whilst the generic principles to increase the efficiency of scarf repairs are always recommended.

REFERENCES

[1] Chotard, T.J., Pasquiet, J., Benzeggagh, M.L., "Residual performance of scarf-repaired pultruded shapes initially impact damaged", *Composite Structures*, vol. 53, pag. 317-331, 2001.

[2] Smith, F.C., Moloney, L.D., Matthews, F.L., "Fabrication of woven carbon fibre/polycarbonate repair patches", *Composites Part A: Applied Science and Manufacturing*, vol. 27, pag. 1089-1095, 1996.

[3] Soutis, C., Duan, D.M., Goutas, P., "Compressive behaviour of CFRP laminates repaired with adhesively bonded external patches", *Composite Structures*, vol. 45, pag. 289-301, 1999.

[4] Sato, C., Ikegami, K., "Dynamic deformation of lap joints and scarf joints under impact loads", *International Journal of Adhesion & Adhesives*, vol. 20, pag. 17-25, 2000.

[5] Campilho, R.D.S.G., de Moura, M.F.S.F., Pinto, A.M.G., Morais, J.J.L., Domingues, J.J.M.S., "Modelling the tensile fracture behaviour of CFRP scarf repairs", *Composites: Part B – Engineering*, vol. 40, pag. 149-157, 2009.

[6] Bikerman, J.J., "The science of adhesive joints", New York, USA: Academic Press; 1968.

[7] Wang, C.H., Gunnion, A.J., "On the design methodology of scarf repairs to composite laminates", *Composites Science and Technology*, vol. 68, pag. 35-46, 2008.

[8] Campilho, R.D.S.G., de Moura, M.F.S.F., Domingues, J.J.M.S., "Stress and failure analyses of scarf repaired CFRP laminates using a cohesive damage model". *Journal of Adhesion Science and Technology*, vol. 21, pag. 855-970, 2007.

[9] Kumar, S.B., Sridhar, I., Sivashanker, S., Osiyemi, S.O., Bag, A., "Tensile failure of adhesively bonded CFRP composite scarf joints", *Materials Science and Engineering: B*, vol. 132, pag. 113-120, 2006.

[10] Odi, R.A., Friend, C.M., "A comparative study of finite element models for the bonded repair of composite structures", *Journal of Reinforced Plastics and Composites*, vol. 21, pag. 311-332, 2002.

[11] Campilho, R.D.S.G., de Moura, M.F.S.F., Domingues, J.J.M.S., "Using a cohesive damage model to predict the tensile behaviour of CFRP single-strap repairs", *International Journal of Solids and Structures*, vol. 45, pag. 1497-1512, 2008.

[12] Campilho, R.D.S.G., de Moura, M.F.S.F., Ramantani, D.A., Morais, J.J.L., Domingues, J.J.M.S., "Buckling behaviour of carbon-epoxy adhesively-bonded scarf repairs", *Journal of Adhesion Science and Technology*, vol. 23, pag. 1493-1513, 2009.

[13] Pipes, R.B., Pagano, N.J., "Interlaminar stresses in composite laminates under uniform axial extension", *Journal of Composite Materials*, vol. 4, pag. 538-548, 1970.

[14] Hart Smith, L.J., "Adhesive-bonded scarf and stepped-lap joints", Long Beach, USA: Mcdonnell-Douglas Corp.; 1973.

[15] Qian, Z.Q., Akisanya, A.R., "An experimental investigation of failure initiation in bonded joints", *Acta Materialia*, vol. 46, pag. 4895-4904, 1998.

[16] Campilho, R.D.S.G., de Moura, M.F.S.F., Ramantani, D.A., Morais, J.J.L., Domingues, J.J.M.S., "Tensile behaviour of three-dimensional carbon-epoxy adhesively-bonded single and double-strap repairs", *International Journal of Adhesion & Adhesives*, vol. 29, pag. 678-686, 2009.

[17] Campilho, R.D.S.G., de Moura, M.F.S.F., Domingues, J.J.M.S., Morais, J.J.L., "Computational modelling of the residual strength of repaired composite laminates using a cohesive damage model", *Journal of Adhesion Science and Technology*, vol. 22, pag. 1565-1591, 2008.

[18] Campilho, R.D.S.G., de Moura, M.F.S.F., Domingues, J.J.M.S., "Modelling single and double-lap repairs on composite materials", *Composites Science and Technology*, vol. 65, pag. 1948-1958, 2005.

[19] Whittingham, B., Baker, A.A., Harman, A., Bitton, D., "Micrographic studies on adhesively bonded scarf repairs to thick composite aircraft structure", *Composites Part A: Applied Science and Manufacturing*, vol. 90, pag. 1419-1432, 2009.

[20] Zimmerman, K., Liu, D., "Geometrical parameters in composite repair", *Journal of Composite Materials*, vol. 29, pag. 1473-1487, 1995.

[21] Hamoush, S., Shivakumar, K., Darwish, F., Sharpe, M., Swindell, P., "Defective repairs of laminated solid composites", *Journal of Composite Materials*, vol. 39, pag. 2185-2196, 2005.

MECANISMOS DE DEFORMACIÓN EN LAMINADOS DE MATRIZ POLIMÉRICA: CORRELACIÓN DIGITAL DE IMÁGENES Y MICROMECÁNICA COMPUTACIONAL

L. P. Canal[1], J. M. Molina-Aldareguía[2], C. González[1,2], J. Segurado[1,2], J. Llorca[1,2]

[1]Departamento de Ciencia de Materiales, ETSI Caminos
Universidad Politécnica de Madrid (UPM).
c/ Profesor Aranguren s/n, 28040, Madrid, Spain.
E-mail: : luisp@mater.upm.es

[2]Instituto Madrileño de Estudios Avanzados de Materiales (IMDEA-Materiales).
c/ Profesor Aranguren s/n, 28040, Madrid, Spain.

RESUMEN

Se ha realizado un estudio micromecánico experimental del comportamiento de laminados unidireccionales sometidos a compresión en la dirección perpendicular a las fibras. Se ha empleado la técnica de correlación digital de imágenes para observar la evolución de los campos de desplazamientos y deformaciones en la microestructura del material compuesto. En los contornos de deformación obtenidos experimentalmente se ha comprobado como las fibras tienen una deformación muy pequeña, mientras que las mayores deformaciones se concentran en las zonas de matriz de menor fracción volumétrica de fibras. Simulando por elementos finitos la microestructura estudiada se han reproducido los resultados experimentales, obteniendo distribuciones de campos de desplazamientos y deformaciones muy similares a las observadas experimentalmente.

ABSTRACT

An experimental micromechanical study has been performed to obtain the behavior of unidirectional laminates subjected to transverse compression. The digital image correlation technique was employed to extract the displacement and strain fields developed in the microstructure of the material. The distribution of the strain fields, driven by the different elastic properties between fibers and matrix has been checked. The maximum strains are located in the matrix, meanwhile the fibers remains with a small strain. The real microstructure of the laminate was simulated by the finite element method, the displacement and strain fields obtained from the simulation were very similar to those experimentally observed.

PALABRAS CLAVE: materiales compuestos, correlación digital de imágenes, micromecánica.

1. INTRODUCCIÓN

En la actualidad el estudio del daño en materiales compuestos es uno de los grandes desafíos de la ciencia de materiales. Mientras que en la mayoría de los materiales homogéneos el fallo se produce por la activación de uno o dos mecanismos, en los materiales compuestos el daño se puede producir por la combinación de muy diversos mecanismos. La aparición de un micromecanismo de daño concreto, o la acción combinada de varios, dependerá tanto de las propiedades mecánicas de las fases que componen el material, como del estado de cargas al que esté sometido.

Para los compuestos de matriz polimérica reforzados unidireccionalmente por fibras largas se distinguen al menos cinco mecanismos de fallo diferentes [1]: la deformación del laminado en tensión en la dirección de las fibras ocasiona la rotura de las fibras, en compresión en la misma dirección el laminado falla por pandeo de las fibras. La deformación en tensión en la dirección perpendicular a las fibras produce la rotura frágil de la matriz y la decohesión fibra/matriz, mientras en compresión se puede observar un comportamiento más dúctil, formándose de bandas de cortante en la matriz. Finalmente, la delaminación entre las distintas capas que componen el laminado es a menudo otro importante mecanismo de daño a tener en cuenta.

En los últimos treinta años la utilización de laminados de matriz polimérica ha crecido rápidamente, como resultado de sus excelentes propiedades mecánicas específicas y de la aparición de nuevas técnicas de procesado y control de calidad. Además, los ingenieros han desarrollado nuevas estrategias de diseño para tratar con la naturaleza anisótropa de estos materiales. Sin embargo, aún no existe un criterio de fallo para los

laminados fiable en todos los posibles estados de carga, lo que en muchos casos obliga a sobredimensionar las estructuras con laminados.

Habitualmente, el comportamiento mecánico hasta el fallo de los materiales compuestos se obtiene mediante resultados experimentales, sin atender a los distintos micromecanismos que ocasionan el daño. Recientemente se ha popularizado el uso de la micromecánica computacional para el estudio de estos micromecanismos de deformación y daño. Varios trabajos han demostrado que el comportamiento del material se puede obtener de forma fiable mediante simulaciones numéricas de un elemento del volumen de la microestructura del compuesto [2-4]. Sin embargo, para conseguir buenos resultados numéricos resulta crítico incluir en las simulaciones las propiedades realistas de las distintas fases que componen el compuesto y los diferentes micromecanismos de daño que se pueden producir.

En este trabajo se presenta una novedosa técnica experimental para el estudio del comportamiento micromecánico de materiales compuestos. Mediante la adquisición de imágenes de la microestructura del material compuesto y su evolución durante un ensayo mecánico, esta técnica permite visualizar los microcampos de desplazamientos y deformaciones que se producen en el seno del material. Los datos obtenidos experimentalmente posibilitarán un mejor conocimiento del inicio y propagación del daño en materiales compuesto, además permitirán mejorar y validar los modelos numéricos.

Para este estudio, se escogieron laminados unidireccionales. Todos los ensayos se hicieron en la dirección perpendicular a las fibras, ya que debido a las grandes diferencias en las propiedades mecánicas de las dos fases las deformaciones en el plano transversal son muy heterogéneas. Se realizaron ensayos de compresión porque en la dirección perpendicular a las fibras son estables y se llega a una gran deformación sin que aparezca una rotura frágil del material.

2. TÉCNICA EXPERIMENTAL Y MATERIALES

La correlación digital de imágenes (DIC) es una novedosa técnica experimental para la medida de deformaciones. Al no requerir el contacto con las muestras, la técnica es fácilmente aplicable en numerosos ensayos, como los realizados a pequeñas escalas, a altas temperaturas o a impacto. Además, esta técnica no sólo proporciona la deformación media de una región de interés de la muestra, si no que también es capaz de resolver la evolución de los microcampos de desplazamientos y deformación local en la superficie del material ensayado. Esta habilidad la hace muy atractiva para ser aplicada en materiales heterogéneos, en los que las distintas propiedades mecánicas de las fases producirán campos de deformación claramente no homogéneos.

La técnica de la correlación digital de imágenes fue desarrollada durante los 80 [5,6], y utilizada posteriormente en numerosas aplicaciones, tanto en la investigación como en la industria. Para la aplicación de esta técnica es necesario tomar diversas imágenes de la muestra durante la realización del ensayo, a diferentes niveles de carga. Comparando las imágenes adquiridas, el software de correlación de imágenes (en este trabajo se ha empleado el software comercial VicSNAP, distribuido por Correlated Solutions, Inc.) obtiene los campos de desplazamiento en la superficie de la muestra y a partir de ellos es capaz de obtener los campos de deformaciones. El programa logra seguir los desplazamientos en la superficie de la muestra evaluando el cambio de posición de numerosos grupos de píxeles en base a la escala de grises de la imagen de la muestra deformada. Así, para que el programa pueda distinguir entre los diferentes puntos de la muestra es necesario que su superficie tenga un patrón irregular.

Los ensayos se llevaron a cabo en una micromáquina de tracción-compresión fabricada por Kammrath & Weiss. Está micromáquina está especialmente diseñada para trabajar en el interior del microscopio electrónico de barrido Zeiss Evo MA15. Durante el ensayo se registraron imágenes con 2000 aumentos de la microestructura del material, posibilitando así su posterior correlación. La utilización de esta técnica requiere de imágenes de alta resolución, por lo que su adquisición en el microscopio electrónico de barrido se convierte en un proceso lento, en el que se necesita emplear aproximadamente un minuto por imagen. Este tiempo de adquisición obliga a detener el ensayo de compresión a una determinada carga, esperar unos minutos para que se produzca la relajación del material, y tomar la imagen. A continuación, se vuelve a incrementar la carga hasta el siguiente punto de adquisición de imágenes.

El material ensayado en este trabajo se preparó a partir de pre-impregnados unidireccionales de fibra de vidrio con resina epoxy, concretamente E-glass/MTM 57 de Advanced Composite Group (UK). Con estos pre-impregnados se prepararon paneles de 350 x 300 mm2 que se calentaron a una velocidad de 3ºC/min y consolidaron en autoclave durante 30 minutos a 120º C y 0.64 MPa de presión. Después fueron enfriados al mismo ritmo de 3ºC/min y se suprimió la presión al llegar a los 80º C. La configuración final de los laminados fabricados fue $[0]_{14}$ y la fracción volumétrica de fibras nominal fue del 54%. Los paneles se inspeccionaron tras su procesado para asegurarse que estaban libres de delaminaciones y otros defectos.

De estos paneles se cortaron las muestras en forma de prismas rectangulares para los ensayos de compresión en la dirección transversal a las fibras, las dimensiones finales de las muestras fueron de 2.5 x 2 mm y 1.6 mm de espesor. Para poder observar la microestructura del material en el microscopio electrónico, una de las caras

fue pulida con papel de carburo de silicio (SiC) hasta la lija de 1000 y terminada con soluciones de polvo de diamante hasta 1 μm. El patrón irregular, necesario para aplicar la técnica de correlación de imágenes, se consiguió dispersando sobre la superficie de la muestra partículas de alúmina (Al_2O_3) de 0.5 μm de tamaño medio. Para dispersar las partículas de forma homogénea se realizó una suspensión del 1% en propanol, utilizando yodo (I_2) como agente dispersante. Esta suspensión de partículas se aplicó sobre las muestras ya pulidas, metalizándolas a continuación con Au-Pd, para observarlas en el microscopio electrónico de barrido. En la figura 1 mostramos una de las imágenes adquiridas de las muestras ensayadas. La región de interés en la que se realizó la correlación digital de imágenes aparece dentro del recuadro blanco.

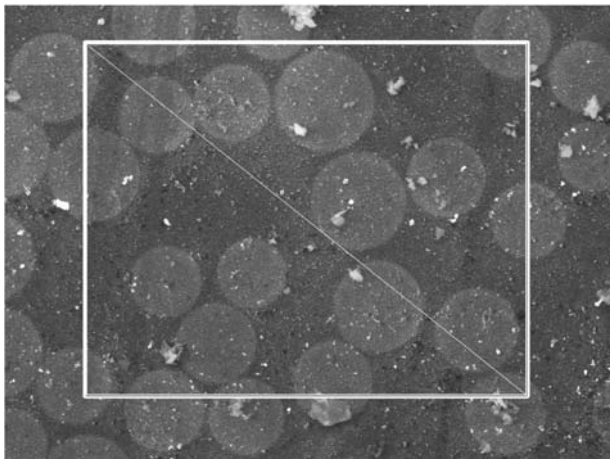

Figura 1. Micrografía de una de las muestras ensayadas y región de interés estudiada. Sobre la superficie se aprecia la dispersión de partículas de alúmina realizada para aplicar la correlación digital de imágenes. La línea que cruza la región de interés representa el camino utilizado posteriormente para representar gráficamente los desplazamientos y deformaciones obtenidos.

3. MODELO NUMÉRICO

La validación numérica de los resultados experimentales se realizó mediante simulaciones por el método de elementos finitos de la microestructura de la región de interés estudiada experimentalmente. Para poder comparar de forma directa la solución numérica con los microcampos de desplazamientos y deformaciones obtenidos utilizando la correlación digital de imágenes, fue necesario generar exactamente la misma microestructura. Para ello, a partir de la imagen del material descargado, se obtuvo el diámetro y la posición inicial de las fibras que componen la región de interés. Con estos datos se pudo reproducir la geometría de la microestructura real del material ensayado. El modelo fue discretizado con elementos cuadráticos de deformación plana (CPE6 y CPE8 en Abaqus [7]). El tamaño de elemento empleado fue suficientemente pequeño para captar los fuertes gradientes en los campos de deformación que se producen en los ligamentos entre fibras. El mallado se realizó utilizando un algoritmo de generación automático disponible en Abaqus CAE. Al final del proceso se obtuvo la malla de elementos finitos mostrada en la figura 2, compuesta aproximadamente por 20000 elementos y 60000 nodos. Los cálculos se realizaron con Abaqus V6.8, en régimen de pequeñas deformaciones.

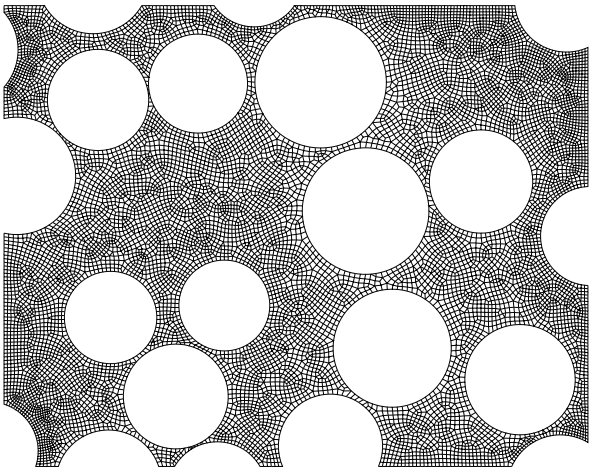

Figura 2. Discretización por elementos finitos de la región de interés estudiada. Las fibras han sido suprimidas para poder observar su posición.

Aunque en la compresión del laminado en la dirección transversal a las fibras aparecen efectos no lineales como la plastificación de la matriz y las decohesiones fibra-matriz, en una primera aproximación no han sido considerados en el modelo numérico, pues el objetivo es reproducir la deformación del laminado para pequeñas cargas, cuando aún todo el material se encuentra en la región elástica. Así, tanto las fibras como la matriz se modelizaron como sólidos lineales, elásticos e isótropos. No se incluyeron elementos cohesivos en las intercaras fibra-matriz, puesto que tampoco se trató de modelizar la decohesión. En la tabla 1 se muestran las propiedades mecánicas utilizadas para modelizar las dos fases del laminado, estas propiedades fueron recopiladas de anteriores trabajos realizados con este material [8].

Tabla 1.Propiedades elásticas de la matriz y las fibras.

	E (GPa)	ν
Fibra de vidrio	74	0.2
Matriz epoxy	3.35	0.35

Para completar el modelo numérico es necesario incluir de forma realista las condiciones de contorno que la compresión del laminado genera en la región de interés estudiada. Esto se consiguió partir de los datos de desplazamientos obtenidos experimentalmente con la correlación digital de imágenes. Mediante un script realizado en MATLAB se impusieron los desplazamientos de cada nodo del contorno del modelo numérico.

4. RESULTADOS

Los contornos de desplazamientos en la dirección de aplicación de la carga, obtenidos con la técnica de correlación de imágenes, se muestran en la figura 3. De estos contornos se podría considerar que la variación de los desplazamientos en el material compuesto se produce de una forma bastante homogénea en toda la región de interés estudiada. Sin embargo, cuando se derivan los campos de desplazamientos para obtener las deformaciones (figura 4) se comprueba que el material se ha deformado de una manera muy heterogénea. Se aprecian claramente mínimos de deformación que se concentran en los lugares ocupados por las fibras, mientra que las máximas deformaciones aparecen en la matriz, en las zonas donde la fracción volumétrica local de fibras es menor. Estos contornos de deformación son fácilmente explicables debido al contraste elástico entre las dos fases que componen el laminado.

Figura 3. Contornos de desplazamientos en la dirección de aplicación de la carga, obtenidos experimentalemente mediante la técnica de correlación digital de imágenes.

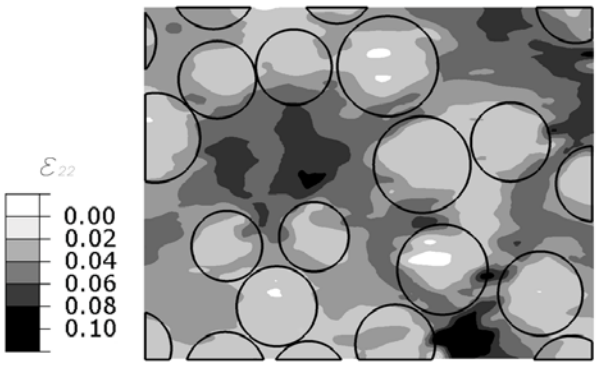

Figura 4. Contornos de deformación en la dirección de aplicación de la carga, obtenidos experimentalemente mediante la técnica de correlación digital de imágenes. La deformación de compresión se ha representado con signo positivo.

En la figura 5 se muestran los contornos de desplazamientos en la dirección vertical obtenidos de las simulaciones por elementos finitos. Al compararlos con los contornos de desplazamientos experimentales (figura 3), se puede observar un extraordinario parecido entre los resultados numéricos y los experimentales. Se comprueba como la forma y la magnitud de los de los contornos de desplazamientos coinciden con gran exactitud.

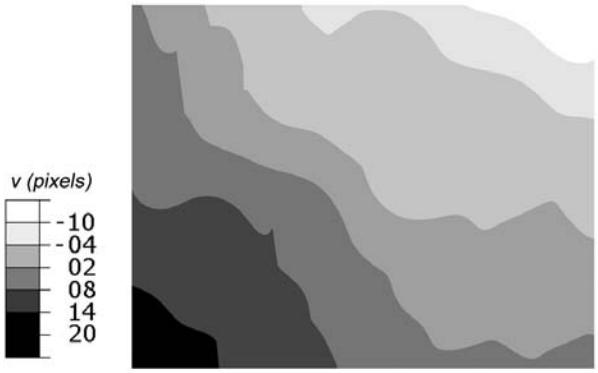

Figura 5. Contornos de desplazamientos en la dirección de aplicación de la carga, obtenidos mediante simulaciones por elementos finitos.

La comparación de los contornos de deformación obtenidos de las simulaciones con los experimentales resulta más compleja. El método de elementos finitos es capaz de recoger los grandes gradientes que se forman entre las fibras y la matriz, mientras que la correlación digital de imágenes obtiene la deformación mediante el gradiente numérico de los campos de desplazamientos, lo que produce un cierto suavizado de los mismos. A pesar de estas diferencias, que afectan principalmente al

valor de los campos en las intercaras fibra-matriz, se puede observar una gran similitud entre los contornos de deformación, en la dirección de aplicación de la carga, experimentales (figura 4) y los obtenidos de las simulaciones por elementos finitos (figura 6).

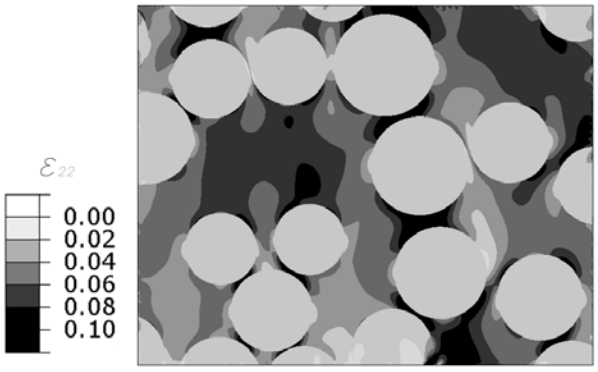

Figura 6. Contornos de deformación en la dirección de aplicación de la carga, obtenidos mediante simulaciones por elementos finitos. La deformación de compresión se ha representado con signo positivo.

Al ser el módulo elástico de las fibras mucho mayor que el de la matriz, la deformación en la dirección de aplicación de la carga (ε_{22}) es mucho más grande en la matriz, quedando las fibras prácticamente sin deformación. Este efecto se puede observar claramente en los contornos de deformación obtenidos mediante las simulaciones numéricas, donde se aprecia que las fibras tienen una deformación homogénea y casi nula, mientras que la práctica totalidad de la deformación es absorbida por la matriz. En los contornos de deformación obtenidos experimentalmente también se puede apreciar este fenómeno. Sin embargo, experimentalmente la correlación digital de imágenes no consigue resolver de una forma tan clara el gradiente de deformaciones que se produce en la interfase fibra-matriz, si no que las deformaciones aparecen suavizadas, con un mínimo de deformación casi nula situado aproximadamente en el centro de la sección transversal de la fibra.

En el contorno de deformación ε_{22} obtenido de las simulaciones también se observa que las máximas deformaciones de la matriz se concentran en zonas entre las fibras orientadas en forma de columna según la dirección de aplicación de la carga. La observación de estos ligamentos es de gran importancia, pues será aquí donde se inicien los micromecanismos de fallo del material. Este efecto no puede apreciarse de una forma clara en los contornos de deformación experimentales, ya que los puntos de máxima deformación son muy pequeños, lo que produce que el programa de correlación digital de imágenes los difumine entre las deformaciones casi nulas de las fibras. Así, para conseguir captar experimentalmente esta concentración de deformaciones se necesitaría tomar imágenes a más aumentos en las zonas donde estas se producirán.

En la figura 7 se representan los desplazamientos en la dirección de aplicación de la carga a lo largo del camino señalado en la figura 1. Se puede comprobar como las gráficas de los desplazamientos experimentales tienen una gran similitud con los obtenidos por simulación. Aunque los desplazamientos experimentales sean un poco más suaves, la posición de todos los máximos y mínimos de desplazamientos coincide por completo.

Las deformaciones en la dirección de aplicación de la carga a lo largo del camino señalado en la figura 1 se recogen en la figura 8. Los máximos de deformaciones localizados en los ligamentos entre las fibras, aparecen en la gráfica obtenida mediante simulaciones como picos muy pronunciados. Aunque experimentalmente sí se aprecia la posición de estos picos, el suavizado que realiza la técnica de correlación digital de imágenes impide obtener los valores de estos picos de máxima deformación. También se comprueba cómo las zonas y los valores de deformación mínima obtenidos experimentalmente, así como los valores medios de deformación a lo largo de todo el camino, son muy similares a los resultados obtenidos de las simulaciones.

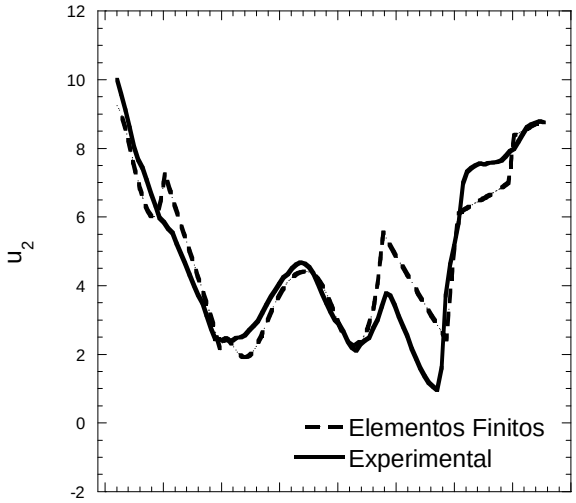

Figura 7. Desplazamientos en la dirección de aplicación de la carga a lo largo del camino señalado en la figura 1.

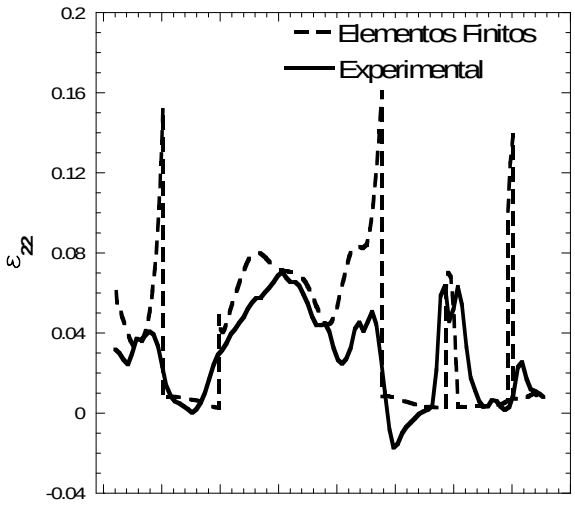

Figura 8. Deformaciones en la dirección de aplicación de la carga a lo largo del camino señalado en la figura 1.

5. CONCLUSIONES

La gran diferencia entre las propiedades mecánicas de las dos fases que componen el material compuesto provoca la aparición de microcampos de deformación muy heterogéneos. La observación de estos microcampos de deformación es de gran importancia, pues determinarán el comienzo del fallo del material. En este trabajo se ha presentado una novedosa técnica experimental para el estudio micromecánico de materiales compuestos. Además, los resultados de esta técnica experimental han sido reproducidos mediante simulaciones micromecánicas por elementos finitos.

Durante la fase experimental se ensayó el laminado unidireccional en compresión en la dirección perpendicular. Estos ensayos se realizaron en el interior de un microscopio electrónico de barrido, lo que permitió adquirir imágenes durante el ensayo de la microestructura del material a distintos niveles de carga. Las imágenes tomadas durante el ensayo posibilitaron la posterior aplicación de la técnica de correlación digital de imágenes. Con esta técnica se pudo comprobar experimentalmente la formación de los microcampos de deformación muy heterogéneos el seno del material.

Para validar la técnica experimental se realizaron simulaciones micromecánicas de la región de interés estudiada experimentalmente. Se pudo comprobar una gran similitud entre los campos de deformaciones observados experimentalmente y los obtenidos de las simulaciones numéricas, probando así el buen funcionamiento de la técnica experimental.

Se ha comprobado que la correlación digital de imágenes es muy adecuada para realizar estudios micromecánicos en materiales compuestos y como esta técnica podrá ser de gran utilidad para posteriores estudios sobre la formación y propagación del daño en este tipo de materiales.

REFERENCIAS

[1] Hinton, M.J., Soden, P.D., Kaddour, A.S. *Failure criteria in fiber-reinforced polymer composites: the World Wide Failure exercise*. Elsevier, 2004.

[2] Cox, B., Yang, Q. *In quest of virtual tests for structural composites*. Science 314, 1102–1107, 2006.

[3] LLorca, J., Segurado, J. *Three-dimensional multiparticle cell simulations of deformation and damage in sphere-reinforced composites*. Materials Science and Engineering A365, 267–274, 2004.

[4] Segurado, J., LLorca, J. *Computational micromechanics of composites: the effect of particle spatial distribution*. Mechanics of Materials 38, 873–883, 2006.

[5] Chu**,** T.C., Ranson**,** W.F., Sutton**,** M.A., Peters**,** W.H. *Applications of digital image correlation technique to experimental mechanics*. Experimental Mechanics 25, 232–244. 1985**.**

[6] Bruck, H.A., McNeill, S.R., Sutton, M.A., and Peters, W.H. *Digital image correlation using Newton–Raphson method of partial differential correction*. Experimental Mechanics 29**,** 261–267, 1989.

[7] Abaqus Users' manual, version 6.8. ABAQUS, Inc. 2008.

[8] Totry, E., González, C., LLorca, J., Molina-Aldareguía, J. M. *Mechanisms of shear deformation in fiber-reinforced polymers: experiments and simulations.* International Journal of Fracture 158, 197-209, 2009.

MECHANICAL BEHAVIOUR OF SANDWICH COMPOSITES WITH DIFFERENT CHARGED FOAM LAYERS

C. Capela[1], J.A.M. Ferreira[2], F.V. Antunes[2], J.D. Costa[2]

[1] CDRsp, Centre for Rapid and Sustainable Product Development, Polytechnic Institute of Leiria,
Morro do Lena - Alto Vieiro,
2400-901 Leiria, Portugal.
E-mail: ccapela@estg.ipleiria.pt

[2] CEMUC, Mechanical Engineering Department, University of Coimbra,
Rua Luís Reis Santos, Pinhal de Marrocos,
3030-788, Coimbra, Portugal.
E-mail: martins.ferreira@dem.uc.pt; fernando.ventura@dem.uc.pt; jose.domingos@dem.uc.pt

ABSTRACT

Hollow glass microspheres are widely used as core material in sandwich construction, particularly in sea water structures, in consequence of their beneficial properties namely: no corrosion effects, design freedom and low density. Microspheres are commercially provided in many different densities, strength and diameter sizes. In the present study a batch of hollow microspheres Verre ScotchitTM-K20 manufactured by 3M was selected along with epoxy 520 resin and hardener 523 to produce the core foams. Two skins were used: net epoxy resin and carbon laminate composite with 2mm thickness, manufactured using twelve woven, balanced, bi-directional, layers of carbon fibres and epoxy resin matrix. Panels sandwich were manufactured using homogeneous and multilayer core foams with the purpose of improving specific flexural stiffness modulus. It was concluded that the panels with carbon reinforced skins exhibit much higher values of strength and stiffness than non-reinforced; multilayered panels with different loads of microspheres (higher percentage of microsphere in the center and lower in the outer) have also higher resistance and stiffness than the panels with homogeneous microsphere percentage core. A tendency to the increase of both properties was observed when the displacement rate increases from 0.5 mm/min to 10 mm/min for all architectures.

KEYWORDS: Composites, sandwich structures, flexure properties, testing.

1. INTRODUCTION

Low-density sheet moulding compounds based in hollow glass microspheres have good properties, namely no corrosion effects and design freedom. Hollow glass microspheres offer also low density and consequent weight reduction. These materials are particularly able to be used as core material in sandwich structures. For this purpose specific monotonic flexural stiffness can be improved using materials with different charged layers: lower density in the centre and standard sheet moulding compounds in the outer layers, according Oldenbo et al [1].

Sandwich structures are widely used in sea water structures, particularly in naval craft. For these applications, both temperature and sea water reduce foam's moduli. However, sea water effect remains confined to a very thin layer near the exposed boundary of the foam and thereby does not degrade its bulk properties [2,3]. A. Siriruk et al [2] estimated the effect of sea water on foam moduli by means of torsional tests on polymeric foams (PVC H100), obtaining degradation of shear modulus and Young's modulus in the saturated region by more than 70% and 60%, respectively. Recently the same authors [4] studied pre-cracked sandwich composite samples, manufactured by a closed cell polymeric foam core and carbon (or glass) fibre reinforced polymeric composite skins, soaked in sea water for extended periods, concluding that the delamination crack propagates close to the interface in the wet case, while it stays within the foam in the dry samples. Also, significant reduction in fracture toughness due to sea water exposure was observed.

At the interfaces among the face sheets of sandwich structures high shear stress gradients occurs as a consequence of the significant different properties of the materials in contact. These regions are critical for design. To prevent premature failures it is necessary to predict accurately the stress fields. High-order models for the analysis of sandwich composites taking into account the core deformability under compression and shear and the stresses continuity at the interfaces are reported, as for example Frostig [5] and Schwarts-Givli et al. [6]. According Fuchiyama et al [7] stress gradient problem in sandwich composites can be reduced by using for core functionally graded materials, with

smooth property variation across the thickness. Recently research in sandwich beams with functionally graded cores has been developed by Sankar [8] and Icardi et al [9].

Panels' behaviour is also influenced by load rate in consequence of microsphere glass foam core compressive properties dependency to strain rate. According P. Li et al [10] both compressive peak and plateau stresses, indicative of fracture resistance and energy dissipation capacity of the foam, respectively, increase almost linearly with the logarithm of strain rate. However, few studies are reported in literature focusing on dynamic properties of glass microspheres syntactic foams, despite their applications at high loading rates. Some examples of these studies are: Woldesenbet et al [11], Capela et al [12] and Song et al [13].

The objective of the present paper is to study the influence of multilayer core foams in the static strength of sandwich panels.

2. MATERIALS PROCESSING AND TESTING

Two types of sandwich panels were manufactured: using homogeneous and multilayer core foams. Hollow glass spheres are commercially provided in many different densities, strength and diameter sizes. The core foams was produced with hollow glass microspheres K20, manufactured by 3M^{TM} (St. Paul, Minnesota; USA), nominally with 50% of particles having diameter lesser than 55 μm. The binding resin was the epoxy 520 and hardener 523 supplied by Ashland Chemical Hispania (Benicarlo, Spain). Two types of face materials were used: epoxy resin and carbon laminate composite with 2mm thickness, the last one manufactured using twelve woven, balanced, bi-directional, layers of carbon fibers, T300 supplied from Toray, and epoxy resin matrix. Core sheets were manufactured by resin transfer molding in vacuum by using an aluminum mould with a rectangular parallelepiped cavity. The mould was cleaned using acetone and treated with a release agent fluid green, methylcyclopropene (MCP). Core sheets with microspheres volume fractions of 19%, 33% and 50% were produced. The panels were manufactured with geometry shown in Fig. 1, using foams sheet layers with 2 mm thickness with different weight fractions adhesively bonded. Skins and core were also bonded. Multilayer core specimens were charged with different formulation layers: lower density in the centre and higher density sheet molding compounds in the outer layers. The specimens were machined from panels with the dimensions of 90x20x12 mm^3 (Fig.1). Five panels' configurations were tested as is summarized in Table 1.

The tests were performed in three-point bending loading with a span of 75 mm, as Figure 2 shows, by using a Shimadzu AG-10 universal testing machine, equipped with a 5kN load cell and TRAPEZIUM software. Fig. 2 shows not only the machine testing and 3PB apparatus and the specimen, but also the ARAMIS technique used to monitor failure evolution. ARAMIS is a non-contact and material independent measuring system providing, for static or dynamically loaded test objects, accurate: 3D surface coordinates, 3D displacements, surface strain values and strain rates.

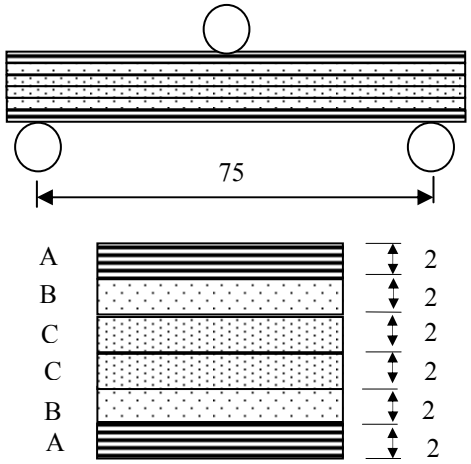

Figure 1. Specimens stacking and dimensions.

Table 1. Summary of the specimen's configuration

Designation	Skin type	Core type	Core Stacking % (in volume)
CHC50	Laminate (C)	Homogeneous (HC)	50/50/50/50
CMC33/50	Laminate (C)	Multilayer (MC)	33/50/50/33
CMC19/50	Laminate (C)	Multilayer (MC)	19/50/50/19
EMC33/50	Epoxy	Multilayer (MC)	33/50/50/33
EMC19/50	Epoxy	Multilayer (MC)	19/50/50/19

The nominal bending stress (σ) was calculated using:

$$\sigma = \frac{3PL}{2bh^2} \tag{1}$$

being P the load, L the span length, b the width and h the thickness of the specimen.

Bending strength was obtained using peak load in equation (1), while the stiffness modulus was calculated by the linear elastic bending beams theory relationship

$$E = \frac{\Delta P \cdot L^3}{48 \Delta u \cdot I} \qquad (2)$$

where I is the inertia moment of the transverse section and ΔP and Δu are, respectively, the load range and flexural displacement range at middle span for an interval in the linear region of load versus displacement plot.

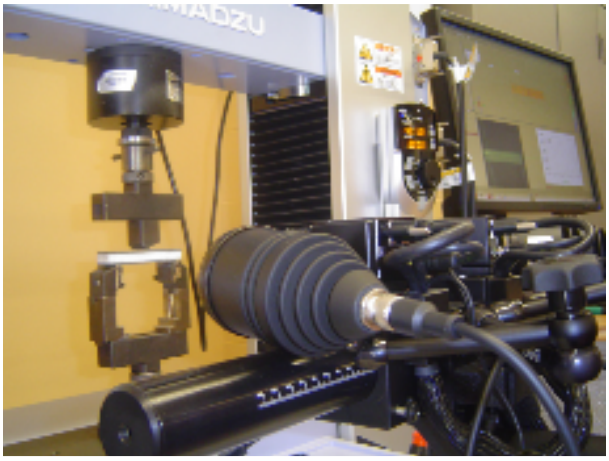

Figure 2. Three-point bending testing apparatus.

3. RESULTS AND DISCUSSION

Fig. 3 a), b) and c) show typical plots of the stress versus bending displacement curves for EMC19/50, CMC19/50 and CHC50 panels, respectively. These curves shows two different aspects which correspond to different failure modes: in epoxy skin panels the failure occurs in the skin and is caused by the bending normal stresses, while in the carbon reinforced panels failure was observed at the foam interlayers as a consequence of shear stress or inside the foam caused by normal stresses. In first case the load increases up to a peak at which occurs an internal break that is followed by a sudden drop of load. The curves for this panel exhibit some nonlinear behavior for high stress level. In the second case the load increase until a peak was obtained corresponding to a core break and a sudden drop of load was observed, but if the displacement continue increasing the load also increase until new core break occurs. Fig. 4a), b) and c) show the aspect and in some cases the evolution of panels failure obtained by ARAMIS technique for EMC19/50, CMC33/50 and CHC50, respectively. These photos confirm the failures modes before indicated.

The displacement rate of the tests influences the values of the stiffness and of the maximum load, but does not influence significantly the aspect of the stress versus displacement curves.

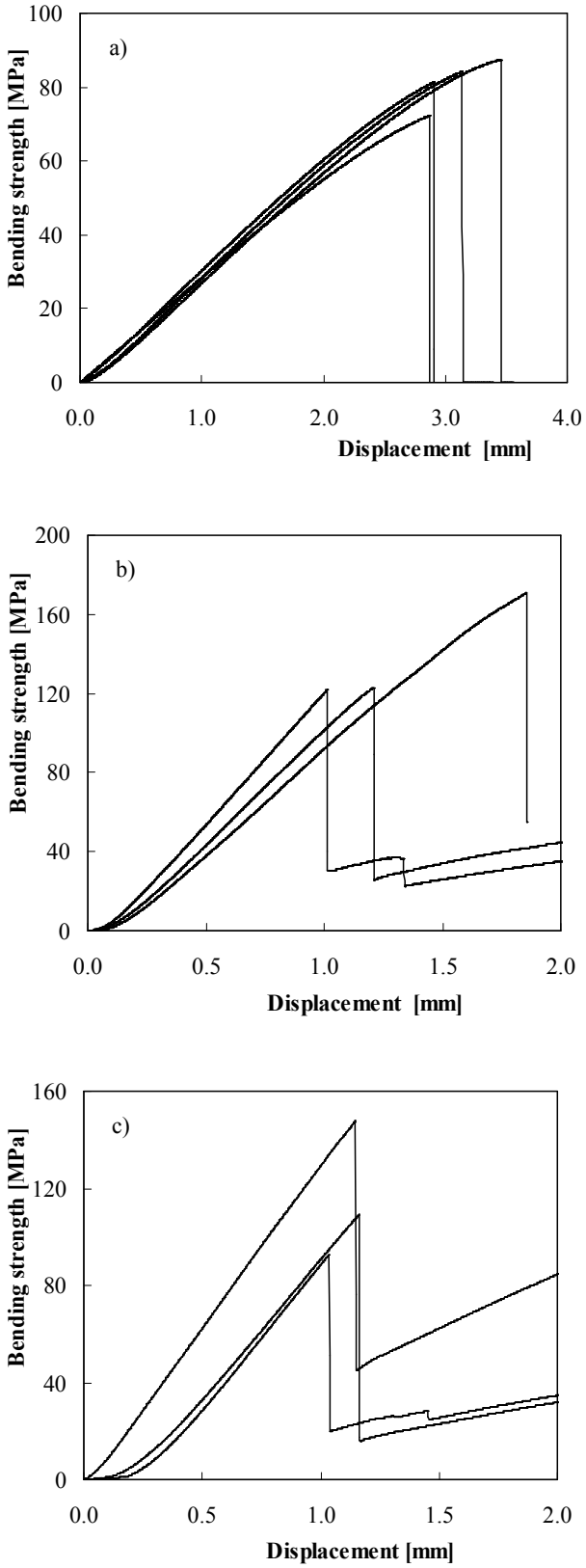

Figure 3. Stress versus displacement curves: a) EMC19/50 b) CMC19/50 c) CHC50 panels.

For each test the stiffness modulus was obtained by linear regression of the load versus displacement curves considering a loading segment ranging from load zero and the maximum displacement value corresponding to a correlation factor at least 99%. Stiffness was calculated using equation (2). The bending strength was calculated for each test using equation (1) for the load corresponding to the first peak of load versus displacement curves.

The average values of the stiffness and bending strength obtained for each test condition are shown in Table 2 and plotted against the displacement rate in Figures 5 and 6, respectively.

In spite the high dispersion obtained for these tests, particularly for those carried out in outer carbon reinforced skins, it can be unequivocally concluded that: the panels with carbon reinforced skins show values of strength and stiffness much higher than non-reinforced ones and the multilayered panels with different microspheres fractions have higher resistance and stiffness than the panels with single foam core. Both properties tend to increase when the displacement rate increases from 0.5 to 10 mm/min.

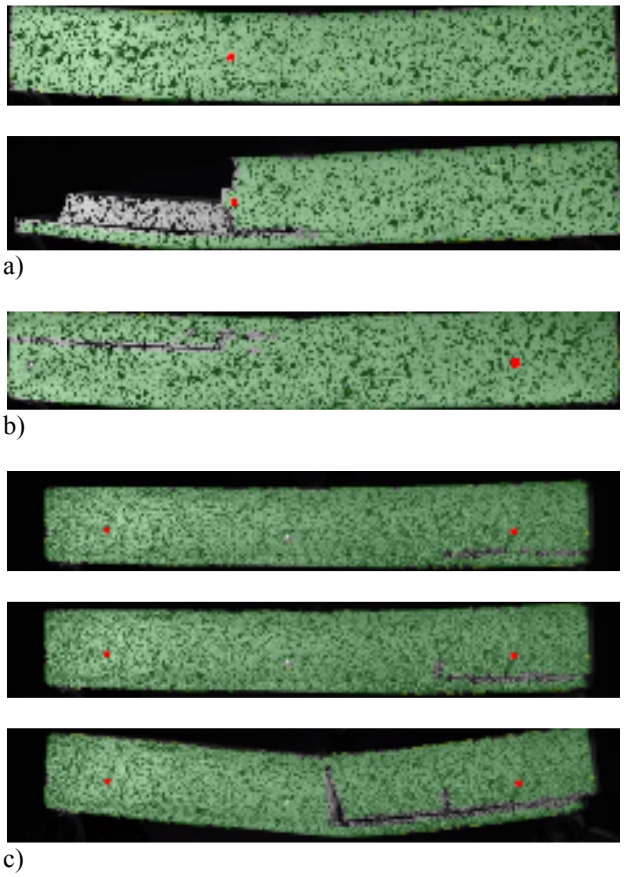

Figure 4. Failure evolution: a) EMC19/50 b) CMC33/50 c) CHC50 panels.

Table 2. Summary of test conditions and average values of the stiffness and strength

Designation	Load Rate (mm/min)	Stiffness (GPa)	Flexural Strength (MPa)
CHC50	10	9305.5	104.1
	0.5	8349.5	85.6
CMC33/50	10	9888.1	113.5
	0.5	8603.5	95.6
CMC19/50	10	10369.8	120.0
	0.5	9135.4	114.3
EMC33/50	10	2472.0	60.0
	0.5	2375.4	52.9
EMC19/50	10	2492.6	88.5
	0.5	2278.0	81.3

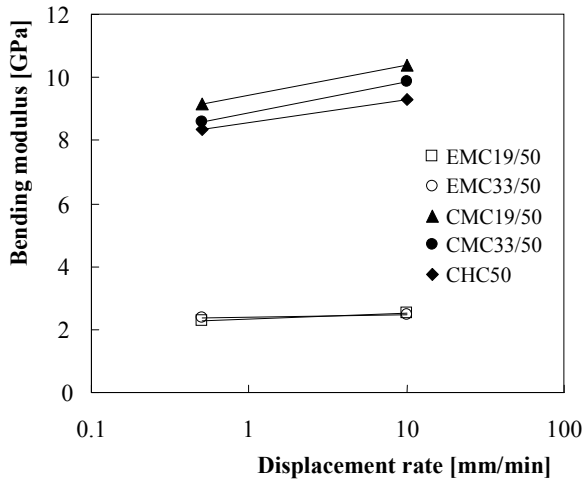

Figure 5. Average stiffness versus displacement rate.

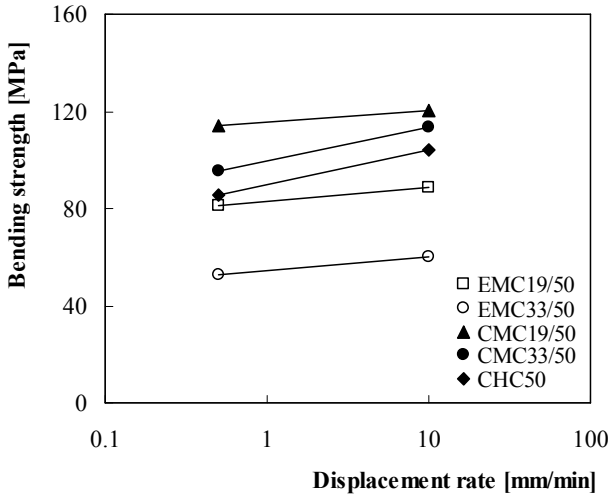

Figure 6. Average strength versus displacement rate.

A 2D numerical model was developed in order to understand the experimental results obtained for the sandwich composites. Only half-specimen was studied with adequate boundary conditions. Figure 7 illustrates the finite element mesh, composed of 21895 linear isoparametric elements and 22312 nodes, the deformed shape and the boundary conditions.

Six layers with distinct material properties were considered. Both the core and the skin of the sandwich composite were assumed to be homogeneous and isotropic with the Young's modulus indicated in table 2. The compressive properties of syntactic foam are slightly different from tension properties, therefore different properties were considered above and below half height of the specimen.

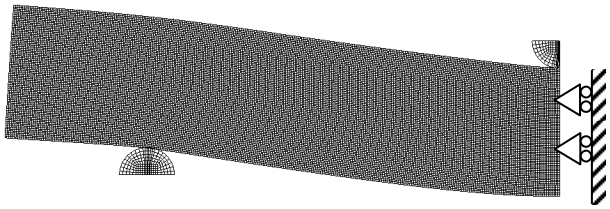

Figure 7. Finite element mesh and deformed shape (x5) (plane strain, F=2000N)

Table 2. Material properties in the numerical model.

Layer	CMC 19/50	E (GPa)	CHC 50	E (GPa)
6	Laminate	58	Laminate	58
5	Foam (19%)	1.24	Foam (50%)	1.12
4	Foam (50%)	1.12	Foam (50%)	1.12
3	Foam (50%)	1.79	Foam (50%)	1.79
2	Foam (19%)	2	Foam (50%)	1.79
1	Laminate	58	Laminate	58

Figure 8 shows the load versus displacement curves for the CMC 19/50 and CHC 50 composites. The stiffness showed variations of 3.1 %, when the volumetric fraction of particles was increased from 19 to 50% in two of the syntactic foam layers. Notice that the global stiffness is mainly controlled by the skin in these composites. The sudden drops of figure are not observed because this preliminary numerical model does not predict failure.

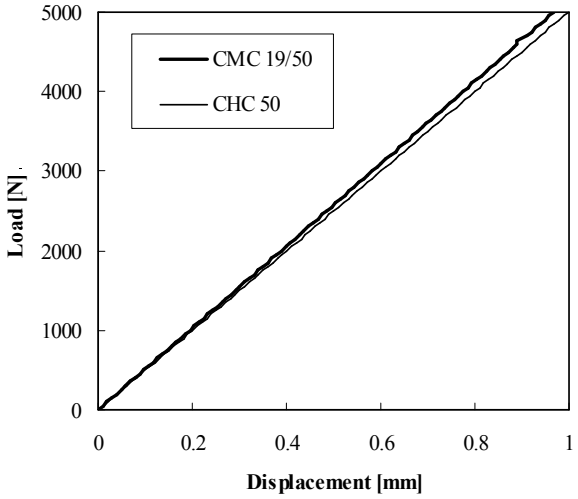

Figure 8. Force versus displacement curves.

Figure 9 shows stresses measured along the thickness of specimen. τ_{xy} was measured at the symmetry line of the specimen, while σ_{yy} was obtained at a distance of 10 mm from central line. The vertical stresses are compressive, as could be expected, and have the highest value near the central pin where the bending stresses had to the contact stresses. The shear stress no longer shows the influence of central pin having maximum values of 5.4 MPa in the section studied. Figure 10 shows the stresses measured along a longitudinal line of the specimen. The line considered is at y=9mm, therefore is the central line of the foam layer immediately below the upper skin. The stresses show a wavy behaviour., where the influence of the central pin is evident for the highest values of d.

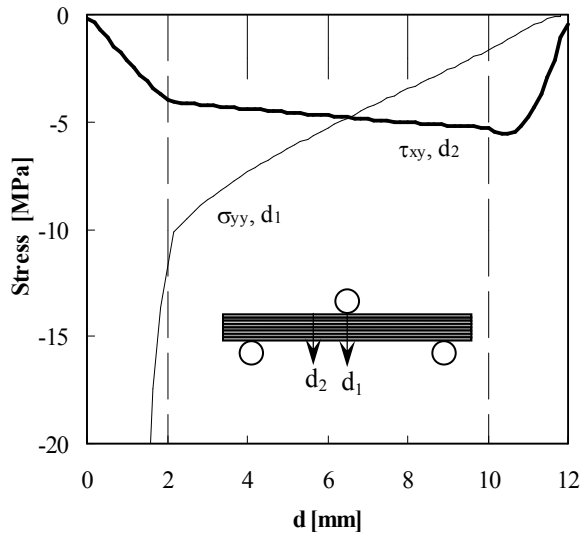

Figure 9. Stress field along thickness.

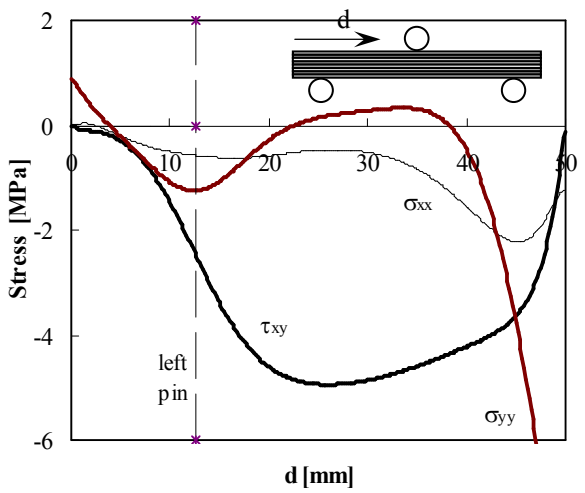

Figure 10. Stress field along longitudinal line.

4. CONCLUSIONS

The bending stiffness and strength of sandwich panels manufactured using homogeneous core and multilayer core foams were obtained. The main conclusions are that: the panels with the skins reinforced with carbon exhibits much higher values of strength and stiffness than non-reinforced; multilayered panels with different loads of microspheres (higher percentage of microsphere in the center and lower in the outer) have also higher resistance and stiffness than the panels with homogeneous microsphere percentage core. A tendency to increasing on both properties was observed when displacement rate increases from 0.5 mm/min to 10 mm/min for the architectures of the panels.

ACKNOWLEDGMENTS

The authors thank Portuguese Foundation to Science and Technology for funding this work, Project nº PTDC/EME-PME/66549/2006.

REFERENCES

[1] M. Oldenbo, S.P. Fernberg, L.A. Berglund, *Mechanical behaviour of SMC composites with toughening and low density additives*, Composites Part A: Appl. Sci. and Manuf., Vol. 34, pp. 875-885, 2003.

[2] A. Siriruk, Y. J. Weitsman, D. Penumadu, *Polymeric foams and sandwich composites: Material properties, environmental effects, and shear-lag modeling*, Composites Science and Technology, Vol. 69, pp. 814–820, 2009.

[3] Li X, Weitsman YJ. *Sea water effects on foam cored composite sandwich layups*, Compos Part B, Vol. 35: pp. 451–459, 2004.

[4] A. Siriruk, D. Penumadu, Y. J. Weitsman, *Effect of sea environment on interfacial delamination behavior of polymeric sandwich structures*, Composites Science and Technology, Vol. 69, pp. 821–828, 2009.

[5] Frostig Y. *Classical and high-order computational models in the analysis of modern sandwich panels*, Composites, Part B: Eng, Vol. 34: pp. 83-100, 2003.

[6] Schwarts-Givli H, Rabinovitch O, Frostig Y. *High-order nonlinear contact effects in the dynamic behaviour of delaminated sandwich panels with a flexible core*, Int J Solids Struct, Vol. 44: pp. 77–99, 2007.

[7] Fuchiyama T, Noda N. *Analysis of thermal stress in a plate of functionally gradient material*, JSAE Rev, Vol. 6: pp. 263- 268, 1995.

[8] Sankar BV. *An elasticity solution for functionally graded beams*. Compos Sci Technol., Vol. 61, pp. 689-696, 2001.

[9] U. Icardi, L. Ferrero, *Optimisation of sandwich panels with functionally graded core and faces*, Composites Science and Technology, Vol. 69, pp. 575–585, 2009.

[10] P. Li, N. Petrinic, C.R. Siviou, R. Froud, J.M. Reed, *Strain rate dependent compressive properties of glass microballoon epoxy syntactic foams*, Materials Science and Engineering A, Vol. 515, pp. 19-25, 2009.

[11] Woldesenbet E, Gupta N, Jadhav A., *Effects of density and strain rate on properties of syntactic foams*, Journal of Materials Science, Vol. 40 (15), pp. 4009-4017, 2005.

[12] C. Capela, J.D. Costa, J.A.M. Ferreira, *Test conditions effect on the fracture toughness of hollow glass micro-sphere filled composites*, Strain-An International Journal for Experimental Mechanics, Vol. 44 (2), pp. 141-146, 2008.

[13] Song, B; Chen, W W; Lu, W Y, *Mechanical characterization at intermediate strain rates for rate effects on an epoxy syntactic foam*, International Journal of Mechanical Sciences, Vol. 49 (12), pp. 1336-1343, 2007.

STUDY OF CRACK ONSET AT HOLES IN PMMA. DIFFICULTIES IN CHARACTERIZING THE MATERIAL

A. Leite [1,2], V. Mantič [1], F. París [1]

[1] Grupo de Elasticidad y Resistencia de Materiales, E.T.S. de Ingenieros
Universidad de Sevilla, Camino de los Descubrimientos s/n
E-41092 Sevilla, España
E-mail: mantic@esi.us.es, paris@esi.us.es

[2] Departamento de Engenharia Mecânica
Instituto Superior de Engenharia de Lisboa
Rua Conselheiro Emídio Navarro,1, 1959-007 Lisboa, Portugal
E-mail: leite@dem.isel.ipl.pt

ABSTRACT

There is still not full confidence in the capability of the actual failure criteria for composites to predict satisfactorily either the onset of the damage in form of cracks or the crack propagation in these materials. Finite Fracture Mechanics (FFM) introduces a new approach to characterize crack onset and may afford a new insight into the analysis of the failure mechanisms in composites. In the present initial work, FFM concepts are applied to characterize damage in a simple configuration, comparing semianalytical predictions with the experimental results obtained. A rectangular plate with a central hole subjected to uniaxial tension at the outer boundary is studied with the objective to elucidate the size effect in failure load, by testing for several hole diameters. The plate material is polymethyl metacrylate (PMMA). The influence of testing parameters such as test velocity on the material characterization is also studied and discussed.

KEY WORDS: crack initiation, stress concentration, Finite Fracture Mechanics, PMMA, composites.

1. INTRODUCTION

Although the Composite Materials applications in the aeronautical industry have considerably increased in recent years, there is still not full confidence in the capability of the actual failure criteria for composites to predict satisfactorily either the onset of the damage in form of cracks or the crack propagation in these materials. New micro- and meso-mechanical studies are required to understand in depth the failure mechanisms in composite materials. Finite Fracture Mechanics (FFM) [1] introduces a new approach to characterize crack onset and may afford a new insight into the analysis of these failure mechanisms. As an ultimate objective of this work, the authors want to apply this formulation to study theoretically and experimentally the onset and propagation of a crack in composite materials on micro-level, namely the problem of the fiber-matrix debonding [2].

In order to achieve an in-depth understanding of the crack onset phenomena, such an analysis is first carried out by applying the FFM concepts to a simple configuration of a plate with a central hole subjected to uniaxial tension at the outer boundary [3], shown in Figure 1. This is used to elucidate the size effects in failure load by testing for several hole diameters. Thus, one of the objectives of this initial work is to clarify the role of parameters that control the appearance of damage and its initial growth in originally undamaged specimens.

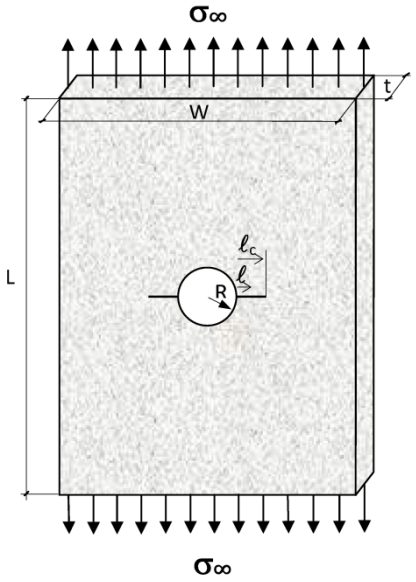

Figure 1. Geometry of the plate with hole and emanating cracks.

The plate height is denoted by L; the width by W, the thickness by t, the hole radius by R, the emanating cracks length at onset by ℓ_c, the intermediate crack lengths by ℓ, the applied remote tension by σ^∞ and the critical remote tension causing the crack onset by σ_c^∞.

The failure criterion proposed is explained in Section 2. The carried out experimental program is described in Section 3, including in the first parts the specimen preparation, the determination of tensile and fracture properties of the material used (polymethyl metacrylate, PMMA), and also observed difficulties. In the last part of this section, the study of crack onset at a hole is presented. First, specimen fabrication and testing are discussed, and then the test results are presented and compared with the FFM predictions. Finally, a discussion of the obtained results and conclusions are given.

2. FAILURE CRITERIA

2.1. Tensile stress criterion

The tensile stress criterion assumes the existence of a critical tension σ_c (material tensile strength), and uses the well known Kirsch's expression for stresses along the symmetry axis of the infinite plate with a circular hole perpendicular to the load. Then, in view of the notation introduced in Figure 1, and assuming that two cracks of the length ℓ_c will abruptly initiate at the hole boundary in the direction perpendicular to the load, the remote critical stress σ_c^∞, should accomplish the following inequality:

$$\sigma_c \le \frac{\sigma_c^\infty}{2}\left(2+\frac{R^2}{(R+\ell)^2}+3\frac{R^4}{(R+\ell)^4}\right),\ \ 0 \le \ell \le \ell_c \qquad (1)$$

2.2. Incremental energy criterion

The following inequality represents the necessary energetic condition for the onset of a crack of the finite length ℓ_c:

$$\int_0^{\ell_c} G(\ell) t d\ell \ge G_c t \ell_c \qquad (2)$$

The energy released during the crack abrupt onset is given by the integral of G (Energy Release Rate, ERR) on the left-hand side of this inequality, whereas the energy required for this crack onset is given by the expressions on its right-hand side, where G_c. is the critical energy release rate.

The stress intensity factor in fracture Mode I, K_I, for two cracks of the length ℓ emanating from a hole, is given by the well known Newman's expression:

$$K_I = \sigma^\infty \sqrt{\pi \ell}\left(1+0.5\frac{R}{R+\ell}\right)\left[1+1.243\left(\frac{R}{R+\ell}\right)^3\right] \qquad (3)$$

Then, the well-known Irwin's relation between the ERR, G, Young Modulus, E, and K_I,

$$G = \frac{{K_I}^2}{E'} \qquad E' = \begin{cases} E & \text{Plane Stress} \\ \frac{E}{(1+\nu^2)} & \text{Plane Strain} \end{cases} \qquad (4)$$

can be substituted into inequality (2).

2.3. Coupled stress and energy criterion

Taking into account that tensions are decreasing with the distance from the hole, the stress criterion (1) leads to the following condition for the critical crack length ℓ_c and the critical remote load σ_c^∞ :

$$\sigma_c^\infty = \frac{2\sigma_c}{\left(2+\frac{R^2}{(R+\ell_c)^2}+3\frac{R^4}{(R+\ell_c)^4}\right)} \qquad (5)$$

Due to the dependence of G on the square of K_I, and consequently on the square of σ^∞, and taking into account that G is increasing with ℓ, the energy criterion (2) leads to another condition for the critical crack length ℓ_c and the critical remote load σ_c^∞ :

$$(\sigma_c^\infty)^2 \int_0^{\ell_c} \hat{G}(\ell) d\ell = G_c \ell_c \qquad (6)$$

where $G = (\sigma^\infty)^2 \hat{G}$. By considering a coupled criterion defined by conditions (5) and (6), we obtain the system of two nonlinear equations for two unknowns σ_c^∞ and ℓ_c. Eliminating σ_c^∞ from the system we arrive to the following nonlinear equation for the unknown ℓ_c:

$$\left(\frac{2\sigma_c}{\left(2+\frac{R^2}{(R+\ell_c)^2}+3\frac{R^4}{(R+\ell_c)^4}\right)}\right)^2 \int_0^{\ell_c} \hat{G}(\ell) d\ell - G_c \ell_c = 0 \qquad (7)$$

This equation can be solved numerically, for example using *Mathematica* package. Once the value of ℓ_c is computed, the corresponding value of σ_c^∞ is easily obtained from equation (5).

3. EXPERIMENTAL PROGRAM

3.1. Tensile Properties

The plate material is polymethyl metacrylate (PMMA). In order to define PMMA elastic properties, we have used standard ASTM D638-03 [4] as guideline.

If the specimen thickness is less than 7 mm type I specimen geometry should be used, as shown in Figure 2. If it is higher than this value type III should be used. The basic difference in these types is the width (and consequently other dimensions). The width for type I is 13 mm and for type III is 19 mm.

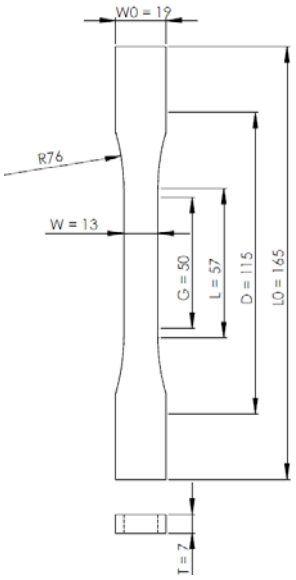

Figure 2. Tension specimen (type I - ASTM D638-03).

The plate of PMMA used to fabricate the specimens had an average maximum thickness of 7 mm. Thus, five specimens of type I were manufactured. In each specimen bidirectional strain gages (one in the longitudinal and the other in transversal direction) were glued to test for the Young modulus, Poisson coefficient and ultimate failure load. Although the standard defines as mandatory to test PMMA at 5 mm/min, this first batch was tested at the velocity of 0.5 mm/min in a electromechanical INSTROM test machine with load cell of 100 kN, equipped with an extensometer. The specimen mounted in the machine is shown in Figure 3.

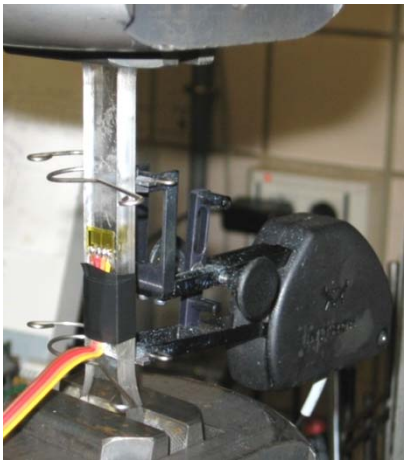

Figure 3. Tension test specimens (type I).

The test results obtained using this velocity are presented in Table 1. The specimens after rupture are shown in Figure 4. The average value of the ultimate failure load was, without taken into account the coupon number 3, σ_c=33.8 MPa.

The stress-strain curves obtained using the longitudinal strain gages, are shown in Figure 5.

Table 1. Test results for tensile specimens type I, tested with 0.5 mm/min.

Spec. No.	Rupture Load [N]	Area [mm^2]	σ_c [MPa]	Observation
1	2557.5	91	28.1	
2	3936.8	91	43.3	
3	2185.7	91	24.0	Broken out of the test length
4	2849.8	91	31.3	
5	2970.5	91	32.6	

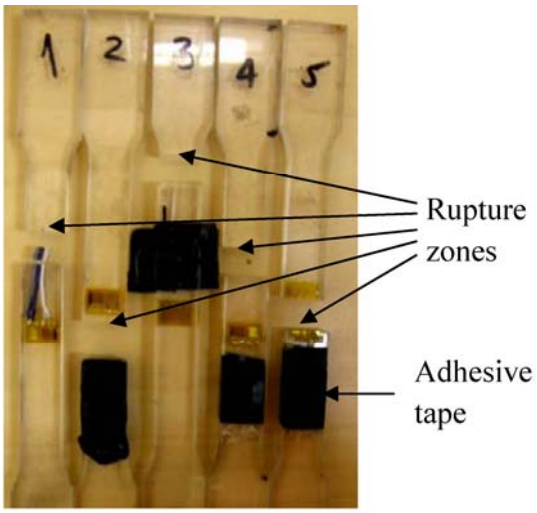

Figure 4. Tension test specimens (type I). Tested at 0.5 mm/min.

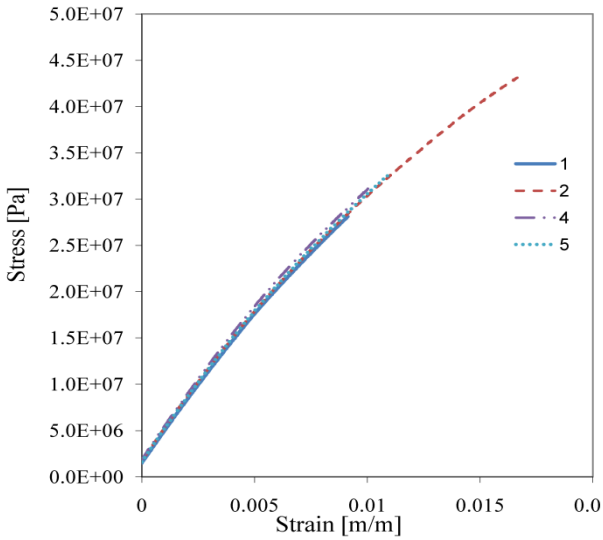

Figure 5. Stress-strain curves obtained from specimens (type I - ASTM D638-03). Tested at 0.5 mm/min.

One can see from Figure 5 that the linear elastic approximation is reasonable for this material. It is also

possible to observe its brittle fracture. The calculated average Young modulus was E=2.85 GPa, and Poisson ratio ν=0.34. These values are within the published PMMA properties, but the ultimate stress σ_c=33.8 MPa seemed to be too much low (less than half of the usual).

Thus, new five, type I, coupons were fabricated and tested now at 5 mm/min velocity (without strain gages). All the specimens broke at the filleted machined parts, invalidating the results. These led us to the decision to manufacture straight specimens (without tabs and strain gages). The results were surprising: the average ultimate stress was more than double (σ_c=73.15 MPa) as shown in Table 2.

Table 2. Test results for straight tensile specimens of type I, tested with 5 mm/min.

Spec. Nr.	Rupture Load [N]	Area [mm^2]	σ_c [MPa]
1	6273.32	84.8	74.4
2	6130.87	82.9	74.0
3	6335.41	87.0	72.8
4	6324.02	87.0	72.6
5	6230.8	86.1	72.3

To see if there were any difference due the change from type I to III, as the specimen thickness was on the limit between the two types, three specimens with 7.05 mm thickness were tested and the results are shown in Table 3, with an average of σ_c=72.7 MPa.

Table 3. Test results for straight tensile specimens of type III, tested with 5 mm/min.

Spec. Nr.	Rupture Load [N]	Area [mm^2]	σ_c [MPa]
1	9974	136.1	73.3
2	9956	136.1	73.2
3	9721	135.7	71.6

3.2. Fracture Properties

To obtain fracture toughness one can use the standard ASTM D5045-07 [5] to design Compact Tension (CT) specimens. In plastics, in general, the main difference to metals in fracture testing is that the natural initial crack cannot be easily made by fatigue cycling, due to the fragility of the specimen. Thus the standard advises making the natural crack by tapping a fresh razor blade into the specimen (with a hammer for example) or if this is not possible, by sliding with the blade into the machined notch. The usual dimensions of CT for our case are B=7 mm; W=4B=28 mm and a=14 mm (machined notch plus natural crack).

To fix the razor blade vertically in order to hammer it against the CT coupon, a jig was necessary. After some research [6-7] that involved hammering, pressing, and drop of a dead weight, the option to tapping our jig with the hammer [6] was taken, as shown in Figure 6. As justified by [6] and other authors, obtaining the natural crack by fatigue, sliding or pressing a razor blade gives higher stress intensity factors, which can induce in erroneous fracture properties.

First nine CT coupons were made using tapping, but that task was not easy because the blade usually collapsed by buckling, as can been seen in Figure 7.

Figure 6. Razor blade support device and application into CT-fracture specimen.

Figure 7. Razor blade damaged after tapping operation.

Then other blades, thicker than the initial razor blades, were adopted, and the crack generation was successful, as shown in Figure 8.

Figure 8. CT-fracture specimen with a successfully obtained natural crack.

To date it was not possible to test for fracture toughness because of necessity of carefully mounted CMOD strain gage and a sufficiently small load cell for such a small CT specimen not available in our laboratory. In virtue of lack of time, we have decided to use three representative values for the range of K_{Ic} for PMMA from [8].

3.3. Crack onset at holes

To study the crack onset in holes, coupons with 300 mm long and 50 mm width with different hole sizes were machined. The hole diameters made were 10, 5, 3, 2, 1 and 0.5 mm. Initially five coupons for each group of diameters were fabricated, but after several machining and testing difficulties, like rupture in the filleted zones, as seen in Figure 9, only four successfully tested coupons for each group have been achieved. Some of the specimens were fabricated as straight with 40 mm width (without fillets). The test velocity was 0.5 mm/min because these tests were initiated before the second and third batches of tensile tests. The test results are shown in Table 4.

Table 4. Test results for plates with holes.

Speci-men	Max Load	Width	Thick-ness	$\sigma_c^\infty / \sigma_c$	
Ø-Nr.	[kN]	[mm]	[mm]	σ_c = 33.8 [MPa]	σ_c = 73.15 [MPa]
10-1	11.3	49.93	6.88	0.98	0.45
10-2	11.3	49.98	6.85	0.98	0.45
10-3	11.0	50.03	7.04	0.92	0.43
10-4	11.6	49.90	7.00	0.98	0.45
5-1	14.0	49.95	6.93	1.19	0.55
5-2	13.9	50.03	6.76	1.22	0.56
5-3	14.3	50.19	7.11	1.18	0.55
5-4	14.1	50.07	7.08	1.17	0.54
3-1	14.3	50.02	7.08	1.19	0.55
3-2	13.8	49.98	6.81	1.20	0.56
3-3	11.2	49.91	6.30	1.05	0.49
3-4	14.7	49.54	6.15	1.42	0.66
2-1	11.5	40.40	6.22	1.35	0.62
2-2	11.8	40.75	6.34	1.35	0.62
2-3	11.1	40.70	6.15	1.31	0.61
2-4	11.9	40.29	6.22	1.41	0.65
1-1	11.6	39.89	6.38	1.34	0.62
1-2	13.1	40.12	6.17	1.56	0.72
1-3	12.6	40.44	6.18	1.49	0.69
1-4	12.1	40.50	6.13	1.44	0.66
0.5-1	14.4	40.10	6.48	1.64	0.76
0.5-2	14.4	40.13	6.54	1.62	0.75
0.5-3	14.3	39.85	6.79	1.56	0.72
0.5-4	16.1	40.03	7.27	1.63	0.75

Figure 10 shows the rupture for the case of a 5 mm hole. All the ruptures were instantaneous.

Figure 9. Plate with 3 mm diameter hole, after rupture near the filleted zone (and not at the hole).

Figure 10. Plate with 5 mm diameter hole, after rupture.

In Figure 11 a rupture in a 0.5 mm hole is shown, that-produced a vertical crack that can be seen in the top half of the hole. This unusual type of crack appeared in the 0.5 mm and in two of the 1 mm diameter holes,

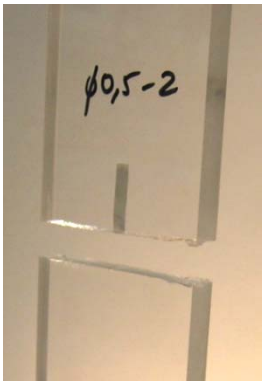

Figure 11. Plate with 0.5 mm diameter hole, after rupture.

In last two columns of Table 1 it can be seen the critical remote load, normalized by the ultimate stress $\frac{\sigma_c^{\infty}}{\sigma_c}$, for the two σ_c obtained from the tensile tests, in order to compare with the FFM predictions. In the latter, plane strain was adopted in calculations, because of the noticeable thickness of the specimens when compared to hole diameters. Three curves were generated by FFM calculations for each σ_c obtained taking different values for K_{Ic} for PMMA material from [8], with the lower, the medium and the higher values (0.8; 1.275 and 1.75 MPa.$\sqrt{m}$). In Figures 12 and 13 comparisons of the experimental results with the FFM predictions can be seen for σ_c=33.8 MPa and σ_c=72.15 MPa, respectively.

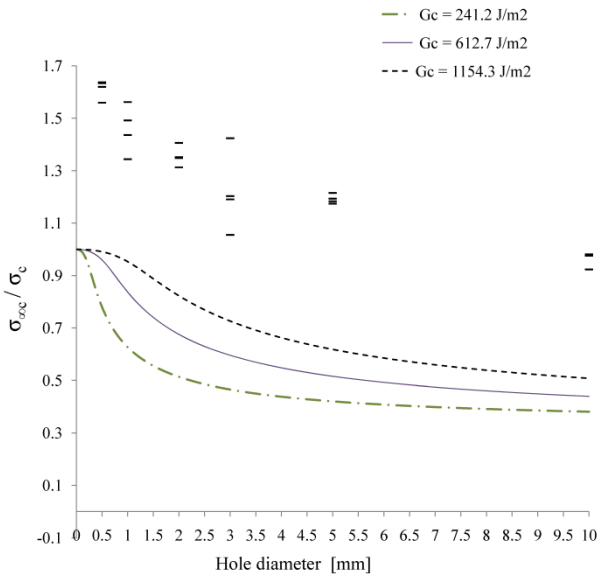

Figure 12. Comparison of the FFM predictions for plate with a hole and of the test results, for σ_c = 33.8 MPa.

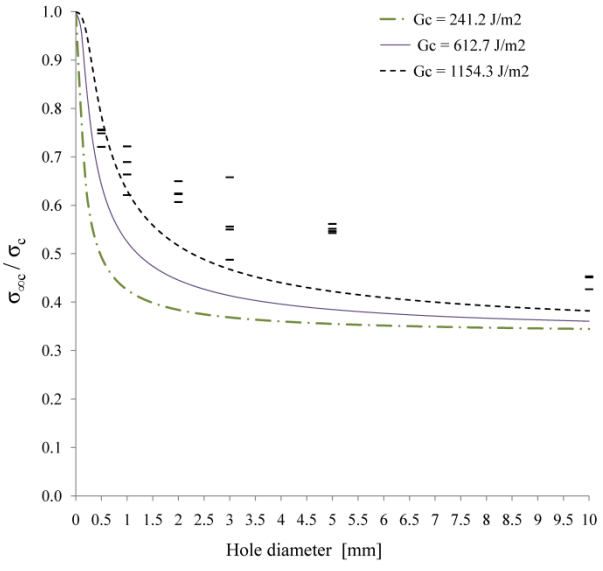

Figure 13. Comparison of the FFM predictions for plate with a hole and of the test results, for σ_c = 73.15 MPa.

4. DISCUSSION AND CONCLUSIONS

Preliminary theoretical and experimental results for characterization of crack onset at circular holes in plates from PMMA subjected to tensile load have been presented. A significant scatter in experimental results, mainly in the plates with small holes has been observed. It appears that PMMA is very sensible to machining and finishing operations and to the existence of fillets, and possibly to heat generation during machining or drilling. Some difficulties were observed in machining some coupons. The mill cutting was not sufficiently smooth. Additionally PMMA has been shown to be clearly sensible to the testing velocities. For example, it is evident in Figure 12 that something is wrong with the ultimate stress, because there are plates with holes supporting much larger tensile stress than plates with no hole. The preliminary results of the Figure 13 show much more reasonable results. It will be important to test plates with holes at a velocity of 5 mm/min and to test CT specimens for K_{Ic} to be able really compare the theoretical predictions by FFM with the experimental results.

REFERENCES

[1] Leguillon, D., *Strength or toughness? A criterion for crack onset at a notch,* European Journal of Mechanics A/Solids, 21, 2002, 61–72.

[2] Mantič, V., *Interface crack onset at a circular cylindrical inclusion under a remote transverse tension. Application of a coupled stress and energy criterion,* International Journal of Solids and Structures 46, 2009, 1287–1304.

[3] Li, J., Zhang, X.B., *A criterion study for non-singular stress concentrations in brittle or quasi-brittle materials*, Engineering Fracture Mechanics 73, 2006, 505–523.

[4] ASTM D638-03. *Standard test method for Tensile Properties of plastic*, ASTM; 2003.

[5] ASTM D5045-99. *Standard test methods for plane-strain fracture toughness and strain energy release rate of plastic materials*, ASTM; 2007.

[6] Souza, J.M.**,** Peres, F. M. and Schön, C.G., *Prática dos Ensaios de Tenacidade à Fratura em Pmma.* Congresso Brasileiro de Engenharia e Ciência dos Materiais – CBECiMat (ref 412-010). 24-28 Nov 2008. Porto de Galinhas, PE, Brasil.

[7] Kim, B.C., Park, S.W., Lee, D.G., *Fracture toughness of the nano-particle reinforced epoxy composite*, Composite Structures 86, 2008, 69–77.

[8] Pilkey, W.D,. *Formulas for Stress, Strain, and Structural Matrices,* Wiley, 1994.

COMPORTAMIENTO TERMOMECÁNICO DE MATERIALES BASADOS EN TITANATO DE CIRCONIO Y CIRCONA CÚBICA

E. López-López, R. Moreno, C. Baudín

Instituto de Cerámica y Vidrio, CSIC
CSIC-Campus de Cantoblanco, Kelsen 5, 28049 Madrid
E-mail: emiliol l@icv.csic.es

RESUMEN

El titanato de circonio presenta anisotropía cristalográfica en su coeficiente de expansión térmica, por lo que tiene un alto interés como componente de materiales con bajo coeficiente de expansión. Por tanto, los materiales de titanato de circonio son candidatos a materiales estructurales, lo que hace preciso caracterizar su comportamiento termomecánico, aspecto no reportado en la bibliografía. En este trabajo se ha realizado la caracterización termomecánica de materiales de titanato de circonio en términos del coeficiente de expansión térmica, módulo de elasticidad, tensión de fractura y tenacidad y trabajo de fractura. La tenacidad y el trabajo de fractura han sido determinados mediante ensayos de fractura controlada. Se discuten los resultados en función de la composición y microestructura de los materiales.

ABSTRACT

Zirconium titanate presents crystallographic anisotropy in thermal expansion. Hence, it can be considered as component of low thermal expansion materials. Thus, zirconium titanate materials are candidates for structural applications for which it is necessary to characterise their thermomechanical behaviour, not reported in the available literature. In this work, the thermomecanical behaviour of zirconium titanate materials has been characterized in terms of thermal expansion coefficient, Young modulus, fracture strength, fracture toughness and work of fracture. Fracture toughness and work of fracture have been determined by controlled fracture tests. Results are discussed on the basis of the composition and microstructure of the materials.

PALABRAS CLAVE: titanato de circonio, propiedades mecánicas, ensayos de fractura controlada.

1. INTRODUCCIÓN

El titanato de circonio presenta anisotropía cristalográfica en el coeficiente de expansión térmica ($\alpha_{a25\text{-}800ºC} = 6.2 \times 10^{-6}$ ºC^{-1}, $\alpha_{b25\text{-}800ºC} = 10 \times 10^{-6}$ ºC^{-1}, $\alpha_{c25\text{-}800ºC} = 8.6 \times 10^{-6}$ ºC^{-1}) [1], por lo que tiene un alto potencial como componente de materiales con bajo coeficiente de expansión, los cuales tienen aplicaciones en el ámbito de la cerámica estructural en condiciones extremas de variación de la temperatura.

Las fases presentes en los materiales de titanato de circonio dependen de la composición de partida, la temperatura y el tiempo de sinterización, y la velocidad de enfriamiento. El titanato de circonio presenta dos fases: de alta ($ZrTiO_4$) y de baja ($Zr_5Ti_7O_{24}$) temperatura [2]. La presencia de Y_2O_3 favorece la formación de la fase de baja temperatura [3].

La fabricación de materiales estructurales requiere de métodos procesamiento que permitan obtener piezas masivas. La sinterización reactiva de compactos en verde obtenidos por colaje de suspensiones acuosas, ha permitido la fabricación de piezas masivas de materiales de titanato de circonio [4, 5].

La caracterización termomecánica de materiales de titanato de circonio es fundamental para su evaluación como componente de materiales estructurales, aspecto sobre el cual no hay ningún dato en bibliografía.

En este trabajo se ha realizado la caracterización termomecánica de materiales de titanato de circonio en términos de las propiedades involucradas en la respuesta a las variaciones de temperatura: coeficiente de expansión térmica, módulo de elasticidad y propiedades mecánicas -tensión de fractura, tenacidad y trabajo de fractura-. La tenacidad y el trabajo de fractura han sido determinados mediante ensayos de fractura controlada.

2. EXPERIMENTAL

Como polvos cerámicos precursores se usaron circona tetragonal policristalina estabilizada con 3 % mol de itria (Y-TZP, TZ3YS, TOSOH, Japón) y titania-anatasa (Merck, 808, Alemania). Presentan un tamaño medio de partícula de 0.4 y 0.3 μm, respectivamente, y una superficie específica de 6.7 y 9.0 m^2/g, respectivamente. Su pureza es superior al 99.9% en ambos casos.

El proceso de conformado por colaje de suspensiones se describe detalladamente en trabajos previos [4,5].

El tratamiento térmico de los compactos en verde fue realizado a 1500ºC/2h con velocidades de calentamiento y enfriamiento de 5ºC/min, obteniéndose materiales sinterizados denominados ZT70 1500 y ZT50 1500, para composiciones de partida con una relación molar de circona y titania 70/30 y 50/50 respectivamente.

Los compactos sinterizados se mecanizaron con discos y muelas de diamante para las distintas caracterizaciones.

Las curvas de dilatación y contracción de piezas de 10 x 10 x 5 mm^3 se registraron en un dilatómetro diferencial (402 EP, Netzsch, Alemania) utilizando velocidades de calentamiento y enfriamiento de 2ºC/min. A partir de estas curvas se calculó el coeficiente medio de expansión térmica. El valor dado es la media de tres medidas, y el error la desviación estándar.

La caracterización microestructural se realizó por microscopía electrónica de barrido de emisión de campo con análisis por dispersión de energías (MEB-EC-EDS, Hitachi S-4700 type I, Japón). Las muestras usadas fueron pulidas con diamante hasta 3µm y posteriormente atacadas térmicamente (1400ºC-1min; velocidades de calentamiento y enfriamiento de 5ºC/min).

La dureza Vickers se determinó usando un microindentador electromecánico (Microtest, España) con una pirámide de diamante (136º). Los ensayos se realizaron a una velocidad de desplazamiento del marco de carga de 0.05mm/min hasta una carga máxima de 100N y un tiempo de permanencia de 10s. El valor de la dureza se calculó usando la ecuación 1, donde P es la carga máxima aplicada en el ensayo y a es la semidiagonal de la huella, medida mediante microscopía óptica de luz reflejada (MOLR) (H-P1, Carl-Zeiss, Alemania).

$$H = \frac{P}{2a^2} \quad (1)$$

El módulo de Young dinámico se determinó a partir de la frecuencia propia de vibración de probetas (4 x 3 x 50 mm^3) en flexión, producida por un impacto mecánico (Grindosonic, J. W. Lemmens, Bélgica). El valor dado es la media de diez medidas, y el error la desviación estándar.

Para la determinación del módulo de Young estático, la tensión de fractura y para la realización de los ensayos de fractura controlada se utilizó una máquina de ensayos electromecánica (EM1/50/FR, Microtest, España).

El módulo de Young estático se calculó a partir de la pendiente de curvas carga-desplazamiento registradas en ensayos de flexión en tres puntos utilizando una velocidad de aplicación de carga 0.05mm/min y una distancia entre apoyos de 40mm. Las curvas fueron corregidas utilizando el valor de 2.0 x 10^{-6} m/N como flexibilidad del conjunto de apoyos y máquina de ensayo. El valor dado es la media de tres medidas, y el error la desviación estándar.

La tensión de fractura se determinó mediante ensayos de flexión en cuatro puntos (probetas de 4 x 3 x 50 mm^3). La velocidad de desplazamiento fue de 0.5mm/min y la distancia entre los apoyos inferiores y superiores fue de 40 y 20mm respectivamente. El valor dado es la media de tres medidas, y el error la desviación estándar.

La tenacidad y el trabajo de fractura se determinaron mediante ensayos de fractura controlada en probetas (6 x 4 x 50 mm^3) sometidas a flexión en tres puntos (distancia de apoyos de 40 mm) y a las que se les introdujeron previamente entallas en forma de V de longitud conocida (SEVNB: single edge V-notched beam en terminología anglosajona). En primer lugar se realizaron pre-entallas con un disco diamantado de 300µm de espesor (Isocut, Buehler, Estados Unidos) hasta una longitud de aproximadamente un 70% del tamaño final de entalla. Usando esta pre-entalla como guía, el resto de entalla se realizó con una cuchilla impregnada con pasta de diamante (Metadi II, Buehler, Estados Unidos) de 15µm y 6µm sucesivamente, siendo el valor del radio del fondo de entalla aproximadamente 30-40 µm (Fig. 1). Para cada material se calculó el tamaño de entalla a partir del cual se producirían ensayos estables si se realizaran en control de posición [6]. El tamaño final de entalla usado fue de una relación a/W de 0.5 para el material ZT50 1500 y de 0.6 para el material ZT70 1500, siendo a la longitud de la entalla y W la altura de la probeta. La longitud de entalla se midió por microscopía óptica de luz reflejada (MOLR) (H-P1, Carl Zeiss, Alemania). Los ensayos de fractura controlada se realizaron usando un nuevo sistema desarrollado que ha sido descrito detalladamente en el trabajo "Controlled fracture tests of brittle ceramics" [7]. Este sistema permite la realización de ensayos de fractura controlada mediante el control de la apertura de la grieta (CMOD: crack mouth opening displacement en terminología anglosajona). A partir de las curvas carga-desplazamiento obtenidas se calcularon los valores de tenacidad y trabajo de fractura. La tenacidad de fractura se calculó de acuerdo con el procedimiento descrito por Guinea et al. [8], y el trabajo de fractura dividiendo el área bajo la curva carga-desplazamiento por el doble de la sección transversal de probeta sin entallar. Los valores dados son la media de tres medidas, y el error la desviación estándar.

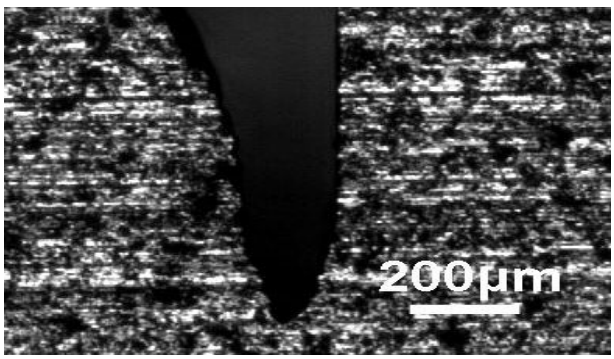

Figura 1. Micrografía MOLR del fondo de entalla característico en una probeta de ZT70 1500 usada en los ensayos de fractura controlada.

3. RESULTADOS Y DISCUSIÓN

El material ZT70 1500 (Fig. 2) es un material bifásico constituido por titanato de circonio ($Zr_5Ti_7O_{24}$) y circona cúbica con titania e itria en solución sólida [5].

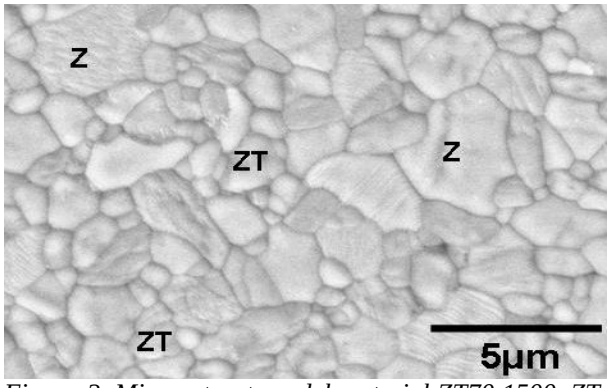

Figura 2. Microestructura del material ZT70 1500. ZT: titanato de circonio. Z: circona cúbica con itria y titania en solución sólida.

El material ZT50 1500 está constituido por una matriz de titanato de circonio ($Zr_5Ti_7O_{24}$), una segunda fase de circona cúbica con titania e itria en solución sólida, y un compuesto de tipo pirocloro como fase minoritaria (Fig. 3) [9].

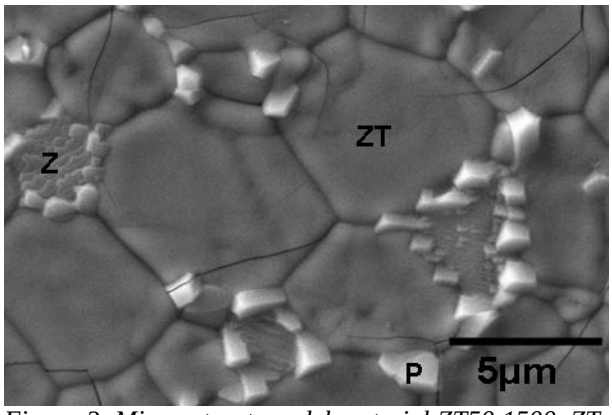

Figura 3. Microestructura del material ZT50 1500. ZT: titanato de circonio. Z: circona cúbica con itria y titania en solución sólida, P: pirocloro.

En ambos materiales se desarrollan tensiones durante el enfriamiento desde la temperatura de sinterización debido a la anisotropía en el coeficiente de expansión térmica del titanato de circonio y a las diferencias entre los coeficientes de expansión térmica de las fases constituyentes. El nivel de las tensiones desarrolladas dependerá de la orientación cristalográfica de granos continuos.

El coeficiente medio de expansión térmica cristalográfico del titanato de circonio ($\alpha \approx 8.2x10^{-6}ºC^{-1}$ [1]) es menor que el coeficiente de expansión térmica de la circona cúbica ($\alpha \approx 11x10^{-6}ºC^{-1}$ [10]), por lo que los granos de circona cúbica quedarán sometidos a tracción en los materiales a temperatura ambiente, lo cual daría lugar a microgrietas circunferenciales, las cuales no se observan. El agrietamiento de los granos de titanato de circonio se produce a partir del tamaño de grano crítico, por lo cual se produce en el material con mayor tamaño de grano (ZT50 1500).

La tabla 1 muestra los valores de densidad de los materiales sinterizados y su coeficiente medio de expansión térmica entre 25 y 850ºC. El menor valor del coeficiente de expansión térmica del material ZT50 1500 se debe tanto a la mayor cantidad de titanato de circonio, de menor coeficiente de expansión, como a la presencia de microgrietas.

Tabla 1. Densidad y coeficiente de expansión térmica medio entre 25-850ºC de los materiales ZT70 1500 y ZT50 1500.

Material	Densidad (g/cm^3)	$\alpha_{25\text{-}850}$ ($x10^{-6}$) ($ºC^{-1}$)
ZT70 1500	5.45 ± 0.01	8.7 ± 0.3
ZT50 1500	5.02 ± 0.01	6.7 ± 0.2

La tabla 2 muestra los valores experimentales de módulo de Young estático y dinámico. Los valores calculados a partir de los modelos de Voigt y Reuss utilizando los datos de la tabla 3 se recogen en la tabla 4. Para el titanato de circonio se ha tomado el valor del modulo de Young determinado para granos de titanato de circonio mediante nanoindentación instrumentada en un trabajo previo [11].

De acuerdo con los valores calculados, los materiales ZT70 1500 y ZT70 1500 deberían presentar valores similares del módulo de elasticidad y superiores a los obtenidos experimentalmente. Sin embargo, los valores experimentales muestran una gran diferencia, siendo muy inferiores para el material ZT50 1500, el cual, además, presenta una diferencia significativa entre los valores del módulo de Young estático y dinámico. El mayor valor del módulo de Young dinámico es debido a que los valores determinados por métodos dinámicos están dominados por la fase más rígida, mientras que los valores determinados por métodos estáticos se ven influidos por las microgrietas presentes, ya que su apertura puede acomodar parte de la deformación impuesta en el ensayo. Por lo tanto, el hecho de que el valor del módulo de Young del material ZT50 1500 sea muy inferior a los valores calculados tiene su explicación en la presencia de microgrietas en dicho material. La diferencia entre los valores calculados y experimentales para el material ZT70 1500 se puede deber a que, en general, los valores obtenidos por nanoindentación son superiores a los determinados por técnicas que caracterizan de manera masiva al material.

Tabla 2. Módulo de Young estático y dinámico de los materiales ZT70 1500 y ZT50 1500.

Material	E estático (GPa)	E dinámico (GPa)
ZT70 1500	155 ± 2	158 ± 2
ZT50 1500	40 ± 3	55 ± 2

Tabla 3. Módulo de Young y fracción volumétrica de las fases presentes en los materiales ZT70 1500 y ZT50 1500.

Fase	Fracción volumétrica ZT70 1500	Fracción volumétrica ZT50 1500	E (GPa)
$Z_5Ti_7O_{24}$	≈ 0.60	≈ 0.83	≈ 170 [11]
c-ZrO_2	≈ 0.40	≈ 0.17	≈ 210 [12]

Tabla 4. Módulo de Young de los materiales ZT70 1500 y ZT50 1500 calculados a partir de los modelos de Voigt y Reuss.

Material	E_{voigt} (GPa)	E_{reuss} (GPa)
ZT70 1500	≈ 186	≈ 184
ZT50 1500	≈ 177	≈ 175

Los valores de la dureza presentan la misma tendencia que los valores del módulo de Young. Los valores calculados a partir de combinación lineal de las propiedades de las fases presentes, relación comprobada de manera empírica en otros sistemas, son similares y muy superiores a los obtenidos experimentalmente (Tabla 5). Por una parte, los valores de la dureza determinados por nanoindetación [11] son también superiores, lo cual explicaría las diferencias en el caso del material ZT70 1500. Por otra parte, el bajo valor de dureza del material ZT50 1500 se explica por la presencia de microgrietas.

Tabla 5. Durezas experimental y calculada de los materiales ZT70 1500 y ZT50 1500.

Material	$H_{experimental}$ (GPa)	$H_{calculada}$ (GPa)
ZT70 1500	10.6 ± 0.2	≈ 16
ZT50 1500	5.5 ± 0.3	≈ 15

La figura 4 muestra las curvas carga-desplazamiento registradas en los ensayos de fractura controlada de los materiales estudiados. En el caso del material ZT70 1500 la gráfica muestra un comportamiento de fractura típico de materiales frágiles, en los que el desplazamiento tiene que disminuir una vez iniciada la fractura para mantener la estabilidad, mientras que el material ZT50 1500 tiene un comportamiento de fractura característico de materiales con curva R.

La figura 5 muestra micrografías de los materiales estudiados donde se observan detalles del tipo de fractura, siendo de tipo mixta en ambos materiales. Los granos de circona cúbica presentan fractura intergranular, mientras que los granos de titanato de circonio muestran fractura transgranular. Las tensiones residuales de tracción desarrolladas en los granos de circona cúbica favorecerían la fractura intergranular observada mientras que la fractura de los granos de titanato de circonio se verá afectada por las grietas presentes en su interior.

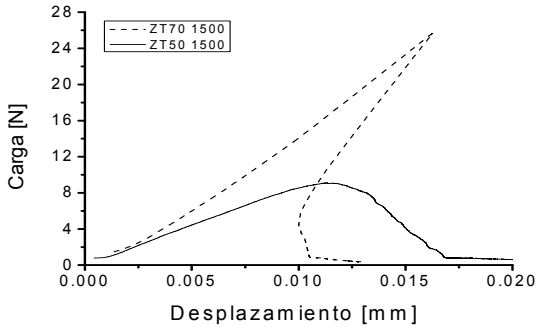

Figura 4. Curvas carga-desplazamiento de los ensayos de fractura controlada de los materiales ZT70 1500 y ZT50 1500.

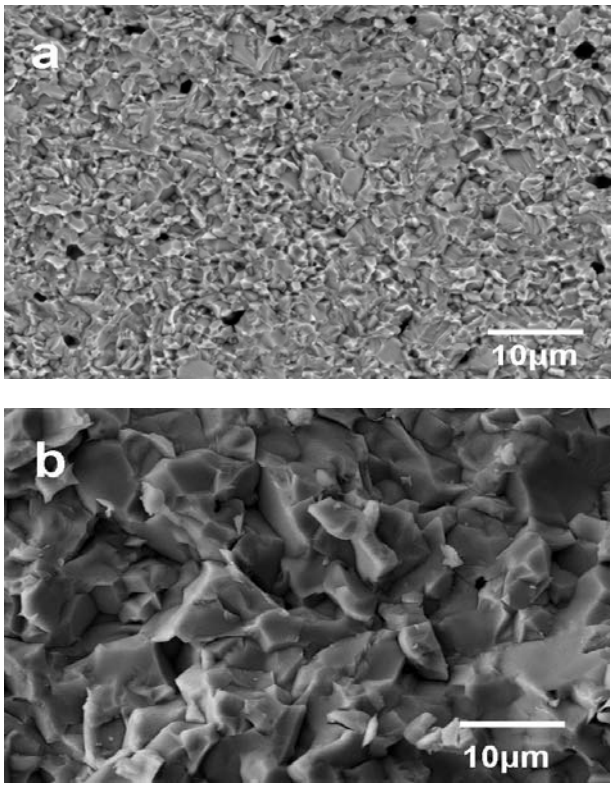

Figura 5. Micrografías MEB de las superficies de fractura de los materiales ZT70 1500 (a) y ZT50 1500 (b).

Tabla 6. Tensión de fractura, tenacidad y trabajo de fractura de los materiales ZT70 1500 y ZT50 1500.

Material	σ_f (MPa)	K_{IC} (MPam$^{1/2}$)	γ_{WOF} (J/m^2)
ZT701500	283 ± 11	2.2 ± 0.2	4.6 ± 0.2
ZT501500	60 ± 3	0.6 ± 0.1	3.9 ± 0.1

La mecánica de la fractura en régimen elástico y lineal (MFEL) establece que en un material sometido a una tensión aplicada σ, las tensiones y deformaciones en el frente de una grieta de longitud c están relacionadas por un factor de proporcionalidad de carácter universal llamado factor de intensidad de tensiones K_I. La grieta se propaga cuando el factor de intensidad de tensiones alcanza un valor crítico K_{IC} que depende sólo del

material. Por lo tanto, este valor crítico es una medida de la tenacidad de fractura del material. La ecuación 2 define la relación entre la tensión de fractura y la tenacidad según la MFEL.

$$\sigma = \frac{K_{IC}}{\sqrt{C}} \tag{2}$$

El tamaño del defecto que produce la fractura es el que relaciona la tenacidad y la tensión de fractura.

$$\frac{K_{ICZT\,701500}}{K_{ICZT\,501500}} = \frac{\sigma_{ZT\,701500}}{\sigma_{ZT\,501500}} \times \frac{\sqrt{C_{ZT\,701500}}}{\sqrt{C_{ZT\,501500}}} \tag{3}$$

Despejando la relación de tamaños de defecto de la ecuación 3 y sustituyendo los valores de K_{IC} y σ de cada material (tabla 6), nos queda la siguiente relación:

$$\frac{C_{ZT\,701500}}{C_{ZT\,501500}} = 1.6 \tag{4}$$

El tamaño de defecto crítico que produce la fractura en el material ZT70 1500 debería de ser mayor (≈1.6 veces) que el que produce la fractura en el material ZT50 1500.

Las figuras 6 y 7 muestran superficies de fractura de ensayos de tensión de fractura. En las probetas del material ZT70 1500 fue posible identificar los defectos críticos y las distintas zonas asociadas a la fractura frágil [13]. Las superficies de fractura del material ZT50 1500 no mostraron defectos críticos (Fig.7 a). Probablemente, la fractura de este material se produce por coalescencia de microgrietas como las que muestra la figura 7b. Esto da lugar a una fractura muy tortuosa, aumentando la superficie de fractura. De hecho, el valor de trabajo de fractura γ_{WOF} del material ZT50 1500 es del mismo orden que el del material ZT70 1500 (tabla 6) a pesar de que los valores de la tenacidad de fractura son muy inferiores para ZT50 1500.

En la tabla 7 se comparan los valores de las propiedades termomecánicas determinadas en este trabajo para el material ZT70 1500 con los valores de estas mismas propiedades existentes en bibliografía para materiales de circona cúbica estabilizada con itria (8-YSZ). El material desarrollado en este trabajo presenta menores coeficiente de expansión térmica y módulo de Young, mientras que los valores de tensión de fractura y tenacidad de fractura son del mismo orden que los de los materiales de circona cúbica, por lo que presentará mejor comportamiento frente a las variaciones de temperatura.

Tabla 7. Módulo de Young, tensión de fractura, tenacidad y trabajo de fractura del material ZT70 1500 y de materiales de circona cúbica.

Material	$\alpha_{25\text{-}850}$ ($x10^{-6}$) ($^oC^{-1}$)	E (GPa)	σ_f (MPa)	K_{IC} ($MPam^{1/2}$)
ZT70 1500	8.7 ± 0.3	155 ± 2	283 ± 11	2.2 ± 0.2
8-YSZ	11 [10]	210 [12]	290 [12]	2.2 [14]

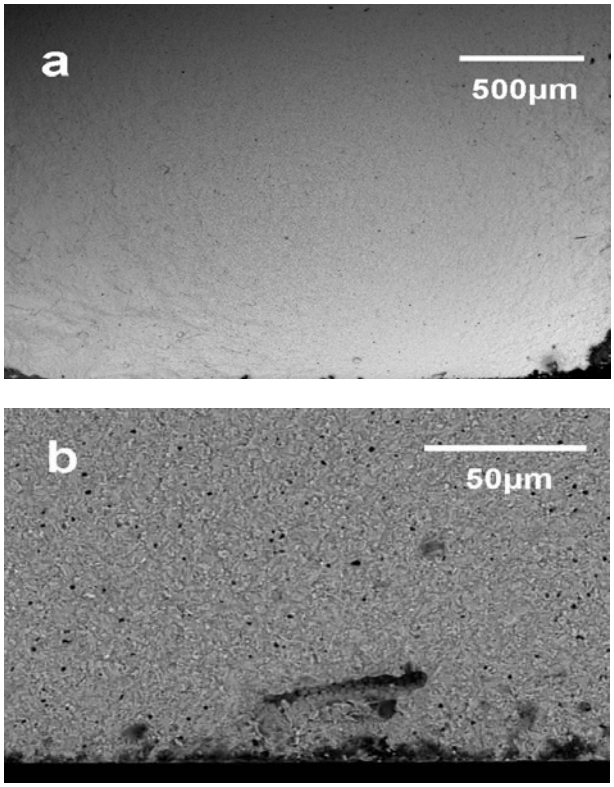

Figura 6. Micrografías MEB de la superficie de fractura de una probeta del material ZT70 1500. La superficie de tracción está localizada en la parte inferior de la micrografía. (a) General, (b) detalle del defecto crítico: *poro longitudinal*.

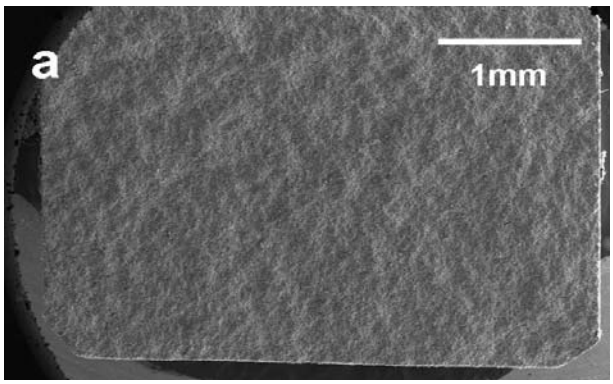

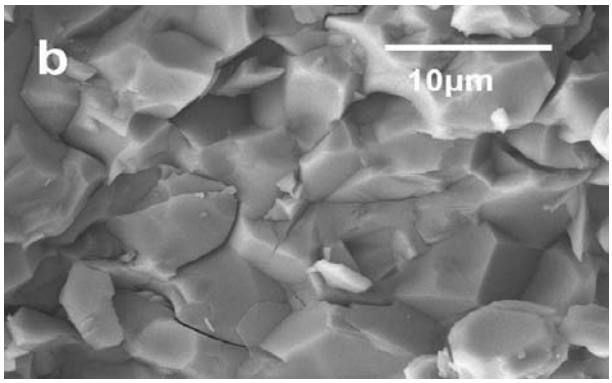

Figura 7. Micrografías MEB de la superficie de fractura de una probeta del material ZT50 1500. La superficie de tracción está localizada en la parte inferior de la micrografía. (a) General, (b) detalle de microgrietas perpendiculares a la superficie de fractura que originan la fractura por coalescencia.

4. CONCLUSIONES

Se ha realizado la caracterización termomecánica de materiales de titanato de circonio de composiciones en del sistema ternario ZrO_2-Y_2O_3-TiO_2 con bajo contenido en Y_2O_3 (< 2.2% mol).

Para composiciones ricas en circona (ZT70 1500), la fase mayoritaria es el titanato de circonio de baja temperatura ($Zr_5Ti_7O_{24}$) y la fase secundaria circona cúbica con solución sólida de titania e itria. Este material presenta mejores propiedades termomecánicas que los materiales de circona cúbica para aplicaciones de variaciones extremas de la temperatura.

Composiciones con relación molar Zr/Ti ≈1 (ZT50 1500) dan lugar a materiales formados por el titanato de circonio de baja temperatura de ($Zr_5Ti_7O_{24}$) como fase mayoritaria, circona cúbica con titania e itria en solución sólida como segunda fase y una tercera fase minoritaria de tipo pirocloro. Este material presenta valores del coeficiente de expansión térmica y del módulo de Young muy inferiores a los de materiales de circona cúbica debido a la presencia de microgrietas.

AGRADECIMIENTOS

Proyectos: MEC MAT2006-13480 C02 y MCI-PET 2008-0113. Microtest S.A.

E. López-López agradece a la Comunidad de Madrid y al Fondo Social Europeo el contrato de investigación CPI/0552/2007.

REFERENCIAS

[1] Ikawa, H., Iwai, A., Iruta, K., Shimojima, H., Urabe, K. and Udagawa, S., *Phase transformation and thermal expansion of zirconium and hafnium titanates and their solid solutions*, J. Am. Ceram. Soc. 71, 120-127, (1988).

[2] McHale A. E. and Roth R. S., *Low-temperature phase relationships in the system ZrO_2-TiO_2*. J. Am. Ceram. Soc., 1986, 69, 827-832.

[3] Bordet P., McHale A., Santoro A. and Roth R. S., *Powder neutron diffraction study of $ZrTiO_4$, $Zr_5Ti_7O_{24}$ and $FeNb_2O_6$*. J. Solid State Chem., 1986, 64, 30-46.

[4] López-López, E., Baudín, C. and Moreno, R., *Synthesis of Zirconium Titanate based materials by Colloidal Filtration and Reaction Sintering*, Int. J. Appl. Ceram. Technol., 2008, 5, 394-400 .

[5] López-López, E., Baudín, C. and Moreno, R., *Thermal expansion of zirconia-zirconium titanate materials obtained by slip casting of mixtures of Y-TZP-TiO_2*, J. Eur. Ceram. Soc., 2009, 29, 3219-3225.

[6] Bar-On I., Baratta F. I. and Cho K., *Crack stability and its effect on fracture toughness of hot- pressed silicon nitride beam specimens*, J. Am. Ceram. Soc., 1996, 79, 2300-2308.

[7] Baudín C., García A., Hernández J. and López M., *Controlled fracture tests of brittle ceramics*, An. Mec. Fractura, 2010, Aceptado.

[8] Guinea G. V., Pastor J. Y., Planas J. and Elices M., *Stress intensity factor, compliance and CMOD for a general three-point-bend bean*, Int. J. Fracture, 1998, 89, 103-116.

[9] López-López, E., Moreno, R. and Baudín, C., *Phase evolution in reaction sintered zirconium titanate based materials*, J. Eur. Ceram. Soc., aceptado.

[10] Liu, Z. G., Ouyang, J. H. and Zhou Y., *Influence of gadolinia on thermal expansion property of ZrO_2-4.5 mol%Y_2O_3 ceramics*, J. Alloys Compd., 2009, 473, 17-19.

[11] López-López E., Botero C. A., Jiménez-Piqué E., Llanes L., Moreno R. and Baudín C., *Determinación de propiedades de interés estructural de materiales de titanato de circonio*, An. Mec. Fractura, 2009, 26, 57-62.

[12] Donzel L. and Roberts S. G., *Microstructure and mechanical properties of cubic zirconia (8YSZ)/SiC nanocomposites*, J. Eur. Ceram. Soc., 2000, 20, 2457-2462.

[13] Bueno S. and Baudín C., *Mechanical behaviour of structural ceramics*, Bol. Soc. Esp. Ceram. V., 2007, 46, 103-118.

[14] Abraham I. and Gritzner G., *Mechanical properties of doped cubic zirconia ceramics*, J. Mater. Sci. Lett., 1993, 12, 995-997.

CHARACTERIZATION OF DELAMINATION FRACTURE SURFACES UNDER MIXED MODE LOADING

R.M.M. Marat-Mendes [1], M.M. de Freitas [2]

[1] Escola Superior de Tecnologia de Setúbal, Campus do IPS,
Estefanilha, 2910-761 Setúbal, Portugal
e-mail: rmendes@est.ips.pt

[2] Instituto Superior Técnico, Universidade Técnica de Lisboa
Av. Rovisco Pais, 1049-001 Lisboa, Portugal
e-mail: mfreitas@dem.ist.utl.pt

ABSTRACT

Delamination is an important mode of failure on laminated composite materials and the characterization of this failure mode is a subject of research. Mode I, mode II, mode III and mixed-mode I+II fracture toughness were obtained using the double cantilever beam test (mode I), the end notch flexure test (mode II), the original and the modified edge crack torsion test (mode III) and the mixed-mode bending test (mixed-mode I+II) respectively. Fracture surfaces obtained during mode III interlaminar fracture toughness of glass/epoxy composites have been also studied using the original and the modified edge crack torsion test geometry. Results were compared with delaminating surfaces obtained during tests of mode I, mode II and mixed-mode I+II. In the original ECT test the hackle marks appears only in the side of the loading pin. In the modified ECT test the hackle marks appears in both sides of the sample and slightly less well defined and smoother fracture features in the middle of the sample.

KEY WORDS: Glass fibre epoxy, interlaminar fracture, fractographic analysis.

1. INTRODUCTION

Interlaminar damage (delamination) is one of the predominant forms of failure in many laminated composites systems. It is usually considered to be a crack propagation between two adjacent layers, in modes I, II or III, in the general case.

Analysis and test techniques for mode I delamination of a composite material have been extensively studied and the preferred technique to obtain the mode I partition is the Double Cantilever Beam test (DCB) [1]. Also mixed-mode I+II analysis and test techniques of laminated composite materials have been extensively studied and standardized with the Mixed Mode Bending test (MMB) [2,3]. Mode II partition has been also extensively studied but up to date, no standard method has been established for measuring mode II critical strain energy release rate, G_{IIC}. The End Notch Flexure (ENF) and the Four Point Bend End-Notch Flexure (4ENF) tests have shown to be the preferred test techniques to obtained mode II partition of the critical strain energy release rate [4-8]. Pure mode III test technique has not been yet achieved however a lot of work concerning mode III partition have been extensively presented in the literature [9-19]. The most recent test technique is the modified Edge Crack Torsion test (ECT) [20] which is a modification of the original Edge Crack Torsion test proposed initially by Lee [21].

In this study, the fracture surfaces obtained during mode III interlaminar fracture of glass/epoxy laminated composites have been investigated using the original and the modified ECT test geometry. It has been reported that with these specimens and test methods a mixed-mode II+III state exists at the delamination front, therefore special attention is focused on this characterization. The fracture surfaces obtained under ECT tests are compared with those obtained with DCB, ENF and MMB tests. The present study aimed at evaluating the adequacy of ECT specimen for the determination of mode III fracture toughness of a glass/epoxy material by combining experimental tests, numerical analyses and specimen fracture observations.

2. MATERIALS

The material used in this work is a unidirectional epoxy prepeg (ET443) reinforced with E glass fibre (UE400REM) supplied by Texipreg®. A 12.7 μm thick Teflon® foil was inserted at the mid-plane of the panels during the lay-up process to define a starter delamination crack. The panels were cured at 125 ºC and 7 bar for 1 h.

The lay-up used in the DCB, ENF and the MMB tests is the one proposed by the mode I [1] and mixed-mode I+II standards [2] which is the $[0]_{24}$. The lay-up used in the ECT test is the $[90/(\pm 45)_3/(\mp 45)_3/90]_s$, this selection of ECT specimen lay-up and dimensions was made considering Li [22] and Carlsson [10] works. Li [22] reported consistent toughness values without transverse cracking problems on this specimen. This stacking sequence is more effective on avoiding transverse cracks in interface 90º plies than the one used recently by Ratcliffe [20], $[90/0/(\pm 45)_3/(\mp 45)_3/0/90]_s$,

Table 1. Lamina Properties.

Test	Lay-up	E_{11} [GPa]	$E_{22}=E_{33}$ [GPa]	$G_{12}=G_{13}=G_{23}$ [GPa]	$\nu_{12}=\nu_{13}$	ν_{21}	V_f [%]
DCB ENF MMB	$[0]_{24}$	43.94	16.71	6.57	0.300	0.114	58.16
ECT	$[90/(\pm 45)_3/(\mp 45)_3/90]_s$	43.42	9.49	6.57	0.316	0.069	56.55

since the incorporation of 0º plies reduces torsional stiffness and strength. Therefore, in view of the ply thickness of the present glass/epoxy material, the stacking sequence used was the one used by Li [22] and Carlsson [10]. Lamina properties were previously determined and are present in Table 1.

Specimens were cut from the panels and the DCB, ENF and MMB nominal dimensions were W=162 mm, b=25 mm with an initial delamination length of a=30 mm and a thickness of $2h$=6.5±0.7 mm (Figure 1). On the other hand, the selected ECT dimensions were L=89 mm, b=38 mm, with five groups of crack lengths $\tilde{a}$= 0, 8, 13, 19 and 23 mm and a thickness of $2h$=8.3±0.3 mm (Figure 2).

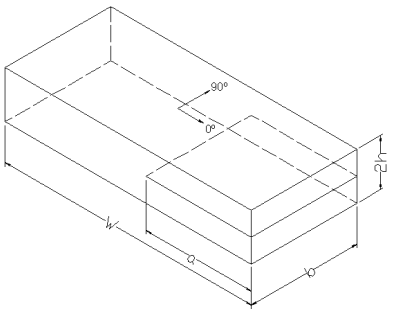

Figure 1. Schematic of DCB, ENF and MMB specimens.

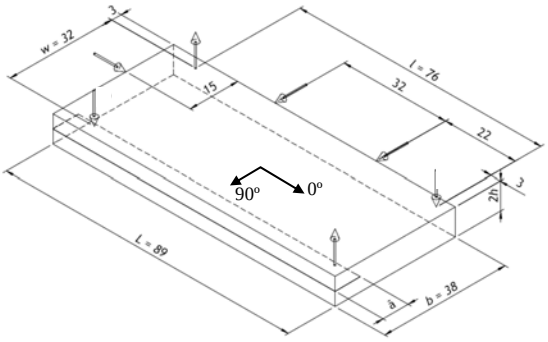

Figure 2. Schematic of ECT specimen.

3. EXPERIMENTAL PROCEDURE

The specimens have been mounted into the test fixtures and static tests were conducted under displacement control at a crosshead displacement rate of 0.5mm/min. This slow rate allowed crack propagation to be followed and recorded easily. Load-displacement plots were recorded during the tests. All fracture tests were performed from the end of the (straight) insert without pre-cracking the specimen.

Mode I, mode II, mixed-mode I+II and mode III fracture toughness were obtained using the DCB, the ENF, the MMB and the original and the modified ECT (O-ECT, M-ECT) tests respectively. The original ECT (O-ECT) fixture (Figure 3) provides supports at three points in three corners, guided by three guide pines to provide perfect alignment and the transverse load is introduced at the fourth point, the unsupported corner, by compression of the loading pin.

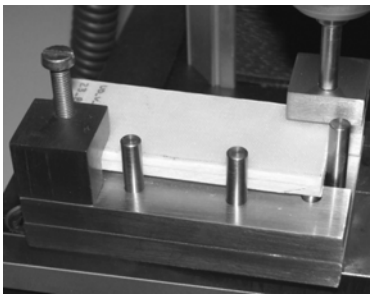

Figure 3. Original ECT test fixture

The modified ECT (M-ECT) test fixture is shown in Figure 4. The ECT specimen is supported in two supports in two corners, guided by three guide pines to provide perfect alignment and the transverse load is introduced symmetrically at the two unsupported corners, by compression of the loading pin.

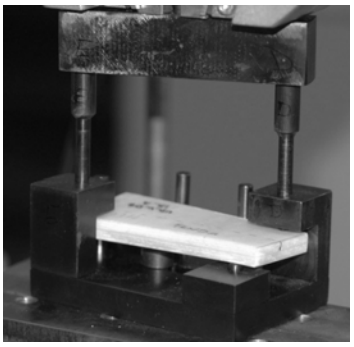

Figure 4. Modified ECT test fixture.

4. ANALYSIS

The virtual crack closure technique (VCCT) [23] was used to calculate the mode I, mode II and mode III strain energy release rate components. Table 2 shows

the fracture toughness obtained through the VCCT from the DCB, the ENF and the M-ECT tests.

Table 2 - Fracture toughness.

	G_{IC} [kJ/m^2]	G_{IIC} [kJ/m^2]	G_{IIIC} [kJ/m^2]
NL	0.845	1.272	0.946
5%/max	0.869	1.309	1.770

5. RESULTS AND DISCUSSION

A scanning electron microscopic (SEM) was used throughout this work to study the fractography of the broken specimens after DCB, ENF, MMB and ECT tests. The specimens were opened after testing and gold sputtering. Analysis of the fracture surfaces using SEM is necessary in order to obtain the maximum information possible concerning the fracture of ECT specimens and compare these fracture surfaces with the DCB, ENF and MMB specimens.

5.1. Mode I fractography

A typical scanning electron micrograph of the fracture surface in Mode I failure mechanism is characterized by fractures localised mainly in the resin and along the resin/fibre interface. SEM images of the crack surfaces in the starter region, Figure 5, clearly shows broken fibres pulled out from the resin as an evidence of the fibre bridging.

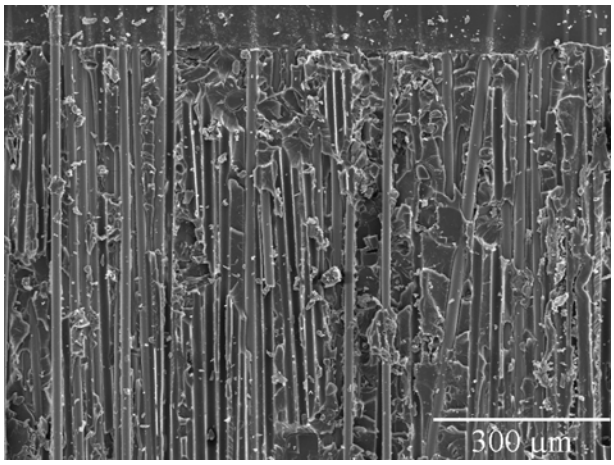

Figure 5. Scanning electron micrographs of DCB fracture surfaces. (Crack propagates from top to bottom).

5.2. Mode II fractography

Fracture surfaces shown in Figure 6 were formed by the characteristic hackle pattern, usually observed after mode-II failure. Mode II failure mechanism consisted of fibre breakage under shearing and is characterized by fractures localised in the resin with many hackles having an orientation of approximately 90º to fibre orientation.

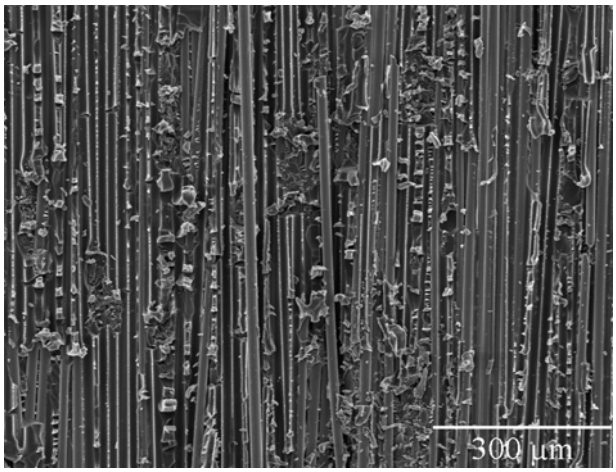

Figure 6. Scanning electron micrographs of ENF fracture surfaces. (Crack propagates from top to bottom).

5.3. Mixed-Mode I+II fractography

In the case of mixed-mode, the mechanisms is more complex consisted of fibre breakage under shearing (mode II) characterized by fractures localised in the resin with *hackles* having an orientation of 90º and others at less than 45º and also fractures localised in the resin and along the resin/fibre interface (mode I), Figure 7.

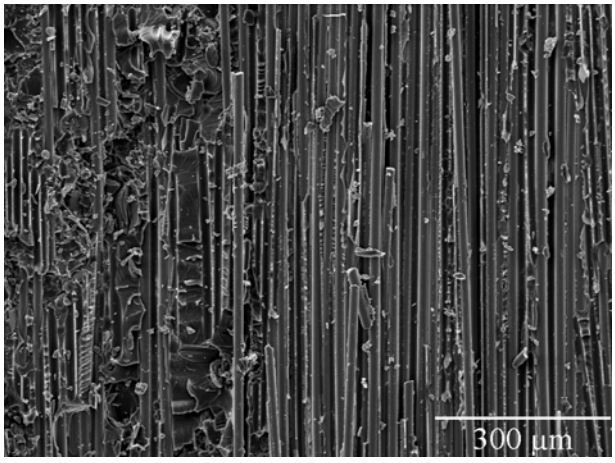

Figure 7. Scanning electron micrographs of MMB fracture surfaces (Crack propagates from top to bottom).

5.4. Mode III fractography

Fracture surfaces of the original and modified ECT specimens have been studied in three different positions. Fracture surfaces of the original ECT specimens have been analysed in the a) loading side, b) middle of the specimen and c) support side. The modified ECT fracture surfaces have been also analysed

in the a) loading side localized upper the starter film, b) middle of the specimen and c) loading side localized outside the starter film.
A schematic of the SEM locations of the fracture surfaces of the original ECT specimens is shown in Figure 8 for the a) loading side (*position 7*), b) middle of the specimen (*position 13*) and c) support side (*position 4*).

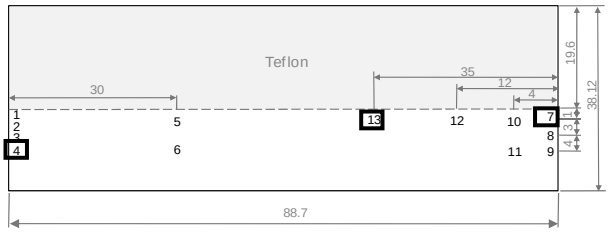

Figure 8. Schematic of the SEM locations of the original ECT sample.

Figure 9 shows the scanning electron micrographs in the side of the loading pin (*position 7* in Figure 8) where it is shown that the fracture surfaces of the original ECT specimens are very different from the fracture surfaces shown earlier in the DCB, ENF and MMB specimens. Here it is clear that the *hackles* are mainly orientated in approximately 45º to the fibre orientation, which indicates a mode III fracture. It can be also observed a presence of *hackles* with a 90º orientation, even in lower amount, like the ones observed in the ENF samples, which indicates a presence of a partition of mode II fracture.

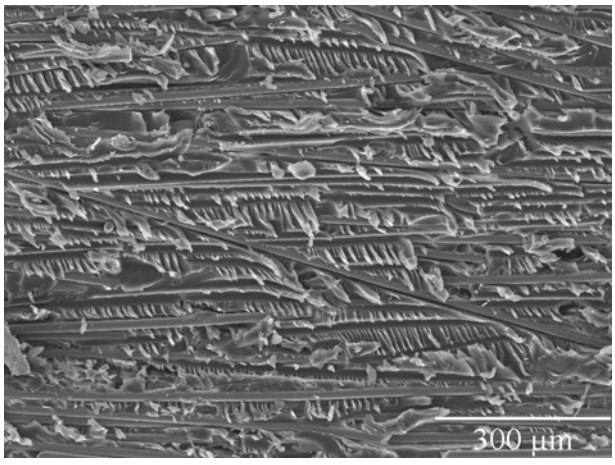

Figure 9. SEM of original ECT sample in the loading side (position 7) (Crack propagates from left to right).

Figure 10 shows the scanning electron micrographs in the middle of the specimen (*position 13* in Figure 8) where it is shown that the fracture surface of the original ECT specimen in this position is very different from the one shown in Figure 9. Here it can be seen that the *hackles* diminishes which indicates a diminishing of mode III presence.

Figure 11 shows the scanning electron micrographs in the support side (*position 4* in Figure 8) where it can be observed a presence of *hackles* orientated in approximately 45º to the fibre orientation indicating a mode III fracture, but this can be only observed when magnified.

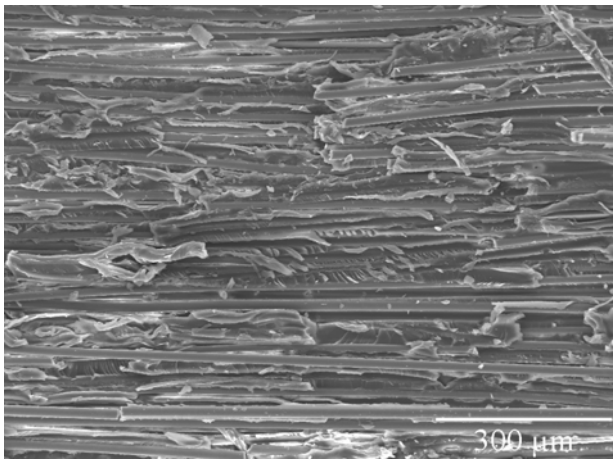

Figure 10. SEM of original ECT sample in the middle of the specimen (position 13) (Crack propagates from left to right).

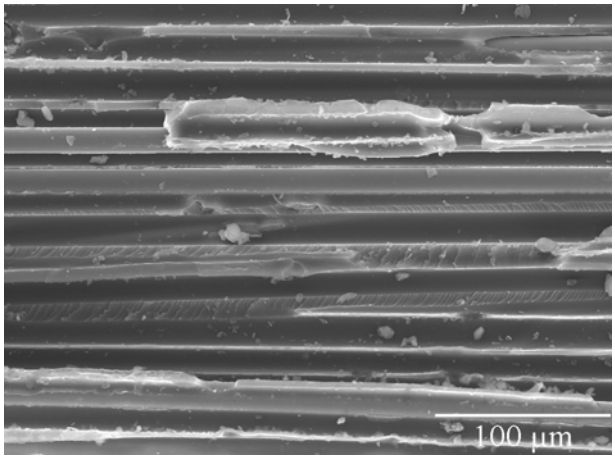

Figure 11. SEM of original ECT sample in the support side of the specimen (position 4) (Crack propagates from left to right).

A schematic of the SEM locations of the fracture surfaces of the modified ECT specimens is show in Figure 12 for the a) loading side localized upper the starter film (*position 1*), b) middle of the specimen (*position 17*) and c) loading side localized outside the starter film (*position 14*).

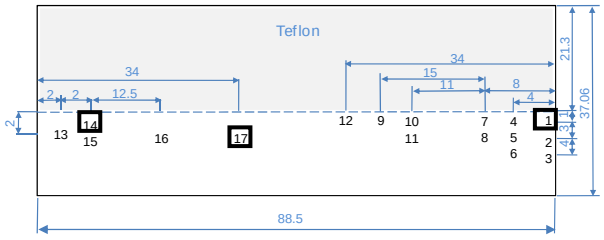

Figure 12. Schematic of the SEM locations of the modified ECT sample.

Figure 13 shows the scanning electron micrographs in the loading side localized upper the starter film (*position 1* in Figure 12) where it is shown that the fracture surfaces of the modified ECT specimens in this position is similar to the fracture surfaces observed in the same side of the original ECT specimen. These fracture surfaces are characterized by *hackles* orientated in approximately 45º to the fibre orientation, which indicates a mode III fracture and also a presence of *hackles* with a 90º orientation, even in lower amount, which indicates a presence of a partition of mode II fracture.

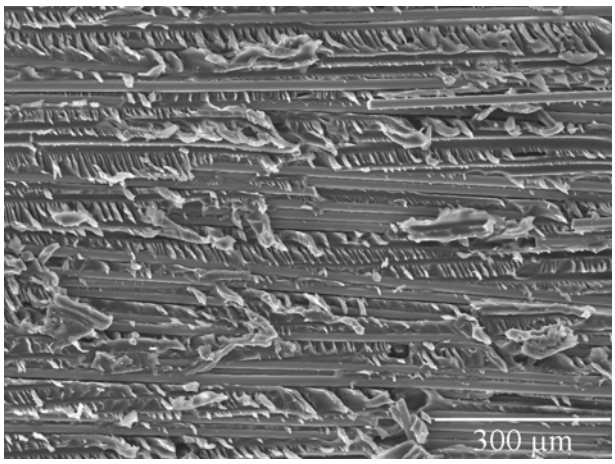

Figure 13. SEM of modified ECT sample in the loading side localized upper the starter film (position 1) (Crack propagates from left to right).

Figure 14 shows the scanning electron micrographs in the middle of the specimen (*position 17* in Figure 12) where it is shown that the fracture surface of the modified ECT specimen in this position is very different from the one shown in Figure 13. Here it can be seen that the *hackles* are less defined with smoother fracture features which indicates a diminishing of mode III presence.

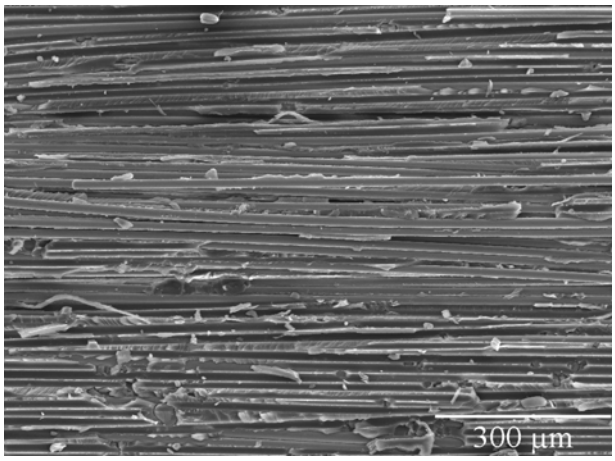

Figure 14. SEM of modified ECT sample in the middle of the specimen (position 17) (Crack propagates from left to right).

Figure 15 shows the scanning electron micrographs in the loading side localized outside the starter film (*position 14* in Figure 8) where it can be observed that the presence of the *hackles* orientated in 45º to the fibre orientation indicating a mode III fracture are similar to the ones observed in the side of the loading upper the starter film. These observations indicate that the modified ECT specimens present a mode III fracture in both sides of the specimen away from the middle of the specimen.

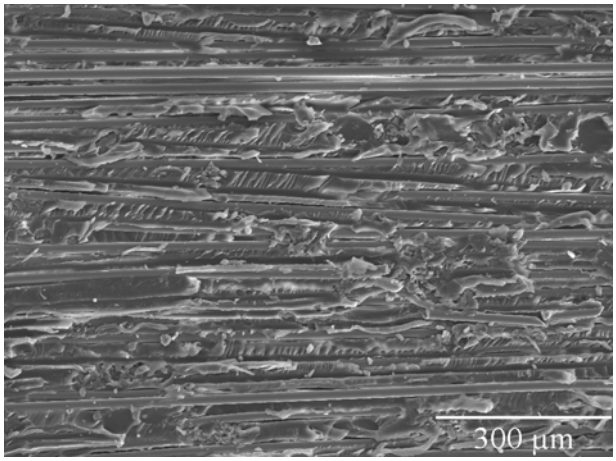

Figure 15. SEM of modified ECT sample in the loading side localized outside the starter film (position 14) (Crack propagates from left to right).

6. CONCLUSIONS

The present investigation has examined the fractographic features associated with delamination in glass/fibre laminated composite comparing the fracture surfaces of the original and modified ECT specimens with the DCB, ENF and MMB fracture surfaces.

The predominant fractographic feature found in mode I testing was broken fibres and pull-out from fibre bridging were observed. In mode II testing, the most predominant morphology was the hackle pattern perpendicular to the fibre orientation. In mixed-mode I+II testing, fractographic observation shows fibre breakage under shearing (mode II) characterized by fractures localised in the resin with *hackles* having an orientation of 90º and others at less than 45º and also fractures localised in the resin and along the resin/fibre interface (mode I).

The mode III fractographic observation shows predominant morphology with hackle pattern oriented at approximately 45º to the crack propagation direction. In the original ECT test the hackle marks appears only in the side of the loading pin. In the Modified ECT test the hackle marks appears in both sides of loading and less defined with smoother fracture features in the middle of the specimen. Mode III characterization concluded that some limited mixed-mode II+III seems to be present for ECT specimen on delamination initiation and growth, but a large majority of mode III delamination is present.

ACKNOWLEDGEMENTS

The authors thank the support from the Portuguese Foundation for Science and Technology (FCT) for the PhD grant no.SFRH/BD/25561/2005.

REFERENCES

[1] *ASTM D 5528 – 01 Standard Test Method for Mode I Interlaminar Fracture Toughness of Unidirectional Fiber-Reinforced Polymer Matrix Composites.* s.l. : American Society for Testing and Materials, 1994. Annual Book of ASTM Standards.

[2] *ASTM D 6671 – 01, Standard Test Method for Mixed Mode I-Mode II Interlaminar Fracture Toughness of Unidirectional Fiber Reinforced Polymer Matrix Composites.* s.l. : ASTM International, 2000.

[3] Marat-Mendes, R. and Freitas, M., *Mode I, mode II, mode III and mixed mode interlaminar fracture of glass/epoxy unidirectional laminates.* Porto, Portugal : Proceedings of EUROMECH 473, 2005.

[4] Blackman, B.R., Brunner, A.J. and Williams, J.G., *Mode II fracture testing of composites: a new look at an old problem.* Vol. 73, pp. 2443-2455, 2006.

[5] Davies, P., Casari, P. and Carlsson, L.A., *Influence of fibre volume fraction on mode II interlaminar fracture toughness of glass/epoxy using the 4ENF specimen.* Composites Science and Technology, Vol. 65, pp. 295-300, 2005.

[6] Pereira, A.B., et al., *Mode II interlaminar fracture of carbon/epoxy multidirectional laminates.* Composite Science and Technology, Vol. 64, pp. 1653-1659, 2004.

[7] Wang, J. and Qiao, P., *Novel beam analysis of end notched flexure specimen for mode-II fracture.* Engineering Fracture Mechanics, Vol. 71, pp. 219-231. 2004

[8] de Morais, A. B., *Analysis of mode II interlaminar fracture of multidirectional laminates.* Composites: Part A, Vol. 35, pp. 51-57, 2004.

[9] Farshad, M. and Flueler, P., *Investigation of mode III fracture thoughness using an anti-clastic plate bending method.* Engineering Fracture Mechanics, Vol. 60 (5-6), pp. 597-603, 1998.

[10] Li, X., Carlsson, L. A. and Davies, P., *Influence of fiber volume fraction on mode III interlaminar fracture toughness of glass/epoxy composites.* Composites Science and Technology, Vol. 64, pp. 1279-1286, 2004.

[11] Moura, M. F., et al., *Finite Element Analysis of the ECT Test on Mode III Interlaminar Fracture of Carbon Epoxy Composite Laminates.* 10th Portuguese Conference on Fracture, 2006.

[12] Moura, M.F., Silva, M.A. and Morais, J.J., *Análise Numérica do Ensaio ECT (Edge Crack Tortion) em Materiais Compósitos.* Granada, España : SEMNI, Congreso de Métodos Numéricos en Ingeniería, 2005.

[13] Pennas, D., Cantwell, W.J. and Compston, P., *The Influence of Strain Rate on the Mode III Interlaminar Fracture of Composite Materials.* Journal of Composite Materials, Vol. 41, pp. 2595-2614, 2007.

[14] Silva, M.A.; Moura, M. F.; Morais, A. B.; Morais, J.J., *Validação Numérica do Provete Edge Crack Torsion (ECT), para determinação experimental de G_{IIIC} em Materiais Compósitos de Carbono-Epóxido.* Ciência & Tecnologia dos Materiais, Vol. 18 (8), 2006.

[15] Suemasu, H. *An experimental method to measure the mode III interlaminar fracture toughness of composite laminates.* Composites Science and Technology, Vol. 59, pp. 1015-1021, 1999.

[16] Zhao, D. and Wang, Y., *Mode III fracture behavior of laminated composite with edge crack in torsion.* Theoretical and Applied Fracture Mechanics, Vol. 29, pp. 109-123, 1998.

[17] de Morais, A.B., Pereira, A.B., Moura, M.F., Magalhães, A.G., *Mode III interlaminar fracture of carbon/epoxy laminates using the edge crack torsion (ECT) test.* Composites Science and Technology, Vol. 69, pp. 670-676, 2009.

[18] Marat-Mendes, R. and Freitas, M., *Characterisation of the edge crack torsion (ECT) test for the measurement of the mode III interlaminar fracture toughness.* Engineering Fracture Mechanics, Vol. 76, pp. 2799–2809, 2009.

[19] Marat-Mendes, R. and Freitas, M., *Failure criteria for mixed mode delamination in glass fibre epoxy composites.* Composite Structures. doi:10.1016/j.compstruct.2009.07.017, 2009.

[20] Ratcliffe, J.G., *Characterization of the Edge Crack Torsion (ECT) Test for Mode III Fracture Toughness Measurement of Laminated Composites.* Langley Research Center, Hampton, Virginia: National Research Council, 2004.

[21] Lee, S.M., *An Edge Crack Tortion Method for Mode III Delamination Fracture Testing.* Journal of Composite Technology & Research, Vol. 15 (3), pp. 193-210, 1993.

[22] Li, J., Lee, S.M, Lee, E.W., O'Brian, T.K., *Evaluation of the Crack Tortion (ECT) Test for Mode III Interlaminar Fracture Toughness of Laminated Composites.* Journal of Composites Technology & Research, Vol. 19 (3), pp. 174-183, 1997.

[23] Ronal Krueger, *The Virtual Crack Closure Technique: History, Approach and Applications*, NASA/CR-2002-211628, April 2002.

MEASUREMENT OF THE ADHESION ENERGY IN A Cu-C INTERFACE

D. Marcos-Gómez[1], J. Tamayo-Ariztondo[1], J. Garagorri[1] D. González[1], J.M. Molina-Aldareguia[2], M.R. Elizalde[1]

[1] CEIT and TECNUN (University of Navarra). Manuel de Lardizábal 15, 20018 San Sebastián, Spain
E-mail: dmarcos@ceit.es

[2]Fundación IMDEA-Materiales, c/Profesor Aranguren s/n, 28040 Madrid, Spain

ABSTRACT

Recently, Cu/C composites have been developed for heat sink applications. Yet, it is known that the adhesion between copper and carbon is weak due to its poor wetting [1]. To improve interfacial properties, Cr or Ti interlayers are used so that the adhesion between Cu and C enhances considerably. In order to measure adhesion in terms of energy, Cu-C flat systems have been prepared. These systems consist of an amorphous carbon substrate with a Cu coating, either with or without a Ti interlayer. Top nanoindentation is performed with a Berkovich tip nanoindenter which penetrates the top surface of the sample, i.e., the coating, and causes debonding of the interface if the driving force introduced by the indentation exceeds the interfacial bond strength. The crack formed in the debonding enables to measure the adhesion energy through an equation derived from the mechanical analysis on layered systems by Marshall and Evans [2].

These experimental results are used to calibrate a cohesive law for a model based on finite elements. The parameters peak stress, maximum equivalent displacement, initial stiffness and adhesion energy of the cohesive law, three of which are independent, have to be determined to this end. Results from the analytical and numerical model are compared. The fact that Marshall-Evans formula does not take into account the plastic energy dissipated by the Cu layer to calculate the fracture energy of the interface from top indentation tests is also discussed.

KEY WORDS: Cu/C composite, adhesion energy, cohesive elements, FEM, nanoindentation

INTRODUCTION

Copper-Carbon Nanofiber (Cu-CNF) composite materials have very promising theoretical properties, specifically, when considering thermal and electrical conductivities. Unfortunately, Cu and CNF show a very weak adhesion as the wetting between them is very poor [1]. This can be solved with interfacial nanometric layers of elements like Ti or Cr. In order to assess the interfacial toughness improvement achieved top nanoindentation tests have been performed on a flat system. This system consists of a Cu layer on top of an amorphous carbon substrate with or without a Ti interlayer. With the data obtained in these experiments, the fracture energy of the interface can be calculated through the equation of Marshall and Evans [2].

Cohesive elements are a very powerful tool to analyse fracture in adhesive layers or in interfaces (for example [3]), but due to their phenomenological nature they demand to be calibrated through experimental data in order to offer realistic results. In addition, some properties of the materials under study may be not entirely or accurately known, which allows for parametric studies of the indentation process, that include other parameters apart from those defining the cohesive elements. Once these are calibrated, complex models of finite elements can be built placing these in the interface between phases, which is the part of the composite prone to fracture, especially for weak interfaces.

EXPERIMENTAL PROCEDURE

The samples tested for mechanical adhesion consist of a 3 μm thick Cu thin film sputtered by Physical Vapour Deposition (PVD) onto a 10 x 10 x 1.5 mm amorphous carbon substrate. In addition, one of the samples contains a very thin (2.5 nm) interlayer of titanium. The notation and description of the samples are shown in table 1.

Table 1. Samples tested with their notation and principal characteristics.

Notation	Interlayer (thickness)	Thickness of Cu layer
17.1	None	3000 nm
17.2	Ti (2.5 nm)	3000 nm

Residual stress analysis

Prior to indentation, residual stresses of the Cu thin films have been measured by the parallel beam glancing X-ray diffraction technique [4]. The diffractometer used

in this work is a Philips X'Pert MRD, which was operated at a voltage of 40 kV and a current of 40 mA. A Cu tube was used to emit in the X-Ray wavelength $K_{\alpha 1}$ = 1.540562 Å [5].

Glancing is a useful method to characterise the spacing between planes in thin films, hence enables to quantify residual stresses in the film. It principally consists on irradiating the material at a very low incident angle with respect to its surface. This enables a very low penetration depth, hence avoiding any interaction with the substrate. The Glancing method was carried out with a linear primary optic. The apertures for the low angle slits at the primary optic were set as 10 for vertical slit and 1/16th for the horizontal slit. A value of ω = 3 º was determined for the incident angle. A solution of free stressed silicon crystals and 2-propanol (isopropyl alcohol) was spread over sample surfaces. The free stressed crystals permit to detect and estimate the errors principally introduced from absorption of the specimen and displacement of the specimen from the diffractometer axis, which is considered as the largest single source of error [6].

Top Nanoindentation tests

The Top Nanoindentation method consists in indenting the thin film on the top surface so that a crack at the interface between the film and the substrate appears [7-9]. The apparatus used in this work to attempt interface debonding on samples 17.1 and 17.2 is a NanoIndenter® II (Agilent, formerly Nano Instruments, Inc.). The indentation tip used for the experiments is a Berkovich tip, a three-sided diamond pyramid. All the indentation tests were carried out under displacement control at a maximum penetration depth varying from 400 nm to 2500 nm.

Adhesion energy was calculated using the Marshall & Evans equation (ME) [2]:

$$G = \frac{h\sigma_I{}^2(1-\nu^2)}{2E} + (1-\alpha)\frac{h\sigma_R{}^2(1-\nu)}{E} - (1-\alpha)\frac{h(\sigma_I-\sigma_B)^2(1-\nu)}{E} \quad (1)$$

where h is the coating thickness, E and ν are the Young's modulus and Poisson's ratio of the coating (110 GPa and 0.343), respectively, and α is a parameter equal to 1 - 1/(1 + 0.902(1 - ν)) when buckling has occurred and equal to 1 when no buckling has been observed. This equation considers the substrate as infinitely rigid, i.e., changes in its strain energy are negligible when the delamination radius is much larger than the film thickness. The film is considered to experience a biaxial stress field.

σ_I is the stress provoked by the indentation and is described as:

$$\sigma_I = \frac{EV_I}{2\pi h a^2(1-\nu)} \quad (2)$$

where V_I is the indented volume and a half of the crack length provoked by the delamination.

σ_R is the residual stress measured in the Cu thin film. If the driving force is sufficiently high, delamination can cause buckling of the Cu layer. The buckling condition is ruled by the critical biaxial buckling stress σ_B, given by [6]:

$$\sigma_B = \mu^2 \frac{h^2 E}{12a^2\left(1-\nu^2\right)} \quad (3)$$

where μ^2 is equal to 14.68 for single buckling and equal to 42.67 for annular buckling or centre-pinned clamped-clamped plate.

A FIB dual beam Quanta FEG 3D (FEI) was used to measure the crack length 2a produced during indentation, in order to calculate the adhesion energy G. A trench was milled across the indentations in order to achieve direct observation of the delamination occurred when indenting a Cu-C sample at different depths with a Berkovich tip.

FINITE ELEMENT MODEL

A finite element (FE) model was prepared using the FE commercial suite ABAQUS to reproduce the nanoindentation experiments. The model consisted in 60º slice of the actual specimen, as the Berkovich tip has mirror and three-fold rotational symmetry. The model is 40 μm high, including the 3 μm thick Cu layer adhered by a zero-thickness cohesive layer (i.e., a layer made of cohesive elements) to the remaining 37 μm of vitreous carbon. This cohesive layer was based on the phenomenological concept of cohesive zone that is used in FE modelling for fracture mechanics and was built with COH3D8 elements. A refined mesh was used around the indentation, both in the Cu and the carbon substrate, and around the expected crack.

Table 2. Elastic properties used to model copper and carbon.

	Young Modulus (GPa)	Poisson's Ratio
Copper [10]	110	0.343
Vitreous Carbon	26[11]	0.343

Table 2 shows the elastic properties of the two materials constituting the model. The substrate was defined as an elastic material in all the simulations so no energy is spent in plastic deformation of the substrate. Poisson's

ratio of the vitreous carbon was unknown and it was assumed to have the same value as for Cu which should not influence the final results. It is important to notice that Cu is four times stiffer than the vitreous carbon, which means that the substrate was noticeably affected by the indentations. Regarding the Cu film, it is modelled as an elastic-plastic material with strain hardening defined by the Hollomon's equation. The behaviour of thin films is a subject open to discussion so yield stress and the strain hardening coefficient are initially considered parameters to study its influence on the calculation of the interfacial fracture energy. Finally, according to experimental measurements, a tensile residual stress of 300 MPa is introduced in the Cu layer (table 3).

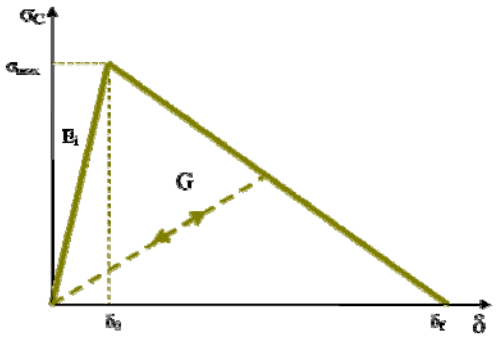

Figure 1. Scheme of the traction-separation law used in the cohesive elements. Four parameters, three of which are independent, define the triangular law: fracture energy (G), peak stress (σ_{max}), initial stiffness (E_i) and final displacement (δ_f),.

A triangular law is used to define the cohesive elements behaviour (fig. 1) [12]. This law is defined by four parameters of which only three are independent. Fracture energy (G), peak stress (σ_{max}) and initial stiffness (E_i) have been used as parameters to calibrate the cohesive law.

EXPERIMENTAL RESULTS

The structure of the Cu coating in samples 17.1 and 17.2 can be observed in figure 2. The effect of the 2.5 nm thick Ti interlayer is noticeable; whereas the sample without interlayer shows a Cu coating with high roughness and porosity, these effects are significantly reduced in the presence of the interlayer.

Figure 3 shows the evolution of crack radius with the penetration depth of the indentation in sample 17.2. It can be observed that the evolution of crack radius is linear with the maximum penetration depth during top indentation. Similar data could not be obtained for sample 17.1 since either no cracks at the interface were generated or the data were not consistent. This is due to the abovementioned roughness and porosity of the Cu coating which is probably related to the poor wetting between Cu and C. An example is shown in figure 4, where at low penetration depth the indenter only came into contact with a unique grain. Thus only data obtained at a penetration depth of 2500 nm have been considered for calculating interfacial fracture energy with ME equation [2]. The results are gathered in Table 3.

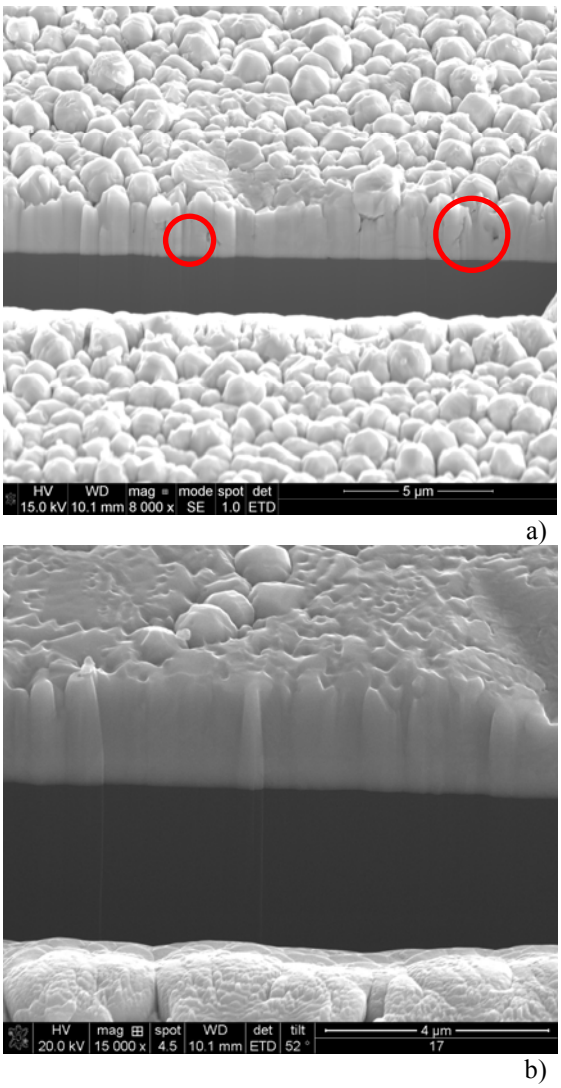

Figure 2. SEM pictures of a trench milled with the FIB on a) sample 17.1 and; b) sample 17.2. Some pores are highlighted with circles in sample 17.1.

Table 3. Average residual stresses, interfacial crack length after a top indentation tests performed at a maximum depth of 2500 nm and calculated adhesion energy using eq. (1) [2] for samples 17.1 and 17.2.

Sample	Residual Stress (MPa)	Adhesion Energy (J/m^2)	Crack Length (µm)
17.1	290 ± 40	24 ± 4	25 ± 1
17.2	307.10 ± 0.05	70 ± 30	19 ± 2

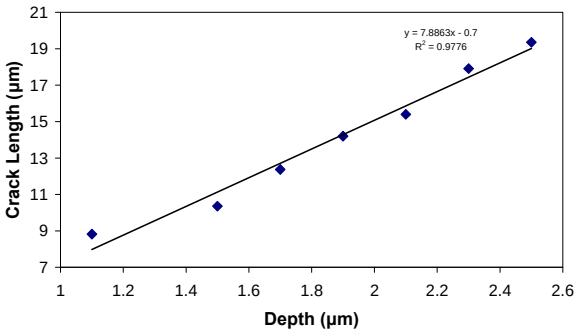

Figure 3. Crack radius against maximum penetration depth during top indentation. Sample 17.2.

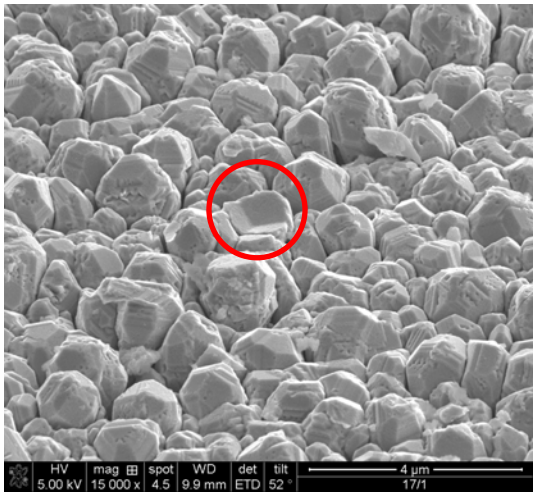

Figure 4. Imprint of a 400 nm depth indentation in a grain of sample 17.1 (circled).

Regarding the effect of the residual stresses in the Cu coating, it can be observed that they are tensile and similar for both samples and hence buckling has not occurred during top indentation tests.

Finally, a significant increase of the adhesion fracture energy is observed in the sample 17.2, so it can be concluded that the 2.5 nm thick Ti interlayer enhances the adhesion between copper and carbon.

COHESIVE LAW CALIBRATION

The crack length vs. penetration depth curve from figure 3 will be used as the reference to calibrate the cohesive elements for the FE model. Only the experimental results obtained for sample 17.2 (with Ti interlayer) are used as a reference because, as mentioned earlier, the data for sample 17.1 were not consistent. Figure 5 shows a comparison between interfacial crack observed in the experiments and the FE simulation results. A very good qualitative agreement between the actual crack and the simulated one can be observed.

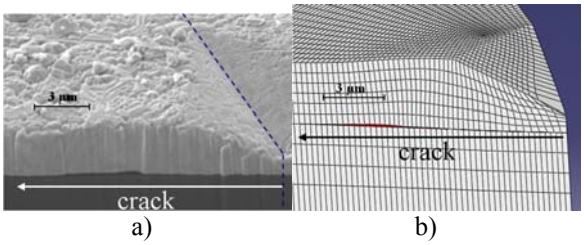

Figure 5. Cross-section view across a top indentation test: (a) SEM image of a FIB milled trench and (b) FE simulation.

A parametric study has been performed in order to calibrate the cohesive law. The parameters considered have been on one hand the fracture energy G, the initial stiffness E_i, and the peak stress σ_{max}, defining the cohesive law, and on the other hand the Cu yield stress σ_y and its hardening coefficient n, defining the plastic behaviour of the Cu film. Several simulations have been performed using as average values 2 J/m^2 for G, 200 GPa for E_i, 150 MPa for σ_{max}, 500 MPa for σ_y and 0 for n. In the case of the cohesive law parameters these values were chosen after some first tries whereas the data for Cu correspond to a 1 µm thick layer [13, 14].

The initial stiffness defines the elastic response of the cohesive elements until damage starts. It has to be big enough not to increase the compliance of the structure but too high values may lead to numerical problems. Simulations varying E_i from 200 to 400 GPa resulted in a decrease of the crack length of around half a micron. It can be concluded that the effect of this parameter is negligible for the problem studied and hence it was decided to fix its value at 200 GPa, roughly twice the elastic modulus of Cu.

Regarding G and σ_{max}, the initial calculations were performed with values of 50 J/m^2 and 500 MPa, respectively, using as reference the fracture energy calculated using ME for sample 17.2 and the elastic limit of Cu. However no cracks were observed in the simulations and thereafter values for both parameters were decreased. G was varied from 30 to 2 J/m^2 and σ_{max} from 400 to 100 MPa. Results of these simulations are shown in Table 4 and figure 6, where the crack radius at the interface for an indentation depth of 2500 nm is gathered for different values of σ_{max} and G. It is noted that snap-back convergence problems appears as σ_{max} is increased or G is decreased. It is shown that the crack increases with peak stress, but the increase is slight (around 1 µm) and saturates for peak stresses above 200 MPa. Concerning the effect of the fracture energy, as expected it is the parameter which affects the delamination to a greater extent: crack radius at the interface increases significantly as fracture energy decreases. However two regimes can be observed in the range simulated, both showing a roughly linear dependence but with different values of the slope. In

fact the ratio crack radius to fracture energy increases in an order of magnitude when G is below 10 J/m^2. For a stronger interface the plastic deformation of the Cu layer will be higher and hence a bigger amount of the energy introduced in the system will be expended in plastic deformation and will not contribute to the crack extension.

Table 4. Interfacial crack radius for different values of fracture energy and peak stress at a nanoindentation depth of 2500 nm. 'X' means simulations not completed due to convergence problems.

Crack Radius a (±0.3 μm)		G (J/m^2)				
		2	5	10	20	30
σ_{max} (MPa)	100	17.7	13.1	8.9	7.7	6.9
	150	18.3	14.2	9.7	8.3	7.4
	200	X	X	10.6	8.6	8.0
	250	X	14.9	X	8.6	8.0
	300	X	X	X	8.6	8.0
	350	X	X	X	0	0
	400	0	0	0	0	0

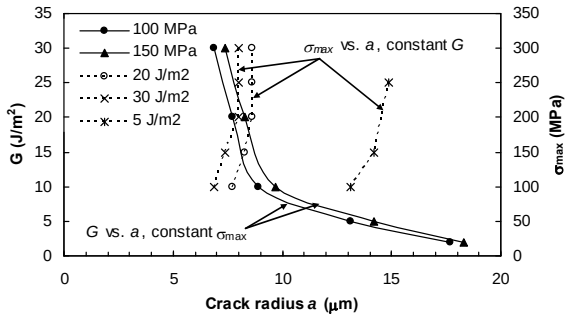

Figure 6. Effect of fracture toughness G and peak stress σ_{max} on the delamination extent (crack radius a). Solid lines curves represent G vs. a for different values of σ_{max} and dotted curves represent σ_{max} vs. a for different values of G.

To study the effect of the plastic behaviour of the Cu on the top indentation test results simulations were performed for yield strength values between 220 and 500 MPa and hardening coefficients between 0 and 0.3. The ranges were selected according to data from literature for different Cu layers [13, 14]. Figure 7 shows the effect of σ_y and n on the crack radius for indentations performed at a maximum depth of 1300 nm and on the slope of the crack radius vs. maximum penetration depth (see fig. 3). It is observed that the effect of the strain hardening coefficient is small and hence it was decided to define Cu as a perfect elasto-plastic material. Regarding the yield strength, a small influence is observed for values between 300 and 500 MPa. Taking this into account and experimental results obtained for Cu layers with different thicknesses [13], a value of 300 MPa is fixed for σ_y.

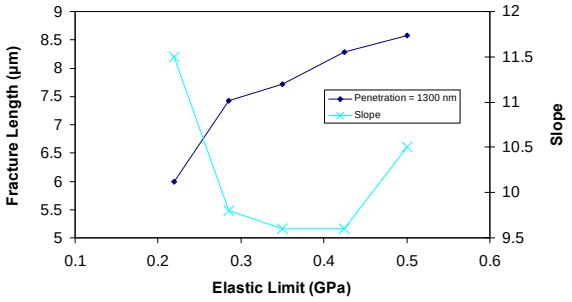

a)

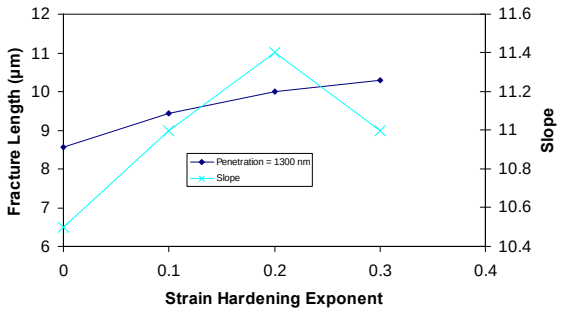

b)

Figure 7. Effect of plasticity variables in the fracture length at a penetration depth of 1.3 μm (left) and in the slope of the fracture length vs. penetration depth curve (right). a) Elastic limit and b) strain hardening exponent

Finally σ_{max} and G were varied taking into account results in table 4 with Cu defined as perfect elasto-plastic with an elastic limit of 300 MPa. Figure 8 shows the experimental and simulated crack radius vs. maximum penetration depth during a top indentation test. As can be noticed a very good agreement is found for G = 2 J/m^2 and σ_{max} = 170 MPa. A deviation from the experimental results is observed for indentation depths below 1300 nm approximately, which can be explained by the structure of the Cu layer described in the previous section.

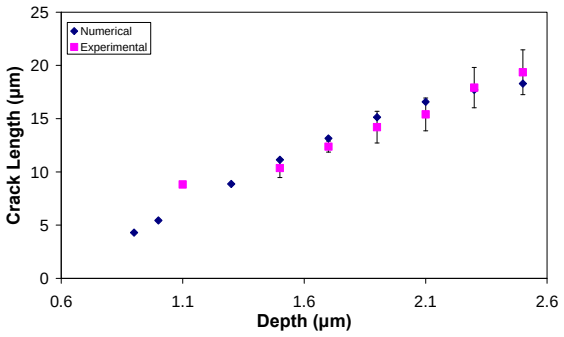

Figure 8. Experimental and simulated (σ_{max} = 150 MPa and G = 2 J/m^2) crack lengths for different indentation depths. Good agreement can be observed.

Additionally, fracture energy is 30 times lower than that calculated through ME for sample 17.2. This effect was also observed in [14], where the plasticity contribution to adhesion was calculated for a 4 point bend test.

CONCLUSIONS

It is shown that top indentation is a suitable technique to determine interfacial adhesion, even if in this work the results are limited due to the structure of the Cu layer (roughness, porosity). However it can be concluded that introducing a Ti nanometric interlayer improves adhesion between Cu and amorphous carbon.

The results from the top indentation tests, in particular the curve crack radius versus penetration depth can be used to calibrate the parameters of a cohesive law which will define adhesion between Cu and amorphous carbon. It is shown that for the system studied the adhesion is overestimated when the analytical models proposed in [2] are used. This is probably related to the plastic energy dissipated during the test and the deformation of the carbon substrate.

REFERENCES

[1] Villard, P., Calvert, L.D., "Pearsons's Handbook of Crystallographic Data", 2nd edR, *ASM International,* Materials Park, Ohio 1991.

[2] Marshall, D.B. and Evans, A.G., "Measurement of adherence of residually stressed thin-films by indentation .1. Mechanics of interface delamination", *J. Appl. Phys.*, Vol. 56, p. 2632 1984.

[3] Segurado, J., *Micromecánca computacional de materiales compuestos reforzados con partículas,* Ph.D. Thesis, Delft, Spain, 2009.

[4] Moreno, C.M., Sanchez, J.M., Ardila, L.C., Molina-Aldareguia, J.M., "Determination of residual stresses in cathodic arc coatings by means of the parallel beam glancing X-ray diffraction technique", *Thin Solid Films*, Vol. 518, p. 206, 2009.

[5] Cullity, B.D., *Elements of X-Ray Diffraction*. Addison-Wesley 2nd ed., 1978.

[6] Kriese, M.D. and Gerberich, W.W., "Quantitative adhesion measures of multilayer films: Part I. Indentation mechanics", *J. Mater. Res.*, Vol. 14, Issue 7 p. 3007, 1999.

[7] Lee, A., Clemens, B.M., Nix, W.D., "Stress induced delamination methods for the study of adhesion of Pt thin films to Si", *Acta. Mater.*, Vol. 52, p. 2081, 2004.

[8] Kese, K.O., Li Z.C., Bergman, B., "Method to account for true contact area in soda-lime glass during nanoindentation with the Berkovich tip", *Mat. Sci. Eng. A*, Vol. 404, Issue 1-2, p. 1 2005.

[9] Gong, J.H., Miao, H.Z., Peng, Z.J., "Analysis of the nanoindentation data measured with a Berkovich indenter for brittle materials: effect of the residual contact stress", *Acta Mater.* Vol. 52, Issue 3, p. 785, 2004.

[10] Matweb, "Copper, Cu; Annealed", *http://www.matweb.com*

[11] Matweb, "Vitreous Carbon", *http://www.matweb.com*

[12] Tvergaard, V. and Hutchinson, J.W., "The influence of plasticity on mixed mode interface toughness", *J. Mech. Phys. Solids*, Vol. 56, p. 2632 1984. Vol. 41, Issue 6, p. 1119, 1993.

[13] Vinci, R. P., Zielinski, E. M., Bravman, J. C., "Thermal strain and stress in copper thin films", *Thin Solid Films*, Vol. 262, Issues 1-2, p. 142, 1995.

[14] Lane M., Dauskardt, R.H., Vainchtein, A., Gao, H.J., "Plasticity contributions to interface adhesion in thin-film interconnect structures", *J. Mater. Res.*, Vol. 15, Issue 12, p. 2758, 2000.

[15] Ocaña, I., Molina-Aldareguia, J.M., Gonzalez, D., Elizalde, M.R., Sánchez, J.M., Martínez-Esnaola, J.M. Gil Sevillano, J.,Scherban, T., Pantuso, D.. Sun, B., Xu, G., Miner, B., He, J. Maiz, J. "Fracture characterisation in patterned thin-films by cross sectional nanoindentation", Acta Mater, Vol 54, p. 3453, 2006.

ACKNOWLEDGEMENTS

Financial support from the EC (Project Interface FP6 STRP 031712) and Basque Government (PhD Grant, project PI07-17) is acknowledged. Dr. Finn Giuliani is acknowledged for providing the samples. D. Marcos is grateful to the Spanish Ministry of Science and Innovation and to the European Social Fund (Torres Quevedo Programme). J. Tamayo-Ariztondo is grateful to the Basque Government for his PhD grant.

ASSESSMENT OF THE MECHANICAL PROPERTIES ON NANOCLAYED POLYMER BASED COMPOSITES

P.N.B. Reis[1], J.A.M. Ferreira[2], J.D.M. Costa[2], S.S. Sauceda[2] and M.O.W. Richardson[3]

[1]CCTA/UBI, Electromechanical Engineering Department
Rua Marquês de Ávila e Bolama
6201-001Covilhã
E-mail: preis@ubi.pt

[2] CEMUC, Mechanical Engineering Department, University of Coimbra,
Rua Luís Reis Santos, Pinhal de Marrocos,
3030-788, Coimbra, Portugal.
E-mail: martins.ferreira@dem.uc.pt; jose.domingos@dem.uc.pt; ss.stewen@gmail.com

[3]RCMI, Department of Mechanical and Design Engineering, University of Portsmouth, England
E-mail: Mel.Richardson@port.ac.uk

ABSTRACT

Nanoscale reinforcement provides opportunities for enhancing polymer systems with unique properties and extended performance, leading, not only to an improvement in the mechanical and fatigue properties but also act as a barrier to slow water permeation. This paper presents the results of a current study concerned to the mechanical properties of a polypropylene binder resin enhanced by using nanoclay reinforcement. The study was centred on the potential benefits obtained by the addition of nanoclays on the stiffness, static and fatigue strength, absorbed impact energy and water absorption resistance. Specimens were produced by injection moulding process with up 3% in weight of nanoclay. Nanoclays improve bending stiffness and bending strength. The immersion in water during 40 days increases the stiffness more than 80% and the bending strength about 40% for all the material compositions. The nanoparticles did not affect significantly the impact energy absorbed and the immersion in water causes a reduction of at least 10%. The addition of 3% of nanoclay promotes a negative effect in G_c, while the water immersion improves significantly the strain energy release rate, particularly for nanoclay filled composites. All material configurations exhibit high cyclic creep showing a faster and intense stress release since the first cycles of fatigue. The 3% nanoclayed composite exhibits fatigue strength higher than the unfilled materials.

KEYWORDS: Nanocomposites, flexure properties, testing.

1. INTRODUCTION

Nanoclay are chemically modified clay where tiny nano level particles that when dispersed throughout a polymer matrix to give remarkably improvements in mechanical and physical properties even at low loading levels eg 1-6 % w/w [1-6].

Unfortunately, dispersion is not easily achieved and the benefits claimed in the literature are, disappointingly, not often realized. It is reported in literature that the key to successful reinforcement with nanoclays is to ensure it completely exfoliates. For this purpose a special silane treatments were developed which radically out-performed commercially available gelcoats in terms of their blister resistance, hardness, stiffness, strength, toughness and fatigue life. Fig.1 shows schematically comparison of non treated and specially treated nano-particles so that they perfectly disperse through polymer matrix systems leading to exceptionally high levels of physical and chemical reinforcement. Studies of Yoshida et al [7] confirm the effectiveness of the silane coupling agent on the interface between silica particles and an epoxy resin. He found that the silane coupling agent has the effect of reducing the degradation of mechanical properties and the adhesiveness of the interface between the resin and silica particle and is satisfactory even after water absorption due to the deformation of a chemical bond.

As mentioned before, the effectiveness of nanoclayed composites increases with the better distribution of the clay in the polymer, being that one of the reasons for which it is not very popular to combine polypropylene (PP) with nanoparticles, once it presents a low rate of nanoparticles distribution onto the matrix. Naturally the PP presents a low compatibility during the mixture

making poor distribution, but new techniques of mixture have been developed to improve exfoliation.

This paper presents the results of a current study concerned to the mechanical properties of a polypropylene binder resin enhanced by using nanoclay reinforcement. The study was centred on the potential benefits obtained by the addition of nanoclays on the stiffness, static and fatigue strength, the absorbed impact energy and water absorption resistance and . Composites sheets were produced by injection moulding process with up to 3% in nanoclay weight.

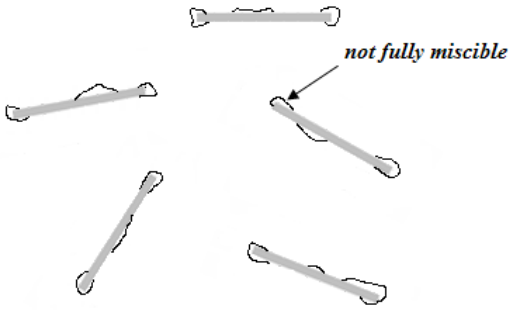

Without Treatment

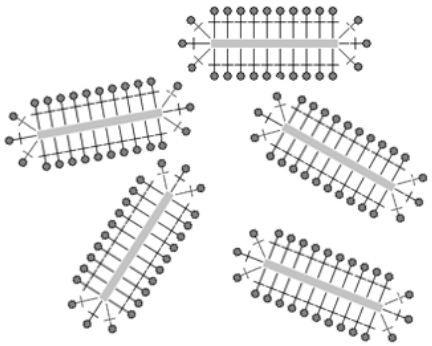

With Treatment

Figure 1. Exfoliates and distributes created by special silane treatment.

2. MATERIALS PROCESSING AND TESTING

Five material formulations were manufactured as summarized in Table 1. Specimens were produced by injection moulding process with 60x10x4 mm^3. 1% w/w pure liquid paraffin (Boots Brand) was added to PP powder along with up to 3% w/w of nanoclays and then stir mixed before injection moulding (PPA3). For PPB3, the liquid paraffin containing small percentage of nanoclays. For PPA and PPB compositions the same procedure was done but without adding nanoclay.

The bending and the strain energy release rate tests were performed in three-point bending loading with a span of 40 mm, by using a Shimadzu AG-10 universal testing machine, equipped with a 5kN load cell and TRAPEZIUM software, at a displacement rate of 1 mm/min. Fatigue tests were performed in three points bending using an imposed displacement electromechanical machine at 10 Hz frequency. All tests were carried out at room temperature.

Table 1. Summary of the specimen's configuration

Code	Composition
PP	Polypropylene
PPA	Polypropylene and paraffin (1% w/w pure liquid paraffin)
PPB	Polypropylene and paraffin (1% w/w pure liquid paraffin containing small percentage of nanoclays)
PPA3	3 % of nanoclays added to polypropylene and paraffin (1% w/w pure liquid paraffin)
PPB3	3 % of nanoclays added to polypropylene and paraffin (1% w/w pure liquid paraffin containing small percentage of nanoclays)

The nominal bending stress (σ) was calculated using:

$$\sigma = \frac{3PL}{2bh^2} \tag{1}$$

being P the load, L the span length, b the width and h the thickness of the specimen.

Bending strength was obtained using peak load in equation (1), while the stiffness modulus was calculated by the linear elastic bending beams theory relationship

$$E = \frac{\Delta P \cdot L^3}{48 \Delta u \cdot I} \tag{2}$$

where: I is the inertia moment of the transverse section and ΔP and Δu are, respectively, the load range and flexural displacement range at middle span for an interval in the linear region of load versus displacement plot.

Charpy impact tests were performed using rectangular 10x4 mm^2 notched specimens, according to ASTM D 6110-97. A 2 mm deep sharp notch with 45º flank angle was machined in each specimen. Afterwards, the tests were carried out on a Ceast 6548/000 pendulum with 50 mm span and an impactor of 2 J. The absorbed energy was directly measured by machine software. The displayed value is obtained from the difference of potential energy between the starting and after-impact highest position of the pendulum.

Water absorption was obtained using the next procedure: the samples are placed in an oven at 80 ºC for 2 hours, cooled and weighted in order to obtain the dry weight (DW), afterwards, the samples are immersed in water and periodically weighted to obtain the current wet weight (CWW). The water absorption in weight percentage (W%) was calculated from equation (3)

$$W\% = \frac{CWW - DW}{DW} x100 \qquad (3)$$

Figure 2 shows the water absorption curves for three material configurations. All these configurations show very small water absorption up to 650 hours. However, for the paraffin additive materials (PPB) and the nanoclay filled configuration (PPB3) lower water absorption was obtained with a tendency to stabilization after only few hours.

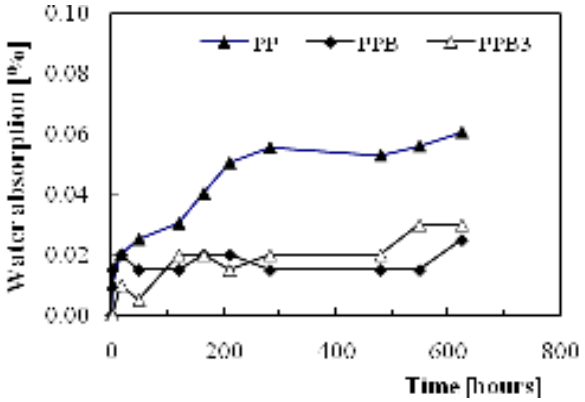

Figure 2. Water absorption curves.

3. RESULTS AND DISCUSSION

3.1. Bending tests

Figure 3 shows typical bending stress versus transversal displacement for three material compositions. The three curves are closed, pointing to a small influence of the filler and additive on stiffness and maximum stress, in spite of a tendency to the improvement in both properties by the nanoclays addition. All compositions exhibit a nonlinear behavior even for low stress level with a high plasticity.

Figure 4 shows the average values of the bending strength obtained for dry specimens and specimens immersed during 40 days in water at 20 ºC. Materials filled by nanoclays exhibit only a slight tendency to increase bending strength. However, surprisingly the immersion in water causes a benefit effect about 40% in all the five material compositions. A benefit in stiffness and strength were also obtained by L. Sobrinho et al. [8], in a vinyl ester resin system that initially presented ductile behavior and modified to brittle after 16 days of hygrothermal ageing at 60 °C due to the increase of crosslink.

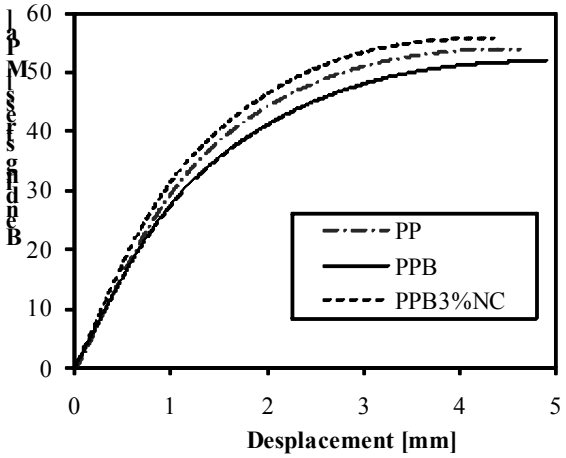

Figure 3. Comparison of stress-displacement curves for nanoclayed and unfilled materials.

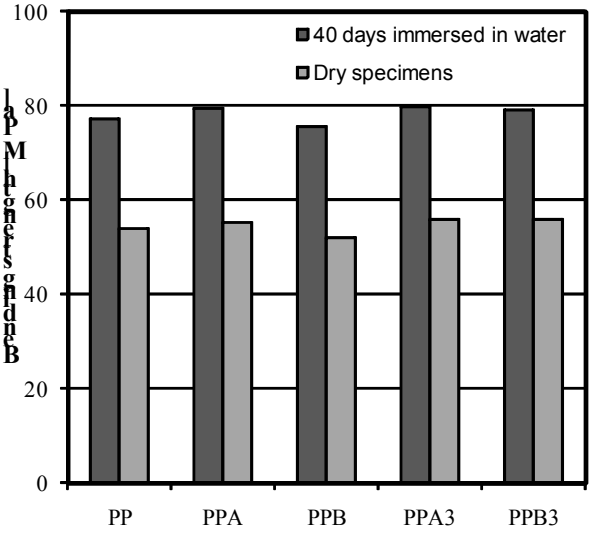

Figure 4.Average bending strength: influence of the material composition and water exposure.

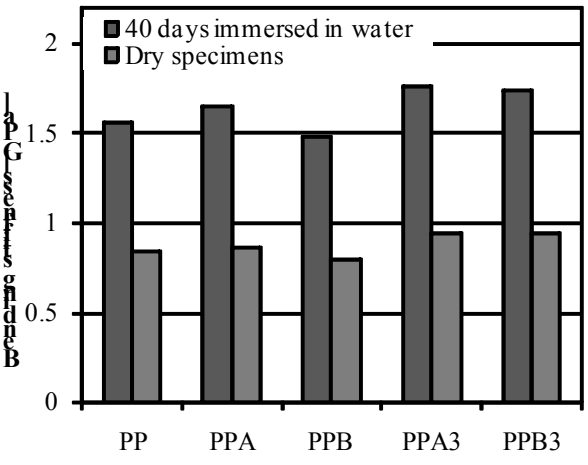

Figure 5.Average bending stiffness: influence of the material composition and water exposure

This is in agreement with the results obtained in this work for bending stiffness and shown in Figure 5 in terms of average values. Materials filled by nanoclays exhibit bending stiffness about 12% higher than unfilled materials. The immersion in water during 40 days increases the stiffness more than 80% for all the five material compositions.

3.2. Impact energy

The results of absorbed impact energy are presented in Fig. 6 in terms of the average value obtained from at least four tests for each test condition. The figure shows the results obtained for all the five configurations studied, using specimens stored in dry air and specimens immersed in water during 40 days. The results show a significant spread, but nevertheless it can be concluded that the filling of nanoparticles did not significantly affect the impact energy absorbed. In addition the immersion in water causes a reduction of the impact energy of at least 10%, confirming the embrittlement of the material previously observed.

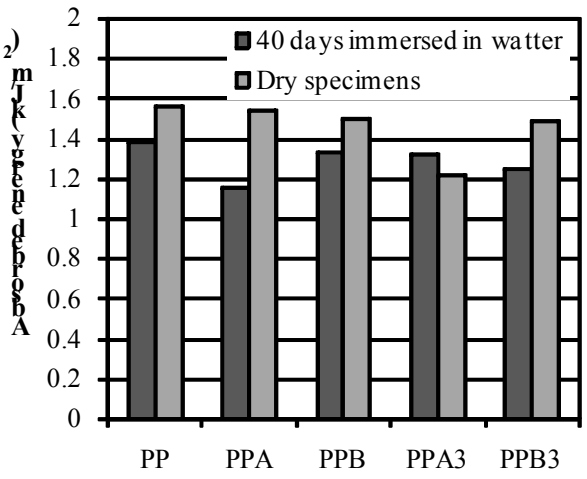

Figure 6. Absorbed impact energy: influence of the material composition and water exposure.

3.3. Strain energy release rate results

The strain energy release rate tests were carried out according ASTM D 5045-96 standard [9]. The average values obtained on dry specimens and on specimens immersed in water during forty days are presented in Figure 7.

For dry specimens a negligible influence of paraffin addition was observed. However, the addition of 3% of nanoclays promotes a negative effect that causes a decrease in G_c of about 20%. The water immersion improves significantly the strain energy release rate, particularly for nanoclay filled composites for which the average increase was over 50%.

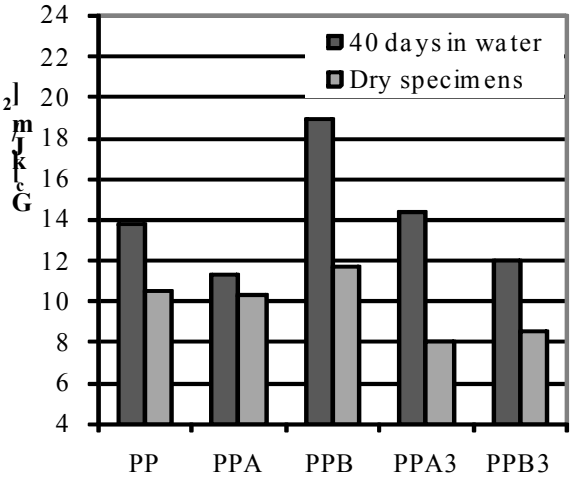

Figure 7.Average strain energy release rate: influence of the material composition and water exposure.

3.4. Fatigue behavior at constant displacement cycles

During fatigue tests the maximum and minimum peak loads were monitored at each cycle. Figures 7a) and b) show the evolution of the normalized stress amplitude versus the normalized number of cycles, where: ΔS is the current stress range, ΔS_i is the initial stress range, N is the current number of cycles and N_{ref} is the failure number of cycles corresponding to 50% decay in maximum stress.

Fig. 7a) shows the influence of the stress level for PPB3 composite while Fig. 7b) shows the influence of the material for 39.6 MPa initial stress amplitude. Matrix resin (PP), PP and paraffin material and 3% nanoclayed composite material exhibit high cyclic creep. The stress release is faster and more intense for higher initial stress levels and also for nanoclayed composites when compared with matrix resin.

Figures 8a) and b) show the initial stress amplitude versus the number of cycles to failure, where the failure is defined for different values on maximum stress decay: 20%, 30%, 40% and 50%. These figures present the results for PPB and PPB3, respectively. For both materials the results show a stress relieve, occurring a decay on maximum stress more than 30% even for low number of cycles.

The performance of the materials in terms of fatigue strength is compared in Fig. 9, where the initial stress range is plotted against the number of cycles for 50% of decay on maximum stress. For this failure criterion the nanoclayed composite PPB3 exhibits a fatigue strength about 10% higher than the paraffin containing small percentage of nanoclays (PPB material) and 20% higher than the PP matrix.

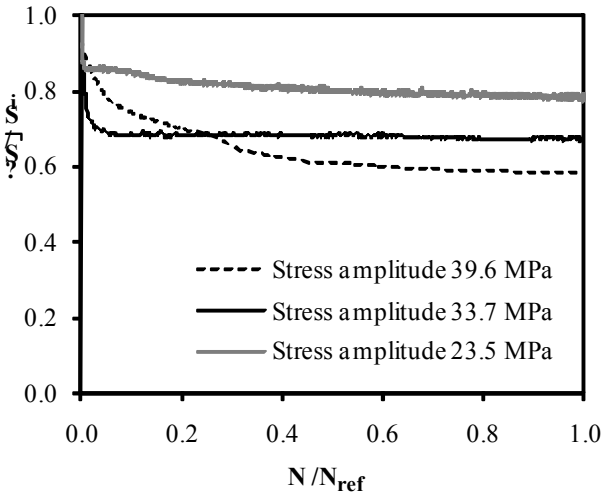

a)

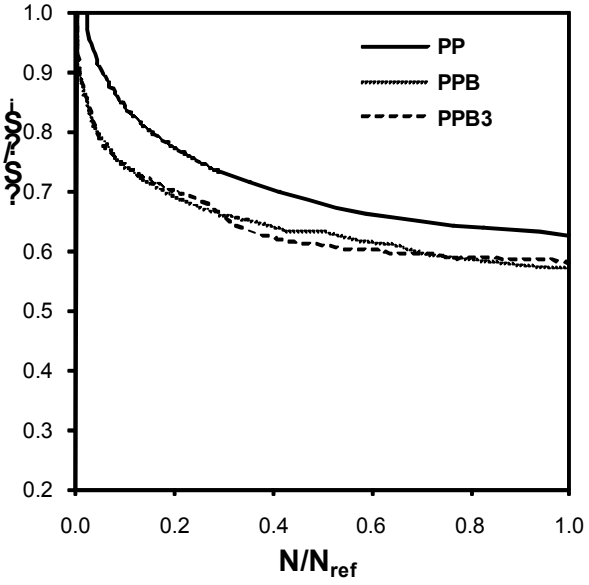

b)

Figure 7. Evolution of the stress amplitude versus the number of cycles: a) PPB3 and various stress levels; b) Different materials and initial stress amplitude 39.6 MPa.

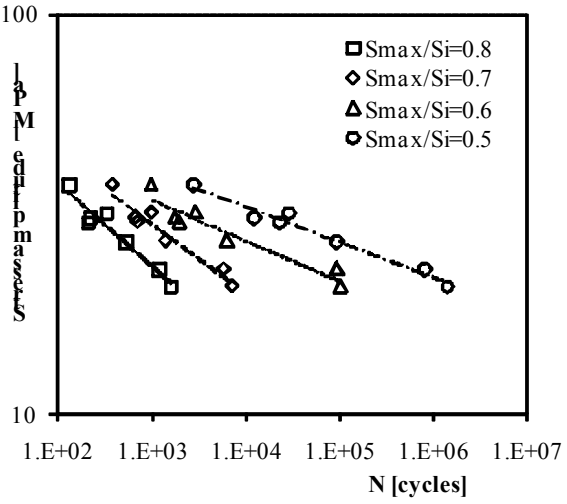

a)

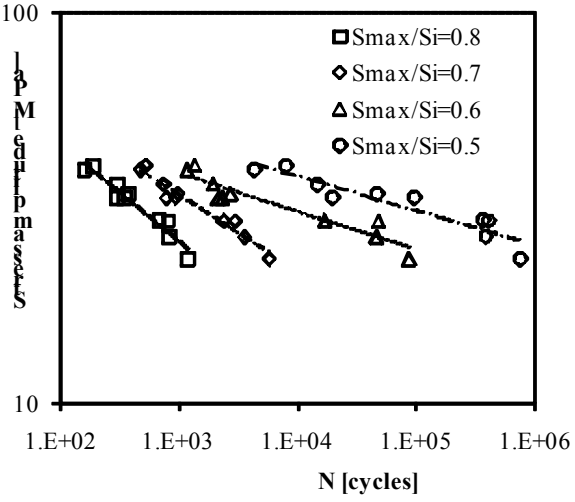

b)

Figure 8. Initial stress range versus number of cycles curves for various maximum stress decay: a) PPB; b) PPB3.

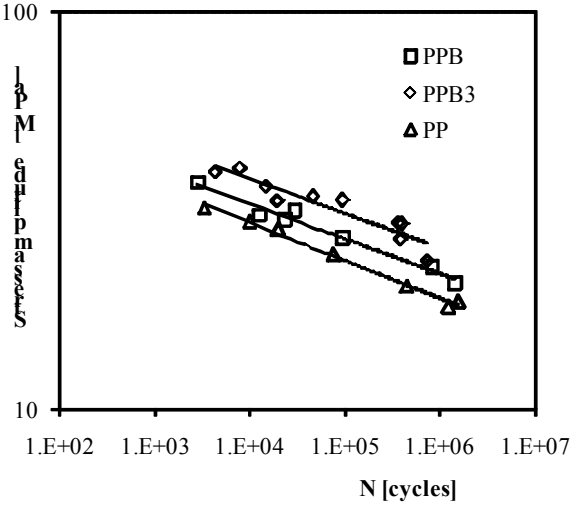

Figure 9. Initial stress range versus number of cycles curves for 50% of maximum stress decay; comparison of the materials.

4. CONCLUSIONS

The effect of the nanoclay addition in polypropylene matrix on the stiffness, static and fatigue strength, absorbed impact energy and water absorption resistance was studied and the main conclusions are:

- Nanoclayed composites exhibit bending stiffness about 12% higher than the unfilled materials and only a slight increase on bending strength. The immersion in water during 40 days increases the stiffness more than 80% and the bending strength about 40% in all the five material compositions.

- The nanoparticles did not affect significantly the impact energy absorbed while the immersion in water causes a reduction of at least 10%, due to an embrittlement of the material.

- The addition of 3% in nanoclays promotes a negative effect that causes a decrease in G_c about 20%. The water immersion improves significantly the strain energy release rate, particularly for nanoclay filled composites for which the average value increases over than 50%.

-The five material compositions exhibit high cyclic creep, showing a fast and intense stress release. For a failure criterion corresponding to 50% on the decay of maximum stress, the nanoclayed composite PPB3 exhibits a fatigue strength about 10% higher than the paraffin containing small percentage of nanoclays PPB material and 20% higher than the PP matrix.

ACKNOWLEDGMENTS

The authors thank Portuguese Foundation to Science and Technology for funding this work, Project nº PTDC/EME-PME/103622/2008.

REFERENCES

[1] Alexandre M, Dubois P, *Polymer-layered silicate nanocomposites: preparation, properties and uses of a new class of materials*, Mater Sci Eng, Vol. 28, pp. 1–63, 2000.

[2] Ke Y, Long C, Qi Z, *Crystallization, properties, and crystal and nanoscale morphology of PET-clay nanocomposites*, J Appl Polym Sci, Vol. 71:pp. 1139–1146, 1999.

[3] Song M, Hourston DJ, Yao KJ, Tay JKH, Ansarifar MA, *High performance nanocomposites of polyurethane elastomer and organically modified layered silicate*, J Appl Polym Sci, Vol. 90, pp. 3239–3243, 2003.

[4] Omar Faruk, Laurent M. Matuana, *Nanoclay reinforced HDPE as a matrix for wood-plastic composites*, Composites Science and Technology, Vol. 68, Issue 9, pp. 2073-2077, 2008.

[5] Weiping Liu, Suong V. Hoa, Martin Pugh, *Fracture toughness and water uptake of high-performance epoxy/nanoclay nanocomposites*, Composites Science and Technology, Vol. 65, Issues 15-16, pp. 2364-2373, 2005.

[6] Saeed Saber-Samandari, Akbar Afaghi Khatibi, Domagoj Basic, *An experimental study on clay/epoxy nanocomposites produced in a centrifuge*, Composites Part B: Engineering, Vol. 38, Issue 1, pp. 102-107, 2007.

[7] Yoshida Y, Higashihara T, Nomura Y, Usui E, Hibi S, *The effects of silane agent on tensile and bending properties of silica-filled epoxy after water absorption by boilding*, Electrical Engineering in Japan, Vol. 129 (2): pp. 1-12, 1999.

[8] Sobrinho L.L., M. Ferreira, F.L. Bastian, *The Effects of Water Absorption on an Ester Vinyl Resin System*, Materials Research, Vol. 12, No. 3, pp. 353-361, 2009.

[9] ASTM, *Standard test method for plane-strain fracture toughness and strain energy release rate of plastic materials*, ASTM D 5045-96, 1996.

COMPORTAMIENTO EN FRACTURA DE UN FIELTRO DE FIBRA DE VIDRIO

Á. Ridruejo [1], C. González [1,2], J. LLorca [1,2]

[1] Departamento de Ciencia de Materiales, E.T.S. de Ingenieros de Caminos, Canales y Puertos, Universidad Politécnica de Madrid, C/ Profesor Aranguren s/n, 28040 Madrid, España.
E-mail: aridruejo@mater.upm.es
cgonzalez@mater.upm.es
jllorca@mater.upm.es

[2] Instituto Madrileño de Estudios Avanzados de Materiales (IMDEA-Materiales), C/ Profesor Aranguren s/n,28040 Madrid, España.

ABSTRACT

The deformation and damage micromechanisms of a glass-fiber non-woven felt were analyzed with a combination of experiments and simulations. Tensile tests were performed on unnotched and notched rectangular specimens to study the physical nature of damage. It was found that fracture was controlled by interbundle bond fracture followed by frictional sliding, leading to the localization of damage in a wide band. A random network model based on finite elements was developed in order to gain a better understanding of the experimental data. The simulations were in very good agreement with the data and contributed to explain features such as the effect of specimen dimensions on the strength of the material and its notch-insensitive behavior.

PALABRAS CLAVE: Modelo micromecánico, fieltros de fibras, daño.

1. INTRODUCCIÓN

Los fieltros de fibras son materiales fabricados a partir de fibras desordenadas que son consolidadas mediante distintos procedimientos, que van desde el entrelazado sencillo de las fibras a procedimientos de unión química o térmica de las mismas. El interés de estos materials reside en su coste relativamente bajo, sobre todo si lo comparamos con sus equivalentes tejidos. Este tipo de materiales ha venido siendo utilizado por el hombre desde la antigüedad -los fieltros de lana desde hace al menos 3500 años-[1] y con profusión, puesto que el papel convencional no es sino un fieltro de fibras de celulosa [2], pero en los últimos años han recobrado interés tecnológico como consecuencia de nuevas aplicaciones en campos tales como la protección balística, el aislamiento térmico, como capas ignífugas, filtros o geotextiles para el refuerzo de suelos. Este interés se ha visto acrecentado desde un punto de vista más fundamental por la analogía estructural de los fieltros con los tejidos biológicos y las agrupaciones de nanotubos de carbono [3].

Las propiedades mecánicas de los fieltros difieren notablemente de las de los tejidos. Mientras que su rigidez y resistencia son menores, su capacidad de deformación y de absorción de energía es superior. Al deformarse un fieltro entran en juego distintos micromecanismos, como la deformación de cada fibra, su reacomodo mediante rotaciones y desplazamientos dentro del fieltro, la rotura de los enlaces entre fibras, el deslizamiento entre ellas y su fractura. La complejidad del estudio de todos estos procesos ha propiciado la utilización de los métodos numéricos, y en particular, del método de los elementos finitos, para obtener una mayor comprensión de los mismos.

Las simulaciones llevadas a cabo hasta la fecha se han basado en redes bidimensionales desordenadas (random fiber networks) que desde los trabajos seminales de Yang [4] y posteriormente Rigdahl [5] han venido incluyendo el efecto de distintas combinaciones de propiedades mecánicas de las fibras y de los enlaces entre ellas [6,7,8]. Sin embargo, dichos modelos han debido recurrir a suposiciones y parámetros no siempre bien justificados desde el punto de vista físico. Por otra parte, gran información disponible tiene como origen la industria manufacturera de fieltros, y en consecuencia está orientada a las propiedades del material y sus aplicaciones, lo que hace que desde el punto de vista fundamental existan lagunas en cuanto al conocimiento preciso de los mecanismos de deformación, daño y rotura de este tipo de material. Dicho conocimiento constituye el objetivo principal de este trabajo. Para ello partimos de un fieltro comercial de fibra de vidrio. Siguiendo un proceso constructivo, se caracterizaron las propiedades mecánicas de las fibras individuales y de los haces de fibras. A continuación, se realizó un estudio de la estructura del fieltro, del que se extrajeron probetas de distintos tipos, que posteriormente fueron ensayadas a tracción uniaxial. Finalmente, a partir de la información experimental, se ha desarrollado un modelo numérico de elementos finitos para simular el comportamiento del material.

2. MATERIAL

El material estudiado es el fieltro Vetrotex M123, fabricado por Saint Gobain. Este fieltro está compuesto

de fibras de vidrio de tipo *E* de 15 μm de diámetro y 50 mm de longitud. Las fibras se agrupan en haces de sección rectangular (360 x 60 μm). Cada uno de estos haces, que contiene 120 fibras, está consolidado por un ligante de poliestireno (PS) que recubre las fibras y constituye la unidad estructural del fieltro. El fieltro se conforma mediante la deposición de los haces de fibras sobre un sustrato plano. Las uniones entre los distintos haces de fibras se deben a las propiedades adhesivas del ligante de poliestireno.

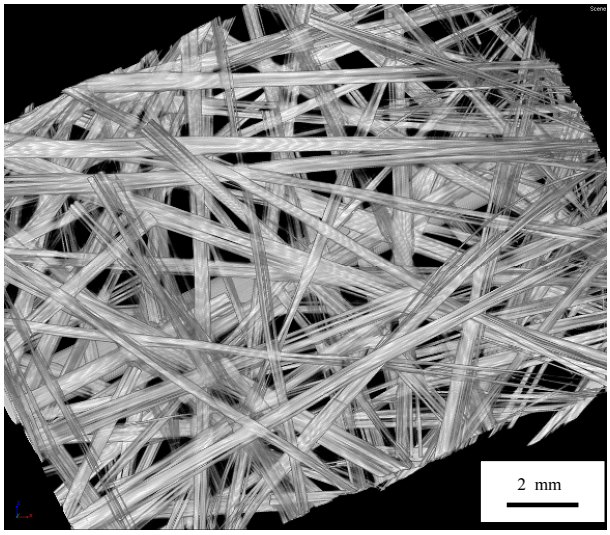

Figura 1. Fieltro Vetrotex M123. Imagen tomográfica

Se efectuaron medidas de la masa del fieltro mediante una balanza electrónica (AND HF 1200G) para hallar la densidad del mismo, que resultó ser de 454 ± 6 g/m^2, en acuerdo con el valor nominal de 450 g/m^2 proporcionado por el fabricante. Las medidas del espesor del fieltro, realizadas mediante un pálmer ofrecieron un valor de 0.54 ± 0.02 mm.

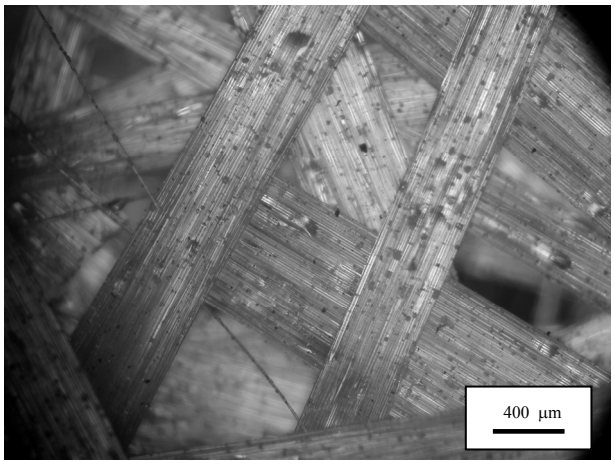

Figura 2. Fieltro Vetrotex M123. Detalle de los haces de fibras

La microestructura del fieltro fue observada mediante técnicas de proyección de perfiles (Nikon V12B) y microscopía óptica convencional (microscopio Nikon Metaphot), así como mediante técnicas de tomografía computerizada de rayos X. Como puede apreciarse en las figuras 1 y 2, se trata de una estructura estratificada e isótropa en el plano que deriva del proceso de deposición de las fibras, según el cual los haces quedan apoyados sobre los depositados anteriormente, permaneciendo rectos y sin entrecruzarse en la dirección perpendicular al plano del fieltro. Las imágenes así obtenidas permitían su tratamiento digital y fueron utilizadas para hallar la densidad de entrecruzamientos y la distancia libre entre uniones. Este último parámetro es básico para el modelo numérico, y en el caso que nos ocupa tiene un valor de 0.75 ± 0.02 mm. Asimismo, las medidas provenientes de las medidas de densidad y las tomografías obtenidas indican que el fieltro está compuesto por el apilamiento de tres capas representativas.

3. TÉCNICAS EXPERIMENTALES

Un estudio completo del material exige la medición de las propiedades mecánicas de los constituyentes del material, partiendo de las fibras y concluyendo con el propio fieltro. Por tanto, en primer lugar se procedió a la extracción de fibras individuales de fibra de vidrio con ayuda de pinzas. Las fibras fueron pegadas a un marco que posteriormente se fijaba a una máquina de tracción. La carga se aplicaba únicamente tras cortar el marco, y quedaba registrada con una célula de carga de precisión ± 1 mN (MTS Nanobionix). Las tensiones ingenieriles se determinaban a partir de dicho registro de fuerza y de los valores del diámetro de la fibra, siempre suponiendo una sección circular. A su vez, las deformaciones se determinaban como el cociente de la elongación de la fibra dividida por su longitud inicial.

En un segundo nivel organizativo, se realizaron ensayos encaminados a la determinación de la resistencia de los haces de fibras de vidrio y de los enlaces entre ellos. El problema con este tipo de ensayos consistía en la determinación precisa de la sección transversal de los haces y en la falta de uniformidad de las muestras enlazadas. Se seleccionaron uniones de fibras alineadas para evitar la aparición de pares de fuerzas, pero aún así era difícil conocer el área exacta de solape. Para reducir en lo posible la dispersión estadística, se realizó un número relativamente grande de ensayos. Finalmente, se extrajeron del rollo muestras rectangulares del material para la realización de ensayos de tracción simple según la norma EN ISO 10319. Las muestras se introducían en dos mordazas diseñadas al efecto y recubiertas de goma para evitar dañar el material. Los ensayos se llevaron a cabo en una máquina universal electromecánica (Instron 1122) equipada con una célula de carga de 5 kN con control de desplazamiento a una velocidad de 0.2 mm/s. Con objeto de estudiar sistemáticamente el posible efecto de la anchura o altura de la probeta, se recortaron muestras de varios tamaños, en particular de 100 mm de altura y 40, 60, 80, 100 y 200 mm de anchura, así como muestras de 100 mm de anchura y 100, 200 y 400 mm de altura. Finalmente, también se prepararon muestras de 200 x 200 mm^2. En

los fieltros de 100 x 200 mm^2 se estudió la sensibilidad a entalla de los fieltros, para lo cual se introdujeron mediante corte con cuchilla entallas centrales de longitud equivalente al 20%, 40% y 60% de la anchura de la probeta.

4. RESULTADOS EXPERIMENTALES

4.1. Fibras individuales

Las fibras individuales extraídas y ensayadas muestran un comportamiento lineal hasta fractura, con una dispersión relativamente grande característica de los materiales frágiles. Los valores obtenidos para el módulo elástico, tensión de rotura y deformación de rotura, que se muestran en la Tabla 1, están en buen acuerdo con los usuales en la literatura [9].

Tabla 1. Propiedades de las fibras de vidrio.

E_f (GPa)	σ_f (GPa)	ε_f (%)
72 ± 2	1.7 ± 0.2	2.3 ±0.3

4.2. Haces de fibras y uniones

Se llevaron a cabo 16 ensayos para medir las propiedades de los haces de fibras. Las curvas carga-desplazamiento eran lineales hasta rotura. Dicha rotura se producía con un valor de carga de 25 ± 6 N. Este valor ha de ser comparado con el obtenido a partir de los 20 ensayos sobre haces unidos, que proporcionó una carga de rotura de 1.2 ± 0.2 N, lo que nos indica que la resistencia de los haces es mucho mayor que la de las uniones y que por tanto el mecanismo dominante en la fractura del fieltro es la rotura de las uniones entre haces de fibras.

4.3. Fieltros no entallados

La Figura 3 muestra el comportamiento en tracción de un fieltro no entallado de fibra de vidrio. A pesar de la dispersión inherente al material, todas las curvas siguen el patrón mostrado, con la carga creciendo linealmente hasta alcanzar un pico agudo.

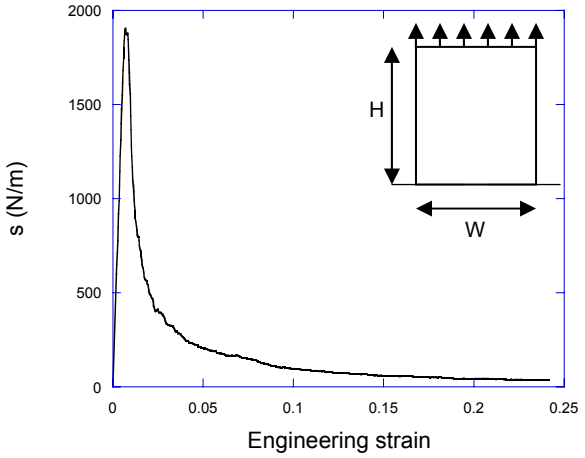

Figura 3. Curva tensión-deformación característica del fieltro M123 ensayado a tracción.

Este pico se corresponde con el inicio de la localización, que se da para una deformación aproximadamente igual al 0.5% por pérdida de adhesión entre los haces de fibras. Los enlaces que hasta entonces no habían soportado carga empiezan a hacerlo debido a los reajustes en el fieltro. A partir del momento en el que estas uniones se rompen, los haces comienzan a deslizar entre sí, y por tanto la resistencia remanente es consecuencia de la fricción entre éstos.

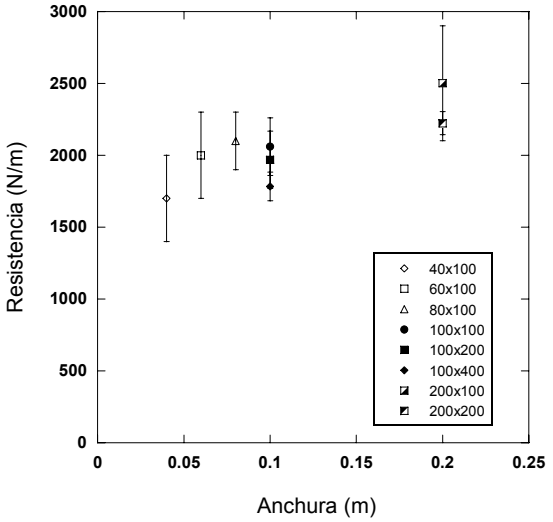

Figura 4. Resistencia del fieltro en función del tamaño.

En la Figura 4 podemos apreciar la influencia del tamaño sobre la resistencia del material. Para una altura dada, la resistencia se incrementa con la anchura, lo que puede interpretarse en términos de efecto de borde, puesto que los extremos de los haces carecen de tensión en la frontera libre. Lógicamente, la importancia de este efecto decae al aumentar la anchura de probeta. Por otra parte, una vez fijada la anchura, nos encontramos con que la resistencia disminuye con la altura de la probeta. Este efecto, más débil que el de la anchura, puede explicarse por la naturaleza frágil de las uniones entre fibras. La resistencia de una unión determinada dependerá de su posición, orientación y conectividad. Como hemos visto, esta variabilidad en la resistencia de los enlaces hace que la deformación se localice en una banda "débil". La probabilidad de aparición de una banda más débil aumenta con la altura de la probeta. Pese a que un análisis probabilístico de Weibull no ha sido llevado a cabo por el limitado rango de tamaños accesibles, la hipótesis de la "banda más débil" tiene un sólido soporte experimental, como se mostrará después.

4.4. Fieltros entallados

Como se ha mencionado antes, la sensibilidad a entalla de los fieltros se estudió en muestras de 100 x 200 mm^2 dotadas de entallas centrales cuyo tamaño a_0 era equivalente al 20%, 40% y 60% de la anchura. Las curvas tensión-deformación correspondientes a las distintas entallas mantenían su forma, indicando así que no se modificaban los procesos de daño. En general, la resistencia del material disminuye con la longitud de la

entalla, pero la dispersión no lo hace, y de hecho algunos fieltros con entallas del 20% y del 40% no localizaban la fractura en la sección de la entalla y mostraban valores anómalamente altos de resistencia, lo que apoya claramente la hipótesis de la "banda más débil".

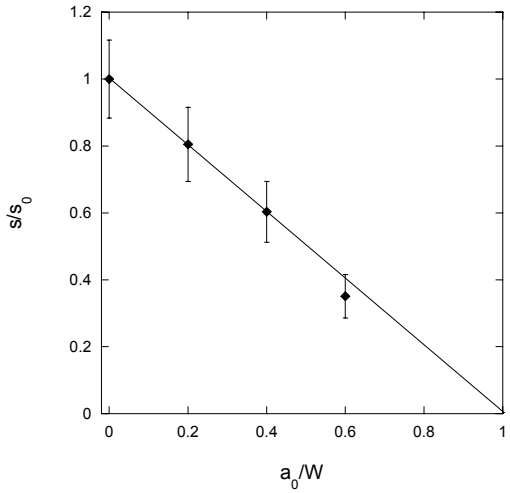

Figura 5. Resistencia del fieltro en función del tamaño de entalla

Por otro lado, la naturaleza frágil de los enlaces haría esperar un comportamiento sensible a entalla, en el que la resistencia fuera inferior a la calculada sin considerar concentración de tensiones, pero sin embargo, la resistencia demostró ser proporcional al ligamento, según la expresión

$$\frac{s}{s_0} = 1 - \frac{a_0}{W}, \qquad (1)$$

donde s es la tensión de rotura, s_0 es la tensión de rotura correspondiente a las muestras no entalladas , a_0 es la longitud de la entalla y W es la anchura de la probeta, tal y como se observa en la Figura 5.

5. DESCRIPCIÓN DEL MODELO NUMÉRICO

Los detalles sobre la generación de malla están recogidos en una referencia anterior [10]. Sucintamente, se comenzó por delimitar un área rectangular de anchura W y una altura H, de dimensiones idénticas a las muestras reales previamente ensayadas. El programa de generación utiliza como inputs el número de fibras a depositar y la longitud de las mismas. Las fibras se construyen a partir de pequeños segmentos. El algoritmo comienza generando un punto con las coordenadas (x_1, y_1) aleatorias del primer punto del primer segmento, junto con su orientación θ_1, también aleatoria. Conocidas la longitud y orientación del segmento, el programa coloca sucesivamente los segmentos hasta agotar la longitud de la fibra. Una vez completada la primera fibra, de nuevo se generan aleatoriamente las coordenadas del punto inicial de la segunda fibra junto con su orientación. El proceso se repite hasta el final de la fibra N-ésima. Si durante el proceso de deposición de segmentos de una fibra se alcanzara alguno de los contornos del área del fieltro, la colocación del siguiente segmento se hace en el lado opuesto del recinto.

La estructura estratificada del fieltro supone una complicación, puesto que un modelo puramente bidimensional no puede mimetizar exactamente dicha estructura. Nuestro objetivo es, pues, el de encontrar una capa representativa bidimensional que reproduzca fidedignamente las propiedades mecánicas del fieltro. Posteriormente será preciso escalar la respuesta según el número de capas que contenga nuestro fieltro. Siguiendo a Kallmes y Corte [11], el parámetro de distancia libre medido l_s= 0.75 ± 0.02 mm, que por su modo de obtención (dispositivos con pequeña profundidad de campo) se refiere a la densidad de una monocapa estructural, nos proporciona una densidad ρ=2.1 mm^{-1}, lo que para el tamaño de 200 x 100 mm^2 supone aproximadamente una longitud total depositada de 41900 mm, equivalente a 836 fibras de 50 mm, con una estimación de 27800 uniones totales, como se aprecia en la Figura 6.

Para discretizar la malla identificamos cada segmento como un elemento viga, tomando sus puntos inicial y final como nodos. Se ha optado por elementos viga de Timoshenko (elementos B21 de ABAQUS). En la definición de las propiedades de la sección se utilizaron las dimensiones medidas de los haces de fibras. El material del elemento viga sigue una ecuación constitutiva elástica lineal caracterizada a partir de las propiedades del material real (fibra de vidrio): un módulo elástico E = 70 GPa, un coeficiente de Poisson ν= 0.2 y una densidad de 2.5 g/cm^3. Para la simulación de las uniones entre vigas se han utilizado elementos conectores sin masa (ABAQUS *connector elements CONN2D2*). El algoritmo compara las distancias entre nodos correspondientes a distintas fibras y coloca un conector cuando dicha distancia está por debajo de determinado umbral.

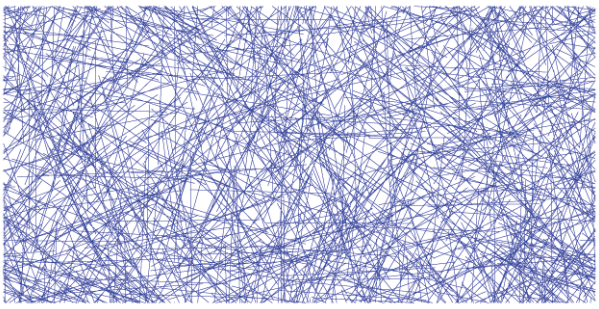

Figura 6. Modelo geométrico del fieltro de fibra de vidrio. Malla sin deformar.

Dada la arquitectura del fieltro, con haces de fibras muy rígidos y resistentes en comparación con las uniones, podemos descartar la ruptura de los haces de fibras y suponer que la rotura del fieltro se produce por la rotura de las uniones entre ellos. Para modelar este proceso se han utilizado un tipo de comportamiento de los conectores basado en la fricción entre haces de fibras. Se supone a las fibras sometidas a una fuerza N normal al plano del fieltro. El programa ABAQUS tiene

definido internamente mediante un pseudopotencial un criterio de deslizamiento de tal modo que cuando las fuerzas tangenciales (en el plano del fieltro) son inferiores al producto del coeficiente de fricción por la normal, el conector se comporta de modo análogo al caso anterior, siguiendo una relación lineal entre la fuerza tangencial ejercida sobre el conector y el desplazamiento relativo de sus nodos. Cuando las fuerzas tangenciales superan dicho umbral (1.2 N, valor experimental de rotura de las uniones) los nodos empiezan a deslizar penalizados con una fuerza de valor μN. En el modelo se toma $\mu = 0.5$, correspondiente al deslizamiento poliestireno-poliestireno [12]. El efecto del debilitamiento del enlace ha sido tenido en cuenta mediante una curva de decrecimiento bilineal de la fuerza normal, de tal modo que su valor se reduce a una décima parte cuando la fibra desliza una distancia equivalente a su anchura (parámetro de ajuste).

Las condiciones de contorno prescritas impedían el movimiento de los nodos de la frontera inferior del fieltro en las direcciones horizontal y vertical e imponían una velocidad de desplazamiento vertical constante en los nodos de la frontera superior de un valor tal que los experimentos virtuales se mantuvieran en régimen cuasiestático, esto es, que la energía cinética fuera despreciable frente al trabajo total, la energía elástica almacenada y la disipada por daño o fricción.

Las simulaciones fueron llevadas a cabo con el programa ABAQUS Explicit (versión 6.8) en modo de doble precisión.

5. RESULTADOS NUMÉRICOS Y DISCUSIÓN

5.1. Fieltros no entallados

En la Figura 8 se muestra cómo el modelo es capaz de seguir el comportamiento experimental del fieltro.

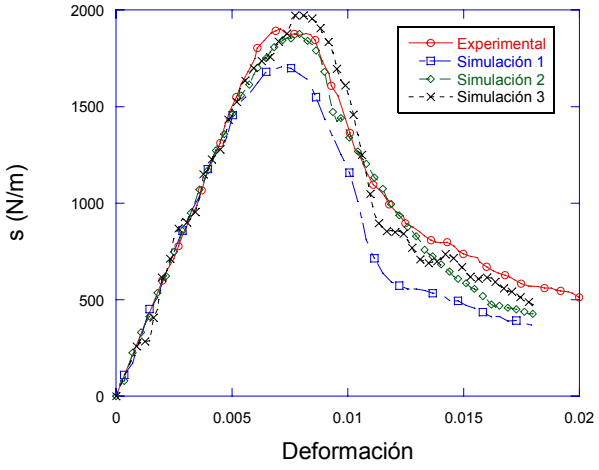

Figura 8. Curvas tensión-deformación. Comparación entre curva experimental y tres realizaciones numéricas

No sólo es relevante que el modelo ofrezca buenos valores tanto para el módulo elástico y para la resistencia del material –puesto que la dispersión experimental es elevada- sino que sea capaz de predecir el comportamiento post-pico hasta las últimas etapas de deformación, cuando el fieltro pierde su capacidad de transmitir carga. Los resultados para distintos tamaños se pueden observar en la tabla 2.

Tabla 2. Efecto del tamaño sobre la resistencia del fieltro .

Anchura (mm)	**Altura** (mm)	**Experimental** (kN/m)	**Simulación** (kN/m)
100	100	2.1 ± 0.2	2.04 ± 0.06
100	200	2.0 ± 0.2	1.83 ± 0.09
200	100	2.5 ± 0.4	2.2 ± 0.1

De nuevo, el modelo captura adecuadamente tanto el efecto de la anchura como el de la altura sobre la resistencia del material sin recurrir a ningún parámetro de ajuste (que sí entra en el comportamiento post-pico).

5.2. Fieltros entallados

El estudio numérico se realizó, al igual que en el caso experimental, sobre fieltros de 100 x 200 mm^2 a los que se les introducía una entalla a_0 igual al 20%, 40% y 60% de su anchura. En el régimen elástico, las tensiones se canalizaban a través de los ligamentos laterales, con las regiones por encima y por debajo de la entalla descargadas (Figura 10). Sin embargo, la concentración de tensiones en la punta de la entalla era limitada ya que los haces de fibras en los que se localiza la tensión la transfieren a zonas más alejadas. Por tanto, las tensiones en los ligamentos son bastante homogéneas incluso bajo carga máxima, lo que conduce a un comportamiento insensible a entalla aun cuando el material es frágil desde el punto de vista de resistencia y tenacidad. Dicha insensibilidad a entalla, también reproducida por el modelo, se muestra en la Figura 9, donde se superponen los resultados numéricos y experimentales.

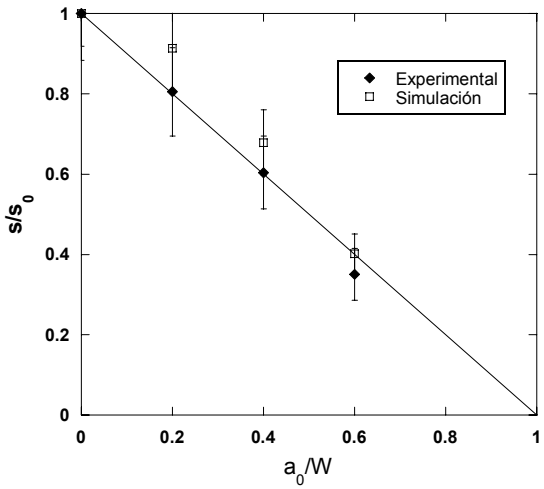

Figura 9. Predicción numérica del efecto de entalla. La línea corresponde a un comportamiento insensible a entalla ideal.

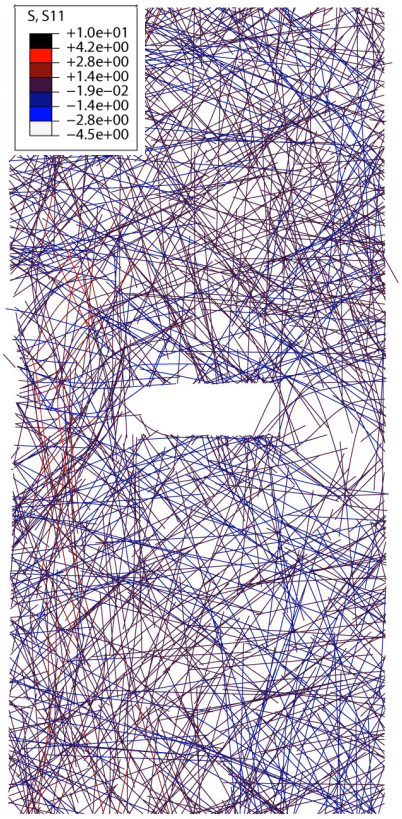

Figura 10. Simulación de la fractura de un fieltro con entalla central $a_0/W=0.4$. Se representa la tensión principal en el haz de fibras (MPa).

Desde el punto de vista de la localización, una vez alcanzado el máximo de carga, una rotura a gran escala de uniones entre haces de fibras conlleva la localización de la deformación en una banda cuyo aspecto es muy similar al observado en los experimentos. La carga se transfiere por fricción en dicha región hasta la pérdida total de cohesión entre los haces de fibras (Figura 10).

6. CONCLUSIONES

Se han estudiado los mecanismos de deformación y rotura de un fieltro de fibra de vidrio mediante ensayos de tracción y simulaciones numéricas. El daño en el material se produce por la rotura de las uniones entre los haces de fibras, frágiles individualmente pero que no conducen a la rotura inmediata del material. El reajuste de los haces de fibra y la disipación friccional de energía hacen que el material mantenga cierta capacidad de transmisión de carga hasta su fallo final. La fractura se localiza en una banda que se desarrolla a lo largo de un "camino de menor resistencia" según la estructura particular de cada muestra de fieltro. Se ha establecido que existe un efecto de la anchura y de la altura sobre la resistencia del material y se ha concluido que en las escalas de estudio el fieltro presenta insensibilidad a entalla por la aparición de bandas débiles y a la limitada concentración de tensiones debida a la estructura poco tupida del material.

AGRADECIMIENTOS

Los autores desean agradecer a Saint Gobain Vetrotex el suministro de material y al Gobierno de la Comunidad de Madrid y el Ministerio de Ciencia e Innovación su apoyo financiero a través de los programas ESTRUMAT-CM (MAT/0077) y MAT2006-2602, respectivamente.

REFERENCIAS

[1] Burkett, M. The *Art of the Felt Maker* Titus Wilson & Son Ltd., 1979

[2] H.L. Cox, *British Journal of Applied Physics,* **3,** 72-79, 1952.

[3] L. Berhan, Y.B. Yi, A.M. Sastry, E. Munoz, M. Selvidge and R. Baughman, *Journal of Applied Physics*, 95-8 (2004) 4335-4345

[4] C.F. Yang. *Plane modelling and analysis of fiber systems.* Ph.D. Thesis. U. of Washington, 1975.

[5] M. Rigdahl, B. Westerlind y H. Hollmark. *Journal of Material Science*, 19 (2004) 3945-3952, 1984.

[6] C. A. Bronkhorst, *Int. J. of Solids and Structures*, 40 (2003) 5441-5454

[7] S. Heyden, Tesis Doctoral. Lund University, 2000.

[8] J. A. Åström y K.J. Niskanen, *Europhys Lett.,* 21, 557-562 (1993).

[9].K. K. Chawla, *Fibrous Materials,* Cambridge University Press*,* 1998**.**

[10] A. Ridruejo, C. González, J. LLorca *Anales de Mecánica de la Fractura,* 26, 394-400 (2009).

[11] O. Kallmes, H. Corte, *Tappi,* **43,** 737-752, 1960.

[12]http://www.roymech.co.uk/Useful_Tables/Tribology/co_of_frict.htm

[13] M. Á. Ramos Carpio. *Ingeniería de los Materiales Poliméricos*. Fundación para el Fomento de la Innovación Industrial, 2007

[14] Vetrotex Chopped Strand Mats. Vetrotex Saint Gobain. http://www.vetrotexeurope.com/products/re_chopstrmat.html , 2005

AN EXPERIMENTAL AND NUMERICAL STUDY OF THE INFLUENCE OF LOCAL EFFECTS ON THE APPLICATION OF THE FIBRE PUSH-IN TESTS.

Jon M. Molina-Aldareguía[1], M. Rodríguez[1], C. González[1,2] and J.LLorca[1,2]

[1]Madrid Institute for Advanced Studies of Materials (IMDEA-Materials)
C/ Profesor Aranguren s/n, 28040 - Madrid, Spain

[2] Departamento de Ciencia de Materiales, E.T.S. de Ingenieros de Caminos, Canales y Puertos, Universidad Politécnica de Madrid, C/ Profesor Aranguren s/n, 28040 Madrid, España.
E-mail: m.rodriguez@imdea.org

ABSTRACT

Several methods have been developed to test interfacial adhesion in composite materials such as pull-out, microbond and push-in/push-out tests. Some of them can only be applied to single fibre matrix composites and others are difficult to perform on brittle fibres due to premature fracture of the fibre. Push-in tests, consisting on pushing the fibre with a micro or nanoindenter on a bulk specimen, constitute a powerful technique that can be applied directly on composite laminates. However, the interfacial adhesion values obtained from different tests (microbond, push in) often differ and even are subjected to a large scatter. This might be due to the fact that the existing analytical solutions that are typically used to interpret the experimental data take into account the constrain effect of the surrounding fibres on a simplified manner. To study this, we have carried out a careful micromechanical modelling of the push-in test, coupled with experimental adhesion testing in a glass fibre reinforced epoxy matrix composite. The model takes into account the interfacial fracture process by means of interface cohesive elements at the fibre–matrix interface and focuses on the study of the constrain effects due to the local configuration of the surrounding fibres.

KEY WORDS: matrix composites; interfacial strength; push-in test; nanoindentation

1. INTRODUCTION

Advanced computational micromechanics has demonstrated its potential to predict the constitutive response of fibre-reinforced composites from the properties of matrix, fibre and their interface [1], [2]. To quantify the interfacial properties, several micromechanical methods exist to test interfacial adhesion in composite materials such as the pull-out test, the microbond test and the push-in and push-out tests. This kind of tests present an ideal interfacial adhesion measure since they carried out on real composite laminates and not on samples fabricated with a particular geometry for such a purpose. This will allow establish the degradation of the interface properties on the real composite under service conditions, as it is widely known that these composites are particularly sensitive to exposition to hot-wet conditions [3]. Other tests suffer from several experimental difficulties: the pull-out test is not easy to perform on brittle fibres due to premature fracture of the fibre and the push-out test [4], [5], requires the preparation of thin membranes (~50μm) of the composite material prior to testing.

In this situation, the push-in test, consisting on pushing one fibre with a micro or nanoindenter on the cross-section of a bulk specimen, [6]-[9], constitutes a powerful technique that can be applied directly on real composite laminates, either before or after degradation under service conditions. Nevertheless, the evaluation of interfacial properties remains a controversial issue among researchers of composite materials due to experimental partly due to the fact that the existing analytical solutions typically used to interpret the experimental data are based on simplified shear lag analytical models [10], [11]. As such, these models only take into account the constrain effect of the surrounding fibres in a simplified way, but the neighboring fibres are distributed in irregular configurations and no solution exists for the stress distribution around an indented fibre in a non-axisymmetric configuration. The axisymmetric models used involve an averaged distance to the nearest-neighbour fibres, which are usually considered perfectly rigid [8], [9]. As such, the derived parameters to account for the effect of neighbour fibres remain somewhat arbitrary.

To overcome this limitation, we have carried out a careful micromechanical modelling of the push-in test, coupled with experimental adhesion tests in a glass fibre reinforced epoxy matrix composite using nanoindentation. The model addresses the interfacial fracture process through the use of interface cohesive elements at the fibre–matrix interface. The study focuses on the constrain effects due to the local configuration of the surrounding fibres and helps to determine the validity of the simplified shear lag models currently used to interpret the results. It is shown that the analytical models are valid when the indented fibre is relatively isolated from its neighbours, but that they tend to overestimate the constrain effect for closely

packed fibres, the scenario usually found in polymer matrix composites. Nevertheless, it is concluded that the simplified shear lag models can be safely used to estimate the interfacial shear strength provided that the constrain effect is carefully derived from the initial part of the push-in loading-displacement curve.

2. MATERIALS AND EXPERIMENTAL TECHNIQUES

A unidirectional glass/epoxy composite was used for this study. Pre-impregnated sheets of E-glass/MTM 57 epoxy resin were purchased from Advanced Composite Group (UK). Rectangular panels of 350 x 300 mm2 were heated at 3 ºC/min and consolidated at 120º C and 0.64 MPa in an autoclave for 30 minutes. They were cooled at the same rate of 3 ºC/min and the internal pressure was released at 80 ºC. The nominal fibre volume fraction was 54%. Blocks of 1 x 1 x 1 cm were cut and polished on SiC paper to 1000 grit finish followed by a diamond slurry up to 1 µm. The samples were mounted on a MTS Nanoindenter XP instrumented equipped with a Berkovich tip. Fibres covering a wide range of diameters (between 14 and 32µm) and different environments (position of the neighbouring fibres) were selected for the tests, as shown in two examples in figure 1.

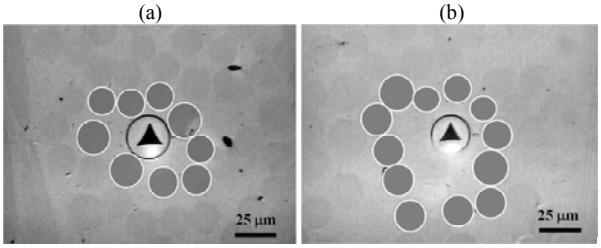

Figure 1. Examples of indented fibres showing the local configuration of the surrounding fibres: (a) a closely packed fibre and (b) a more isolated fibre.

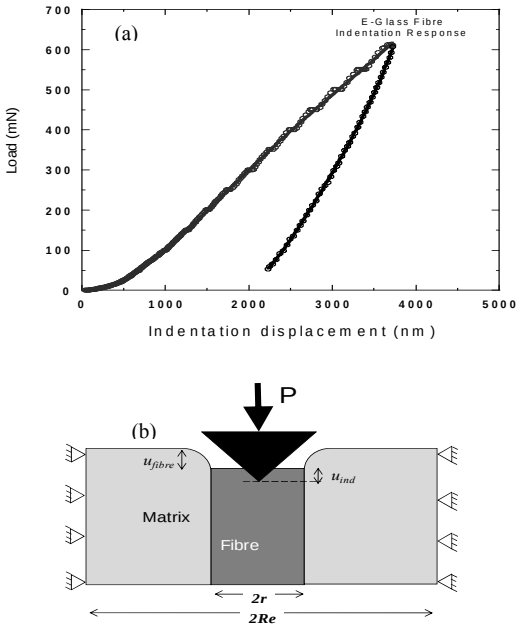

Figure 2. (a) Typical indentation load-displacement curve performed on a glass fibre and (b) sketch illustrating the indentation response of the fibre showing the two components of the indenter displacement: the penetration of the indenter in the fibre cross-section u_{ind} and the compression of the fibre and deflection of the matrix u_{fibre}.

The push-in test consists of pushing the indenter into the cross-section of a fibre which is perpendicular to the polished section. The indentations were performed at a displacement rate of 50 nm/s at various levels of maximum load ranging between 20 mN and 700 mN.
Figure 2 (a) shows a typical load-displacement curve obtained during indentation of one fibre. As shown previously in polymer matrix composites [12] no significant discontinuity in the load-displacement curve is observed at the onset of debonding. Several authors [8], [9], have thoroughly work on the treatment of the indentation curves in order to obtain a debonding load without the need for time-consuming load step procedures and optical inspection of the indented fibres. But for the sake of clarity, the most important aspects are briefly discussed below in conjunction with the experimental results obtained in this work.

3. EXPERIMENTAL RESULTS

3.1 Extraction of load-fibre displacement curve

The treatment relies on the identification of two components in the indenter displacement. The first is related to the penetration of the indenter in the fibre crosssection u_{ind}, and the second is associated with the compression of the fibre in the surrounding epoxy matrix and the deflection of the matrix u_{fibre}, (figure 2 (b). In order to derive the elastoplastic indentation response of E-glass one can either indent a piece of bulk glass or derive it from finite element simulations. The second approach was used in this work.
Once the elastoplastic indentation response of bulk glass is known, the fibre displacement u_{fibre} can be simply obtained by subtracting the elastoplastic component of indentation (u_{ind}) from the total displacement u recorded during the test, as shown in figure 3 (a). The curve in figure 3 (b) shows the typical behaviour found elsewhere [8], [9], for the fibre compression once the displacement due to the elastoplastic indentation is removed.
The initial linear part corresponds to the elastic response of the fibre/matrix system, while most authors interpret the departure from linearity at the critical load P_{crit} as the result of interfacial debonding. In this work, the test was interrupted at increasing loads for optical inspection of the indented fibres.
As shown in figure 3 (c), it was difficult to establish whether the departure from linearity marked the onset of plastic deformation of the matrix or the onset of interfacial debonding, especially because debonding was gradual and did not occur on the entire periphery of the fibre simultaneously.

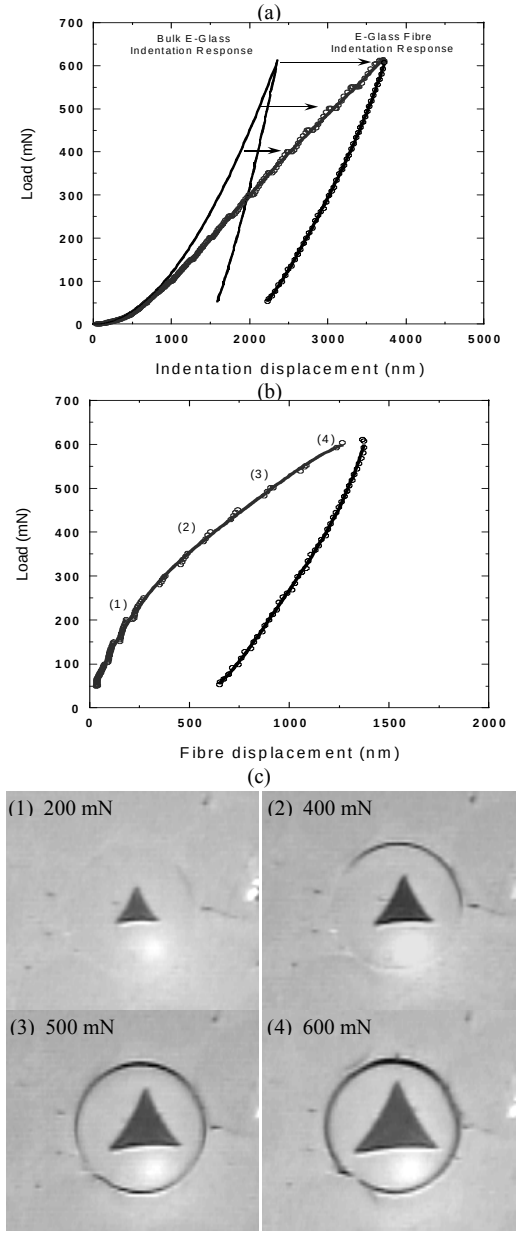

Figure 3. (a) Load-displacement curve of E-glass fibre and bulk glass (as predicted by FEM); (b) the load-fibre displacement behaviour obtained by subtracting the elastoplastic component of indentation (u_{ind}) from the total displacement u recorded during the test; (c) optical images of the indented fibre showing that the debonding is gradual.

3.2. Analytical shear lag model

The analytical shear-lag models currently used to interpret the load-displacement curves obtained in the push-in test assume a perfect hexagonal fibre packing, elastic deformation of the matrix and a perfectly bonded interface. The proximity of the surrounding fibres is taken into account through the parameter *Re*, as illustrated in figure 2(b), which represents the distance from the indented fibre to the ring of neighbouring fibres. The model assumes that the longitudinal displacement of the matrix equals zero at distance *Re*. Under this assumption, a linear relationship is obtained between the displacement of the fibre u_f and the applied load P [8], [9].

$$u = \frac{P}{\pi \cdot r \cdot n \cdot E_f} \quad (1) \qquad \text{with} \qquad n^2 = \frac{2G_m}{E_f \ln\left(\mathrm{R_e}/r\right)} \quad (2)$$

where r is the fibre radius, σ_f is the fibre axial stress, G_m is the matrix shear modulus and E_f is the fibre Young's modulus. Finally, the maximum shear stress at the onset of debonding can be assimilated to the interfacial shear strength:

$$u = \frac{n \cdot P_{crit}}{2\pi \cdot r^2} = \frac{n}{2}\sigma_f^{crit} \quad (3)$$

where σ_f^{crit} is the axial stress at the cross-section of the fibre at debonding. It is interesting to note that the analytical model tries to account for the effect of the surrounding fibres through the parameter *(Re/r)*. This parameter *(Re/r)* has no physical interpretation but it has been shown to correlate to the local packing of the indented fibre and can be denoted as the constraint factor. In the treatment proposed in [8], the linear part of the indentation curve is used to estimate *n* and *(Re/r)* through equations (1) and (2). Once n is determined, the interfacial strength can be derived from the critical load for debonding P_{crit} through equation (3).

3.3. Effect of fibre diameter and neighbouring fibres

The shear-lag model presented above was applied to the experimental results obtained in this work. Overall over 30 fibres were tested. Figure 4 (a) displays seven representative load-displacement curves, showing the large differences that can be found for fibres of different diameters or located in different environments (for the sake of clarity only the loading portions of the curves are displayed). As mentioned above, the linear part of the curves was used to estimate the constraint factor *(Re/r)* through equations (1) and (2). As expected from equation (1), the slope of the linear part in this graph was constant for all the fibres, but the onset of departure from linearity was very sensitive to the local environment of the fibres.

Figure 4 where the load was normalized by the fibre diameter and *n* clearly shows the behaviour of fibres with similar diameters. Fibres with a smaller constraint factor *Re/r*, i.e. having more closely packed fibres around, showed a more marked departure from linearity, corroborating the strong effect of the local environment of the neighbouring fibres on the push-in test.

Finally, the calculated interface shear strength (calculated from the load at the onset of the departure from linearity) is plotted in figure 5 as a function of the constraint factor. An average value of 83 MPa was obtained although the uncertainty was large due to the difficulty on determining the critical load. The axial fibre stress at the onset of debonding varied linearly with the constraint factor (figure 5), as expected.

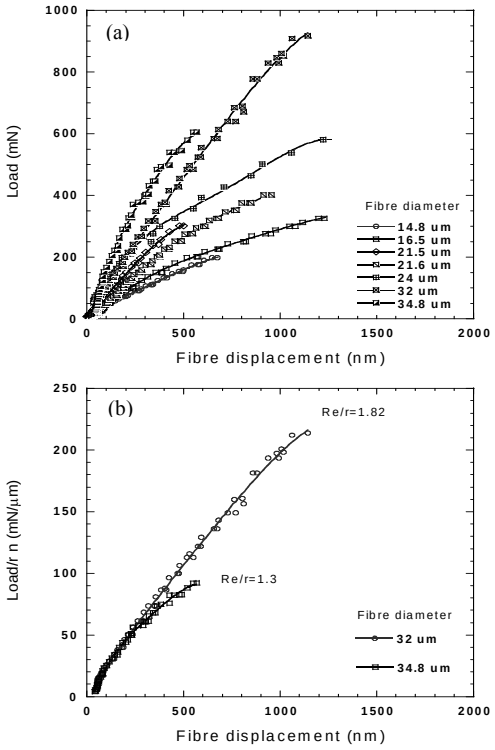

Figure 4. (a) Load-fibre displacement behaviour for some representative fibres of different diameter; (b) Normalized load curves for fibres with 32-35 µm diameter showing the effect of the confinement parameter Re/r.

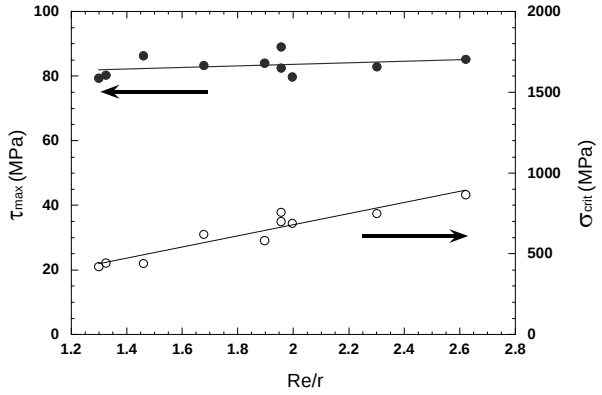

Figure 5. Interface shear stress and axial fibre stress at the onset of departure from linearity as a function of the constraint factor.

It is interesting to note that the ratio Re/r can be related to the fibre volume fraction V_f under the assumption of hexagonal fibre packing according to:

$$\ln(Re/r) = \frac{1}{2}\ln\left(2\pi/\sqrt{3}V_f\right) \qquad (4)$$

which for a nominal fiber volume fraction of 54% leads to *Re/r* =2.6. The fact that the reported values are considerably lower reflects that the configuration of the fibres was far from the ideal hexagonal packing, as can be clearly seen in figure 1. In fact, the constraint factors obtained were very small and one should wonder whether this approach is valid for composites with very high volume fractions of fibres. In addition, it was difficult to establish whether the onset of departure is due to interface decohesion or local plastic deformation of the matrix, which has a shear yield stress of 80 MPa, similar to the interfacial strength. To elucidate this, the validity of the approach is discussed in the following sections based on the results of finite element simulations.

4. MODELLING

The experimental results above demonstrate that the effect of the local environment of the surrounding fibres is not negligible, especially in cases where the volume fraction of fibres is very large. Advanced numerical simulations that take into account the details of the microstructure are thus critical to understand the role played by the surrounding fibres on the test results and to determine the minimum distance from the tested fibre to its nearest neighbours to minimize the constraint effect on the measured interfacial properties. The modelling strategy to simulate the push-in test is depicted in Fig. 6.

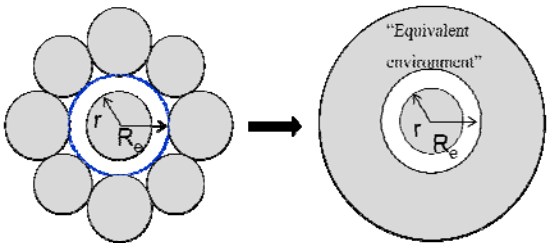

Figure 6. Simplification assumed in this work to model the effect of the local environment of the fibres as a solid ring with the same properties than the fiber located at a distance Re from the indented fibre.

For the sake of simplicity, the effect of the surrounding fibres in (a) at a distance *Re* from the centre of the fibre has been modelled as a solid ring, displaying the same properties that the fibres. A fibre diameter of 20*µm* was assumed and the position of the solid ring was varied in the range $Re/r \in (1.0, \infty)$ to account for the constraint effect of the neighbouring fibres.

The numerical analysis of the indentation of the fibre cross-section was carried out using the finite element method. The simplification depicted in figure 6 allowed for the implementation of an axisymmetric model. The fibres and matrix were meshed using two-dimensional four–node linear axisymmetric elements with reduced integration. The Berkovich indenter was modelled as a rigid conical indenter with an included angle of 70.3º. The specimen dimensions were large enough so that the effects of the boundary conditions were negligible and the mesh was refined near the indented zone, to avoid numerical instabilities at the contact between fibre and indenter. Glass fibres were modelled as linear elastoplastic isotropic solids using a Von Mises plasitification criterion, with the properties given in Table 1. The yield stress of the glass fibres was fixed by fitting the numerical simulations to the indentation behaviour of the fibres. The MTM57 epoxy matrix was

assumed to behave as an isotropic, elastoplastic solid. The matrix elastic constants were obtained from the data sheet of ACG and are reported in Table 1. The yield stress of the MTM57 epoxy matrix was fixed at 140 MPa by fitting numerical simulations to the indentation behaviour of the matrix [13], giving a shear yield stress of 80 MPa.

Table 1. Material Properties

Material	E (GPa)	ν	σ_y (MPa)
E-Glass	70	0.18	4200
MTM57 epoxy	3.4	0.35	140

Interface decohesion was simulated through a cohesive crack model, using first-order interface elements of Abaqus (COHAX4) inserted at the fibre/matrix interface which follow a traction-separation *(t-δ)* constitutive law. In the absence of damage, the interface behaviour was linear with an initial stiffness large enough to ensure the displacement continuity at the interface and to avoid any modification of the stress fields around the fibres in the absence of damage. This linear behaviour ends at the onset of damage, which occurs when the traction acting on the interface reaches the interface strength, t_c.
From the viewpoint of the interface properties, the interface behaviour is controlled by two parameters, namely the interface strength tc and the fracture energy, G_i, which stands for the area under the curve t-δ. The interface strength was fixed at t_c= 80 MPa, based on the preliminary experimental results obtained based on the shear-lag model. Regarding the interface fracture energy, this parameter should not significantly affect the onset of debonding and a value of 100 J/m2 was used, as in previous analyses [14].

5. NUMERICAL RESULTS AND COMPARISON WITH EXPERIMENTS.

5.1. Effect of the surrounding fibres on the linear slope of the loading curve

The load-displacement curves obtained by FEM, for fibres with different constraint factors *Re/r* are plotted in figure 7 assuming a perfect interface. As in the experiments, an initial linear response was obtained and the stiffness increased with the constraint of the surrounding fibres (lower *Re/r*). It is interesting to notice that the curves departed earlier from linearity as the constraint increased, marking the onset of plastic deformation of the matrix around the fibres (indicated by the gray arrows in the figure). At this point, the shear stresses reached τ_{matrix}=80 MPa, as expected from the matrix yield stress (table 1).
Comparison between the FEM results and the results that would be obtained on applying the shear lag model leads to the conclusion that the latter tends to overestimate the constraint effect of the neighbouring fibres when the confinement effect is large (*Re/r* < 3).

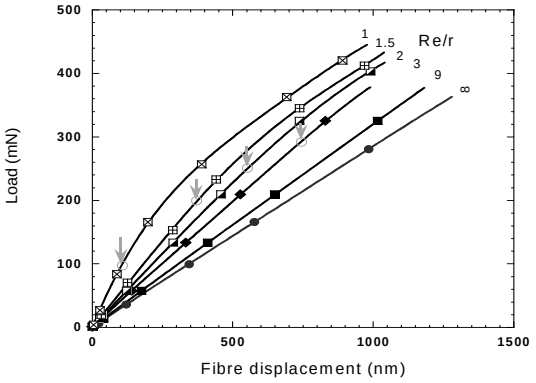

Figure 7. Load-fibre displacements results obtained by FEM, for fibres with different constraint factors Re/r, assuming a perfect interface. As the constraint increases (lower Re/r), the stiffness of the response increases.

This is shown in figure 8 where the parameter *n* as obtained from the slope of the FEM load-displacement curves and from equation (2) is plotted as a function of the confinement. The shear lag model overestimates the confinement effect of the surrounding fibres on the stiffness of the load-displacement curve as much as 30%, for Re/r<3.

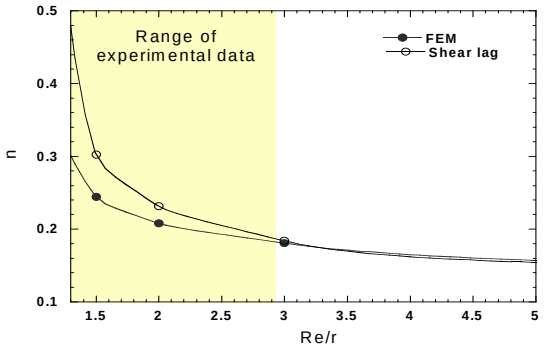

Figure 8. Comparison between the shear lag model results and the FEM results. Value of n versus Re/r as measured by FEM and as calculated using equation (2).

5.2. Effect of the interfacial strength

The load-displacement curves obtained by FEM are plotted in figure 9 for fibres with different constraint factors *Re/r* and an interfacial strength of 80 MPa. The dashed line indicates the equivalent behaviour assuming a perfect interface.
In all cases, the departure of linearity, as indicated by the gray arrows, marked the onset of debonding of the indented fibre, even if the interfacial shear strength was comparable to the matrix shear yield stress. An interesting situation would be that in which the matrix shear yield stress were lower than the interfacial strength, which will be the subject of future studies.
Finally, figure 10 shows the comparison between one experimental push-in test and the corresponding FEM simulation for different values of the constrain factor *Re/r*. A perfect match is obtained in this case for *Re/r*=1.5. It is worth mentioning at this point that the same value of interfacial strength, i.e. 80 MPa, was obtained using the shear lag model, but with *Re/r* = 2.

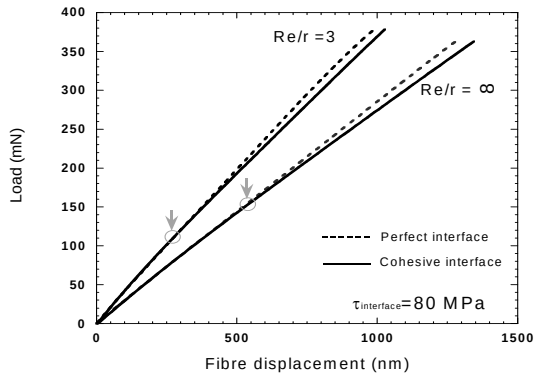

Figure 9. Load-fibre displacements results obtained by FEM, for fibres with different constraint factors Re/r, assuming a perfect interface and a cohesive interface with an interfacial strength of 80 MPa.

This means that the simplified shear lag models used constitute an appropriate method to analyse the push-in test, provided that the parameter (*Re/r*) is obtained by fitting the linear slope of the load displacement curve using equations (1) and (2). However, it should be stressed out that the values of (*Re/r*) obtained in this way act as fitting parameters and are larger than the real distance to the neighbouring fibres, because the shear lag model overestimates the constrain effect, as shown in figure 8.

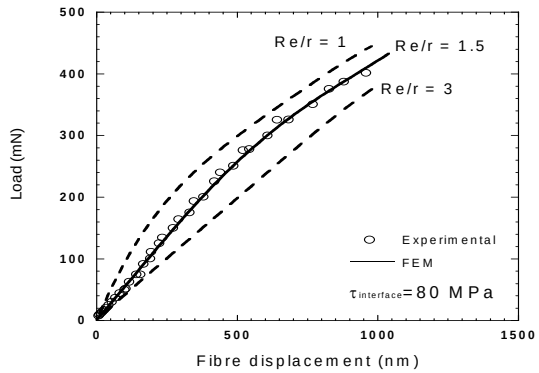

Figure 10. Comparison between experimental results on a 20 μm diameter fibre and FEM results with different Re/r and an interfacial strength of 80 MPa. A perfect match is obtained for Re/r=1.5.

6. CONCLUSIONS.

A detailed micromechanical modelling of the push-in test, coupled with experimental tests, was carried out in a glass-fibre reinforced epoxy matrix composite using nanoindentation. The model took into account the interfacial fracture process using interface cohesive elements at the fibre–matrix interface and focused on the constrain effects of the nearest neighbouring fibres to determine the validity of the simplified shear lag models currently used to interpret the results of the test.
The results showed that the analytical models currently used are valid when the indented fibre is relatively isolated from its neighbours. For closely packed fibres (Re/r < 3), which is the normal situation in polymer matrix composites, the shear lag model tends to overestimate the constraint effect of the neighbouring fibres. However, according to the FEM results, the simplified shear lag models used constitute an appropriate method to analyse the push-in test even in this case, provided that the parameter (*Re/r*) is obtained by fitting the linear slope of the push-in load displacement curve. In this case, the values of (*Re/r*) obtained act as fitting parameters and are larger than the real distance to the neighbouring fibres. The simulations also showed that plasticity effects in the matrix are not negligible for large local volume fraction of fibres and can give rise to erroneous interpretations of the push-in test. The results showed that in the case of the composite tested, with comparable matrix shear yield stress and interfacial strength, the push-in test can be applied safely to determine the interfacial strength. Further work is needed to determine the relative matrix shear yield stress to interfacial strength ratios at which this is not the case.

7. RERERENCES

[1] Cox, B., Yang, Q., 2006. Science 314, 1102-1107.
[2] González, C., LLorca, J. 2006. Acta Mater., 54, 4171.
[3] Saud A., Ghydaa A., Safaa A.R. 2009. Materials and Design 30, 1835–1840.
[4] González, C., LLorca, J. 2001. Acta Mater., 49, 3505.
[5] Rollin, M., Jouannigot, S., Lamon, J., Pailler, R. 2009. Composites Science and Technology 69, 1442–1446.
[6] Mandell, J.F., Chen, J.H. and McGarry, F.J. 1980. Znt. J. Adhes. Adhes. I, 40.
[7] Kalinka, G., Leistner, A. and Hampe, A. 1997. Composites Science and Technology 51, 845-851
[8] Kharrat, M., Chateauminois A., Carpentier, L. and Kapsa, P. 1997, Composite Part A 28A, 39-46.
[9] Zidi, M., Carpentier L., Chateauminois A., Sidorof, F. 2000. Composites Science and Technology 60, 429-437.
[10] Cox, H.L. 1942, Br. J. Appl. Phys. 3, 72.
[11] Kelly, A. and Tyson, W.R. 1965. J. Mech. Phys. Solids 13, 329.
[12] Desaeger, M. and Verpoest. I. 1993. Compos. Sci. Technol. 48, 215.
[13] Molina-Aldareguia, J.M., Rodríguez, M., González, C., LLorca, J. 2009, *in preparation.*
[14] Gonzalez, C., LLorca, J. 2007b. Composites Science and Technology 67, 2795-2806.

8. ACKNOWLEDGEMENTS

This investigation was supported by the European Union through the project MAAXIMUS and by the Comunidad de Madrid and the ERA-NET MATERA through the program DEFCOM. The composite materials used in this investigation were manufactured at INTA (Instituto Nacional de Técnica Aerospacial), and the authors want to express their gratitude to Dr. J. M. Pintado and to Dr. M. A. de la Torre.

ACCURATE SIMULATION OF DELAMINATION GROWTH UNDER MIXED-MODE LOADING USING COHESIVE ELEMENTS WITH MODE-DEPENDENT PENALTY STIFFNESS

A.Turon[*,1] , E.V. González[*], P. Maimí[*], P. Camanho[†], J. Costa[*]

[*]AMADE, University of Girona
Campus Montilivi, s/n. 17071 Girona, Spain
Albert.turon@udg.edu
Emilio.gonzalez@udg.edu
Pere.maimi@udg.edu
Josep.costa@udg.edu

[†]DEMec, Universidade do Porto
Rua Dr. Roberto Frias 4200-465 Porto, Portugal
pcamanho@fe.up.pt

ABSTRACT

The cohesive zone model approach, in conjunction with a damage formulation has been used by many authors to simulate delamination using finite element codes. Most of these models available in the literature are developed for pure mode loading, and then extended to analyze mixed-mode loading situations. However, these models have not been validated correctly under mixed-mode loading conditions where an incorrect selection of the parameters of the model can result in inaccurate simulation predictions. To obtain accurate simulation results, the cohesive formulation previously developed by the authors has been modified. Mode-dependent penalty stiffness has been introduced in the formulation as well as the damage evolution law has been redefined. Different loading scenarios are simulated to validate the accuracy of the new formulation presented.

KEY WORDS: Delamination, mixed-mode, cohesive zone model.

1. INTRODUCTION

Delamination is one of the most common types of damage in laminated fiber-reinforced composites due to their relatively weak interlaminar strengths. Delamination or interlaminar damage may arise under mode I loading and under mode II loading, however in practical applications, delamination is more likely to grow under mixed-mode loading conditions. An effective method to analyze delamination is using cohesive zone models [1-5].

Cohesive zone models provide and ideal representation of the delamination process of advanced composite materials. The excellent performance of cohesive zone models in the simulation of delamination is due to the accurate kinematics representation of the fracture process, based on a strong discontinuity in the displacement field and to the possibility to use constitutive models that correctly account for the different loading modes.

The cohesive zone model approach, in conjunction with a damage formulation has been used by many authors to simulate delamination using finite element codes. Moreover, the latest versions of commercial nonlinear finite element codes incorporate the capability to simulate delamination. Most of these models available in the literature are developed for pure mode loading, mode I or mode II loading, and then extended to analyze mixed-mode loading situations. However, these models have not been validated correctly under mixed-mode loading conditions where an incorrect selection of the material properties can result in inaccurate simulation results [6]. To obtain accurate simulation results, a reformulation of the cohesive formulation developed by the authors [3,5] is presented in this paper. The formulation is modified by introducing mode-dependent penalty stiffness and redefining the damage evolution law. Different mixed-mode loading scenarios are simulated to validate the accuracy of the formulation presented.

2. REFORMULATION OF THE COHESIVE DAMAGE MODEL

The constitutive behaviour of cohesive elements is implemented using a cohesive damage zone model that relates the tractions, τ, to the displacement jumps, Δ, at the interfaces where crack propagation occurs. Damage

[1] Corresponding author

initiation is related to the interfacial strength of the material, τ^o. When the energy dissipated is equal to the Fracture Toughness of the material, G_c, the traction is reduced to zero and new crack surfaces are formed. The constitutive law used in this work is a bilinear relation between the tractions and the displacement jumps [5,7]. The bilinear cohesive law uses an initial linear elastic response before damage initiation, as shown in Figure 1. This linear elastic part is defined using a penalty stiffness parameter, K, that ensures a stiff connection between the surfaces before crack propagation. The interfacial strength and the penalty stiffness define an onset displacement jump, Δ^o, related to the initiation of damage.

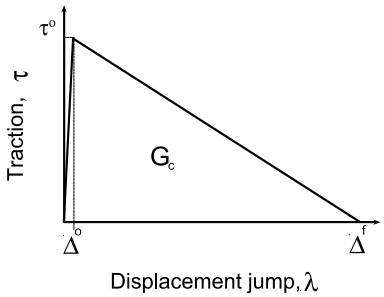

Figure 1 Bilinear constitutive law used for quasi-static loading.

The displacement jump across the interface is obtained from the displacements of the points located on the top and bottom sides of the interface in the local coordinate system.
Further detail of the boundary value problem and the kinematics of the model are detailed in [3,5]. In the following sections the reformulation of the constitutive equations is described.

2.1 Constitutive equations

The Helmholtz free energy by unit surface of the interface under isothermal conditions is divided in two terms:

$$\Psi(\boldsymbol{\Delta},d)=\Psi(\boldsymbol{\Delta},d)_{coh}+\Psi(\boldsymbol{\Delta})_{con} \qquad (1)$$

where $\Psi(\boldsymbol{\Delta},d)_{coh}$ and $\Psi(\boldsymbol{\Delta})_{con}$ refer tot he cohesive and contact energy contributions, respectively. The vector $\boldsymbol{\Delta}=\{\Delta_1,\Delta_2,\Delta_3\}^T$ contents the displacement jumps between the two homologous points of the respective adjacent surfaces, and d is the scalar isotropic damage variable. It should be noted that $\boldsymbol{\Delta}$ acts as the free variable (i.e. displacement driven formulation) and d is the internal variable that ensures the irreversibility of the model [5,10].
The definition of the energy terms should be selected such as it yields to a unilateral and a symmetric constitutive behaviour for propagation mode I and shear modes, respectively. The corresponding expressions are:

$$\Psi(\boldsymbol{\Delta},d)_{coh}=\frac{1}{2}(1-d)\left[\Delta_i K_{ij}\Delta_j+\Delta_3\delta_{i3}K_{33}\langle-\Delta_3\rangle\right] \qquad (1)$$

$$\Psi(\boldsymbol{\Delta},d)_{con}=-\frac{1}{2}\Delta_3\delta_{i3}K_{33}\langle-\Delta_3\rangle \qquad (1)$$

where $\langle x\rangle$ are the Macaulay brackets defined as $\langle x\rangle=\frac{1}{2}(x+|x|)$, and δ_{ij} is the Kroenecker delta. K_{ij} are the components of the stiffness matrix.

The stiffness matrix is defined as a diagonal matrix, therefore only the diagonal terms: K_{11}, K_{22} and K_{33} are non zero. K_{11}, K_{22} and K_{33} are the penalty stiffness for modes II, III and I, respectively. Applying Coleman's method [2], the constitutive equation reads:

$$\tau_i=\tau_{i,coh}+\tau_{i,con} \qquad (2)$$

where

$$\tau_{i,coh}=(1-d)\left[K_{ij}\Delta_j+\delta_{i3}K_{33}\langle-\Delta_3\rangle\right] \qquad (3)$$

$$\tau_{i,con}=-\delta_{i3}K_{33}\langle-\Delta_3\rangle \qquad (4)$$

2.1 Equivalent mixed mode norms

To formulate the damage evolution law, a mixed-mode norms of the tractions, τ, and the displacement jumps, λ, have been to be defined. In the original model [3,5] they were defined as the Euclidean norm of the individual tractions and displacement jumps, respectively. However, in the reformulation of the model using different penalty stiffness, these mixed-mode norms need to be redefined. The relation between the mixed-mode traction τ and the mixed-mode displacement jump λ is defined as:

$$\tau=(1-d)k_B\lambda \qquad (5)$$

where k_B is a mode-dependent interfacial stiffness.

The mixed-mode traction τ is defined as the Euclidean norm of the individual tractions τ_1, τ_2, τ_3. The mixed-mode displacement jump λ reads:

$$\lambda=\frac{K_{ii}\left[\Delta_i^2-\delta_{3i}\langle-\Delta_3\rangle^2\right]}{\sqrt{K_{ii}^2\left[\Delta_i^2-\delta_{3i}\langle-\Delta_3\rangle^2\right]}} \qquad (6)$$

and the mixed-mode interfacial stiffness k_B is defined as:

$$k_B=\frac{K_{ii}^2\left[\Delta_i^2-\delta_{3i}\langle-\Delta_3\rangle^2\right]}{K_{ii}\left[\Delta_i^2-\delta_{3i}\langle-\Delta_3\rangle^2\right]} \qquad (7)$$

To completely define the evolution of the damage variable under mixed-mode loading, a local mixed-mode ratio B is defined as:

$$B = \frac{\Psi_1 + \Psi_2}{\Psi} = \frac{K_{11}\Delta_1^2 + K_{22}\Delta_2^2}{K_{11}\Delta_1^2 + K_{22}\Delta_2^2 + K_{33}\langle -\Delta_3 \rangle^2} \quad (8)$$

Defining $K_{sh}=K_{11}=K_{22}$ and using equation (8) in equation (7), the mixed-mode interfacial stiffness results in a condensed form as:

$$k_B = K_{33}(1-B) + BK_{sh} \quad (9)$$

2.3 Damage activation function and evolution law

The damage activation function is defined as:

$$F(\boldsymbol{\Delta}) = \mathrm{H}(\boldsymbol{\Delta}) - r_d \leq 0 \quad (10)$$

where $\mathrm{H}(\boldsymbol{\Delta})$ is a monotonic loading function which depends on the jump displacement vector, and r_d is the threshold function. Both functions are updated at every time t, and they are respectively defined as:

$$\mathrm{H}(\boldsymbol{\Delta}) = \min\left\{\frac{\lambda - \Delta^o}{\Delta^f - \Delta^o}, 1\right\} \quad (11)$$

$$r_d = \max\left\{0, \max_s[H(\boldsymbol{\Delta})]\right\} \quad 0 \leq s \leq t \ \ \forall t \quad (12)$$

It should be noted that the first term of equation (11) is directly the ratio of the energy dissipated during the damage process and of the critical energy release rate, i.e. G_d/G_c [6]. Therefore, from equations (11) and (12) the expression which defines the damage variable d reads:

$$d = \frac{r_d \Delta^f}{r_d \Delta^f + (1 - r_d)\Delta^o} \quad (13)$$

To complete define the constitutive model it is necessary to define the displacement jumps corresponding to delamination onset, Δ^o, and to delamination propagation, Δ^f, under mixed-mode conditions. The Benzeggagh and Kenane criterion [8] is used to define these parameters, yielding to [5]:

$$\Delta^o = \left(\frac{K_{33}\left(\Delta_3^o\right)^2 + \left[K_{sh}\left(\Delta_{sh}^o\right)^2 - K_{33}\left(\Delta_3^o\right)^2\right]B^\eta}{k_B} \right)^{\frac{1}{2}} \quad (14)$$

$$\Delta^f = \frac{1}{k_B \Delta^o}\left(K_{33}\Delta_3^o\Delta_3^f + \left[K_{33}\Delta_{sh}^o\Delta_{sh}^f - K_{33}\Delta_3^o\Delta_3^f\right]B^\eta\right) \quad (15)$$

where Δ_{sh}^o and Δ_3^o are the displacement jumps corresponding to delamination onset in pure mode I and shear mode respectively, and Δ_{sh}^f and Δ_3^f are the displacement jumps corresponding to delamination propagation in pure mode I and shear mode respectively [5].

2.4 Rate of energy dissipation

To ensure the thermodynamic consistency of the model, the dissipated energy by surface unit during the damage propagation process, Ξ, has to be equal or greater than zero:

$$\Xi = Y\dot{d} \geq 0 \quad (16)$$

where the thermodynamic force Y associated with the internal variable d is defined as:

$$Y = \frac{1}{2} d\left[\Delta_i K_{ij} \Delta_j + \Delta_3 \delta_{i3} K_{33} \langle -\Delta_3 \rangle\right] \quad (17)$$

Equation (17) demonstrates that the thermodynamic force Y is always equal or greater than zero; therefore the term $\dot{d}$ must be positive. Since the damage variable is a function of r_d and the local mixed-mode ratio B, the following equation must be satisfied:

$$\dot{d} = \frac{\partial d}{\partial r_d}\dot{r_d} + \frac{\partial d}{\partial B}\dot{B} \geq 0 \quad (18)$$

The threshold function r_d is always positive according to equation (12), and the term $\frac{\partial d}{\partial r_d}$ is also always positive:

$$\frac{\partial d}{\partial r_d} = \frac{\Delta^o \Delta^f}{\left[r_d \Delta^f + (1 - r_d)\Delta^o\right]^2} \quad (19)$$

Therefore, since the local mixed-mode ratio B can either increase or decrease, the term $\frac{\partial d}{\partial B}$ must be zero to ensure the thermodynamic consistency of the model:

$$\frac{\partial d}{\partial B} = \frac{\partial \frac{\Delta^o}{\Delta^f}}{\partial B} \quad (20)$$

Previous equation is equivalent to the condition given in [6] for the selection of the pure mode interfacial stiffness. Using the initiation and propagation criteria given in previous section, the condition to ensure the thermodynamic consistency reads:

$$K_{sh} = K_{33}\frac{G_{Ic}}{G_{IIc}}\left(\frac{\tau_{shear}^o}{\tau_3^o}\right)^2 \quad (21)$$

3. VALIDATION EXAMPLES

Simulations of delamination propagation under pure mode I, pure mode II, and mixed-mode loading are performed. The double cantilever beam (DCB) and the end-notched flexure (ENF) test specimens are used to simulate delamination propagation under pure mode I and under pure mode II loading respectively. The mixed-mode bending (MMB) test specimen is used to simulate delamination growth under mixed-mode loading. The configurations of the DCB, ENF and MMB test specimens are shown in Figure 1.

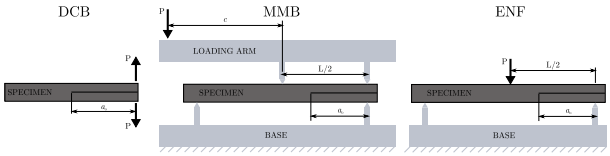

Figure 2. DCB, MMB, and ENF test specimens.

Four-node cohesive elements implemented as Abaqus user elements [3,5] and two-dimensional plane stress elements (Abaqus CPE4 elements) are used to simulate DCB, MMB, and ENF tests in unidirectional carbon-fiber reinforced epoxy composite. The specimens simulated are 150mm long, 20mm wide, with two 1.55mm thick arms, with an initial crack length of 3 mm. A mode I penalty stiffness of $K_{33}=10^6$N/mm^3 is used. The remaining material properties are $E_{11}=120$GPa, $E_{22}=E_{33}=10.5$GPa, $G_{12}=G_{13}=5.25$MPa, $G_{23}=3.48$MPa, $\nu_{12}=\nu_{13}=0.3$, $\nu_{23}=0.5$, $G_{Ic}=0.260$kJ/m^2 and $G_{IIc}=1.002$kJ/m^2.

Models using 0.15mm long cohesive elements along the length of the specimen, and 10 plane stress elements along the specimen's thickness are created to simulate the DCB, MMB and ENF tests with the different interface strengths τ_3^o and τ_{sh}^o. The initial size of the delamination in the DCB and MMB specimens is simulated by removing the corresponding cohesive elements. For the ENF specimen, pre-damaged cohesive elements are placed in the pre-cracked region to avoid interpenetration of the crack faces.

Several simulations with the same elastic and fracture properties but with different values of τ_3^o using the DCB test specimen are performed. The results are compared with the analytical expressions obtained using LEFM which depend only on the fracture toughness. The relation between the applied load and the displacement in shown is Figure 3 where it can be observed that the results during crack propagation match the LEFM solution, regardless of the interface strength. Lower values of the interlaminar strength result in lower values of the maximum applied load. Nevertheless, there are no differences in the load-displacement curve when steady state delamination growth takes place.

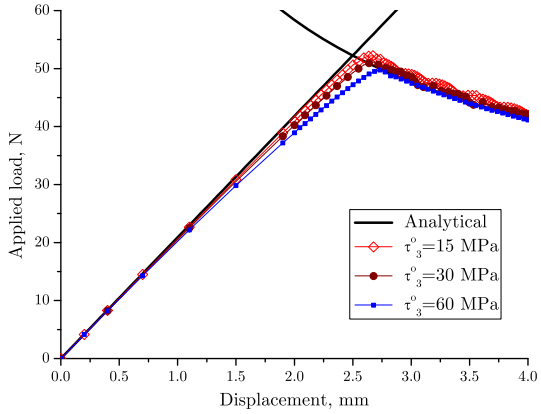

Figure 3. Load displacement curve obtained for different interface strengths in a DCB test.

Similar simulations are performed to predict delamination growth under pure mode II loading for different values of τ_{sh}^o using the ENF test specimen. The relation between the applied load and the displacement is shown in Figure 3. As observed in the pure mode I tests, the results obtained match the LEFM curve during self-similar delamination growth, regardless of the interface strength.

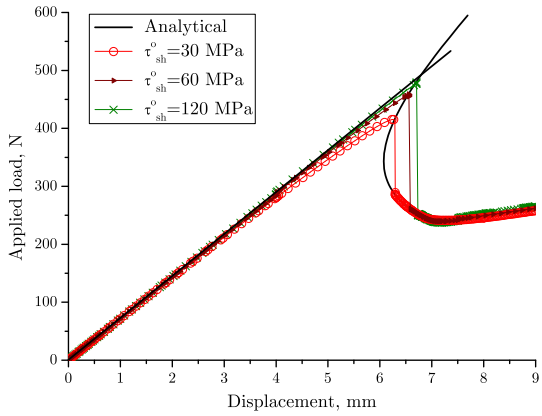

Figure 4. Load displacement curve obtained for different interface shear strengths in a ENF test.

A similar exercise is performed for specimens under mixed-mode loading. A mixed-mode ratio of 50% is simulated by setting the distance c shown in Figure 1 to 63.18mm [9]. Several simulations with the same elastic and fracture properties but with different interface strengths are performed. The interface strengths are varied to investigate their effect on the results. The results obtained are presented in Figure 4, where it can be observed that the load-displacement relation during crack propagation is independent on the strength used.

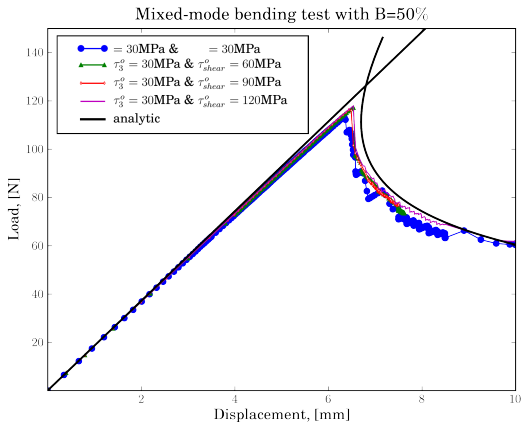

Figure 5. Load displacement curve obtained for different interface strengths in a MMB test with 50% of mode II.

From Figure 5 is also observed that the computed energy dissipation during delamination grow is independent of the interlaminar shear strength.

4. CONCLUSIONS

The cohesive element formulation previously developed by the authors has been reformulated to get accurate predictions under mixed-mode loading. The formulation has been modified by introducing mode-dependent penalty stiffness and redefining the activation function, the damage evolution law, and the equivalent mixed-mode norms of the displacement jump. It has demonstrated that exist a relation between the pure mode interface stiffness and the cohesive properties (pure mode Fracture Toughness and pure mode interface strengths). The accuracy of the new model has been demonstrated by simulating delamination under different mixed-mode loading conditions. It has shown that the computed energy dissipation under delamination propagation is independent of the interface strengths selected.

ACKNOWLEDGEMENTS

The authors would like to acknowledge the useful discussions with Dr. Carlos G. Dávila, NASA Langley Research Center, U.S.A.
This work has been partially funded by the Spanish government through DG- GICYT under contract: MAT2006-14159-C02-01 and the research visit of the first author at the University of Porto funded by the grant JC2008-00400 of the José Castillejos" program.
The financial support of the Portuguese Foundation for Science and Technology (FCT) under the project PTDC-EME-PME-64984-2006 is acknowledged.

REFERENCES

[1] G. Alfano, M. Crisfield, Finite element interface models for the delamination analysis of laminated composites: mechanical and computational issues, International Journal for Numerical Methods in Engineering, 77 (2) (2001), 111-170.
[2] U. Mi, M. Crisfield, G. Davies, Progressive delamination using interface elements, Journal of Composite Materials, 32 (1999), 1246-1272.
[3] P.P. Camanho, C.G. Dávila, M. de Moura, Numerical simulation of mixed-mode progressive delamination in composite materials, Journal of Composite Materials, 37 (2003), 1415-1438.
[4] V. Goyal-Singhal, E. Johnson, C.G. Dávila, Irreversible constitutive law for modeling the delamination process using interfacial surface discontinuities, Composite Structures, 64 (2004), 91-105.
[5] A. Turon, P.P. Camanho, J. Costa, C.G. Dávila, "A damage model for the simulation of delamination in advanced composites under variable-mode loading", *Mechanics of Materials,* 38:1079-1089, 2006.
[6] A. Turon, P.P. Camanho, J. Costa, J. Renart, Accurate simulation of delamination growth under mixed-mode loading using cohesive elements: definition of interlaminar strengths and elastic stiffness, Journal of composite materials, (2009), submitted.
[7] E. Reddy Jr., F. Mello, T. Guess, Modeling the initiation and growth of delaminations in composite structures, Journal of Composite Materials, 31 (1997), 812-831.
[8] M.L. Benzeggagh, M. Kenane, Measurement of Mixed-Mode delamination Fracture Toughness of Unidirectional Glass/Epoxy Composites With Mixed- Mode Bending Apparatus, Composites Science and Technology, 49 (1996), 439-49.
[9] N. Blanco, A. Turon, J. Costa, An exact solution for the determination of the mode mixture in the mixed-mode bending delamination test, Composites Science and Technology 66 (10), (2006), 1256-1258.
[10] E.V. González, P. Maimí, A. Turon, P.P. Camanho and J. Renart, Simulation of delamination by means of cohesive elements using an explicit finite element code, CMC - Computers, Materials and Continua, 9, 51-92, (2009).

COMPLIANCE REAL TIME MONITORING IN MODE II DELAMINATION FATIGUE TESTS

J. Vicens [1], J. Costa [1], J. Renart [1]

[1] AMADE. Analysis and Advanced Materials for Structural Design,
Escola Politècnica Superior, EPS. Universitat de Girona, UdG,
Campus Montilivi s/n. 17071 Girona, Spain
E-mail: pep.vicens@udg.edu

ABSTRACT

An experimental investigation of crack growth under fatigue loading on epoxy resin reinforced with unidirectional carbon fibre and which focuses on the introduction of a new methodology based on real-time monitoring of the compliance is presented. The new methodology is based on a new definition of the compliance as the ratio of load and displacement amplitudes applied in fatigue tests. This new definition allows the value of the compliance of the specimen, in spite of the non-linearities introduced by fixtures and load application during the test, to be obtained. In the experimental program to validate the new methodology, 3ENF fatigue tests were carried out to obtain the onset of crack growth and the associated da/dN-G_{max} curves for ratio R=0.1 and 5 Hz frequency. The fatigue tests were carried out for different G_C rates (10%, 20%, 30%, 40%, etc.). Onset curve and crack growth rate for AS4/3501 are presented.

KEY WORDS: fatigue, crack growth, three point bending, end notched flexure, real time monitoring, compliance.

1. INTRODUCTION

Nowadays, the information provided by fatigue tests, the onset point (initiation of crack growth) and crack growth rate (evolution of the crack once it has started), requires long duration tests, which are labour intensive. All the information is provided by the study of the evolution of the specimen's compliance and/or the measure of the crack length. For fatigue tests in mode I [1] a variation of 1% or 5% of the compliance is considered as an indication of crack onset. The normalized procedure to obtain the onset point requires stopping the test periodically to carry out static tests on the lineal zone of the material in order to evaluate the specimen's compliance. The accuracy of this method depends on the frequency of the stops, and requires the continuous intervention of the technician. Therefore, the fatigue tests become extremely costly and produce scattered results.

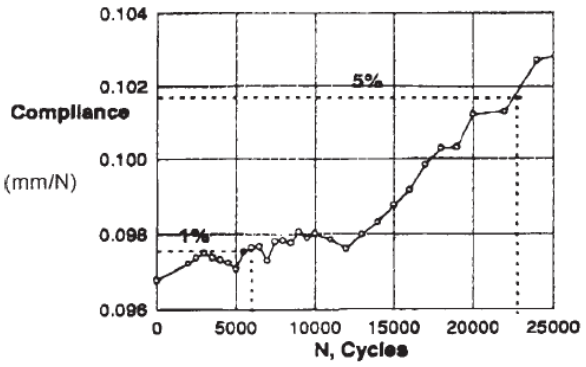

Figure 1.Evolution of the compliance in front of the Number of cycles. ASTM D6115 – 97 p:5.

To attain the crack growth rate, the crack length have to be measured by visual inspection along the specimen edges. A set of a(N) points are then obtained. Ideally, the crack growth rate da/dN corresponds to the derivate of the a(N) curve of the specimen. Great efforts have been made to automate fatigue procedures in composites with the aim of determining the damage evolution on real time. Some authors have proposed different methodologies to determine the damage onset point. For example, acoustic emissions [2], optical fibre sensors [3] or a variation of the conductivity of the material [4] have been some solutions presented. These methods require a lot of time for specimen preparation and involve the use of sensors for the test.

In this work a methodology to determine the fatigue crack growth behaviour (onset and crack growth rates) of delamination in composite materials is presented. This methodology is based on the real-time monitoring of the specimen compliance.

2. EXPERIMENTAL

Composite material manufactured from 3501 resin reinforced with unidirectional carbon fibres AS4 cured in an autoclave under standard aeronautical conditions was used. The laminate configuration consists of 16 plies with 0º orientation /insert/ 16 plies with 0º orientation, employing a PTFE foil insert of 30µm of thickness and 60 mm length in order to produce an artificial delamination to initiate the crack in the mid plane. The samples were approximately 25mm wide, 5.5mm thick and 210mm long approximately.

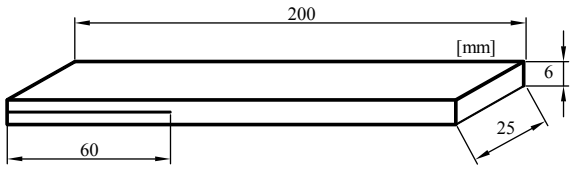

Figure 2.Specimen dimensions.

17 samples have been tested to obtain the onset curve. For this experimental program validation in mode II a variation of 2% of the compliance is considered to indicate crack onset. The limit for the initiation of the crack growth has been considered as 2.5 million cycles. The da/dN-G_{max} graph has been built up with the information provided by the 10%Gc to 50%Gc samples. All tests have been carried out at R=0.1 and 5Hz frequency.

Table 1. Initial conditions for fatigue tests in R=0.1.

# samples	%Gc	δ_{min} [mm]
2	10	-0.370
3	20	-0.524
3	30	-0.642
2	40	-0.741
3	50	-0.828
2	70	-0.980
2	90	-1.111

A three point bending, 3ENF, fixing tool has been used to reproduce the mode II testing conditions used in this study. The parameters of the fixing tool were L=50mm (distance between the load applicator and roller support) and an initial crack length of 25mm (distance from the end to the insert and the roller support).

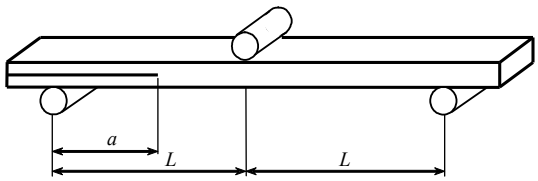

Figure 3.3ENF fixing too.l

A clip-on-gage extensometer Epsilon 3541-008M-025M has been used to measure the displacement values. The fatigue tests were carried out under displacement control.

3. DYNAMIC COMPLIANCE

The compliance of any structural component is defined by LEFM as the ratio between displacement and load, C=δ/P. Assuming a perfect linear behaviour of the material, the compliance value is the slope on a load-displacement graph assuming the it passes through the origin of coordinates. The value of the slope remains constant until any damage on the material occurs (matrix cracking, fibre breaks, fibre kinking, delamination...) and thus provokes a variation of the slope. Any non-linear effect causes a loss of stiffness in the material. When the material is being damaged the value of the compliance varies, it can increase suddenly as in a sudden crack growth in delamination tests or it can be noticed as a smooth loss of linearity as in the formation of micro-cracks.

The geometry and manufacture of the three point bending fixing tool used in this study introduces a non-linearity at small displacements. The slope on the load-displacement increases in the initial zone until it reaches a constant slope value corresponding to the value of compliance of the specimen tested. Plays between pieces of the fixing tool, an inaccurate load introduction on the specimen or geometrical non-linearities of the samples are the principal causes that produce these non-linearities.

Due to the initial non-linearity produced by the fixing tool, the implementation of the LEFM definition to calculate the compliance during a fatigue test exhibits uncertainty on the compliance value. In fatigue tests, controlled by displacement, cyclic displacement following a sinus wave is applied producing a corresponding sinus wave force response. In figure 4 the displacement *δ'* and *δ''* applied corresponds to point *A* and point *B* respectively on the displacement-force curve. The compliance calculated as LEFM definition, the slope between the chosen point and the origin of coordinates, gives different values depending on the chosen point. The compliance during dynamic tests does not remain constant and varies from the minimum value, *C'*, (corresponding to the minimum displacement), to a maximum value of compliance, *C''*.

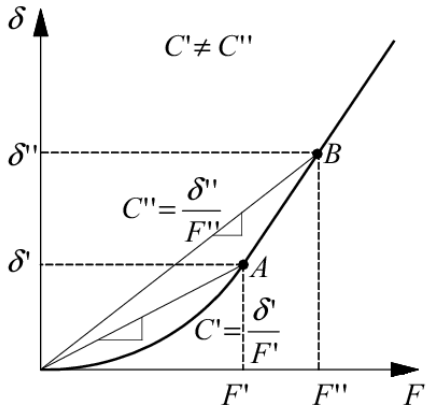

Figure 4.Classical definition of Compliance.

In an attempt to avoid the effect of the initial non-linearity a new definition to calculate the compliance is proposed. The idea begins by defining the compliance as the ratio between the displacement amplitude and load amplitude applied during a cyclic period in a dynamic test.

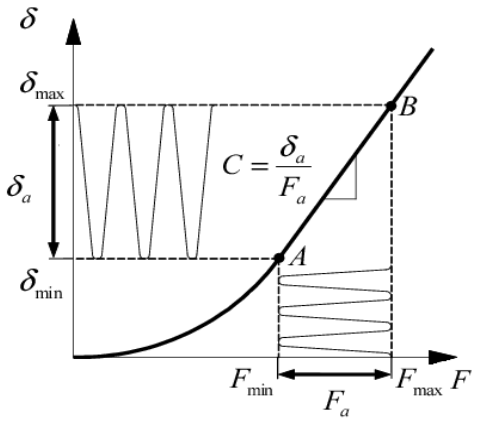

Figure 5.New definition of compliance.

The definition of the compliance corresponds to the secant line between two points in any shape of the load-displacement curve. On a fatigue test controlled by displacement, the displacement signals are set up at the beginning of the test. In Figure 5 the minimum displacement, δ_{min}, and the maximum displacement, δ_{max}, are chosen to produce on the sample a, F_{min}, and F_{max}, respectively at a chosen frequency. The newly calculated compliance is the slope of the line that connects point B and point A and corresponds to the ratio of the displacement amplitude, δ_a, and force, F_a.

The amplitude of both, force and displacement can be calculated from the instantaneous signals provided by the load cell and extensometer following the outlined procedure below:
The sensors of force and displacement acquire signals which follow a sinus wave form (see equation 1 and 2).

$$F(t)= F_m + F_a \sin\left(\frac{2\pi}{T}t + \theta\right) \quad (1)$$

$$\delta(t)= \delta_m + \delta_a \sin\left(\frac{2\pi}{T}t\right) \quad (2)$$

Where, F_m and δ_m are the mean value of load and displacement, F_a and δ_a are the actual amplitude of force and displacement respectively. T, is the period of one cycle and, t, is the time.

$$F^2(t)= F_m^2 + F_a F_m \sin\left(\frac{2\pi}{T}t\right) + F_a^2 \sin^2\left(\frac{2\pi}{T}t\right) \quad (3)$$

$$\delta^2(t)= \delta_m^2 + \delta_a \delta_m \sin\left(\frac{2\pi}{T}t\right) + \delta_a^2 \sin^2\left(\frac{2\pi}{T}t\right) \quad (4)$$

$$\int_0^T F^2(t)dt= \int_0^T F_m^2 dt + \int_0^T F_a F_m \sin\left(\frac{2\pi}{T}t\right)dt + \int_0^T F_a^2 \sin^2\left(\frac{2\pi}{T}t\right)dt \quad (5)$$

$$\int_0^T \delta^2(t)dt= \int_0^T \delta_m^2 dt + \int_0^T \delta_a \delta_m \sin\left(\frac{2\pi}{T}t\right)dt + \int_0^T \delta_a^2 \sin^2\left(\frac{2\pi}{T}t\right)dt \quad (6)$$

Secondly, to obtain equations function of the mean and the amplitude value the equations 1 and 2 have to be squared. By squaring these equations the signal-noise from the sensors is also squared. A robust method to calculate the new compliance is required particularly after squaring the signals acquired and the noise of the values. The integration of the sinus wave form signal during one period, T, provides an averaged value and reduces the signal-noise ratio and so providing a robust method to obtain the compliance.

$$F_a^2 = \frac{\int_0^T F^2(t)dt - F_m^2 T}{\pi} \quad (7)$$

$$\delta_a^2 = \frac{\int_0^T \delta^2(t)dt - \delta_m^2 T}{\pi} \quad (8)$$

Finally, the Dynamic Compliance (DC) is defined as the ratio between the square root of the amplitudes of displacement and load found in equations 7 and 8.

$$C = \frac{\delta_a}{F_a} \quad (9)$$

The Dynamic Compliance is implemented on the control software of the MTS servo-hydraulic testing machine. The algorism calculates the values of the new compliance from the input signals (force and displacement) from the sensors (load cell and extensometer). The algorism is based on arithmetic operations and recalculates the value of the compliance every clock interval between each response of the servovalve allowing a real time monitoring compliance that can be stored or visualized to be obtained.

3.1 Experimental Compliance Calibration

To determine the crack length, it is necessary to obtain the crack growth length, and so the Experimental Compliance Calibration, CCE, is used in spite of the visual crack determination. The crack length and the sample compliance are correlated in a lineal relation between the compliance and the crack length cubed.

Load and unload testing in the elastic range for different crack lengths provides the information required to determine the slope, m, of the regression line on a C in front of a^3 graph. ESIS [5] proposes a complete characterization of the compliance using 0, 15, 20, 25, 30, 35, 40mm of crack length. Implementing the values of the regression line obtained permits the crack length on real time to be obtained.

ESIS standard for static test in mode II proposes static test on elastic range before testing to determine the Experimental Compliance Calibration, CCE. This paper

proposes calculating the CCE using dynamic tests in spite of static tests for different crack length because the tests simulate the same fatigue testing conditions on the sample and allow the use of the dynamic compliance, DC, to obtain the different compliance values consequently reducing the testing time spent.

Static and dynamic test were carried out on the same sample to compare the static and dynamic values of, *m* for an Experimental Compliance Calibration for different ranges of energy release rates. The sample between one static test and the dynamic test remains on the fixing tool without moving ensuring the exact same test conditions are repeated. The static test was carried out on the elastic range and the dynamic test between the displacements that produce different energy release rates with a ratio of R=0.1.

Figure 6 shows the slopes of compliance in function of crack length cubed for first order polynomial regression of the static values on the elastic range, m_{st}. Figure 7 depicts the first order polynomial regression line of the load-displacement dynamic test values, m_{dyn}; and in figure 8 the new method of dynamic compliance, DC, calculated directly from the testing machine, m_{DC}.

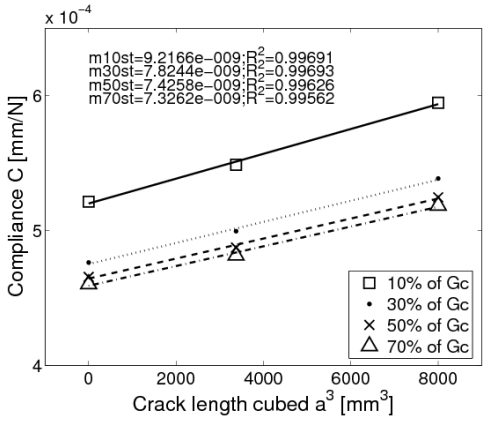

Figure 6.CCE Static Compliance Calibration R=0.1.

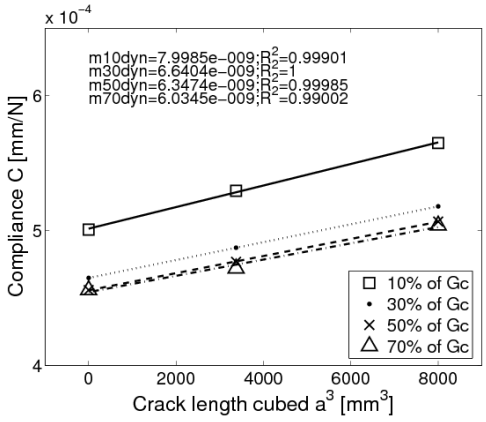

Figure 7.Regression Dynamic Compliance Calibration R=0.1.

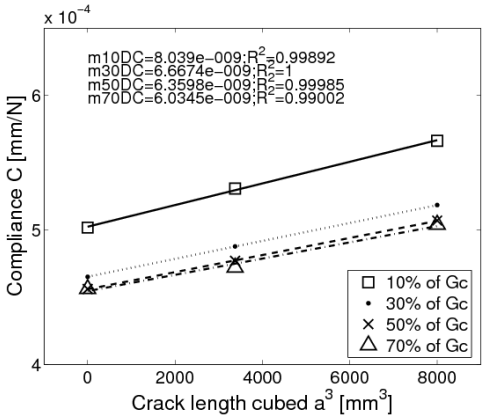

Figure 8.DC Calibration R=0.1.

The slope results using the same method are summarized in table 1. The difference between the static and dynamics results of the compliance calibration is about 15%. The values obtained with the new method proposed in this paper are practically equal to those obtained with the first order polynomial regression line of the load- displacement of the dynamic values for all the cycles of the dynamic test.

Table 2. Comparasion of results of static and dynamic experimental compliance calibration.

%G	m_{st}	m_{dyn}(regression)	m_{DC}
10	9.216e-9	7.998e-9	8.039e-9
30	7.824e-9	6.640e-9	6.667e-9
50	7.425e-9	6.347e-9	6.360e-9
70	7.326e-9	6.034e-9	6.034e-9
mean	7.948e-9	6.755e-9	6.775e-9

In conclusion, the standard method proposed by ESIS [5] to calculate the compliance calibration is not useful in fatigue test because it does not take into account the fatigue test conditions.

3.2 Range of use

When the Dynamic Experimental Compliance Calibration, CCEdyn, is carried out, the effect of the number of cycles on the specimen have to be taken into consideration because the cycles applied have to be added later, (i.e. after the running the test), to the value of the onset point. Besides, the number of cycles applied to the sample at low rates of energy release rate does not damage the specimen. However, for fatigue tests at rates of energy release rate close to the critical energy release rate a few cycles could damage the sample even when the CCEdyn is done.

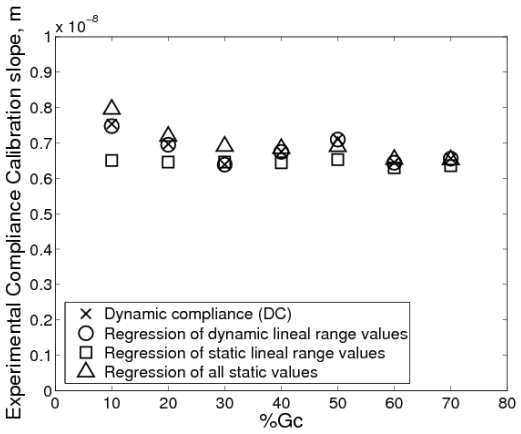

Figure 9.Comparison of parameter m in function of %G.

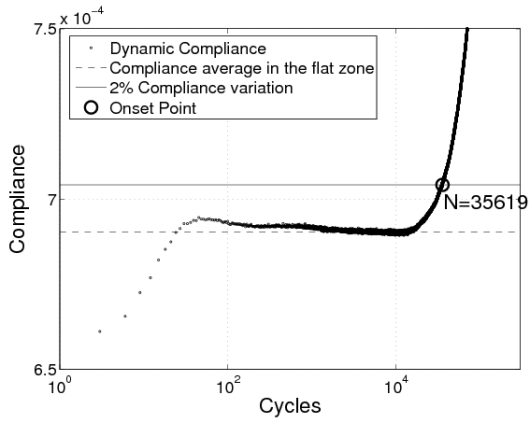

Figure 10.Compliance–cycle graph for 5L41G04 specimen.

Figure 9 compares the slope of the CCE for different %Gc and different calculation methods. The most constant method in front of the variation of the G_c is the one based on the LEFM method. This method calculates the slope as a regression of all the values of the constant slope of a displacement force graph. The DC method gives similar values in the range of 30 to 70 % of Gc. This range allows carrying out the CCE for each sample independent of which conditions will be tested. The option to choose the rate of Gc to calculate the CCE avoids the effects of fixing tool non-linealities at low rates of Gc or damaging the sample at close Gc rates.

4. RESULTS AND DISCUSSION

The experimental results obtained are presented.

4.1 Experimental result for sample

The new dynamic compliance (DC) allow the storage of the experimental values of every cycle providing a nearly continuous C(N) and a(N) graph if the CCE is used in the second case. The door is open to improve the accuracy in the determination of the onset point and the determination of the da/dN-Gmax graph. Furthermore, man-labour dependence is drastically reduced achieving a virtually automatic fatigue test.

Figure 10 shows the experimental data results for one test. At least one hundred cycles are required to reach a constant value of DC because the extensometer requires some cycles to reach the command values. The compliance remains constant until the sample is damaged. The onset point is calculated as the intersection between the 2% compliance variation line and the DC values. The accuracy of the determination on the onset point depends on the frequency of the cycles stored.

4.2 Beginning of delamination

Figure 11 presents the fatigue curve characterization of the material (crack growth onset). The curve is obtained by adjusting the experimental data.

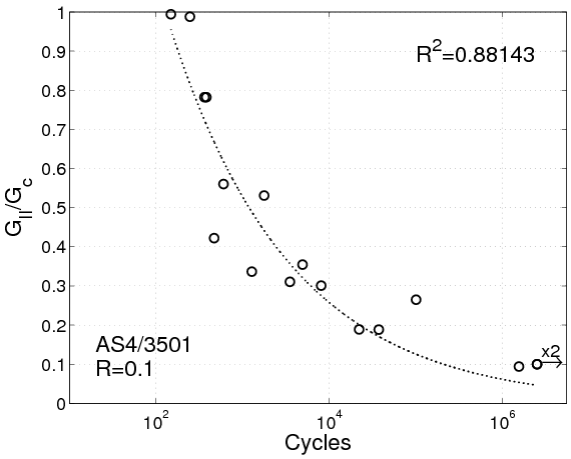

Figure 11.Onset curve for AS4/3501.

The energy release rate of each specimen in figure 11 is different to the initial conditions in table 1. The initial test conditions are calculated based on information provided by static tests. The experimental %G is calculated using experimental values (initial crack length, force) in every cycle by:

$$G_{\max} = \frac{3mF_{\max}^2 a^2}{2B} \quad (10)$$

The new methodology presented in this paper allows real test fatigue conditions to be calculated more accurately.

4.3 da/dN- G_{max} curve

The calculation of da/dN is not a direct result. From the real time compliance stored and by using the

experimental compliance calculation the crack length in front of cycles graph is obtained. The velocity of the crack growth is the slope of the *a* vs *N* graph. The slope is calculated by using a first degree polynomial regression for different vector length of *a* and *N*. The maximum energy release rate is calculated from the crack length and force values of the vectors, used to calculate the slope, using equation 10. Figure 12 shows the result.

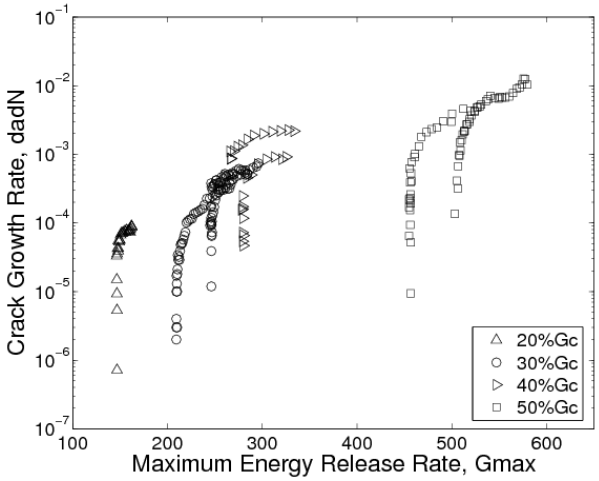

Figure 12.Crack growth rate for AS4/3501.

The mode II test is an unstable test. Once the crack starts growth reaches high energy release rate values quickly. The 3NF test has the limitation that when the crack length grow enough and arrives near the load applicator, local effects provide wrong experimental values. There is only a small range that can be used.

A threshold for each specimen corresponding the time before the crack starts to grow is observed. The Paris law could be determined but it would have to be done by parts, using some samples.

5. CONCLUSIONS

In conclusion, the new method presented permits the real time monitoring of the evolution of the compliance during a fatigue test. From the Compliance data stored continuously during the test, the C(N) graph can be produced. With this graph, the onset point can be determined with the accuracy of one cycle. Then, the a(N) graph results from fitting the C(N) curve to a first order polynomial and the da/dN, is calculated. More experimental values of the da/dN-G_{max} graph are obtained with this method.
This new methodology reduces man-labour dependence and permits an automation of fatigue tests.

ACKNOWLEDGEMENTS

The authors would like to acknowledge in particular the Instituto Nacional de Técnica Aerospacial, INTA for providing the samples. The authors also acknowledge the Spanish Government for funding this work in the MAT2009-07918 project.

REFERENCES

[1] ASTM D6115 - *97 Standard Test Method for Mode I Fatigue Delamination Growth Onset of Unidirectional Fiber-Reinforced Polymer Matrix Composites* (2004).

[2] S. Benmedakhene, M. Kenane, M.L. Benzeggagh (1999). *Initiation and growth of delamination in glass/epoxy composites subject to static and dynamic loading by acoustic emission monitoring.* Composite Science and Technology, 59:201-208.

[3] H.Y. Ling, K.T. Lau, Z. Su, E.T.T. Wong (2007). *Monitoring mode II fracture behaviour of composite laminates using embedded fiber-optic sensors.* Compsites: Part B, 38:488-497.

[4] R. Schueler, S.P. Joshi, K. Schulte (2001). Damage detection in CFRP by electrical conductivity mapping. Composites Science and Technology, 61:921-930.

[5] European Structural Integrity Society Polymers & Composites Task Group (1992). Protocol for interlaminar fracture testing nº 2. Protocols for Interlaminar testing of Composites.

Concrete, cement

EFECTO DE LAS CONDICIONES DE CURADO DEL HORMIGÓN EN SU COMPORTAMIENTO FRENTE A LOS CICLOS HIELO-DESHIELO

Ghaida Al-Assadi[1], María Jesús Casati[2], Jaime Fernández[1], Jaime C. Gálvez[1]

[1] Departamento de Ingeniería Civil: Construcción, E.T.S. de Ingenieros de Caminos, Canales y Puertos, Universidad Politécnica de Madrid, C/ Profesor Aranguren s/n, 28040 Madrid, España
E-mail: ghaida@caminos.upm.es; jfernandez@intemac.es; jcgalvez@caminos.upm.es

[2] Departamento de Vehículos Aeroespaciales, E.U.I.T. Aeronáutica,
Pl. Cardenal Cisneros s/n, 28040 Madrid, España.
E-mail: mariajesus.casati@upm.es

RESUMEN

El objetivo de este trabajo es relacionar las condiciones de curado del hormigón y la adición de un inclusor de aire, con los daños producidos por los ciclos hielo-deshielo en hormigones curados con baja humedad y alta temperatura. Para ello se ha realizado una campaña experimental sobre probetas de hormigón curadas en condiciones extremas reales "in situ" de humedad y temperatura con y sin aire ocluido sometida a ciclo de hielo deshielo. El trabajo presenta la correlación de la evaluación del comportamiento mecánico del hormigón sometido a ciclos hielo-deshielo frente al grado de hidratación del hormigón y el volumen y tamaños de los poros. De los resultados obtenidos se concluye que las probetas sin aireante muestran un deterioro de sus propiedades mecánicas tras el ensayo de hielo-deshielo. Sin embargo, la inclusión de aire beneficia el comportamiento del hormigón frente a los ciclos hielo-deshielo, de modo que incluso mejoran sus propiedades mecánicas tras el ensayo. Este comportamiento anómalo se explica porque el proceso de hidratación del cemento continúa durante los ensayos hielo-deshielo, cerrando la red porosa. Este aspecto se ha podido confirmar con los ensayos de ATD y TG realizados.

ABSTRACT

The main objective of this is to analyze the simultaneous potential damage of concrete specimens exposed to different curing conditions (high temperature and low relative humidity) and freeze-thaw cycles. This experimental campaign was realized on concrete specimen cured in real extreme conditions of humidity and temperature of 30°C and 37 % relative humidity, and with and without air-entraining admixtures subjected to freeze-thaw cycles. Concretes with characteristics strength of 30 y 45MPa, with and without air- entraining admixtures (AEA), were subjected to two different curing conditions: wet and air dried conditions. In addition to the freezing- thawing test, additional durability tests were performed including: mercury intrusion porosimetry, the differential thermal analysis (ATD), termogravimetric analysis (TG). From the obtained results, it can be concluded that the specimens without air-entraining experienced deterioration in their mechanical properties as a result of the freeze-thaw test. The inclusion of air benefited the behaviour of concrete against the freeze-thaw cycles, to the extent that some of the specimens experienced an improvement in their mechanical properties after the freeze-thaw testing. The pore volume and size seems to be higher in the specimens before exposure to the freeze-thaw cycles. These results are attributed to the fact that the hydration process of the cement continued during the freeze-thaw cycles.

PALABRAS CLAVE: Hormigón, ciclos hielo-deshielo, hidratación, porosidad, curado.

1. INTRODUCCIÓN

El hormigón y los compuestos del cemento son materiales tolerantes y con una larga vida en servicio a temperatura ambiental extrema. Las temperaturas extremas en climas calientes y fríos no constituyen una amenaza, porque el hormigón seco tiene un coeficiente de expansión térmica suficientemente bajo y los movimientos moderados pueden considerarse en el diseño.

Sin embargo, surgen problemas de durabilidad cuando el hormigón húmedo en climas fríos está expuesto a los ciclos repetidos de temperatura que causan el hielo y el deshielo del agua de los poros. La expansión del hormigón húmedo puede ser alta y las tensiones inducidas dentro del hormigón pueden ser inaceptables.

En estos casos las inadecuadas condiciones de curado determinan cambios en la microestructura del materia, principalmente en el grado de hidratación que se alcanza y este hecho lleva asociado cambios importantes en la estructura porosa con un debilitamiento importante de su función protectora frente a la entrada de agentes agresivos. Un buen curado permitiría conseguir una consistencia de fraguado tal que nos permita obtener un grado de dureza capaz de garantizar la máxima resistencia física y química en obra.

Entre los estudios sobre el efecto del curado a temperatura elevada en la resistencia al hielo-deshielo del hormigón, Klieger 1958 [1] demostró que la resistencia al hielo-deshielo del hormigón con aireante curado a temperatura elevada no disminuyó. En otro estudio Khurana & Torresan (1997) [2] obtuvieron que la resistencia al hielo-deshielo del hormigón sin aireante mejoró cuando la temperatura de curado pasaba de 20 a 60°C. También Jacobsen (1997) [3] obtuvo valores de la resistencia al descascarillamiento del hormigón sin aireante generalmente bajas cuando la temperatura de curado aumentó de 20 a 60°C. Jonsson & Olek (2004) [4] demostraron que la resistencia al hielo-deshielo de probetas de hormigón curadas hasta los 69ºC se comportaron mejor que las curadas a 28ºC.

El objetivo de este trabajo es relacionar las condiciones de curado del hormigón y la adición de un inclusor de aire, con los daños producidos por los ciclos hielo-deshielo en hormigones curados con baja humedad y alta temperatura. El trabajo presenta la correlación de la evaluación del comportamiento mecánico de hormigón sometido a ciclos hielo-deshielo frente al grado de hidratación del hormigón. Para realizar este estudio se ha realizado una campaña experimental en la que se ha estudiado la porosimetría por intrusión de mercurio, el análisis térmico diferencial (ATD) y el análisis termogravimétrico (TG) a tres edades diferentes 28, 90 y 365 días, en hormigones con distintos curados y con y sin adición de aire.

2. DESCRIPCIÓN DE LA CAMPAÑA EXPERIMENTAL

2.1 Preparación de las probetas y curado

Se fabricaron cuatro tipos de hormigones, de dos resistencias características: 30 MPa y 45 MPa. De cada hormigón se confeccionaron dos tipos, uno con la adición de un aireante (Sika Aer 5), en proporción 0,05% en peso del cemento, y el otro sin aireante. La relación agua/cemento fue 0,5 para en hormigón H30 y 0,4 para el hormigón H45. Las proporciones de la dosificación se recogen en la siguiente referencia de los autores [5].

Se realizaron dos variantes al tipo de curado en las probetas de hormigón curadas en condiciones extremas reales “in situ” de humedad y temperatura a 30ºC de temperatura y a 37% de humedad relativa y con y sin aire ocluido sometidas a ciclo de hielo deshielo. El denominado “B = curado húmedo” se hizo regando diariamente las probetas, en el interior de la cámara climática, durante la primera semana, según recomienda la Instrucción Española de Hormigón Estructural (EHE). El “M = curado seco” se hizo suprimiendo el riego diario antes indicado. De este modo de obtuvieron ocho grupos de probetas:

- Hormigón sin aireante curado húmedo (H30-00-B) y (H45-00-B), amasadas nº.1 y 5.
- Hormigón con aireante curado húmedo (H30-0.05-B) y (H45-0.05-B), amasadas nº.2 y 6.
- Hormigón sin aireante curado seco (H30-00-M) y (H45-00-M), amasadas nº.3 y 7.
- Hormigón con aireante curado seco (H30-0.05-M) y (H45-0.05-M), amasadas nº.4 y 8.

2.2 Tipos de Ensayos

Propiedades mecánicas:
Se ensayaron seis probetas cilíndricas de cada grupo para determinar la resistencia a compresión, módulo de deformación estático y la resistencia a tracción, según las normas UNE 83-304-84, UNE 83-316-96 y UNE 83-306-85, respectivamente.

Porosimetría por intrusión de mercurio (MIP):
En este trabajo se empleó un equipo de la casa Micromeritics, modelo Autopore IV 9500, que opera hasta una presión de 33,000 psi (228 MPa) cubriendo un rango de diámetro de poro desde 0,006 a 175 μm. La metodología empleada para los análisis es similar a las directrices de la norma ASTM D4404, que tiene como objetivo el análisis de rocas y suelos.

La obtención de la muestra siguió un proceso en el que se extrae un fragmento de hormigón del interior de la probeta, a 5 cm de los extremos para las muestras antes de los ciclos. Para las muestras después de la aplicación de los ciclos hielo-deshielo se consideró la media de los valores obtenidos en 4 puntos a distintas profundidades de la probeta en sentido radial. Mediante tenazas de corte se extrajeron los áridos gruesos más visibles y se separaron con aire a presión los restos de árido fino y polvo superficial que se desprende de la matriz. El resultado es una masa redondeada de “mortero” de aproximadamente entre 2 y 4 g.

La técnica de porosimetría por intrusión de mercurio ha sido desarrollada para determinar el volumen y distribución del tamaño del poro de sólidos en el rango de los macroporos. Esta técnica se basa en la propiedad del mercurio de ser líquido que no moja las superficies debido a la alta tensión superficial, el ángulo de contacto con la superficie sólida es mayor de 90°, por lo que requiere elevar la presión para forzarlo a entrar en los poros. La ecuación (1) que relaciona la presión ejercida por el sistema con el radio del poro penetrado, es según [Washbunm, 1921], para poros cilíndricos:

$$p = \frac{-4\gamma \cos\theta}{d} \qquad (1)$$

donde:

- γ Tensión superficial (N/nm);
- θ Ángulo de contacto;
- d Diámetro de poro (nm);
- p Presión necesaria para que el mercurio penetre en un poro de diámetro d (N/nm^2).

ATD/TG:

La caracterización de los productos hidratados se llevó a cabo mediante la realización de análisis térmicos. El tipo de muestra que se emplea es en polvo, con un tamaño de partícula inferior a 0,2 mm. Se analizaron muestras en polvo procedente de secciones completas de muestra. Se llevó a cabo la interrupción del proceso de curado de las probetas a 28, 90 y 365 días, para todas las amasadas. La finalidad de este proceso era evaluar el estado de hidratación de cada una de las muestras a las distintas edades.

En el análisis térmico diferencial (ATD), la información viene dada por los cambios térmicos producidos en la muestra calentada paralelamente a una muestra inerte de referencia. La señal obtenida en un ATD muestra la diferencia de temperatura que se establece entre la muestra objeto de estudio y el material de referencia, cuando ambos se someten al mismo programa de calentamiento. Habitualmente se presentan los datos en forma de curvas, % incremento de masa frente a la temperatura o la derivada de ésta con la temperatura, frente a la temperatura.

Ciclo hielo-deshielo:

Se ensayaron seis probetas cilíndricas de cada grupo para el ensayo de hielo/deshielo según la norma ASTM C 666 [6], y una se dejó como referencia en cámara a 20ºC de temperatura y 45-50% de humedad relativa. Los 300 ciclos hielo-deshielo de acuerdo con el diagrama temperatura/tiempo de la Figura 1. Los detallas de este método se recogen en la siguiente referencia de los autores [5].

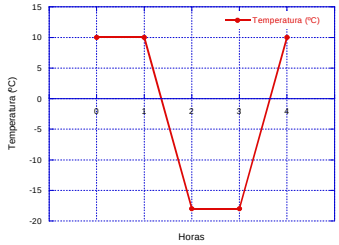

Figura 1. Esquema del ciclo hielo-deshielo.

3. RESULTADOS

La tabla 1 muestra los resultados de los ensayos de resistencia a compresión y porosidad de las probetas antes y después de los ciclos hielo/deshielo.

Las probetas sin aireante muestran un deterioro de sus propiedades mecánicas tras el ensayo de hielo/deshielo en los hormigones H30, mientras no se observa esa tendencia tan clara en el H45. Sin embargo, la inclusión de aire beneficia el comportamiento del hormigón frente a los ciclos hielo/deshielo, de modo que incluso mejoran sus propiedades mecánicas tras el ensayo debido al incremento de la edad (90 días aproximadamente) y a su mejor comportamiento frente al ataque del efecto hielo/deshielo.

Tabla 1. Resultados de los ensayos

Tipo de Hormigón	R. compresión	Porosidad de mercurio	Diámetro Crítico
	(Mpa)	(%)	(nm)
H30-00-B (Antes)	34.35	11,94	50,3635
H30-00-B (Después)	21.43	12,19	40,2834
H30-0,05-B (Antes)	30.86	15,98	62,5151
H30-0,05-B (Después)	36.96	14,33	40,2850
H30-00-M (Antes)	40.84	12,91	40,2908
H30-00-M (Después)	30.01	11,62	40,2821
H30-0,05-M (Antes)	27.91	16,24	40,2951
H30-0,05-M (Después)	31.28	14,97	40,2851
H45-00-B (Antes)	59.13	13,18	32,3730
H45-00-B (Después)	50.63	11,51	32,3710
H45-0,05-B (Antes)	35.11	19,23	40,2796
H45-0,05-B (Después)	39.38	19,00	40,2830
H45-00-M (Antes)	56.99	12,16	62,5305
H45-00-M (Después)	63.39	9.65	32,3770
H45-0,05-M (Antes)	36.34	18,31	62,5212
H45-0,05-M (Después)	40.64	15,30	40,2809

Con respecto a la porosidad, parecen detectarse en casi todos los casos, valores más bajos después de los ciclos hielo-deshielo que antes de los ciclos, sin que se vea una influencia notable de la incorporación del aireante. En casi todos los casos los curados húmedos parecen tener una porosidad mayor después de los ciclos que los correspondientes secos, como se observa en la Figura 2.

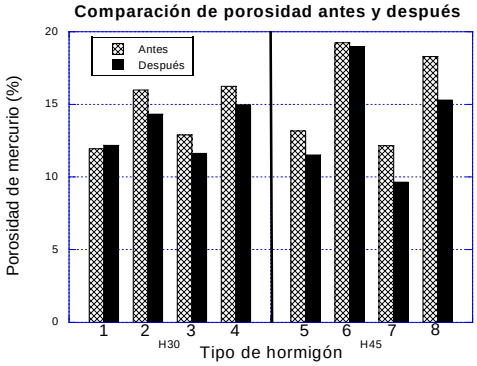

Figura 2. Comparación de la Porosimetría entre los ocho tipos de hormigón.

Con respecto al diámetro crítico que es el tamaño de poro interconectado que más se repite de forma continua, y se corresponde con la pendiente máxima de la curva de porosidad acumulada, parece ser mayor con el curado seco especialmente con el hormigón H45, como se muestra en la Figura 3, tendiendo a igualarse estos valores después de los ensayos hielo/deshielo.

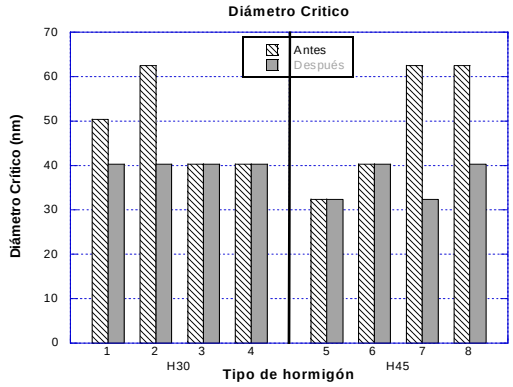

Figura 3. Comparación del diámetro crítico entre los ocho tipos de hormigón.

Si el proceso de deterioro causado por la exposición a los ciclos hielo-deshielo fuera la única razón de las variaciones microestructurales, la distribución de tamaño de poro observado después de los ciclos cambiaría de modo que el pico que representa la variedad dominante de los poros, en la curva de distribución diferencial, debería desplazarse hacia los diámetros más grandes. Se observa en las Figuras 4 a 11 para el hormigón H45 y H30 que este pico no se mueve en alguno de los casos y se desplaza hacia la izquierda (poros más pequeños) en los hormigones H30 curado húmedo y H45 curado seco, mostrándose un aumento significativo de pequeños poros después de los ciclos hielo-deshielo. Esto puede deberse a que se detuvo el proceso de hidratación, y al suministrar agua a al muestra durante los ciclos hielo-deshielo, se reanudó. Esto significaría que el contenido inicial de agua del hormigón no era suficiente para evitar el efecto de auto-desecación, y el proceso de rehidratación en algunas muestras ha sido relevante.

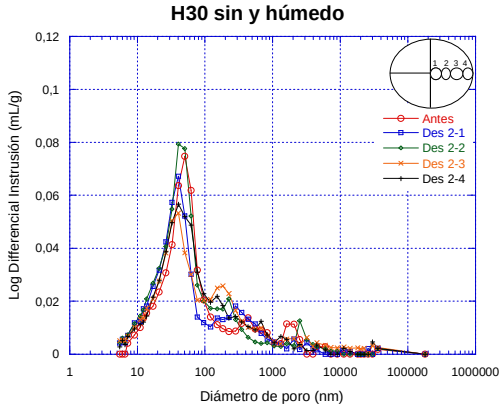

Figura 4. Logaritmo de la intrusión diferencial del hormigón H30 sin aireante curado húmedo antes y después del ensayo de hielo-deshielo.

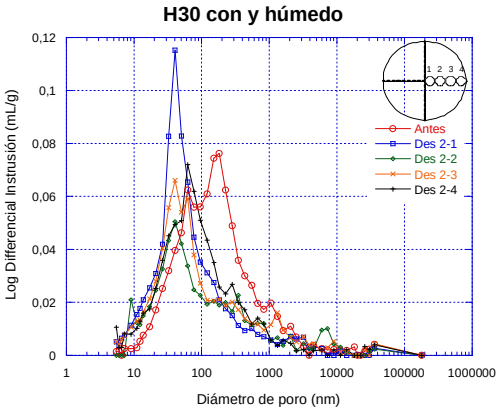

Figura 5. Logaritmo de la intrusión diferencial del hormigón H30 con aireante curado húmedo antes y después del ensayo de hielo-deshielo.

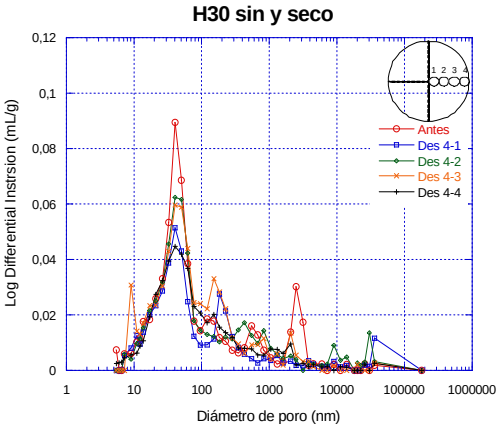

Figura 6. Logaritmo de la intrusión diferencial del hormigón H30 sin aireante curado seco antes y después del ensayo de hielo-deshielo.

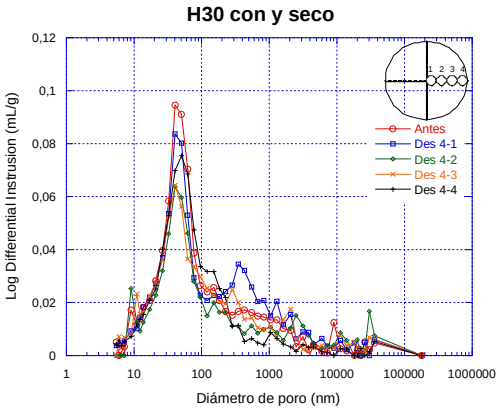

Figura 7. Logaritmo de la intrusión diferencial del hormigón H30 con aireante curado seco antes y después del ensayo de hielo-deshielo.

Y también se observa a través la Tabla 1 que el volumen total de poros antes de los ciclos es mayor en todos los hormigones, mostrando valores más altos los

que contienen aireante. También se observan valores más altos para el hormigón H45

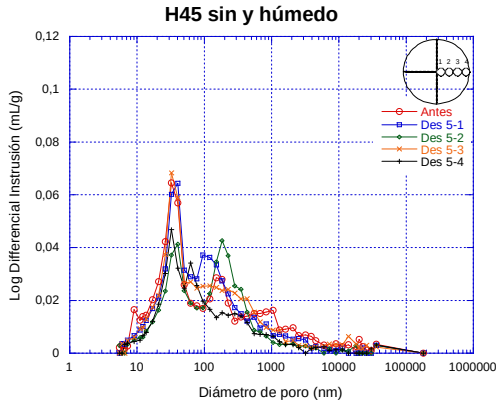

Figura 8. Logaritmo de la intrusión diferencial del hormigón H45 sin aireante curado húmedo antes y después del ensayo de hielo-deshielo.

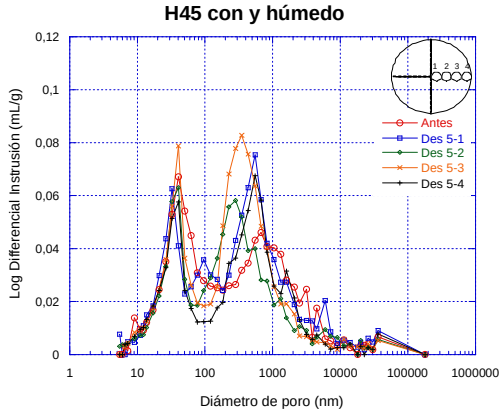

Figura 9. Logaritmo de la intrusión diferencial del hormigón H45 con aireante curado húmedo antes y después del ensayo de hielo-deshielo.

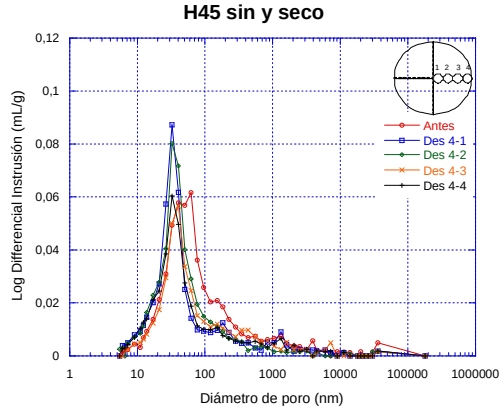

Figura 10. Logaritmo de la intrusión diferencial del hormigón H45 sin aireante curado seco antes y después del ensayo de hielo-deshielo.

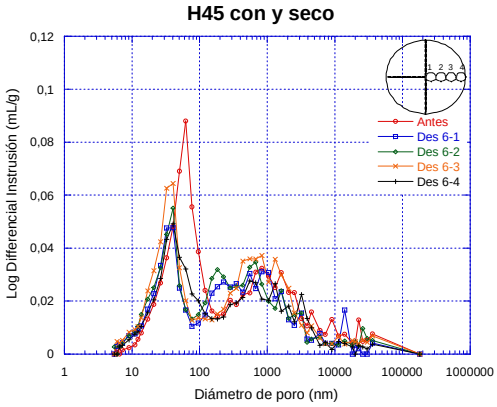

Figura 11. Logaritmo de la intrusión diferencial del hormigón H45 con aireante curado seco antes y después del ensayo de hielo-deshielo.

El grado de hidratación influye en la resistencia a la helada del hormigón, ya que un alto grado de hidratación reduce la porosidad capilar de la pasta de cemento y por tanto la cantidad de agua susceptible de congelación. Además, aumenta la resistencia de la pasta de cemento y por consiguiente, aumenta su resistencia contra la presión hidráulica provocada por la congelación del agua.

(a)

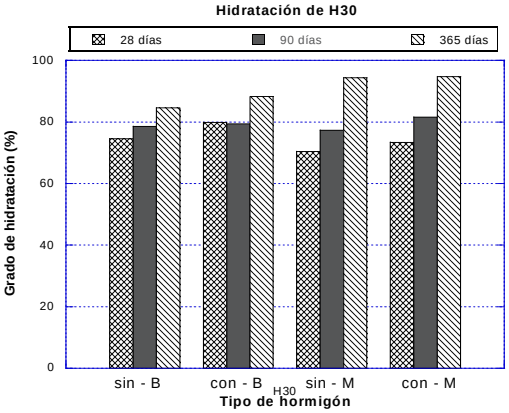

(b)

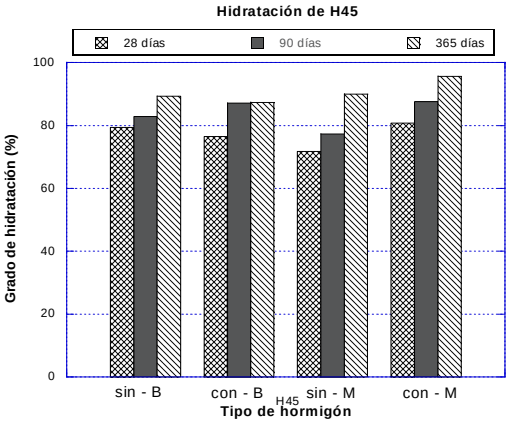

Figura 12. Grado de hidratación
a) para los cuatro tipos de hormigón H30
b) para los cuatro tipos de hormigón H45

En la Figura 12 (a y b) se han representado el grado de hidratación del hormigón a las edades de 28, 90 y 365. Se observa como todos los hormigones aumentan su grado de hidratación a los 365 días. El grado de hidratación que alcanza el hormigón H45 es mayor que el del H30, ya que tiene algo más de cemento 400 kg/m^3, frente a 380 kg/m^3 del H45.

También se observa, a 28 días, en todos los hormigones con curado seco, un grado de hidratación más bajo que en los hormigones con curado húmedo, como cabría de esperar, siendo esta diferencia más acusada en el hormigón H45. A la vista de estos resultados se puede concluir que los hormigones de curado húmedo tienen una velocidad de hidratación mas rápida que los de curado seco. Los hormigones de curado seco retrasan la hidratación, dejando más grano accesible a la humedad exterior, con lo que mejoran sus propiedades para resistir los ciclos de hielo/deshielo, este dato concuerda con el mayor porcentaje de poros determinado en los hormigones con curado seco, sobre todo para el H30. A 90 días se mantiene esa tendencia con diferencias menos acusadas para todos los hormigones. A los 365 días, tiempo en que las probetas han seguido en la cámara de curado, en las probetas curadas en las condiciones más extremas, todos los hormigones alcanzan grados de hidratación más altos que en las que recibieron los riegos la primera semana de curados.

3. CONCLUSIONES

1. Las probetas sin aireante muestran de forma bastante generalizada un deterioro de sus propiedades mecánicas tras el ensayo de ciclos hielo-deshielo. Las probetas con adición de aireante se comportan mejor frente a los ciclos hielo-deshielo que las que carecen de aireante.

2. Las propiedades de durabilidad del hormigón sometido a los ciclos hielo-deshielo están muy relacionadas con su estructura porosa. El volumen, el radio y la distribución del tamaño de poros deciden el punto de congelación de la solución del poro y la cantidad de hielo formado en los poros. Aparentemente el volumen y tamaño de poros es mayor antes de los ciclos hielo-deshielo que después. Este resultado se achaca a que durante el ensayo de hielo-deshielo se completa la hidratación del cemento, insuficientemente desarrollada al principio por el curado extremo aplicado.

3. El grado de hidratación alcanzado en las probetas al inicio del ensayo hielo/deshielo es entorno a un 10% mas bajo en las de curado húmedo y un 24% también más bajo para las de curado seco, concuerda con los resultados obtenidos en los resultados del volumen y tamaño de poros mayor antes de los ciclos hielo/deshielo que después. Al finalizar los ciclos se completa la hidratación del cemento, insuficientemente desarrollada al principio por la baja humedad y la alta temperatura de curado.

4. En general, ambos curados permitieron que continuara la hidratación del hormigón y el fortalecimiento de la zona de transición entre el árido y la pasta de cemento durante los ciclos hielo-deshielo. Con riegos se hidrata más el exterior de las probetas, alcanzando una estructura porosa externa más cerrada. Por el contrario sin riegos la estructura porosa externa es más abierta permitiendo mayor accesibilidad entre los poros conectados, lo que beneficia el comportamiento al hielo-deshielo.

5. El tipo de curado con o sin riegos diarios durante la primera semana, para las condiciones ambientales impuestas de humedad (37%) y temperatura (30°C) y para un hormigón con una relación a/c de 0,5, no parece tan relevante frente al deterioro por los ciclos hielo-deshielo, que el resto de las variables estudiadas. Parece detectarse incluso, y en algunos casos, un mejor comportamiento del curado seco.

AGRADECIMIENTOS

Los autores desean agradecer al Ministerio de Ciencia e Innovación la concesión del proyecto BIA2008-03523 y al Ministerio de Fomento del proyecto MFOM 01/07.

REFERENCIAS

[1] Klieger P., "Effect of mixing and curing temperatures on concrete strength", *J. Amer. Conc. Inst*, 29, 12, 1063–1081, 1958.

[2] Khurana & Torresan, "New Admixtures for Eliminating Steam Curing and its Negative Effects on Durability", ACI SP-173, American Concrete Institute, Farmington Hills, MI, pp.83-103, 1997.

[3] S. Jacobsen, D.H. Saether, E.J. Sellevold, "Frost testing of high strength concrete: frost/salt scaling at different cooling rates*", Materials & Structures*, Vol.30, pp.33-42, 1997.

[4] J.A. Jonsson & J. Olek, "Effect of Temperature-Match-Curing on Freeze-Thaw and Scaling Resistance of High-Strength Concrete", *Cement, Concrete and Aggregates*, ASTM International, Vol.26, No.1, pp.21-25, 2004.

[5] Al-Assadi, G., Casati, M.J., Fernández, J., Gálvez, J.C., "Evaluación del deterioro del hormigón sometido a ciclos Hielo-Deshielo", *Anales de Mecánica de la Fractura,* 26 (2), 2009, pp. 472-477

[6] [ASTM 666, 2003], ASTM C666/C666M-03, *Standard Test Method for Resistance of Concrete to Rapid Freezing and Thawing,* American Society for Testing and Materials.

ESTUDIO EXPERIMENTAL SOBRE LAS TRANSICIONES ENTRE LOS MODOS DE FALLO EN VIGAS DE HORMIGÓN ARMADO SIN CERCOS

A. Carpinteri [1], **J. R. Carmona** [2], **G. Ventura** [1]

[1] Dept. Structural and Geothechnical Engineering, Politecnico di Torino,
Corso Duca degli Abruzzi, 24, 10129, Torino, Italy
[2] E.T.S. de Ingenieros de Caminos,
Canales y Puertos, Universidad de Castilla la Mancha
Avenida Camilo José Cela s/n, 13071 Ciudad Real
E-mail: jacinto.ruiz@uclm.es

RESUMEN

El presente articulo muestra los resultados de una reciente campaña experimental diseñada con el objeto de investigar la relación entre la propagación de las fisuras y el tipo de fallo en vigas de hormigón armado sin cercos. Se realiza un análisis de la forma, extensión y posición de inicio de la fisura que durante su desarrollo provoca el fallo del elemento de hormigón. Se han ensayado 16 vigas de geometría similar y armadas con 4 cuantías de armado diferentes. Se ensayaron 4 vigas de cada tipo. Los resultados experimentales son analizados con la ayuda del modelo denominado "Bridged Crack Model". El modelo de forma sencilla permite estudiar de forma analítica la transición entre los diferentes modos de fallos y como afecta el tamaño de los elementos de hormigón. Se pretende establecer de forma racional y contrastada experimentalmente un modelo que de forma sencilla permita explicar la relación entre los diferentes procesos de fisuración que tienen lugar en las vigas de hormigón armado sin cercos y los modos de fallo.

ABSTRACT

This paper presents the results of a recent experimental research program aimed at investigating the relation between cracking processes and failure mode and at the validation of a recently developed mechanical model. In the analysis of the experimental results, a special emphasis is given to the the shape, extension and initial location of the failure crack and their relation to the rupture mode of the reinforced concrete beam. The experimental program investigated five different reinforcement percentages with four samples each, for a total of 16 beams subjected to three point bending test. The experimental results are discussed with the help of the bridged crack model. The model unifies the theoretical treatment of yielding, shear and crushing failures to predict collapse mode transitions and related size effects, and the experimental program is targeted to validating and discussing the choice of some model parameters.

ÁREAS TEMÁTICAS PROPUESTAS: Fracture of materials (Concrete)/ experimental techniques

PALABRAS CLAVE: Hormigón armado, modos de fallo, efecto de escala

1. INTRODUCCIÓN

En elementos de hormigón armado durante el proceso de carga diferentes procesos de fisuración tienen lugar. La trayectoria de las fisuras y su longitud van a definir el tipo de fallo; por ejemplo en vigas sometidas a flexión en tres puntos las primeras fisuras se forman en las regiones de máximo momento flector, en la cara donde las tensiones de tracción son mayores. Estas fisuras de flexión han sido ampliamente estudiadas, sobre todo en el caso de de las vigas débilmente armadas, donde su formación y progreso esta relacionado con la cuantía mínima de armadura a disponer para evitar la rotura frágil [1].

Al incrementar la cuantía de armado y antes del fallo nuevas fisuras se generan y progresan a la largo de la viga en áreas más alejadas de la zona de máximo momento flector. Esta fisuras crecen en presencia de una combinación de esfuerzo cortante y flector. Si la cuantía de armado es suficiente una de estas fisuras se propaga, antes de alcanzarse la carga de plastificación de las armaduras, de forma inestable provocando el fallo de la viga [2]. En tecnología de estructuras este tipo de fallo se denomina convencionalmente como fallo por tracción diagonal o fallo por cortante [3]. No obstante y dependiendo de las características geométricas de las vigas y mecánicas de los materiales se puede producir el fallo por compresiones excesivas en la parte superior de la viga.

En el presente articulo se analiza la relación entre la cuantía de armado, la posición inicial de la fisura, la trayectoria de las mismas y el tipo de fallo, en vigas de hormigón armado armadas sin cercos. Un total de 16 vigas con 4 cuantías diferentes de armado han sido ensayadas. El articulo se centra en la descripción de los resultados experimentales con especial atención a las trayectorias de las fisuras y la transición entre modos de fallo. Este estudio forma parte de una investigación más amplia con

el objeto de establecer de forma racional la cuantía en la que se produce en la transición entre fallos y como el tamaño del elemento y propiedades del hormigón influyen en ella.

2. PLANTEAMIENTO DEL PROGRAMA EXPERIMENTAL

El estudio se ha planteado con el fin de analizar la influencia del la cuantía de armado en el mapa de fisuración. Aunque al aumentar la cuantía de armado las fisuras acaban extendiéndose a toda la viga, nos hemos centrado en el estudio de la posición inicial y forma de la fisura que determina el fallo del elemento, en adelante denominada *fisura crítica*, en relación con la cuantía de armado. Las cuantías de las vigas fueron definidas en base a los siguientes requerimientos:

- La cuantía más baja corresponde aproximadamente al mínimo mecánico para evitar el fallo frágil;
- La siguiente cuantía se fijó aproximadamente en la transición entre el fallo por flexión y el fallo por cortante;
- La tercera cuantía se determino para que el fallo de la viga se produjera por tracción diagonal;
- La mayor de las cuantías se definió de tal forma que se indujera en la viga un fallo por compresiones excesivas en la parte superior.

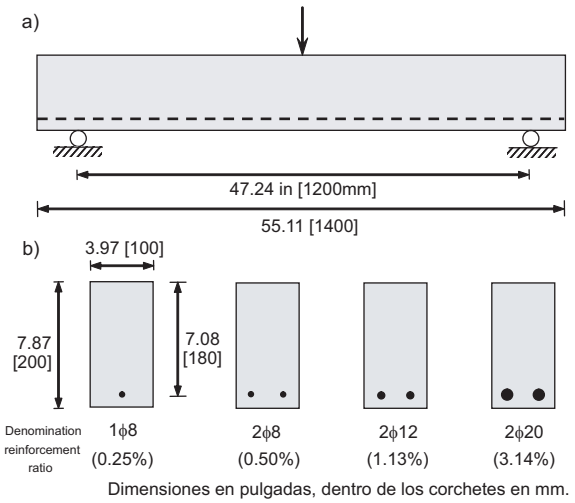

Figura 1: Geometría y armado de las vigas

La geometría de las vigas y cuantías son mostradas en la Figura 1. Las dimensiones de las vigas se determinaron de tal forma que su manipulación en el laboratorio fuera razonablemente sencilla. La distancia entre apoyos es igual a seis veces el canto de la viga. La Figura 1b muestra la sección central de las secciones consideradas. Cada viga se denomina por las barras de armado que contiene, entre paréntesis se muestra la cuantía de armado.

La caracterización de los materiales fue realizada mediante ensayos independientes de acuerdo con Normativas y recomendaciones vigentes. Los detalles de estos ensayos de caracterización son presentados en el siguiente apartado. Todos los ensayos se han realizado en el laboratorio de materiales y estructuras del Departamento de Estructuras y Geotécnia del Politécnico de Turín

3. CARACTERIZACIÓN DE LOS MATERIALES

Un único hormigón fue utilizado en la ejecución de todas las vigas. Se realizó un estricto control del proceso de fabricación de las vigas para minimizar las desviaciones. Tanto las vigas como las probetas para caracterización se fabricaron en la planta de Buzzi-Unicem sita en Santhià, localidad cercana a Turín.

Los ensayos forman parte de una mas extensa campaña que se ha realizado con el objeto de estudiar el comportamiento de vigas ejecutadas con hormigón con fibras metálicas y armado. La determinación de la energía de fractura y tenacidad se realizó de acuerdo a la recomendación RILEM TC-89 [4] y siguiendo el procedimiento recomendado por Elices, Guinea y Planas [5]. La tenacidad se determinó a partir de la relación $K_{IC} = \sqrt{G_f E}$, donde G_f y E son la energía de fractura y el módulo de elasticidad respectivamente. La resistencia a compresión, f_{ck}, fue medida en cubos de dimensiones $150 \times 150 \times 150$ mm. El modulo de elasticidad se determino sobre probetas prismáticas de dimensiones de $100 \times 100 \times 300$ mm. La resistencia en probeta cilíndrica, f_c, fue evaluada a partir de la resistencia en probeta cúbica a través de la expresión $f_c = 0{,}85 f_{ck}$.

En la tabla 1 mostramos los resultados obtenidos.

	f_c [a] MPa	E_c GPa	G_F N/m	K_{IC} [b] Nmm$^{3/2}$
mean	49.4	33.1	111.5	60.7
cov.(%)	11.5	2.5	13.0	-

[a] probeta cilíndrica
[b] $K_{IC} = \sqrt{E G_F}$

Tabla 1: Características mecánicas del hormigón

Para realizar el armado de las vigas se han utilizado barras de $8\ mm$, $12\ mm$ y $20\ mm$ de diámetro. El limite elástico al $0{,}2\,\%$ de deformación se midió en 519 MPa y la resistencia última en 623 MPa. El armado utilizado era corrugado.

4. METODOLOGÍA EXPERIMENTAL

Todas las vigas fueron ensayadas en un dispositivo de flexión en tres puntos tal y como se muestra en la Figura 1. Los ensayos se realizaron en una maquina dinámica servo-hidráulica tipo MTS 204.71 con una capacidad

de 250 kN. La carga fue aplicada sobre una placa de 50 mm de ancho situada en el centro del vano. Para medir el desplazamiento vertical se dispusieron dos transductores lineales (LPT) con un rango de medida de 100 mm. El desplazamiento vertical, δ, se determinó como la media de la medida dada por ambos LPTs. Adicionalmente en los apoyos se dispusieron otros LPTs para medir el desplazamiento en éstos y corregir el desplazamiento del centro de vano.

El desplazamiento en centro de vano fue tomado como parámetro de control de los ensayos. Durante los ensayos la velocidad del desplazamiento vertical se mantuvo constante con un valor igual a $8\mu\text{ms}^{-1}$. La carga maxima se alcanzaba aproximadamente unos 15-20 minutos tras comenzar el ensayo dependiendo de la cuantía de armado. La duración total de cada ensayo fue de unos 30-45 minutos. La carga, P, y el desplazamiento bajo el punto de carga, δ, fueron monitorizadas durante todo el ensayo. Finalmente y para completar la información de cada ensayo los mapas de fisuración de ambas caras fueron tomados fotografiando ambas caras con una cámara de alta resolución. De cada tipo de viga se ensayaron al menos 4 probetas.

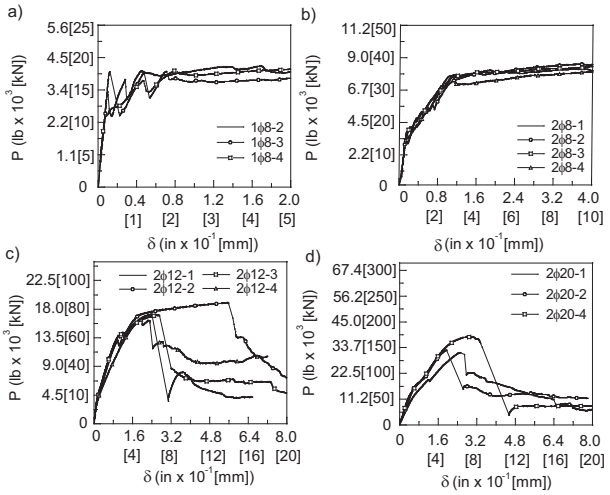

Figura 2: Curvas carga-desplazamiento (P-δ)

5. RESULTADOS EXPERIMENTALES

Todas las curvas carga desplazamiento son mostradas en la Figura 2. El eje y esta escalado de acuerdo con la cuantía de armado para poder comparar las curvas. Para facilitar la comparación entre vigas del mismo tipo se ha corregido la pendiente inicial de las curvas a la teórica que se obtendría mediante la teoría de la elasticidad [6]. Se ensayaron correctamente 14 de las 16 vigas planteadas.

El comportamiento de las vigas es siempre lineal en el primer tramo. En las vigas más débilmente armadas la carga de fisuración (primer pico) es aproximadamente igual a la carga última, que vienen dada por el tramo horizontal. Al aumentar la cuantía de armado se aprecia un cambio en la pendiente inicial coincidente con el punto donde se fisura la viga lo que provoca una perdida de rigidez. Para las dos cuantías más bajas, $0{,}25\,\%$ y $0{,}50\,\%$, observamos como en la parte final de las curvas se produce un tramo prácticamente horizontal, que indica que las armaduras han plastificado, aumentando el desplazamiento vertical sin un aumento significativo de la carga. El fallo de estas vigas es dúctil y se identifica con el fallo por flexion. En cambio para las cuantías más altas, $1{,}13\,\%$ and $3{,}14\,\%$, un repentino descenso en la carga es medido, sin que se haya alcanzado la plastificación de las armaduras. Las vigas fallan de forma frágil.

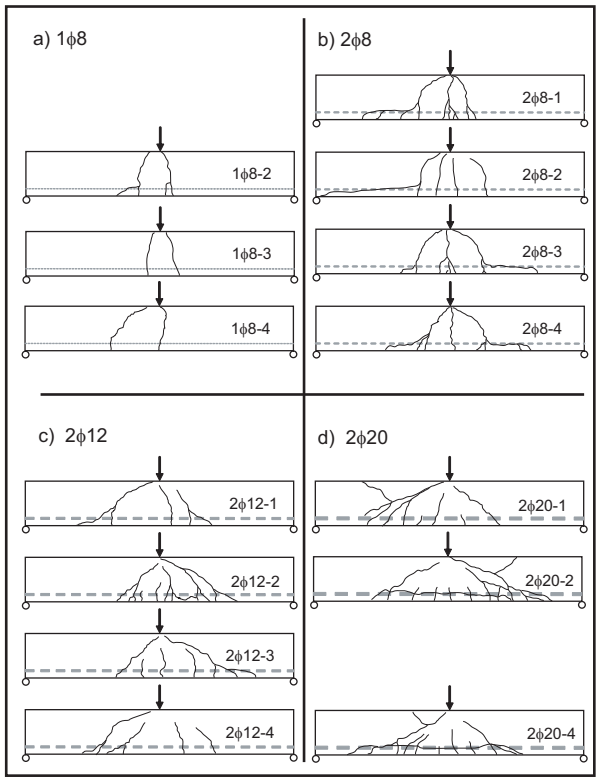

Figura 3: Patrones de fisuración

Los patrones de fisuración de las vigas ensayadas son mostrados en la Figura 3. Durante el proceso de carga las primeras fisuras son de flexión en zonas cercanas al centro de vano. Para la menor de las cuantías ($0{,}25\,\%$), Figura 3a, el acero plastifica rápidamente tras la carga de fisuración, en una de las fisuras formadas, de esta forma la deformación se localiza en la barra de acero y se bloquea el progreso de más fisuras en el elemento de hormigón armado. Para las vigas armadas con una cuantía del $0{,}50\,\%$, Figura 3b, la longitud de vano donde aparecen fisuras se amplía, aunque el comportamiento mecánico es bastante similar al caso de vigas con un $0{,}25\,\%$ de cuantía: el acero plastifica en una de las fisuras y se localiza la deformación en la barra provocando un fallo dúctil. Se observa en algunos casos que aparece una fisura horizontal a la altura del armado provocada por la movilización en las fases finales del ensayo de la adherencia entre hormigón y acero. Estas fisuras también se deben a la movilización del efecto pasador al producirse una desplazamiento ver-

tical entre los labios de la fisura. Para las vigas con una cuantía del $1{,}13\,\%$, Figura 3c, tanto fisuras de flexión y de flexión cortante aparecen a lo largo del vano. Comparando el patrón con los casos anteriores la zona afectada por las fisuras aumenta de forma sensible. El fallo del elemento se genera al propagarse una de estas fisuras de forma inestable al no poder controlar su progreso el armado y liberando gran parte de la energía contenida por el elemento [3]. El armado no llega a plastificar y un subito y frágil fallo tiene lugar. Durante el crecimiento inestable de la fisura una redistribución de la forma en la que la carga es soportada se produce desde el conjunto armado–ligamento de hormigón comprimido a efecto pasador de las barras a través de las fisuras. El hormigón que rodea el refuerzo no es capaz de de soportar la carga transmitida por las barras y se originan fisuras longitudinales a la altura del armado tras la carga máxima. Finalmente para las vigas más armadas $(3{,}14\,\%)$, véase la Figura 3d, se obtiene el patron más extenso. Las fisuras de flexión y cortante aparecen a lo largo del vano y se desarrollan hasta que en la parte central de la viga se produce en su cara superior el fallo por compresiones excesivas, caracterizado por la aparición de una fisuración en forma de cuña cerca del punto de aplicación de la carga.

6. INFLUENCIA DE LA CUANTÍA DE ARMADO

La influencia de la cuantía de armado es bien conocida en la vigas de hormigón armado, la máxima carga y el modo de fallo dependen fuertemente de ésta. Este efecto es observado en la Figura 4a, donde representamos una curva P-δ para cada uno de los tipos de vigas ensayadas. Al aumentar la cuantía la carga aumenta, también se observa la transición desde un fallo dúctil, predominantemente en flexión para las vigas con menor cuantía a un fallo frágil de las vigas con la mayor cuantía de armado.

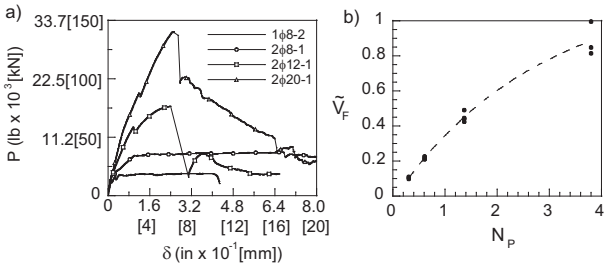

Figura 4: Influencia de la cuantía de armado; a) curvas P-δ; b) curva $\tilde{V}_F$-N_P

En la Figura 4b representamos la carga máxima en cada ensayo expresada de forma adimensional en abscisas, $\tilde{V}_F$, frente a denominado numero de fragilidad de Carpinteri, N_P [7]. Este numero de fragilidad es proporcional a la cuantía de armado. La expresión del número de fragilidad, N_P y del cortante en el apoyo de forma adimensional, $\tilde{V}_F$ es:

$$N_P = \frac{f_y h^{\frac{1}{2}}}{K_{IC}}\rho; \qquad \tilde{V}_F = \frac{V_F}{K_{IC} h^{\frac{1}{2}} b} \tag{1}$$

donde K_{IC} es la tenacidad en fractura del hormigón, f_y el límite elástico del acero y V_F es el cortante en la sección que se analiza. Cada uno de los puntos representa el valor de uno de los resultados realizados. Se ha dibujado una linea de interpolación para ver más claramente la tendencia. Las curvas muestran una variación no lineal de la carga máxima, más evidente al aumentar el numero de fragilidad. La respuesta no lineal esta relacionada con el cambio en el modo de fallo (flexión→cortante→compresión).

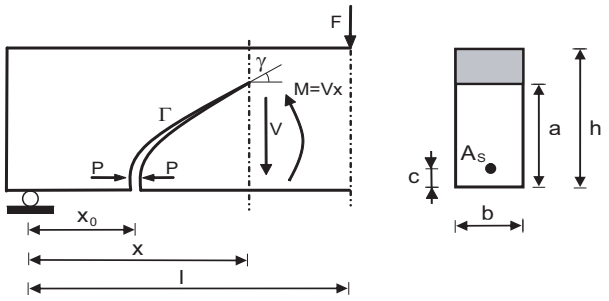

Figura 5: fisura critica

7. FISURA CRÍTICA

En ensayos a flexión en tres puntos, el fallo se desarrolla generalmente por la formación y desarrollo de una serie de fisuras de flexión-corte a lo largo del vano, hasta que en una de ellas se localiza una deformación excesiva de la armadura y se provoca el fallo de la viga

Aunque los mapas de fisuración en vigas de hormigón presentan una alta densidad de fisuras, nos vamos a centrar en el presente estudio en la fisura cuya apertura determina el fallo de la viga. Para poder interpretar los resultados experimentales la trayectoria real observada en los ensayos va a ser descrita de forma matemática a partir de la ecuación definida para las trayectoria de las fisuras definida para su modelación con el *bridged crack model* [8]. La trayectoria de la fisura, Γ, queda caracterizada en por dos partes. La primera parte, Γ_1, es vertical y va desde la parte inferior de la viga hasta la posición del armado. La segunda parte, Γ_2, se modela con una función exponencial que se desarrolla desde la intersección de la primera parte y el armado hasta el punto de aplicación de la carga. La trayectoria de la fisura $\Gamma = \Gamma_1 \cup \Gamma_2$ es definida analíticamente por la función:

$$\Gamma(a) = \begin{cases} x_0 & c \geq a \\ x_0 + \left(\dfrac{a-c}{h-c}\right)^{\mu} (l - x_0) & c \leq a \leq h \end{cases} \tag{2}$$

donde h es el canto, l es la luz de cortante, a es la altura del fondo de la fisura, c es el recubrimiento, x es la abscisa del fondo de fisura, x_0 es la abscisa del punto de iniciación de la fisura y μ es el exponente de la función exponencial que define la trayectoria de la fisura. Para facilitar la comparación entre diferentes trayectorias la Eq. (2) puede ser escrita en forma adimensional mediante las variables:

$$\alpha_0 = \frac{x_0}{l}; \qquad \alpha = \frac{x}{l}; \qquad \xi = \frac{a}{h}; \qquad \zeta = \frac{c}{h}; \qquad \lambda_l = \frac{l}{h} \tag{3}$$

La ecuación de las trayectorias quedaría como:

$$\alpha(\zeta,\xi) = \begin{cases} \alpha_0 & \zeta \geq \xi \\ \alpha_0 + \left(\dfrac{\xi-\zeta}{1-\zeta}\right)^{\mu}(1-\alpha_0) & \zeta \leq \xi \leq 1 \end{cases} \tag{4}$$

donde α es la abscisa desde el apoyo escrita de forma adimensional, ξ es la altura del fondo de fisura relativa al canto, α_0 es la abscisa del punto inicial de la fisura desde el soporte y ζ es el recubrimiento expresado de forma relativa al canto. Todas esta variables tienen un rango de variación de 0 a 1. Finalmente λ_l es la esbeltez de la luz de cortante, $(\lambda_l = \frac{l}{h})$.

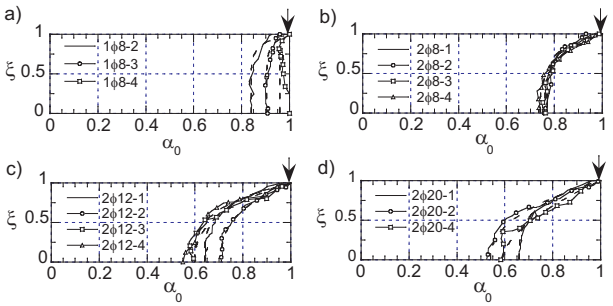

Figura 6: Trayectorias de las fisuras adimensionalizadas

La Figura 6 muestra las diferentes *fisuras críticas* observadas en cada uno de los ensayos realizados. Las fisuras se muestran de forma adimensional. Únicamente se represente la mitad de la viga. La flecha dibujada representa el punto de aplicación de la carga y el apoyo se describe con la abscisa $\alpha_0 = 0$.

Cada una de las fisuras críticas se discretizo en puntos y para hallar los parámetros que caracterizan la trayectoria de la fisura (6) μ y α_0 se realizó una regresión no lineal. Los resultados obtenidos se muestran en la tabla 2. Complementariamente mostramos el coeficiente de correlación de Pearson R, la carga máxima expresada de forma adimensional $\tilde{V}_{test}$ y el modo de fallo observado.

Probeta	α_0	μ	R [a]	$\tilde{V}_{test}$ [b]	modo fallo [c]
1ϕ8-2	0.84	8.70	0.50	0.10	F
1ϕ8-3	0.91	9.10	0.59	0.09	F
1ϕ8-4	0.96	24.9	0.48	0.10	F
2ϕ8-1	0.77	5.29	0.98	0.21	F
2ϕ8-2	0.78	6.05	0.92	0.22	F
2ϕ8-3	0.76	3.76	0.99	0.23	F
2ϕ8-4	0.74	3.21	0.99	0.21	F
2ϕ12-1	0.64	3.59	0.98	0.44	C
2ϕ12-2	0.72	2.74	0.99	0.49	C/F
2ϕ12-3	0.60	2.60	0.98	0.44	C
2ϕ12-4	0.61	3.30	0.97	0.42	C
2ϕ20-1	0.64	3.40	0.99	0.82	C/CM
2ϕ20-2	0.54	2.32	0.99	0.85	C/CM
2ϕ20-4	0.58	1.78	0.95	0.99	C/CM

[a] coeficiente de correlación de Pearson's
[b] ver Eq. (1)
[c] modo de fallo F=flexión; C=cortante; CM=compresión

Tabla 2: Resultados de la caracterización de la trayectoria de las fisuras.

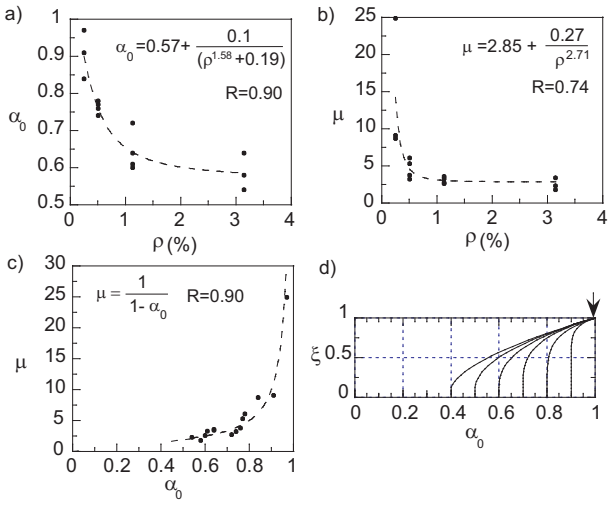

Figura 7: (a) Influencia del punto de iniciación de la fisura con la cuantía de armado; (b)influencia del exponente de caracterización de la trayectoria con el armado; (c) relación entre el punto de iniciación y el exponente; (d) familia de fisuras críticas obtenida a partir de los resultados experimentales

La figura 7a analiza la influencia de la cuantía de armado, ρ, en la posición inicial de la fisura crítica, α_0. La linea de puntos representa una regresión no lineal con la siguiente ecuación:

$$\alpha_0 = 0{,}57 + \frac{0{,}10}{0{,}19 + \rho^{1{,}58}} \tag{5}$$

Al incrementar la cuantía de armado el valor de α_0 decrece. Esto significa que la fisura critica se origina mas cerca del apoyo al aumentar la cuantía. También observamos que al aumentar la cuantía las fisuras el valor de α_0 es

aproximadamente $0{,}50$ lo que indica que las fisuras tienden a iniciarse en la parte central de la luz de cortante. La relación entre la cuantía de armado y el exponente de la ecuación que define la trayectoria de la fisura es mostrada en la Figura 7b. Este exponente tiende a disminuir su valor cuando la cuantía de armado aumenta. Esta tendencia es interpretada como que al aumentar la cuantía las fisuras tienden a ser mas inclinadas respecto a al directriz de la viga. Las líneas de puntos representa un regresión no lineal de los resultados obtenidos a partir de los ensayos con ecuación:

$$\mu = 2{,}85 + \frac{0{,}27}{\rho^{2{,}71}} \tag{6}$$

Las expresiones mostradas anteriormente, ecuaciones (5) y (6), y los datos geométricos, materiales y resultados de los ensayos pueden ser utilizados para contrastar diferentes modelos experimentales. La Figura7c representa la relación entre el exponente que caracteriza la trayectoria y el punto de iniciación de la fisura. Las fisuras tienden a ser más tendidas al acercarse al apoyo. Por último en la figura 7d se representa la familia de *fisuras críticas* que tendríamos en un elementos de hormigón armado. Cada una de las trayectorias está asociada a una cuantía de armado y a un tipo fallo. Las mas cercanas al centro de vano aplicarán el el fallo por flexión y conforme nos vayamos alejando las fisuras criticas provocarán el fallo del elemento por tracción diagonal (cortante). Con la ayuda del modelo presentado en la referencia [8] se puede establecer la transición entre ambos tipo de fallo.

8. CONCLUSIONES

El presente articulo presenta los resultados de una campaña experimental realizada ensayando a flexión en tres puntos vigas de hormigón armado con diferentes cuantías de armado. El programa experimental fue diseñado para estudiar la influencia de la cuantía en los mapas de fisuración con especial atención al modo de fallo y la fisura donde se localiza la rotura (*fisura crítica*). Se ha realizado un análisis de la posición inicial de las fisuras criticas y de su forma con la ayuda de la formulación matemática descrita para su análisis con el *bridged crack model* [8].

Los mapas de fisuración y el comportamiento mecánico es muy sensible a la cuantía de armado. Para cuantías bajas las fisuras críticas se localizan en zonas cercanas a la posición de la carga y son prácticamente verticales, además el fallo de la viga se produce por flexión. Al aumentar la cuantía de armado la posición inicial de la fisura critica se desplaza hacia el apoyo y el fallo se produce por tracción diagonal (cortante). La cuantía de armado controla la posición de la fisura critica y en consecuencia el tipo de fallo del elemento. En base al estudio se proponen unas expresiones para determinar su posición y forma. a cada cuantía se le asocia una trayectoria crítica. Los resultados pueden servir para contrastar modelos teóricos. En nuestro caso se utilizaran para contrastar el modelo *bridged crack model*, unificando los distintos tipos de fallo en un único modelo.

A partir de las observaciones realizadas se pueden analizar problemas tecnológicos como son el establecimiento de zonas para realizar la comprobación del fallo por cortante, o la determinación de la cuantía minima por debajo de la cual no sera necesaria la comprobación a cortante de elementos de hormigón armado ya que fallarían por flexión. Estos puntos serán abordados en próximos trabajos y muestran como problemas tecnológicos dentro del campo de las estructuras de hormigón pueden ser abordados de forma racional bajo el punto de vista de teoría relacionadas con la mecánica de la fractura.

AGRADECIMIENTOS

Los autores expresan su agradecimiento a la Junta de Comunidades de Castilla-La Mancha por el Proyecto PAI08-0196-8210. Un agradecimeinto particuar a la empresa Buzzi-Unicem y al Ing. Enrico Moretti por su ayuda en la preparación de todas las probetas y su transporte hasta el Politecnico di Torino

REFERENCIAS

[1] Carpinteri, A. Ed, *Minimum Reinforcement in Concrete Members.* Number 24 in ESIS Publication. Elsevier. London. 1999

[2] Karihaloo, B., *Fracture Mechanics & Structural Concrete.* Longman, Scientific & Technical. 1995

[3] J. R. Carmona, G. Ruiz and J. R. del Viso, Mixed-mode crack propagation through reinforced concrete. *Engineering Fracture Mechanics*, 74(17):2788–2809, 2007.

[4] RILEM TC 89-FMT, Determination of the fracture energy of mortar and concrete by means of three-point bend tests on notched beams. *Materials and Structures*, 23:457–460, 1985.

[5] Z. P. Bažant, and J. Planas, *Fracture Size Effect in Concrete and Other Quasibrittle Materials*. CRC Press, Boca Raton. 1998.

[6] Planas, J. and Guinea, G. V. and Elices, M., Stiffness associated with quasi-concentrate loads. *Materials and Structures*, 27:311–318, 1992.

[7] Carpinteri, A., Stability of fracturing process in RC beams. *Journal of Structural Engineering-ASCE*, 110:544–558, 1984.

[8] Carpinteri, A. and Carmona, J. R. and Ventura, G., Propagation of flexural and shear cracks through reinforced concrete beams by the brided crack model. *Magazine of Concrete Research*, 59(10):743–756, 2007.

ENERGÍA DE FRACTURA DE PANELES DE MORTERO DE CEMENTO REFORZADOS CON FIBRAS DE VIDRIO (GRC) SOMETIDOS A IMPACTOS DE BAJA VELOCIDAD

A. Enfedaque [1], V. Sánchez-Gálvez [2]

[1] Departamento de Ingeniería Civil: Construcción, E.T.S. de Ingenieros de Caminos, Canales y Puertos, Universidad Politécnica de Madrid, C/ Profesor Aranguren s/n, 28040 Madrid, España.
E-mail: alejandro.enfedaque@upm.es

[2] Departamento de Ciencia de Materiales, E.T.S. de Ingenieros de Caminos, Canales y Puertos, Universidad Politécnica de Madrid, C/ Profesor Aranguren s/n, 28040 Madrid, España.
E-mail: vsanchez@mater.upm.es

RESUMEN

El uso de morteros reforzados con fibras cortas de vidrio (GRC) se ha generalizado durante años en el mundo de la construcción. Sus aplicaciones en edificación y en la industria de la construcción se benefician de sus excelentes propiedades mecánicas. Durante los últimos 40 años se han realizado numerosos trabajos que reflejan el comportamiento tanto a tracción como a flexión de este material. Sin embargo, las propiedades dinámicas del GRC no se han estudiado con anterioridad. Para caracterizar el comportamiento frente a los impactos se ha realizado una extensa campaña de ensayos de torre de caída. Los ensayos han mostrado que el comportamiento del GRC está determinado por el espesor de los paneles ensayados. Hay una relación lineal entre la energía absorbida por las placas y el espesor de las mismas. Se ha desarrollado un sistema de filtrado de datos que permite eliminar los efectos indeseables registrados durante el ensayo**.**

ABSTRACT

Glass fibre reinforced cement (GRC) has been used in many applications in the past. GRC great mechanical properties have been widely used in architecture and civil engineering applications. In the last 40 years tensile and bending behaviour of GRC has been thoroughly studied. However, GRC dynamic behaviour has never been studied before. A wide experimental programme has been carried out using a drop weight machine. Test results showed that GRC impact behaviour is mainly determined by GRC thickness. Energy absorbed by GRC plates is linearly related with thickness. Data has been filtered using a new approach that discard useless data registered during the tests.

KEY WORDS: GRC, impacto, fractura.

1. INTRODUCCION

El GRC es un material que está formado por la unión de dos materiales con propiedades totalmente diferentes: mortero de cemento y fibras de vidrio cortadas y proyectadas aleatoriamente junto con el mortero en dos dimensiones [1]. La unión de los dos materiales nos proporciona un material que reúne las mejores propiedades de ambos y que mejoran las propiedades individuales de cada uno. En el caso del mortero de cemento la inclusión de fibras de vidrio mejora la ductilidad del mismo y la resistencia a tracción; así como la presencia de mortero de cemento mejora los problemas de esbeltez que pueden aparecer cuando se comprimen las fibras de vidrio. Por lo tanto cuando tenemos la unión de ambos materiales lo que se obtiene es un material que tiene una resistencia a tracción y ductilidad mayor que el mortero de cemento y que tiene también una resistencia a compresión alta ya que la que proporciona el mortero de cemento no se ve reducida por la inclusión de las fibras de vidrio.

Por lo tanto con la unión de estos materiales tenemos un compuesto de cemento el cual se caracteriza por las buenas propiedades mecánicas y que no necesita armaduras. Esto nos da un material que tiene una versatilidad de diseño enorme ya que se pueden lograr elementos con casi cualquier forma con espesores de alrededor de 10 mm.

A pesar de los problemas de fragilización que se ha comprobado que aparecen con el paso del tiempo [2-5], las aplicaciones del GRC en edificación y en la industria civil son numerosas [6].

El GRC es un material idóneo para la fabricación de paneles ligeros de fachada además de por las buenas propiedades ya citadas por su notable resistencia al fuego y a la corrosión.

Los paneles de GRC pueden sufrir impactos tan variados como son el lanzamiento piedras, impacto de granizo, caída de herramientas durante su construcción

o bien la proyección de elementos del mobiliario urbano (farolas, semáforos…) causada por tornados u otros fenómenos meteorológicos.
El interés principal de este trabajo es caracterizar el comportamiento del GRC frente a los impactos a bajas velocidades, puesto que no hay apenas referencias previas y en ocasiones adolecen de rigor científico.
Mediante una serie de ensayos de torre de caída se ha obtenido información sobre el comportamiento del GRC cuando está sometido a velocidades bajas de deformación.

2. DESCRIPCIÓN DE LOS ENSAYOS

La torre de caída empleada en los ensayos es el modelo Dynatup 8250. Un esquema de la torre utilizada se puede ver en la figura 1.

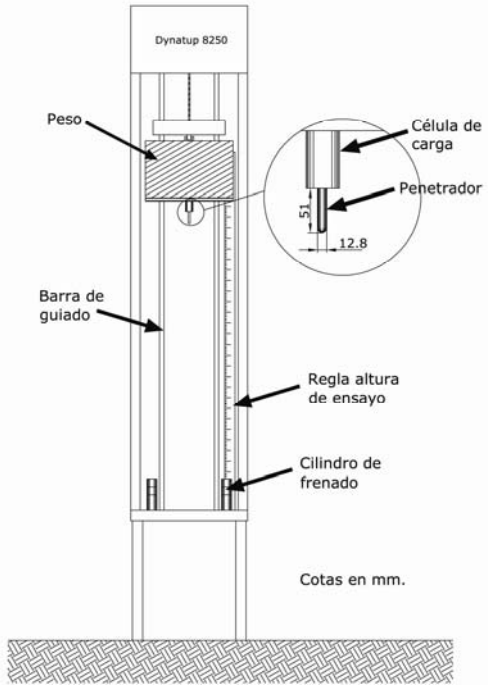

Figura 1. Torre de caída.

Esta torre de caída permite realizar ensayos desde diferentes alturas con pesos que varían desde los 2.21 kg hasta los 44.02 kg. Los pesos se colocan en un marco que, en su parte baja y unida a él, tiene una célula de carga que va conectada a un penetrador o impactador. Este impactador es un cilindro de 12.70 mm de diámetro rematado en su parte baja por una semiesfera del mismo diámetro fabricado en acero. La célula de carga, que está conectada al impactador, está a su vez conectada a un ordenador que dispone de un sistema de adquisición de datos. Este sistema de adquisición a través de los datos proporcionados por la célula de carga, da listados de velocidades, energías y cargas registradas durante el ensayo.

Las muestras que se desean ensayar se colocan en la parte inferior de la torre de caída donde se puede fijar un soporte sobre el que disponer las probetas. La torre de caída también dispone de un hueco en su parte inferior que permite ensayar elementos cuyo tamaño es mayor que la distancia existente entre las barras que guían el conjunto de peso, célula de carga e impactador.

Para realizar los ensayos, se monta en el marco el peso deseado y posteriormente se eleva el mismo a la altura desde la que se dejará caer el conjunto peso, célula de carga e impactador. Posteriormente, se acciona el botón de disparo, el gancho que sujeta el peso se abre liberando el conjunto y dejándolo caer.

3. MATERIAL ENSAYADO

Se han realizado ensayos de impacto a baja velocidad sobre probetas de GRC realizado sin adiciones pero con plastificante para ayudar a dar docilidad al mortero fresco. Las cantidades que se han empleado son las que aparecen en la tabla 1.

Tabla 1. Formulación del mortero de cemento

Cemento	50 Kg.
Arena	50 Kg.
Agua	20 litros.
Plastificante	0.5 litros.

Se realizaron con la colaboración de PREINCO S.A. una serie de paneles de 1.2x1.2m y 10 mm de espesor. De estos paneles se desechó un marco de 5 cm alrededor del contorno para evitar las condiciones de contorno que surgen en la fabricación de los mismos. Una vez eliminada esta parte se realizó el corte de las probetas para los ensayos.

Se usaron probetas de dimensiones similares a la de los paneles reales en los ensayos realizados con la torre de caída para reproducir el efecto de la flexión en el comportamiento del material. Las dimensiones de las probetas fueron de 250x250 mm. Estas dimensiones no permiten colocar las placas en la parte superior de la torre de caída ya que el espacio que hay entre las barras de guiado del peso es menor. Hubo que colocar las probetas entre las patas de la torre. Para conseguir que se produzca el impacto sobre las muestras, el penetrador y célula de carga pasaban a través de un agujero en el suelo de la torre de caída. Los ensayos se han realizado a 28 días de edad del material aproximadamente.

El soporte de las probetas en los ensayos fue un marco de acero rígido. Este marco dispone de dos mitades entre las que se sitúa la muestra a impactar. Se usó un marco ya que se quería reproducir un empotramiento perfecto en los contornos de las muestras. Para conseguir un empotramiento lo más perfecto posible, se colocaron tornillos a cada lado del marco para presionar las probetas al apretar los mismos.

En la figura 2 se puede ver una sección del soporte una vez colocado en la posición en la que se realizan los ensayos y una vista de la planta del mismo. El marco y una de las probetas ensayadas se pueden ver en la figura 3.

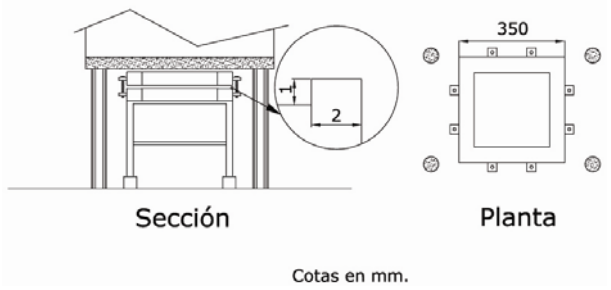

Figura 2. Colocación marco.

Figura 3. Marco fijación probeta.

Se colocó en el marco un peso de 11.72 kg para perforar las muestras. La altura desde la que se dejó caer el peso fue la máxima permitida por la torre de caída. Teniendo en cuenta que la muestra estaba colocada debajo del suelo de la torre, la distancia que existía entre el impactador y las muestras fue de 103 cm. Los impactos se realizaron en el centro de las placas. Antes de cada ensayo se bajó el conjunto formado por el peso, el impactador y la célula de carga hasta estar casi en contacto con las muestras para colocar la muestra y lograr que el impacto se produjese en el centro de las placas. Se elevó el conjunto de peso, célula de carga e impactador a la altura deseada y se realizó el ensayo.

4. RESULTADOS DE LOS ENSAYOS

Los resultados de los ensayos con perforación se pueden ver en las gráficas que aparecen en la figura 4. En ellas se muestran los registros de cargas frente a la deflexión de la muestra. En la leyenda de cada una de ellas se detalla el espesor de cada placa en la zona de impacto.

Los resultados de los ensayos realizados sobre placas de GRC sin adiciones mostraron cierta dispersión. La carga máxima que soportaron las muestras varió desde los 3.45 kN hasta los 8.75 kN.

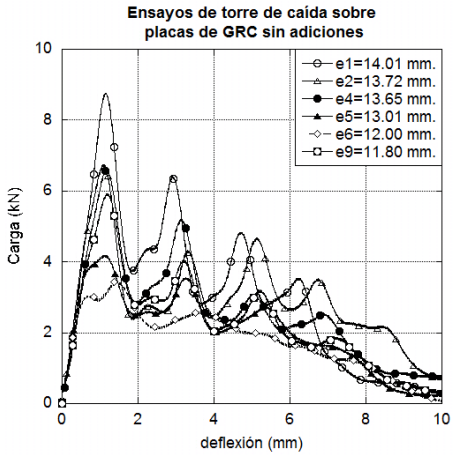

Figura 4. Ensayos torre caída sobre GRC.

Estas diferencias se produjeron, en la mayoría de los casos, debido a las diferencias de espesor que había entre las placas. Sin embargo, la placa de menor espesor en la zona impactada registró cargas mayores que otras muestras de mayor espesor. Por lo tanto, no se puede fijar una tendencia que relacione la carga máxima con el espesor de la muestra en la zona de impacto.

5. ANALISIS DE LOS RESULTADOS

Durante un ensayo de torre de caída la instrumentación registra una serie de medidas de la variación de la carga en el impactador. Con estas medidas, mediante la ecuación 1 se determina la energía perdida por el peso durante el impacto.

$$E = \frac{1}{2} m \left(v_i^2 - \left(v_i - \frac{1}{m} \int_0^t P dt \right) \right) \qquad (1)$$

Donde E es la pérdida de energía de la masa, m es la masa de caída, v_i es la velocidad de impacto y la integral de P con respecto al tiempo es el área debajo de la curva carga-tiempo. Puesto que la carga del impactador es proporcional a su aceleración, mediante una doble integración respecto del tiempo se puede obtener el desplazamiento del mismo. Será necesario evaluar la pérdida de energía del conjunto masa impactador y de otros mecanismos de disipación de energía para conocer la capacidad de absorción de carga de la muestra ensayada.

La relación que existe entre la tensión y la deformación de la muestra está encubierta por una serie de fenómenos que tienen lugar durante el ensayo. Los fenómenos que se registran y que no proporcionan información sobre el comportamiento del material tienen que ver con las oscilaciones armónicas y con las fuerzas de inercia.

Durante el impacto se producen oscilaciones en el penetrador y en la muestra ensayada. Estas vibraciones se producen a la frecuencia propia de cada uno de estos

elementos y quedan registradas junto con el comportamiento del material en los datos que se obtienen de la célula de carga. Para conseguir obtener datos sobre el comportamiento mecánico del material hay que determinar tanto los elementos que producen vibraciones como las frecuencias a las que se producen dichas vibraciones para poder realizar un filtrado que los elimine.

Los efectos de las inercias, que aparecen en los ensayos dinámicos de compuestos cementíceos, tienen gran importancia [7]. Las fuerzas de inercia aparecen durante el ensayo al acelerar la muestra ensayada desde el reposo hasta la velocidad de caída del conjunto formado por peso y penetrador. Las cargas inerciales se caracterizan por un tener un pico agudo, seguido normalmente por unas oscilaciones que se van atenuando al comienzo de las curvas carga-tiempo. La magnitud de estas cargas inerciales se puede considerar como proporcional a la velocidad de impacto, ya que la carga inercial, ejercida por la muestra en el penetrador, es igual al producto del peso y la aceleración de dicha masa.

En la parte inicial del impacto, se acelera la muestra y se induce una carga inercial que se añade a la carga que causa la flexión y la deformación local de la muestra ensayada. Como resultado de esto, la carga que se registra es notablemente mayor que la resistida por la muestra, siendo la resta de ambas el efecto de las inercias en el resultado del ensayo. Dichos efectos aparecen como oscilaciones en las curvas carga-tiempo obtenidas en el ensayo. La duración de este efecto inercial es breve [8]. Para que las medidas realizadas en ensayos de impacto tengan la precisión adecuada, el tiempo durante el que se produce el registro de las cargas debe ser, al menos, 3 veces superior al periodo de dicha oscilación inercial. Para tiempos superiores las medidas obtenidas corresponden a la flexión de la muestra durante el ensayo.

Hay que eliminar las oscilaciones del impactador y de la propia muestra. Para eliminar las oscilaciones del impactador, que aparecen en el registro tomado en el ensayo, se halló la frecuencia propia del impactador mediante ensayos en la torre de caída realizados sobre muestras de un material frágil. Se hicieron dos ensayos en torre de caída sobre placas de mortero de cemento obteniéndose los resultados que se ven en la figura 5.

A partir de los resultados de estos ensayos, se establecieron las curvas amplitud-frecuencia de las cargas registradas en el impactador y se escogió el intervalo de frecuencias más representativo mediante la utilización de las transformadas de Fourier.

Se realizaron las transformadas de Fourier de las gráficas que se ven en la figura 5 para determinar el rango de frecuencias dentro del cual se encuentra la frecuencia propia del impactador.

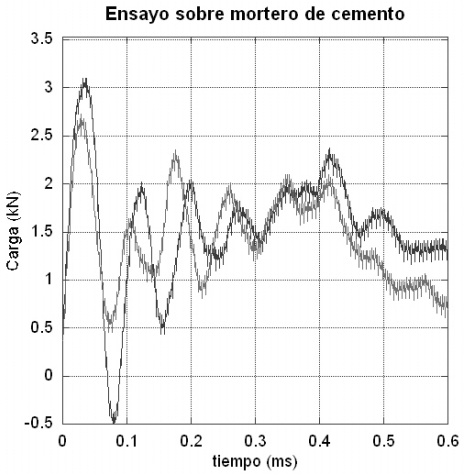

Figura 5. Carga frente a tiempo en mortero de cemento.

En la figura 6 se puede ver una parte de la gráfica de frecuencia-amplitud de la señal registrada. En la figura 6 se ve que el último pico de la amplitud que se ha registrado para ambos ensayos está en torno a los 20 kHz. Puesto que el registro que se obtiene en la célula de carga parte tan sólo de las vibraciones del penetrador, se realizó un filtrado de los datos obtenidos en los ensayos, descartando las medidas obtenidas a frecuencias mayores de 20 kHz.

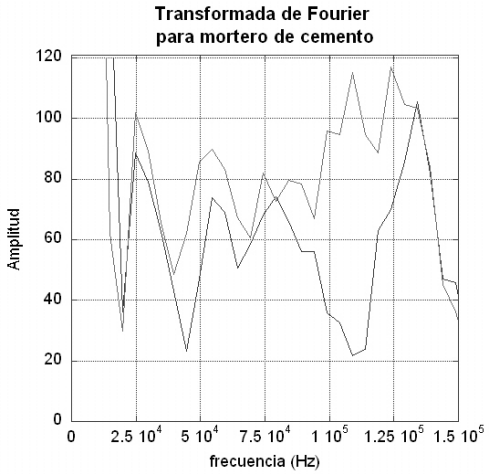

Figura 6. Transformadas de Fourier de la señal de carga.

Para hallar la frecuencia propia del GRC hay que realizar un ensayo sobre una placa circular de espesor homogéneo Para realizar este ensayo el material debe ser isotrópico. Aunque no lo sea, el espectro de frecuencias obtenidas puede indicar el rango dentro del que se encuentra la frecuencia propia del material [9]. Esto fue realizado en los primeros estudios sobre el comportamiento del GRC [10] y se concluyó que las frecuencias propias de vibración del material están cerca de los 3.2 kHz. Sin embargo, un cambio de espesor provocará el cambio de las frecuencias propias del material porque estas son proporcionales al espesor de la muestra. Por lo tanto, si se produce un cambio del espesor, se producirá un cambio del espectro de frecuencias estudiadas. Las placas de GRC que se han

analizado en este estudio tienen un espesor variable y por lo tanto no se puede asegurar que la frecuencia propia del material sea la encontrada en la literatura.

Para eliminar la influencia de las vibraciones del material se realizó un análisis de la velocidad de las ondas en un material cementíceo con módulo de elasticidad 20 GPa. y con una densidad de 2200 kg/m^3. Sabiendo que la velocidad de las ondas en un medio se halla mediante la ecuación 2, se concluyó que la frecuencia de vibración de las ondas en el material era de unos 100 kHz. Por tanto, mediante el filtrado realizado para eliminar las vibraciones debidas al penetrador, se eliminaron también las correspondientes al GRC.

$$v = \sqrt{\frac{E}{\rho}} \tag{2}$$

Las vibraciones propias de la placa ensayada es otro de los efectos que se registran en los ensayos de torre de caída. Estas proceden de la perturbación introducida por el impactador al contactar con la muestra. Para saber la frecuencia de dichas oscilaciones se acudió a la solución analítica de las frecuencias de vibración de una placa isótropa y de espesor constante. Esta formulación se obtuvo de la literatura [11] y se muestra en la ecuación 3

$$\Omega = \sqrt{\frac{\rho}{D}} w a^2 \tag{3}$$

Donde Ω es la frecuencia natural de vibración, ρ es la densidad del material, w es la frecuencia circular, a es el lado de la membrana cuadrada y D es la rigidez del material para una placa de espesor uniforme e isótropa que se expresa según el análisis de Love-Kirchoff en la ecuación 4.

$$D = \frac{Eh^2}{12\left(1-\nu^2\right)} \tag{4}$$

Donde D es la rigidez de la placa, E es el módulo de elasticidad del material, h es el espesor de la placa y v es el coeficiente de Poisson el material. Tomando los datos que se muestran en la tabla 2, se halló que el periodo de vibración de una placa cuadrada, sometida a una perturbación introducida por el impactador, era de 2 ms. Las oscilaciones de carga que aparecieron en los ensayos tienen periodos de vibración similares.

Tabla 2. Propiedades material..

Frecuencia natural (Ω)	3.367
Densidad (ρ)	2200 kg/m^3
Dimensiones placa (a)	0.25 m.
Espesor placa (h)	0.01 m.
Modulo elasticidad (E)	20 GPa
Coeficiente Poisson (v)	0.3

Por lo tanto, para obtener datos del comportamiento del material se realizó un filtrado de las frecuencias que introdujo el penetrador y posteriormente se hizo un suavizado en el que la curva se aproximó a un polinomio de grado 8. Se empleó este tipo de suavizado porque eliminaba de manera clara y sin introducir distorsiones la vibración de la placa de los datos obtenidos. El resultado que se obtuvo para una de las muestras se puede observar en la figura 7.

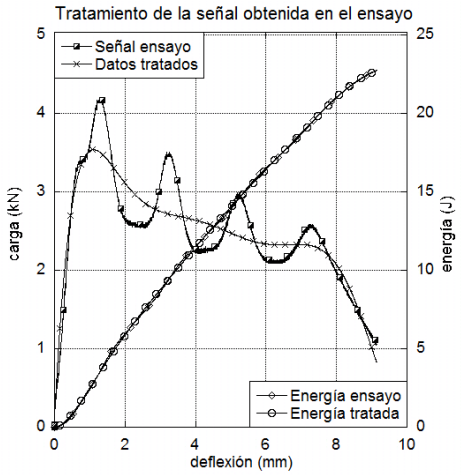

Figura 7. Filtrado y suavizado de los datos obtenidos en los ensayos.

Como se puede ver en la figura 7, se conservó la cantidad de energía absorbida en el ensayo. Esto prueba que, a pesar del tratamiento de señales realizado, no se produjeron modificaciones que falseen los datos registrados en los ensayos. Las curvas que se han obtenido después de estos procesos de suavizado y filtrado pueden ser interpretadas de manera más sencilla sin perder precisión en las medidas realizadas.

Las curvas obtenidas después de filtrar y suavizar las gráficas obtenidas en los ensayos se pueden ver en la figura 8. A pesar del proceso de filtrado el comportamiento de las muestras siguió siendo diferente.

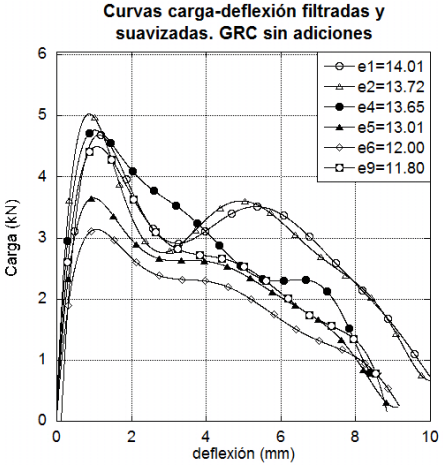

Figura 8 Ensayos torre caída sobre GRC con suavizado.

Aparecieron dos modos de fallo distintos debido a las diferencias de espesor de las muestras. En las placas más delgadas la penetración produjo la extracción de un tapón de material, mientras que en las placas de mayor espesor el GRC se abrió formando un cono de salida debajo del punto de impacto.

Es muy complicado encontrar una tendencia en la energía absorbida por las placas de GRC en el impacto debido a las diferencias en los modos de fallo del material.

A pesar de lo expuesto con anterioridad se relacionó la energía que absorben las probetas ensayadas con el espesor de las mismas. Las diferencias que se observaron en las medidas obtenidas en placas con espesores similares, fueron pequeñas y pueden ser atribuidas a la dispersión propia de los resultados y a las diferencias de sustentanción de las mismas. Los cambios de espesor en las placas hizo que las placas no estuvieran empotradas en todo su contorno.

En la figura 8 se ve la relación existente entre la energía absorbida por la placa en el impacto y el espesor de la misma para una energía de impacto de 118J.

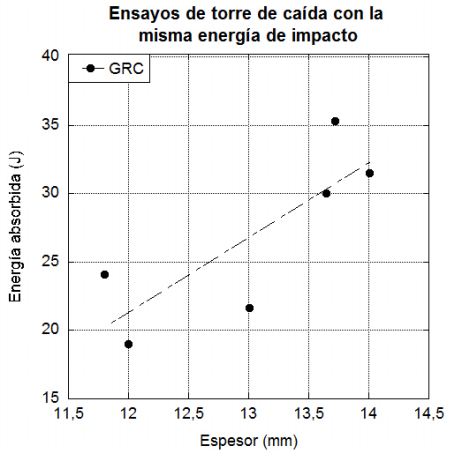

Figura 8. Relación entre espesor y energía absorbida.

La relación entre la absorción de energía en el impacto y el espesor de las placas para la formulación estudiada se muestra en la ecuación 5

$$E_{GRC} = -44.061 + 5.4471e \qquad (5)$$

En esta ecuación E_{GRC} es la energía absorbida por la placa en el impacto y e es el espesor de la placa en mm. Esta ecuación es válida para una energía de impacto de 118 J.

6. CONCLUSIONES

Se ha llevado a cabo un programa experimental de ensayos de impacto a velocidades medias en torre de caída.
Las diferencias en los mecanismos de fallo en los ensayos de torre de caída, a igualdad de energía de impacto, vienen determinados por el espesor de las placas ensayadas.
Parece que existe una relación lineal entre la energía absorbida y el espesor a igualdad de energía de impacto.
Se ha desarrollado un sistema de filtrado de datos que permite eliminar los efectos indeseables registrados durante el ensayo

AGRADECIMIENTOS

Los autores desean agradecer al Ministerio de Educación y Ciencia la financiación de este trabajo a través del proyecto BIA 2004-07336.

REFERENCIAS

[1] L. Sánchez Paradela, V. Sánchez-Gálvez *Los cementos reforzados con fibras de vidrio*, Hormigón y Acero, V.173, 4º trimestre 1989, pp.113-126.
[2] B. Mobasher, , S.P. Shah, *ACI Mater. J. 1989, nº 86* pp 448-458.
[3] A.J. Majumdar, *Fibre reinforced cement and concrete.Construction Press: Lancaster, PA (1975),* pp 279-314.
[4] S.P. Shah, D. Ludirdja, J.I: Daniel, B. Mobasher. *ACI Material Journal (1988)*, número 85, pp. 352-360.
[5] S.P. Shah, D. Ludirdja, J.I: Daniel. *Prestressed Concrete Inst. (1987)* numero 32, pp. 82-99.
[6] Cian, D. y Della Bella, B., *Structural applications of GRC for Precast floors*, GRC Proceedings 2001.
[7] Suaris, W. y Shah, S. P. (1983). *Properties of concrete subjected to impact*. Journal of Structural Engineering, Vol. 109: pp. 1727–1741.
[8] Server, W. L., Wullaert, R. A. y Sheckhard, J. W. *Evaluation of current procederes for dynamic fracture toughness testing*. Flaw Growth and Fracture, 1977 pp. 446–461.
[9] Liew, K. M. *Frequency solutions for circular plates with internal supports and discontinuous boundaries*. International Journal of Mechanical Sciences, 1992 Vol. 34, nº7: pp. 511–520.
[10] Glinicki, M. A., Vautrin, A., Soukatchoff, P. y Francois-Brazier, J. *Plate impact testing method for GRC materials.* Cement and Concrete Composites, 1994. Vol. 16, nº 4:pp. 241–251.
[11] Felix, D. H., Rossit, C. A., Laura, P. A. A. y Bambill, D. V. (2005). Mecánica computacional Vol. XXIV.

ANÁLISIS DEL HORMIGÓN EN MODO MIXTO DE FRACTURA UTILIZANDO UN MODELO MESO-ESTRUCTURAL CON ELEMENTOS JUNTA

C.M. López[1], M. Rodríguez[1], I. Carol[1]

[1] Departamento de Ingeniería del Terreno, Cartográfica y Geofísica
ETSECCPB, Universitat Politècnica de Catalunya, 08034 Barcelona. España
E-mail: carlos.maria.lopez@upc.edu, mariana.rodriguez@upc.edu, ignacio.carol@upc.edu

RESUMEN

En este trabajo se presentan resultados de la simulación numérica de algunos ensayos experimentales sobre muestras de hormigón sometidas a carga biaxial que combina tracción y corte [1]. Para ello se emplea una modelización en la que se representan explícitamente los principales componentes de la estructura interna del hormigón a nivel mesoescala. Los ensayos experimentales se realizaron mayoritariamente en muestras de 200 mm de lado, si bien en algunos casos de carga también se emplearon muestras de 100 y 50 mm. En un trabajo anterior presentado en el Congreso del Grupo Español de Fractura del año 2009 se ha estudiado una muestra de 200 mm con tamaño máximo de árido de 16 mm. En este artículo se analiza ahora la muestra de 50 mm de lado con un tamaño máximo de árido similar al de las probetas empleadas en los experimentos (2mm). Los resultados obtenidos en uno de los estados de carga han permitido reproducir satisfactoriamente el comportamiento carga-desplazamiento (tensión-desplazamiento), así como la formación y evolución de la tendencia de fisuración detectada en los ensayos llevados a cabo en [1] y similares en [2].

ABSTRACT

This paper presents the results of the numerical simulation of some of the experimental tests on concrete samples subjected to different biaxial loading paths combining tension and shear [1]. The study uses a meso-structural model which explicitly represents the main components of the internal structure of concrete at meso-scale level. The experimental tests were conducted mostly in samples of 200 mm side, although in some load cases were also used samples of 100 and 50mm side. In a previous work presented in the Congress of the Spanish Group of Fracture (2009) a sample of 200 mm side with maximum aggregate size 16mm has been studied. This paper now examines the sample of 50 mm side with a maximum aggregate size similar to the used in the experimental test (2mm). The numerical results obtained in one of the loading conditions have allowed satisfactorily reproduce the load-displacement behaviour (tension-displacements) and the cracking patterns detected in the experimental tests conducted in [1] and similarly in [2].

PALABRAS CLAVE: Modo mixto de fractura en hormigón, Análisis mesomecánico, Elemento junta.

1. INTRODUCCIÓN

En ensayos experimentales en modo mixto de fractura, llevados a cabo en diferentes tipos y tamaños de probetas de hormigón, se ha puesto de manifiesto la importante influencia de la componente de corte [1,2]. Por ejemplo, al imponer un estado combinado de desplazamientos de apertura (normal) y de corte en una proporción fija, se detecta una variada relación entre las fuerzas normales y tangenciales, que puede incluso dar lugar a estados de carga en compresión-corte, a pesar de estar imponiéndose un desplazamiento normal de separación. Este comportamiento resulta más acentuado en la medida en que el desplazamiento de corte que se impone resulta mayor.

En un artículo del anterior Congreso del Grupo Español de Fractura [3], se han presentado simulaciones numéricas de algunos ensayos experimentales llevados a cabo en [1] sobre muestras de 200 mm de lado. Se han analizado allí dos de las trayectorias de carga, correspondientes a los casos 4 y 6 de los ensayos experimentales, los cuales han sido utilizados con frecuencia para contrastar la capacidad de diversos modelos [4-7].

En este trabajo se analiza ahora la muestra de 50 mm de lado con un tamaño máximo de árido similar al de las probetas empleadas en los ensayos experimentales (2mm). En este caso, los ensayos se realizaron en muestras prismáticas de hormigón de 50 mm de lado y 50 mm de espesor, que contienen dos entallas de 6.25 mm de largo y 5mm de altura ubicadas de forma simétrica en el centro de la altura (en la figura 1 izquierda se muestra un esquema de la configuración del ensayo experimental).

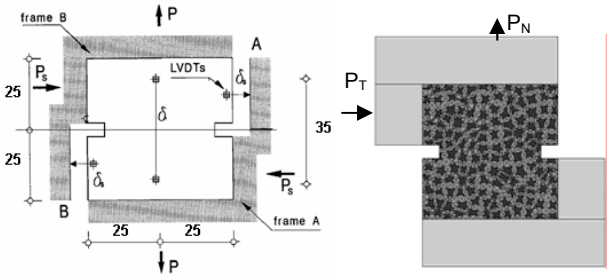

Figura 1: Representación esquemática del ensayo experimental (izquierda) y malla de EF utilizada en la modelización (derecha) para la muestra de 50 mm.

2. MODELIZACIÓN MESOESTRUCTURAL

El modelo consiste en discretizar la estructura interna del material mediante piezas irregulares que representan a los áridos de mayor tamaño, rodeadas por una matriz representativa del comportamiento del mortero y los áridos de menor tamaño. A fin de posibilitar la no linealidad de comportamiento, mecanismos de rotura y fisuración, etc., la malla de elementos finitos incluye elementos junta sin espesor. Estos elementos se distribuyen a lo largo de todos los contactos entre elementos de árido-mortero (interfase) y entre algunos de los contactos de elementos de la matriz, con el objeto de representar las principales direcciones potenciales de fisuración. Para los elementos junta se utiliza una ley constitutiva no lineal basada en la teoría de la elastoplasticidad y en conceptos de la mecánica de fractura, formulada en términos de las tensiones en el plano medio de la junta y los desplazamientos relativos correspondientes. El criterio de fractura F se define mediante una hipérbola de tres parámetros (la resistencia a tracción χ, y los parámetros $tan\phi$ y c de la asíntota que representan el ángulo de fricción entre las caras de la fisura y la cohesión aparente, respectivamente). Una vez iniciada la fisuración, la superficie de fractura se contrae mediante el decrecimiento de los parámetros de la hipérbola en función de unas leyes basadas en el trabajo consumido en el trabajo de fractura. Para controlar el proceso de fractura, el modelo posee dos parámetros que representan la energía de fractura clásica en modo I, G_F^I, y un denominado Modo IIa definido para corte con alta compresión sin dilatancia, G_F^{IIa}. La regla de flujo es no asociada, con una ley de dilatancia que disminuye progresivamente con el nivel de compresión $\sigma \rightarrow \sigma^{dil}$ y con la degradación de la junta $c \rightarrow 0$. Se dispone de parámetros α_χ, α_ϕ y α_c que controlan la forma de evolución del reblandecimiento, y α_d que controla la evolución de la dilatancia en compresión. Una descripción más detallada se ha presentado en anteriores Congresos del GEF, así como en diversas publicaciones [8,9]. Resultados del modelo mesomecánico en 2D y 3D para ensayos de tracción y compresión uniaxial, biaxial, ensayo brasileño, etc. pueden consultarse en [9-12]. En la figura 1 derecha se presenta la malla para el hormigón, junto con las placas de carga, empleada en este trabajo.

3. RESULTADOS

Se analiza la trayectoria de carga denominada 6 en los ensayos experimentales [1], en la cual se aplica una evolución en control de desplazamientos de manera que la relación δ_N/δ_T se mantiene constante. Se adoptaron tres valores de δ_N/δ_T iguales a 1, 2 y 3, denominados tendencias de carga 6a, 6b y 6c, respectivamente. Los parámetros del hormigón para los elementos de medio continuo son: E = 73000 MPa (áridos), E = 27000 MPa (mortero) y υ = 0.2 (ambos); para las juntas de interfase: $K_N = K_T$ = 500000 MPa/mm, $tan\phi_0$ = 0.80, χ_0 =1.5 MPa, c_0 = 7MPa, G_F^I = 0.05 N·mm, G_F^{IIa} = 10 G_F^I, σ^{dil} = 40 MPa, α_d = -2, y demás parámetros igual a cero; para las juntas de mortero-mortero, los mismos parámetros excepto para χ_0 =3 MPa, c_0 = 14MPa, G_F^I = 0.1 N·mm. Los ensayos se han realizado en tensión plana.

3.1. Influencia de una relación impuesta de los desplazamientos en la muestra de 50 mm de lado

En [1] se ha analizado el efecto tamaño ensayando muestras de 200, 100 y 50 mm de lado. En nuestra modelización, a partir de la muestra de 200 mm se ha obtenido por reducción la correspondiente de 50 mm, con lo cual se tiene un tamaño de árido mucho más aproximado al de los experimentos (figura 1 derecha). En la adaptación de la malla sólo ha debido corregirse la altura de las entallas para mantenerla en 5mm. En la figura 3 se muestran los resultados numéricos obtenidos junto con los experimentales para el caso de carga 6, caso 6a en la parte superior, caso 6b en el centro y caso 6c abajo. En la columna izquierda de esta figura se muestran los diagramas en términos de la carga vertical normalizada con respecto a la carga máxima de tracción de cada caso y el desplazamiento vertical. La columna de la derecha corresponde a las curvas de la fuerza de corte en función de los desplazamientos correspondientes. Para el caso de carga 6a, se puede apreciar en la figura la incidencia del desplazamiento lateral en el comportamiento de la fuerza vertical, que luego del pico en tracción pasa a la zona de compresión, como ocurre en la muestra de 200 mm [3]. Sin embargo, dentro del rango de desplazamientos considerados, en la muestra de 50 mm se produce un pico de compresión seguido de una reducción que tiende asintóticamente a anularse. En correspondencia con el pico de compresión y su decrecimiento, el diagrama de fuerza-desplazamiento lateral alcanza un máximo seguido del reblandecimiento. A pesar de la diferencia en la máxima carga horizontal obtenida, la simulación numérica captura satisfactoriamente el comportamiento detectado experimentalmente (gráficos superiores de la figura 3 en los que, a título ilustrativo, se incluyen también los resultados de la malla sin corregir la altura de las entallas). Esto se puede apreciar más claramente en la figura 4, en la que también se ha normalizado la carga horizontal, y ambos desplazamientos se presentan en términos relativos al desplazamiento normal en el pico de compresión. En la figura 3, parte central e inferior, se muestran las curvas correspondientes a los casos de

carga 6b y 6c, respectivamente. Se puede apreciar que los resultados numéricos, si bien de forma más reducida a medida que aumenta la proporción δ_N/δ_T, mantienen la tendencia en la carga vertical con un máximo en la zona de compresión, que se corresponde con un pico en las curvas de carga horizontal. En los experimentos, las curvas de carga normal tienden a anularse del lado de tracción, y la carga lateral presenta un comportamiento tipo meseta al alcanzar su valor máximo.

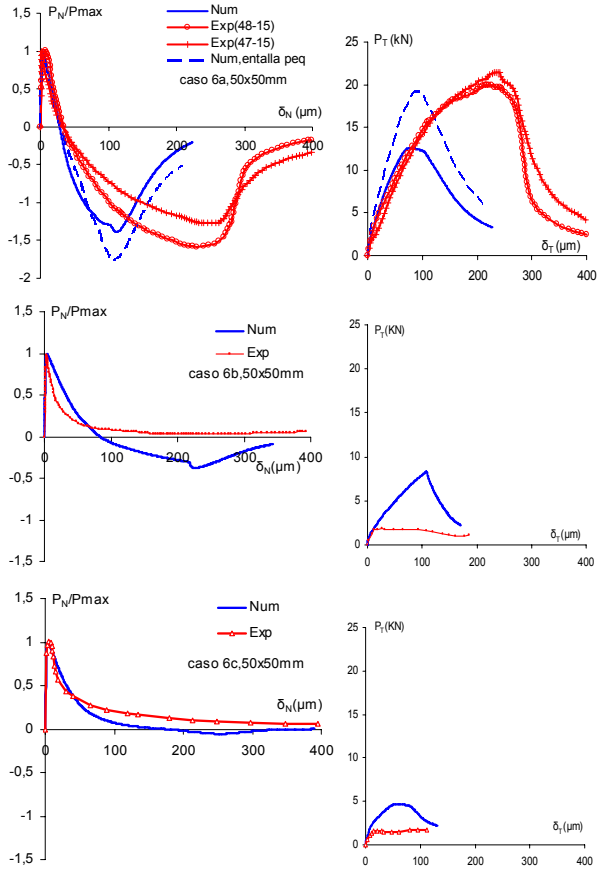

Figura 3. Curvas de fuerza vertical (normalizada) vs. desplazamiento vertical (izquierda) y de fuerza horizontal vs. desplazamiento horizontal (derecha), para los casos de carga 6a, 6b y 6c (de arriba a abajo).

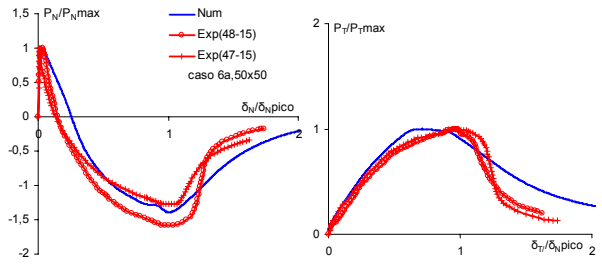

Figura 4. Curvas de fuerza vs. desplazamiento vertical normalizados (izquierda) y curvas de fuerza vs. desplazamiento horizontal normalizados (corte), para el caso de carga 6a en la muestra de 50x50 mm^2.

En la figura 5 se presenta la tendencia de fisuración del modelo numérico en términos del trabajo de fractura disipado, representado por el espesor de línea en cada punto de las juntas (izquierda), junto con la experimental (derecha), para los casos de carga 6a, 6b y 6c de arriba hacia abajo, respectivamente. Resulta especialmente interesante el comportamiento del caso 6a, que se comenta en detalle en el apartado 3.3.

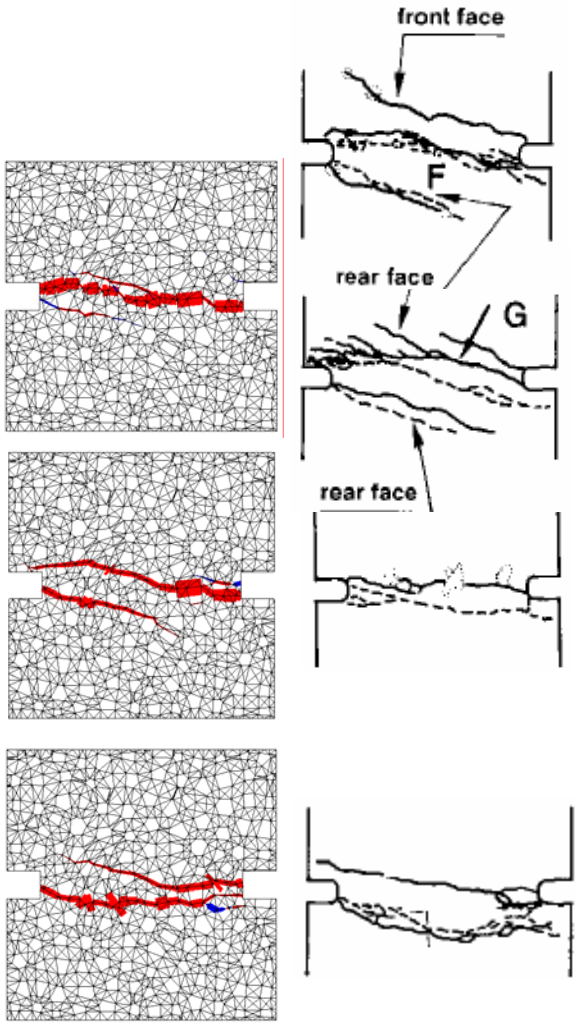

Figura 5. Tendencia de fisuración en el ensayo experimental (derecha) y en la simulación numérica (izquierda) para los casos de carga 6a, 6b y 6c en las muestras de 50x50 mm^2.

3.2. Comparación con otros resultados de modo mixto

El comportamiento experimental de la zona de proceso de fractura del hormigón en modo mixto también ha sido estudiado por Hassanzadeh [2]. Estos ensayos se han realizado en probetas prismáticas de hormigón de 60 mm de altura y 70x70 mm^2 en su sección transversal, que presenta una entalla perimetral de 15 mm de ancho (área neta de 40x40 mm^2). Durante la primera parte del ensayo, la muestra está sometida a tracción pura hasta que se alcanza el pico de tensiones normales. A partir de este punto, se aplican simultáneamente desplazamientos relativos normal y de corte en una proporción fija caracterizada por el ángulo tan θ =

δ_N/δ_T. Los ensayos fueron realizados con valores de θ = 30º, 60º, 75º. Nooru-Mohamed (1992) ha comparado sus resultados con los de Hassanzadeh, empleando las muestras de 50x50 mm^2 para los casos de carga 6 con δ_N/δ_T iguales a 1 (θ = 45º), 2 (θ = 63.4º) y 3 (θ = 71.6º), en términos de las tensiones y los desplazamientos correspondientes.

En las figuras 6 y 7 se presentan estos resultados junto con los obtenidos con el modelo numérico, diferenciando para su mayor claridad los casos 6a, 6b y 6c, que se comparan respectivamente con los ensayos de θ = 30º, 60º, 75º de Hassanzadeh. En la figura 6 se muestran los gráficos tensión-desplazamiento vertical (normal) de postpico. Para δ_N/δ_T = 1 y θ = 30º los tres resultados muestran comportamientos cualitativos similares: luego del post-pico de tracción, cambia el signo de las tensiones, se alcanza un pico de compresión y finalmente las tensiones tienden a anularse asintóticamente desde el lado de compresión. Cuando la relación δ_N/δ_T pasa a 2 y 3, los resultados numéricos mantienen la tendencia anterior aunque de manera más atenuada, lo cual concuerda con los resultados obtenidos por Hassanzadeh, mientras que en los experimentos de Nooru-Mohamed las curvas siguen un reblandecimiento que tiende a anularse del lado de tracción. En la figura 7 se muestran los gráficos tensión-desplazamiento lateral (de corte). Para δ_N/δ_T = 1 y θ = 30º, los resultados experimentales presentan entre sí una gran diferencia en el pico de la tensión de corte y en el comportamiento de reblandecimiento que en el caso de Hassanzadeh resulta mucho más atenuado. La curva numérica presenta un pico más parecido al de Hassanzadeh, si bien la caída de reblandecimiento resulta más acentuada como en el caso de Nooru-Mohamed. Los resultados numéricos de los casos 6b y 6c concuerdan mejor con los correspondientes de Hassanzadeh, ya que presentan un pico en la tensión de corte en correspondencia con un máximo en la zona de compresión.

3.3. Comparación de resultados entre las muestras de 200 y de 50 mm de lado

En un artículo anterior [3], se han presentado los resultados completos de la simulación numérica del estado de carga 6 sobre la muestra de 200 mm de lado. En la figura 8 izquierda se muestran las respectivas curvas de fuerza vertical versus desplazamiento vertical obtenidas con el modelo junto con los resultados experimentales. Se puede apreciar en esta figura la influencia del desplazamiento lateral en relación al desplazamiento normal, que genera que las curvas pasen al sector de compresión con un comportamiento más acentuado con el aumento de la proporción de corte. En la muestra de 50 mm de lado este comportamiento se mantiene en un principio (figura 3 izquierda), sin embargo, posteriormente en los resultados numéricos se produce un pico de compresión seguido de una reducción que tiende asintóticamente a cero. En los ensayos experimentales, este comportamiento se aprecia claramente en el caso 6a de [1]. También en los tres casos considerados en [2], como puede apreciarse en la figura 6. En la muestra de 50 mm, en correspondencia con el pico de compresión y su decrecimiento, el diagrama de fuerza-desplazamiento lateral alcanza un máximo seguido del reblandecimiento.

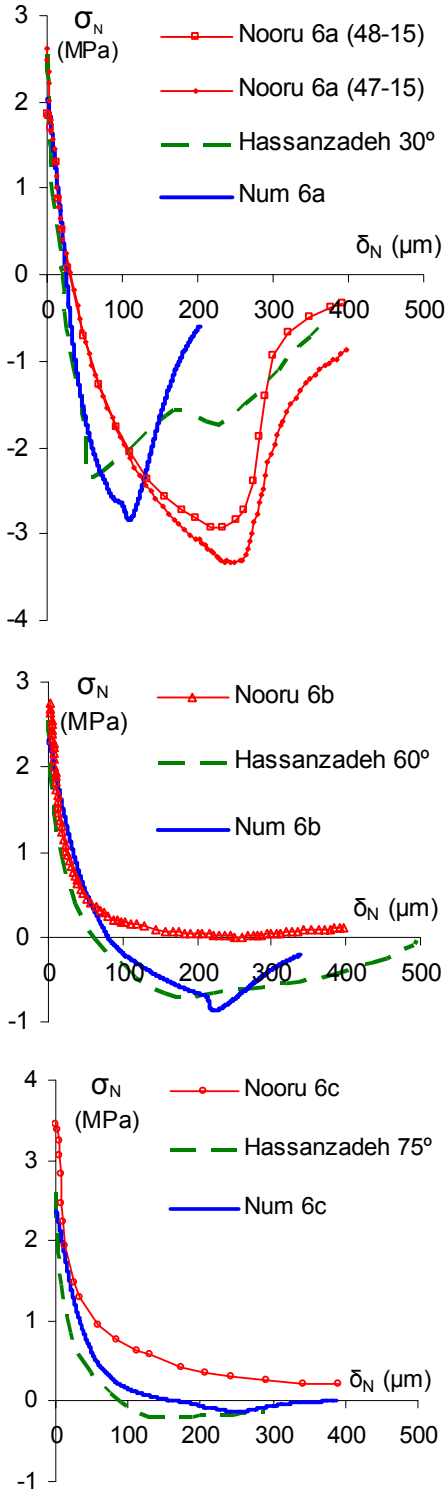

Figura 6. Curvas de tensión vs. desplazamiento vertical (normal) para los casos de carga 6a ,6b y 6c (de arriba a abajo).

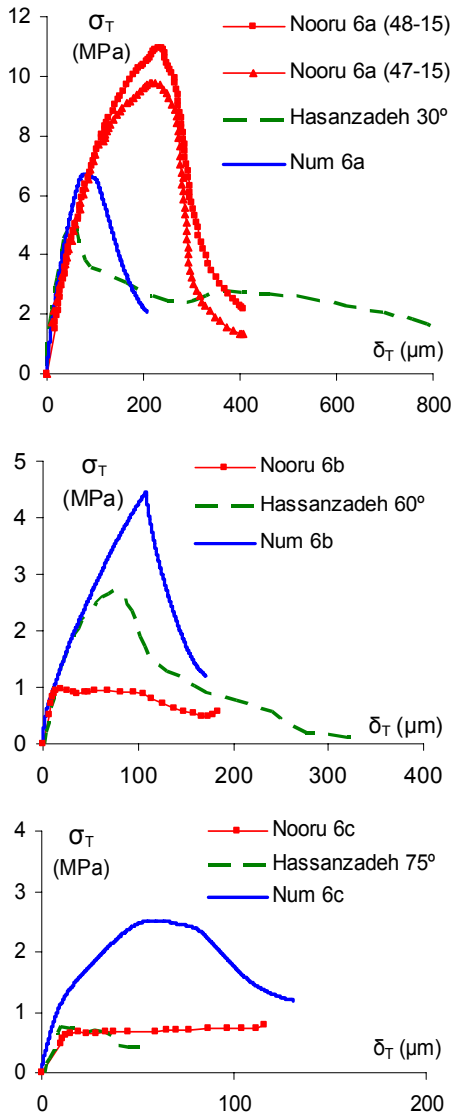

Figura 7.Curvas de tensión vs. desplazamiento horizontal (corte) para los casos de carga 6a ,6b y 6c (de arriba a abajo).

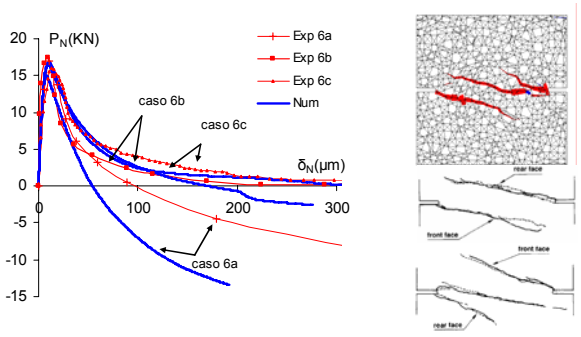

Figura 8. Curvas de fuerza vs. desplazamiento vertical (izquierda) y tendencia de fisuración (derecha) en la simulación numérica (arriba) y experimental (abajo) para el caso 6a de la muestra de 200 mm.

Por el contrario, en el caso 6a de la muestra de 200 mm, dentro del rango de desplazamientos considerados, la fuerza lateral y la vertical siguen en aumento (tanto en los experimentos como en la modelización). En la figura 8 derecha se muestra la trayectoria de fisuración de la simulación numérica (arriba) y la experimental (abajo) para el caso 6a de la muestra de 200 mm. En ambos casos se puede apreciar una tendencia inclinada a partir de cada entalla. Por su parte, en la figura 5 superior se observa la fisuración correspondiente al caso 6a de la muestra de 50 mm, a la izquierda la del modelo y a la derecha la experimental. En [1] se han realizado dos ensayos experimentales en las muestras denominadas 47-15 y 48-15. Se comenta en esta referencia, que tanto la fisura F para la muestra 47-15 como la fisura G para la muestra 48-15 (figura 5 superior derecha), se convierten en cada caso en la fisura dominante (tanto en la cara frontal como dorsal), mientras las otras fisuras inclinadas se cierran. Más aún, se dice que la caída en la capacidad resistente de corte está asociada con la apertura de las fisuras F y G, que presentan una trayectoria tortuosa. Para apreciar la evolución de la tendencia de fisuración en la simulación numérica del caso 6a, en la figura 9 se muestran varios estados representados en este caso en términos del módulo del vector desplazamiento plástico (en rojo fisura activa y en azul en descarga), que permite apreciar más claramente la incidencia de cada modo de fractura (en los gráficos en función de la energía disipada de la figura 5 izquierda, en la apreciación visual incide la diferencia entre los valores de los parámetros G_F^I y G_F^{IIa}). En la figura 9a se observan tres fisuras inclinadas, de las cuales posteriormente dos de ellas evolucionan de forma activa y la restante ubicada en la parte superior de la entalla de la derecha entra en descarga (figuras 9b y 9c correspondientes a δ_N = 42 μm y δ_N = 76 μm, respectivamente). En la figura 9d, para δ_N = 110 μm, en una situación cercana a donde se producen los picos tanto de la carga vertical como de la horizontal de corte (ver figura 3 superior), se aprecia que progresa desde la entalla izquierda una fisura aproximadamente horizontal (que ya se observa de forma incipiente en la figura 9c), que se une a la fisura desarrollada desde la entalla derecha, formando una tendencia aproximadamente horizontal, a la vez que se cierran las tendencias inclinadas. En la figura 9e, para δ_N = 226 μm, se observa que se acentúa la fisura orientada de una a otra entalla, cuyo desarrollo completo propicia la disminución progresiva hasta anularse de ambas cargas, vertical de compresión y lateral de corte. En la figura 9f se muestra la malla deformada para δ_N = 226 μm, en la cual puede apreciarse la fisura completamente formada, que presenta una tendencia más o menos tortuosa motivada por la representación explícita de la mesoestructura, que determina que la fisuración tienda a bordear los áridos ("aggregate interlock").

El modelo mesoestructural captura correctamente el comportamiento mecánico cuando se impone una proporción fija de los desplazamientos, lo cual puede atribuirse al efecto de la dilatancia. Mientras la relación fija entre los desplazamientos impuestos se mantenga inferior al efecto de dilatancia de la muestra, ésta verá

impedido su progreso y se desarrollarán tensiones de compresión crecientes, hasta que la evolución de la degradación propicia un pico de las tensiones de compresión y la posterior tendencia a cero. Este fenómeno detectado en la muestra de 50x50 mm^2 cabría esperar que se produjera en la muestra de 200x200 mm^2 (figura 8) si se prolongaran los rangos de carga (limitados en los experimentos de Nooru-Mohamed, para las muestras de 100x100 y 200x200 mm^2, por la capacidad de carga de la máquina de ensayo).

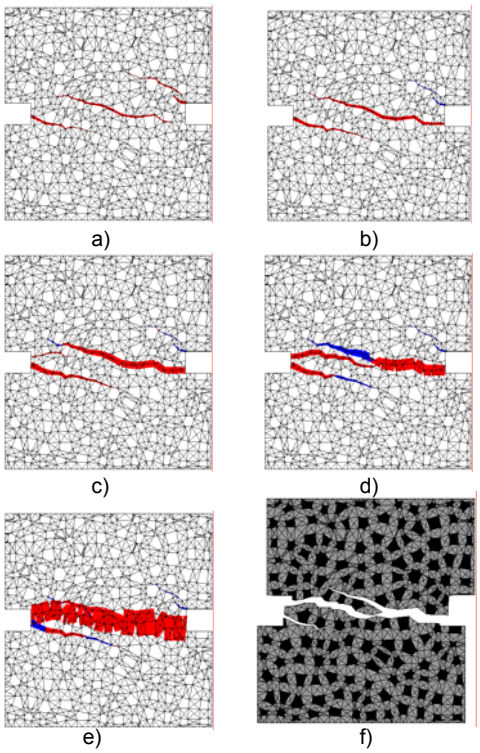

Figura 9. Evolución de la fisuración para el caso 6a en la muestra de 50 mm, en términos del módulo del vector desplazamiento plástico, para valores de a) δ_N = 17 μm, b) δ_N = 42 μm, c) δ_N = 76 μm, d) δ_N = 110 μm, e) δ_N = 226 μm y f) malla deformada para δ_N = 226 μm.

4. CONSIDERACIONES FINALES

En este artículo se ha empleado un modelo numérico mesoestructural para simular algunos ensayos experimentales llevados a cabo en [1] sobre una muestra de 50 mm de lado, que se han comparado con resultados previos obtenidos en la muestra de 200 mm [3]. Se ha conseguido reproducir satisfactoriamente el comportamiento de las curvas de carga-desplazamiento (tensión-desplazamiento) de los ensayos de Nooru-Mohamed y similares de Hassanzadeh. Este comportamiento no resulta nada trivial puesto que una imposición de desplazamientos combinados de apertura y de corte, dan lugar a una evolución de las fuerzas axial y lateral (tensiones normales y de corte) que puede variar considerablemente desde estados en tracción/corte a estados de compresión/corte. Cabe señalar que si bien existen numerosos trabajos de modelización numérica de estos ensayos, todos los artículos consultados se refieren a la malla de 200 mm y no aparece el comportamiento con pico y posterior reblandecimiento en compresión. Los trabajos en curso incluyen completar el análisis del efecto tamaño, extendiendo los cálculos a las mallas de 100 y 200 mm con un tamaño de áridos similar al de los experimentos.

AGRADECIMIENTOS

Los autores agradecen al MICINN (Madrid) la ayuda recibida a través del proyecto BIA2009-10491 y la beca FPI concedida al segundo autor.

REFERENCIAS

[1] Nooru-Mohamed, M. B. "*Mixed-Mode Fracture of concrete: An experimental approach*". PhD thesis, University of Technology, Delft, Holanda (1992).

[2] Hassanzadeh, M. "Determination of fracture zone properties in mixed mode I and II". *Engineering Fracture Mechanics,* 35 (4/5), pp. 845-853 (1990).

[3] Rodríguez, M., López, C.M., Carol, I. "Análisis meso-estructural de la fractura del hormigón en modo mixto". *Anales de la Mecánica de Fractura*, 26, vol. 2, pp. 452-457 (2009).

[4] Cusatis, G., Bazant, Z., Cedolin, L. "Confinement-shear lattice CSL model for fracture propagation in concrete", *Comput. Methods Appl. Mech. Engrg.* 195, 7154-7171 (2006).

[5] Oliver, J., Huespe, A., Pulido, M.D., Blanco S. "Computational modeling of cracking of concrete in strong discontinuity settings", *Computers and Concrete*, Vol. 1, Nº 1, 61-76 (2004).

[6] Di Prisco, M., Ferrara, L., Meftah, F., Pamin, J., de Borst, R., Mazars, J., Reynouard, J. "Mixed mode fracture in plain and reinforced concrete: some results on benchmark tests". *International Journal of Fracture*, Vol. 103, pp. 127-148 (2000).

[7] RFGC, Revue française de génie civil. 7 (5), 2003.

[8] Carol, I., Prat, P. C., y López, C. M. "A normal/shear cracking model. Application to discrete crack analysis", *J. Engng. Mech. ASCE*, 123, pp. 765–773 (1997).

[9] López, C. M. *"Análisis microestructural de la fractura del hormigón utilizando elementos finitos tipo junta. Aplicación a diferentes hormigones"*, Tesis Doctoral, ETSECCPB, Universitat Politècnica de Catalunya, Barcelona (1999).

[10] López C.M., Carol I., Aguado A. "Meso-structural study of concrete fracture using interface element. I: numerical model and tensile behaviour". *Materials and Structures*, 41, Nº 3, pp. 583-599 (2008).

[11] López C.M., Carol I., Aguado A. "Meso-structural study of concrete fracture using interface element II: compression, biaxial and Brazilian test". *Materials and Structures*, 41, Nº 3, pp. 601-620 (2008).

[12] Caballero, A., López, C.M., Carol, I. "3D meso-structural analysis of concrete specimens under uniaxial tension". *Comput. Methods Appl. Mech. Engrg.*, 195, 7182-7195 (2006).

COMPORTAMIENTO MECÁNICO A ALTAS TEMPERATURAS DE CEMENTOS DE CENIZA VOLANTE ACTIVADOS ALCALINAMENTE

Antonia Martín[a], Ana Fernández-Jiménez[b], José Ygnacio Pastor[a], Ángel Palomo[b]

[a] Departamento de Ciencia de Materiales, E.T.S. de Ingenieros de Caminos, Canales y Puertos, Universidad Politécnica de Madrid, C/ Profesor Aranguren s/n, 28040 Madrid, España.
E-mail: amartin@mater.upm.es

[b]Instituto Ciencias de la Construcción Eduardo Torroja (IETcc) del C.S.I.C
E28033-Madrid, España

RESUMEN

En este trabajo se realiza un estudio comparativo del comportamiento mecánico, en función de la temperatura, entre un cemento Portland comercial, utilizado de referencia y dos nuevos materiales cementantes. Los ensayos realizados se han centrado en muestras de cemento portland , muestras de cenizas volantes activadas con un 100% de silicato sódico y muestras con un 70% de ceniza y un 30% de cemento activadas con un activador en estado sólido.Se realizaron dos tipos de ensayos: 1) post tratamiento térmico, donde se evaluó la resistencia mecánica residual tras una hora de exposición térmica a diferentes temperaturas, y 2) ensayos mecánicos a altas temperaturas , donde se determino el comportamiento mecánico y la tenacidad a la fractura a distintas temperaturas.
Técnicas de Rayos X y microscopía electrónica de barrido han sido utilizadas para analizar las variaciones microestructurales en los materiales, como consecuencia de la exposición a altas temperaturas.

ABSTRACT

In this work a comparative study of the mechanical behaviour is realized, depending on temperature, between a commercial Portland cement, used of reference and two materials cementicious. The realized tests have centred on Portland cement samples, 100% sodium silicates-activated fly ash samples and a blend of 70% ash + 30% clinker activated with solid state activators. Two types of test were conducted 1) post-thermal treatment tests to evaluate the residual strength after one hour of exposure to temperatures different, and, 2) high temperature strength test, where it determine the mechanical behaviour and fracture toughness to different temperatures. XRD and SEM techniques were also deployed to track the mineralogical and microstructural variations in the materials as a result of such exposure.

KEY WORDS: cementos alcalinos, ceniza volante, comportamiento mecánico, alta temperatura.

1. INTRODUCCIÓN

La fabricación del cemento Pórtland es un proceso energérticamente muy costoso y en el que se emiten a la atmósfera elevadas concentraciones de CO_2 y otros gases causantes del efecto invernadero. Por eso durante las últimas décadas, se han realizado numerosas investigaciones sobre el empleo de subproductos industriales como, por ejemplo, las cenizas volantes, para el desarrollo de materiales cementantes alternativos al cemento Pórtland tradicional. Estas cenizas volantes tienen que ser activadas alcalinamente, lo que consiste en un proceso químico que permite la transformación de una estructura, parcial o totalmente vítrea en un compacto esqueleto cementante. El principal producto de reacción obtenido es un aluminosilicato alcalino, que diferentes autores describen como "precursor zeolítico". Este aluminosilicato se caracteriza por presentar una estructura tridimensional y un desorden a largo y medio alcance que lo hace amorfo a los rayos X.
Las investigaciones mas recientes han demostrado que con estos materiales se pueden alcanzar resistencias mecánicas a compresión superiores a 60MPa tras un corto período de tiempo de curado (1-3). Además, el material resultante posee buenas propiedades de durabilidad, especialmente en lo que se refiere a su resistencia al ataque de disoluciones ácidas, reacción árido-álcali etc. (4-7)

Otro aspecto importante a destacar de estos cementos es su elevada resistencia al fuego y a la exposición a altas temperaturas. Hasta ahora la mayoría de los trabajos publicados hacen referencia al comportamiento de cementos y hormigones alcalinos preparados en base a cenizas volantes antes y después de su exposición a altas temperaturas. Si embargo muy pocos de los ensayos realizados hasta ahora estudian lo que le ocurre al material cuando simultáneamente se expone a una temperatura elevada y se le somete a condiciones de carga hasta rotura.

Por ello el objetivo de este trabajo es determinar el comportamiento mecánico a altas temperaturas bajo cargas de cementos cuya característica mas destacable es la de no contener cemento Pórtland entre sus constituyentes o en todo caso contener proporciones muy bajas de dicho conglomerante, así como su resistencia residual una vez que el material se ha enfriado.

1. PROCEDIMIENTO EXPERIMENTAL

2.1 .Materiales

Como material de referencia se utilizó un cemento Pórtland (denominado T1C), y como materiales cementantes se ha utilizado una ceniza volante silicoaluminosa procedente de la central térmica de Puente Nuevo (Córdoba, España), (denominada T3FW) y otro material cementante que contiene un 25% de cemento y un 59% de ceniza volante (denominada T4CF). En la tabla I aparece la composición de dichos materiales, los tipos de soluciones alcalina, la relación líquido /sólido (L/S) y las condiciones de curado usado en cada caso.

Tabla 1. Características de los materiales estudiados

Name	*Material*		*Activator*	*L/S ratio*	*Curing conditions*
	Cement	*Fly ash*			
T1C	100%	0%	-	0.27 H_2O	20 h curing chamber (22 ºC, 98% H_R)
T3FW	0%	100%	[1]Sodium silicate solution	0.29 Solu.	4h. a 50ºC + 16h a 85ºC (98% H_R)
T4CF	25%	59%	[2]Solid activator (16 %)	0.3 H_2O	20 h curing chamber (22 ºC, 98% H_R)

La ceniza volante se caracteriza por presentar un contenido en fase vítrea del 63% aproximadamente y un 45,05% de sílice reactiva.

El régimen de curado para las muestras T1C fue de 20 horas a temperatura ambiente en la cámara de curado (22 ºC ± 1 ºC y 98% humedad). A continuación las muestras se desmoldaron y se guardaron en la cámara de curado durante 28 días, procediéndose a continuación ha realizar los ensayos de rotura.

Las muestras T3FW se curaron inicialmente durante 4 horas a 50 ºC y una humedad relativa >90%. A continuación se desmoldaron y se curaron otras 16 horas a 85ºC y humedad relativa >90%. Y por último las muestras T4CF tuvieron el mismo régimen de curado que las T1C.

Las condiciones de curado se seleccionaron basándose en estudios previos [8,9].

Para la caracterización mecánica se realizaron dos tipos de ensayos:

- **Ensayos mecánicos a altas temperaturas**, que se llevaron a cabo sobre muestras prismáticas de 8x4x50 mm. En este caso se determine la resistencia a compresion, la resistencia a flexion y la tenacidad de fractura, en los dos últimos casos mediante ensayos de flexion en tres puntos, a varias temperaturas entre 25 ºC y 600 ºC. No se realizaron esayos a temperaturas superiores pues se producian deformaciones muy elevadas o la rotura espontánea de la muestra durante el calentamiento. Para realizar los ensayos se utilizó una máquina Instron modelo 4505, sobre la cual se instaló un horno que permitio realizar los ensayos mecánicos a alta temperatura. La medida del desplazamiento de la cruceta durante los ensayos se realizó con un extensómetro LVDT situado fuera del horno. La velocidad de calentamiento de las muestros fue de 4 ºC/min. Una vez alcanzada la temperatura asignada , se espero 30 minutos con el fin de estabilizar la temperatura, tras lo cual se realizó el ensayo.

- **Ensayos post-tratamiento térmico,** en los que se utilizaron muestras prismáticas de 19x10x60 mm para los materiales. En cada ensayo el horno se calentó a la temperatura de 200, 400, 600, 800,1000, tras lo cual se introdujo la muestra en el mismo, manteniéndola durante una hora a esa temperatura. Transcurrido ese tiempo se sacó la muestra del horno y se dejó enfriar bruscamente a temperatura ambiente. A continuación, se procedió a evaluar a temperatura ambiente la resistencia mecánica residual mediante ensayos de flexión en tres puntos y de compresión. Estos ensayos se realizaron en una prensa Ibertest, a una velocidad de carga de 2,4 KN/S de acuerdo con la norma EN 196-1. La resistencia a flexión en tres puntos se calculó aplicando la teoría de vigas de Bernouilli [10], y la tenacidad de fractura con la ecuación generalizada para vigas entalladas dada por Guinea et al. [11].

2. RESULTADOS Y DISCUSIÓN.

En la figura 1 se muestran los resultados de las resistencias a flexión y compresión de los tres materiales en función de la temperatura.

Tanto en los ensayos de flexión como en los de compresión el cemento Pórtland de referencia presenta

buena resistencia a temperatura ambiente, pero sufre una importante disminución en su resistencia a flexión entre 400 y 600 ºC, y en compresión es a partir de 600 ºC, mientras que los otros materiales, tanto en los ensayos de flexión como de compresión no presentan una resistencia tan elevada como la del cemento, y a partir de 400 ºC en el material T3FW se observa la misma disminución en su resistencia a flexión que la que presenta el cemento Pórtland. El material T4CF presenta un comportamiento similar en su resistencia, tanto en flexión como en compresión.

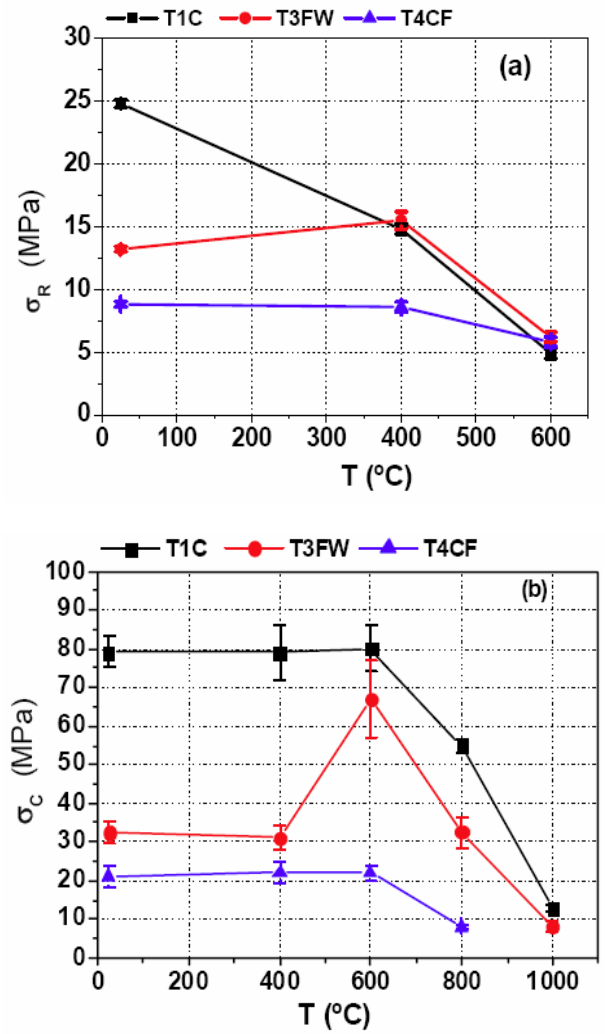

Fig.1. Resistencia a flexión a altas temperaturas.
a) Resistencia a flexión y b) resistencia a compresión.

La tenacidad de fractura de los materiales fueron bajas, pero se observa que el material T3FW es el que mejor tenacidad de fractura muestra frente a las altas temperaturas. Por el contrario el material T4CF presenta los menores valores de tenacidad al igual que ocurría con los valores de resistencia mecánica. Los valores de tenacidad del material T3FW permiten predecir que con el nuevo material cementante se puede mejorar la rotura frágil de los elementos sometidos a tracción o flexión a la temperatura de servicio durante la vida útil de la estructura.

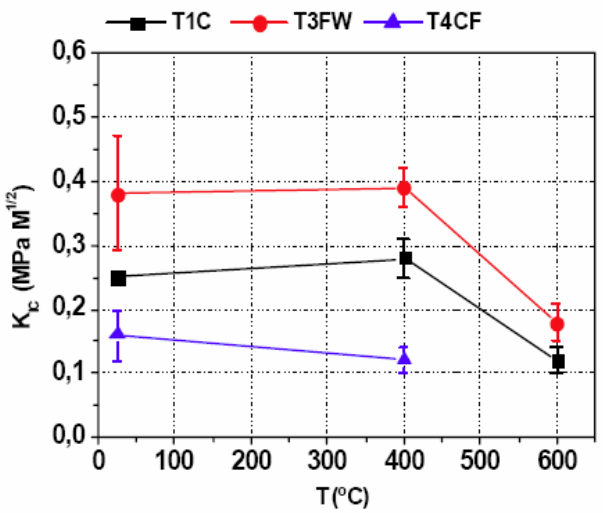

Fig. 2. Tenacidad de fractura a altas temperaturas.

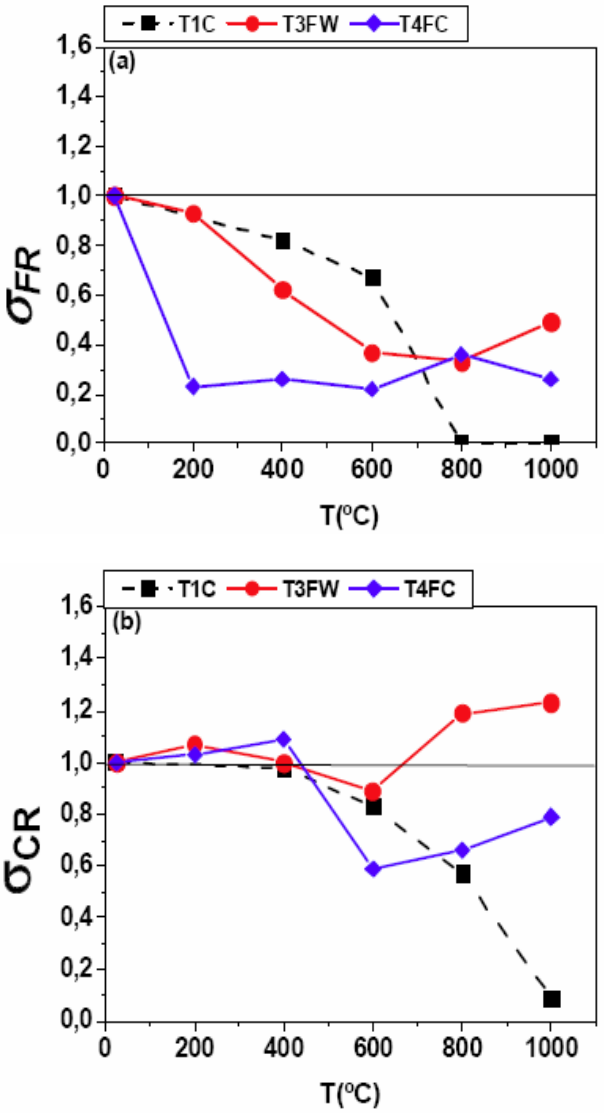

Fig.3. Resultado de los ensayos post-tratamiento térmico a) resistencia residual a flexión y b) resistencia residual a compresión.

En la figura 3 se muestran los resultados de las tensiones residuales a flexión y compresión tras ser expuestos los materiales a 1 hora a distintas temperaturas y después enfriados rápidamente a temperatura ambiente.
En estos ensayos, al no estar el material sometido a una pequeña carga durante el ensayo, estos se pueden realizar a temperaturas superiores a 600 ºC. A temperaturas de 800 y 1000 ºC se observa que aunque las muestras elaboradas en base ceniza pierden su estabilidad dimensional, lo que afecta principalmente a los valores de flexión, figura 3a, siguen siendo lo suficientemente compactas como para poder ser ensayadas. En la figura 3b, que corresponde a las resistencias mecánicas a compresión, se puede observar que para el material T3FW aumentan con la temperatura, incluso el matorral T4FC que presenta una importante caída de resistencias a compresión a 600 ºC, incrementa sus resistencias a temperaturas inferiores. Para el material T1C a partir de 600 ºC las muestras aparecen macroscópicamente fisuradas lo cual imposibilita ensayar el material una vez que se ha enfriado.

A continuación se han caracterizado estos materiales tras su exposición a altas temperaturas mediante microscopia electrónica de barrido y difracción de RX. Desde el punto de vista físico, entre 25 y 400 ºC no se observan grandes diferencias entre los tres materiales, pero a temperaturas superiores a 600 ºC las muestras de cemento aparecen muy fisuradas, mientras que las muestras de ceniza presentan variaciones dimensionales e incluso cambio de color, asociado a variaciones en el grado de oxidación del hierro presente en estos materiales. En lo que respecta a las variaciones dimensionales el hecho más relevante es que el comportamiento "pseudos-plástico" descrito en trabajos anteriores [12], cuando se empleo como activador una disolución de NaOH 8M y el material estaba sometido a carga elevada a temperatura, no es observado en los materials T3FW ni en el T4CF.

El material T3FW muestra una microestructura bastante similar entre 25 y 400 ºC y se observa existencia de partículas de ceniza intactas o parcialmente atacadas embebidas en una matriz compacta de gel de aluminio silicato hidratado, principal producto de reacción en la activación alcalina de las cenizas volantes.

Por el contrario, el material T4CF presenta entre 25 y 400 ºC una mayor cantidad de partículas sin reaccionar, y junto al gel también aparecen partículas ricas en cálcico procedentes del cemento Portland. En general, este material muestra una matriz menos cohesionada y con una mayor cantidad de partículas de ceniza sin reaccionar, lo cual justifica su menor resistencia mecánica y su rápida degradación con la temperatura. Los estudios realizados por SEM destacaron la presencia de partículas en forma de aguja compuestas básicamente por sodio. Estas partículas se detectan para intervalos de temperaturas entre 25 y 400 ºC, pero no a 600 ºC. Su presencia se asocial a restos de activador que no ha reaccionado con la matriz. A 600 ºC la temperatura es lo suficientemente elevada como para que este sodio actúe como fase fundente y reaccione con el material.

La presencia de esta fase fundente justifica que, en los materiales ensayados a temperaturas iguales o superiores a 600 ºC una vez enfriados, se observe la formación de una matriz más compacta, con un aspecto más vítreo. Además al enfriarse el material de esta fase fundente actúa sellando defectos, fisuras o grietas que debilitan el material. Este fenómeno es más acusado en el material T3FW y menor en la T4CF, donde el contenido observado de partículas ricas en sodio es aparentemente menor.

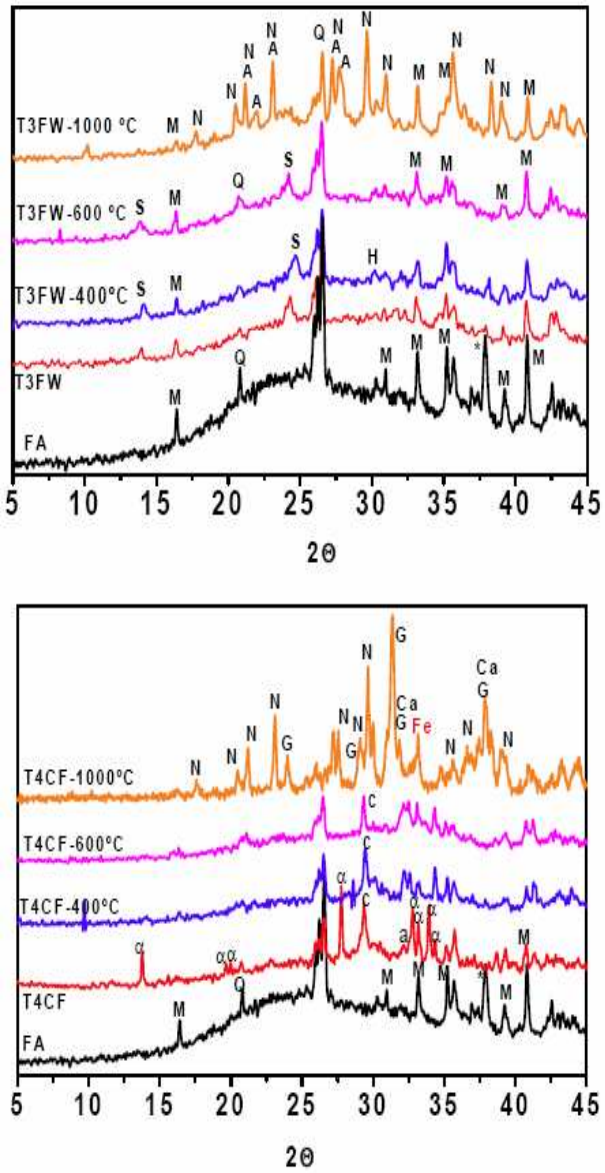

Fig. 4. Diagrama de RX para los materiales a) T3FW y b) T4CF después de ser calentados a 25, 400, 600 y 1000 ºC.

En la figura 4 se presentan los difractogramas de los materiales T3FW y T4FC. En cada figura aparece en primer lugar el difractograma de la ceniza sin

reaccionar, el del material activado y el de dicho material después de ser sometido al tratamiento térmico a altas temperaturas (400, 600 y 1000 ºC). En los difractogramas del material T3FW se observa a todas las temperaturas ensayadas , la presencia de las dos fases cristalinas minoritarias presentes en la ceniza de partida, lo cual indica que estas fases apenas si se ven afectadas por el proceso de activación o por la exposición del material a altas temperaturas . También se observa una reorganización microestructural del componente vítreo de la ceniza de partida como consecuencia del ataque alcalino.

En lo que respecta al material T4CF no se detecta la formación de zeolitas como consecuencia de la reacción de la ceniza, ni de portlandita como consecuencia de la reacción del cemento. Cuando dicho material es sometido a altas temperaturas, los difractogramas obtenidos a 400 ºC y 600 ºC son bastante parecidos. Se ha producido la descomposición del carbonato cálcico sódico, pero se observa la presencia de calcita. A temperaturas superiores (1000 ºC) la calcita se ha descompuesto y aparecen nuevas fases.

3. CONCLUSIONES

Los resultados de este trabajo ponen de manifiesto que los cementos elaborados por activación alcalina de la ceniza volante sin añadir cemento Pórtland, presenta un mejor comportamiento a altas temperaturas que los cementos tradicionales. El cemento Pórtland a partir de los 400 ºC presenta una caída drástica de la resistencia mecánica. Por el contrario, el cemento elaborado con ceniza volante activada alcalinamente mantiene, e incluso aumenta, los valores de resistencia mecánica residual a compresión tras ser expuesto durante una hora a alta temperatura.

Debido principalmente al elevado contenido de álcalis que presentan estos materiales, a temperaturas en torno a 600-700 ºC se forma una fase vítrea fundida. La solidificación de esta fase fundida durante el proceso de enfriamiento puede explicar el excelente comportamiento a compresión de las cenizas activadas alcalinamente. El mayor o menor grado de deformación del material parece estar relacionado con la composición del material, y sobre todo con el contenido de álcalis libres o fijados en el sistema. Este comportamiento puede ser un problema a la hora de utilizar este material, sobre todo si está sometido a importantes cargas, pero sin embargo presenta la ventaja frente al cemento en base cemento Pórtland de que nos dejaría un margen de seguridad donde el material avisaría antes de colapsar, mientras que a estas temperaturas el cemento Pórtland rompería catastróficamente.

4. AGRADECIMIENTOS

Los autores quieren agradecer la financiación recibida del Ministerio de Ciencia e Innovación a través d elos proyectos MAT2009-13979-C03-02, ISOOC-06-1410 y CSD00C-06-1410, y de la Comunidad de Madrid a través del proyecto ESTRUMAT S-0505/MAT/0077. Además, la autora Fernández-Jiménez quiere agradecer al Ministerio de Ciencia e Innovación la beca Ramón y Cajal en su edición 2008, y al programa L'OREAL-UNESCO el premio Women in Science Fellowship for Materials Science, que en su tercera edición ha permitido financiar el proyecto "Low environmental impact, high resistance binders"

5. REFERENCIAS

[1] Fernández-Jiménez, A., Palomo, A., Composition and Microestructure of alkali activated fly ash mortars. Effect of the activator, **Cem. Concr. Res.,** 35, 1984-1992, 2005.

[2] Duxson P., Provis J.L., Lukey G.C., Mallicoat S.W., Kriven W.M.,Van Deventer J.S.J. Understanding the relationship between geopolimer composition, microstructure and mechanical properties. **Colloids and Surfaces A.,** 269, 47-58, 2005.

[3] Fernández-Jimenez, A., Palomo, A., López-Hombrados, C. Some engineering properties of alkali activated fly ash concrete. **ACI Materials Journal**, 103 [2] 106-112, 2006.

[4] Fernández-Jimenez, A., Garcia- Lodeiro, I, Palomo, A. Durability of alkali-activated fly ash cementitious materials. **J. Materials Science**, 42, 3055-3065, 2007.

[5] Garcia- Lodeiro, I., Palomo, A., Fernández-Jiménez, A. The alkali-aggregate reactions in alkali activated fly ash mortars. **Cem. Concr. Res.,** 37, [2], 175-183, 2007.

[6] Allahverdi, A., Skvara, F. Nitric acid attack on hardened paste of geopolymeric cements. **Ceramics-Silikaty**, 45, (4), 143-149, 2001.

[7] Allahverdi, A., Skvara, F. Sulfuric attack on hardened paste of geopolymer cements. Part.1. Mechanisms of Corrosion at Relatively Hihg Concentrations. **Ceramics-Silikaty**, 49, (4), 225, 2005.

[8] Palomo,A., Alonso, A., Fernández-Jimenez, A. Sobrados, I. Sanz, J. Alkali activated of fly ashes. A NMR study of the reaction products. **J. Am. Ceramic. Soc.,** 87, [6], 1141-1145, 2004.

[9] Fernández-Jimenez, A. Palomo, A., Sobrados, I., Sanz, J. The role played by the reactive alumina content in the alkaline activation of fly ashes. **Microporous and Mesoporous Materials**, 91 111-119, 2006.

[10] Thimoshenko, S.P., Strength of Materials, 3d ed., part II, pag. 169, **D. Van. Nostrand Company, Inc.,** Princenton, New Jersey, 1956

[11] Guinea, G., Pastor, J.Y., Planas, J., Elices, M., **International Journal Fracture**, 89, 103-116, 1998.

[12] Fernández-Jiménez, A., Palomo, A., Pastor, J.Y., Martín, A. New cememtitious materials based on alkali activated fly ash: Performance at high temperature. **Journal American Ceramic Society,** 91 (80) 3308-3314, 2008.

ESTUDIO SOBRE PANELES ESBELTOS DE HORMIGÓN DÉBILMENTE ARMADOS

R. Porras-Soriano, **G. Ruiz**, **J. R. Carmona** y **R.C.Yu**

E.T.S. de Ingenieros de Caminos, Canales y Puertos,
Universidad de Castilla-La Mancha
Avenida Camilo José Cela s/n, 13071 Ciudad Real
E-mail: rocio.porras@uclm.es
Tfno: 926 29 53 00 Ext. 6311. Fax: 926 29 53 91

RESUMEN

El presente trabajo muestra los resultados de una investigación sobre el comportamiento frente a pandeo de paneles esbeltos de hormigón débilmente armados. A partir de las observaciones experimentales se ha realizado un estudio con dos modelos numéricos capaces de reproducir la pérdida de rigidez del panel durante el proceso de carga debido a la iniciación y progreso de fisuras en el hormigón.

Los resultados obtenidos en los modelos se contrastan con los resultados experimentales, analizando la sensibilidad de la esbeltez del panel, la excentricidad de la carga y la cuantía de armado. Los resultados obtenidos pueden ayudar a una mejor comprensión de los mecanismos de propagación de las fisuras y del fallo de paneles esbeltos de hormigón débilmente armado. Complementariamente se analizan, en base a los resultados experimentales, los patrones de fisuración de las probetas.

ABSTRACT

This work reports the results of tests performed on lightly reinforced concrete panels subjected to buckling load. According to these test we made two simple models to disclose the behaviour of the lightly reinforced concrete panels subjected to buckling. Both models reproduce the loss of stiffness of these structures, due to the initiation and development of cracks during loading.

The numerical model was validated against experimental data. The sensitivity of the slenderness of the panel, the reinforcement ratio and the characteristics of the concrete was determined. The resultant crack patterns are also analyzed and compared to their experimental counterparts.

PALABRAS CLAVE: Hormigón armado, pandeo, modelo cohesivo

1. INTRODUCCIÓN

Los paneles que se estudian en esta investigación son paneles de fachada con capacidad portante. Los cuales, debido a su disposición en la edificación reciben cargas excéntricas. Para el estudio del comportamiento a flexocompresión de estos se planteó la campaña experimental que se describe en el artículo Porras, Ruiz, Carmona y Yu [1]. En esta experimentación los ensayos fueron diseñados a escala reducida sobre paneles, con el fin de facilitar tanto el control de los materiales utilizados en la ejecución de las probetas como la propia realización de los ensayos, minimizando la dispersión de los resultados experimentales. La metodología experimental seguida fué análoga a la empleada para el estudio de vigas débilmente armadas realizado dentro de este mismo grupo [4, 5], adaptando los dispositivos experimentales al objeto de la presente investigación.

En la parte final del artículo se comparan los resultados obtenidos con los resultados obtenidos en dos modelos. El primero de ellos es un modelo que ya se presentó, y que se describe en el artículo de Carmona, Ruiz y Porras [6]. También se contrastan con los resultados obtenidos con un modelo de fisura distribuida en bandas resuelto con el programa ATENA.

2. RESULTADOS DE LA CAMPAÑA EXPERIMENTAL

La campaña experimental realizada constaba de 27 tipos de paneles diferentes, que se corresponden con 3 tamaños, 3 configuraciones de armado y 3 excentricidades iniciales diferentes. Las probetas de hormigón armado fueron ensayadas en un dispositivo que simula el proceso de carga en compresión, aplicando la carga con una cierta excentricidad inicial, denominada e_0. Durante el ensayo se medía el desplazamiento del punto de aplicación de la carga, el valor de la carga aplicada y el desplazamiento horizontal en el punto central de las probetas, sobre la cara comprimida, denominado e_a.

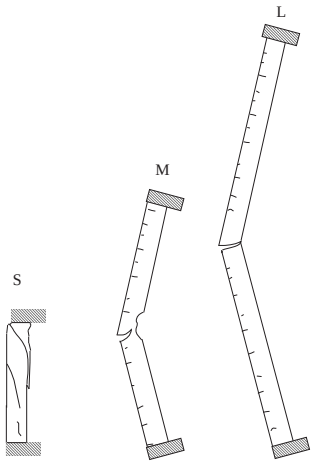

Figura 1: Esquema de los modos de fallo

Para designar a cada probeta, tal y como se describe en el ya mencionado artículo, se utiliza una combinación de una letra mayúscula según el tamaño de la probeta (S-pequeño-30cm, M-mediano-60cm y L-grande-120cm), un número que indica el número de barras de armado (1, 2 y 3) y una letra minúscula según la excentricidad inicial aplicada (a-2mm, b-25mm, c-50mm). Se han ensayado al menos dos probetas de cada tipo. Así pues, una probeta cuya denominación sea L2b-1 indica que es la primera de las dos probetas ensayadas de longitud 120 cm con dos barras de armado longitudinal y que ha sido ensayada aplicando la carga con una excentricidad de 25 mm.

Los resultados obtenidos de carga máxima y excentricidad adicional, son los que se resumen en las gráficas de la Figura 2. En la primera fila de tres gráficas se presenta la excentricidad adicional frente a la cuantía de armado. La tendencia de estas gráficas indica que la excentricidad adicional obtenida en los ensayos es mayor según aumenta la cuantía de armado de las probetas. Esta tendencia es más pronunciada en las probetas de mayor esbeltez (M y L). Este hecho indica que una mayor cuantía de armado retrasa la aparición del proceso de inestabilidad. Además se puede apreciar que se produce una dispersión de los resultados obtenidos para las probetas de excentricidad *a*. Esta dispersión está relacionada con el modo de fallo del panel, puesto que para la menor excentricidad, se produce un fallo predominantemente por compresión, como comentaremos más adelante.

En cuanto a la carga máxima, como tendencia general en los ensayos con excentricidades *b* y *c*, se aprecia que a mayor cuantía de armado, mayor es la carga máxima alcanzada en el ensayo. El efecto es contrario para la excentricidad *a*. Este comportamiento está asociado al tipo de rotura, pues para la excentricidad menor, excentricidad *a*, el fallo de la pieza se produce predominantemente por compresión, mientras que para la excentricidad *b* comienza a apreciarse la flexión en el momento de fallo y para los ensayos realizados con la excentricidad mayor, excentricidad *c*, se extrae como conclusión que la rotura se produce completamente por flexión.

Si relacionamos la cuantía de armado con los patrones de fisuración, se puede observar cómo, a mayor cuantía la fisuración es menor. Así por ejemplo en el caso de tres barras y longitud L, en la mayoría de los ensayos, la probeta se fisura sin llegar a romper.

Analizando la influencia de la esbeltez en los patrones de fisuración, se aprecia, según vemos en los esquemas de la Figura 1, que en las probetas de menor esbeltez, tamaño S, el fallo es predominantemente por compresión, cómo así lo demuestra la fisuración vertical. En las probetas de tamaño M se produce una fisura por tracción en la cara externa, y un fallo por compresión en la cara interna. Por otro lado, en las probetas de tamaño L se produce una fisuración por flexión, formándose una fisura predominante, generalmente próxima al centro de vano. Este comportamiento es más acusado, cuando las probetas más pequeñas se cargan con excentricidad tipo a, y las probetas de mayor esbeltez con excentricidades b y c.

En los gráficos mostrados en la Figura 3 se puede apreciar como al aumentar la excentricidad inicial de la carga, la carga máxima alcanzada en el ensayo es menor. Siendo cada uno de los puntos representados en las gráficas la media de los dos ensayos realizados de cada tipo. Esta disminución de la carga máxima se produce de forma mucho más pronunciada cuando se pasa de ensayar con una excentricidad *a* a ensayar con la excentricidad *b*, que de esta a la *c*. De nuevo en los resultados se refleja un cambio de comportamiento en el fallo de las probetas ensayadas.

En la Figura 4 se analiza la relación existente entre la excentricidad inicial de aplicación de la carga y la excentricidad adicional alcanzada durante el ensayo. Como conclusión se aprecia que, por lo general, cuanto mayor es la excentricidad inicial de aplicación de la carga mayor es la excentricidad adicional, como demuestra la tendencia ascendente de los puntos en cada una de las tres gráficas de la citada figura.

3. MODELOS NUMÉRICOS

3.1. Presentación del modelo cohesivo de fisura discreta.

Este modelo es el que se presentó en el artículo "Modelo numérico para analizar el comportamiento a pandeo de paneles esbeltos de hormigón armado"[6]. Se trata de un panel que se encuentra biarticulado y la carga se aplica con una excentricidad inicial, e_0, que es constante y del mismo signo a lo largo del panel o pilar. Al existir simetría con respecto a la sección central, se modela únicamente la mitad del panel. Presenta una única fisura cohesiva, situada en la sección central del panel se representa por medio de unos elementos tipo muelle que siguen la función de ablandamiento del hormigón. La masa del hormigón se discretiza de modo continuo usando elementos triangulares de 6 nodos.

Para la implementación y resolución de este modelo hemos utilizado el programa de elementos finitos ANSYS.

TAMAÑO *S* TAMAÑO *M* TAMAÑO *L*

a) b) c)

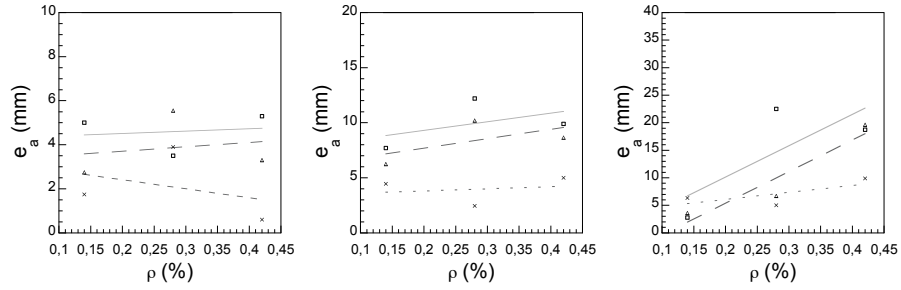

d) e) f)

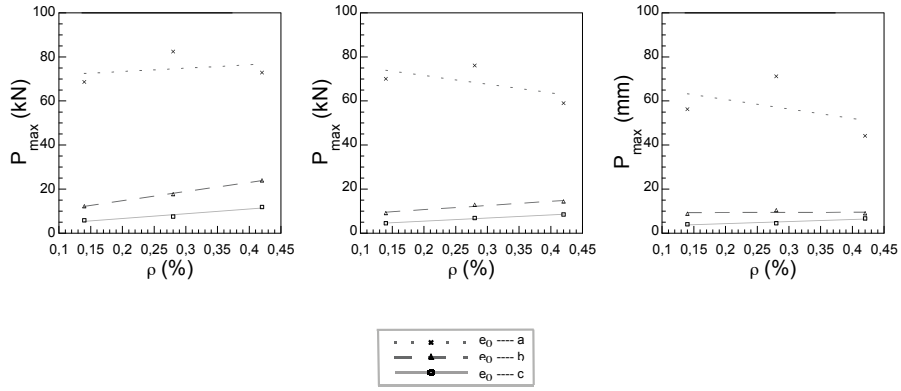

Figura 2: Relación de la excentricidad adicional y la P_{max} con la cuantía de armado.

a) b) c)

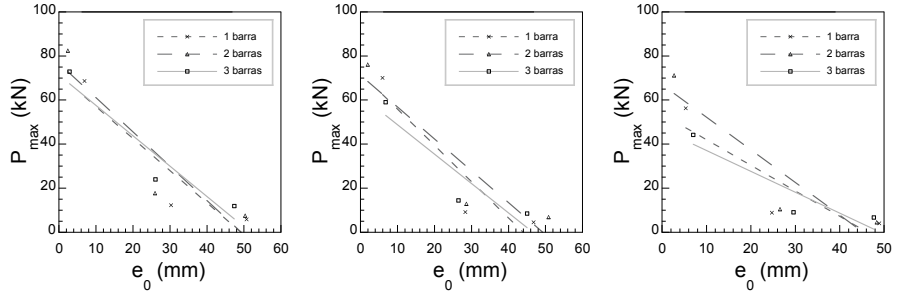

Figura 3: Relación P_{max} - excentricidad inicial (e_0). a) Tamaño S. b) Tamaño M. c) Tamaño L.

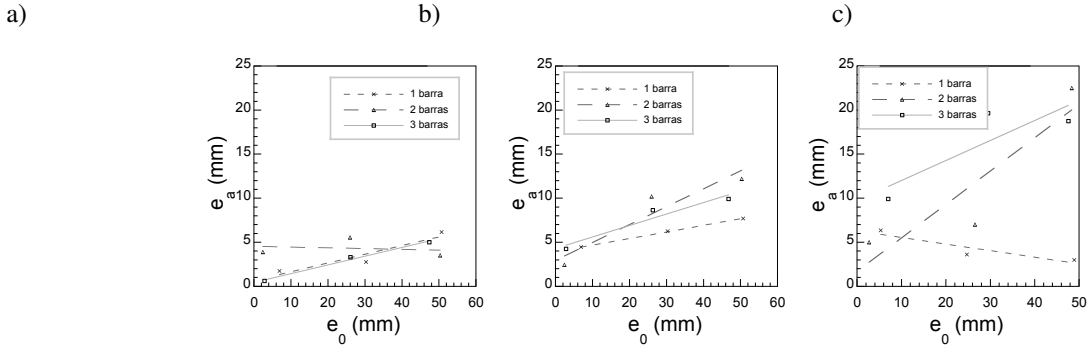

Figura 4: Relación excentricidad adicional (e_a) - excentricidad inicial (e_0). a) Tamaño S. b) Tamaño M. c) Tamaño L.

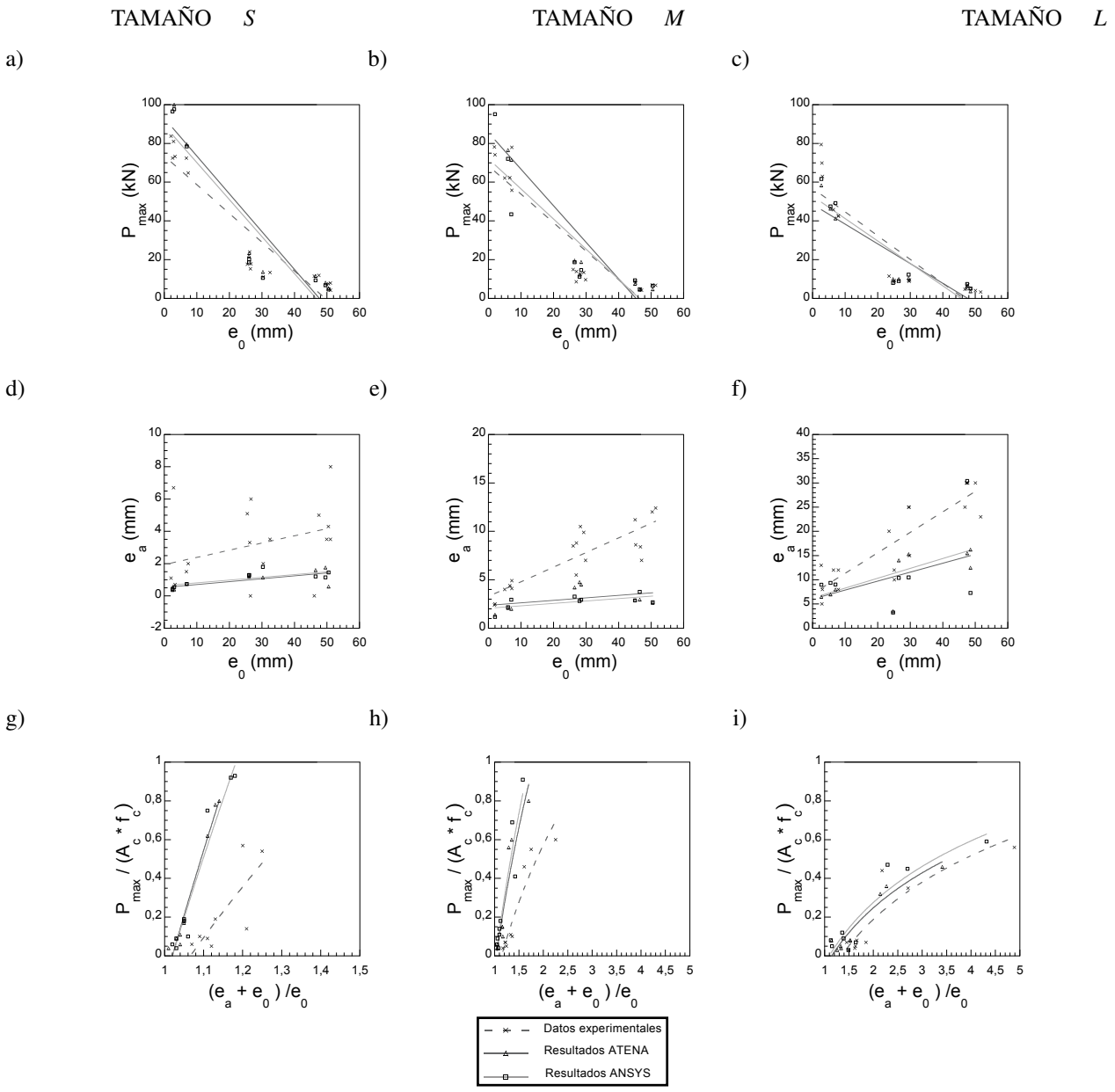

Figura 5: Comparación resultados experimentales y numéricos. a) Tamaño S. b) Tamaño M. c) Tamaño L. d) Tamaño S. e) Tamaño M. f) Tamaño L.

3.2. Presentación del modelo de fisuración distribuida en banda

Éste es un modelo realizado con un programa comercial llamado ATENA. Se trata de un modelo en 2D, de elementos triangulares. Cómo modelo constitutivo del hormigón se ha empleado un modelo de fisuración distribuida en banda definido en el mencionado programa. Este modelo se basa en las teorías propuestas por Baẑant y Oh [7]. Según éste, la deformación se concentra en una región del material (banda), que se representa mediante un plano en el análisis mediante elementos finitos. En tracción esta deformación es una fisura, y en compresión es un plano de aplastamiento.

Para modelar los materiales se han introducido las características mecánicas del hormigón empleado, obtenidas en la campaña experimental.

3.3. Validación de los modelos

La carga se introduce en los modelos a través de un desplazamiento impuesto sobre una placa con una rigidez muy superior a la del hormigón situada en el extremo superior del panel modelado. De esta forma podemos evaluar la carga de pandeo del panel para diferentes excentricidades. En los cálculos no hemos tenido en cuenta el peso propio del panel, el cual, para paneles muy esbeltos, puede ser una fracción importante en la carga resistida. No obstante, introducir este parámetro en los cálculos sería relativamente sencillo. Por último indicamos que los modelos mecánicos presentados son extrapolable a tres dimensiones, con lo que se podría estudiar el problema del pandeo con flexión esviada.

Los resultados obtenidos en los modelos numéricos desarrollados, son los que se recogen en las gráficas de la Figura 5 y en las Tablas 1 y 2.

Tanto el modelo de una única fisura, como el modelo de fisura distribuida en bandas, son sensibles al aumento de la esbeltez, puesto que la carga máxima alcanzada disminuye al aumentar la esbeltez del panel.

Otra tendencia que se puede apreciar es que, tanto en los modelos numéricos como en los datos experimentales la P_{max} disminuye al incrementar la e_0. Este comportamiento se puede apreciar en las tres primeras gráficas de la Figura 5. Cabe mencionar, que los valores obtenidos para la carga de pandeo (P_{max}) han sido reproducidos por los modelos de forma sensiblemente correcta.

Si analizamos los resultados obtenidos en los modelos de la excentricidad adicional asociada a carga máxima (Tabla 4), podemos apreciar cómo ambos modelos se comportan de forma algo más rígida a cómo lo hacen los ensayos del laboratorio. Esta diferencia se debe al contacto que existe entre la placa de aplicación de la carga y el panel, puesto que en los modelos es un contacto más rígido y uniforme. Si bien, las tendencias se mantienen. Así por ejemplo, se puede afirmar, tal y cómo se puede apreciar en las gráficas d, e y f de la Figura 5, que la excentricidad adicional es mayor para mayores valores de excentricidades iniciales de aplicación de la carga. Si compramos cada una de estas tres gráficas, que representan los tamaños S, M y L, respectivamente, se puede apreciar cómo, tanto para los modelos, como para los resultados experimentales, la excentricidad adicional en carga máxima es mayor para mayores esbelteces.

En las tres últimas gráficas de la Figura 5 se presentan los resultados de carga máxima y excentricidad adicional adimensionalizados. La adimensionalización de ambos valores se ha hecho conforme a las ecuaciones 1 y 2.

$$\frac{P_{max}}{A_c \times f_c} \tag{1}$$

$$\frac{e_a + e_0}{e_0} \tag{2}$$

La tendencia en estas gráficas indica que la excentricidad inicial de aplicación de la carga, influye de forma más notable para las probetas de mayor esbeltez. En estas gráficas se observa también que, para mayores valores de e_0, la relación e_t/e_0 es menor.

Con carácter general las tendencias observadas experimentalmente y los valores obtenidos para la carga de pandeo han sido reproducidos por los modelos de forma sensiblemente correcta.

4. CONCLUSIONES

En este artículo se han presentado los resultados obtenidos en una campaña experimental realizada para estudiar el comportamiento a flexocompresión de paneles esbeltos de fachada. Dichos resultados han servido para validar dos modelos numéricos.

Se han obtenido resultados muy similares tanto en la campaña experimental, como en los modelos realizados . Por lo que se da como validado el modelo.

Se ha obtenido que tanto la resistencia a compresión del hormigón cómo la excentricidad adicional son valores muy importantes para determinar el comportamiento a pandeo. Así pues, la dispersión entre los resultados experimentales y los numéricos es mucho mayor para el tamaño S, que para el resto de tamaños. Esto se debe a que en los tamaños más pequeños, pequeñas variaciones en la medida de la e_0, provocan grandes variaciones en los resultados.

		P_{max} (kN)		
-	e_0	EXPER.	FIS. DIST.	FIS. BANDA
S1-a	6.9	64.8 - 72.4	79.5	78.5
S1-b	30.3	13.4 - 11.1	13.6	10.5
S1-c	50,5	4.2 - 7.5	5.3	4,6
S2-a	2,5	83.8 - 81.0	102.7	96.5
S2-b	26	17.6 - 17.8	22.0	18.6
S2-c	49,5	7.9 - 7.1	8.1	6.7
S3-a	3	72.4 - 73.3	100.0	97.7
S3-b	26,1	- - 24	23.4	20.1
S3-c	46,5	11.5 - 11.9	11.6	9.3
M1-a	6	62.1 - 78	76.5	72.1
M1-b	28	9.6 - 8.6	12.3	11.3
M1-c	46,5	4.8 - 4.2	4.5	4.7
M2-a	2	78.2 - 74.1	102.7	95.1
M2-b	28,5	12.5 - 13.4	18.8	14.6
M2-c	50,5	6.95 - 6.8	4.7	6.5
M3-a	7	55.8 - 62.3	71.5	43.4
M3-b	26,5	14.9 - 13.9	19.5	18.7
M3-c	45	8.9 - 8.0	7.5	9.5
L1-a	5,5	42.6 - 69.9	46.3	47.5
L1-b	24,7	9.2 - 8.5	10.0	8.0
L1-c	48,5	4.7 - 3.3	3.7	3.2
L2-a	2,7	79.4 - 63	58.4	61.7
L2-b	26,5	9.5 - 11.5	10.0	9.0
L2-c	48,5	4.0 - 5.0	5.1	5.1
L3-a	7	45.8 - 42.5	41.2	49.2
L3-b	29,5	9.1 - 8.9	10.5	12.2
L3-c	47,5	6.3 - 7.0	6.5	7.4

Tabla 1: Resultados de los modelos numéricos: P_{max}

		e_a (mm)		
-	e_0	EXPER.	FIS. DIST.	FIS. BANDA
S1-a	6.9	2.0 - 1.5	0.75	0.74
S1-b	30.3	3.5 - 2.0	1.15	1.79
S1-c	50.5	8.0 - 4.3	0.58	1.46
S2-a	2.5	1.1 - 6.7	0.36	0.42
S2-b	26	5.1 - 6.0	1.27	1.28
S2-c	49.5	3.5 - 3.5	1.76	1.15
S3-a	3	0.5 - 0.7	0.40	0.53
S3-b	26,1	- - 3.3	1.20	1.30
S3-c	46,5	- - 5.0	1.60	1.20
M1-a	6	4.0 - 4.9	2.10	2.16
M1-b	28	7.0 - 5.5	4.75	2.80
M1-c	46,5	8.4 - 7.0	2.96	3.75
M2-a	2	2.4 - 2.5	1.40	1.16
M2-b	28,5	10.5 - 9.9	4.50	2.94
M2-c	50,5	12 - 12.4	2.61	2.67
M3-a	7	4.1 - 4.4	2.00	2.95
M3-b	26,5	8.5 - 8.8	4.20	3.26
M3-c	45	11.2 - 8.6	2.89	2.87
L1-a	5,5	8.0 - 5.0	7.00	9.35
L1-b	24,7	10.0 - 12.0	3.50	3.24
L1-c	48,5	25.0 - 23.0	12.5	23.70
L2-a	2,7	13.0 - 8.0	6.50	8.97
L2-b	26,5	15.0 - 20.0	14.00	10.36
L2-c	48,5	30.0 - 30.0	16.25	7.27
L3-a	7	12.0 - 12.0	8.00	9.00
L3-b	29,5	25.0 - 25.0	15.30	10.50
L3-c	47,5	30.0 - 30.0	15.50	30.40

Tabla 2: Resultados de los modelos numéricos: e_a

Por la forma de modelar el hormigón a partir de todas sus características, incluyendo los parámetros en fractura, los modelos son susceptibles de ser utilizados para estudiar el comportamiento frente a pandeo de paneles fabricados con otros tipos de hormigones como hormigones con fibras, hormigones ligeros, de alta resistencia... y otros materiales considerados quasifrágiles como fabricas de ladrillo o columnas de materiales pétreos, siempre que estén convenientemente caracterizados.

AGRADECIMIENTOS

Los autores expresan su agradecimiento a la empresa INDAGSA perteneciente al Grupo Ortiz por la financiación concedida para realizar esta investigación. Así como a la ayuda PAI08-0196, de la Junta de Comunidades de Castilla-La Mancha.

REFERENCIAS

[1] Porras-Soriano, R., Ruiz, G., Carmona, J. R., and Yu, C. *Estudio experimental de los paneles de hormigón débilmente armados*, Anales de Mecánica de la Fractura 26, 2:787–792, 2009.

[2] Carmona, J. R. *Study of cracking processes in reinforced concrete structures*, Ph. D. Thesis, Universidad de Castilla-La Mancha. Ciudad Real. 2006.

[3] Bažant, Z. P. and Cedolin, L., *Stability of structures*, Dover, Mineola, New York, 2003.

[4] Ruiz, G., Elices, M. and Planas J. *Experimental Study of Fracture of Lightly Reinforced Concrete beams*, Materials and Structures, 31:683–691, 1998.

[5] Ruiz, G. and Carmona, J. R. *Estudio experimental sobre propagación de fisuras en modo-mixto en vigas de hormigón armado*, Anales de Mecánica de la Fractura 23, 353–358, 2006.

[6] Carmona, J. R., Ruiz, G. and Porras-Soriano, R. *Modelo numérico para analizar el comportamiento a pandeo de paneles esbeltos de hormigón armado*, Anales de Mecánica de la Fractura 25, 2:787–792, 2008.

[7] Baẑant, Z.P. y Oh, B.H. *Crack Band Theory for Fracture of Concrete*, Materials and Structures, RILEM, 16:155–177, 1983.

COMPARISON OF THE CRACK PATTERN IN ACCELERATED CORROSION TESTS AND IN FINITE ELEMENTS SIMULATIONS

B. Sanz[1], J. Planas[1], J.M. Sancho[2]

[1]Departamento de Ciencia de Materiales, E.T.S. de Ingenieros de Caminos, Canales y Puertos, Universidad Politécnica de Madrid, C/ Profesor Aranguren s/n, 28040 Madrid, España.
E-mail: bsanz@mater.upm.es
E-mail: jaime.planas@upm.es

[2]Departamento de Estructuras de Edificación, E.T.S. de Arquitectura, Universidad Politécnica de Madrid, Avda. Juan de Herrera 4, 28040 Madrid, España.
E-mail: jose.sancho@upm.es

ABSTRACT

In this work, the crack pattern obtained in accelerated corrosion tests is compared to the one obtained in numerical simulations for reinforced steel concrete samples. In the simulations, an expansive joint element is used to simulate the oxide layer behaviour together with finite elements with embedded adaptable cohesive crack to simulate the concrete fracture. In parallel, some samples are artificially corroded imposing constant current and after corrosion they are impregnated with resin containing fluorescein to improve the detection of the cracks. In the paper, the main features of the model and the experimental procedure are described and the crack pattern is analysed. A main crack across the concrete cover is easily seen in both cases, but also secondary cracks are observed after treating the concrete surface, in accordance with the model predictions, which gives further support to the ability of the numerical approach to simulate the real cracking processes.

KEY WORDS: Accelerated corrosion tests, Cohesive crack, Finite Elements simulations

1 INTRODUCTION

Corrosion of rebars is an important pathology in reinforced steel concrete structures. It consists of the generation of an oxide layer at the steel surface that induces internal pressure on the surrounding concrete, due to the greater specific volume of the oxide with respect to the steel, and thus cracks the concrete cover [1, 2, 3].

Focussing on the prediction of the mechanical effects of the oxide expansion over the concrete, a numerical model to simulate the oxide layer behaviour was programmed, assuming that the corrosion depth is given at any specified time [4]. It was called *expansive joint element* and it has already been presented in previous conferences. That model consists in an interface element with zero initial thickness that incorporates both the expansive and the mechanical behaviour of the oxide, which is characterised by its debonding ability, with nearly free sliding (very small shear stiffness) and nearly free separation (strongly reduced normal tension stiffness). Concrete cracking is simulated by finite elements with embedded adaptable cohesive cracks [5] that follow the basic cohesive crack model proposed by Hillerborg et al [6].

In parallel, accelerated corrosion tests have been carried out in order to verify the ability of the model to simulate real processes. The samples are concrete prisms with a steel tube inside simulating a rebar, that are artificially corroded by the imposition of constant current. After corrosion, the samples are cut into slices to study the cracking along the bar and they are impregnated under vacuum with resin containing fluorescein to improve the detection of the cracks.

The crack pattern obtained in the tests is compared to the one obtained in numerical simulations of the same process. In both cases, a main crack is observed from the steel to the concrete surface, but also some secondary cracks and some microcracks can be seen when looking under the microscope or after impregnating the concrete surface with resin and fluorescein, in accordance to the model predictions.

In the paper, the main features of the model and the experimental procedure are described and the crack pattern is analysed.

2 NUMERICAL SIMULATIONS

2.1 Finite element model

In the simulations, finite elements with embedded adaptable cohesive crack [5] are used to model the concrete cracking. Those elements follow the basic cohesive crack model [6] and they are programmed in C++ within the finite element framework COFE (*Continuum Oriented Finite Elements*).

To model the oxide layer behaviour, an interface finite element called *expansive joint element* was programmed

by the authors [4] within the finite element framework COFE. It consists in a four-node element with zero initial thickness and it is defined by the initial length and the normal direction. The model works assuming elastic behaviour, small strain and direct integration at the nodes. The main parameters of the model are the corrosion depth x (the amount of steel that is transformed into oxide) and a factor β that indicates the volumetric expansion of the oxide respect to the initial steel section and which depends on the ratio of the specific volumes of oxide and steel. A sketch of the model is shown in figure 1. It must be remarked that only the part corresponding to the volumetric expansion is considered as expansive joint element and the steel section is kept constant during the calculations, so mechanical equivalence between the element and the real oxide needs to be established. The main equations of the model are detailed in the appendix at the end of the paper.

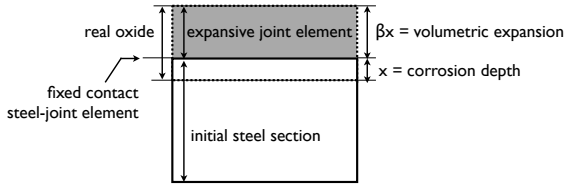

Figure 1: Sketch of the expansive joint element

2.2 *Parameters of the simulations*

The samples in the simulations are concrete prisms of 90 mm height and 100 mm width with a 20 mm diameter smooth steel bar cast-in, centred with respect to the width, and with a concrete cover equal to the diameter of the bar. The concrete is modelled with elements with embedded adaptable cohesive crack, the steel with linear elastic elements and the oxide with expansive joint elements. The mesh is generated using the pre-post FE mesh processor Gmsh [7]. The elements are constant strain triangles.

The mechanical properties of steel and concrete were experimentally determined by mechanical tests (compression, brazilian and three point bending tests) [8, 9, 10, 11], so the parameters of the materials in the simulations are the same as the real ones. They are shown in table 1.

Two *linear* approximations for the softening curve have been used. The first one has a fracture energy $G_F = 0.1$ N/mm (100 N/m), which corresponds to the actual total fracture energy of the material, and, except for the tail, lies well above the actual softening function, as shown in Fig. 2. The second one has a fracture energy $G'_F = 0.5G_F = 0.05$ N/mm (50 N/m) and corresponds to the linear approximation of the initial portion of the softening curve, as shown in Fig. 2. These approximations provide lower and upper bounds for the brittleness of the behaviour.

However, there are no experimental results available for the properties of the oxide, so the values have to be assumed at a this stage of the research and need to be verified in future by tests. A value equal to one is assumed for β as found in the literature [2] and the other values have been chosen to have a reasonable stiffness for the oxide layer in compression while keeping the computations stable. A previous study revealed some essential features of the model: first, nearly free sliding, that is obtained by reduced shear stiffness, and second, nearly free separation, that is obtained by strongly reduced stiffness in tension. The adopted values are shown in table 2. The total radial expansion is 25 μm and it is imposed in 50 steps.

Table 1: Mechanical properties of steel and concrete, where E is the elasticity modulus, ν is the Poisson coefficient, α' is the adaption factor of the crack, f_t is the tensile strength and G_F is the fracture energy.

	Steel	Concrete
E (GPa)	200	30
ν	0.3	0.2
α'	–	0.2
f_t (MPa)	–	3.0
G_F (N/mm)	–	0.1

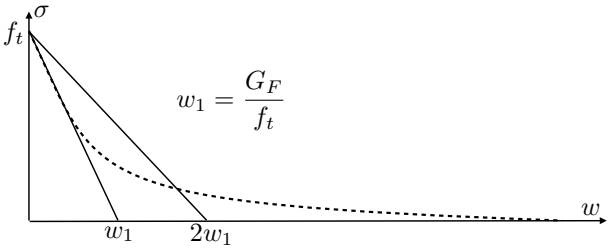

Figure 2: Sketch of the curvilinear softening curve, and the two linear approximation used in the paper

Table 2: Properties of the oxide, where β is the volumetric expansion factor, x_0 is the cut-off corrosion depth, k^0_{nc} is the initial compression stiffness, k^0_t is the initial shear stiffness and η_t is the directionality factor.

β	1.0
x_0 (mm)	$1.0e^{-3}$
k^0_{nc} (N/mm^3)	$7.0e^{6}$
k^0_t (N/mm^3)	$7.0e^{-14}$
η_t	$1.0e^{-11}$

2.3 *Crack pattern obtained in the simulations*

The crack patterns obtained in the simulations are shown in Figs. 3 and 4 for corrosion depths x of 4 and 25 μm, respectively. The crack width (in mm) and the maximum principal stress (in MPa) are represented; the top picture in each figure corresponds to linear softening with $G_F = 0.1$ N/mm and x100 magnification of displacements and the bottom one to the linear softening with $G'_F = 0.05$ μm, and undeformed mesh.

Figure 3 shows that in both cases a main crack has formed across the concrete cover, while a ring of radial cracks of similar extent forms around the bar; the only difference is that for the tougher softening the crack width nowhere exceeds 6.7 μm, while for the more brittle softening reaches a width of 10.5 μm at the concrete surface; this is closer to the expected behaviour, since the maximum opening is well within the initial linear portion of the softening curve ($w_1 = 33.6$ μm in Fig. 2).

Figure 4 shows that the main crack width for $x = 25$ μm is very similar for the two softening lines (122 vs. 124 μm); however, the secondary crack pattern is much more localised in the more brittle concrete.

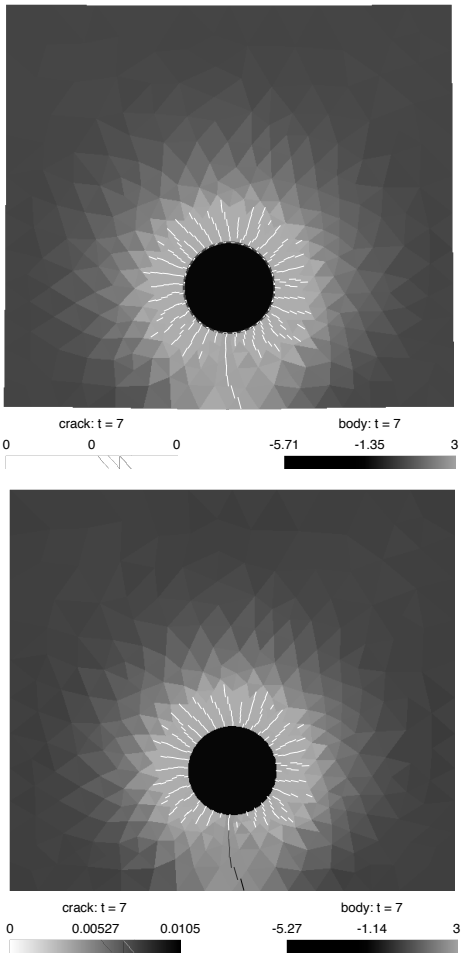

Figure 3: Crack pattern for a corrosion depth of 4μm for linear softening with $G_F = 0.1$ N/mm (top) and $G_F = 0.05$ N/mm (bottom).

3 EXPERIMENTAL PROCEDURE

3.1 Accelerated corrosion tests

The samples are concrete prisms with the same cross-sectional dimensions of the simulated prisms, with the bar substituted by a steel tube of the same outer diameter (20 mm).

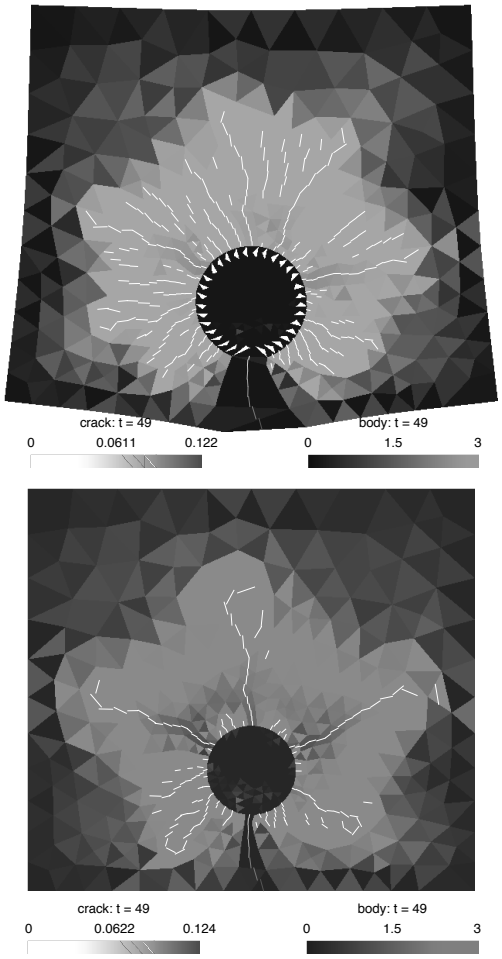

Figure 4: Crack pattern for a corrosion depth of 25μm for linear softening with $G_F = 0.1$ N/mm (top) and $G_F = 0.05$ N/mm (bottom).

The samples were artificially corroded by the imposition of a constant current density of 400 μA/cm^2. This current is much higher than the maximum values observed in actual structures, which may affect to the type of oxide that is generated, but these tests are only intended to analyse crack patterning and the ability of the numerical approach to reproduce it; slower tests will be conducted in the future. The imposition of the current was maintained until a noticeable crack appeared at the concrete surface. The counter electrode was a tube of stainless steel and the conductor medium was water without any additives. The sample is placed with the tube in vertical position. Figure 5 shows a view of the test assembly.

After corrosion, the samples were cut into four slices with a radial saw and a grinding machine was used to improve the smoothness of the surfaces of the cuts. A picture of one of the central slices is shown in figure 6. A main crack is easily seen across the concrete cover, in good agreement with the numerical predictions; a much thinner crack opposite to the main crack is hardly visible, but detecting further secondary cracks requires the help of magnifying devices.

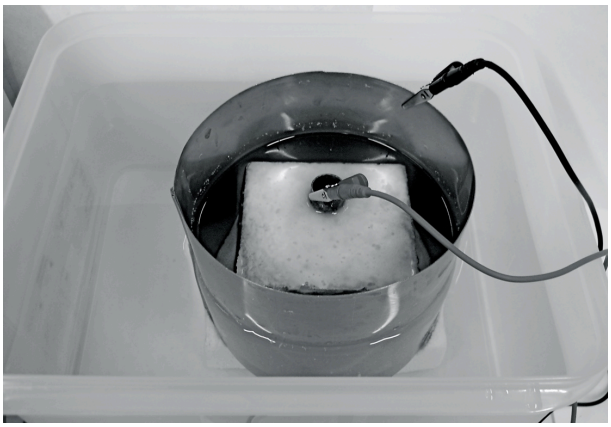

Figure 5: View of the assembly of an accelerated corrosion tests

When looking under the microscope, thin secondary cracks and radial micro-cracks are detected, in accordance with the results of the simulations, as shown in figures 7 and 8. Bright vertical lines on the steel surface can be observed that have been produced during the grinding process.

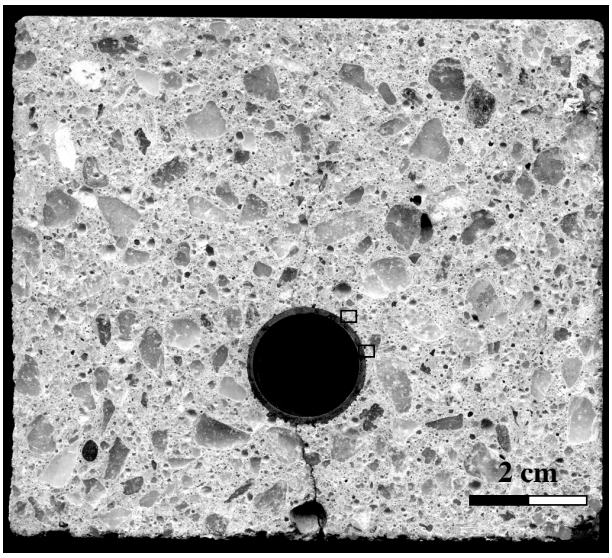

Figure 6: General view of the crack pattern observed in a corroded sample

3.2 Resin impreganation

In order to improve the detection of the cracks, the slices were impregnated with resin and fluorescein under vacuum. A low viscosity resin was selected to facilitate its penetration. The concentration of fluorescein was adjusted by selecting among a set of five concentrations the smaller concentration that delivered good visibility of the mix under ultra violet (UV) light; a concentration of $1,5$ mg of fluorescein per millilitre of resin was finally used.

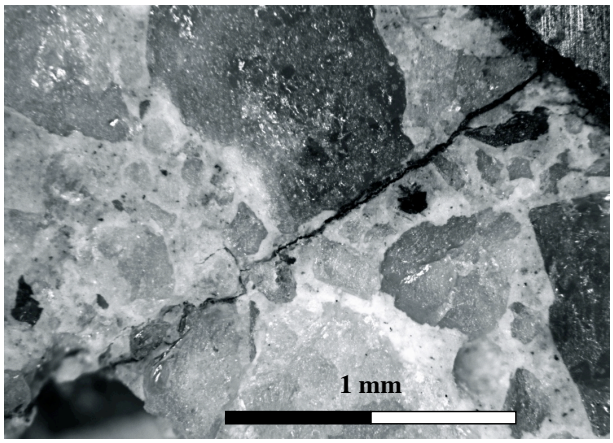

Figure 7: Secondary cracks observed in a corroded sample when looking under the microscope

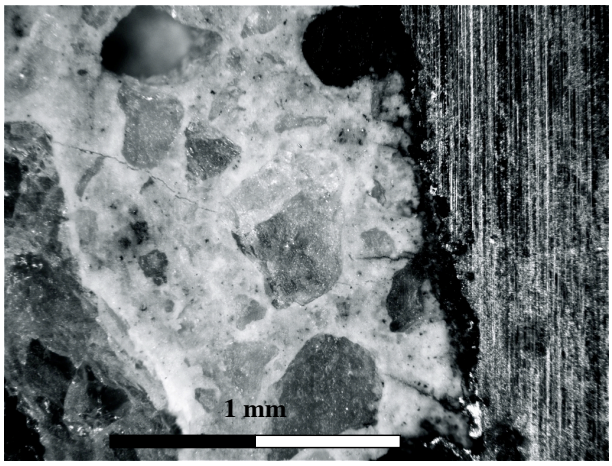

Figure 8: Radial micro-cracks observed in a corroded sample when looking under the microscope

The slices were impregnated under vacuum to improve the resin penetration through the cracks and pores of concrete. For that, a vacuum pump and a pressure cooker were utilised. A vacuum of 600 mmHg was reached. Firstly, vacuum was applied to the slice of concrete to empty of air the pores. Then, the resin was injected while keeping the vacuum. And finally the valve that controls vacuum was opened allowing the air to get inside. After curing the resin during two days at room temperature, the surfaces of the resin were ground again to eliminate the excess of resin and to expose undisturbed material.

In figure 10 a picture of the same slice that was studied in figures 6-8 is shown after impregnation and under UV lighting. The secondary cracks and some microcracks that were only observable under microscope before applying the surface treatment are now easily seen, and the overall pattern strikingly resembles the pattern in figure 4.

A further interesting observation is that the main crack, which can be seen by the naked eye without impregna-

tion, does not seem to have taken much resin during impregnation. The reason seems to be that the crack is full of compact black iron oxide. This seems to be true also for the root (next to the steel) of some secondary cracks.

Figure 9: Vacuum impregnation assembly. Pump, control of the pump and pressure cooker

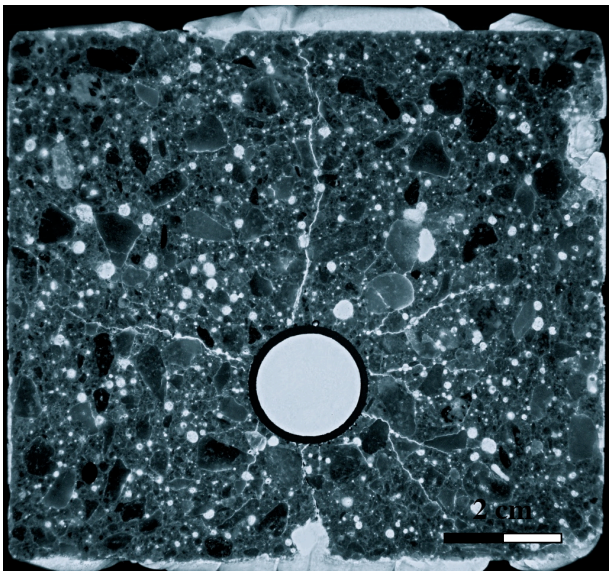

Figure 10: General view of the crack pattern obtained in a corroded sample after impregnating the surface with resin and fluorescein and lighting it with UV light

4 CONCLUSIONS

An interface finite element called *expansive joint element* was programmed to simulate the expansion of the oxide layer that is generated when the rebars in reinforced concrete structures are corroded and to study the mechanical effects of it over the surrounding concrete. The simulations with that model predict a wide main crack across the concrete cover but also six or seven long secondary cracks and other smaller cracks, all of them much less opened than the main crack.

Very similar results are obtained when acceleratedly corroding real samples. Although only the main crack is clearly visible by the naked eye, secondary cracks and microcracks can be seen under the microscope, although in this way the wide-field view is lost, unless a wide micrograph covering is built.

The wide-field crack detection can be achieved by vaccuum-impregnating the samples with low viscosity resin containing fluorescein and observing them under UV light. The overall pattern of the fluorescent cracks closely resembles the patterns obtained numerically. The main crack and the root of some of the secondary cracks seems to be filled up with compact oxide.

ACKNOWLEDGEMENTS

The authors gratefully acknowledge the *Ministerio de Ciencia e Innovación, Spain,* for providing financial support for this work under grant BIA2005-09250-C03-01, and for providing, within the Spanish National Research Program CONSOLIDER-INGENIO 2010, funds for the research framework SEDUREC, within which the authors carried out their work. The authors also thank Mr. José Miguel Martínez for his help and advice during the setup of the experiments.

REFERENCES

[1] C. Andrade, M.C. Alonso, and F.J. Molina. Cover cracking as a function of bar corrosion: Part i - experimental test. *Materials and Structures*, 26:453–464, 1993.

[2] F.J. Molina, M.C. Alonso, and C. Andrade. Cover cracking as a function of bar corrosion: Part ii - numerical model. *Materials and Structures*, 26:532–548, 1993.

[3] M.C. Alonso, C. Andrade, J. Rodriguez, and J.M. Diez. Factors controlling cracking of concrete affected by reinforcement corrosion. *Materials and Structures*, 31:435–441, 1997.

[4] B. Sanz, J. Planas, A. M. Fathy, and J. M. Sancho. Modelización con elementos finitos de la fisuración en el hormigón causada por la corrosión de las armaduras. *Anales de Mecánica de la Fractura*, 25:623–628, 2008.

[5] J. M. Sancho, J. Planas, D. A. Cendon, E. Reyes, and J. C. Galvez. An embedded cohesive crack model for finite element analysis of concrete fracture. *Engineering Fracture Mechanics*, 74:75–86, 2007.

[6] A. Hillerborg, M. Modéer, and P.E. Petersson. Analysis of crack formation and crack growth in concrete by means of fracture mechanics and fracture elements. *Cement and concrete research*, 6:773–782, 1976.

[7] C. Geuzaine and J.-F. Remacle. Gmsh: a three-dimensional finite element mesh generator with built-in pre- and post-processing facilities. *International Journal for Numerical Methods in Engineering*, 79(11):1309–1331, 2009.

[8] G. V. Guinea, J. Planas, and M. Elices. A general bilinear fitting for the softening curve of concrete. *Materials and Structures*, 27:99–105, 1994.

[9] M. Elices, G. V. Guinea, and J. Planas. On the measurement of concrete fracture energy using three point bend tests. *Materials and Structures*, 30:375–376, 1997.

[10] J. Planas, G. V. Guinea, and M. Elices. Size effect and inverse analysis in concrete fracture. *International Journal Fracture*, 95:367–378, 1999.

[11] J. Planas, G. V. Guinea, J. C. Galvez, B. Sanz, and A. M. Fathy. Experimental determination of the stress-crack opening curve for concrete in tension. report 39. chapter 3. indirect tests for stress-crack opening curve. Technical report, RILEM TC 187-SOC Final Report, 2007.

APPENDIX: EQUATIONS OF THE EXPANSIVE JOINT ELEMENT

The *expansive joint element* is defined by two parameters as explained in the main text: the corrosion depth x and the volumetric expansion factor β. The latter depends on the relation between the specific volumes of oxide and metal (per mole of metal):

$$\beta = \frac{v_{ox}}{v_{met}} - 1 \tag{1}$$

When external actions are applied simultaneously to the expansion of the oxide, the traction vector $\mathbf{t}$ can be assumed (in the simplest model) to be linearly related to the apparent mechanical displacement $\mathbf{w}^a$ and thus written as

$$\mathbf{t} = \mathbf{K_n}\mathbf{w}^a \qquad \text{with} \qquad \mathbf{w}^a = \mathbf{w} - \beta x \mathbf{n}, \tag{2}$$

where $\mathbf{K_n}$ is the stiffness tensor, $\mathbf{w}$ is the total displacement, $\mathbf{n}$ is the unit normal vector to the metal surface, and $\mathbf{w}^a$ is calculated as the difference between the total displacement and the free expansion displacement of the oxide. The stiffness tensor $\mathbf{K_n}$ is a second order and objective tensor that explicitly depends on the unit vector $\mathbf{n}$. It can be separated into the normal and tangent projections to the surface as

$$\mathbf{K_n} = k_n \mathbf{n} \otimes \mathbf{n} + k_t(\mathbf{1} - \mathbf{n} \otimes \mathbf{n}) \tag{3}$$

where $\mathbf{1}$ is the second order identity tensor, $\otimes$ expresses tensorial product of two vectors and k_n and k_t are the normal and tangent stiffness constants. Substituting equation (3) in equation (2), the stresses vector is finally given by

$$\mathbf{t} = k_n(\mathbf{w} \cdot \mathbf{n} - \beta x)\mathbf{n} + k_t[\mathbf{w} - (\mathbf{w} \cdot \mathbf{n})\mathbf{n}] \tag{4}$$

Considering a pure shear stress τ that is applied to the oxide surface, the real displacement u at the application point is given by the sum of the shear displacement of the metal layer plus that of the oxide layer:

$$u = h - x\frac{\tau}{G_{met}} + (1+\beta)x\frac{\tau}{G_{ox}} \tag{5}$$

where h is the height of the layer of steel and G_{met} and G_{ox} are the shear stiffness moduli of metal and oxide. The same displacement is calculated using the expansive joint element (which does not subtract thickness to the metal layer) as

$$u = h\frac{\tau}{G_{met}} + \frac{\tau}{k_t} \tag{6}$$

Mechanical equivalence between the expansive joint element and the real metal-oxide system is established by identifying the displacements given by equations (5) and (6), so that the expansive joint shear stiffness is given by

$$k_t = \frac{G^*_{ox}}{\beta x}, \text{ with } G^*_{ox} = \frac{\beta G_{ox}}{1+\beta}\left[1 - \frac{G_{ox}}{(1+\beta)G_{met}}\right]^{-1} \tag{7}$$

where G^*_{ox} is the equivalent transversal stiffness modulus of the expansive joint element. Imposing mechanical equivalence when a normal stress is applied, similar results are obtained for the normal stiffness:

$$k_n = \frac{K^*_{ox}}{\beta x}, \text{ with } K^*_{ox} = \frac{\beta K_{ox}}{1+\beta}\left[1 - \frac{K_{ox}}{(1+\beta)K_{met}}\right]^{-1} \tag{8}$$

where K^*_{ox}, K_{ox} and K_{met} are the normal stiffness moduli of the expansive joint element, the oxide and the metal. It turns out, from the foregoing equation, that stiffness moduli of the element are inversely proportional to the corrosion depth x. To avoid numerical instability, a cut-off stiffness is established for a certain small value x_0 of corrosion depth and thus we write where k^0_t and k^0_n are the shear and normal stiffness corresponding to x_0.

$$k_t = \begin{cases} k^0_t \\ k^0_t \dfrac{x_0}{x} \end{cases}, k_n = \begin{cases} k^0_n & \text{if } x \le x_0 \\ k^0_n \dfrac{x_0}{x} & \text{if } x > x_0 \end{cases} \tag{9}$$

In the model, there is the possibility to distinguish two cases of normal stiffness for compression and tension. It is introduced by a directionality factor η so that

$$k^0_n = \eta k^0_{nc} \tag{10}$$

where k_{nc} is the value of the stiffness for compression and η is given by

$$\eta = \begin{cases} 1 & \text{if } \mathbf{w} \cdot \mathbf{n} - \beta x \le 0 \text{ (compression)} \\ \eta_t & \text{if } \mathbf{w} \cdot \mathbf{n} - \beta x > 0 \text{ (tension).} \end{cases} \tag{11}$$

where η_t is a constant much less than one.

MODELING THE STATIC-DYNAMIC FRACTURE IN REINFORCED CONCRETE

Luis Saucedo[1], Rena C. Yu[2] and Gonzalo Ruiz[3]

Departamento de Mecánica Aplicada e Ingeniería de Proyectos,
E.T.S. de Ingenieros de Caminos, Canales y Puertos,
Universidad de Castilla-La Mancha, Avda Camilo José Cela s/n, 13005 Ciudad Real, España

[1]E-mail: luis_saucedo@hotmail.es
[2]E-mail: rena@uclm.es
[3]E-mail: Gonzalo.Ruiz@uclm.es

ABSTRACT

We aim to model the static-dynamic fracture, often propagates in mixed-mode in lightly reinforced concrete beams. When a beam does not have enough shear reinforcement, fracture can initiate and propagate unstably and lead to failure through diagonal tension. In order to study this phenomenon numerically, a model capable of dealing with both static and dynamic crack propagation as well as the natural transition of these two regimes is necessary. A cohesive model for concrete fracture and an interface model for the deterioration between concrete and steel re-bar, both combined with an insertion algorithm, are chosen for this task. The static process is solved by dynamic relaxation (DR) method together with a modified technique to enhance the convergence rate. This same DR method is used to detect a dynamic process and switch to a dynamic calculation. The numerically obtained load-displacement curves, load-CMOD curves and crack patterns fit very well with their experimental counterparts, having in mind that we fed the calculations only with parameters measured experimentally.

KEY WORDS: Diagonal-tension failure, Dynamic relaxation.

1. INTRODUCTION

In this paper we investigate the evolution of 3D mixed-mode fracture in notched reinforced concrete beams subjected to static loading. As observed in the experimental results of Carmona, Ruiz & Del Viso 2007, under static loading conditions, mix-mode fracture can propagate in static or dynamic regime. The conditions of transition between these two regimes vary with beam geometry, reinforcement ratio, location and inclination of the rebar. Knowing those conditions beforehand is essential to beam design and safety of a whole structure, since without a rebar to slow down and eventually stop the dynamic fracture, the beam would collapse. The idea of adding reinforcements to transform a brittle behavior --beam collapsing-- into a ductile one --rebar yielding-- is many times more important than sole increasing of peak loads. In other words, mere high peak load may present false high load capacity if ductility is lacking.

When a beam is not sufficiently reinforced to resist shear, the crack initiated from the notch can run unstably and leads to diagonal tension failure, see Figure 1. To numerically reproduce this entire progress of the crack initiation, propagation and "hinge" forming, is undoubtedly a challenging task. A computational model that is able to not only handle both static and dynamic fracture but also detect the transition in between is required. To tackle this problem, we adopt an explicit discrete cohesive model, with a three-dimensional discretization, incorporated with a modified dynamic relaxation (DR) method. The modified DR, see Yu and Ruiz, 2004, is served both as a solver and a detector for dynamic processes.

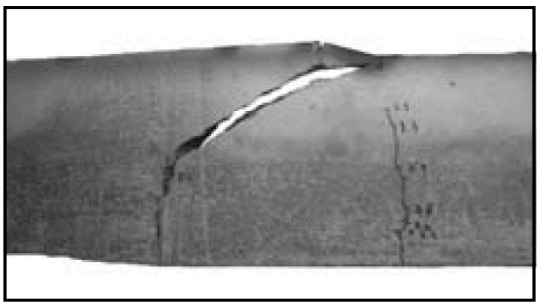

Figure 1. A lightly reinforced concrete beam failed through diagonal tension.

2. FINITE ELEMENT METHODOLOGY

We model the concrete bulk using the Neo-Hookean material extended to the compressible range. The fracture in concrete is modeled using a 3D cohesive model developed by Ortiz & Pandolfi 1999, with a linear-decreasing cohesive law. The steel rebar is explicitly represented using 10-node tetrahedrons and follows an elastic perfectly-plastic constitutive law. The steel-concrete interface is simulated through an interface

element endorsed with a perfectly plastic bond-slip law. Both the cohesive elements and the interface elements are inserted upon crack initiation or bond deterioration, the geometry is updated through an effective fragmentation algorithm, see Pandolfi & Ortiz, 2002. The whole process is solved using a modified dynamic relaxation method (Yu & Ruiz 2004). All the material properties were measured through independent experiments and their values are listed in Table 1, where E represents the material elastic modulus, f_t ,G_F are the tensile strength and the specific fracture energy of the concrete, $S_{c0.2}$ stands for the 0.2% yield strength of the steel rebar, T_c is the bond strength of the steel-concrete interface. Note that the value 174 GPa is the nominal modulus measured for a ribbed rebar.

Table 1. Mechanical properties of concrete, steel and the interface in between given in Carmona, Ruiz & Del Viso 2007.

Material	E (GPa)	f_t (MPa)	G_F (N/m)	$S_{c0.2}$ (MPa)	T_c (MPa)
Concrete	*36.3*	*3.8*	*43.4*	-	-
Steel	*174*	-	-	*563*	-
Steel-Concrete interface	-	-	-	-	*6.4*

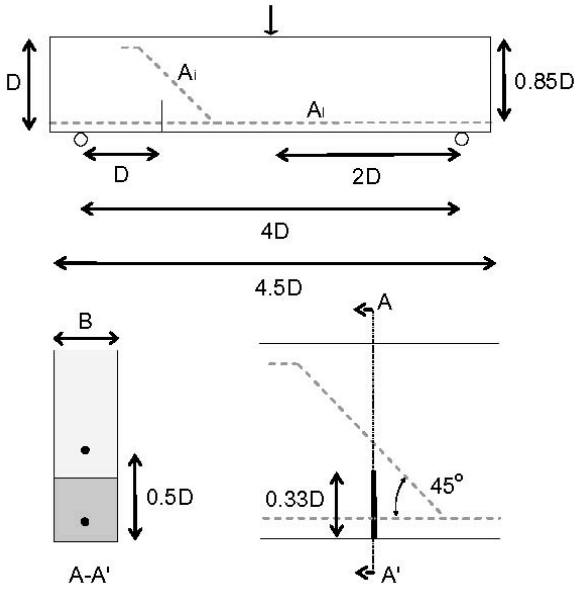

Figure 2. Geometry for the beams tested by Carmona, Ruiz & Del Viso (2007), where D is of 75, 150 and 300 mm for small (S), middle (M) and large (L) specimens.

3. NUMERICAL RESULTS

3.1. Validation

In Figure 2, we show the geometry of the notched beams tested by Carmona, Ruiz and Del Viso (2007) and follow their nomenclature for a beam of different size (S, M or L), reinforced with longitudinal or shear steel bars. For example, S01 is a small size beam, with zero longitudinal, one transversal rebar. This was designed to provoke a single propagating crack in beams of different sizes and to facilitate the study of crack trajectories, peak loads and their relation with the amount and location of the reinforcements.

Beams M00 and M20 are chosen as validation examples. The complete load-displacement and load-CMOD curves are plotted against their experimental counterparts in Figure 3, where letters A to E mark different stages of the crack propagation. Taking into consideration that all fed material parameters are measured ones, the fit is remarkable.

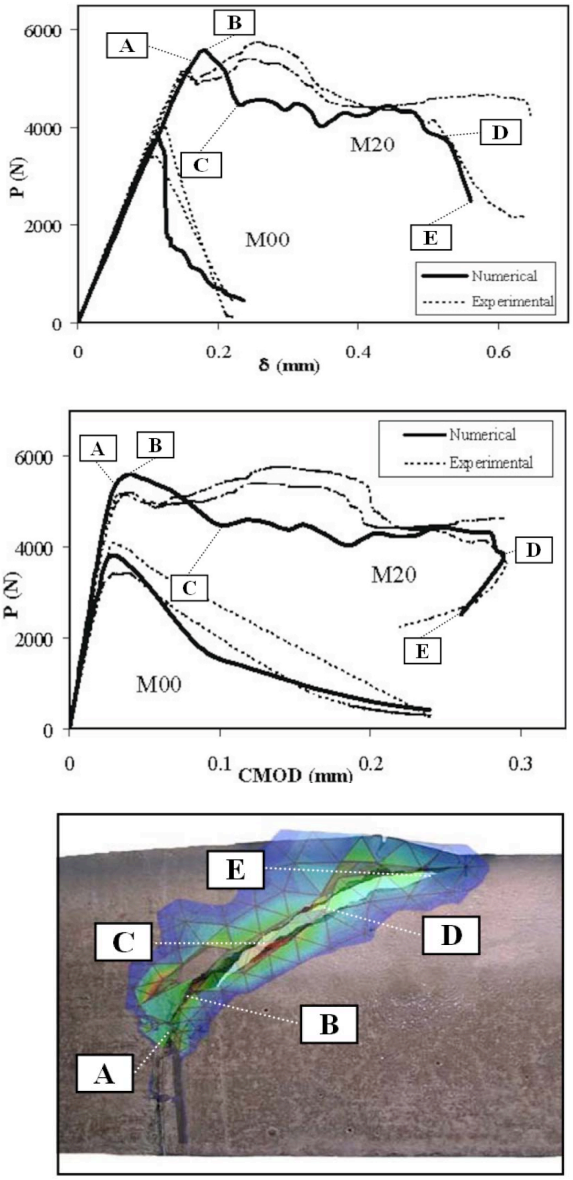

Figure 3. Numerical-experimental comparison for (from top to bottom) load-displacement, load-CMOD curves and crack patterns.

It needs to be pointed out that, the calculations shown in Figure 3 had gone through a static-dynamic-static transition. In particular, at the last stage of M20, the crack closes due to the formation of the "hinge" after the diagonal-tension failure. This last part cannot be captured by any sophisticated solvers if considering it static, since the crack propagation is intrinsically dynamic. The lower numerical load at post-peak compared to the experimental one is attributed to the material hardening of the rebar is not yet included in the numerical model.

3.2. Dynamic fracture under static loading

When a structural element fails due to surpassing of its loading limit, the collapsing process is usually unstable, and is accompanied with dynamic fracture. Such a dynamic fracture propagation under static loading is demonstrated in Figure 4 for the case of a small beam without any reinforcements S00. Figure 4(top) shows the numerical crack trajectory superimposed upon the experimental one. A perfect match is obtained. In Figure 4(bottom), the discontinuous lines with empty symbols represent the experimentally recorded load-displacement curve. Note that, at post-peak stage, from peak load to zero load, no intermediate points were recorded due to the rapid failure of the beam. In other words, we cannot directly compare the load-displacement data after peak load, nevertheless, one can observe that the numerical softening curve tends to the experimental one taken at the end of the experiment. The matching of both the load-displacement curves and crack trajectories validates both the amount and the location of the energy spent. It needs to be pointed out that since the test was done with displacement control, it was the self-weight that provoked the dynamic fracture when the crack was advanced towards the loading plane. For a beam with reinforcements, the static-dynamic transition could occur (a) when the interface is broken and (b) when the rebar is yielded or broken, see Figure 3 B-C and D-E, and Figure 4 B-C. Figure 3 shows that the longitudinal reinforcement of M20 actually stopped the dynamic crack propagation, consequently there was a dynamic-static transition from point C to D, apart from the static-dynamic ones B-C and D-E. Such transitions are determined by the reinforcement ratio and the beam geometry.

3.3. Effect of longitudinal and transversal reinforcements

From Figure 3, comparing the case of M00 and M20, we observe that longitudinal rebars help to augment both the peak and the ultimate loads. Consequently, M20 is more ductile compared to the non-reinforced one M00. From Figures 4 and 5, for beam S01, however, the peak load is lower than the beam S00. By looking at the crack trajectories, we observe that the transversal rebar served to change the main crack trajectory at point D. This is clearly seen in Figure 6, where the experimental trajectories are put together for beams S00, S01, S10 and S11. The fractures paths remained the same at the first stage of the crack propagation, this shows neither the longitudinal nor the transversal rebar was activated.

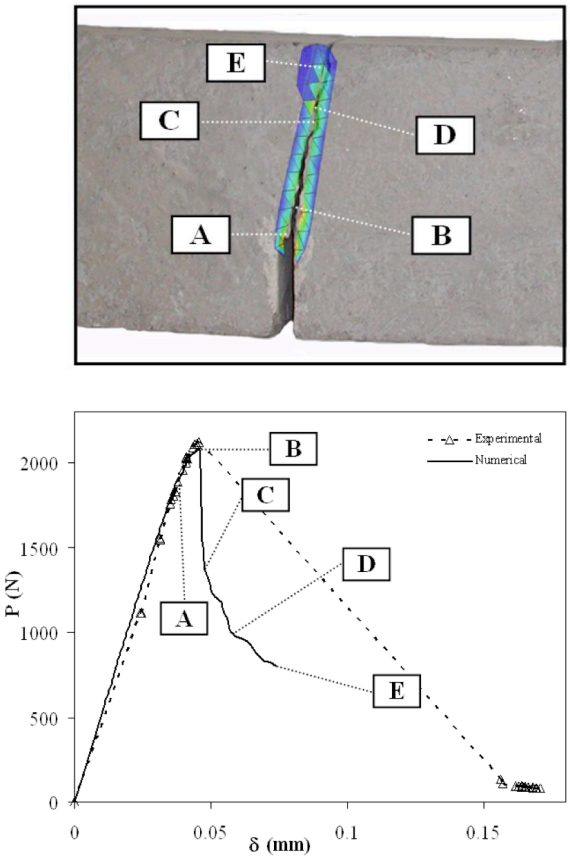

Figure 4. Experimental and numerical comparison for (top) crack patterns and (bottom) load-displacement curve for the case of S00, a small beam with neither longitudinal nor transversal reinforcements.

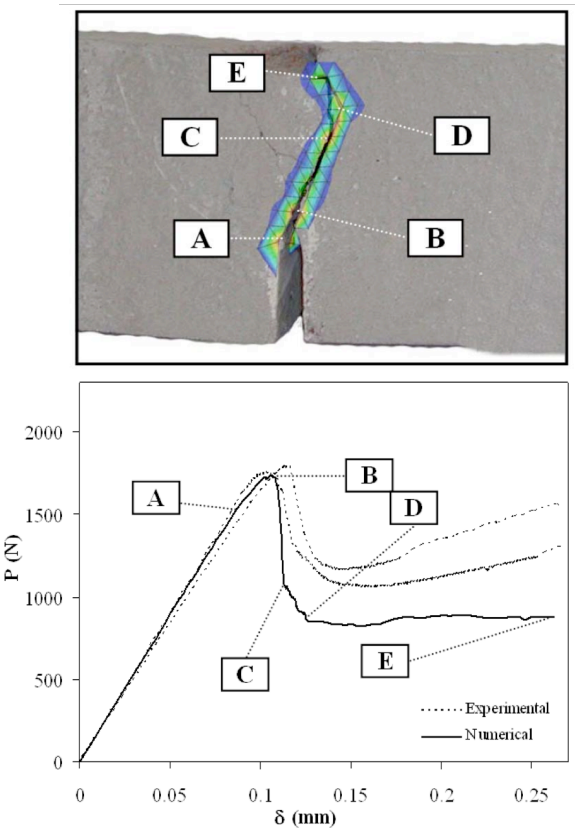

Figure 5. Numerical and experimental crack patterns and load-displacement curve for S01, a small beam reinforced with one transversal re-bar.

Then the crack path curved towards the loading plane for S10, whereas it went the opposite direction for S01. The crack followed a straight line in the case of S00. S11 is a mixture of S01 and S10, but closer to S10 than to S01. This reveals the stronger influence of the longitudinal reinforcement than the transversal on fracture path. It bears emphasis that such complicated trajectory would be an impossible task for those methods that work with only pre-embedded cracks.

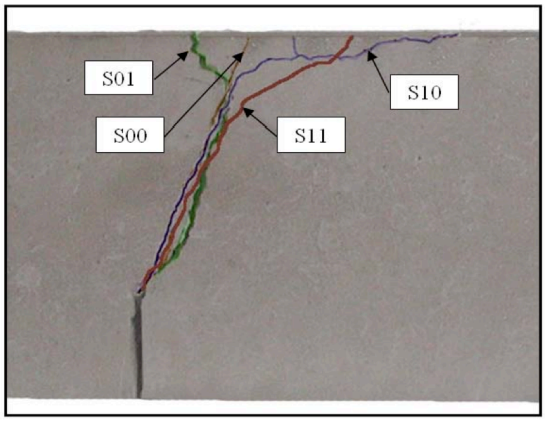

Figure 6.Main crack trajectories observed in experiments for beams S00, S01, S10 and S11.

3.4 Size effect in reinforced beams

According to the size effect law, two geometrically similar beams, the smaller one resists proportionally more than the larger one. However, Figure 7 shows the well-distinguished smaller-is-stronger rule in plain concrete beams do not equally reproduce for reinforced ones. In Figure 7(top), the load-displacement values for S10 are doubled to compare better with M20. Surprisingly, S10 resists less peak load than M20.

By looking at the movements of the two crack surfaces individually, see Figure 7(bottom), we observe that S10 and M20 show different failure mechanisms. Larger absolute amount of reinforcement in M20 has resulted that the left part of the beam is being dragged towards the loading plane. In other words, even though S10 and M20 share the same crack patterns, but the loading capacity do no follow the size effect law as observed in plain concrete beams. This phenomenon would not be captured by a non-explicit representation of the rebar and cracks.

3.5. Dowel action and sewing effect of the rebar

Figure 8 is a snapshot of the fractured beam S11, reinforced with one longitudinal and one transversal rebar. Note that the phenomenon of dowel action as shear transfer mechanism across cracks is reproduced naturally as a result of the explicit representation of rebar and the bond-slip interaction between concrete bulk and the rebar. Additionally observed is the sewing effect of both rebars and secondary cracks in concrete bulk. Correctly model each physical phenomenon individually and the interactions between reinforcement and concrete is fundamental for a right design of an reinforced concrete structure, since all those aforementioned factors contribute to the entire energy consumption therefore the resistance and global behavior of the beam.

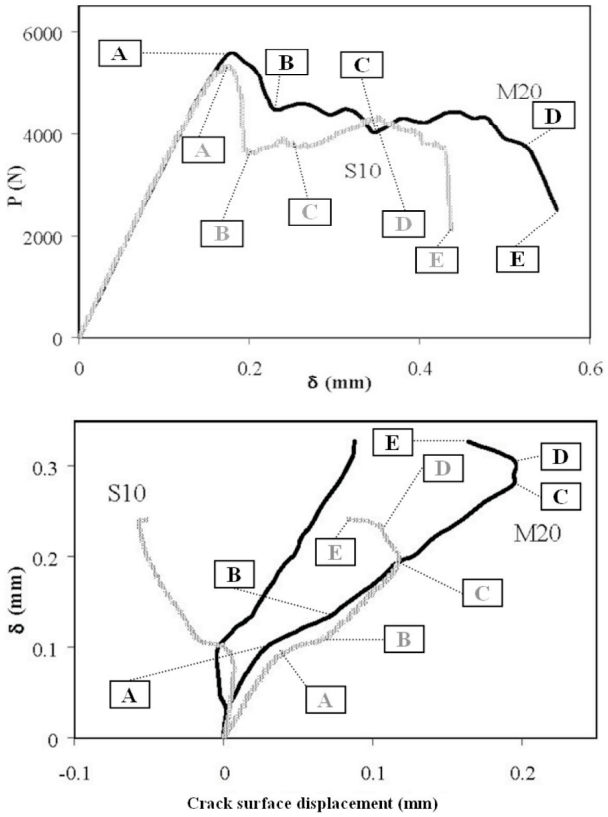

Figure 7. Load-displacement comparison for S10 and M20 (top) and crack surface displacements versus loading-point displacement for S10 and M20 (bottom).

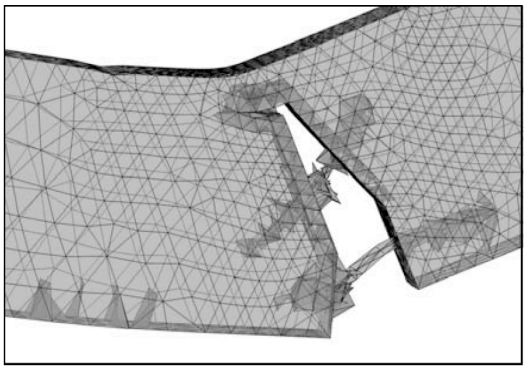

Figure 8. The dowel action, sewing effect of the rebar and secondary cracks modeled in beam S11.

4. CONCLUSIONS

We have modeled the static-dynamic mixed-mode fracture in reinforced concrete. The concrete bulk, steel rebar and the interface in between are all explicitly represented. A modified relaxation method is employed to solve the static process and detect a dynamic one. The methodology was validated against experimental results of Carmona, Ruiz and Del Viso. The salient features, such as micro cracking, changing of crack trajectory, pull out and the dowel action of the rebar, are all naturally reproduced through the discrete fracture and explicit representation of the rebar. As a by-product, the fundamental role of fracture mechanics in reinforced concrete structure design is thoroughly demonstrated.

ACKNOWLEDGEMENTS

The authors acknowledge the financial support from *Ministerio de Ciencia e Innovación,* Spain, under grant MAT 2006-09105 and the Consejería de Educación y Ciencia, JCCM, Spain, under grant PAI08-0196.

REFERENCES

Yu, R.C. and Ruiz, G. 2004 Multi-cracking modeling in concrete solved by a modified DR method. *Computers and Concrete*, **1(4)**, 371-388.

Carmona, J.R., Ruiz, G. and Del Viso, J.R. Mixed-mode crack propagation through reinforced concrete. Engineering Fracture Mechanics. *Engineering Fracture Mechanics,* **74**, 2788-2809.

Ortiz, M. and Pandolfi, A. 1999 Finite-deformation irreversible cohesive elements for three-dimensional crack-propagation analysis. *International Journal for Numerical Methods in Engineering*, **44**:1267-1282.

Pandolfi, A. and Ortiz, M. 2002 An efficient adaptive procedure for three-dimensional fragmentation simulations. *Engineering with Computers*, **18**:148-159.

DEVELOPMENT AND GROWTH OF THE FRACTURE PROCESS ZONE IN HSC UNDER A WIDE RANGE OF LOADING RATES

Rena C. Yu[1], XiaoXin Zhang[1,2], Gonzalo Ruiz[1], Manuel Tarifa[1], Miguel Camara[1]

[1] E.T.S. de Ingenieros de Caminos, Canales y Puertos, Universidad de Castilla-La Mancha
Avda. Camilo José Cela s/n, 13071 Ciudad Real, Spain
E-mail: zhangxiaoxinhrb@gmail.com

[2] Harbin Engineering University, Harbin 150001, China.

ABSTRACT

Compared with the extensive research on properties of the fracture process zone (FPZ) under quasi-static loading conditions, much less information is available on its dynamic characterization, especially for high-strength concrete (HSC). This paper presents the very recent results of an experimental program aimed at disclosing the loading rate effect on the size and velocity of the FPZ in HSC. Eighteen three-point bending specimens were conducted under a wide range of loading rates from from 10^{-4} mm/s to 10^{3} mm/s using either a servo-hydraulic machine or a self-designed drop-weight impact device. Four strain gauges mounted along the ligament of the specimen were used to measure the FPZ size. Surprisingly, the FPZ size remains almost constant (around 20 mm) when the loading rate varies seven orders of magnitude. This is clearly different from NSC, in which the FPZ size actually decreased with loading rate. Moreover, at low loading rates, the crack propagates with increasing velocity. Under high loading rates, the crack propagates with slightly decreasing velocity, though the maximum crack speed reached up to 20.6% of the Rayleigh wave speed of the tested HSC. Furthermore, the loading-rate effect on crack velocities is pronounced within the low loading rate regime, whereas it is minor under the high loading-rate range.

KEY WORDS: Fracture process zone, crack velocity, loading rate, high-strength concrete

1. INTRODUCTION

For cementitious materials, the inelastic zone around a crack tip is termed as fracture process zone (FPZ) and dominated by complicated mechanism, such as microcracking, crack deflection, bridging, crack face friction, crack tip blunting by voids, crack branching, and so on. Due to the length of the FPZ is related with the characteristic length of the cementitious materials, the size, extent and location of the FPZ has been the object of countless research efforts for several decades. For instance, Cedolin et al. [1] have used an optical method based on the moiré interferometry to determine FPZ in concrete. Castro-Montero et al. [2] have applied the method of holographic interferometry to mortar to study the extension of the FPZ. The advantage of the interferometry method is that the complete FPZ can be directly observed on the surface of the sample. Swartz et al. [3] have adopted the dye penetration technique to illustrate the changing patterns observed as the crack progress from the tensile side to the compression side of the beam. Hu and Wittmann [4] have used a multicutting technique together with the conventional compliance method to determine the extent of the FPZ on a wedge-opening loaded specimen with a ligament length of 110 mm. The results show that the length of the FPZ in mortar varies from around 43 mm to 12 mm while the crack is approaching to the boundary.

Moreover, acoustic emission (AE) is also an experimental technique well suited for monitoring fracture process. Haidar et al. [5] and Maji et al. [6] have studied the relation between acoustic emission characteristics and the properties of the FPZ. Mihashi et al. [7] has adopted three-dimensional AE techniques to study the FPZ. The results show that micro-cracking occurs randomly around the macro-crack and that the FPZ expands after peak load due to the presence of aggregates. Furthermore, X-ray [8], fibre optics [9] ultrasonic pulse velocity [10,11] techniques are also available for estimating the extent of the FPZ in concrete.

With regard to the crack-propagation velocity, the crack propagation in concrete occurs relatively slowly compared with the theoretical value [12]. Yon et al. [13,14] have verified the existence of low crack velocities in concrete by using strain gauges in a displacement-controlled dynamic fracture test system, though the strain rate of the crack tip was as high as 0.24 s^{-1}, the average crack velocity only reached 152 m/s. Mindess [15] measured crack velocity in plain concrete under impact loading by using a high-speed video camera (1000 frames per second). The results showed that the crack velocities were all in excess of 254 m/s (the limit of measurement for these tests) for the plain concrete under impact loading conditions, impact velocities were from 2.99 m/s to 4.72 m/s. The measured crack velocities are different from the theoretical ones could be an indication of the amount of internal microcracking that occurs in concrete during failure [15]. In addition, Biolzi et al. [16] pointed out that the crack velocity increases considerably with the concrete strength. Nevertheless, relatively little is

known about the physical process of crack development during dynamic loading conditions, detailed information about loading rate effect on crack velocities in concrete is scant, especially for high-strength concrete (HSC).

In the present work, we chose strain-gauge technology to measure the crack-propagation velocity and the size of FPZ in HSC at a wide range of loading rates, from 10^{-4} mm/s to 10^{3} mm/s. Two testing devices, a hydraulic servo-controlled testing machine and a self-designed drop-weight impact device were adopted. Furthermore, the detailed information from the strain history records will undoubtedly facilitate the validation of numerical models aimed at disclosing rate dependency.

2. EXPERIMENTAL PROCEDURE

2.1. Material characterization

A single HSC was used throughout the experiments, made with porphyry aggregates of 12 mm maximum size and ASTM type IV cement, I42.5L/SR. Micro silica-fume slurry and super plasticizer (Glenium ACE 325, B255) were added to the concrete composition. The mixing proportions by weight were 1:0.336:3.52:1.62:0.3:0.043 (cement: water: coarse aggregate: sand: micro-silica fume slurry: super plasticizer).

Table 1: Mechanical and fracture properties of the HSC tested.

	f_c (MPa)	f_t (MPa)	G_F (N/m)	E (GPa)	ρ kg/m^3
Mean	102.7	5.4	141	31	2368
Std. Dev.	2	0.8	9	2	1

There was a strict control of the specimen-making process to minimize scattering in test results. All of the specimens were cast in steel molds, vibrated by a vibrating table, wrap cured for 24 hours, de-molded, and stored for 4 weeks in a moist chamber at 20º C and 98% relative humidity until testing. Compressive tests were conducted according to ASTM C39 and C469 on 75 mm × 150 mm (diameter × height) cylinders. Brazilian tests were also carried out using cylinders of the same dimensions and following the procedures recommended by ASTM C496. Eight cylinders were cast, four for compressive tests and four for splitting tests. The mechanical properties as determined from various characterization and control tests are shown in Table 1.

2.2. Three-point-bend fracture tests

As aforementioned, in order to study the loading-rate effect in HSC, three-point bending tests on notched beams were conducted over a wide range of loading rates, from 10^{-4} mm/s to 10^{3} mm/s. Two testing apparatus were employed, one was a hydraulic servo-controlled testing machine, the other was a self-designed drop-weight impact instrument. The beam dimensions were 100 mm×100 mm (B×D) in cross section, and 420 mm in total length L. The initial notch-depth ratio a_0/D was approximately 0.5, and the span S was fixed at 300 mm during the tests, see Figure 1. Each specimen was removed from the moist room one day before the test and restored to the chamber after bonding the strain gauges. The specimen surface was polished and all four strain gauges (SG01-SG04, Model: LY 11 6/120A, 6 mm in length and 2.8 mm in width) were bonded to that surface, with a distance of 10 mm between each neighbouring gauge. Since a running crack in concrete is often deflected by aggregates along its path, the four strain gauges were bonded 10 mm apart from the centerline of the beam, see Figure 1. Those strain gauges provided not only the strain history at the bonded positions, but also the time at which the crack tip of the FPZ passed each strain gauge.

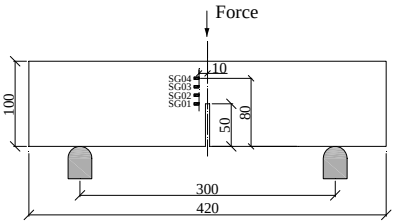

Figure 1: Specimen with bonded strain gauges (units in mm).

2.2.1. Tests under loading rates from 10^{-4} mm/s to 10^{1} mm/s

Within this low loading-rate range, the tests were performed employing the hydraulic servo-controlled testing machine under position control. Three loading rates, from quasi-static level (5.50×10^{-4} mm/s) to rate dependent levels (0.55 mm/s and 17.4 mm/s), were applied. Three specimens were tested at each loading rate. A MGCplus data acquisition system from HBM, with integrated strain amplifier and oscilloscope, was used to collect the data from the strain gauges; the sample rate was set at 2.4 kHz.

2.2.2. Tests under loading rates from 10^{2} mm/s to 10^{3} mm/s

Within this high loading-rate range, all tests were conducted using the instrumented, drop-weight impact apparatus, which was designed and constructed in the Laboratory of Materials and Structures at the University of Castilla-La Mancha. It has the capacity to drop a 316 kg mass from heights of up to 2.6 m, and can accommodate flexural specimens with spans of up to approximately 1.6 m. In this study, an impact hammer of 120.6 kg was employed to drop from three heights 40, 160 and 360 mm. The corresponding impact speeds were 8.81×10^{2} mm/s, 1.76×10^{3} mm/s and 2.64×10^{3} mm/s, respectively. Three specimens were tested at each impact speed. A detailed description of the instrument is given in reference [20]. The impact force is measured by a piezoelectric force sensor. In addition, the reaction

force is determined by two force sensors located between the support and the specimen. A strain amplifier DEWETRON-30-8 and two oscilloscopes TDS3014B were used to acquire the data from the strain gauges, the sample rate was set at 250 kHz.

2.2.3. Crack-velocity measurement

When the fracture initiates, an unloading stress wave is generated and travels to the strain gauge, the sudden decrease of strain as a function of time indicates the crack initiation, see Figure 2 for a typical strain history record from one of the four strain gauges.

The crack velocity naturally refers to the speed in which this initiated cohesive crack tip, i,e. the FPZ front, will propagate. The time interval t_f is the crack initiation time. Additionally shown in Figure 2 are $t_{\varepsilon\max}$ and $t_{\varepsilon r0}$, which indicate the time at peak strain and the time at which the strain is relaxed to zero, respectively. We define the time interval between $t_{\varepsilon\max}$ and $t_{\varepsilon r0}$ as the strain relaxation time t_r.

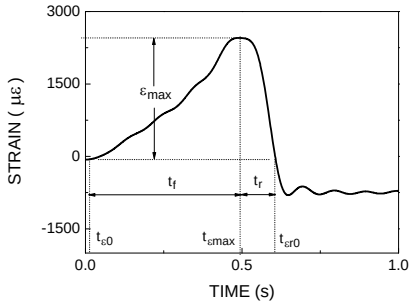

Figure 2: A typical strain versus time curve (shown in the record of SG01), taking the example of the loading rate at 0.55 mm/s.

Since the stress wave speed is much greater than the crack propagation velocity [15], the time taken by the unloading stress wave to propagate from the crack line to SG0n (the offset distance from the center line is 10 mm) need not be taken into account. Thus an average crack-velocity between two neighboring strain gauges can be obtained through dividing the distance in between–10 mm– by the time interval across the two corresponding peak signals recorded.

Furthermore the peak load is also an important parameter, which reflects the loading capacity of a given structural element, in our case, a three-point-bend beam, consequently all the information related to the peak load is also essential. In Figure 3, we give all the peak-load related information in one typical load history curve for low loading rate. The terms t_p and t_{pr} are defined as the pre- and post-peak crack propagation time. The elapsed time between $t_{\max}$ at SG04 and t_{p0} is used to obtain the crack velocity along the last 20 mm where no strain gauge was bonded. In addition, knowing the crack length at peak load a_p, the pre- and post-peak crack propagation velocity υ_1 and υ_2 are also calculated as a_p/t_p and $\left(D-a_0-a_p\right)/t_{pr}$ respectively and given in the next section.

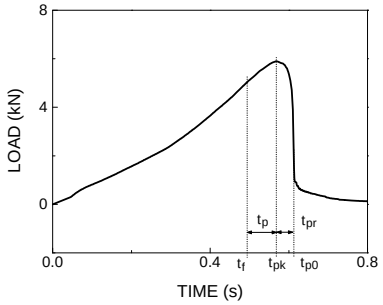

Figure 3: The typical load history for low loading rates, taking example of 0.55 mm/s.

2.2.4 FPZ measurement

Hillerborg et al. [18] first proposed a fictitious crack model for fracture of concrete as shown in Fig. 4. Where the newly formed crack surfaces and the corresponding fracture process zone are simply simulated by a cohesive zone located in the front of the initial crack tip. As a result, the energy dissipation for a crack propagation can be completely characterized by the cohesive stress-separation relationship.

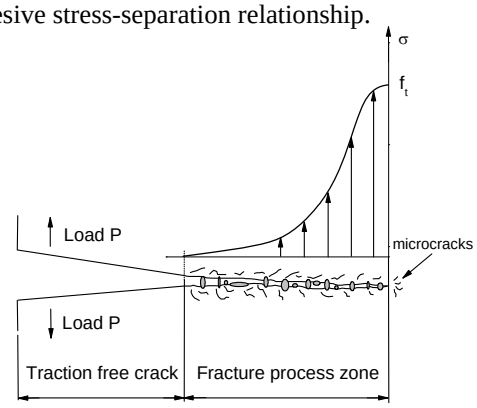

Figure 4. Sketch of concrete crack and FPZ

Here, we explore the advantage of the strain-gauge technology, having in mind that the attainment of peak stains signals pass of the cohesive crack tip, and strain values relaxed to zero represent a traction-free crack tip.

3. RESULTS AND DISCUSSION

The measured load histories are depicted in Figure 5. It needs to be pointed out that under high loading rates, the load refers to the impact force, i.e., the inertial force is also included.

Information related to the peak load, such as the dynamic increase factor (DIF), the time intervals t_{pk}, t_p and t_{pr} are reported in Table 2. The measured velocities υ_{sg}, the pre- and post-peak crack propagation velocities υ_1 and υ_2 are all listed in Table 3.

3.1 loading rate effect on peak loads

From Figure 5, note that the peak load increases proportionally with the loading rate, such rate effect is minor at low loading rates while it is pronounced at high loading rates. We define the dynamic increase factor (DIF) as the ratio of peak load and its corresponding quasi-static value (5.50×10^{-4} mm/s in this case). The DIF for peak loads are 1.4 and 25.0, for the loading rates of 17.4 mm/s and 2.64×10^{3} mm/s, respectively. In other words, the DIF at high loading rates is approximately one order higher than that at low loading rates.

It also needs to be pointed out that in Figure 5 (bottom row), we have scaled the load-axis by a factor proportional to its loading rate. Note that the peak load increases slightly faster than its loading rate. This is mainly due to the significant increase of inertia forces, see [19].

It is noteworthy that, at low loading rates, when the load peak is achieved, the crack length increased from 10 mm and 4 mm (5.5×10^{-4} and 5.5×10^{1} mm/s) to 37 mm (17.4 mm/s); while at high loading rates, the crack length varied from between 5 to 14 mm for all three cases, see Table 2. In particular, for the loading rate of 17.4 mm/s, when the peak load is achieved at t_{pk} of 21 ms, SG02 is deformation free at $t_{\varepsilon 02}$ of 19.9 ms, this shows the first 10-mm stretch from the notch tip is already traction free.

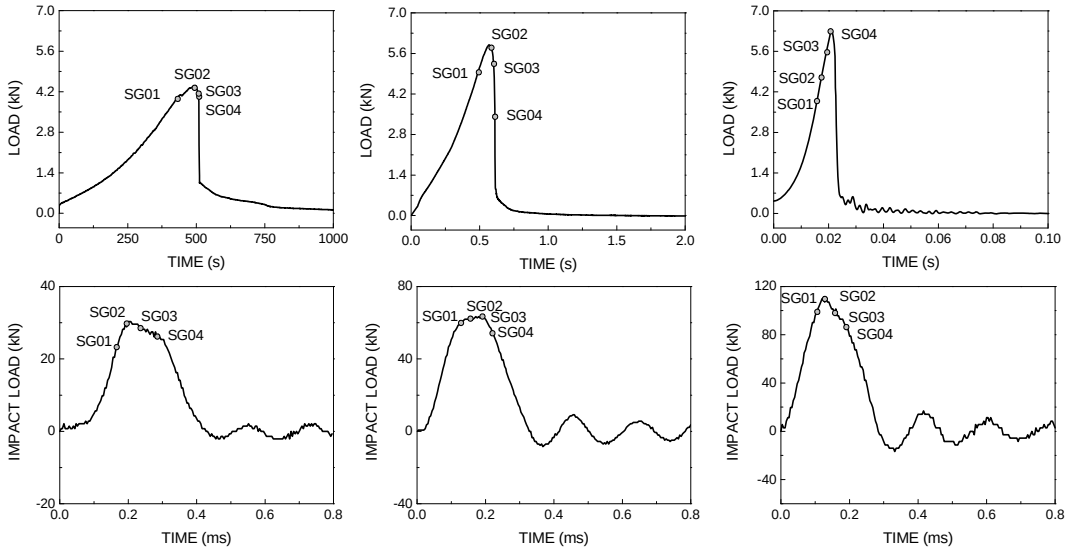

Figure 5: Load history for low loading rates (top row): 5.5×10^{-4} (left), 0.55 (middle) and 17.4 (right) mm/s, and high loading rates (bottom row): 8.81×10^{2} (left), 1.76×10^{3} (middle) and 2.64×10^{3} (right) mm/s, where SG0n marks the time at which the strain peak is obtained for strain gauge SG0n (n=1, 2, 3,4). Note that for the bottom row, the load-axis is proportionally scaled to its loading rate.

Table 2: Peak load and information related to peak load.

Loading rate	*Peak load*	*DIF*	t_f	t_{pk}	$t_p\ (t_{pk}-t_f)$	t_{p0}	$t_{pr}\ (t_{p0}-t_{pk})$	a_p
(mm/s)	*(kN)*		(s)	(s)	(s)	(s)	(s)	(mm)
5.5×10^{-4}	4.4	1.0	432	494	62	512	18	10
(mm/s)	*(kN)*	-	(ms)	(ms)	(ms)	(ms)	(ms)	(mm)
5.5×10^{-1}	5.9	1.3	490	567	77	614	47	4
1.74×10^{1}	6.3	1.4	15.8	21	5.2	23.8	2.8	37
(mm/s)	*(kN)*	-	(μs)	(μs)	(μs)	(μs)	(μs)	(mm)
8.81×10^{2}	30.3	6.9	168	200	32	428.5	228.5	11
1.76×10^{3}	63.4	14.4	128	172	44	331.0	159	14
2.64×10^{3}	209.9	25.0	108	120	12	284	164	5

3.2 loading rate effect on crack velocity

The crack velocities are listed in Table 3. In the low loading rate range, on the one hand, for each loading rate, the crack advances with increasing speed; on the other hand, as the loading rate increases, the crack velocity increases proportionally. For instance, at 5.5×10^{-4} mm/s, the crack velocity increased by a factor of 38 from 0.19 mm/s for υ_{sg1} to 7.3 mm/s for υ_{sg3}; while at the loading rate of 2640 mm/s, the crack speed varied from 417 m/s to 357 m/s. When the loading rate increased by a factor of 1000 (from 5.5×10^{-4} mm/s to 0.55 mm/s), the first-stage crack velocity υ_{sg1} increased by 4100, while the late-stage velocities υ_{sg3} and υ_{sg4}

only increased by a factor of 1369 and 1476 respectively. This indicates that, when the loading condition changes from quasi static to low loading rates, the loading rate effect on the early-stage crack velocity is almost three times stronger than its effect on the late-stage crack propagation; however, within the low loading rate range, when the loading rate increased by 34, from 0.55 mm/s to 17.4 mm/s, the increase factor from υ_{sg1} to υ_{sg3} remained practically the same (from 14.4 to 17.3). Within the high loading rate range, on the contrary, the crack advances with decreasing speed, and as loading rate increases, the crack propagation speed tends to be uniform, this is clearly seen from the pre and post-peak crack velocities. The maximum crack velocity reached approximately 20.6% of the Rayleigh wave speed.

Table 3: Average crack velocity evolution.

Loading rate (mm/s)	v_{sg1} SG01-SG02 (m/s)	v_{sg2} SG02-SG03 (m/s)	v_{sg3} SG03-SG04 (m/s)	v_{sg4}* (m/s)	v_{max}/v_R %	Pre-peak v_1 (m/s)	Post-peak v_2 (m/s)
5.5×10^{-4}	1.9×10^{-4}	2.7×10^{-4}	7.3×10^{-3}	2.1×10^{-3}	-	2.3×10^{-4}	1.2×10^{-3}
5.5×10^{-1}	0.78	0.73	1.05	3.1	-	0.58	0.73
1.74×10^{1}	11.2	12.6	16	4.2	-	6.8	4.2
8.81×10^{2}	292	250	208	138	14.4	344	171
1.76×10^{3}	357	278	357	187	17.6	327	224
2.64×10^{3}	417	417	387	200	20.6	417	275

* V_{SG4}, crack velocity along the last 20 mm distance

Comparing the numerically-predicted two-stage crack propagation in [19], the experimentally observed pre- and post-peak velocities in Table 3 suggest that, at low loading rates, pre-peak crack propagation is stable in a sense that, continuous loading is necessary for continuous crack advancing, whereas post-peak one is unstable, since less external load leads to faster crack propagation. On the contrary, at high loading rates, impact loads result fast crack propagation from the very beginning, less external load at post-peak is accompanied by a slower crack extension.

3.3 loading rate effect on the size of FPZ

Figure 6 shows the method to determine the growth and development of the FPZ, taking the example of the loading rate at 2640 mm/s.

The upper half of the figure gives four strain histories recorded in the four strain gauges, with the time at peak strain $t_{\in max}$ and the time when the strain relaxed to zero $t_{\in r0}$ marked with filled squares and circles respectively. The time at peak load t_{pk} is also shown to distinguish the pre and post-peak crack propagations. The lower half of Figure 6 shows the FPZ evolution with time during loading.

Table 4: FPZ size

Loading rate (mm/s)	FPZ size (mm)
5.5×10^{-4}	14-20-17
5.5×10^{-1}	25-47
1.74×10^{1}	17-21-14
8.81×10^{2}	23-21-16
1.76×10^{3}	16-19-15
2.64×10^{3}	18-21-16

The upper limit of the shaded zone shows the evolution of the cohesive crack tip, while the lower one represents the traction-free crack tip. For instance, in order to know the FPZ ended at SG02, i.e., when $\sigma = 0$ is reached at $t_{\in r02}$, one needs to know the current location of the

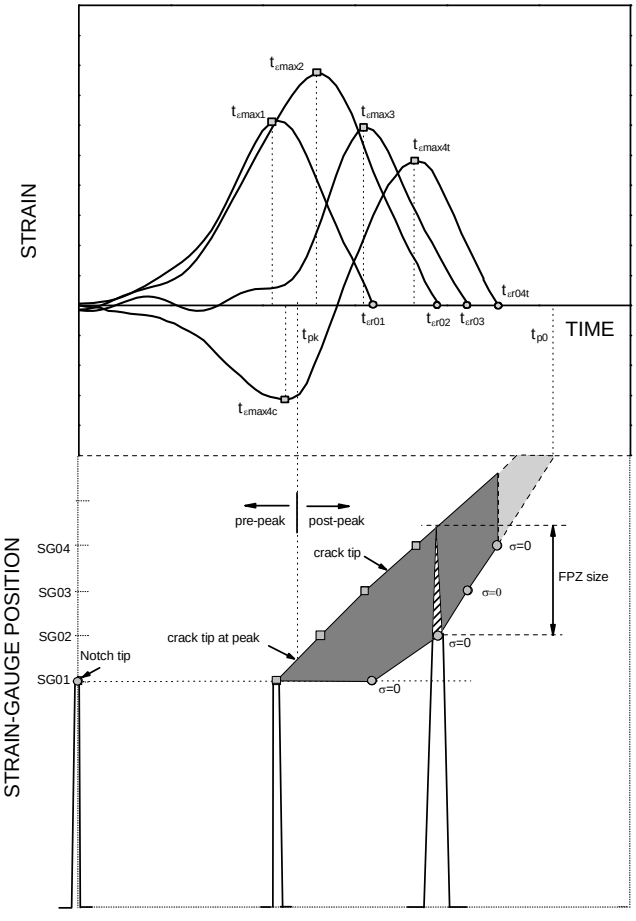

Figure 6: Methodology to estimate the development and growth of FPZ. Filled square symbols represent time at peak strain, whereas filled circles stand for time when the strain relaxed to zero. The upper half shows the strain histories recorded in the four strain gauges; the lower part illustrates the initiation and propagation of

the main crack, where the shaded zone is the evolution of the FPZ during loading. The dashed-line-surrounded shadow indicates unconfirmed information due to lack of further measurements. Shown is the case of the loading rate at 2640 mm/s.

cohesive crack tip. From the upper part of Figure 6, we find the intersection point between the line $t = t_{\epsilon r02}$ and the upper limit of the dark shaded zone, the distance between this intersection point and SG02 is the sought FPZ size. Note that, the FPZ was not completely developed either within the first nor the last 20 mm due to boundary effects. Since four strain gauges were employed to measure the strain history, at most three FPZ sizes can be directly obtained, more values can be obtained through interpolation as in Figure 6. We nevertheless list only those directly obtained FPZ sizes in Tab. 4 separated by a dash "-" sign. If we exclude the possible boundary effects of the notch and final ligament of each specimen, the central FPZ size in Tab. 4 should be considered as the material FPZ size. Surprisingly, the FPZ size remained almost the same when the loading rate varied seven orders of magnitude. This is clearly different from NSC, in which the FPZ size actually decreased with loading rate, see Du et al. [13,14] and Wittman [23].

4. CONCLUSIONS

Using strain-gauge technology, employing a servo-hydraulic machine and a drop weight impact device, we have measured crack propagation velocities and the size of the FPZ for a HSC loaded over a wide range of loading rates, from 10^{-4} mm/s to 10^{3} mm/s. The following conclusions can be drawn. (a) The peak load is sensitive to the loading rate. Under low loading rates, the rate effect on the peak load is minor, while it is pronounced under high loading rates. (b) The measured time to peak load t_{pk}, a measure of the initial CMOD rate, varied from 0.12 ms to 494 s. (c) Unlike normal strength concrete, the FPZ size varied only slightly for loading rates of seven orders of magnitude. (d) Under low loading rates, the main crack advances with increasing velocity, the late-stage velocity is one-order higher than the early-stage one; the rate effect on the crack velocity is remarkable. At high loading rates, the main crack propagates with a decreasing crack velocity of several hundred m/s, the rate effect on crack velocity is minor. In addition the crack propagation velocity in the high loading-rate range reached 20% of the material's Rayleigh wave speed.

REFERENCES

[1] Cedolin, L., Dei Poli, S., and Iori, I., Experimental determination of the fracture process zone in concrete. *Cement and Concrete Research*, **13**, pp. 557-567, 1983.

[2] Castro-Montero, A., Shah, S. P., and Miller, R. A., Strain field measurement in fracture process zone. *Journal of Engineering Mechanics*, **116**, pp. 2463-2484, 1990.

[3] Swartz, S. E., and Go, C. G., Validity of compliance calibration to cracked concrete beams in bending *Experimental Mechanics*, **24**, pp. 129-134, 1984.

[4] Hu, X., and Wittmann, F. H., Experimental method to determine extension of fracture-process zone. *Journal of Materials in Civil Engineering*, **2**, pp. 15-23, 1990.

[5] Haidar, K., Pijaudier-Cabot, G., Dubé, J. F., and Loukili, A., Correlation between the internal length, the fracture process zone and size effect in model materials. *Materials and Structures*, **38**, pp. 201-210, 2005.

[6] Maji, A., and Shah, S. P., Process zone and acoustic-emission measurements in concrete. *Experimental Mechanics*, **28**, pp. 27-33, 1988.

[7] Mihashi, H., Nomura, N., and Niiseki, S., Influence of aggregate size on fracture process zone of concrete detected with three dimensional acoustic emission technique. *Cement and Concrete Research*, **21**, pp. 737-744, 1991.

[8] Otsuka, K., Detection of fracture process zone in concrete by means of x-ray with contrast medium. Fracture mechanics of concrete structures. *Proc. of FraMCoS-1*, pp. 485-490, 1992.

[9] Denarié, E., Saouma, V. E., Iocco, A., and Varelas, D., Concrete fracture process zone characterization with fiber optics. *Journal of Engineering Mechanics*, **127**, pp. 494-502, 2001.

[10] Berthaud, Y., Damage measurements in concrete via an ultrasonic technique. Part i experiment. *Cement and Concrete Research*, **21**, pp. 73-82, 1991.

[11] Selleck, S. F., Landis, E. N., Peterson, M. L., Shah, S. P., and Achenbach, J. D., Ultrasonic investigation of concrete with distributed damage. *ACI Materials Journal*, **95**, pp. 27-36, 1998.

[12] Mindess, S., and Bentur, A., A preliminary study of the fracture of concrete beams under impact loading, using high speed photography. *Cement and Concrete Research*, **15**, pp. 474-484, 1985.

[13] Yon, J. H., Hawkins, N. M., and Kobayashi, A. S., Strain-rate sensitivity of concrete mechanical properties. *ACI Materials Journal*, **89**, pp. 146-153, 1992.

[14] Du, J., Yon, J. H., Hawkins, N. M., Arakawa, K., and Kobayashi, A. S., Fracture process zone for concrete for dynamic loading. *ACI Materials Journal*, **89**, pp. 252-258, 1992.

[15] Mindess, S., Crack velocities in concrete subjected to impact loading. *Canada Journal of Physics*, **73**, pp. 310-314, 1995.

[16] Biolzi, L., and Tognon, G., Strain rate effect on crack propagation in concrete. *Theoretical and Applied Fracture Mechanics*, **7**, pp. 201-206, 1987.

[17] Zhang, X. X., Ruiz, G., and Yu, R. C., A new drop-weight impact machine for studying fracture processes in structural concrete. *Strain, doi:10.1111/j.1475-1305.2008.00574.x.*, 2008.

[18] Hillerborg, A., Modéer, M., and Petersson, P. E., Analysis of crack formation and crack growth in concrete by means of fracture mechanics and finite elements. *Cement and Concrete Research*, **6**, pp. 773-781, 1976.

[19] Zhang, X. X., Ruiz, G., and Yu, R. C., Experimental study of combined size and strain rate effects on the fracture of reinforced concrete. *Journal of Materials in Civil Engineering*, **20**, pp. 544-551, 2008.

[20] Wittmann, F. H., Crack formation and fracture energy of normal and high strength concrete. *Sadhana - Academy Proceedings in Engineering Sciences*, **27**, pp. 413-423, 2002.

ANÁLISIS MESO-MECÁNICO DEL HORMIGÓN BAJO LA ACCIÓN DE PROCESOS EXPANSIVOS INTERNOS

A. Campos[1], C.M. López[2], A. Aguado[1]

[1] Departamento de Ingeniería de la Construcción
[2] Departamento de Ingeniería del Terreno, Cartográfica y Geofísica
ETSECCPB, Universitat Politècnica de Catalunya, 08034 Barcelona. España
E-mail: andre.campos@upc.edu, carlos.maria.lopez@upc.edu, antonio.aguado@upc.edu

RESUMEN

Es conocido que la existencia de procesos expansivos en el hormigón inducidos por reacciones químicas, puede provocar una considerable degradación de sus propiedades mecánicas. Este comportamiento puede ser la respuesta a diferentes causas como la reacción álcali-árido, las reacciones de oxidación de sulfuros, el ataque sulfático (externo o interno), etc. Los procesos reactivos, en general, provocan cambios de volumen diferencial en la estructura interna del material, aspecto que viene a acentuar la importancia de realizar análisis mediante modelos mesomecánicos, en los que se representa explícitamente la estructura interna de primer nivel (meso-estructura). En este trabajo se presentan resultados de simulaciones numéricas meso-mecánicas de un hormigón sometido a acciones expansivas internas. Se han obtenido curvas de la degradación del módulo de elasticidad y de la resistencia a tracción en función del grado de expansión, que se comparan con resultados experimentales [1]. También se muestran aspectos de la fisuración y de la energía disipada, que se correlacionan con el nivel de expansión y la evolución de los parámetros mecánicos.

ABSTRACT

It is known that the existence of expansive processes in concrete induced by chemical reactions can cause considerable degradation of its mechanical proprieties. This phenomenon may have several causes such as alkali-aggregate reaction, sulphides oxidation reaction, the sulfate attack (internal or external), among others. The reactive processes, in general, cause differential volume changes in the internal structure of the material, aspect that accentuates the importance of analysis by meso-mechanical models that take into account the explicit representation of the first level internal structure (meso-structure). This paper presents results of meso-mechanical simulations of a concrete subjected to internal expansion actions. Curves have been obtained for the degradation of the elastic modulus and tensile strength in function of the degree of expansion and compared with experimental results [1]. Furthermore, this work shows aspects of the evolution of cracking and energy dissipation, both of which can be correlated with the degree of expansion and the variation of the mechanical parameters.

PALABRAS CLAVE: Análisis mesomecánico, Elemento junta, Expansiones internas.

1. INTRODUCCIÓN

Algunas deformaciones expansivas detectadas en el hormigón pueden ser causadas por procesos reactivos en que los productos generados, tales como el gel de las reacciones álcali-árido, la etringita secundaria en ataques sulfáticos, entre otros, provocan cambios de volumen diferencial en la estructura interna del material, lo cual da lugar a un estado de tensiones internas que puede ser causa de microfisuración, degradación de las propiedades mecánicas macroscópicas, e incluso en estados avanzados del proceso puede generar un grado de fisuración considerable.

La formación de etringita a edades muy tempranas (comúnmente llamada etringita primaria), con el hormigón en estado plástico, no produce degradación y daño. Sin embargo cuando se forma con posterioridad, a partir de días, meses o años (denominada etringita secundaria), la expansión no uniforme asociada puede producir la degradación del material y una fisuración de tipo enramada característica de los procesos reactivos. Existen varios procesos que pueden causar la formación de etringita secundaria, como el ataque sulfático externo (ASE) en que los iones sulfato provienen de una fuente externa, o el ataque sulfático interno (ASI) donde la fuente de sulfatos se encuentra en el interior de la masa de hormigón. Una forma de ASI puede ocurrir en hormigones fabricados con áridos que presentan contenidos de sulfuros de hierro (en forma de pirita o pirrotina) que al oxidarse (reacción primaria) causan una primera expansión y liberan sulfatos que reaccionan con los aluminatos del cemento (reacción secundaria), dando lugar a la formación de etringita asociada a una

segunda expansión de mayor magnitud que la reacción primaria. Este tipo de reacción expansiva ha sido detectado en algunas presas del Pirineo español como Graus, Tavascán y Rumedo, cuya problemática viene estudiándose desde hace años dentro del grupo de trabajo de la UPC [2,3]. En el marco de esta temática, se ha empleado un modelo numérico mesoestructural para estudiar la influencia de una expansión diferencial actuando en los áridos, junto con diferentes niveles de confinamiento [2-4]. Los resultados obtenidos han permitido explicar el comportamiento y tipo de fisuración observado en distintas zonas de las presas afectadas, tales como elementos auxiliares en los que la acción expansiva actúa libre y zonas visibles del cuerpo de presa con función resistente. Sin embargo, dada la ausencia de ensayos de laboratorio en este tipo de ASI (poco frecuente y de lento desarrollo en el tiempo), el modelo no se pudo contrastar cuantitativamente con resultados experimentales que registren por ejemplo la degradación de parámetros mecánicos con el nivel de expansión, datos que sí se disponen para expansiones debidas a otro tipo de reacciones químicas. Estudios experimentales de hormigones afectados por formación tardía de etringita han constatado reducciones de hasta el 60% en el módulo de Young [1,5,6]. Un grado similar de reducción del módulo también ha sido detectado en hormigones afectados por la reacción álcali-sílice [7-9] y por ASE [10]. En estas referencias también se han constatado reducciones apreciables de las resistencias a tracción y compresión. En general, se asocia la degradación de dichas propiedades a la microfisuración del hormigón provocada por la expansión.

Otro tipo de ASI es causado por un elevado contenido de sulfatos en el cemento y la acción de una alta temperatura que puede provenir de una fuente externa (como sucede durante un curado en caliente), o una fuente interna (calor de hidratación en un hormigón masivo). La etringita primaria ("early ettringite formation") no es estable a altas temperaturas, y durante el curado en caliente se descompone en monosulfato y yeso, pero se recompone y con efectos expansivos al bajar la temperatura en el hormigón endurecido, dando lugar a la denominada en este caso formación tardía de etringita ("delayed ettringite formation", DEF), [5,11]. En Rocco et al. [1] se ha ensayado experimentalmente un hormigón afectado de DEF, y se han determinado propiedades mecánicas como el módulo de Young, la resistencia a tracción y la energía de fractura para diferentes niveles de expansión.

En este trabajo se presentan simulaciones numéricas meso-mecánicas de un hormigón sometido a acciones expansivas internas, cuyos resultados obtenidos en términos de la degradación del módulo de elasticidad y de la resistencia a tracción se comparan con los obtenidos experimentalmente en [1]. También se muestran aspectos de la fisuración y de la energía de fractura disipada, que se correlacionan con el grado de expansión y la evolución de los parámetros mecánicos.

2. MODELIZACIÓN MESOESTRUCTURAL

Un planteamiento bastante completo y potente de abordar el estudio de materiales heterogéneos como el hormigón consiste en representar explícitamente la estructura interna de primer nivel (meso-estructura), y reproducir el comportamiento "macro" del material como resultado del análisis mecánico a nivel "meso". Desde hace aproximadamente unos 15 años, dentro del grupo de investigación del Departamento de Ingeniería del Terreno de la ETSECCPB-UPC, se viene desarrollando una metodología inicialmente en 2D y más recientemente en 3D, para el análisis mesomecánico de materiales heterogéneos, en especial para hormigón. El modelo consiste en la representación explícita en una discretización por el método de los elementos finitos (FEM), de las tres fases componentes principales de la estructura interna del hormigón a un nivel de observación a mesoescala. Por un lado, los áridos de mayor tamaño (aproximadamente el tercio mayor de la granulometría), cuya distribución y forma se genera de forma aleatoria mediante un procedimiento basado en la teoría de Voronoi-Delaunay. Rodeando a la fase granular se discretiza una matriz homogénea, que representa al mortero más los áridos de menor tamaño. Finalmente, se incluye en la malla una retícula de elementos junta sin espesor, distribuidos a lo largo de todos los contactos entre elementos de áridos y mortero (interfase) y entre algunos contactos de la matriz. Estos elementos junta se insertan *a priori* entre los elementos estándar del medio continuo, de modo que puedan quedar representadas las principales potenciales trayectorias de fisuración. En la figura 1 se presenta una malla de elementos finitos 2D, a la izquierda los áridos de mayor tamaño en color azul y la matriz en color gris, y a la derecha la retícula de elementos junta.

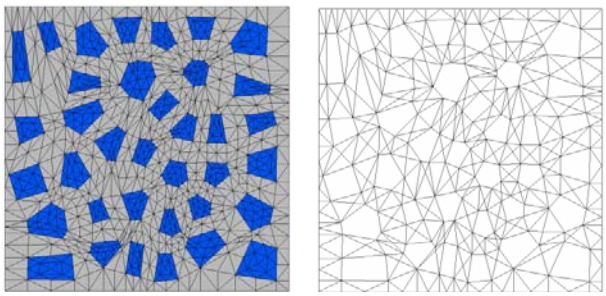

Figura 1. Malla de elementos finitos (izquierda) y retícula de elementos junta (derecha).

Para el comportamiento de los elementos junta se utiliza una ley constitutiva no lineal basada en la teoría de la elastoplasticidad y en conceptos de la mecánica de fractura, formulada en términos de la componente normal y tangencial de las tensiones en el plano medio de la junta y los desplazamientos relativos correspondientes. El criterio de fractura F se define mediante una hipérbola de tres parámetros (la resistencia a tracción, χ, y los parámetros $tan\phi$ y c de la asíntota que representan el ángulo de fricción entre las caras de la fisura y la cohesión aparente,

respectivamente). Una vez iniciada la fisuración, la superficie de fractura se contrae mediante el decrecimiento de los parámetros de la hipérbola en función de unas leyes basadas en el trabajo consumido en el proceso de fractura. Para controlar este proceso, el modelo posee dos parámetros que representan la energía de fractura clásica en modo I, G_F^I (tracción pura) y un segundo modo denominado Modo IIa definido bajo corte y alta compresión sin dilatancia, G_F^{IIa}. La regla de flujo es no asociada, con una ley de dilatancia que disminuye progresivamente con el nivel de compresión $\sigma \rightarrow \sigma^{dil}$ y con la degradación de la junta $c \rightarrow 0$. Se dispone de parámetros adicionales α_χ, α_ϕ y α_c que controlan la forma de evolución de las curvas de reblandecimiento. Una descripción más detallada se ha presentado en anteriores Congresos del Grupo Español de Fractura, así como en diversas publicaciones [4,12,13]. Resultados del modelo mesomecánico tanto a nivel 2D como 3D para distintas situaciones de carga pueden consultarse en [13-15].

3. RESULTADOS

Se analiza una muestra de 10x10 cm, con un arreglo de 6x6 áridos de 20 mm de tamaño máximo y que representan un 27% en volumen (figura 1). Los parámetros del hormigón para los elementos de medio continuo son: *E=60000 MPa* (áridos), *E=27000 MPa* (mortero) y *υ=0.2* (ambos); para las juntas de interfase: $K_N = K_T = 100000$ *MPa/mm*, $\tan\phi_0 = 0.70$, $\chi_0 = 2$ *MPa*, $c_0 = 7$ *MPa*, $G_F^I = 0.12$ *N/mm*, $G_F^{IIa} = 10\ G_F^I$, σ^{dil} = 40 MPa; para las juntas de mortero-mortero, los mismos parámetros excepto para $\chi_0 = 4$ *MPa*, $c_0 = 14$ *MPa*, $G_F^I = 0.24$ *N/mm*, $\alpha_d = -2$, $\alpha_\phi = 2$ *y* demás parámetros igual a cero. Los principales parámetros se han adoptado de modo de ajustar adecuadamente las propiedades del hormigón sin expansión ensayado en [1]. El cálculo, en condiciones de tensión plana, se realizó aplicando primero de forma progresiva unas deformaciones impuestas hasta un determinado nivel de expansión, y luego una tracción uniaxial en control de desplazamientos. Para cada ensayo numérico correspondiente a un nivel de expansión seguido de una tracción uniaxial, se ha obtenido su curva completa tensión-deformación, y en particular el módulo de Young y la resistencia a tracción (valor de pico).

Dado el tipo de ASI considerado, se han impuesto deformaciones sólo en la fase de la matriz. La acción expansiva se ha aplicado mediante deformaciones impuestas en cada nodo de la matriz, de manera equivalente al caso de incrementos de temperatura. En nuestra modelización mesoestructural la matriz representa una fase en realidad heterogénea constituida por la pasta de cemento (donde se producirían las expansiones), arena y los áridos de menor tamaño, distribuidos de forma aleatoria, por lo cual cabría esperar una distribución no uniforme de la expansión en un medio homogéneo equivalente. En primer término se efectuaron cálculos con una evolución de deformaciones constantes en la matriz, y posteriormente se ha obtenido una distribución no uniforme mediante una variación aleatoria en cada nodo, a partir de un rango establecido de distorsión alrededor del valor uniforme.

En las figuras 2 y 3 se muestran los resultados numéricos de la variación del módulo de elasticidad y la resistencia a tracción para el caso de deformaciones variables en la matriz. También se incluyen los resultados experimentales de Rocco et al. [1], que han utilizado 5 cementos distintos con diferentes contenidos de sulfatos a fin de obtener los distintos niveles de expansión. Si bien los ensayos experimentales y los numéricos se han realizado de distinta manera, los resultados son comparables (en los experimentos la resistencia a tracción se obtuvo mediante el ensayo brasileño y el módulo de Young a partir de una viga de tres puntos). Como se puede apreciar en ambas figuras, los resultados del modelo concuerdan en un alto grado con los experimentales. Se puede observar que en los resultados numéricos la reducción del módulo de Young presenta una caída brusca en los primeros niveles de expansión, seguida de una evolución más atenuada, aspecto que no puede constatarse en los experimentos dada la ausencia de datos en ese rango de expansiones.

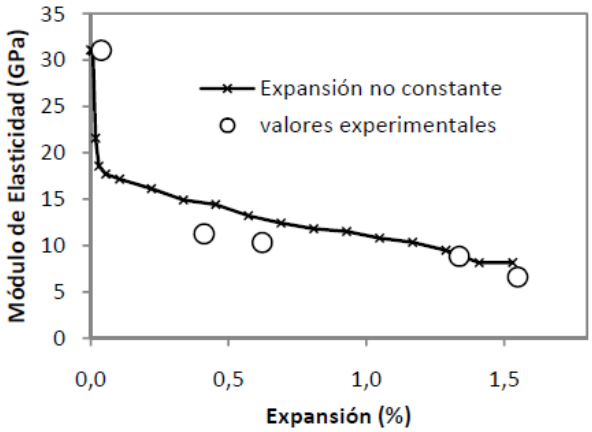

Figura 2. Variación del módulo de elasticidad con la expansión.

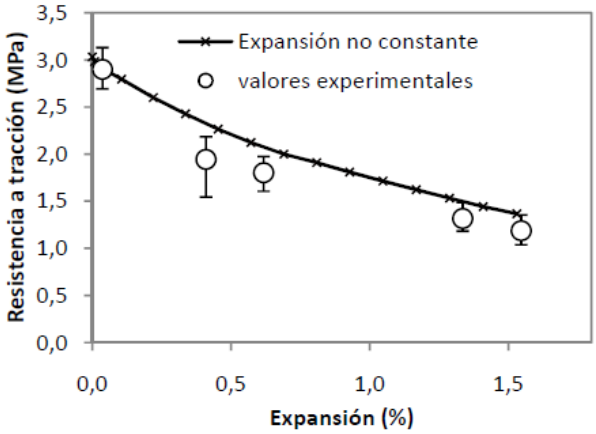

Figura 3. Variación de la resistencia a tracción con la expansión.

La figura 4 muestra el estado de fisuración de la malla con 1,53% de expansión (no uniforme), en términos de la energía disipada en el proceso de fractura, representada por el espesor de línea en cada punto de las juntas, en color rojo si la fisura está activa y en azul si se encuentra en descarga elástica. Se puede observar en la figura de la izquierda que la degradación se localiza principalmente en las juntas de interfase, y en menor medida en la matriz cuya distribución se muestra a una escala mayor en la figura de la derecha.

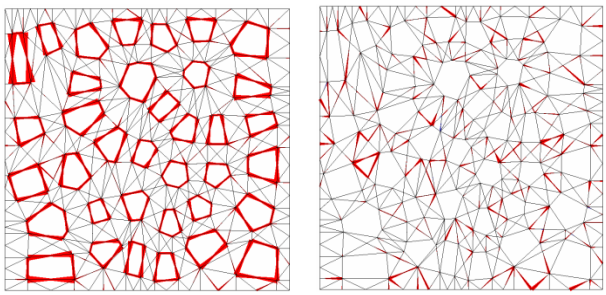

Figura 4. Estado de fisuración al 1,53% de expansión (izq) y sólo para la matriz a una escala mayor (der).

La figura 5 muestra las curvas tensión-desplazamiento en tracción uniaxial para distintos niveles de expansión no uniforme. Se puede apreciar que con el aumento de la expansión disminuyen progresivamente el módulo de Young y el valor máximo de tensión (con aumento de la deformación de pico), si bien no se aprecian diferencias significativas en las ramas de reblandecimiento ("softening"), que resultan bastante similares en todas las curvas. Esto es indicativo de un similar gasto de energía en el proceso de nucleación y localización de la fractura en cada uno de los casos, tal como puede observarse en la figura 6. En los gráficos de la izquierda se aprecia que la energía disipada en la macrofisura para el caso sin expansión, se mantiene aunque superpuesta con un aumento creciente de la degradación en las interfases (que mayoritariamente entran en descarga con la localización), a medida que aumenta el nivel de expansión. Como en los gráficos en términos de la energía disipada influye considerablemente el modo de fractura actuante (diferentes valores de G_F^I y G_F^{IIa}), el efecto de localización se puede apreciar más claramente en los gráficos de la malla deformada (fig. 6 derecha). Este aspecto concuerda cualitativamente con los resultados de [1], que han registrado similares valores de la energía de fractura con la variación de expansión.

Desde el punto de vista de los resultados del modelo numérico, resulta interesante reflejar la influencia diferenciada de la degradación de las juntas de interfase y las de la matriz. Una deformación uniforme impuesta en la matriz sólo afecta a las juntas de interfase árido-matriz. En las figuras 7 y 8 se presenta la variación en función del nivel de expansión, del módulo de elasticidad y la resistencia a tracción en valores normalizados con respecto al caso sin expansión, para los dos ejemplos numéricos (expansión uniforme y no uniforme), junto con los resultados experimentales.

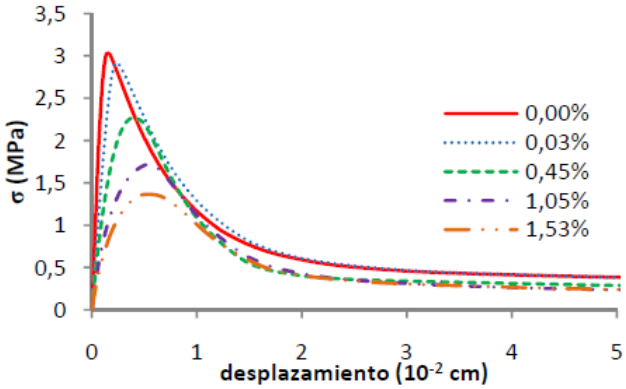

Figura 5. Curvas de tensión-desplazamiento en tracción pura para diferentes niveles de expansión.

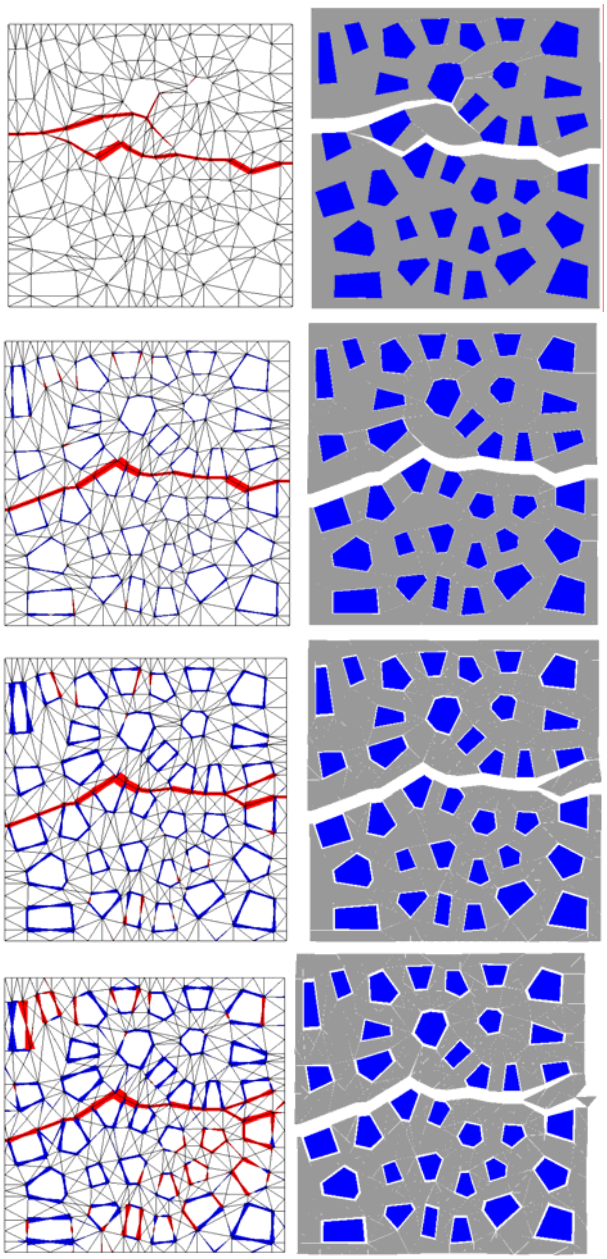

Figura 6. Estado de fisuración (izquierda) y malla deformada (derecha) en el estado final para una expansión de 0, 0.45, 1.05 y 1.53%, de arriba a abajo.

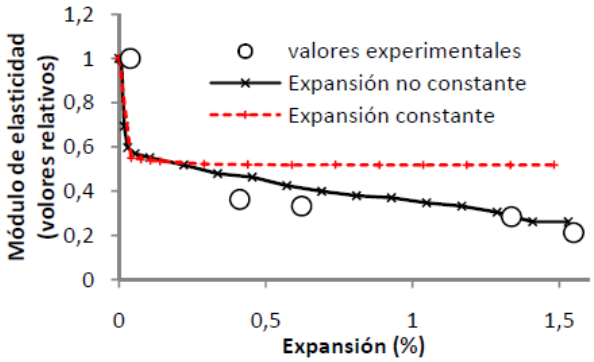

Figura 7. Variación del módulo de elasticidad normalizado con la expansión.

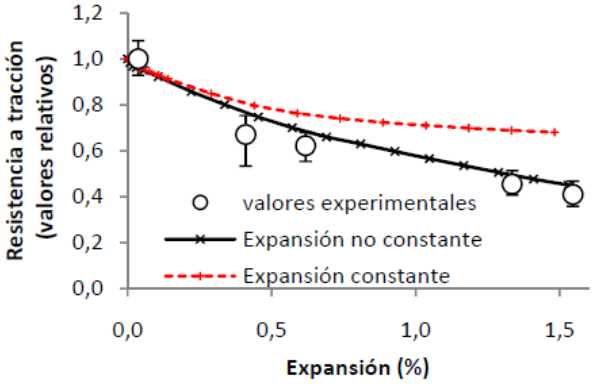

Figura 8. Variación de la resistencia a tracción normalizada con la expansión.

En la figura 7 se puede apreciar que los dos casos numéricos prácticamente coinciden hasta una expansión de aproximadamente el 0,03%, en que ambas tendencias cambian, y mientras el caso no uniforme sigue una degradación más atenuada, en el caso uniforme el módulo permanece constante con el aumento de la expansión, incluso para valores muy elevados. Por su parte, en la figura 8 se observa que en los dos casos numéricos hay una degradación progresiva de la resistencia a tracción con la expansión, lógicamente de mayor magnitud para la deformación impuesta variable. Los resultados parecen indicar que la evolución del módulo de elasticidad depende de la extensión de la degradación, mientras que la reducción de resistencia se ve afectada también por la intensidad del deterioro. A fin de evaluar estos factores, para cada nivel de expansión se ha calculado la longitud total de fisuración, obtenida como la suma de la longitud de todas las juntas abiertas en la malla, y el total de energía disipada, resultado de integrar la energía a lo largo de las juntas abiertas (expresada en: energía disipada [N/mm] x longitud [mm]). En la figura 9 se presenta la relación entre el grado de expansión y la longitud total de fisuración. Se observa que inicialmente se activan las juntas de interfase hasta completar toda su longitud en un rango relativamente bajo de expansión. Luego, en el caso no uniforme se van abriendo progresivamente juntas de la matriz de una forma mucho más atenuada con respecto al aumento del nivel de expansión.

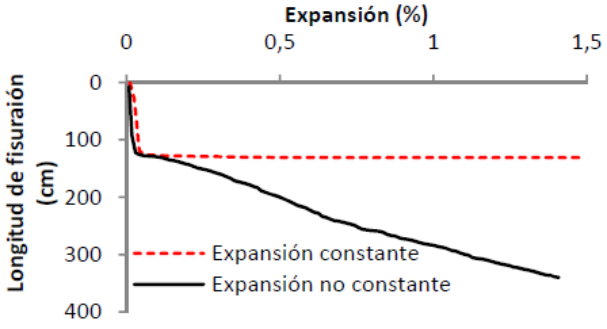

Figura 9. Variación de la longitud total de fisuración con la expansión

En la figura 10 se presenta la relación entre el nivel de la expansión y la energía disipada total. Para cada caso, se incluye también la energía disipada sólo por las juntas de interfase. Se puede apreciar en el gráfico una relación aproximadamente proporcional entre la energía disipada total del caso no uniforme y la expansión. También se observa que prácticamente coincide la evolución de la energía total disipada en las juntas de interfase para ambos casos de expansión.

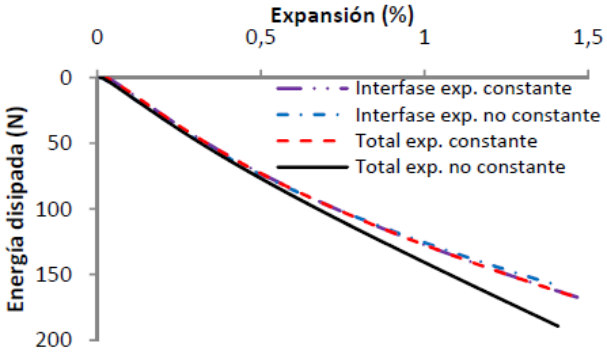

Figura 10. Variación de la energía disipada con la expansión.

Las figuras 9 y 10 muestran que el comportamiento de las juntas de interfase es muy similar en ambos casos, deformaciones uniformes y variables en la matriz, y por lo tanto su diferencia corresponde a la degradación de las juntas de mortero en el caso no uniforme. En el modelo numérico, en primer lugar se abren todas las juntas de interfase, debido a las propiedades resistentes más débiles que las de mortero que se han adoptado (a fin de reflejar las características de un hormigón convencional) y al efecto diferenciado de unas deformaciones impuestas sólo en la matriz. El caso de deformaciones uniformes pone de manifiesto que una vez abiertas todas las interfases, al continuar el deterioro (disminución de resistencia al aumentar la energía disipada en estas juntas) con el aumento del nivel de expansión, se afecta lógicamente la resistencia a tracción de la muestra, pero no el módulo de Young. Las similares características entre las figuras 7 y 9 indican una relación directa entre la degradación del módulo de elasticidad y el aumento de la longitud total de fisuración, tal como se refleja en la figura 11. Se

puede apreciar en la figura una tendencia aproximadamente lineal, con una reducción de la pendiente al comenzar la degradación de las juntas de mortero. De manera similar, las figuras 8 y 10 permiten relacionar la resistencia a tracción y la energía disipada total, cuya evolución se muestra en la figura 12.

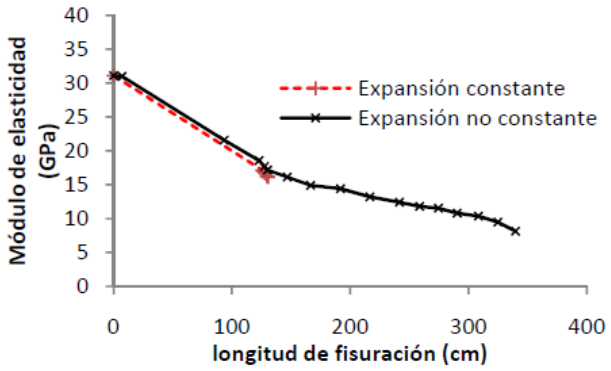

Figura 11. Variación del módulo de elasticidad con la longitud de fisuración.

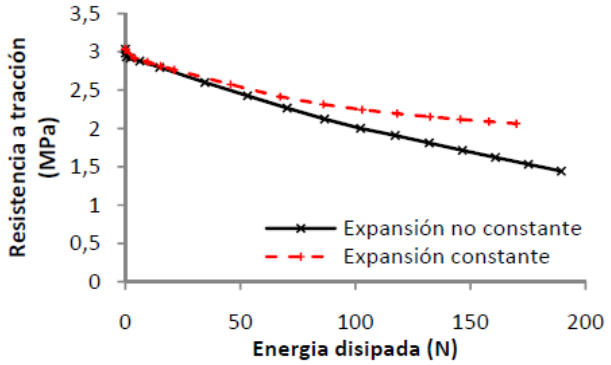

Figura 12. Variación de la resistencia a tracción con la energía disipada.

4. CONSIDERACIONES FINALES

Se ha empleado un modelo mesoestructural con elementos junta para estudiar la degradación de algunas propiedades mecánicas de un hormigón sometido a acciones expansivas internas. Los resultados numéricos obtenidos concuerdan en un alto grado con resultados experimentales realizados en un hormigón afectado por la formación tardía de etringita. Un aporte interesante de la modelización es que ha permitido relacionar el nivel de expansión con el grado de deterioro y microfisuración de la muestra, definido en términos de la longitud total de fisuración en las juntas que se ha visto que incide de forma determinante en la degradación del módulo de Young, y la energía disipada a lo largo de las juntas activadas que influye de manera directa sobre la disminución de la resistencia a tracción. Los trabajos en curso se orientan a profundizar estudios previos sobre expansiones del hormigón debidas al ataque sulfático interno originado por la oxidación de sulfuros de hierro contenidos en los áridos utilizados en algunas presas ubicadas en el Pirineo español.

AGRADECIMIENTOS

El trabajo se ha desarrollado en el marco de los convenios entre UPC y las empresas Endesa Generación S.A. e Iberdrola S.A (Proyecto Horex). Se hace constar la beca FPU (MEC) concedida al primer autor. El segundo autor agradece la ayuda recibida a través del proyecto BIA2009-10491 (MICINN).

REFERENCIAS

[1] Rocco, C., Giandrasso, F., Bergol, L., Di Pace, G., Planas, J., "Fracture properties of concrete exposure to delayed ettringite formation", *Proceedings of the 5th Int. Conference on fracture Mechanics of Concrete an Concrete Structures,* Vail, pag. 623-630, 2004.

[2] Aguado, A., Agulló, L., Casanova, I., López, C. M., "Estudio de fenómenos expansivos en presas de hormigón. De la micro a la macro estructura." *Comité Español de Grandes Presas*. *Premio Torán*, 103 p, 1998.

[3] Casanova, I., López, C.M., Aguado, A., Agulló, L., "Micro and mesoscale modeling of expansion in concrete dams". In Berga, L (Ed.), *Dam Safety*, Balkema, Rotterdam, pag. 661-667, 1998.

[4] López, C. M., "Análisis microestructural de la fractura del hormigón utilizando elementos finitos tipo junta. Aplicación a diferentes hormigones", *Tesis Doctoral, ETSECCPB, UPC*, Barcelona, 1999.

[5] Brunetaud, X., Divet, L., Damidot, D., "Impact of unrestrained delayed ettringite formation-induced expansion on concrete mechanical proprieties", *Cement and Concrete Research,* 38, pag. 1343-1348, 2008.

[6] Zhang, Z., Olek, J., Diamond, S., "Studies on delayed ettringite formation in early-age, heat-cured mortars I. Expansion measurements, changes in dynamic modulus of elasticity, and weight gains", *Cement and concrete Research*, 32, pag. 1729-1736, 2002.

[7] Larive, C., "Apport combinés de l'expérimentation et de la modélisation à la compréhension de l'alcali-réaction et ses effets mécaniques", *PhD, LCPC*, Paris, 1997.

[8] Capra, B., Sellier, A., "Orthotropic modeling of alkali-aggregate reaction in concrete structures: numerical simulations", *Mech. of Materials,* 35, pag 817-830, 2003.

[9] Jones A. E. K., Clark, L. A., "The effect os AS Ron the properties of concrete and implications for assessment", *Engineering Structures,* 20, pag. 785-791, 1998.

[10] Piasta, W. G., Schneider, U., "Deformations and elastic modulus of concrete under sustained compression and sulphate attack", *Cement and Concrete Research,*22, pag. 149-158, 1991.

[11] Glasser, F. P., "The stability of ettringite", *Int. RILEM TC 186-ISA Workshop on Internal Sulfate Attack and Delayed Ettringite Formation,* Villars, pag. 43-64, 2002.

[12] Carol, I., Prat, P. C., López, C.M. "A normal/shear cracking model. Application to discrete crack analysis", *J. Engng. Mech. ASCE*, 123, pag. 765–773, 1997.

[13] López, C. M., "Meso-structural study of concrete fracture using interface element. I: numerical model and tensile behavior". *Materials and Structures,* 41, nº3, pag. 583-599, 2008.

[14] López, C. M., Carol, I., Aguado, A., "Meso-structural study of concrete fracture using interface element II: compression, biaxial an Brazilian test". *Materials and Structures*, 41, nº3, pag. 601-620, 2008.

[15] Caballero, A., López, C.M., Carol, I., "3D meso-structural analysis of concrete specimens under uniaxial tensión". *Comput. Methods Appl. Mech. Engrg.,* 195, pag. 7182-7195, 2006.

Experimental methods

CONTROLLED FRACTURE TESTS OF BRITTLE CERAMICS

C. Baudín[1], A. García[1], J. Hernández[2], M. López[2]

[1] Instituto de Cerámica y Vidrio, CSIC
CSIC-Campus de Cantoblanco, Kelsen 5, 28049 Madrid, Spain
e-mail: cbaudin@icv.csic.es

[2] Microtest S.A.
Valle de Tobalina 10, 2801 Madrid, Spain
e-mail: mla@microtest-sa.com

ABSTRACT

Controlled fracture tests are required for the accurate determination of the toughness parameters of materials in order to assure the full conversion of the supplied energy into crack surface energy. From the three parameters involved in the test, load, displacement of the load frame and crack mouth opening displacement (CMOD), this latter is the only one that continuously increases as fracture proceeds. Therefore, the CMOD has been proposed as control variable for the stable fracture tests. In this work, a new equipment to perform stable fracture tests of ceramics controlled by the CMOD is presented. The developed equipment allows performing stable fracture tests of extremely brittle ceramics such as fine grained magnesium-aluminium spinel. The developed equipment is presented together with results obtained for fine grained ceramic using different experimental conditions.

KEY WORDS: ceramics, stable fracture, toughness

1. INTRODUCTION

Stable crack growth is necessary to get reliable and accurate fracture toughness data. If the fracture toughness values are determined from test configurations that do not allow stable crack growth, then the measurement have to be solely related to crack initiation [1]. In such cases, the calculated value of the fracture toughness may be over-evaluated. In addition to the conventional fracture toughness, stable fracture tests allow the determination of fracture energy and crack-growth resistance curves.

Controlled fracture tests for brittle materials as most ceramics are difficult to accomplish, therefore, they are not usually performed. The chevron notched geometry allows reaching stable fracture in brittle specimens using the displacement of the loading frame as control parameter [2] but specimens are difficult to fabricate especially for fine grained materials. For other geometries such as straight notch beams in flexure and load frame displacement controlled tests, stable fracture is only reached for materials with some extent of R curve behaviour [3-4]. The load frame displacement should decrease after the peak load for stable testing of brittle materials.

The crack mouth opening displacement (CMOD) is the only parameter which increases throughout the whole test. CMOD controlled stable fracture tests have been reported for advanced ceramics with R-curve behaviour such as yttria-partially-stabilized zirconia [5] but not for extremely brittle ceramics such as fine grained magnesium-aluminium spinel. Such kind of tests is performed using specific experimental laboratory set ups.

In this work, a new equipment to perform stable fracture tests of ceramics controlled by the crack mouth opening displacement (CMOD) is presented.

2. EQUIPMENT

2.1 Loading device

The MICROTEST EM1/50 (Figure 1) is a single screw, dual column, servo-controlled electromechanical test machine. Electromechanical or universal testing machines are most commonly used for static testing in a tensile or compression mode within a single frame. The control is performed by an electronic system that generates the control signal to make the actuator move the crosshead in an upward or downward direction via a drive system. The different test set ups are placed between the rigid frame (stiffness $< 2.10^8$ N/m) and the moving crosshead.

The maximum load range is 50kN, both tension and compression. The displacement range is 0-100mm and the maximum speed is 100mm/min. The actual applied loads are measured by extensometric load cells mounted

in the line of force application. The displacement of the moving crosshead can be controlled and measured by means of an optical encoder placed in the motor axis.

The SCM3000 electronic controller includes load and position channels as well as position auxiliary ones with the option to add additional strain channels for extensometers. In this case, the signal from the contactless optical measurement system for CMOD determination is directed to one of these auxiliary channels. Therefore, the control parameters can be not only force and displacement but also CMOD.

Figure 1. Test machine MICROTEST EM1/50 with the experimental set up.

The test specimen is placed between the rigid frame and the moving crosshead in a stainless steel three points bending test fixture with a span of 40 mm (Figs. 1-2) with a load cell of 5KN. This load cell was selected to assure high stiffness of the loading setup. The stiffness of the machine, load cell, and supports arrangement was determined experimentally using an uncracked alumina bar (4mm x 6mm x 50mm); the obtained values were $1.6x10^6$ N/m up to 20N and $1.7x10^7$ N/m up to 150N.

2.2 Crack mouth opening displacement measurement unit.

For the CMOD measurement and control, a high precision optical micrometer KEYENCE LS7010 is used (Figures 1 and 2). This optical system provides a measurement accuracy of ± 0.5μm and repeatability of ± 0.06μm. The measurement range of this optical system goes from 0.04mm to 6mm. The equipment carries out a continuous measurement, averaging up to 2400 samples/s, and so very stable readings are obtained.

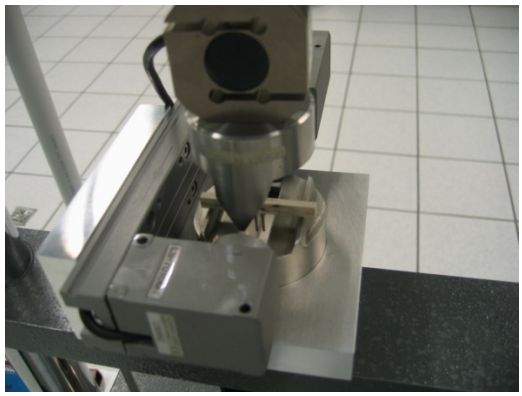

Figure 2. Detail of the three point bending device with the optical micrometer.

The principle of measurement of the optical system is as follows (Figure 3). A high-intensity GaN green LED radiates light, which is changed into uniform parallel light through the special diffusion unit and collimator lens and emitted to the target in the measuring range. This parallel beam "illuminates" measurement area. Then the shadow image of the target appears on the HL-CCD (high-speed linear CCD) through the telecentric optical system. With the telecentric system of lenses the size of the image on the CCD does not change even if it moves, thus, the same precision all along is maintained

The output incident signal of the HL-CCD (charge coupled device) is processed by the DE processor (by means of a digital edge-detection algorithm) in the controller and CPU. The detection threshold is an adjustable parameter. As final result, it is possible to obtain the separation between two pins such as those used, as described below.

The measuring head incorporates a CMOS (complementary metal oxide semiconductor) camera to capture real-time image of the target.

The controller of the optical system incorporates a function of elimination of abnormal values, to improve the precision of the measurement. This function ignores the abnormal values exceeding a preset value to prevent malfunctions caused by dust or other irrelevant factors. Figure 3 shows other interfaces not used in the present setup (RS-232C input/output, 2 channel BCD output, 2 I/O channels, and 2 analog output channels).

2.3 Setup

The optical micrometer is attached to the lower loading support; in this way the mechanical interferences are avoided and a correct orientation of the light beam with respect to the axis of load and the bending fixture is assured.

Given the small opening displacement of the notch, in order to be able to detect and measure its width during the test (the size of detectable minimum object by the system is of 0.04mm), pins of 1.5mm in diameter and 12mm length are adhered to both sides of the notch so that they are perpendicular to the light beam. In this way the equipment detects the edges of these elements giving the straightforward values of CMOD variations.

The analog output signal from the optical device is connected to the control and measurement system SCM3000 of the electromechanical MICROTEST testing machine, so the CMOD can serve as control variable during the test. This allows performing fracture tests at constant CMOD rate.

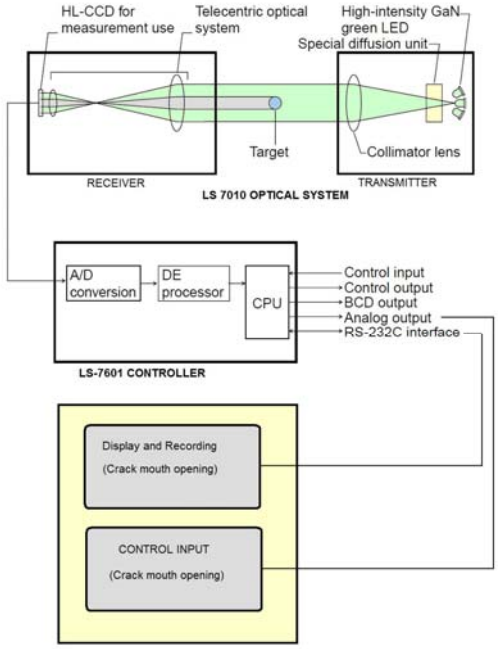

Figure 3. SCM 3000 system

The analog channel in the SCM3000 electronics receives the CMOD. The 16 bits A/D converter in the SM3000 system converts the continuous CMOD analog signal to discrete digital numbers proportional to the magnitude of the voltage of this signal. The whole output analog range corresponds with the measurement range of the optical micrometer (6mm) and this is converted in 2^{16} levels (65536 values). That means that a theoretical resolution of 0.1µm is obtained for this maximum range. In order to reach the highest accuracy the tests were performed at 20 ºC, with a separation between edges of pins bonded to the sides of the crack of about 1mm. The repeating accuracy of the optical micrometer for this separation was checked to be ± 0.06µm with 1.0 mm-diameter round bar located in the centre of the measuring area.

The output analog range of the optical micrometer selected by this test is ±50µm that corresponds with the scaling value of 5 µm/V. That means that a theoretical resolution of about 0.02µm is obtained. This converted signal is used to control the CMOD rate by the microprocessor in the SCM3000 system. The process makes use of a PID algorithm with adjusted parameters to perform and maintain the desired CMOD speed during the test. The equipment carries out a continuous measurement of the value average of 512 samples/s, and so a very stable reading of the separation of the edges of the crack mouth is obtained.

The motor driver uses the control signal from the SCM3000 system to generate the suitable current that operates over the motor to adjust the CMOD rate. The measurement of the CMOD by the LS7010 allows the control loop to be closed (Fig. 3).

3. SPECIMEN PREPARATION

A fine grained magnesium-aluminium spinel labelled SP, with density of 3.46 ± 0.03g/cm^3 and Young's Modulus of 251 ± 13GPa, was prepared from a commercial spinel $MgO.Al_2O_3$ powder and sintered at 1750ºC for 2h [6].

Single Edge V-Notch Beams (SEVNB) of 4mm x 6mm x 50mm were diamond machined. The notch was initially cut with a 300 µm wide diamond wheel. Using this pre-notch as a guide, the remaining part of the notch was done with a 150 µm wide razor blade sprinkled with diamond pastes of successively 15 and 6µm. Tip radii of about 25 µm were obtained (Fig. 4). The relative notch length, a/D (a=notch length, D=width of the specimen), was 0.64.

One cylindrical steel pin was glued at each side of the notch. The diameter of the pins was 1.5 mm and the length was 12 mm.

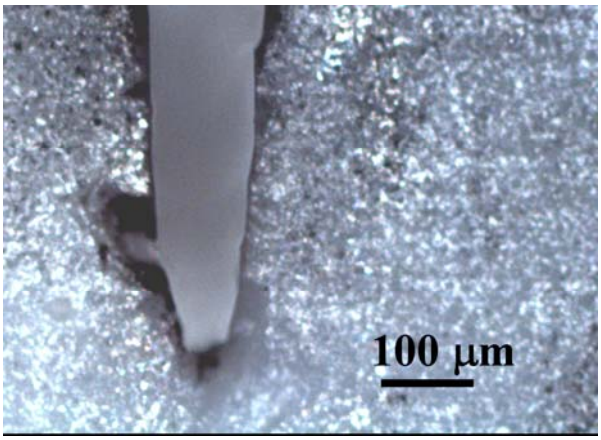

Figure 4. Notch for SP specimens. The black coloration of the tip corresponds to the diamond used.

4. TESTS AND DATA ANALYSIS

Figures 5 and 6 show the CMOD-time plots corresponding to tests performed at different constant CMOD rates.

The programmed CMOD rates were reached in all cases. Variations of less than about, 0.02 μm were obtained in all cases, demonstrating the very stable reading of the separation of the CMOD obtained.

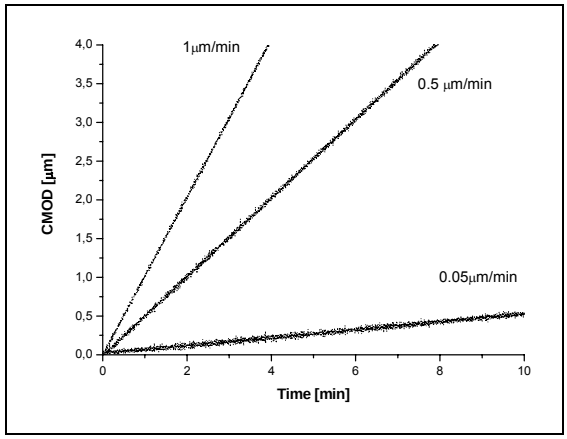

Figure 5. CMOD-time for tests performed at three different CMOD rates.

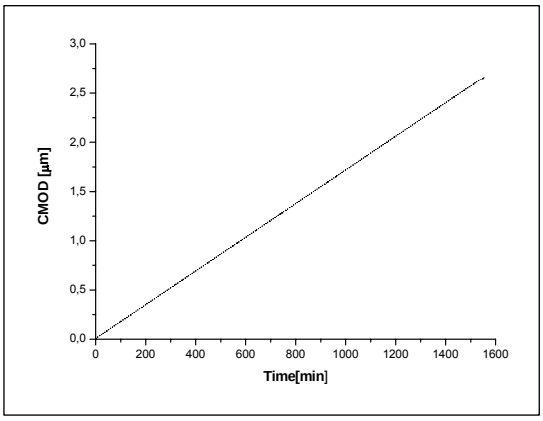

Figure 6. CMOD-time curve for SP tested at 0.1 μm/min.

Figure 7 is characteristic of a setup leading to stable tests in CMOD control. It increases throughout of the whole test.

Figure 8 shows the load-displacement curve corresponding to the tests of figures 6 and 7. From the maximum load, decreases in the displacements are needed to reach stable tests.

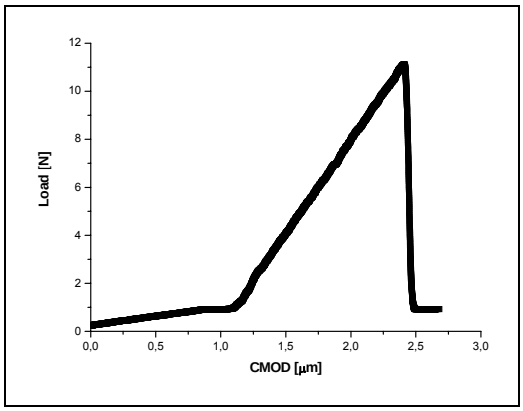

Figure 7: Load-CMOD plot.

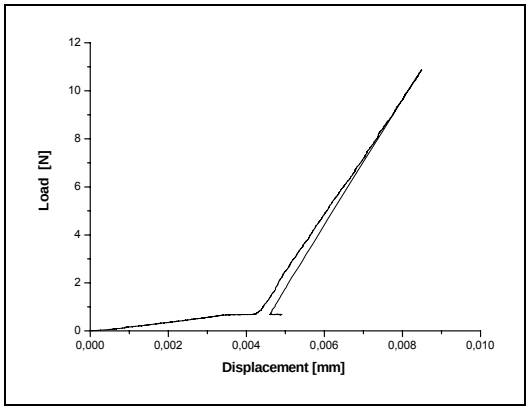

Figure 8: Load-displacement plot.

Using the stiffness values determined for maximum loads lower than 20N, the properties of the material and the analysis in ref [7], stable fracture tests could not be obtained under displacement control for this spinel. On the contrary, stable fracture tests have been possible for specimens with relative notches of about 0.64 using CMOD control.

The CMOD for a general three point bend specimen, can be derived by superposing the solution for a reference beam with fixed L/D ratio (=4) and the solution for pure bending in adequate proportions so as to give the same law of bending moments over the central part [8]. General expressions have been determined for the CMOD and its inverse function, giving the crack length as a function of CMOD, equations (1), (2) and (3). These expressions are valid for any crack length and for span-to-depth ratios larger than 2.5.

$$\alpha = \frac{\gamma^{3/3} + m_1(\beta)\gamma}{[\gamma^2 + m_2(\beta)\gamma^{3/2} + m_3(\beta)\gamma + m_4(\beta)]^{3/4}} \quad (1)$$

where γ is given by

$$\gamma = \frac{w_M BE'}{6P} \tag{2}$$

and

$$\begin{aligned} m_1(\beta) &= \beta(0.25 - 0.0505\beta^{1/2} + 0.0033\beta) \\ m_2(\beta) &= \beta^{1/2}(1.155 - 0.215\beta^{1/2} + 0.0278\beta) \\ m_3(\beta) &= -1.38 + 1.75\beta \\ m_4(\beta) &= 0.506 - 1.057\beta + 0.888\beta^2 \end{aligned} \tag{3}$$

For three-point-bend beams, the values of K_{IC} can be determined from the notch depths and the maximum loads reached in the tests according to a general expression, equation (4), for the stress intensity factor , valid for any value of the crack-to-depth ratio ($0 \le \alpha \le 1$) and span-to-depth ratios larger than 2.5 ($2.5 \le \beta \le 16$):

$$\begin{aligned} K_I / K_0 (\alpha, \beta) &= \frac{p_\infty(\alpha) + 4/\beta[p_4(\alpha) - p_\infty(\alpha)]}{(1-\alpha)^{3/2}(1+3\alpha)\sqrt{\pi}} \\ K_0 &= \frac{3LP}{2BD^2}\sqrt{\pi a} \end{aligned} \tag{4}$$

where w_M is the crack opening displacement, L is the span, P is the maximum load, B and D are the width and the depth of the bars, , a is the crack length, α is the crack-to-depth ratio (α = a/D), β is the span-to-depth ratio (β = L /D).

The $p_4(\alpha)$ and $p_\infty(\alpha)$ given by equations (5) and (6) are cubic polynomial for β = 4 and β = ∞ (formally equivalent to pure bending).

$$p_4(\alpha) = 1.9 + 0.41\alpha + 0.51\alpha^2 - 0.17\alpha^3 \tag{5}$$

$$p_\infty(\alpha) = 1.99 + 0.83\alpha - 0.31\alpha^2 + 0.14\alpha^3 \tag{6}$$

The fracture toughness value, K_{IC}, was calculated using the general expression of the stress intensity factor (eq. 4) and the value of the maximum load attained during the test. The onset of crack propagation was considered in the peak load. The value of K_{IC} obtained was 1.4 MPa $m^{1/2}$. It was 50% lower than the value determined in unstable tests (≈3 MPam$^{1/2}$ [6]).

From K_{IC} and Young`s modulus, G_{IC}, can be calculated according to the analysis of Irwin that relates the stress-derived fracture toughness (K_{IC}) and the energy-derived fracture toughness (G_{IC}) for plane strain conditions [4]:

$$G_{IC} = \frac{K^2_{IC}}{E'} \tag{7}$$

where $E' = E/(1-\nu^2)$ is the generalized Young´s modulus for plane strain (E is the Young´s modulus and ν is the Poisson´s ratio). The value of G_{IC} obtained was 7.5 J/m^2

6. CONCLUSIONS

An experimental device to perform stable fracture tests of ceramics by controlling the CMOD has been developed. Stable fracture tests for extremely brittle ceramics such as a fine grained magnesium-aluminium spinel have been performed using this device. A toughness value is about 50% lower than ref. [6].

ACKNOWLEDGEMENTS

Projects: MEC MAT2006-13480 C02 and MCI-PET 2008-0113

REFERENCES

[1] B.F. Sorensen , A. Horsewell, O. Jorgensen and A.N. Kumar, "Fracture Resistance Measurement Method for in situ Observation of Crack Mechanisms", *J. Am. Ceram. Soc.*, 1998, 81, [3], 661-69.

[2] A. Ghosh, M.G. Jenkins, K.W. White, A.S. Kobayashi and R.C. Bradt, "Elevated-Temperature Fracture Resistance of a Sintered α-Silicon Carbide", *J. Am.Ceram. Soc.,* 1989, 7, [2], 242-247.

[3] H. Wieninger, K. Kromp and R.F. Pabst, "Crack resistance curves of alumina and zirconia at room temperature", *J. Mat. Sci.,* 1986, 21, 411-418.

[4] S. Bueno, M.H. Berger, R. Moreno and C. Baudín, "Fracture behaviour of microcrack-free alumina-aluminium titanate ceramics with second phase nanoparticles at alumina grain boundaries", *J. Eur. Ceram. Soc*, 2008, 28, 1961-1971.

[5] J.Y. Pastor, J. Planas and M. Elices, "Ambient and High-Temperature Stable Fracture Tests in Ceramics: Applications to Yttria-Partially-Stabilized Zirconia", *J. Am. Ceram. Soc*, 1993, 76 [11], 2927-29.

[6] C. Baudín, R. Martinez and P. Pena, "High-Temperature Mechanical Behaviour of Stechiometric Magnesium Spinel", *J .Am. Ceram. Soci*.,1995, 78 [7], 1857-62.

[7] I. Bar-On, F. I. Baratta and K. Cho, "Crack Stability and Its Effect on Fracture Toughness of Hot-Pressed Silicon Nitride Beam Specimens", *J. Am. Ceram. Soc*., 1996, 79 [9], 2300-308.

[8] G.V. Guinea, J.Y. Pastor, J. Planas and M. Elices, " Stress intensity factor, compliance and CMOD for a general three-point-bend beam", *Int. J. Fract*., 1998, 89, 103-116.

APLICACIÓN DE LA TOMOGRAFÍA AXIAL COMPUTERIZADA AL ESTUDIO DE MATERIALES Y PIEZAS FABRICADAS

P. M. Bravo[1], J. M. Alegre[1], I. I. Cuesta[1], M. Preciado[1]

[1] Departamento de Ingeniería Civil, Escuela Politécnica Superior,
Universidad de Burgos C/Villadiego s/n 09001 Burgos, Spain
Email: pmbravo@ubu.es

RESUMEN

La tomografía axial computerizada es una técnica que permite el análisis no destructivo de piezas y materiales en todo su volumen.
En general, es una técnica que genera una imagen de una sección delgada transversal de una pieza. El haz de energía habitualmente de Rayos X y el detector están en el mismo plano que la superficie de la que se va a obtener la imagen. La señal del detector se obtiene mientras la muestra gira en el eje perpendicular al plano considerado. Mediante un procedimiento de cómputo se calcula y representa la atenuación relativa de la energía del haz que pasa a través de las estructuras de la sección delgada de la pieza.
La imagen de TC representa punto a punto los coeficientes de atenuación lineal en la sección, que dependen de la densidad del material, del número atómico efectivo del material y de la energía del haz de rayos X.
Posteriormente las imágenes de TC pueden ser procesadas mediante programas de análisis de imagen plana o tridimensional. Se puede utilizar un conjunto de imágenes de TC para caracterizar el volumen de la pieza, geometría, porosidad, fases materiales, grietas.
En el presente trabajo se presenta la aplicación de esta técnica a diferentes tipos de estudios:

- Determinación de porcentajes de fases minerales en materiales pétreos.
- Obtención de mapas de porosidad en piezas de inyección de aleaciones de magnesio o aluminio.
- Estudio de grietas en probetas de hormigón ensayadas a fatiga.
- Extracción de superficies para un análisis geométrico detallado o su mallado mediante programas de elementos finitos.
- Medida de geometrías sobre el volumen extraído.
- Comparación entre geometría teórica y real de piezas fabricadas.
- Separación de piezas, materiales o partes de materiales de diferente densidad.

En estos trabajos se ha utilizado el tomógrafo instalado en la Universidad de Burgos de la marca YXLON y el programa de análisis de imagen tridimensional VGStudio MAX.
La aplicación de esta técnica es de gran interés para diferentes tipos de estudios no solo en el campo de aplicación industrial sino también en investigación y permite obtener información mas detallada, de forma menos costosa o a veces imposible de obtener por otros medios.

PALABRAS CALVE: Tomografía axial computerizada, análisis de imagen, medida de porosidad, obtención de superficies.

ABSTRACT

Computed tomography CT is a technique that allows non-destructive analysis of parts and materials throughout its volume.
This technique generates an image of a transverse thin section of a piece. The X-ray energy beam and detector are in the same plane as the surface of the obtained picture. The detector signal is collected while the sample rotates in the axis perpendicular to the plane considered. The relative attenuation of the beam energy passing through the structures of the thin section of the piece is calculated and represented using a computational procedure.
The CT image represents point by point the linear attenuation coefficients in the section, which depend on the density of the material, the effective atomic number of material and the X-ray beam energy.
Then the CT images can be processed using an image analysis software bi- or three-dimensional. A set of CT images can be used to characterize the sample volume, geometry, porosity, material phases, and cracks.
This paper presents the application of this technique to different types of studies:

- Determination of percentages and distribution of mineral phases in stone materials.
- Obtaining maps of porosity injection parts made of magnesium or aluminium alloys.

- Study of cracks in concrete specimens tested in fatigue.
- Extraction of surfaces for a detailed geometric analysis or meshing with finite element programs.
- Measure the volume extracted geometries.
- Comparison between theoretical and real geometry of produced parts.
- Separation of parts, materials or parts of materials with different densities.

The CT installed at the University of Burgos (YXLON brand) and the three-dimensional image analysis software VGstudio MAX have been used in this work.
The application of this technique is of great interest for different types of studies, not only in the field of industrial application but also in research. It allows obtaining more detailed information, less expensive or sometimes impossible to obtain by other means.

KEY WORDS: Computed tomography, image analysis, porosity measurement, surface extraction.

1. INTRODUCCIÓN

La tomografía industrial computerizada puede ser una herramienta de gran ayuda para el investigador o el ingeniero a la hora de caracterizar o simular el comportamiento mecánico de materiales y piezas.

Las propiedades mecánicas de los materiales y de los diseños fabricados con ellos dependen directamente de su estructura, de su composición y de los defectos inducidos por el proceso de fabricación.

Si se quieren introducir modelos micromecánicos basados en la distribución de fases cristalinas o minerales, en la distribución de porosidad, o en la distribución del refuerzo en un material compuesto es necesario obtener un mapa de distribución que permita obtener los datos suficientes para aplicar los correspondientes modelos.[1],[5]

Habitualmente se requiere la utilización de técnicas destructivas para la aplicación de cortes que permitan la posterior aplicación de un modelo estadístico.

Desde el punto de vista de inspección y control de calidad esta técnica permite obtener un mapa de porosidad de toda la pieza analizada pudiendo observarse su distribución espacial dentro de la pieza y la medida del tamaño de los diferentes poros observados. Desde el punto de vista dimensional se puede, previa calibración, realizar medidas directamente sobre la imagen de la pieza tomografiaza.[7]

Si lo que se pretende es realizar una simulación, la obtención de la geometría de la pieza mediante la extracción de superficies puede ser de gran ayuda a la hora de mallar un modelo en 3D. También puede ser viable la introducción de la distribución de porosidad de la pieza tomografiaza con la finalidad de observar su influencia. [2]

2. TOMOGRAFIA INDUSTRIAL COMPUTERIZADA DE RAYOS X

La tomografía computerizada (TC) es una técnica que genera imágenes de secciones transversales de una pieza. Esta técnica difiere de la radiografía en que el haz de energía y el detector están en el mismo plano que la superficie de la que se va a obtener la imagen.

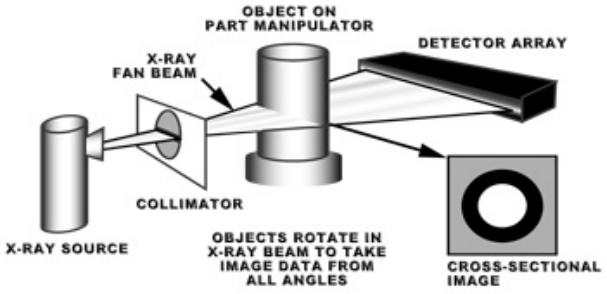

Figura 1. Esquema de la tomografía computerizada.

Esta técnica genera las imágenes a partir de la señal de atenuación del haz obtenida para diferentes ángulos de proyección de la sección considerada. La atenuación que sufre el haz está directamente relacionada con la densidad, el espesor atravesado y la composición del material así como la energía del haz de rayos X.

La TC utiliza esta información obtenida desde diferentes ángulos para determinar la configuración de la sección transversal con ayuda de un algoritmo de reconstrucción. De esta manera se determina cuantitativamente la distribución punto a punto de los coeficientes de atenuación. La imagen de la sección se puede visualizar asignando un nivel en una escala de grises a cada valor de atenuación.

Posteriormente las imágenes pueden ser procesadas mediante programas de análisis de imagen plana o tridimensional. Se puede utilizar un conjunto de imágenes de TC para caracterizar el volumen total de la pieza.

Con los datos transformados se pueden representar planos a través de la pieza, superficies tridimensionales o estructuras dentro de la misma [7].
Partiendo de la misma calidad de imagen de TC será el potencial del sistema de análisis de imagen el que nos permita obtener mayor o menor rendimiento.
También la habilidad del analista permitirá alcanzar mejores resultados.

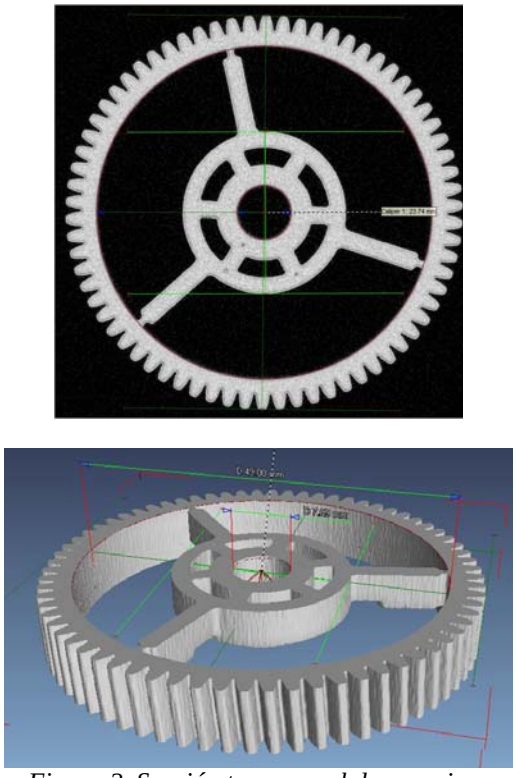

Figura 2. Sección transversal de una pieza tomografiaza y su reconstrucción 3D.

Habitualmente las limitaciones de los equipos de TC vienen derivadas de los siguientes puntos:

1. Tamaño del manipulador y por lo tanto de la pieza que se puede introducir.
2. Capacidad de penetración del haz de RX. Depende del material de la pieza y de la potencia del tubo de RX del equipo utilizado.
3. Resolución del sistema. Depende del sistema de detección del equipo, del tamaño del foco del tubo de RX, del número de proyecciones y de los algoritmos de reconstrucción de la imagen.

3. LAS IMÁGENES

El proceso de reconstrucción da lugar a una matriz bidimensional de números que corresponden a la sección transversal del objeto. Cada número es un punto (píxel) de la imagen.

El valor de cada píxel es proporcional al coeficiente de atenuación lineal medio en el correspondiente volumen (voxel). El coeficiente de atenuación lineal es aproximadamente proporcional a la densidad del material y es función del número atómico efectivo del material y de la distribución del espectro del haz de rayos X.

Para permitir la interpretación de la información contenida en la matriz de datos, esta información es representada como una imagen.

Las imagines de TC son mucho más fáciles de interpretar que las imágenes radiográficas convencionales porque los detalles de la imagen no se superponen. Se puede identificar la posición concreta de cada detalle.

Además, las diferencias de densidad dentro del objeto son fácilmente identificables y cuantificables y pueden ser relacionadas con características deseables o no deseables del objeto o material analizado.

Los parámetros de funcionamiento como es el espesor de la sección (distancia entre secciones) o los tiempos de recogida de datos pueden ser ajustados para obtener la combinación más adecuada entre tiempo de inspección y calidad de la imagen.

La capacidad de la tomografía computerizada para mostrar determinadas características variara con el equipo utilizado y los parámetros utilizados.

Suponiendo unas condiciones adecuadas se pueden hacer algunas consideraciones sobre la idoneidad del método para la observación de varios tipos de defectos:

- Huecos e inclusiones. Observar las figuras 2 y 3. Son defectos fácilmente detectables y de alto contraste. Defectos de menor tamaño que la resolución del sistema se pueden observar pero con menos contraste respecto del material base.
- Porosidad y microrechupes como los de la Figura 4. Reducen la densidad del material y son visibles si están distribuidos sobre un área con muchos pixels. El porcentaje de porosidad puede cuantificarse con procedimientos controlados.

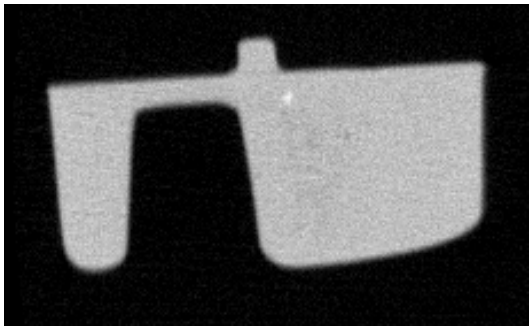

Figura 3. Inclusión en una sección de una pieza tomografiada.

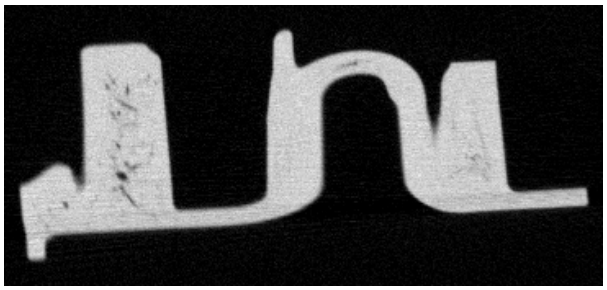

Figura 4. Porosidad visible en una sección de una pieza tomografiada

- Densidad relativa entre materiales con el mismo número atómico efectivo.

- Grietas abiertas o desplazadas como las de la Figura 5. Se pueden detectar. Como en los poros, la separación de la grieta puede estar por debajo de la resolución del sistema. El contraste disminuirá al reducir la apertura de la grieta.

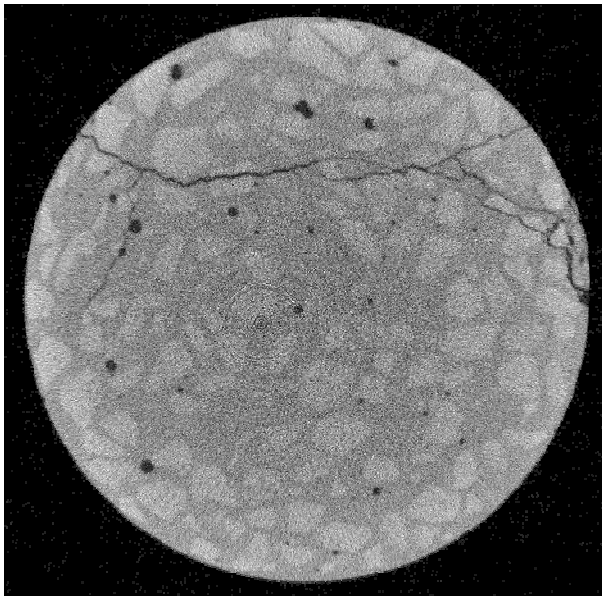

Figura 5. Grieta en una probeta de hormigón ensayada. Se puede observar la distribución del árido grueso y el camino que ha seguido la grieta.

- Despegues y delaminaciones en materiales compuestos son detectables si están suficientemente separadas. La orientación similar de las estructuras del material puede dificultar aun más su detección. [4]

- Material residual en las fundiciones se ve fácilmente en el material en masa. Las capas delgadas superficiales pueden ser difíciles de detectar tal como se observa en la figura 6.

- Los defectos de mecanizado como el sobre-taladrado o los defectos de ensamblaje se pueden ver fácilmente.

4. ANALISIS DE IMAGEN 2D Y 3D.

4.1. Reconstrucción 3D

Para transformar el conjunto de imágenes obtenidas en el equipo de TC en un volumen 3D se ha de utilizar un programa de análisis de imagen tridimensional. Las imágenes presentadas en el presente trabajo han sido obtenidas mediante el programa VGStudioMax 2.0.

Cuando se importan las imágenes se indica el tamaño del pixel y la distancia entre cortes de manera que el volumen reconstruido tenga las dimensiones correctas.
Se ha de asignar además el tamaño de la escala de grises que se quiere utilizar para representar los datos de las secciones.

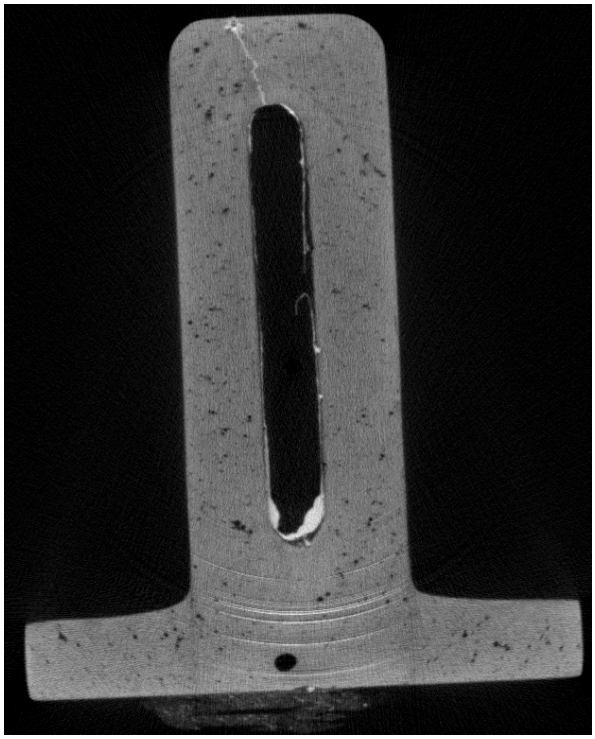

Figura 6. Sección de una pieza de cerámica con restos de fundición de aluminio. Se observa porosidad y una grieta rellena de fundición de aluminio.

La calibración de las imágenes en cuanto a los rangos de la escala de grises que corresponden al material o materiales y al fondo de las imágenes permite determinar la superficie de la pieza como una iso-superficie en la escala de grises. Este paso es fundamental ya que todos los análisis posteriores se basan en esta calibración.

4.2. Medidas geométricas en 2D y 3D.

Apoyándonos en esta superficie y utilizando las herramientas disponibles en el programa de análisis se pueden definir elementos geométricos auxiliares (puntos, planos, rectas, cilindros, conos) que nos permitan definir ejes de referencia y realizar medidas

geométricas (ángulos, distancias, radios, espesores. ver figura 7).

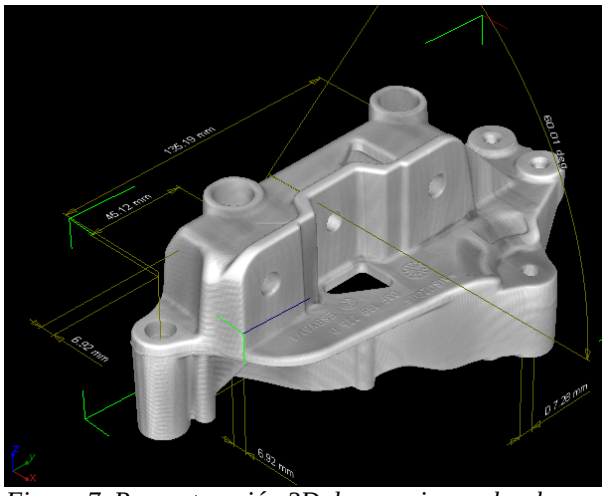

Figura 7. Reconstrucción 3D de una pieza sobre la que se han realizado diferentes medidas.

4.3. Análisis de porosidad.

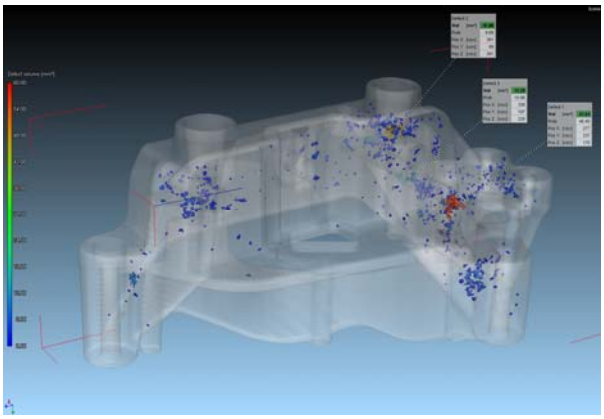

Figura 8. Vista 3D de la distribución de porosidad en una pieza inyectada.

La determinación de la porosidad se basa en la calibración inicial realizada. Esta calibración permite determinar aquellas zonas que no están dentro del rango de densidades (niveles de gris) que corresponden al material y que por lo tanto pueden considerarse como poros. Estas zonas tienen que estar dentro del volumen delimitado por la superficie de la pieza que es la región de interés considerada. Si realizamos esta selección a partir del histograma podremos obtener el volumen total de porosidad. En la figura 8 se puede observar un análisis de porosidad de este tipo sobre una pieza de magnesio inyectada.

El programa utilizado en este trabajo dispone de una subrutina específica que determina la conectividad de los diferentes puntos considerados como porosidad y delimita la extensión de cada poro, su volumen y su posición.

Este mismo resultado se podría obtener manualmente utilizando herramientas disponibles que permiten seleccionar áreas crecientes a partir de un punto en función del rango de grises considerado y realizando este trabajo para cada uno de los poros. Generando una región de interés para cada poro. A partir de ahí obtener todos los datos necesarios. Evidentemente este trabajo es mucho más costoso.

4.4. Extracción de superficies.

Desde el punto de vista del análisis estructural se pueden extraer superficies a partir de la calibración realizada para posteriormente mallar el volumen interior y realizar los análisis que se consideren necesarios mediante el programa de calculo (MEF) correspondiente.

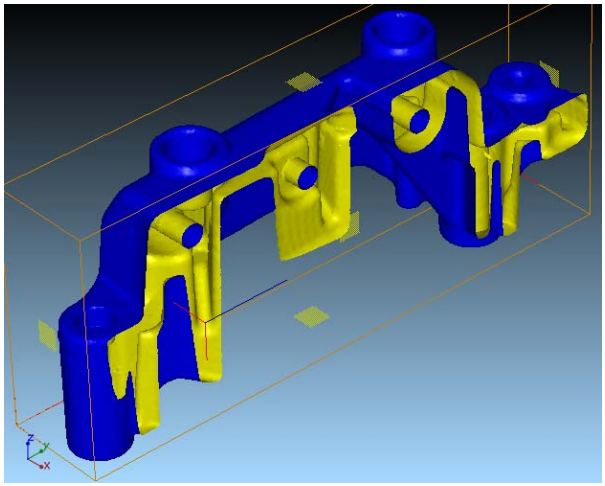

Figura 9. Superficie extraída de la pieza 3D calibrada. Sección según el plano YZ

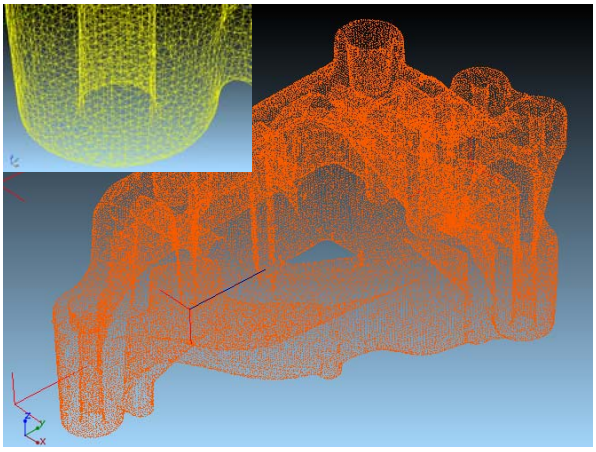

Figura 10.Nube de puntos de la superficie de la pieza. Detalle de la malla triangulada generada.

La presencia de porosidad se puede tener en cuenta de dos maneras distintas:

1. Generando las superficies de los poros dentro del volumen de la pieza. Este método es adecuado para poros de tamaño grande.
2. Seleccionando zonas de micro-porosidad con diferente nivel en la escala de grises y

asignando a estas zonas diferentes propiedades mecánicas.

4.5. Separación de zonas con diferente absorción.

Este tipo de separación es factible cuando se pueden observar partes de una pieza o de un material con densidades suficientemente diferenciadas en la escala de grises.

En estos casos se pueden extraer los volúmenes y las geometrías de las diferentes partes (fases minerales, componentes de una pieza, etc.) como se puede ver en las imágenes de la figura 11.

En estos casos las operaciones (sustracción, adición) realizadas con las diferentes regiones de interés permiten obtener modelos complejos que se pueden exportar a programas de cálculo o de diseño.

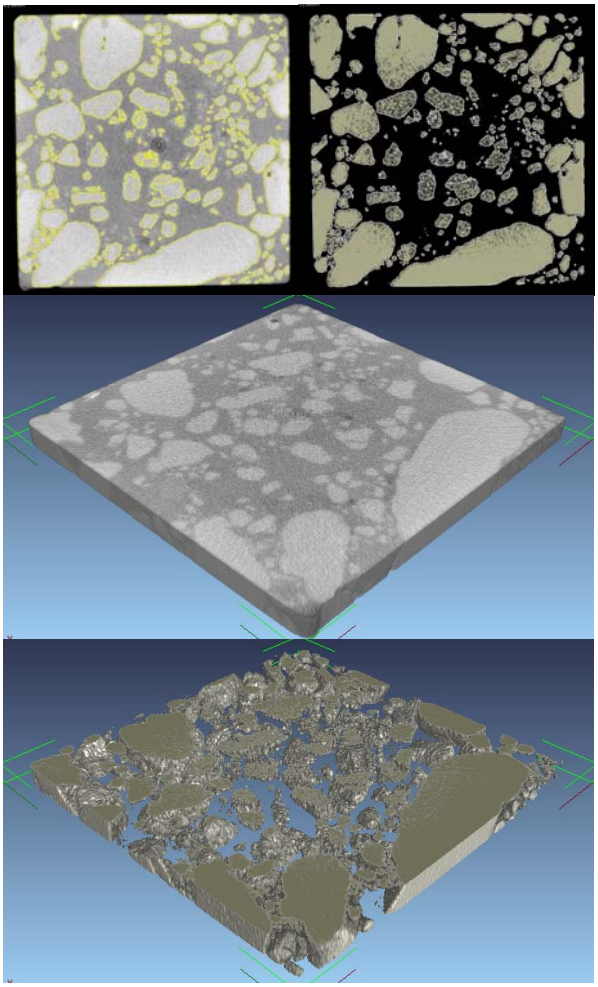

Figura 11. Separación de fases minerales de una piedra.

5. CONCLUSIONES.

La tomografía axial computerizada de rayos X es una técnica disponible con un grado desarrollo importante que permite su aplicación en es campo de los materiales y el estudio estructural de piezas.

Una parte importante de su aplicabilidad depende del uso de programas de análisis de imagen con herramientas adecuadas. Sin ellas no se podría obtener un rendimiento elevado.

Las principales limitaciones que tiene esta técnica dependen del equipo de tomografía en cuanto a sus prestaciones del tamaño máximo de la pieza, capacidad de penetración del haz de rayos X, resolución y calidad de la imagen. Dependiendo de la resolución necesaria se deberán utilizar los equipos de tomografía o microtomografía adecuados.

La posibilidad o no de aplicación de esta técnica a un determinado tipo de estudio dependerá directamente

REFERENCES

[1] H. A. Crostack, et al., "*Analysis of the material behaviour of metal-matrix composites under tension by synchrotron radiation based microtomography and FE-calculations*," Developments in X-Ray Tomography Iv, vol. 5535, pp. 493-504, 2004.

[2] J. P. Weiler and J. T. Wood, "*Modeling fracture properties in a die-cast AM60B magnesium alloy II-The effects of the size and location of porosity determined using finite element simulations*," Materials Science and Engineering a-Structural Materials Properties Microstructure and Processing, vol. 527, pp. 32-37, 2009.

[3] W. Y. Jang and S. Kyriakides, "*On the crushing of aluminum open-cell foams: Part II analysis*," International Journal of Solids and Structures, vol. 46, pp. 635-650, 2009.

[4] C. C. Tsao and H. Hocheng, "*Computerized tomography and C-Scan for measuring delamination in the drilling of composite materials using various drills*," International Journal of Machine Tools & Manufacture, vol. 45, pp. 1282-1287, 2005.

[5] Z. P. You and Q. L. Dai, "*Dynamic complex modulus predictions of hot-mix asphalt using a micromechanical-based finite element model*," Canadian Journal of Civil Engineering, vol. 34, pp. 1519-1528, 2007.

[6] ASM Handbook vol. 17. Non-destructive Evaluation and Quality Control. Metals Park,Ohio: ASM International, 1996

[7] VGstudioMax v2.0 Manual.

INFLUENCIA DE DIFERENTES VARIABLES DEL ENSAYO DE TRACCIÓN EN LA DEFORMACIÓN DE ROTURA

D. A. Cendón, J. M. Atienza y M. Elices

Departamento de Ciencia de Materiales, E.T.S. de Ingenieros de Caminos,
Canales y Puertos, Universidad Politécnica de Madrid, C/ Profesor Aranguren s/n,
28040 Madrid, España.
E-mail: dcendon@mater.upm.es

RESUMEN

Entender hasta qué punto la deformación de rotura es una propiedad del material resulta fundamental para estudiar cómo rompen los materiales y, especialmente, para poder realizar simulaciones representativas de los procesos que se están produciendo durante la rotura y establecer criterios que nos permitan predecirla. En este trabajo se ha estudiado la deformación de rotura obtenida en el ensayo de tracción de probetas planas de diferentes espesores. Para ello se ha realizado una campaña experimental de ensayos de tracción extensamente instrumentados sobre acero perlítico. Mediante un sistema de extensometría óptica se han obtenido los mapas de deformación en la superficie de las probetas durante todo el ensayo. Paralelamente, se han realizado simulaciones numéricas encaminadas a reproducir los ensayos con la mayor fidelidad posible. Se ha estudiado la influencia de la sección inicial y la base de medida del extensómetro en la deformación y la forma de rotura y en la dispersión de los resultados. Las simulaciones numéricas han permitido, además, caracterizar la triaxialidad de las diferentes probetas en el momento de rotura.

ABSTRACT

Strain localisation, necking and fracture phenomena during a tensile test are far from being completely understood. At present, advanced experimental techniques are available to allow measuring the strain localization phenomena during a tensile test. In this work, strain localisation and failure of steel specimens subjected to uniaxial tension is investigated. Rectangular specimens with different thicknesses of pearlitic steel were tested. Strain maps of the specimen surfaces during the whole tensile test were obtained using an optical extensometer. Detailed finite element simulations of the tests were conducted. The influence of different variables, like the area of the specimens, the length of the extensometer or the triaxiality, on the form of rupture and the strain at rupture have been discussed

KEY WORDS: uniaxial tensile test, ductile failure, failure criteria, stress triaxiality.

1. INTRODUCCION

El ensayo de tracción es la técnica experimental más utilizada para medir las propiedades mecánicas de los materiales metálicos [1]. Con él se obtienen los parámetros que definen el comportamiento del material, ya sea en rango elástico, plástico, e incluso en rotura. Uno de los parámetros básicos es la ductilidad, que está relacionada con la deformación que puede llegar a alcanzar el material previo a su rotura.

En un ensayo de tracción normalmente distinguimos entre la deformación bajo carga máxima y la deformación de rotura. La primera es fácil de medir y suele dar resultados bastante repetitivos. Sin embargo, la segunda es algo más complicada de obtener. La deformación de rotura se suele definir a partir del alargamiento medido justo antes de que se produzca una pérdida de carga apreciable producida por la fractura del material, lo cual es posible si se están utilizando extensómetros y la rotura se produce dentro de la longitud captada por el extensómetro. El problema es que si la rotura sucede fuera de la longitud recogida por el extensómetro, la deformación de rotura calculada de esta forma no es representativa y puede experimentar grandes variaciones en función de la posición del punto de rotura con respecto al extensómetro.

Otras veces, los valores de la deformación de rotura se obtienen de forma manual juntando las dos partes de la probeta de tracción rota y midiendo la distancia final entre dos marcas que se hicieron al principio del ensayo. Tal y como se recoge en la Norma ASTM E8-96a (Standard Test Methods for Tension Testing of Matellic Materials) [2], estas dos formas para calcular la deformación en rotura no son generalmente intercambiables, recomendando como más precisa la primera.

La misma Norma advierte que los resultados de la deformación de rotura son muy sensibles a variables como: la velocidad del ensayo, la geometría de las

probetas, los extensómetros utilizados, los defectos geométricos de las probetas y la falta de alineamiento de la carga. En un test interlaboratorios realizado por la ASTM (Practice E691) se observó que de todas las propiedades que se obtienen en el ensayo de tracción, la de menor repetitividad y reproducibilidad era la deformación en rotura, seguida de cerca por la reducción en área. Esto ha llevado a que normalmente prefiramos utilizar la deformación bajo carga máxima como propiedad del material y dejemos la deformación de rotura como parámetro más bien marcado por la forma en que se ha realizado el ensayo.

No obstante, cuando se persigue conocer algo más sobre la ductilidad y la rotura del material la información que aporta la deformación bajo carga máxima no es suficiente. Entender hasta qué punto la deformación de rotura es una propiedad del material resulta fundamental para estudiar cómo rompen los materiales y, especialmente, para poder realizar simulaciones representativas de los procesos que se están produciendo durante la rotura y establecer criterios que nos permitan predecirla. En la actualidad, empezamos a disponer de herramientas ópticas experimentales capaces de medir la localización de las deformaciones y que pueden aportar una información decisiva en estos aspectos.

En este trabajo se presenta parte de una investigación enfocada a estudiar los mecanismos de rotura de los aceros de construcción. Se han estudiado los fenómenos de estricción y rotura en probetas planas de diferentes espesores. Para ello se ha realizado una campaña experimental de ensayos de tracción extensamente instrumentados sobre acero perlítico. Mediante un sistema de extensometría óptica se han obtenido los mapas de deformación en la superficie de las probetas durante todo el ensayo. Puesto que para caracterizar adecuadamente la rotura resulta fundamental conocer, no sólo las deformaciones, sino también el estado tensional en el instante de rotura [3-5], se han realizado simulaciones numéricas encaminadas a reproducir los ensayos con la mayor fidelidad posible.

Se ha estudiado la influencia de la sección inicial en la deformación y la forma de rotura y en la dispersión de los resultados. Las simulaciones numéricas han permitido, además, caracterizar la triaxialidad de las diferentes probetas en el momento de rotura.

2. CAMPAÑA EXPERIMENTAL

2.1. Material

El material estudiado en este trabajo es acero eutectoide empleado para la obtención de los alambres de pretensado. Se ha utilizado el alambrón de partida (12mm diámetro) previo al proceso de trefilado en frío. El material fue suministrado en rollos por la fábrica EMESA-Trefilería (Arteixo-La Coruña).

La microestructura perlítica, obtenida gracias a un enfriamiento controlado desde la temperatura de austenización, está formada por finas láminas de ferrita y cementita. En el alambrón, antes del proceso de trefilado, no se percibe una orientación preferencial de dichas láminas, lo que permite suponer que se trata de un material isótropo en sus propiedades mecánicas. Ensayos de dureza realizados sobre las diferentes direcciones [6] han confirmado esta hipótesis de isotropía.

2.2. Probetas

A partir del alambrón de partida de 12mm de diámetro se obtuvieron probetas con una región de estudio plana de cuatro espesores diferentes (1, 2, 3 y 4 mm). La forma y dimensiones de las probetas se recogen en la Figura 1 y la Tabla 1. En total se obtuvieron 4 probetas para cada espesor.

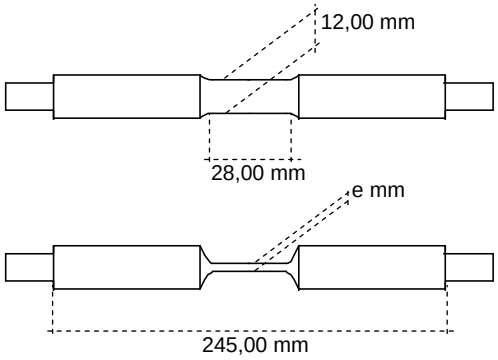

Figura 1. Probetas utilizadas para los ensayos de tracción.

Tabla 1. Sección transversal de las probetas

Nombre	e (mm)	área (mm^2)
E1	1.00	12.00
E2	2.00	24.00
E3	3.00	36.00
E4	4.00	48.00

2.3. Ensayos e instrumentación

Se realizaron ensayos de tracción sobre las 16 probetas. Se empleó una máquina universal estática marca Suzpecar con control en desplazamiento. La velocidad de solicitación durante todo el ensayo fue 0.5 mm/s (velocidad de deformación aproximada de 2%/min). La carga se midió con una célula de carga HBM, modelo U2, de 10 TN de capacidad.

Para obtener la máxima información sobre el proceso de deformación, las probetas se instrumentaron de forma intensiva utilizando dos extensómetros resistivos gemelos, uno a cada lado de la probeta, abarcando toda la zona plana. De esta forma se aseguraba que la rotura de las probetas se produjera siempre dentro de la zona controlada por el extensómetro.

También se utilizó un sistema de medida de desplazamientos y deformaciones mediante óptica de alta resolución (Vic-2D) [7]. Este sistema mide el desplazamiento de un conjunto aleatorio de puntos que se marcan en la superficie de la probeta antes de empezar el ensayo. Después, mediante un software específico, interpola el campo de desplazamientos en toda la superficie utilizando funciones a trozos, tipo "splines", obteniendo de esta manera un campo continuo que puede derivarse para obtener el campo de deformaciones. Mediante este sistema se obtuvo el contorno de deformaciones en la superficie de las probetas durante todo el proceso de carga y, en particular, en el instante de la rotura de las mismas (con una resolución temporal de 1 segundo).

3. SIMULACIÓN NUMÉRICA

Para obtener información sobre la distribución de tensiones en la sección de las probetas durante los ensayos, se realizaron simulaciones numéricas en 3D de los cuatro espesores ensayados. Para ello se utilizó el programa ABAQUS 6.8, mallando la probeta completa. La malla se realizó utilizando elementos hexaédricos de 8 nodos, empleando un total de 28000 elementos y 34746 nodos. La Figura 3 muestra una imagen de una de las mallas utilizadas.

Con el fin de poder simular correctamente los cuellos de estricción, las simulaciones se realizaron en grandes desplazamientos. La carga se aplicó con control en desplazamientos, imponiendo un desplazamiento creciente en los nodos del extremo superior de la probeta, manteniendo inmovilizados los nodos del extremo inferior, emulando de esta manera el proceso experimental de aplicación de carga. La curva tensión-deformación utilizada se obtuvo a partir de los datos experimentales según se explica en trabajos anteriores [8]. En dicho trabajo se calibró el modelo numérico, mostrando que era capaz de reproducir adecuadamente el comportamiento posterior a la carga máxima.

4. RESULTADOS Y DISCUSIÓN

4.1. Influencia del espesor y de la base de medida del extensómetro en las propiedades mecánicas.

Una de las principales ventajas del ensayo a tracción simple es que permite obtener parámetros como el módulo de elasticidad, el límite elástico o la resistencia máxima, de forma bastante sencilla. Estos parámetros pueden obtenerse con independencia de la sección de la probeta, ya sea ésta circular o rectangular [2]. Cabe hacerse la pregunta de si el mismo resultado será aplicable a la deformación en rotura.

Las Figuras 4a, 4b, 4c y 4d muestran, respectivamente, el límite elástico al 0,2%, la resistencia máxima, la deformación bajo carga máxima y la deformación de rotura[1], todos ellos en función del espesor de las probetas. En dichas figuras se muestra el resultado en forma valor medio ± la desviación típica. Puede apreciarse claramente cómo mientras los tres primeros resultados son independientes del espesor, la deformación de rotura es claramente dependiente, aumentando ésta a medida que lo hace el espesor.

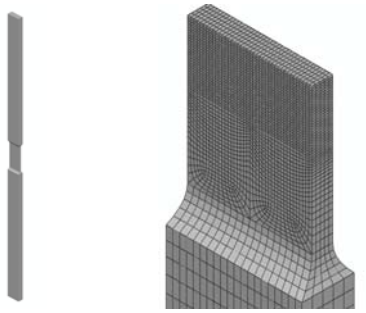

Figura 3. Geometría utilizada en las simulaciones (derecha) y detalle de la sección de la malla en la zona central de análisis (izquierda).

La norma ASTM señala que la deformación de rotura puede depender de la sección transversal de la probeta ensayada. Concretamente, señala que la deformación de rotura *generalmente aumenta en aquellas probetas en las que la relación* $L_0/(A_0)^{1/2}$ *disminuye*, siendo L_0 la longitud de la base extensométrica y A_0 el área inicial. Según esta indicación, valores mayores de la sección transversal, conducirían a valores mayores de la deformación de rotura. No obstante, al norma no llega a especificar hasta qué medida puede llegar a cambiar la deformación de rotura.

La norma ASTM señala también que, en caso de medir la deformación última de rotura, este dato debe ir acompañado por la longitud de la base de medida utilizada. De esta forma, la propia norma está asumiendo que los resultados pueden depender de la base extensométrica, sin llegar a especificar en qué medida pueden variar. Para estudiar este efecto, se han analizado los resultados de deformación bajo carga máxima y de deformación de rotura, utilizando una segunda base extensométrica más larga que la primera (28 mm en la segunda, por 24 mm en la primera). Los resultados de ambas bases extensométricas se muestran en la Figura 5. En ambos casos ambos extensómetros muestran la misma tendencia, obteniéndose menores deformaciones con el extensómetro de mayor base de medida, lo cual es lógico si pensamos que en el cuello de estricción se produce una localización de deformaciones en la cual se concentran los desplazamientos que después promediamos a lo largo de toda la longitud del extensómetro, si bien en el caso de la deformación bajo carga máxima, la diferencia apenas supera el 5%, mientras que en el caso de la deformación de rotura la diferencia alcanza el 20%.

[1] Solamente los ensayos válidos para medir deformación de rotura que, según ASTM E8, son aquellos en los que la rotura se produce en la mitad central de la zona adelgazada.

En este sentido, dado que la deformación de rotura depende claramente de la base extensométrica utilizada, parece más interesante obtener la deformación local de rotura, es decir, la deformación logarítmica en la zona de rotura como si se utilizase un extensómetro de base de medida idealmente nula. Este parámetro sería mucho más útil para incorporar un criterio de rotura en una simulación de Elementos Finitos. Obtener dicha deformación ha sido posible mediante la utilización del sistema de correlación digital de imágenes. La Figura 6 muestra la deformación local vertical de rotura frente al espesor de las probetas con rotura válida. Puede verse cómo la tendencia es similar a la de la Figura 4d.

El hecho de que la dispersión en la deformación de rotura de la Figura 6 aumente claramente con el espesor podría deberse al hecho de que la rotura está gobernada básicamente por la existencia de defectos en la sección de la probeta. Los mayores espesores, debido a la estado tensional, posibilitan deformaciones máximas mayores, pero también aumentan las probabilidades de defectos, lo cual haría que los resultados puedan ser más variables.

4.2. Influencia del espesor en la forma de la rotura.

Se he estudiado también la influencia del espesor en los mecanismos de rotura. En este sentido, en la literatura puede encontrarse cómo los resultados experimentales obtenidos por diversos autores muestran patrones de rotura distintos para los espesores más finos, en comparación con los demás espesores [9]. Ello ha llevado a algunos autores a suponer que para espesores finos la rotura está gobernada por un mecanismo de rotura distinto y, por tanto, el criterio de rotura que la explica, también debe ser distinto según se trate de espesores finos o gruesos [10].

Los resultados obtenidos en la campaña experimental que aquí se he realizado, en efecto, han mostrado un patrón de rotura distinto en las probetas de 1mm, en comparación con el resto de espesores (ver Figura 7). Mientras que en el espesor más fino se aprecian dos bandas diagonales de rotura (Figura 7a), para los espesores mayores las probetas muestran el típico patrón de rotura por copa y cono, con un plano de rotura perpendicular a la dirección de carga (Figura 7b).

Sin embargo, observando la Figura 4d, en la que se representan las deformaciones de rotura frente al espesor, vemos cómo ésta crece con el espesor de forma aparentemente bastante continua, no siendo apreciable ningún cambio de tendencia entre las probetas de 1, 2, 3 y 4 mm. De esta forma, aunque el espesor sí parece provocar un cambio brusco en la forma final de la superficie de rotura, aparentemente este cambio brusco no se aprecia en la deformación de rotura, que varía con el espesor de forma bastante suave. Este resultado no parece apoyar la hipótesis de utilizar criterios de rotura distintos en función del espesor.

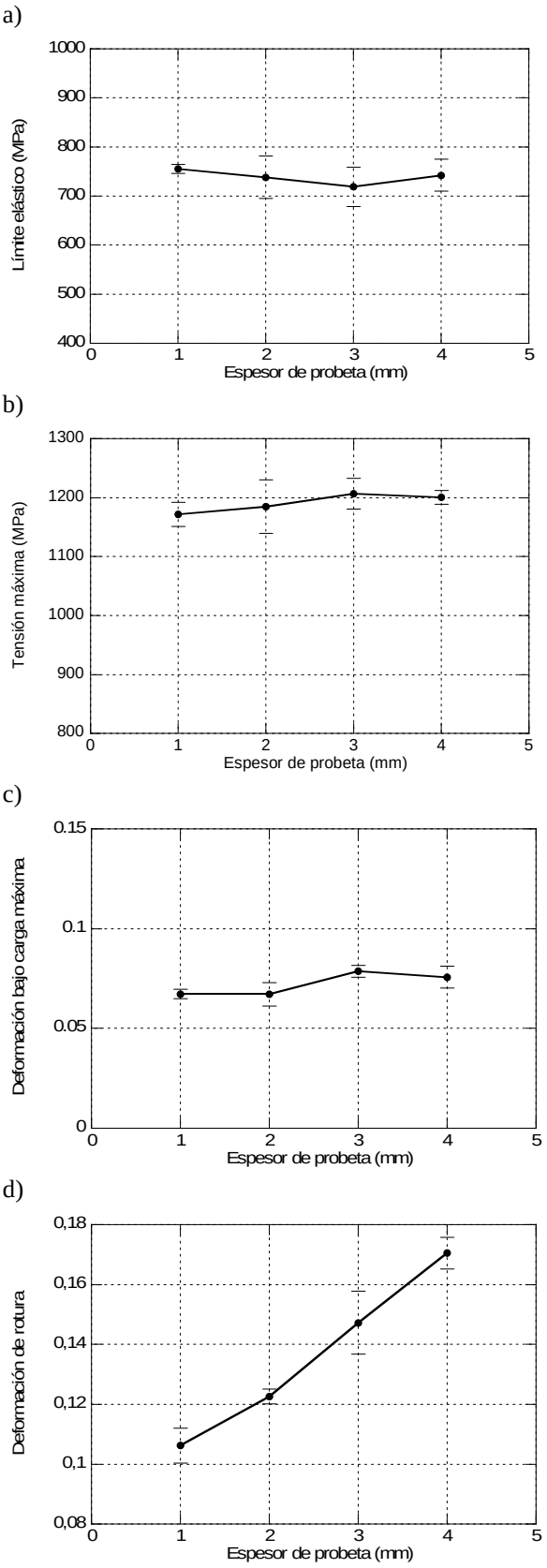

Figura 4. a) Límite elástico al 0,2% frente al espesor; b) tensión (ingenieril) máxima frente al espesor; c) deformación (logarítmica) bajo carga máxima frente al espesor; d) deformación (logarítmica) de rotura frente al espesor.

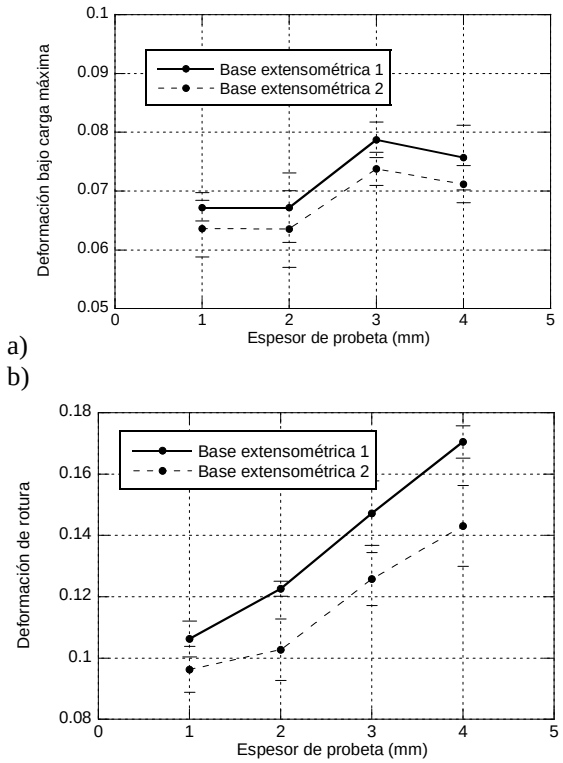

Figura 5. a) deformación (logarítmica) bajo carga máxima frente al espesor, obtenida con dos bases extensométricas distintas; b) análogamente, con la deformación de rotura.

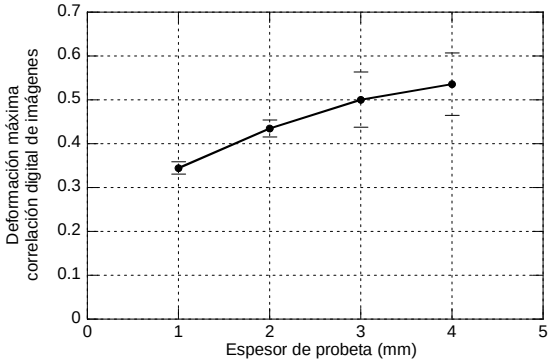

Figura 6. Deformación (logarítmica) de rotura local, frente al espesor.

Cabría pensar si tal vez la ausencia de un cambio brusco en la deformación de rotura en la probetas de 1 mm de espesor es una consecuencia del promediado en la deformación de rotura introducido por estar midiendo las deformaciones con un extensómetro cuya base de medida es muy superior a la longitud de la zona en la que se localiza la estricción y en la que, posteriormente, se produce la rotura. Sin embargo, los resultados mostrados en la Figura 6, que de nuevo muestran un cambio sueva en las deformaciones de rotura medidas con un extensómetro ideal de base 0, desmienten esta hipótesis.

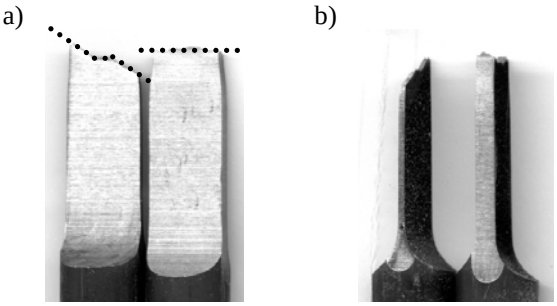

Figura 7. a) Vista frontal de la superficie de rotura de dos probetas, una de 1 mm y otra de 3 mm; b) análogamente, en vista lateral .

4.3. Influencia de la triaxialidad en la rotura.

Las simulaciones numéricas han permitido obtener información sobre el estado de deformaciones y tensiones del interior del alambre en los momentos próximos a la rotura. Esto resulta fundamental para tratar de entender qué parámetros son los responsables de desencadenar el proceso de rotura, lo cual es clave para ajustar los diferentes modelos de rotura

Un primer análisis que podría ser interesante es el de los contornos de deformación plástica equivalente en el momento de la rotura. En la Figura 7, pueden apreciarse los contornos de deformación plástica equivalente en el momento de la rotura, para los 4 espesores. La principal diferencia entre los espesores reside en que a medida que aumenta éste, las bandas diagonales de deformación se van achatando, de forma que la deformación se concentra en una zona cada vez más estrecha. Aún así, esta evolución parece gradual, especialmente entre las probetas de 1 y 2 mm, lo cual no explicaría el cambio importante que se produce en su forma de rotura.

Para intentar profundizar más en los motivos que originan la variación de la deformación de rotura con el espesor, se ha analizado el valor de la triaxialidad en los diferentes espesores durante el ensayo. Siguiendo a Bao y Wierzbicki [11], utilizaremos como índice de triaxialidad al cociente $\sigma_m / \overline{\sigma}$, siendo σ_m la presión (la tercera parte de la traza del tensor de tensiones), y $\overline{\sigma}$ la tensión equivalente de Von Mises. Este parámetro de triaxialidad es habitual en algunos criterios de rotura, como por ejemplo el de Johnson-Cook [3].

La Figura 8 muestra el citado índice de triaxialidad en función de la deformación extensométrica de la probeta hasta la rotura (con la misma base de medida empleada en la Figura 4d), en el punto de mayor triaxialidad, que corresponde al punto central de la sección de estricción. Puede apreciarse cómo la triaxialidad aumenta de forma más rápida en los espesores más finos, si bien, una vez más, no se aprecia una diferencia drástica entre la probeta de 1 mm y las probetas de mayores espesores. Observando el valor de la triaxialidad en el instante de la rotura, se observa cómo la tendencia es a que la rotura

se produzca más o menos cuando las probetas alcanzan el mismo valor de la triaxialidad. A la vista de los resultados, en esta campaña experimental, la triaxialidad aparentemente no puede explicar las diferencias entre las deformaciones últimas de rotura para los distintos espesores.

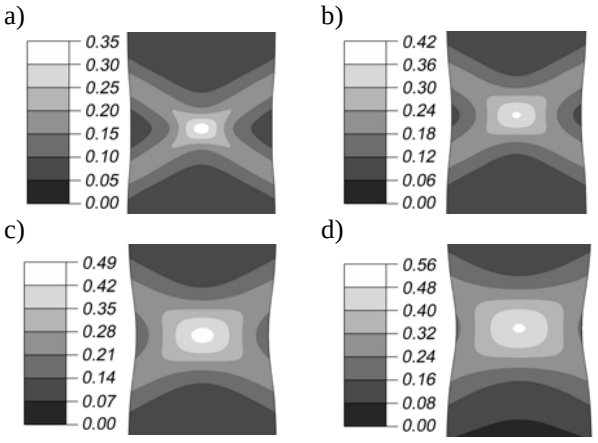

Figura 8. Contornos de deformación plástica equivalente para los espesores: a) 1mm; b) 2mm; c) 3mm; d) 4 mm.

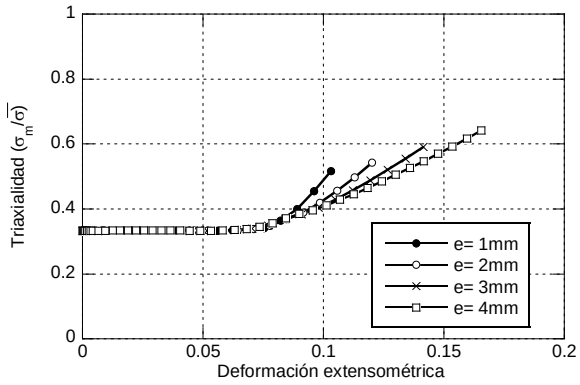

Figura 9. Índice de triaxialidad hasta la rotura, obtenido con las simulaciones numéricas para los distintos espesores.

5. CONCLUSIONES

Con una campaña experimental extensamente instrumentada sobre probetas planas de diferentes espesores se han puesto de manifiesto los diferentes factores que afectan al parámetro deformación de rotura obtenido en un ensayo de tracción. También se ha mostrado que aunque en el rango de espesores estudiados se observa un importante cambio en la forma de rotura, esto no se ha visto reflejado en un cambio brusco de la deformación de rotura.

Los resultados obtenidos muestran que no es posible considerar la deformación de rotura como un parámetro del material, al menos no en el mismo sentido en que se consideran otros parámetros como el módulo de elasticidad o el límite elástico, pero sin duda proporciona una información muy valiosa. Entender cómo se localiza la deformación durante el ensayo de tracción y cómo se produce la rotura resulta fundamental para interpretar los resultados experimentales y por ende las propiedades mecánicas que se pueden extraer de ellos.

AGRADECIMIENTOS

Los autores desean agradecer el apoyo del Ministerio de Ciencia y Tecnología a través del proyecto CONSOLIDER-INGENIO 2010. También desean mostrar su gratitud a D. Luis del Pozo y Dª. Luisa Villares de EMESA Trefilerías, por su ayuda con el material y al profesor Jaime Planas por sus útiles comentarios.

REFERENCIAS

[1] Sánchez-Gálvez, V., Física de la Plasticidad, ETSI Caminos, Canales y Puertos, 1988.

[2] ASTM Annual Book of ASTM Standards.

[3] Johnson, G. and Cook, W.H., Fracture characteristics of three metals subjected to various strains, strain rates, temperatures and pressures, Eng. Frac. Mech. Vol. 21. pag. 31-48, 1985.

[4] Bao, Y. and Wierzbicki, T., On fracture locus in the equivalent strain and stress triaxiality space, Int. J. Mech. Sciences Vol. 46. pag. 81-98, 2004.

[5] Bao, Y., Dependence of ductile crack formation in tensile tests on stress triaxiality, stress and strain ratios, Eng. Frac. Mech. Vol. 72. pag. 505-522, 2005.

[6] Atienza, J.M., Tensiones residuales en alambres de acero trefilados, Tesis Doctoral, 293 pag., Universidad Politécnica de Madrid, 2001.

[7] Vic 3D/2D User Manual. Correlated Solutions Inc. 2005.

[8] Cendón, D.A., Atienza, J.M y Elices, M. Localización de la deformación durante un ensayo a tracción: resultados experimentales y numéricos. Anales de la Mecánica de la Fractura, Vol. 26 (1). Pp. 154-159. 2009.

[9] Wierzbicki, T. and Bao, Y. Calibration and evaluation of seven fracture models. Int. J. of Mech. Sci., Volume 47, Issues 4-5. Pp. 719-743. 2005.

[10] Kamoulakos A, Culiere P, Araki T. Prediction of ductile metal rupture with the E-W Model in PAM-CRASH. In: IBEC 2003 Chiba, Japan; 2003.

[11] Y. Bao & T. Wierzbicki. A comparative study of various ductile crack formation criteria. Journal of Eng. Mats. and Tech., Vol. 126. Pp. 314-324. 2004.

ESTUDIO DE LAS TÉCNICAS PARA LA OBTENCIÓN DE PROBETAS SPT PREFISURADAS

I.I. Cuesta[1], C. Rodriguez[2], F.J. Belzunce[2], J.M. Alegre[1]

[1]Grupo de Integridad Estructural. Universidad de Burgos. Escuela Politécnica Superior. C/Villadiego s/n, 09001, Burgos
E-mail: iicuesta@ubu.es

[2]Escuela Politécnica Superior de Ingeniería de Gijón. Universidad de Oviedo. Campus de Gijón, 33203, Gijón

RESUMEN

En aquellos casos en los que no se dispone de material suficiente para llevar a cabo ensayos convencionales, con los que poder determinar las propiedades mecánicas del material analizado, existen en la actualidad diferentes ensayos no normalizados para tal fin. Uno de éstos, es el ensayo de probetas miniatura o small punch test (SPT), el cuál consiste básicamente en un punzonado sobre una probeta pequeña, mediante un punzón de gran rigidez, estando la periferia de la probeta empotrada por una matriz. Uno de los grandes retos en estos momentos es la posibilidad de obtener las propiedades a fractura del material con el ensayo de este tipo de probetas miniatura. La gran mayoría de los trabajos sobre este tema hasta el momento han sido realizados con probetas convencionales de SPT, siendo muy pocos los autores que han utilizado probetas prefisuradas. Para la realización de esta fisura inicial en la probeta SPT, previa al ensayo, se están utilizando en la actualidad dos procedimientos principalmente, el primero de ellos mediante micromecanizado de alta precisión y el segundo a través de microfisuración por láser. El objetivo principal del presente trabajo es estudiar el efecto en los resultados obtenidos con estos dos procedimientos experimentales.

ABSTRACT

In those cases where there is not enough material for conducting conventional tests to determine the mechanical properties of the material analyzed, there are now several non-standard tests for this purpose. One of these is the Small Punch Test (SPT), which basically consists of deforming a miniature specimen using a high-strength punch. The sides of the specimen are firmly held between two dies. One of the greatest challenges at present is the possibility of obtaining the fracture properties of a material with this type of SPT specimens. The vast majority of papers on this topic to date have involved conventional SPT specimens. Very few authors have utilized pre-cracked specimens. To achieve this initial crack in the SPT specimen prior to testing, two procedures are at present mainly being used. The first of them use high-precision micromachining, and the second using laser-induced microcracking. The main objective of this paper is to study the effect of these procedures on the obtained results.

KEY WORDS: Ensayo Small Punch, Micromecanizado, Microfisuración por láser.

1. INTRODUCCIÓN

En la década de los 80, en el campo nuclear, para solventar el problema que suponía caracterizar material irradiado de componentes en servicio, donde la escasez de material para mecanizar probetas convencionales era un serio inconveniente, se desarrolló el ensayo miniatura de punzonado o small punch test (SPT).

Dicho ensayo consiste básicamente en la ejecución de un punzonado sobre una probeta miniatura, con un punzón de gran rigidez, estando la periferia de la probeta empotrada en una matriz. Estas probetas miniatura generalmente son cuadradas de dimensiones 10x10*mm*, o bien son circulares de diámetro 3*mm*, este reducido tamaño de probeta supone que el ensayo SPT se pueda considerar como un ensayo no destructivo del componente en servicio analizado.

En las últimas décadas han sido numerosos los autores que han centrado sus investigaciones en la utilización del SPT con el fin de obtener las propiedades mecánicas del material, en los casos que no se dispone de una cantidad suficiente de material para poder realizar ensayos normalizados. Extendiendo su aplicabilidad a otros campos a parte del nuclear como, por ejemplo, a los procesos de soldadura para la evaluación de las propiedades del material en las zonas afectadas térmicamente.

Actualmente, uno de los grandes retos es la posibilidad de obtener las propiedades a fractura del material con el

ensayo de este tipo de probetas miniatura. La gran mayoría de los trabajos [1-3] sobre este tema hasta el momento han sido realizados con probetas convencionales de SPT, siendo muy pocos los autores que han utilizado probetas prefisuradas [4-6].

En este sentido, el ensayo SPT convencional, donde no existe una fisura inicial, no parece adecuado para la determinación directa de los parámetros de fractura convencionales (K ó J). Puede ser utilizado, eso sí, para determinar parámetros de daño, que inician y desarrollan la rotura final de la pieza. A priori, la utilización de probetas prefisuradas, por el hecho de tener mecanizada una grieta inicial, podría suponer una mejor opción a la hora de estimar las propiedades a fractura, ya que tienen una mayor similitud con las probetas convencionales (Charpy o CT) usadas para tal fin. Han sido varias las geometrías analizadas en el entorno de trabajo en el que se ha desarrollado el presente estudio. Inicialmente, las opciones que se han barajado aparecen reflejadas en la Figura 1.

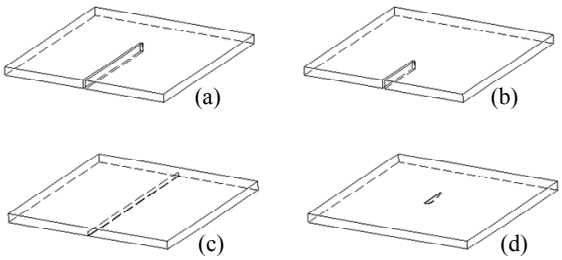

Figura 1. Tipos de fisura inicial en probetas SPT.

Se han considerado fisuras pasantes en todo el espesor, de diferentes longitudes, sobrepasando el eje de carga (a) y sin llegar al citado eje (b). Evidentemente, la elección de un tipo u otro de fisura debe obedecer a criterios científicos, pero también deben considerarse criterios de viabilidad. La fisura tipo (d), central no pasante, en unas dimensiones tan reducidas de probeta resulta a priori de muy difícil ejecución.

Las fisuras tipo (a) y (b) no han resultado muy prácticas desde el punto de vista de la longitud de propagación, y en cualquier caso el espesor de la probeta haría que el valor de K fuese muy cercano a condiciones de tensión plana. La fisura tipo (c), longitudinal no pasante, parece en primera instancia una de las opciones factibles, aunque evidentemente también presenta sus limitaciones (reducido espesor e inicio de propagación de fisura en la zona cercana al punzón). Sin embargo, se estima que podría utilizarse para estimar las condiciones de inicio, con las particularidades que los resultados obtenidos puedan presentar.

La prefisura tipo (c) en la probeta SPT se puede realizar principalmente mediante dos procedimientos, el primero de ellos mediante micromecanizado de alta precisión y el segundo a través de microfisuración por láser. El objetivo principal del presente trabajo es estudiar el efecto en los resultados obtenidos con estos dos procedimientos experimentales, para determinar las ventajas e inconvenientes, que podrían presentar cada uno de ellos a la hora de utilizarlos para estimar las propiedades a fractura del material.

2. PROBETAS SPT PREFISURADAS

El material utilizado en el presente estudio es un acero inoxidable martensítico endurecido por precipitación. Sus principales características son alto límite elástico (1100 *MPa*), buena resistencia a la corrosión, buenas propiedades mecánicas a temperaturas superiores a $316^{o}C$ y alta tenacidad tanto en la dirección longitudinal como en la transversal. Presenta un comportamiento isotrópico cercano a un material elástico-perfectamente plástico, por lo que puede ser considerado como un material con elevado grado de ductilidad.

A priori, los resultados obtenidos con este material podrán ser extrapolados a otros tipos de aceros, siempre que su comportamiento no sea muy disimilar al de este acero. En caso contrario, habría que realizar un nuevo estudio con el material deseado.

Las probetas SPT empleadas, han sido obtenidas a partir del corte en rebanadas de una probeta tipo Charpy, resultando directamente probetas cuadradas de 10 *mm* de lado. Se han empleado dos técnicas para la realización de dicho corte, la primera por corte con disco de alta precisión y la segunda por electroerosión. En el corte por disco el tiempo de preparación de la probeta es mucho mayor, ya que después de realizar el corte, en el que se obtiene una probeta SPT de espesor mayor del deseado, hay que reducirlo mediante desbaste y pulido.

Por otro lado, en el corte por electroerosión, tras los ajustes necesarios, el espesor de la probeta es el deseado y no es necesario realizar ninguna operación adicional. Una vez obtenidas las probetas SPT de dimensiones 10x10 *mm* y espesor 0.5 *mm*, se procede a mecanizar la fisura inicial de tipo longitudinal no pasante (Figura 1.c). Para ello, como ya se ha comentado anteriormente, se ha empleado el micromecanizado de alta precisión y la microfisuración por láser.

En el micromecanizado se ha empleado una herramienta en forma de V con ángulo de 37º y radio de redondeo en la punta de $100\mu m$. La profundidad de fisura deseada se obtiene aplicando la herramienta longitudinalmente a partir de la cara inferior, desde el centro de un lado de la probeta hacia el centro del lado opuesto. La geometría de la fisura inicial que se obtiene con esta técnica se puede ver en la Figura 2, la cuál reproduce fielmente la forma de la herramienta con la que se ha mecanizado. Cabe destacar el buen acabado superficial de la fisura y la homogeneidad conseguida de la profundidad de fisura a lo largo de toda su longitud.

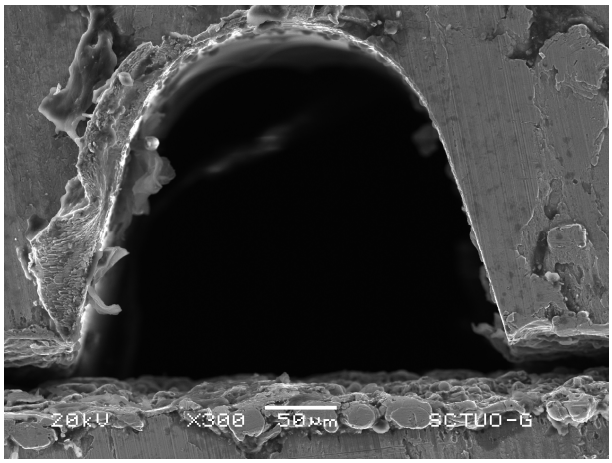

Figura 2. Sección de la fisura inicial obtenida con el micromecanizado de alta precisión.

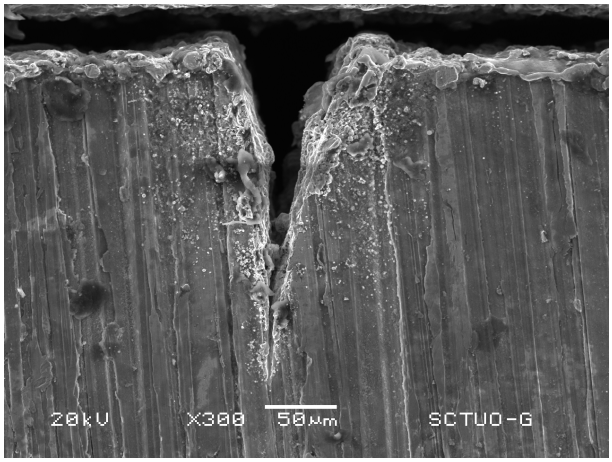

Figura 3. Sección de la fisura inicial obtenida con la microfisuración por láser.

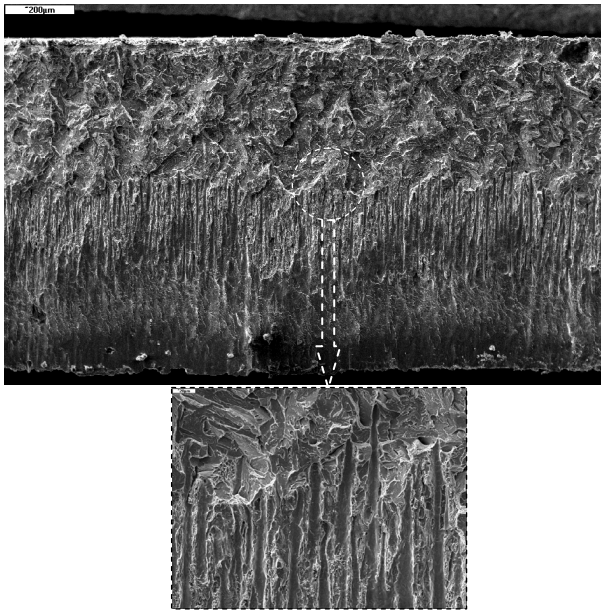

Figura 4. Frente de fisura obtenido con la microfisuración por láser.

En la microfisuración por láser, tras una calibración inicial, el láser, es aplicado en forma de haz de pulsos de $30\mu m$ de diámetro. Al igual que en la técnica anterior, la fisura se realiza de forma longitudinal, a partir de la cara inferior, desde el centro de un lado de la probeta hacia el centro del lado opuesto.

En la Figura 3 se muestra la sección de la fisura inicial obtenida con esta técnica, donde se puede observar que en este caso es mucho más aguda, y la punta de fisura es afilada, asemejándose más a una fisura perfecta sin redondeo en la punta. Sin embargo, presenta el inconveniente de conseguir un frente de fisura más irregular, como se puede ver en la Figura 4, donde la profundidad de fisura es ligeramente variable en longitud, ya que los pulsos láser van dejando picos y valles a lo largo del extremo de fisura conforme ha ido avanzando, como se puede ver en el detalle de la Figura 4. Los ensayos realizados requerirán una medida posterior de la fisura obtenida, y un ajuste de los mismos en función de las diferencias observadas respecto de la medida nominal.

En los ensayos SPT se pueden utilizar probetas SPT prefisuradas con diferentes profundidades de fisura (a). Dicha profundidad se puede adimensionalizar con respecto al espesor de probeta (t), obteniendo de esta manera diferentes valores de la relación a/t, siendo los más habituales valores teóricos de a/t entre 0.2 y 0.5. En el presente trabajo se ha utilizado una relación $a/t = 0.5$, por lo que la profundidad de fisura teórica fue de 0.25 *mm*, ya que el espesor de probeta era 0.5*mm*. Una vez realizadas las fisuras iniciales en las probetas SPT se ha procedido a medir mediante SEM los valores de la profundidad real en los dos extremos de la fisura, para cada una de las probetas. Con el micromecanizado la media de a fue de $252\mu m$ ($a/t = 0.5$), mientras que con la microfisuración por láser se obtuvo un valor medio de $225\mu m$ ($a/t = 0.45$).

3. ENSAYO SPT

Una vez medidas las fisuras iniciales en las probetas SPT se procedió a ensayarlas, obteniendo para cada una de las probetas la curva carga-desplazamiento del punzón. La Figura 5 presenta las curvas típicas carga-desplazamiento obtenidas en el ensayo SPT con probetas prefisuradas, en función de si la relación a/t es mayor o menor de 0.5, para el material considerado en el presente trabajo. Analizando la forma de la curvas, es posible distinguir diferentes regiones en cada una de ellas. Para una mayor comprensión de estas curvas, también se han representado las obtenidas en un ensayo SPT sin fisura y la simulación de una fisura completamente pasante, es decir, como si estuviese formada por dos mitades unidas sólo por las fuerzas de contacto (probeta rota en dos mitades).

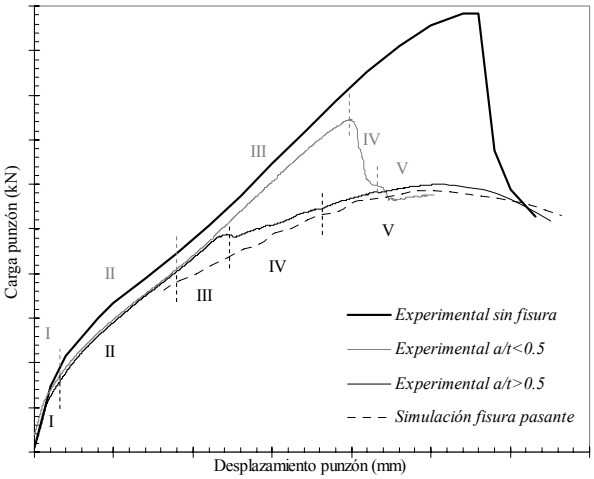

Figura 5. Curvas carga-desplazamiento del ensayo SPT sobre probeta prefisurada.

Para la curva correspondiente a una relación $a/t > 0.5$, la región I correspondería al comportamiento puramente elástico de la probeta. En esta región tanto la probeta como el utillaje se reposicionan ligeramente y se produce el fenómeno de indentación. La región II correspondería con la transición elastoplástica, ya que en algunas zonas de la probeta comienza a predominar la deformación plástica, especialmente la zona en contacto con el punzón. En la tercera región tiene lugar la progresiva abertura de los labios de la fisura y la plastificación creciente de la probeta, y como consecuencia final de esto, el comienzo y propagación de la fisura, hasta llegar al quiebro que se produce en la curva, entre la región III y IV, en el cuál la fisura se hace pasante a lo largo del espesor de la probeta. A partir del inicio de la región IV se produce rápidamente el desgarro de la probeta hasta alcanzar los bordes de la matriz, instante en el que la probeta tiende a comportarse como dos mitades desacopladas (fisura pasante). La quinta y última región se puede decir que comienza cuando la curva carga-desplazamiento se ajusta al comportamiento de dos mitades, como se puede ver en la Figura 5.

En la curva correspondiente a una relación $a/t < 0.5$ se puede llegar a distinguir de nuevo hasta cinco regiones más o menos diferenciadas. Las tres primeras se corresponderían con las de la curva anterior, con la salvedad de que la región III es mucho mayor en este caso, alcanzando la probeta una mayor capacidad de carga al ser mayor el ligamento resistente. A lo largo de la región III se inicia la fisura y crece hasta hacerse pasante, cuyo valor en este caso coincide con el máximo de la curva carga-desplazamiento. En ese instante se produce un descenso brusco de la capacidad resistente de la probeta. La región IV comprende dicho decremento, y en ella la fisura propaga en ambos sentidos por todo el espesor, hasta llegar a la zona de empotramiento, momento en el que la probeta, al igual que antes, se comporta como dos mitades desacopladas. La última región correspondería al traspaso total del punzón, a través de las dos mitades desacopladas.

Como se ha podido intuir, la diferencia existente entre las dos curvas radica principalmente en la capacidad de carga que puede soportar la probeta hasta el instante en el que la fisura se hace pasante a lo largo del espesor, propagando rápidamente hasta la zona del empotramiento. Una vez alcanzado este instante el comportamiento de la probeta se intenta estabilizar de una forma u otra, asemejándose al exhibido por dos mitades desacopladas.

Se ha podido comprobar que el instante de inicio de la propagación no queda claramente manifestado en la curva carga-desplazamiento de la probeta SPT prefisurada. En cambio, el instante en el que la fisura se hace pasante en todo el espesor si que se identifica en ambas curvas, por el quiebro de la curva en la primera y por el descenso brusco de la capacidad resistente en la segunda.

La Tabla 1 recoge tanto la técnica de generación de la fisura inicial, como el tipo de corte realizado y el espesor de cada una de las probetas SPT prefisuradas utilizadas en el presente trabajo. Como se puede observar en dicha tabla, también se han realizado ensayos SPT sobre probetas sin fisura inicial. Debido a la escasez de material, en esta primera comparación, no se han realizado excesivos ensayos para salvaguardar el mayor número de probetas SPT prefisuradas para ensayos posteriores, que se llevarán a cabo en función de las conclusiones alcanzadas en este trabajo.

Tabla 1. Probetas SPT ensayadas.

Probeta SPT	***Tipo de corte***	***Técnica de fisuración***	***Espesor (mm)***
GI03	Disco	Sin fisura	0.501
GI04	Disco	Sin fisura	0.503
BU01	Electroerosión	Sin fisura	0.479
BU21	Electroerosión	Láser	0.488
BU22	Electroerosión	Láser	0.480
GI12	Disco	Láser	0.503
BU09	Electroerosión	Micromecanizado	0.489
BU14	Electroerosión	Micromecanizado	0.489
BU17	Electroerosión	Micromecanizado	0.488

4. RESULTADOS

Tras el ensayo de todas las probetas de la Tabla 1, se han obtenido las curvas carga-desplazamiento que se pueden ver en las siguientes figuras, resultados que se discutirán en el apartado siguiente.

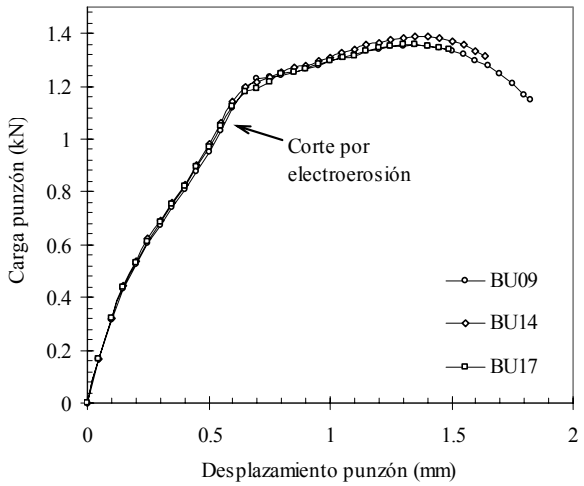

Figura 6. Curvas carga-desplazamiento del ensayo SPT sobre probetas prefisuradas por micromecanizado.

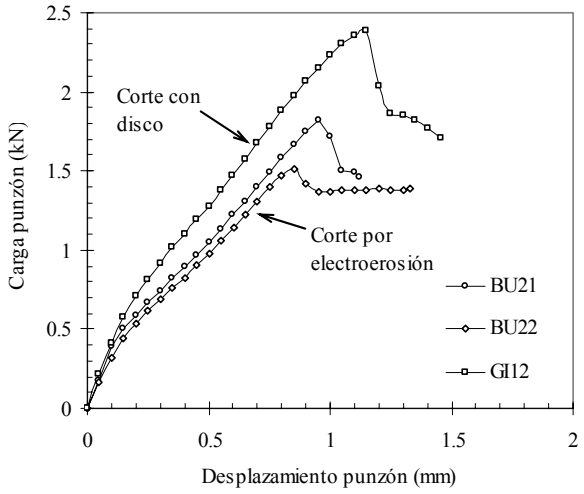

Figura 7. Curvas carga-desplazamiento del ensayo SPT sobre probetas prefisuradas por láser.

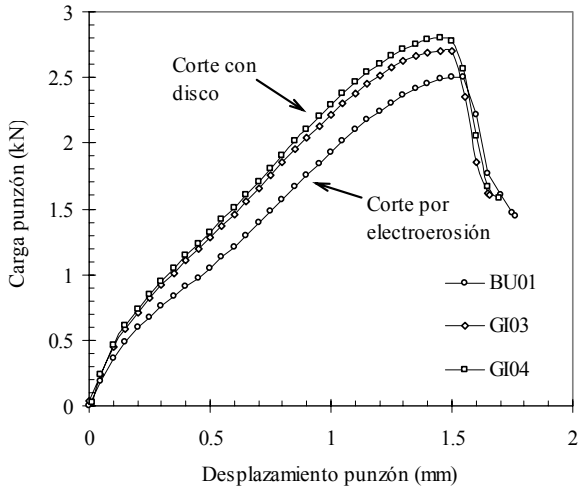

Figura 8. Curvas carga-desplazamiento del ensayo SPT sobre probetas sin fisura inicial.

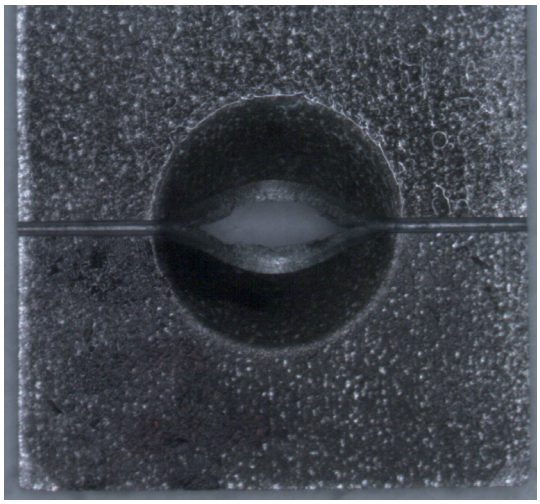

Figura 9. Probeta SPT BU17 ensayada, cortada por electroerosión y prefisurada por micromecanizado.

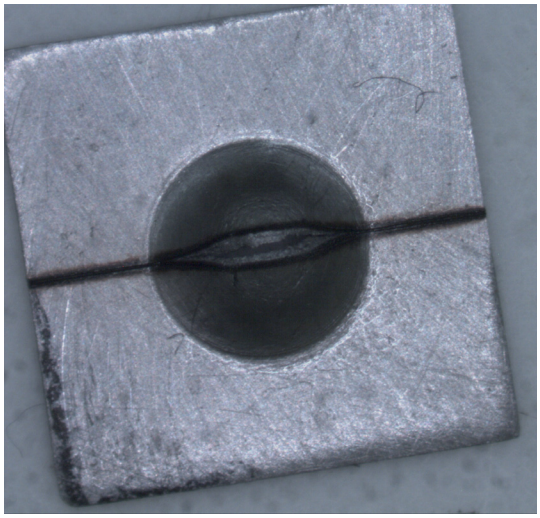

Figura 10. Probeta SPT GI12, cortada con disco y prefisurada por láser, tras el ensayo.

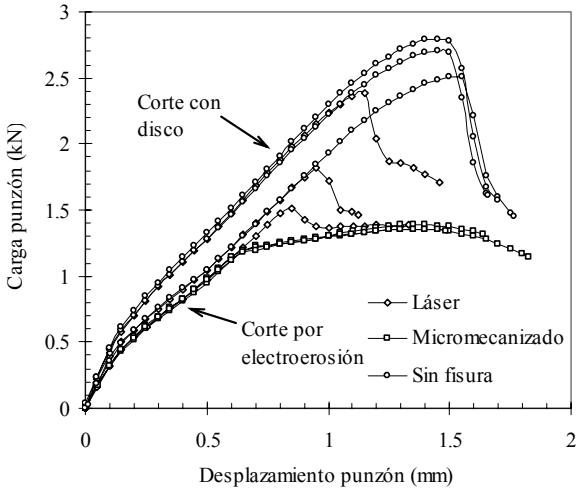

Figura 11. Comparación de las curvas carga-desplazamiento de los ensayos SPT realizados.

5. DISCUSIÓN

En la Figura 6 se puede observar la buena repetibilidad que presenta el ensayo SPT con probetas prefisuradas por micromecanizado, hecho que se justifica en virtud de la homogeneidad de la fisura obtenida con la herramienta utilizada. También el comportamiento de las curvas mostradas en esta figura se ajusta al típicamente observado en probetas SPT prefisuradas con una relación $a/t > 0.5$ (Figura 5), por lo que se deduce que la profundidad de fisura real coincide con la que se deseaba en un principio, que se recuerda era de $0.25mm$.

La Figura 7 muestra los resultados obtenidos con las probetas SPT prefisuradas por láser. Se puede ver que la dispersión es mayor y que el comportamiento de dichas probetas se ajusta más al correspondiente a una relación $a/t < 0.5$, lo que hace suponer que la profundidad de fisura real es menor que en las probetas prefisuradas por micromecanizado. Esto hace que el ligamento resistente de la probeta sea mayor, implicando una mayor capacidad de carga. En esta figura queda también de manifiesto que el comportamiento de las probetas también depende del tipo de corte empleado para obtenerlas (corte por disco o corte por electroerosión).

La Figura 8 recoge las curvas carga-desplazamiento obtenidas en los ensayos SPT con las probetas sin fisura inicial y de nuevo se observa una diferencia en el comportamiento de las probetas en función del tipo de corte con el que se han obtenido. Dicha diferencia también se hace patente visualmente como se puede apreciar en las Figuras 9 y 10, que muestran dos de las probetas ensayadas hasta la rotura. Se trata de la probeta BU17, cortada por electroerosión y prefisurada por micromecanizado, y de la probeta GI12, cortada con disco y prefisurada por láser, respectivamente. En la primera (BU17) se puede distinguir el aspecto rugoso que deja el corte por electroerosión y el buen acabado de la fisura mecanizada, mientras que la segunda (GI12) tiene un aspecto brillante debido al pulido realizado, y en ella se observa una pequeña zona que corresponde a la región afectada térmicamente por el láser.

Por último, en la Figura 11 se han representado conjuntamente todas las curvas de las figuras anteriores, observando claramente que el tipo de corte con el que se obtiene la probeta influye notablemente sobre la capacidad resistente de la probeta. En dicha figura se pueden diferenciar dos conjuntos de curvas en función del tipo de corte, pudiendo destacar en cada uno de ellos, la pequeña dispersión existente en las primeras regiones de las curvas. Por otro lado, se puede observar como todas las curvas correspondientes a las probetas SPT prefisuradas y cortadas por electroerosión, una vez que la fisura se ha hecho pasante y ha propagado hasta la zona de empotramiento, tienden a estabilizar su comportamiento al de dos mitades desacopladas. En las primeras regiones de dichas curvas no se aprecian diferencias notables debidas a la técnica de prefisuración, sin embargo en las últimas regiones si que se aprecia una diferencia notable, debida principalmente a que la profundidad de fisura en las probetas prefisuradas por láser es menor que en las prefisuradas por micromecanizado, por lo que su capacidad de carga, como se observa en la figura, es mayor.

6. CONCLUSIONES

Las dos técnicas estudiadas para la prefisuración de la probeta SPT presentan ventajas e inconvenientes en ambos casos. Del micromecanizado se puede destacar el buen acabado superficial de la fisura y la homogeneidad conseguida de la profundidad de fisura, implicando esto la repetibilidad de las curvas obtenidas en el ensayo. Como desventaja se podría decir que la forma de la fisura inicial se asemeja más al de una entalla que al de una fisura afilada. Todo lo contrario sucede con la prefisuración por láser, donde la fisura lograda si es afilada, pero presenta el inconveniente de no conseguir una profundidad de fisura homogénea y del valor deseado, por lo que es necesario un posterior análisis SEM de la fisura. A pesar de todo esto, se ha comprobado que el tipo de corte, con el que se obtienen las probetas SPT, tiene una mayor influencia en los resultados obtenidos que la técnica con la que se realiza la fisura inicial en la probeta.

AGRADECIMIENTOS

Los autores desean agradecer la financiación recibida del proyecto MCI Ref: MAT2008-06879-C03-03/MAT.

REFERENCIAS

[1] X. Mao and H. Takahashi, *Development of a further-miniaturized specimen of 3 mm diameter for tem disk small punch tests*, Journal of Nuclear Materials 150 (1987), 42-52.

[2] X. Mao, H. Takahashi and T. Kodaira, *Supersmall punch test to estimate fracture toughness Jic and its application to radiation embrittlement of 2.25Cr-1Mo steel*, Materials Science and Engineering, AI50 (1992), 231-236.

[3] Jai-Man Baik, J. Kameda, and O. Back, *Small Punch Test evaluation of intergranular embrittlement of an alloy steel*, Scripta Metallurgica et Materialia, Vol. 17 (1983), 1443-1447.

[4] Jang-Bog Ju, Jae-il Jang, Dongil Kwon, *Evaluation of fracture toughness by small-punch testing techniques using sharp notched specimens*, International Journal of Pressure Vessels and Piping 80 (2003), 221–228.

[5] I. I. Cuesta, J. M. Alegre, R. Lacalle, J. A. Álvarez, F.Gutiérrez-Solana, *Cálculo de la integral J en probetas SPT para la estimación de la tenacidad a fractura*, Anales de Mecánica de la Fractura Vol. II (2008), 486-491.

[6] I. I. Cuesta, J. M. Alegre, P.M. Bravo, *Evaluación de la tenacidad a fractura mediante la combinación del diagrama FAD y de ensayos SPT sobre probetas fisuradas*, Anales de Mecánica de la Fractura Vol. II (2009), 382-387.

NUEVO PROCEDIMIENTO EXPERIMENTAL PARA EL CÁLCULO DE FACTORES DE INTENSIFICACIÓN DE TENSIONES A PARTIR DEL ANÁLISIS DE IMÁGENES FOTOELÁSTICAS

F.A. Díaz[1] , A. García-Collado[1], P. Siegmann[3], E.A. Patterson[3]

[1] Departamento de Ingeniería Mecánica y Minera
Universidad de Jaén, Campus las Lagunillas, Edif. A3,
23071 Jaén, España.
E-mail: fdiaz@ujaen.es, acollado@ujaen.es

[3] Departamento de Teoría de la Señal y Comunicaciones
Universidad de Alcalá, Campus universitario,
28805 Alcalá de Henares (Madrid), España
E-mail: philip.siegmann@uah.es

[2] Department of Mechanical Engineering,
Michigan State University,
2555 Engineering Building, East Lansing MI 48824-1226, USA
E-mail: eann@msu.edu

RESUMEN

En el presente trabajo se propone un nuevo método para el cálculo de factores de intensificación de tensiones a partir de datos isocromáticos. El método se basa en el cálculo del ángulo de retardo empleando exclusivamente dos imágenes fotoelásticas obtenidas para dos posiciones diferentes del polarizador y el analizador en un polariscopio de transmisión. El retardo experimental es comparado con el retardo teórico calculado mediante el modelo de Westergaard empleando un número discreto de puntos en la de zona alrededor del vértice de la grieta. De esta forma, se evita la necesidad de hacer un desenvolmiento de la imagen (unwrapping), eliminándose fuentes potenciales de error. Seguidamente, K_I, K_{II} y T-stress (σ_{ox}) son calculados mediante la minimización de una función de error. Para ilustrar el potencial y eficacia del método propuesto, se han obtenido valores de K a partir de de imágenes fotoelásticas capturadas durante un ensayo de fatiga con una probeta tipo Center-Cracked-Tension (CCT). Los resultados muestran un extraordinario nivel de concordancia con los obtenidos a partir de simulaciones realizadas empleando el método de los elementos finitos, poniendo de manifiesto el potencial de la metodología propuesta.

KEY WORDS: Grieta por fatiga, factor de intensificación de tensiones, fotoelasticidad, procesado de imagen.

ABSTRACT

A novel experimental approach for the calculation of the stress intensity factor from the analysis of photoelastic images is presented. The method is derived from the six image phase-stepping method proposed by Patterson but only two images are used to obtain the retardation angle. The experimental retardation is compared with the theoretical one predicted by Westergaard's model using a discrete number of data points around the crack tip region. In this way, the necessity of unwrapping is avoided and a large potential source of errors is eliminated. Subsequently, K_I, K_{II} and T-stress (σ_{ox}) are inferred by minimizing an error function. To demonstrate the efficacy of the proposed approach, stress intensity values have been obtained from photoelastic images captured during fatigue tests conducted in polycarbonate Center-Cracked Tension (CCT) specimen. The results are very promising, showing a high level of agreement with those predicted from theory.

KEY WORDS: Fatigue crack, stress intensity factor, photoelasticity, image analysis.

1. INTRODUCCIÓN

La detección precisa de grietas así como la evaluación del daño ocasionado por fatiga en componentes industriales han centrado la atención de múltiples investigadores durante mucho tiempo. En este contexto, la habilidad para medir tensiones y deformaciones de forma precisa en las cercanías de una grieta, son un aspecto fundamental en el estudio y análisis del proceso de fatiga.

Desde que Post y Wells [1, 2] mostraron inicialmente en los años 50 el potencial de la técnica de fotoelasticidad para el estudio de problemas de fractura han sido muchos los autores que han centrado su interés en aplicar la mecánica de la fractura al análisis estructural. Uno de los mayores avances en el cálculo del factor de intensificación de tensiones a partir del análisis de imágenes fotoelásticas fue el llevado a cabo por Sanford and Dally [3] con el método Multi-Point Overdeterministic (MPOD). Desde entonces, este procedimiento ha sido extensamente empleado para el análisis de diferentes problemas de fractura. Además, este método se ha extendido de forma satisfactoria a otras técnicas experimentales [4, 5], convirtiéndose en un procedimiento estándar para el cálculo de parámetros en problemas de mecánica de la fractura.

Aunque el MPOD es un método robusto y simple de utilizar, sin embargo tiene algunas limitaciones. Así, es necesario conocer el valor exacto del orden franja en todos los puntos empleados para el análisis. Ello implica tener que emplear puntos correspondientes a valores de orden de franja enteros o mitad obtenidos a partir de las posiciones del polarizador y analizador que proporcionan un polariscopio circular en campo claro y oscuro, con la consiguiente identificación manual de los órdenes de franja [6]. Otra posibilidad pasa por realizar un desenvolvimiento de la imagen (unwrapping) empleando algoritmos específicos de procesado de imágenes [7]. Este último procedimiento se ha hecho muy popular en los últimos tiempos. Sin embargo, ambos procedimientos pueden resultar difícil de implementar de forma satisfactoria en regiones con altos valores o gradientes de tensión y por consiguiente, gran densidad de franjas en los alrededores del vértice de grieta. Esto resulta especialmente problemático para grietas presentes en componentes industriales complejos, siendo necesario que el operador de la técnica posea experiencia previa y aptitudes para poder obtener de forma satisfactoria el factor de intensificación de tensiones.

Los continuos avances en la informática han hecho posible el desarrollo de nuevos métodos de procesado de imágenes dando lugar a lo que hoy día se conoce como fotoelasticidad digital (digital photoelasticity). Diferentes técnicas de procesado de imágenes han hecho posible la obtención de mapas de campo de completo de tensión/deformación en componentes mecánicos mediante el procesado de imágenes fotoelásticas [7]. En particular, los métodos de variación de fase (phase-stepping methods) son los más extensamente empleados en la extracción de la información relativa a la fase a partir de procesado de imágenes de franjas. Mediante el empleo de métodos de desenvolvimiento de la fase (unwrapping methods), es posible obtener mapas continuos de orden de franja a partir de distribuciones periódicas ángulo de retardo. De esta manera, las técnicas de desenvolvimiento de fase han incrementado enormemente el potencial y utilidad de método inicial propuesto por Sanford y Dally [3]. Así, los datos necesarios para aplicar el método MPOD pueden ser empleados de cualquier parte de la imagen o incluso es posible emplear la imagen completa. Sin embargo, el empleo de algoritmos de desenvolvimiento de la fase previo al empleo del método MPOD implica un incremento en tiempo y complejidad en la evaluación del factor de intensificación de tensiones; por tanto sería ventajoso si directamente fuera posible utilizar las imágenes de retardo para el cálculo del factor de intensificación de tensiones directamente sin necesidad de realizar el proceso de unwrapping.

Con el presente trabajo se propone un nuevo método para el cálculo del factor de intensificación de tensiones basado en el análisis de imágenes isocromáticas. El método se basa en la determinación de la distribución del ángulo de retardo relativo mediante la combinación de dos imágenes fotoelásticas, y su posterior comparación con la distribución obtenida empleando modelos teóricos. De esta manera, se evita el proceso de desenvolvimiento de la fase como se ha comentado anteriormente, pudiéndose adquirir datos de toda la imagen. Los resultados muestran con claridad que el método propuesto es muy robusto y proporciona resultados precisos en tan solo unos segundos. Para mostar el potencial del método, éste se ha empleado para calcular el factor de intensificación de tensiones en una probeta tipo CCT (Centered-Cracked-Specimen) fabricada en policarbonato con una grieta de 12.18 mm a la que se ha aplicado diferentes niveles de carga. Los resultados obtenidos con el método propuesto reproducen fielmente los obtenidos mediante el método de los elementos finitos, poniendo de manifiesto la viabilidad y el potencial de la metodología propuesta.

2. METODOLOGÍA Y PROCEDIMIENTO EXPERIMENTAL

El procedimiento propuesto se basa en el cálculo del ángulo de retardo a partir del análisis de dos imágenes fotoelásticas. Las dos imágenes son capturadas para los estados de un polariscopio circular en campo oscuro y campo claro respectivamente. En estas dos configuraciones del polariscopio, la intensidad de la luz capturada por la cámara digital situada frente al polariscopio se puede describir según las siguientes expresiones:

$$I_1 = i_m + i_v \cos(\alpha_{\exp})$$
$$I_1 = i_m - i_v \cos(\alpha_{\exp})$$
(1)

Donde i_v es la intensidad resultante cuando los ejes del polariscopio y la probeta son paralelos, i_m considera el término de luz fondo [8]. De acuerdo con la ecuación (1), el ángulo de retardo α_{exp}, se puede obtener experimentalmente restando las imágenes 1 y 2 como denota la ecuación (2).

$$\alpha_{exp} = \cos^{-1}\left(\frac{I_1 - I_2}{2 i_v}\right) \; with \; \alpha_{\exp} = 2\pi N \quad (2)$$

Donde N denota el orden de franja.

Adicionalmente, es también posible calcular el ángulo de retardo, α empleando cualquiera de los modelos matemáticos que describen campo de tensiones den los alrededores e una grieta disponibles en la literatura [9]. En este caso se ha empleado para ilustrar el método el modelo de Westergaard [10, 11] mostrado en la ecuación (3).

$$\left(\frac{N f^2}{t}\right) = Function\left(r, \theta, K_I, K_{II}, \sigma_{ox}\right) \quad (3)$$

Donde f representa la constante de franja del material, t la longitud del camino de la luz en el material fotoelástico, r y θ son coordenadas en un sistema polar centrado en el vértice de la grieta con x en la dirección de crecimiento de la misma.

En el método propuesto se lleva a cabo un ajuste matemático de la distribución teórica del ángulo de retardo, α_{theo} a los datos experimentales, α_{exp}. Como resultado del ajuste es posible obtener K_I, K_{II} y σ_{ox}. El método se ha dividido en seis pasos que se describen en las siguientes líneas.

Inicialmente, el ángulo de retardo experimental se obtiene combinando las imágenes 1 y 2 como se ha indicado previamente (paso 1). Seguidamente la posición del vértice de la grieta debe ser identificada mediante la inspección visual de la imagen resultante del paso 1 (paso 2).

Para asegurar la validez del modelo matemático adoptado basado en condiciones lineales elásticas, es necesaria la aplicación de una máscara a la imagen en la región cercana al vértice de la grieta y a lo largo de las caras de la grieta. El propósito perseguido es eliminar del análisis la zona plástica en los alrededores de la grieta. Posteriormente, se seleccionan una serie de puntos cercanos a la grieta con los que con posterioridad se llevará cabo el ajuste (paso 3). El tamaño de la región en la que se pueden asegurar la validez de los puntos capturados ha sido definido por Nurse y Patterson [6] como un anillo de radio interior igual a diez veces el radio de la grieta y radio exterior aproximadamente 0.4 veces la longitud de la grieta. Sin embargo en el presente trabajo se ha empleado un área rectangular comprendida entre estos límites.

Las coordenadas de los puntos capturados son empleadas para evaluar la ecuación (3) y obtener una imagen teórica del ángulo de retardo de acuerdo con el modelo de Westergaard (paso 4). Para ello, es preciso definir valores iniciales para K_I, K_{II} y σ_{ox}. La imagen obtenida es continua puesto que se obtiene a partir del orden de franja teórico. Sin embargo, la imagen experimental está wrapeada, y por consiguiente, las dos imágenes no pueden ser directamente comparadas. Para evitar este problema la distribución teórica es wrapeada empleando una rutina escrita en Matlab (paso 5) basada en las matrices de Jones para simular un polariscopio virtual [12]. De esta manera, es posible obtener un mapa para α_{theo}, que puede ser directamente comparado con el obtenido experimentalmente, α_{exp}. Para calcular K_I, K_{II} y σ_{ox} es preciso definir una función error:

$$g = \alpha_{\exp} - \alpha_{theo} \quad (4)$$

Para ello se lleva a cabo un ajuste por mínimos cuadrados (paso 6). Puesto que el sistema resultante de ecuaciones no es lineal, es preciso resolverlo de forma iterativa. Para la resolución se decidió emplear el método Downhill Simplex [13].

Finalmente, se obtienen loa valores de K_I, K_{II} y σ_{ox}. La calidad del ajuste es evaluada empleando dos parámetros estadísticos como son la media y la varianza de la diferencia entre los valores de ángulo retardo teóricos y experimentales para los puntos evaluados.

3. DESCRIPCIÓN DEL ENSAYO

Para comprobar la calidad de la metodología propuesta se llevaron a cabo un a serie de experimentos empleando una probeta tipo CCT de 2 mm de espesor fabricada en policarbonato con una entalla inicial de 10mm. Para generar la grieta se empleo una cuchilla (figura 1).

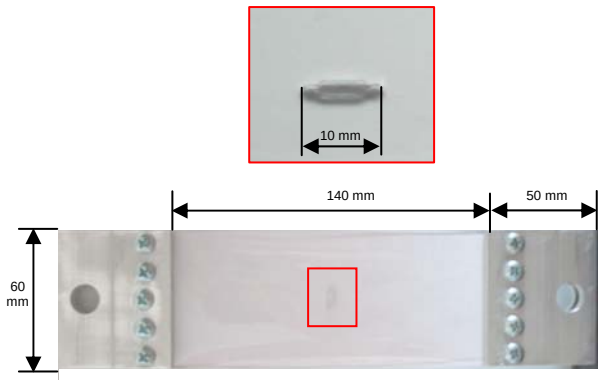

Figura 1. Ilustración que muestra la geometría y dimensiones de las probetas empeladas durante los ensayos.

Para aplicar la carga a la probeta se empleó una máquina universal de ensayo INSTRON 5567 con una capacidad de carga máxima de 30 kN (figura 2) controlada desde un PC de mesa (Dell - Pentium 4 Intel processor).

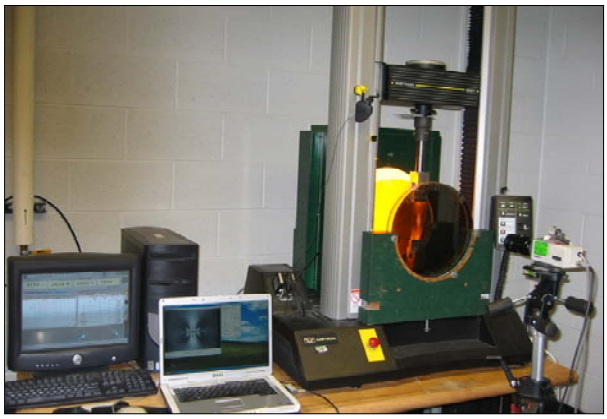

Figura 2. Foto ilustrativa del equipo y el montaje experimental empleado para los ensayos

Durante los ensayos se capturaron imágenes fotoelásticas a intervalos de carga 100 N para un rango de carga comprendido entre 0 y 700 N. La figura 3 muestra una imagen del mapa de retardo en escala de grises para una grita de 12.18mm con una carga aplicada de 500 N.

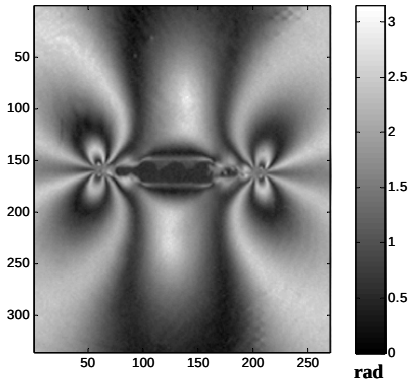

Figura 3. Mapa de ángulo de retado calculado empleando la metodología propuesta. Imagen correspondiente a una grieta de longitud 2a=12.18mm con una carga aplicada de 500 N.

Para los ensayos, se empleó un polariscopio de transmisión con una fuente de luz monocromática. Para capturar las imágenes se utilizó una cámara CCD Panasonic VW-BP100 controlada por un ordenador portátil (DELL - Centrino Intel Mobile Technology processor) a través de una tarjeta de video (Imperx Inc. VCE-B5A01). Además, se utilizó una lente de zoom de 70-210mm (Tamron model 58A) para aumentar la resolución espacial en la región cercana al vértice de la grieta (figura 3).

Seguidamente, las imágenes fueron analizadas empleando un programa escrito en Matlab® que implementaba los pasos previamente descritos. Como resultado del programa se obtuvieron los valores de K_I, K_{II} y σ_{ox}. Los resultados experimentales se compararon con los obtenidos mediante un modelo de elementos finitos para la misma geometría y condiciones de carga ensayadas.

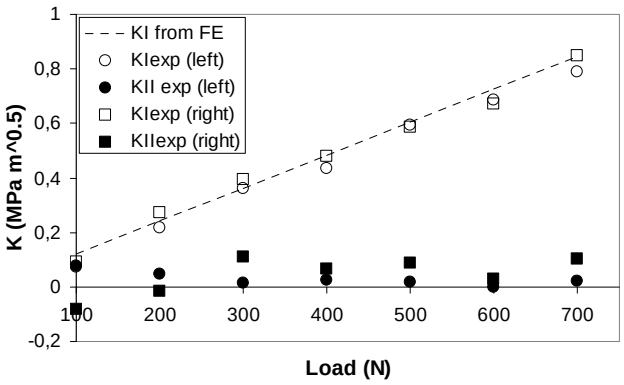

Figura 4. Resultados para K_I y K_{II}, empleando la metodología propuesta con una grieta de longitud 12.18mm para un intervalo de carga de 0 a 700 N.

4. RESULTADOS Y DISCUSIÓN

Las figuras 4 y 5 muestran los valores de K_I, K_{II} y σ_{ox} obtenidos a partir del análisis de imágenes fotoelásticas empleando la metodología propuesta. Los resultados experimentales han sido comparados con lo obtenidos mediante el método de los de elementos finitos.

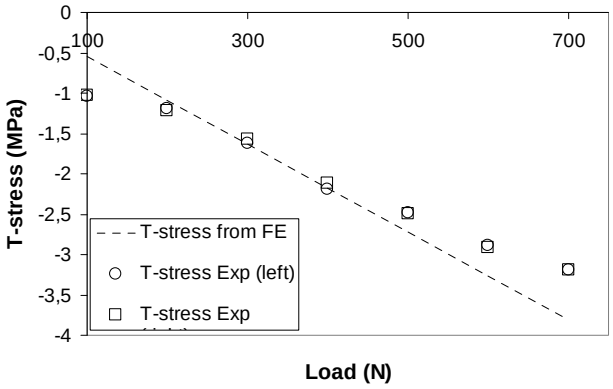

Figura 5. Resultados para σ_{ox}, empleando la metodología propuesta con una grieta de longitud 12.18mm para un intervalo de carga de 0 a 700 N.

Los resultados experimentales muestran un excelente nivel de concordancia con los obtenidos mediante el método de los elementos finitos (figures 4 y 5). Existe una pequeña dispersión en los datos que puede ser atribuida a la presencia de ruido en las imágenes. Otra posible razón de esta dispersión en los resultados puede ser atribuida a errores cometidos durante la fase de localización del vértice de la grieta, puesto que la identificación de realizó manualmente mediante observación directa de la imagen de franjas. Sin embargo, en todos los casos las calidad del ajuste está avalada por valores muy pequeños del error medio normalizado (menor de 6.25×10^{-3}) y de la varianza (menor de 2.4×10^{-3}). Esto también se pone de manifiesto en la figura 6 en la que se muestra una comparativa entre el ángulo de retardo experimental y el obtenido empleando el modelo de Westergaard con los

valores de K_I, K_{II} y σ_{ox} obtenidos tras realizar el ajuste matemático. Como se puede observar ambas imágenes son prácticamente idénticas con muy pequeñas diferencias de forma localizada. Estas diferencias son razonables teniendo en cuenta que la solución analítica adoptada se basa en condiciones lineales elásticas y asume las condiciones de una grieta en una placa infinita.

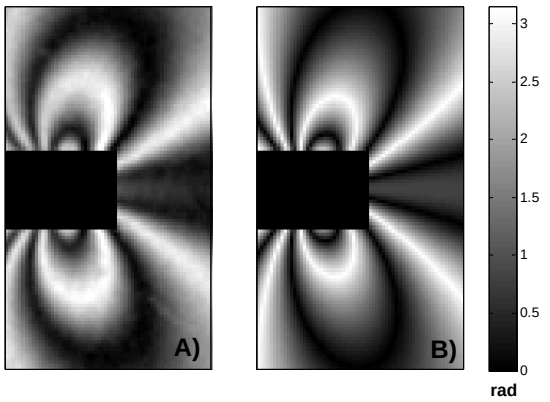

Figura 6. Comparativa entre mapas del ángulo de retardo para una grieta de 12.18 mm de longitud. a) retardo obtenido experimentalmente combinando las imágenes correspondientes a un polariscopio circular en campo claro y oscuro respectivamente y b) calculadas empleando el modelo de Westergaard tras realizar el ajuste matemático.

5. CONCLUSIONES

Con el presente trabajo se ha mostrado un nuevo método para el cálculo del factor de intensificación de tensiones a partir del análisis de imágenes fotoelásticas. Con el método propuesto es posible obtener resultados precisos en tan solo unos segundos capturando solo dos imágenes fotoelásticas correspondientes a dos posiciones diferentes del analizador. El nuevo método evita la necesidad de aplicar algoritmos de desenvolvimiento de la fase en el cálculo del factor de intensificación de tensiones, eliminando fuentes potenciales de error. El método ha sido ensayado con una probeta tipo CCT fabricada en policarbonato de 2mm de espesor. Los resultados muestran un extraordinario nivel de concordancia con los obtenidos mediante el método de los elementos finitos, mostrando el potencial del método propuesto para otras aplicaciones en ingeniería.

AGRADECIMIENTOS

Este trabajo se ha llevado a cabo con la financiación de la Junta de Andalucía a través del proyecto de investigación de Excelencia TEP 2009-5177 y del proyecto del Plan Nacional del I+D del Ministerio de Educación y Ciencia MAT2009-09058. Los autores también quieren agradecer la generosidad del Departamento de Ingeniería Mecánica de Michigan State University al poner a disposición de los autores sus instalaciones.

REFERENCIAS

[1] Post, D. (1954), 'Photoelastic stress analysis for an edge crack in a tensile field', Proc. SESA, Vol. 12, no. 1, pp. 99-116.

[2] Wells, A., Post, D. (1958), ' Dynamic stress distribution surrounding a running crack- a photoelastic analysis', Proc. SESA, Vol. 16, no. 1, pp. 69-92.

[3] Sanford, R. J., Dally, J. W. (1979), 'A general method for determining the mixed mode stress intensity factor form isochromatic fringe patterns', Engineering Fracture Mechanics, 11, pp. 621-683.

[4] Diaz, F. A., Patterson, E. A., Tomlinson, R. A., Yates, J.R. (2004), 'Measuring stress intensity factors during fatigue crack growth using thermoelasticity', Fatigue and Fracture of Engineering Materials and Structures, Vol. 27, no. 7, pp. 571-584.

[5] Lopez-Crespo, P., Shterenlikht, A., Patterson, E.A., Withers, P.J., and Yates, J.R., (2008), 'The stress intensity of mixed mode cracks determined by digital image correlation', J. Strain Analysis, 43(8):769-780.

[6] Nurse, A. D., Patterson, E. A. (1993), 'Determination of predominantly mode II stress intensity factor from isochromatic data', Fatigue and Fracture of Engineering Materials and Structures, Vol. 16, no. 12, pp. 1339-1354.

[7] Patterson, E. A. (2002), 'Digital photoelasticity: Principles, practice and potential', Strain, Vol. 38, pp. 27-39.

[8] Wang, Z. F., Patterson, E. A. (1995), 'Use of phase-stepping with demodulation and fuzzy sets for birefringence measurement', Optics, Lasers and Engineering, Vol. 22, pp. 91-104.

[9] Ewalds, H. L. and Wanhill, R. J. H. (1989), 'Fracture Mechanics'. Published by Edward Arnold, Netherlands.

[10] Westergaard, H. M. (1939), 'Bearing pressures and cracks', Journal of Applied Mechanics, Vol. 6, pp. 49-53.

[11] Dally, J.W., Riley, W.F., 'Experiental Stress Analysis', 4th edition, Mc-Graw Hill, 2005.

[12] Ramesh, K. (2000), 'Digital photoelasticity. Advanced techniques and applications', Springer, Berlin,

[13] Nelder, J. A. and Mead, R. (1965), 'A Simplex Method for Function Minimization', The Computer Journal, Vol. 7, pp. 308-313

METODOLOGÍA PARA LA OBTENCIÓN DE LA TENACIDAD DE FRACTURA DINÁMICA. APLICACIÓN A UN ACERO ESTRUCTURAL

N. García, D. Cendón, F. Gálvez, V. Sánchez-Gálvez

Departamento de Ciencia de Materiales, E.T.S. de Ingenieros de Caminos,
Canales y Puertos, Universidad Politécnica de Madrid, C/ Profesor Aranguren s/n,
28040 Madrid, España.
E-mail: fgalvez@mater.upm.es

RESUMEN

Este trabajo propone una nueva metodología para la obtención de la tenacidad de fractura dinámica en materiales cuyo comportamiento en fractura dinámica se puede asimilar al elástico y lineal. La metodología se basa en el ensayo de flexión en tres puntos en barra Hopkinson. Consiste en obtener la historia del factor de intensidad de tensiones y determinar el tiempo en el que se inicia la propagación de la fisura. Para ello es necesario medir la deformación en un lugar próximo a la punta de la fisura mediante cualquier técnica de extensometría aplicable a alta velocidad de deformación. La nueva metodología se basa en la proporcionalidad entre la deformación de la probeta y el factor de intensidad de tensiones en condiciones dinámicas en puntos cercanos a la punta de la fisura. Para determinar con precisión el instante de rotura, se empleó una técnica mixta contraponiendo la medida de COD con la deformación de la probeta en un lugar determinado. La metodología se ha aplicado con éxito al acero estructural Armox 500T, obteniéndose unos valores de tenacidad de fractura dinámica muy similares a los valores de tenacidad de fractura estática de este material, en línea con lo esperable para un acero de alta resistencia.

ABSTRACT

This work proposes a new methodology to obtain the dynamic toughness of materials that behave linear elastic. The methodology is based on the three point bending test on a Hopkinson bar. It consists in obtaining the history of the stress intensity factor and measure the instant when the crack starts to propagate. To reach this, it is necessary to measure the strains near the crack tip using any technique applicable at high strain rate. The methodology is based on the proportionality between the strains and the stress intensity factor near the crack tip. To measure with enough precision the failure time a mixed technique was used, representing the COD against strains near the crack tip. This methodology has been successfully applied to the steel Armox500, and similar values of the dynamic toughness have been obtained when compared to static. This result was as expected, since this is a very high strength steel with a negligible strain rate effect.

PALABRAS CLAVES: Alta velocidad de deformación, Tenacidad de Fractura Dinámica, Acero de Blindajes, Correlación digital de imágenes, Barra Hopkinson.

1. INTRODUCCIÓN

Resulta de gran importancia conocer las propiedades mecánicas de materiales estructurales a alta velocidad de deformación a la hora de estudiar fenómenos tales como explosiones, impactos de proyectiles, ondas de presión, etc. En especial, la tenacidad de fractura en régimen dinámico (K_{ICd}) debe tenerse en cuenta en el diseño de elementos estructurales con una extensa superficie de material expuesta al daño, como sucede por ejemplo en blindajes de protección de vehículos o instalaciones frente a explosiones. En este caso, los defectos o grietas presentes en el material pueden reducir su resistencia, la cual no puede ya ser estimada simplemente en base a los parámetros de resistencia a tracción, sino que debe estar caracterizada también por la tenacidad de fractura dinámica. A pesar de su gran relevancia, la fractura en régimen dinámico no ha sido muy estudiada hasta el momento. Así como en régimen estático, la metodología de obtención de la tenacidad de fractura está recogida en una serie de normas ampliamente utilizadas, en régimen dinámico no existe todavía ningún procedimiento comúnmente aceptado y validado. Esto se debe a que la obtención de K_{ICd} presenta dificultades tales como el carácter de pulso de onda de la tensión aplicada y la falta de equilibrio en la probeta. El problema ha sido abordado por parte de algunos investigadores, entre los cuales puede citarse a Weisbrod y Rittel [1], mediante metodologías mixtas experimental-numéricas. Éstas proponen elaborar numéricamente la historia del factor de intensidad de tensiones $K_I(t)$ por un lado y determinar de manera experimental el instante de rotura por otro. El valor del factor de intensidad de tensiones en el instante justo de rotura proporcionaría la tenacidad de fractura dinámica $K_{ICd} = K_I(t_R)$. Sin embargo, los autores de este trabajo intentaron aplicar este método sobre el acero Armox 500T en anteriores estudios [2] sin obtener resultados satisfactorios [3]. Siguiendo en esta línea de trabajo, se identificó un factor crítico principal: las simulaciones numéricas del ensayo no eran lo suficientemente representativas en cuanto a los tiempos de propagación de las ondas. En efecto, medir experimentalmente el tiempo de rotura requiere una gran precisión, tanto en

los procedimientos experimentales como en las simulaciones numéricas. Sin embargo, el tiempo en la simulación obtenido en nuestro estudio, presentaba un adelanto con respecto al tiempo medido en el ensayo real, lo cual invalidaba las medidas encontradas. La dificultad radicaba esencialmente en simular numéricamente los contactos entre la probeta ensayada y el dispositivo experimental, factores clave a la hora de reproducir tiempos, como se comprobó posteriormente [4]. A la vista de esto, se ha desarrollado una nueva metodología que no presenta los problemas encontrados en las metodologías experimental-numéricas y que es, en principio, aplicable a cualquier material elástico y lineal. Dicha metodología se presenta a continuación.

2. FUNDAMENTO TEÓRICO Y METODOLOGÍA PROPUESTA

En régimen estático, existe proporcionalidad entre la carga aplicada y el factor de intensidad de tensiones [5], según:

$$K_I = G(geom)P\sqrt{a} \quad (1)$$

Siendo G una función que depende de la geometría, a el tamaño de fisura y P la carga aplicada.

Particularizando esto para una probeta con un tamaño inicial de fisura y una geometría dados, se tiene:

$$K_I = \beta \cdot P \quad (2)$$

Siendo β el factor de proporcionalidad entre la carga aplicada P y el factor de intensidad de tensiones K_I para esa probeta. Por otra parte, por estar en régimen elástico y lineal, existe proporcionalidad entre la carga aplicada P y la deformación ε medida en cualquier punto de la probeta. Es decir:

$$P = \alpha \cdot \varepsilon \quad (3)$$

De las expresiones (2) y (3), se puede obtener la proporcionalidad entre el factor de intensidad de tensiones y la deformación de la probeta medida en cualquier punto, según:

$$K_I = \alpha \cdot \beta \cdot \varepsilon \quad (4)$$

Sin embargo en régimen dinámico esta relación deja de ser válida debido a varios factores. Por una parte, tiene que transcurrir un cierto tiempo desde que se aplica la carga hasta que las tensiones alcanzan la punta de la fisura. Por otra parte, las fuerzas de inercia no son despreciables. Sólo parte de la carga aplicada se invierte en inducir un campo tensional en la punta de la fisura, ya que el resto se requiere para poner en movimiento la probeta.

No obstante, en puntos muy cercanos a la punta de fisura, sí puede verificarse la proporcionalidad descrita en (4). Esto se debe a que la menor distancia entre el punto de medida de la deformación y la punta de fisura anula prácticamente el efecto de retardo en la propagación de las ondas, a la vez que reduce drásticamente la masa a movilizar, lo cual establece unas condiciones muy similares al caso estático.

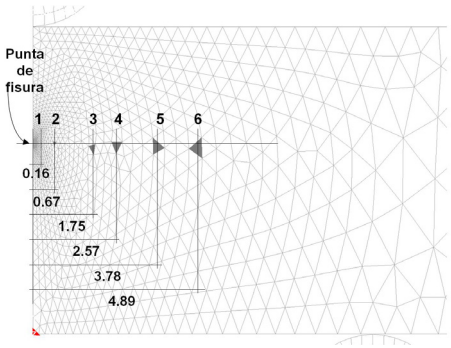

Figura 1. Puntos correspondientes a seis elementos de la malla de la probeta y sus respectivas distancias (en mm) a la punta de fisura

Todo esto se ha comprobado en el presente trabajo mediante simulaciones numéricas del ensayo, tanto en régimen estático como en dinámico. Así, se sometió la probeta a un desplazamiento del punto de aplicación de carga similar al que experimenta la probeta en el ensayo real y se extrajo la historia del factor de intensidad de tensiones y la historia de deformaciones, en una serie de elementos cada vez más alejados de la punta de fisura, como puede verse en la Figura 1.

Representando K_I frente a la deformación en cada elemento, se obtuvo su coeficiente de proporcionalidad, tanto en estático y en dinámico, como puede verse en la Figura 2. Así en régimen estático, se apreció una linealidad a cualquier distancia de la punta de fisura, mientras que en dinámico esta proporcionalidad sólo se cumplió a pequeñas distancias de la punta de fisura. Para el material utilizado, esta distancia límite en el punto de medición de la deformación se estableció en 2mm aproximadamente.

El fundamento teórico expuesto permite por tanto obtener un valor proporcional a K_I mediante la medida de la deformación en un punto situado a una distancia máxima de 2mm de la punta de fisura, en el caso de nuestro material. Teniendo en cuenta que el factor de proporcionalidad es el mismo en estático y en dinámico (Figura 2), basta obtener dicho factor de proporcionalidad, es decir, el producto $\alpha \cdot \beta$, en condiciones estáticas, para cada probeta. Para ello se registra la relación entre la carga aplicada y la deformación en el punto de medición mediante un ensayo estático a baja carga, sin llegar a propagar la fisura, obteniendo así el factor α. La relación entre la carga aplicada en régimen estático y el factor de intensidad de tensiones (factor β) se puede obtener mediante simulación numérica o en manuales. Multiplicando estos dos factores por la deformación de la probeta en condiciones dinámicas registrada durante el ensayo en el punto de medición, se obtiene la historia del factor de intensidad de tensiones dinámico. Identificando el instante de rotura en el ensayo dinámico de la manera que se describe a continuación, se puede conocer el valor de la tenacidad de fractura dinámica.

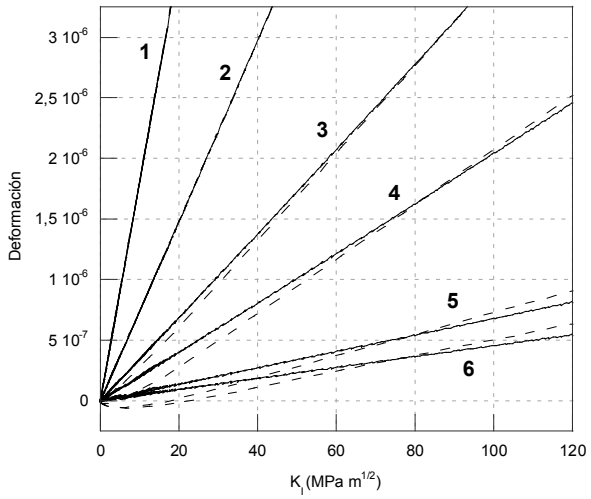

Figura 2. Deformaciones normales al plano de fisura de los puntos 1, 2, 3, 4, 5 y 6 en función de K_I, en el caso estático (líneas continuas) y dinámico (líneas de puntos)

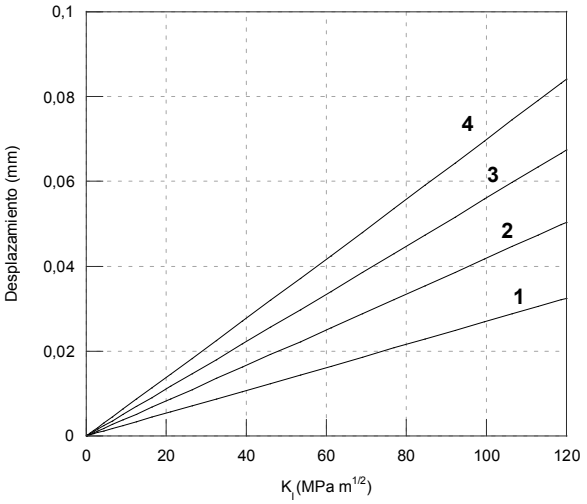

Figura 3. Desplazamientos normales al plano de fisura de los puntos 1, 2, 3 y 4 en función de K_I, en simulación dinámica.

2.1. Medición del tiempo de rotura

El tiempo de rotura ha sido siempre un punto crítico en el estudio de la fractura dinámica. En la nueva metodología elaborada este problema se resolvió mediante la sencilla confrontación de dos registros experimentales: la deformación en un punto cercano a la punta de fisura y la abertura de los labios de la entalla o COD. En efecto, ambos son proporcionales al factor de intensidad de tensiones y por tanto entre sí, hasta el momento de rotura. La proporcionalidad del COD con el factor de intensidad de tensiones se comprobó mediante simulación numérica como puede verse en la Figura 3, donde se representan los desplazamientos horizontales de varios puntos tomados a diferentes distancias a lo largo de la entalla, frente al factor de intensidad de tensiones en régimen dinámico.

Cuando la grieta se empieza a propagar, dicha proporcionalidad deja de existir. La deformación en el punto de medición tiende a disminuir, mientras que el COD tiende a aumentar, lo cual hace todavía más patente la pérdida de proporcionalidad entre ambos y la consiguiente identificación del instante de rotura. Para poder medir correctamente el COD, se decidió emplear un sistema de Correlación Digital de Imágenes (CDI en lo sucesivo) y una cámara de alta velocidad. La CDI es un método de extensometría sin contacto que correlaciona, mediante algoritmos, sucesivas imágenes tomadas en el ensayo, de manera a obtener mapas de desplazamientos y deformaciones en una zona seleccionada de la imagen. Para ello, se necesita pintar previamente la superficie de la probeta para que el programa pueda identificar con facilidad puntos de referencia.

Representando la deformación de la banda frente al COD, y aplicando a esta gráfica un criterio de pendientes al 95% similar al que indica la norma ASTM para hallar la fuerza crítica en el gráfico Fuerza-abertura de fisura, se obtuvo la deformación a rotura, que nos reveló a su vez el instante de rotura.

En base a las ideas anteriores y a los dispositivos experimentales disponibles, la secuencia metodológica para obtener la tenacidad de fractura dinámica se establece del siguiente modo:

1. Preparación de las probetas. En una cara lateral, se pegó una banda extensométrica y en la otra se pintó según un patrón reconocible por el CDI.
2. Ensayo estático de calibración, sin llegar a rotura, para cada probeta, y obtención del factor α, que relaciona la carga estática aplicada y la deformación estática de la banda.
3. Ensayo dinámico de la probeta, grabando la cara pintada con cámara de video de alta velocidad y registrando la historia de la deformación dinámica de la banda frente al tiempo $\varepsilon(t)$.
4. Procesamiento con el CDI de las imágenes tomadas por la cámara y obtención del COD frente al tiempo. Determinación de la deformación y tiempo de rotura ε_r por comparación del COD frente a la deformación de la banda.
5. Medida del tamaño de fisura sobre la probeta rota, siguiendo el procedimiento indicado en la norma ASTM E399.
6. Obtención del factor β, que relaciona la carga estática frente al factor de intensidad de tensiones, mediante simulación numérica estática, utilizando como input el tamaño de fisura medido y el desplazamiento de los apoyos registrado en el ensayo.
7. Determinación de la tenacidad de fractura dinámica multiplicando los tres factores obtenidos mediante la expresión:

$$K_{ICd} = \alpha \cdot \beta \cdot \varepsilon_r \qquad (5)$$

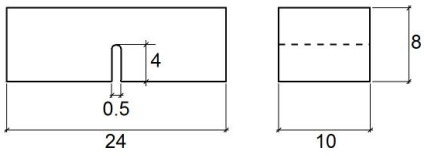

Figura 4. Geometría de las probetas (en mm)

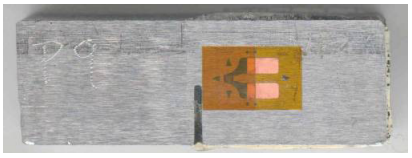

Figura 5. Probeta instrumentada

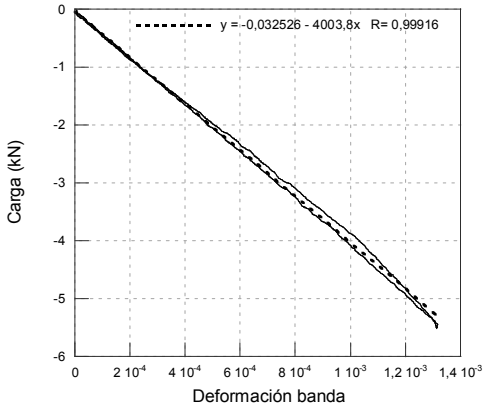

Figura 6. Obtención de α en la calibración estática

3. CAMPAÑA EXPERIMENTAL

3.1. Material y probetas

La nueva metodología se aplicó sobre el acero de alta resistencia Armox 500T fabricado por la empresa sueca SSAB. Sus propiedades mecánicas, suministradas por el fabricante [6], se recogen en la Tabla 1 y sus ecuaciones constitutivas y criterio de rotura pueden encontrarse en [4]. Este material se utiliza como blindaje de vehículos, mostradores de bancos, protecciones contra robo, etc, y se eligió precisamente por la gran importancia de la tenacidad de fractura en sus aplicaciones.

Se utilizaron probetas de flexión en tres puntos de tipo Charpy, prefisuradas por fatiga según la norma ASTM E399 [7], con las dimensiones mostradas en la Figura 4 y fisuras propagadas al menos 1.5mm de profundidad.

Las probetas se prefisuraron utilizando una máquina servohidráulica y un sistema de monitorización de la fisura consistente en un telescopio y una cámara de video enfocada sobre la probeta.

Las probetas fueron instrumentadas por una cara (Figura 5), con una banda de pequeño tamaño de rejilla, colocada a 2mm de la fisura en horizontal, y a la altura de la punta de fisura en vertical.

El otro lado de la probeta se pintó de blanco con puntos negros, por ser éste el patrón que ofrecía mejores resultados en la CDI.

Tabla 1. Propiedades mecánicas del acero Armox 500T

Módulo de elasticidad E	207 GPa
Coeficiente de Poisson	0.3
Densidad	7850 kg/m3
Límite elástico	1250 MPa
Tensión de rotura	1450-1750MPa
Elongación	8%-10%
Dureza	480-540 HB
Velocidad de propagación de las ondas	5135 m/s

3.2. Calibración estática de la probeta: obtención de α

Los ensayos estáticos de calibración de flexión en tres puntos se llevaron a cabo en una máquina servohidráulica con una célula de carga de 25kN con un error menor de 25N. Se realizaron en control en desplazamiento con una velocidad de 0.1mm/min. Se alcanzó una carga de 6kN (equivalente a un factor de intensidad de tensiones de unos 50 MPa·m^{½}, un 60% aproximadamente de la tenacidad de fractura medida en régimen estático), y a continuación se descargó a la misma velocidad.

Con estos ensayos, se obtuvo la relación entre la carga aplicada y la deformación de la banda extensométrica, es decir, el factor α. La Figura 6 muestra un ejemplo de la relación carga-deformación medida mediante la banda extensométrica en una de las probetas ensayadas. El factor α es la pendiente de la recta de ajuste obtenida.

3.3. Ensayo dinámico: obtención de la deformación a rotura de la banda ε_r

Una vez calibradas en estático, las probetas se sometieron a ensayos dinámicos a rotura de flexión en tres puntos, mediante la técnica experimental de la barra Hopkinson, representada en la Figura 7.

Con estos ensayos se obtuvo: por un lado, la historia de deformación dinámica de la banda, y por otro, la historia del COD mediante el sistema de CDI. La adquisición de imágenes en el ensayo dinámico se hizo mediante una cámara de alta velocidad, capaz de obtener hasta un millón de imágenes por segundo.

Las imágenes de la cámara, unas 300 para cada probeta, se trataron con el software Vic 2D [8]. Se configuró un extensómetro digital seleccionando sobre la imagen dos puntos a un lado y otro de la entalla, a una distancia media entre la punta de fisura y el borde de la probeta. (Figura 8)

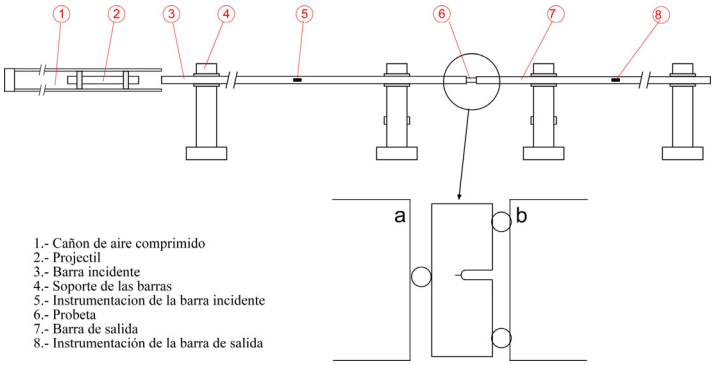

Figura 7. Esquema de los ensayos a alta velocidad de deformación en la barra Hopkinson.

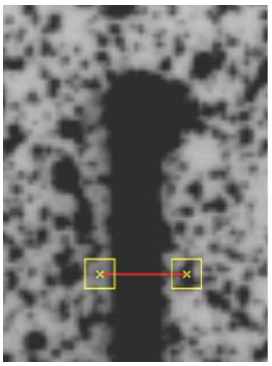

Figura 8. Extensómetro digital del Software Vic 2D

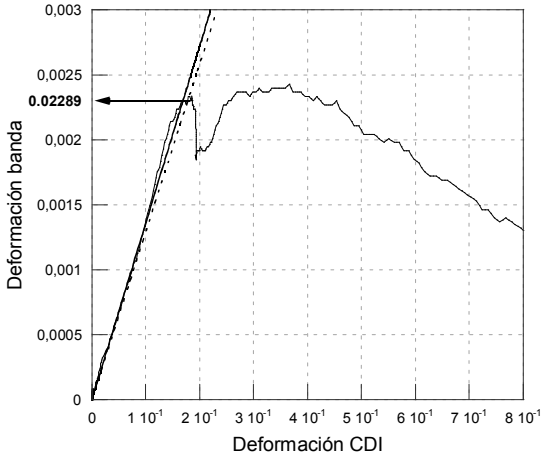

Figura 9. Obtención de la deformación a rotura mediante los registros experimentales

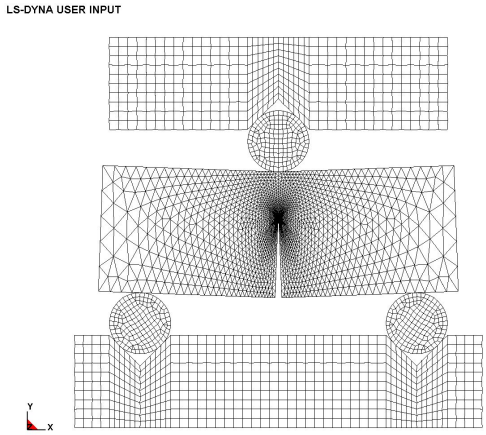

Figura 10. Mallado del ensayo de flexión en tres puntos

Representando en un mismo gráfico la deformación de la banda en dinámico y la medida con el extensómetro digital, se obtuvieron curvas como la representada en la Figura 9. Se identificó sobre estas curvas la deformación a rotura, es decir, la deformación correspondiente a la pérdida de linealidad de la curva, según lo explicado en el apartado anterior.

3.4. Simulación numérica: obtención de β.

Para conocer la relación entre la carga aplicada y el factor de intensidad de tensiones, es decir, el factor β, se realizaron simulaciones del ensayo estático mediante el programa LS-DYNA [9]. Las simulaciones, en configuración de dos dimensiones (Figura 10), incluyeron la probeta, los soportes y los rodillos de apoyo. Se malló sólo la mitad del dispositivo experimental por ser simétrico y se asumieron condiciones de deformación plana. Se impuso un desplazamiento creciente en el borde del apoyo superior y desplazamientos impedidos en la base del soporte inferior.

La malla se afinó especialmente en la punta de fisura, con un tamaño medio de elemento en esta zona de $a/1000$ siendo a el tamaño de la fisura. Para conseguir el mayor realismo posible en la simulación, se impuso el tamaño de fisura medido sobre la probeta ensayada. El factor de intensidad de tensiones para un valor unitario de carga se obtuvo mediante el método de los desplazamientos nodales [10], según la expresión:

$$K_I = \frac{E\sqrt{2\pi}}{(1+\nu)(\kappa+1)} \frac{u_1\sqrt{r_2^3} - u_2\sqrt{r_1^3}}{\sqrt{r_2^3 r_1} - \sqrt{r_1^3 r_2}} \qquad (6)$$

Siendo u_1 y u_2 las historias de los desplazamientos normales al plano de fisura de los nodos 1 y 2, r_1 y r_2 sus respectivas distancias a la punta de fisura, E el módulo de elasticidad y ν el coeficiente de Poisson del material. El parámetro elástico κ vale $3-4\nu$ en caso de deformación plana, y $(3-\nu)/(1+\nu)$ en caso de tensión plana. El factor β se obtuvo como la relación entre el valor de K_I obtenido y la carga unitaria.

3.5. Obtención de K_{ICd}

A partir de los parámetros α, β y ε_r hallados en los epígrafes anteriores, se utilizó (5) para hallar K_{ICd}.

4. RESULTADOS

Los resultados obtenidos para las seis probetas ensayadas están recogidos en la Tabla 2.

Estos valores proporcionaron una K_{ICd} promedio para el acero Armox 500T de 87.6 MPa·m^{½} con una desviación típica de 8,9 MPa·m^{½}.

Los valores de K_{ICd} encontrados son prácticamente idénticos a los hallados en régimen estático [2]. Esto es lo esperable para un acero de alta resistencia, por lo que los resultados pueden considerarse fiables y la presente metodología desarrollada para este material validada.

Tabla 2. Valores obtenidos de K_{ICd}, factor α, factor β y deformación dinámica a rotura ε_r

probeta	Factor α (kN)	Factor β (MPa√m / kN)	ε_r	K_{ICd} (MPa√m)
A7	2693	7.610	0.00439	90.0
A12	4071	7.248	0.00335	99.0
A20	4055	7.985	0.00265	85,9
A21	4004	9.392	0.00228	86,1
A27	4657	9.910	0.00193	89,2
P9	3581	9.151	0.00224	73,2

5. CONCLUSIONES

- Se ha puesto a punto y validado una nueva metodología para la obtención de K_{ICd} en aceros estructurales. Esta metodología está basada en la proporcionalidad en régimen dinámico entre K_{ICd} y la deformación en puntos cercanos a la punta de la fisura. Consiste en hallar K_{ICd} como el producto de tres factores α, β y ε_r. Los factores α y β se obtienen de calibraciones estáticas (experimental y numérica, respectivamente) de cada probeta; y el factor ε_r, deformación a rotura dinámica, se obtiene del ensayo dinámico, a partir del registro de una banda extensométrica colocada cerca de la punta de fisura. La metodología sería en principio aplicable a cualquier material que tenga un comportamiento en fractura elástico y lineal.

- La metodología desarrollada no presenta las complicaciones encontradas en las metodologías mixtas experimental-numéricas. Se basa en datos tomados principalmente de los ensayos experimentales, prescindiendo de simulaciones numéricas que pueden no ser suficientemente representativas del ensayo dinámico, como se vio en estudios anteriores.

- Se ha ideado un sistema para la determinación fiable del instante de rotura en el ensayo dinámico. Este sistema consiste en contrastar el registro de deformación que proporciona la banda en el ensayo dinámico, en un punto cercano a la punta de fisura, con un registro de COD del mismo ensayo. El instante en que ambos registros dejan de ser proporcionales es el instante en que la fisura comienza a propagarse.

- Se ha probado y validado el sistema de Correlación Digital de Imágenes para la medida de COD en ensayos dinámicos. El sistema consta del software Vic-2D y de una cámara de alta velocidad, con una frecuencia de toma de imágenes de 3 μs^{-1}.

- Aplicando la nueva metodología a seis probetas de acero Armox 500T, se ha obtenido un valor promedio de tenacidad de fractura dinámica de 87.6 MPa·m^{½}. Este valor es muy similar a la tenacidad de fractura en condiciones estáticas, tal y como se espera de un acero de alta resistencia.

AGRADECIMIENTOS

Los autores desean agradecer al Ciencia e Innovación la financiación del proyecto a través de el programa CONSOLIDER INGENIO 2010 y el proyecto BIA2008-06705-C02-01 “SEGACEX”

REFERENCIAS

[1] G. Weisbrod and D. Rittel, *A method for dynamic fracture toughness determination using short beams,* International Journal of Fracture 104, (2000) 89-103

[2] F. Gálvez, D.A. Cendón, A. Enfedaque, y V. Sánchez-Gálvez, *Medida de la tenacidad de fractura dinámica de un acero de blindaje de alta resistencia*, Anales de la Mecánica de la Fractura 25, (2008) 695-700

[3] N. García. *Desarrollo de una nueva metodología para la obtención de K_{ICd} en un acero estructural*. Proyecto fin de Carrera. Ingeniero de Materiales, UPM. (2009)

[4] F. Gálvez, D.A. Cendón, N. García, A. Enfedaque. and V. Sánchez-Gálvez. *Dynamic fracture toughness of a high strength armor steel*. Engineering Failure Analysis 16 (2009) 2567-2575

[5] Broek D. *Elementary Engineering Fracture Mechanics*. Kluwer Springer (1982)

[6] Armox 500T Datasheet. SSAB AB (2007)

[7] ASTM E399–08. *Standard Test Method for Linear-Elastic Plane-Strain Fracture Toughness K_{ICd} of Metallic Materials.* (1993).

[8] Vic-2D/3D. Correlated Solutions, Inc. (2005)

[9] LS-DYNA 970. Livermore Software Technology Corporation. (2003)

[10] G.V. Guinea, J. Planas, and M. Elices, *K_I evaluation by the displacement extrapolation technique,* Engineering Fracture Mechanics 66, (2000) 243-255

DETERMINACIÓN DE LA TENACIDAD A FRACTURA MEDIANTE EL ENSAYO SMALL PUNCH Y CURVAS ISO-A

R. Lacalle[1], D. Ferreño[1], J. García[1], J.A. Álvarez[1], F. Gutiérrez-Solana[1]

[1]Departamento de Ciencia e Ingeniería del Terreno y de los Materiales
E.T.S de Ingenieros de Caminos, Canales y Puertos. Universidad de Cantabria
Avenida de los Castros s/n 39005 Santander

E-mail: lacaller@unican.es

RESUMEN

El ensayo Small Punch representa una de las alternativas a la caracterización convencional de materiales metálicos, con particular interés en aquellas situaciones donde el material es escaso. En este trabajo, se propone una nueva metodología para la estimación de la tenacidad a fractura de materiales metálicos mediante el uso exclusivo de probetas Small Punch entalladas. El método planteado se basa en una combinación del ensayo de probetas Small Punch entalladas y de curvas iso-a, obtenidas mediante sencillas simulaciones por elementos finitos. La técnica desarrollada ha sido aplicada a dos aceros distintos (acero naval Grade A y acero estructural E690), utilizando además probetas con distintas longitudes de entalla inicial. Los resultados obtenidos, muestran la adecuación de este método y además permiten realizar recomendaciones sobre la longitud de entalla óptima a emplear en los ensayos.

PALABRAS CLAVE: Small Punch, Tenacidad a Fractura, Curvas iso-a

ABSTRACT

The Small Punch Test represents one of the alternative ways to the conventional characterisation of metallic materials, with a particular interest in those situations with a limited amount of available material. In this paper, a new methodology for the estimation of fracture toughness of metallic materials by means of notched Small Punch specimens is proposed. This method is based on a combination of Small Punch Test on notched specimens plus iso-a curves obtained in simple Finite Element simulations. The developed technique has been applied to two different steels (Grade A ship building steel and E690 structural steel), using specimens with different initial notch lengths. The obtained results show the suitability of this method and, in addition to that, some key recommendations about the optimum notch length to be used in the tests can be done.

KEYWORDS: Small Punch Test, Fracture Toughness, iso-a Curves

1. INTRODUCCIÓN

El ensayo miniatura de punzonamiento, o *Small Punch* se enmarca dentro de la familia de técnicas alternativas para la caracterización mecánica de materiales metálicos. Por sus reducidas dimensiones puede ser considerado como un ensayo de naturaleza quasi-no-destructiva, lo que le hace idóneo para la caracterización de aquellas situaciones [1,2] donde la escasez del material impide el empleo de probetas con las dimensiones requeridas por las metodologías de ensayo convencionales [3-5].

El ensayo *Small Punch* ha sido empleado con éxito, entre otros ámbitos, en la caracterización de las propiedades de tracción de materiales metálicos [6,7]. Se han realizado además numerosos intentos para la estimación de la tenacidad a fractura a partir exclusivamente de ensayos de tipo *Small Punch* [8-10]. Sin embargo, la mayoría de las aproximaciones propuestas para la determinación de la tenacidad presentan, o bien una notable dificultad analítica (complejos modelos de elementos finitos), o bien su aplicación queda reducida a situaciones de carácter muy concreto.

En este trabajo se propone una nueva vía para la estimación de la tenacidad a fractura en régimen Elasto Plástico de materiales metálicos en base a ensayos tipo *Small Punch*. Esta nueva aproximación se basa en el ensayo de probetas *Small Punch* con una entalla lateral [11], y el empleo posterior de curvas iso-a [12] obtenidas tras una simulación por el método de los elementos finitos. La técnica desarrollada ha sido

aplicada a dos materiales distintos, una acero naval Grade A y un acero estructural E690, valorándose además el efecto sobre los resultados de la longitud de la entalla inicial.

2. EL ENSAYO SMALL PUNCH

El ensayo *Small Punch* puede definirse de forma simple como un punzonado hasta rotura de una probeta plana de pequeñas dimensiones. Durante el transcurso de la prueba se registra de forma continua tanto la carga ejercida por el punzón como el desplazamiento experimentado por éste, obteniendo, de este modo, una curva carga-desplazamiento característica de cada ensayo.

Las probetas empleadas en este trabajo presentan unas dimensiones de 10x10 mm y un espesor de referencia de 0.5 mm. Además en cada una de las probetas y previamente a la realización del ensayo, se practicó una entalla lateral mediante electroerosión por hilo (Figura 1). La misión de esta entalla es crear en la probeta un defecto preexistente, al igual que en los ensayos convencionales de tenacidad a fractura [5]. La presencia de esta entalla permite, además, la caracterización del material según la orientación deseada, situación imposible en el caso de ensayar probetas *Small Punch* convencionales sin entalla [13]. El radio de la entalla realizada en las probetas es igual a 0.15 mm, que según [14] en el ámbito de la Mecánica de la Fractura Elasto-Plástica, puede asimilarse sin consecuencias a un defecto tipo fisura.

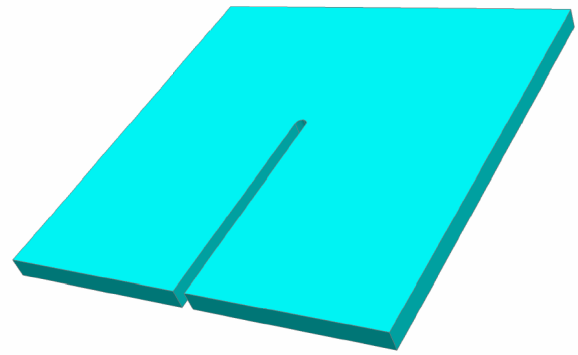

Figura 1. Esquema de las probetas Small Punch con entalla lateral.

Por otra parte en la Figura 2, puede observarse un esquema del utillaje que, acoplado a una máquina universal de ensayos mecánicos, se ha empleado para la realización de estos ensayos. En la Figura 2, se plasman además las dimensiones más relevantes de este útil de ensayo.

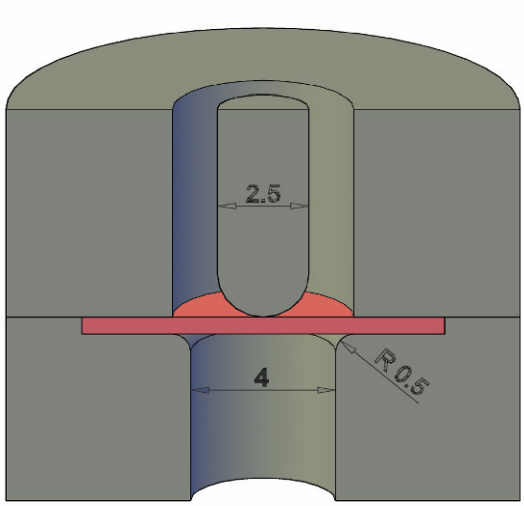

Figura 2. Esquema del utillaje de los ensayos Small Punch. Dimensiones en mm.

3. MATERIALES

En este trabajo han sido empleados dos materiales con propiedades mecánicas bien diferenciadas, un acero naval grade A y un acero estructural E690. Las composiciones químicas de estos materiales pueden consultarse en la Tabla 1. La Tabla 2 muestra, por su parte, los parámetros característicos del comportamiento en tracción de estos materiales. Con el objeto de disponer de materiales con tenacidades a fractura claramente diferenciadas se seleccionaron para ser caracterizadas la orientación T-L en el acero Grade A y la orientación L-T en el acero E690. Las curvas J correspondientes a estos materiales y orientaciones, obtenidas por el procedimiento convencional [5] empleando para ello probetas CT, pueden observarse en la Figura 3.

Tabla 1. Composición química de los aceros empleados en este trabajo (resultados en % en peso).

	Grade A	E690
C	0.13	0.135
Si	0.24	0.241
Mn	0.66	1.1
Ni	<0.02	1.518
Cr	<0.02	0.496
Mo	<0.005	0.465
Cu	<0.02	0.18

Tabla 2. Parámetros característicos del comportamiento a tracción de los aceros empleados.

	Grade A	E690
s_y (MPa)	288	840
s_u (MPa)	450	940
E (GPa)	210	200

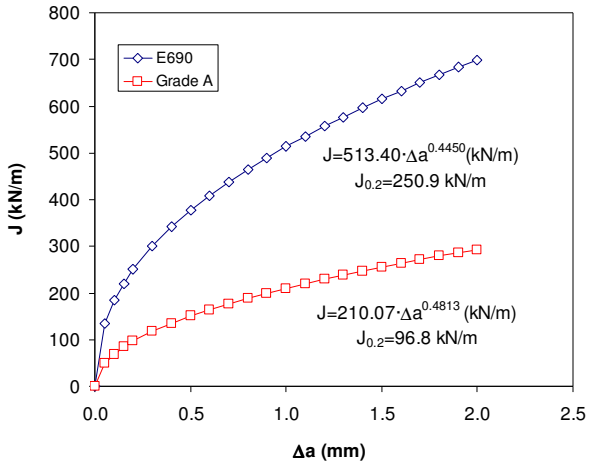

Figura 3. Curvas J de los aceros Grade A y E690.

4. METODOLOGÍA EXPERIMENTAL Y ANÁLITICA

4.1 Ensayos sobre probetas entalladas

De cada uno de los dos aceros se prepararon un total de 4 probetas Small Punch sobre las que se practicaron entallas laterales con las dimensiones que se indican en la Tabla 3. En la Figura 4 se muestran las 4 curvas obtenidas para las probetas de acero Grade A, mientras que la Figura 5 muestra las curvas correspondientes al acero E690.

Tabla 3. Longitudes de entalla inicial (mm).

Probeta	Grade A	E690
1	3.78	3.84
2	4.36	4.29
3	4.81	4.86
4	5.22	5.45

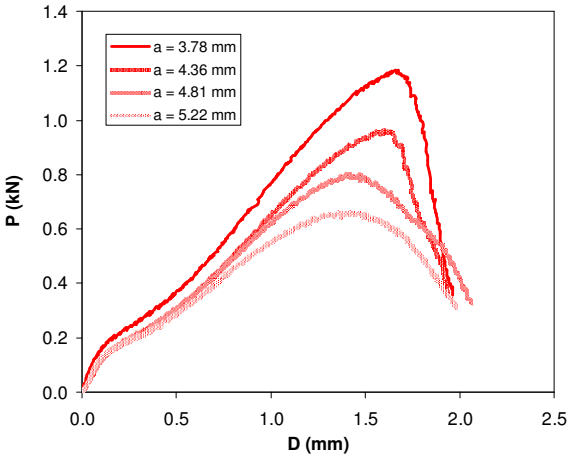

Figura 4. Curvas Small Punch experimentales (Grade A).

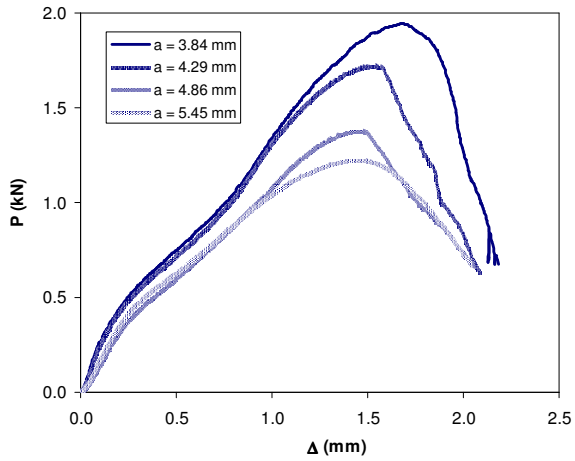

Figura 5. Curvas Small Punch experimentales (E690).

4.2 Metodología para la obtención de la curva J-Δa

Para la determinación de la tenacidad a fractura en términos de la curva J-Δa, directamente se empleó la definición de la integral J como tasa de liberación de energía [15] dada por la expresión (1).

$$J = -\frac{1}{B}\cdot\left(\frac{\partial U}{\partial a}\right)_{\Delta} \qquad (1)$$

Donde "B" es el espesor de la probeta, "U" es la energía de deformación, "a" es la longitud de fisura y "Δ" es el desplazamiento. De esta forma, la expresión (1) puede interpretarse como el incremento de energía por unidad de espesor para un incremento diferencial de la longitud de fisura siendo constante el desplazamiento.

Si se dispone de curvas iso-a (como su nombre indica sin crecimiento de grieta) de la geometría y material de interés, es posible, tras una serie de pasos [12] llegar a la expresión (1) que define la resistencia a fractura en rango elasto-plástico. Dichas curvas iso-a, no pueden, en principio, ser obtenidas por vía experimental, ya que en el transcurso del ensayo, inevitablemente se produciría crecimiento de grieta. Por ello se debe recurrir al método de los elementos finitos. En este caso, partiendo del modelo que se muestra en la Figura 6 y empleando el código ANSYS [16], se obtuvieron para cada uno de los dos materiales las curvas iso-a mostradas en las Figuras 7 y 8 que cubren un especto de fisuras desde 4.15 hasta 5.95 mm, contando desde el borde lateral de la probeta. En la simulación, de carácter elástoplástica, se emplearon elementos tipo SOLID95, habiéndose simulado además los contactos entre punzón y probeta y probeta y utillaje.

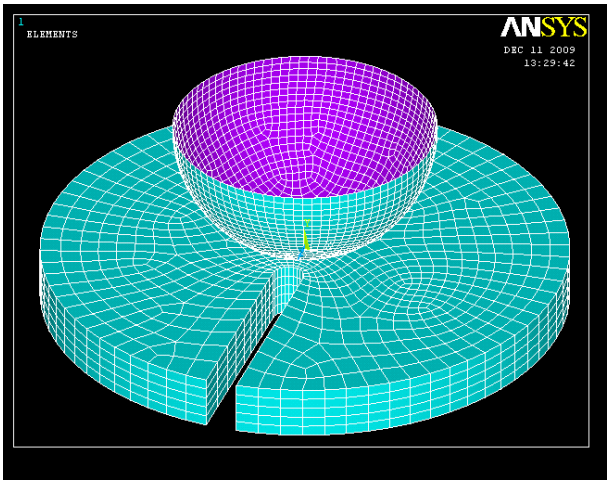

Figura 6. Modelo de elementos finitos utilizado para la obtención de las curvas iso-a. Se simula simplemente la zona de proceso, ya que el resto de la probeta permanece empotrada (Figura 1).

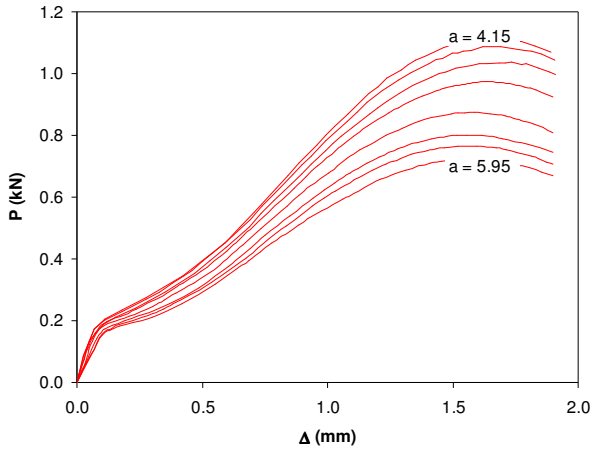

Figura 7. Curvas iso-a correspondientes al acero Grade A.

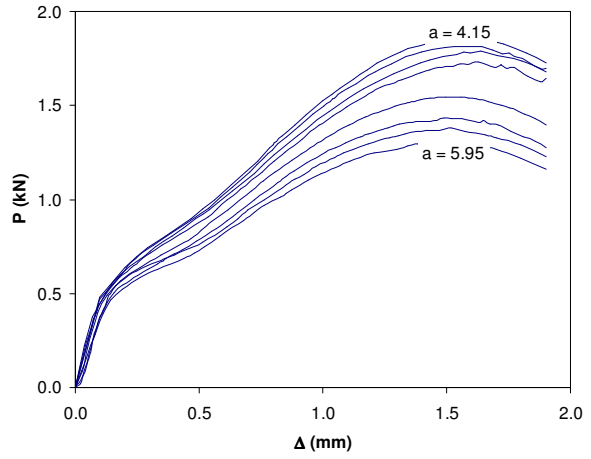

Figura 8. Curvas iso-a correspondientes al acero E690.

Una vez que se dispone de las curvas iso-a, la integral J, para cada valor de crecimiento de grieta, puede ser calculada mediante la siguiente secuencia de pasos [12]:

1. La curva U(Δ) debe ser obtenida para cada valor de "a" simplemente por integración de las curvas iso-a.

2. Las intersecciones entre las curvas de ensayo y las curvas iso-a (Figura 9) ofrecen pares de valores de interés Δ- Δa.

3. Para cada valor de interés de Δ es posible, acudiendo a las curvas estimadas en el punto 1, obtener curvas U(a).

4. Las curvas U(a), características de cada valor de Δ, pueden ser derivadas en función de "a" sin más que ajustarlas una función que en el caso analizado respondió al tipo de la propuesta en (2).

$$U = A_0 + A_1 \cdot \ln(a) \qquad (2)$$

5. Una vez se dispone del incremento diferencial de "U" frente a "a" para un desplazamiento y valor de fisura dados, el valor de J se puede calcular sin más que recurrir a (1).

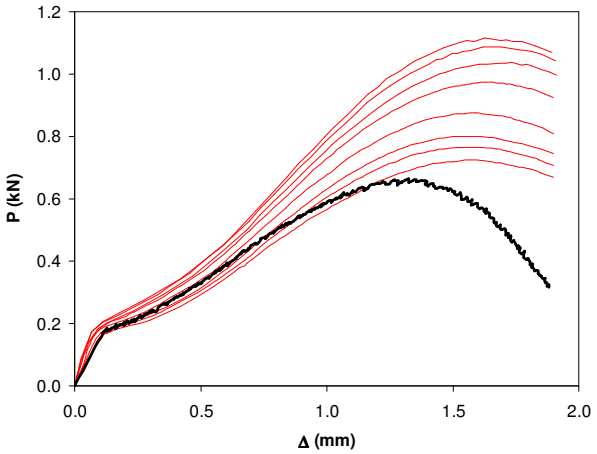

Figura 9. Ejemplo de curva experimental frente a curvas iso-a.

5. ANÁLISIS DE RESULTADOS

Aplicando el procedimiento que acaba de ser descrito a cada una de las probetas de los dos materiales, se obtuvieron las curvas J- Δa que se muestran en las Figuras 10 y 11, donde también se incluyen, a modo de referencia, las curvas J-Δa obtenidas por métodos convencionales mediante probetas CT. En todos los casos, los puntos obtenidos experimentalmente fueron ajustados según una ley potencial del tipo (3).

$$J = C_1 \cdot \Delta a^{C_2} \qquad (3)$$

Como se aprecia en las Figuras 10 y 11, el comportamiento observado es claramente función de la longitud de entalla inicial. Así, para fisuras "cortas" se aprecian altos valores de resistencia, en consonancia con las teorías generales de Mecánica de la Fractura, pero no crecientes con el incremento de la longitud de fisura. Este hecho puede ser explicado atendiendo a que, si bien para que se produzca la iniciación de grieta se necesitan altos valores energéticos, no es posible suministrar dicha energía exclusivamente al fondo de la entalla, sino que parte de la energía contribuye al daño del resto de la probeta. Por ello, cuando la grieta se inicia, su propagación resulta más sencilla en un material tanto o más dañado cuanto más corta es la entalla inicial.

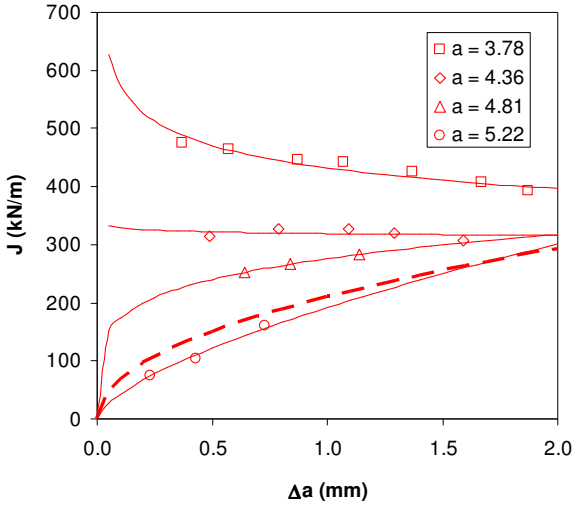

Figura 10. Curvas J-Δa para distintas longitudes de entalla (Grade A).

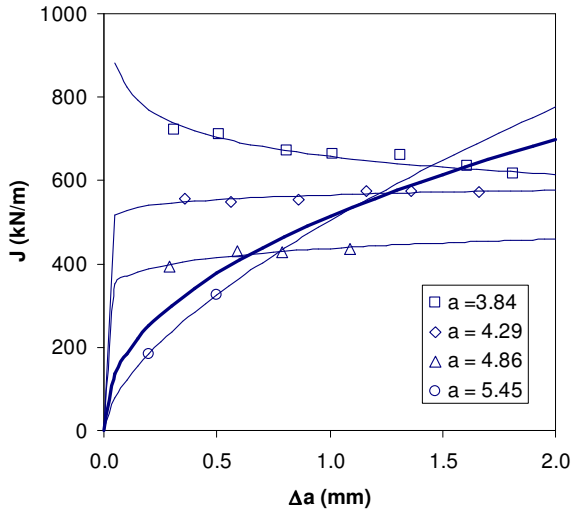

Figura 11. Curvas J-Δa para distintas longitudes de entalla (E690).

Si, para cada uno de los casos se representan los valores de los coeficientes de ajuste C_1 y C_2, se observa que se obtienen valores equivalentes a los obtenidos por la vía convencional para longitudes de entallas iniciales cercanas a 5 mm (Figuras 12 y 13).

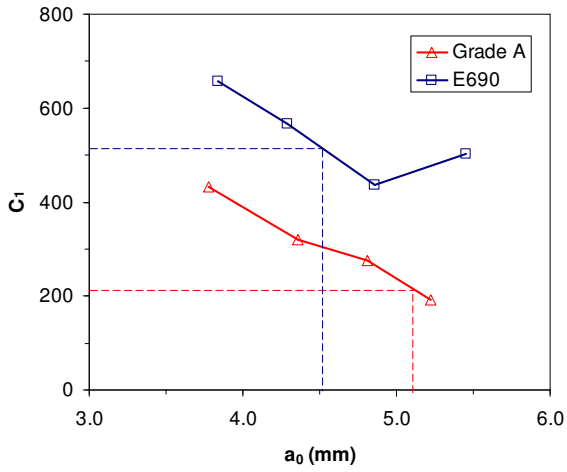

Figura 12. Evolución del parámetro de ajuste C_1 con la longitud de entalla inicial.

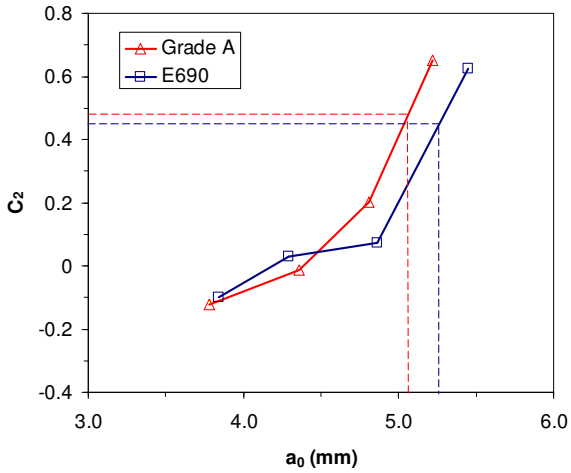

Figura 13. Evolución del parámetro de ajuste C_2 con la longitud de entalla inicial.

Puede representarse también el valor de tenacidad de iniciación $J_{0.2}$, definido como el valor de J correspondiente a un crecimiento de grieta de 0.2 mm, frente a las distintas longitudes de entalla iniciales. Se comprueba nuevamente, que para entallas ligeramente superiores a 5 mm se alcanzan valores semejantes a los obtenidos en ensayos normalizados de fractura. Partiendo de los resultados mostrados, y atendiendo a la semejante tendencia que presentan las curvas de la Figura 14, puede proponerse la expresión (4) para la determinación de $J_{0.2}$ con independencia de la longitud de entalla empleada.

$$J_{0.2} = J_{0.2,a_0} + 333 \cdot (a_0 - 5.1) \qquad (4)$$

En (4), "J" viene expresada en kN/m y "a" en mm. Por otro lado, $J_{0.2,a0}$ representa la tenacidad de iniciación aparente calculada con una probeta con entalla inicial a_0.

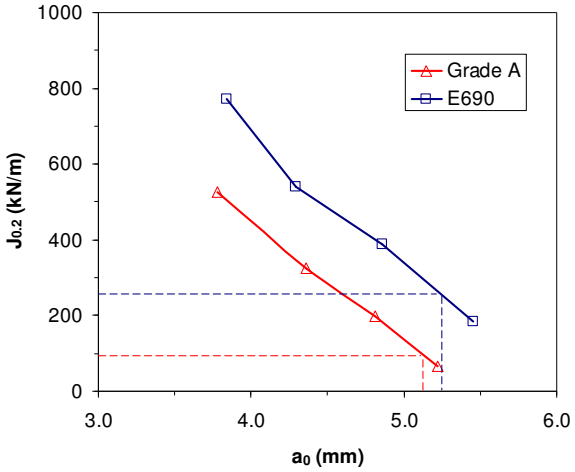

Figura 14. Evolución del valor de $J_{0.2}$ con la longitud de entalla inicial.

6. RESUMEN Y CONCLUSIONES

En este trabajo se ha desarrollado una nueva metodología para la estimación de la tenacidad a fractura a partir de probetas Small Punch con una entalla lateral. El método propuesto se basa en superponer a las curvas experimentales obtenidas con probetas entalladas una colección de curvas iso-a. Las curvas iso-a son obtenidas mediante simulaciones elasto-plásticas por elementos finitos.

La metodología ha sido aplicada a dos materiales distintos -un acero Grade A y un acero estructural E690- empleando en ambos casos distintas longitudes de entalla inicial en las probetas ensayadas en laboratorio. Tras analizar los resultados, pueden extraerse las siguientes conclusiones:

- Para valores de entallas "cortas" se obtienen valores de resistencia a fractura elevados (claramente por encima de los estimados mediante ensayos convencionales), con curvas de J decrecientes.

- Los valores de entalla entre 5 y 5.2 mm ofrecen resultados equivalentes a los obtenidos en los ensayos normalizados.

- Para el caso de los valores de tenacidad ligados a la iniciación, $J_{0.2}$, se ha propuesto una expresión que permite su estimación con independencia de la longitud de entalla inicial empleada.

En base a todo lo anterior, se propone el empleo de probetas con entallas iniciales comprendidas entre 5.0 y 5.2 mm siempre que se pretenda determinar la curva completa J- Δa. Cuando simplemente se busque el valor de iniciación, puede ahorrarse, sin embargo, el coste ligado a la precisión a la hora de materializar la entalla y emplear cualquier longitud comprendida entre 4 y 5.5 mm.

REFERENCIAS

[1] S. Cicero, R. Lacalle, F. Gutiérrez-Solana, "Application of Small Punch Techniques for the Determination of Gold Mechanical Properties", Strain, in press.

[2] D. Finarelli, M.Roedig, F.Carsughi, "Small Punch Test on Austenitic and Martensitic Steels Irradiated in a Spallation Environment with 530 MeV Protons" Journal of Nuclear Materials, 328, 2004, pp. 146-150.

[3] ASTM E8-00, "Standard Test Methods for Tension Testing of Metallic Materials", Annual Book of ASTM Standards, 2000.

[4] ASTM E23-01, "Standard Test Methods for Notched Bar Impact Testing of Metallic Materials", Annual Book of ASTM Standards, 2000.

[5] ASTM E1820-99a, "Standard Test Method for Measurement of Fracture Toughness", Annual Book of ASTM Standards, 1999.

[6] M. Eskner, R. Sandström, "Mechanical property using the small punch test", Journal of Testing and Evaluation, vol 32, Nº 4, January 1995, pp. 282-289.

[7] R. Lacalle, J. García, J.A. Álvarez, F. Gutiérrez-Solana, "Obtención Mediante el Ensayo Small Punch de las Propiedades de Tracción de Materiales Metálicos", Anales de Mecánica de la Fractura 26, 2009.

[8] A. Shekhtel, A.B. Croker, A.K. Hellier, "Towards the correlation of fracture toughness in an exservice power generator rotor", *International Journal of Pressure Vessels an Piping*, vol 77, 2000, pp. 113-116.

[9] J.S.Ha, E. Fleury, "Small Punch test to estimate the mechanical properties of steels for steam power plant: II Fracture Toughness", *Internacional Journal of Pressure Vessels and Piping*, vol 75, 1998, pp. 707-713.

[10] I.I. Cuesta, J.M. Alegre, P. Bravo, "Evaluación de la Tenacidad a Fractura mediante la Combinación del Diagrama FAD y de Ensayos SPT sobre Probetas Fisuradas", Anales de Mecánica de la Fractura 26, (2009)

[11] R. Lacalle, J.A. Álvarez, F. Gutiérrez-Solana, "Use of Small Punch Notched Samples in the Determination of Fracture Toughness", *Proceedings of ASME PVP 2008*, Chicago.

[12] D. Ferreño, S. Cicero, R. Lacalle, I. Gorrochategui, F.Gutiérrez-Solana, "Obtaining the J–Da curves of an X-750 alloy from rising load test results and iso-a curves obtained by means of finite elements model", Engineering Failure Analysis 16 (2009), pp. 409-420.

[13] R. Lacalle, J.A. Álvarez, F. Gutiérrez-Solana, "Analisys of Key Factors for the Interpretation of Small Punch Test Results", Fatigue and Fracture of Engineering Materials and Structures, 31, 2008, pp. 841-849.

[14] O.Akourri, M.Louah, A. Kifani, G. Gilgert, G. Pluvinage, "The Effect of Notch Radius on Fracture Toughness J_{Ic}", *Engineering Fracture Mechanics* 65, 2000, p. 491-505.

[15]T.L. Anderson, "Fracture Mechanics, Fundamentals and Applications", CRC Press, 1991.

[16] ANSYS Inc., 2008, Release 11.0.

ICE NECK FRACTURE EXPERIMENTS

A. Luque[1], J. Aldazabal[1], A. Martín–Meizoso[1], J.M. Martínez–Esnaola[1], J. Gil Sevillano[1], R.S. Farr[2], A. Hoodle[3]

[1] CEIT and Tecnun (University of Navarra). Paseo Manuel Lardizábal 15, 20018 San Sebastián. Spain.
E–mail: aluque@ceit.es. Phone: +34 943212800. Fax: +34 943213076.
[2] Unilever R&D. Olivier van Noortlaan 120, AT3133 Vlaardingen. The Netherlands.
[3] Unilever R&D, Colworth House. Sharnbrook, MK44 1LQ Bedford. United Kingdom.

ABSTRACT

This paper summarizes the results of fracture experiments carried out on ice necks at –18 ºC. The neck geometry is a meniscus. This shape is attained freezing water between a flat plate and a spherical probe which are moved apart during the tensile test. Two types of fracture are observed: adhesive fracture and cohesive fracture. Adhesive failure occurs by propagation of a crack between the sample and one of the parts which "attaches" the sample to the equipment. Cohesive failure takes place by propagation of an internal crack within the solidified water. Each fracture behaviour is characterised by a different fracture stress. In this work, we also try to estimate the Young's modulus of ice.

KEY WORDS: Tensile test, ice, fracture stress, adhesive failure, cohesive failure, Young's modulus.

1. ICE MECHANICAL PROPERTIES

Mechanical properties of ice are relevant to those natural and artificial environments in which liquid water and low temperatures can be found at the same time. Some illustrative examples of this are the breakup of glaciers and avalanche event prediction (Glaciology) or the icing of structures in cold climates (Civil, Naval and Aeronautical Engineering). In Food Science, this topic is of interest to the preservation of optimal consumption conditions of frozen foods: microstructural details (ripening of ice particles and formation and growth of ice–ice necks) affect the sensory properties which are eventually felt by consumers.

These are some of the mechanical properties of ice:

- Monocrystalline hexagonal I_h ice shows a moderate anisotropy with C_{11} = 13.7 GPa, C_{12} = 7.0 GPa, C_{13} = 5.6 GPa, C_{33} = 14.7 GPa and C_{44} = 3.0 GPa (3–axis coincides with the c_{Ih} direction) [1,2].
- For randomly–oriented ice polycrystals, values of Young's modulus, E, between 9.0 and 9.5 GPa are reported, and Poisson's ratio, ν, ranges from 0.3 to 0.325 [1–5].
- The inelastic behaviour of ice is also markedly anisotropic. The critical resolved shear stress for non–basal slip is several times greater than that for basal slip [1–4]. This leads to the build–up of internal stresses at grain–size scale which can initiate cracks. Ice exhibits macroscopically ductile or brittle behaviour depending on the tolerance to these cracks [6].
- Tensile strength, σ_f, of polycrystalline ice ranges from 0.7 MPa to 3.1 MPa [5,6], between –20 ºC and –10 ºC, with the typical scatter associated to fracture measurements.
- Ice fracture toughness, K_{Ic}, ranges from 50 kPa√m to 110 kPa√m [1,2,5,7,8].

In this work, we carry out tensile tests of ice samples at –18 ºC, in order to study the fracture behaviour of ice particles when they have joined and form a neck. As the implementation of such an experiment can be difficult [9], the chosen geometry is a meniscus of solidified water formed between the two parts of a tensile tester which are moved apart during the experiment.

2. EQUIPMENT AND PROCEDURE

The fracture tests are performed in an Instron 4501 tensile tester. It is provided with a load cell of 100 N and it can carry out the tests in either force or displacement control.

The generation of ice necks and the experiments take place within a cold chamber which is kept at –18 ºC. The temperature control is also provided by Instron: an income flow of cold N_2 gas to the chamber is established to reach the target temperature. However, the pump of gas is discontinuous (~10 s) and thus, the temperature control may not be very precise.

In order to perform these experiments, a flat plate and a spherical probe of Ø5 mm are introduced into the cold chamber and clamped to the fixed part and to the crosshead, respectively. Then, we let these two parts freeze. Before generating the samples, an ice layer is grown on the spherical probe with the help of a pipette (Figure 1.a). Finally, the probes approach one another until they are 1 mm or 2 mm away. In that moment, load and displacement signals are set to zero. Next, a very small amount of water is placed between the probes with the help of a syringe (Figure 1.b). Only 5 mm^3 or 10 mm^3 are enough to form a meniscus (Figure 1.c).

Finally, the experiment can start and is carried out under displacement control. The test can be divided into two parts: the cooling step and the loading step. During

cooling, the sample is kept at –18 ºC for 2 min and the crosshead does not move. During the loading step, the crosshead starts to move at a rate of 0.1 mm/min and the loading of the sample occurs.

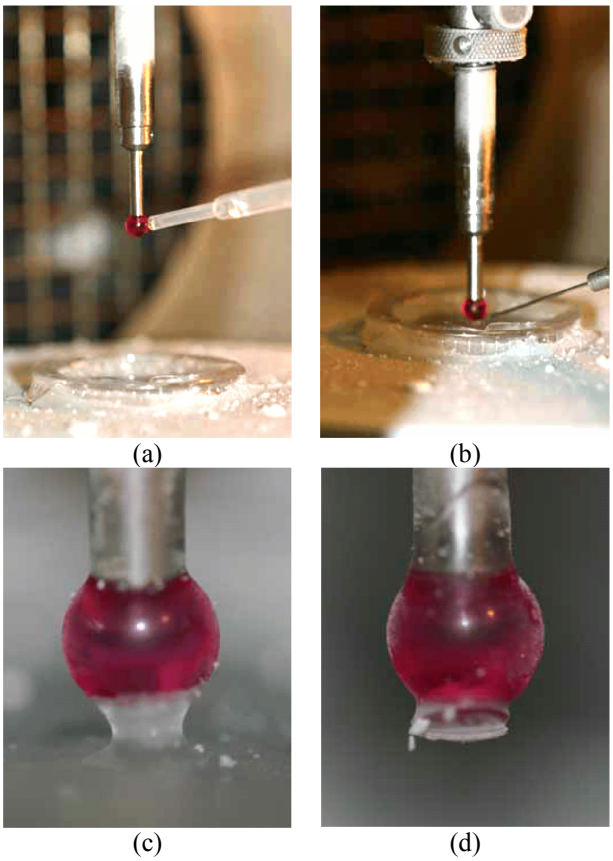

Figure 1. (a) *Preparation of the Ø5 mm spherical probe.* (b) *Generation of an ice neck between the probes.* (c) *Ice neck (meniscus) before tensile test.* (d) *Ice neck after fracture (cohesive failure).*

3. RESULTS

Although the (deliberate) loading of the sample takes place during the loading step, some of the samples broke during the cooling step. This can be understood if we recall that the liquid meniscus freezes during this step. Due to the displacement control of the equipment, the crosshead is impeded to move during cooling. Nevertheless, the meniscus contracts during its solidification. Therefore, a net tensile load is applied on the meniscus and that is registered by the equipment. Whether or not the load introduced during the cooling step is enough to break the neck depends on its production and solidification. If fracture does not take place during the first step of the experiments, then it occurs during the second part, as expected (Figure 1.d).

Figure 2.a shows the load *vs.* time $F - t$ curves of the menisci that broke during the cooling step. Figure 2.b shows the load *vs.* displacement $F - \Delta L$ curves of the necks that broke during the loading step.

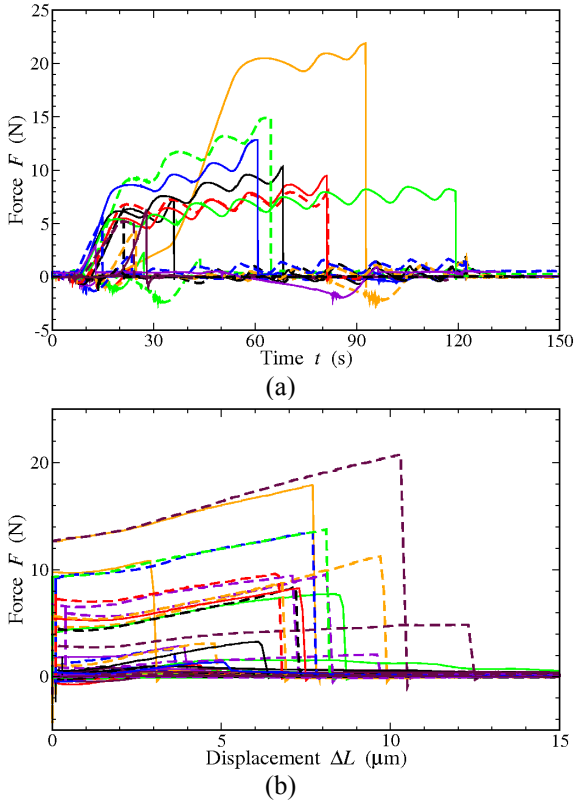

Figure 2. (a) *Load – time curves corresponding to necks broken during cooling.* (b) *Load – displacement curves corresponding to necks broken during loading.*

Apart from the classification of broken necks in terms of the moment of their actual fracture, they can also be classified in terms of the fracture type that they exhibit. A simple inspection permits classifying fracture into adhesive and cohesive. Adhesive failure corresponds to a crack appearing between ice and the spherical probe (Figure 3.a), whereas cohesive failure corresponds to a crack propagating through the ice (Figure 3.b).

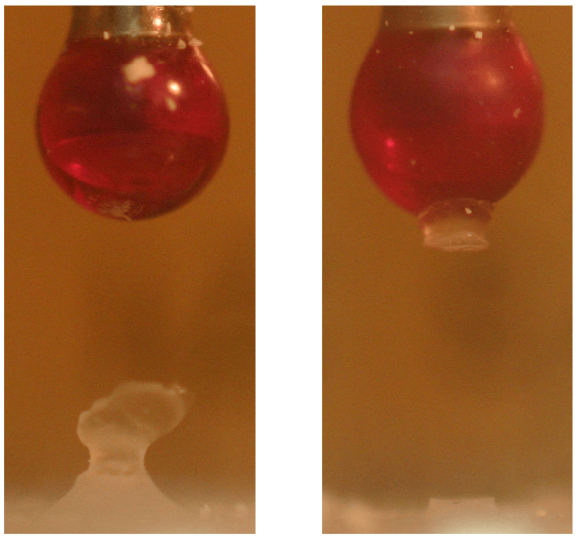

Figure 3. Different types of fracture observed: (a) *adhesive failure and* (b) *cohesive failure.*

Nevertheless, this new division is independent of the aforementioned one. This is: the two types of failure were observed both during cooling and during loading.

From the $F - \Delta L$ curves (Figure 2.b), we can calculate the ice Young's modulus and the value of fracture stress, σ_f, of both adhesive and cohesive failure. However, from the $F - t$ curves (Figure 2.a), we can only calculate σ_f The obtained values of σ_f and E are summarized in the following sections.

3.1. Fracture stress

The first approach to obtain the fracture stress is simply to calculate the average stress in the neck, σ_{ave}, *i.e.* the applied force, F, divided by the section, A, of the neck. However, this value must be corrected by a term, namely f_{corr}, in order to take into account the triaxiality contribution to σ_f, such that $\sigma_f = f_{corr} \cdot \sigma_{ave}$. This factor has been computed using Abaqus and considering different neck sizes, X, neck curvatures, ρ, and neck lengths, L_{neck}. The geometry employed in Abaqus to obtain this factor mimics the meniscus geometry, as shown in Figure 4.

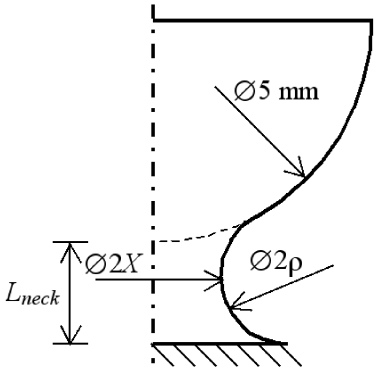

Figure 4. Geometry of the neck simulated in Abaqus for the estimation of the triaxiality correction factor, f_{corr}.

Within the analyzed range of X/ρ, which contains the X/ρ values of the experiments, the correction factor can be fitted to

$$f_{corr} = 1.33 + 0.18 \ln(X/\rho) \qquad (1)$$

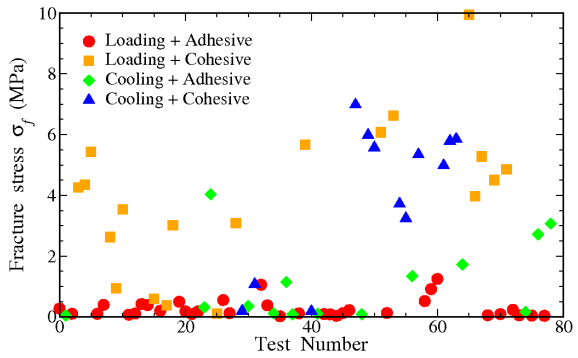

Figure 5. Fracture stress, σ_f, associated to each neck.

Figure 5 shows the fracture stress associated to these experiments. The colour/shape code indicates the moment and the type of failure. The mean fracture stresses are summarized in Table 1.

Table 1. Mean values of fracture stress, σ_f, and Young's modulus, E, of the observed failure types.

	σ_f (MPa)	E (MPa)
Loading + Adhesive	0.3 ± 0.3	70 ± 50
Loading + Cohesive	4 ± 2	200 ± 100
Cooling + Adhesive	1 ± 1	
Cooling + Cohesive	4 ± 2	

We can observe that the ice necks showing cohesive failure yield a mean fracture stress of approximately 4 MPa. The obtained value of σ_f is slightly higher than those reported in the literature (0.7 MPa – 3.1 MPa [5]). Nevertheless, the scatter associated to these results is high and, thus, the differences are not really relevant.

In relation with adhesive failure, we can observe more differences between the ice samples broken during cooling and those broken during loading (on average, 1 MPa *vs.* 0.3 MPa). In both cases, the scatter is high. The scatter is such that a possible result for σ_f is zero. That would mean that there is very small adhesion between the surfaces. This would indicate that more attention should have been paid during the surface preparation and the sample production. This could also have reduced the number of adhesive events.

It is interesting to analyse these fracture stress results in terms of Weibull distribution [10]

$$P(\sigma_f) = 1 - \exp[-(\sigma_f / \sigma_{f0})^k] \qquad (2)$$

where k is the shape parameter and σ_{f0} is the scale parameter, which corresponds to the value for which the ~63% of the measured fracture stresses is below σ_{f0}. For this purpose, all the results of adhesive failure and those of cohesive failure have been grouped in two different data sets, as shown in Figure 6.

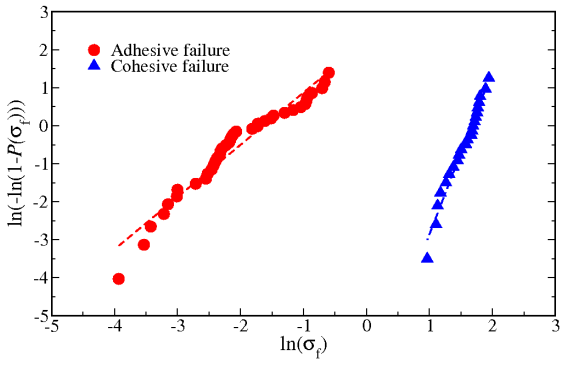

Figure 6. Weibull distribution of fracture stress, σ_f, associated to the observed fracture types.

For adhesive fracture, we have obtained a shape parameter of 1.4 and a size parameter of 0.20 MPa. Nevertheless, the fit is not as good as for the cohesive fracture, for which the shape parameter increases up to 4.3 and the size parameter is approximately 5.3 MPa. This is 25 times bigger than the value obtained for adhesive failure, a similar result if we consider the mean values of σ_f. This is in good agreement with the scatter shown in Table 1, which indicates that the estimates for the fracture stress for cohesive failure are more reliable than those for adhesive failure. Some authors [9,11] attribute this difference to the existence of a liquid–like layer between the surfaces. This layer, whose existence may be possible from a thermodynamical point of view, represents an easily separable zone. Thus, failure can proceed preferentially through that layer. However, the existence of this layer could not be demonstrated experimentally in these samples. Finally, the shape parameter value for cohesive failure obtained in this work is of the same order as the values reported in the literature, which range between 3 and 5 [5,8].

3.2. Young's modulus

If we now consider the deformation undergone by the ice necks during the cooling step, we can estimate the value of Young's modulus, E. We have already mentioned that the geometry of the sample induces stress triaxiality during the tensile test. The axial stress is not uniform through the neck, nor is the axial strain. As a first approximation, we are going to calculate E as

$$E = \frac{\sigma_{ave} - \sigma(0)}{\varepsilon_{ave}} = \frac{F_{max} - F(0)}{A}\frac{L_{neck}}{\Delta L} \qquad (3)$$

where $\sigma(0)$ is the average axial stress at the beginning of the loading step, calculated from the load at that particular instant, $F(0)$, ε_{ave} is the uniform axial strain and ΔL is the change in the "length" of the neck. The change of neck section during the tensile test is neglected. Figure 7 presents the values of Young's modulus along the axial direction, obtained from these experiments. Obviously, no estimations for E can be obtained from the necks broken during the cooling step ($\varepsilon = 0$). Table 1 also summarizes the mean values of Young's modulus for the different failure types.

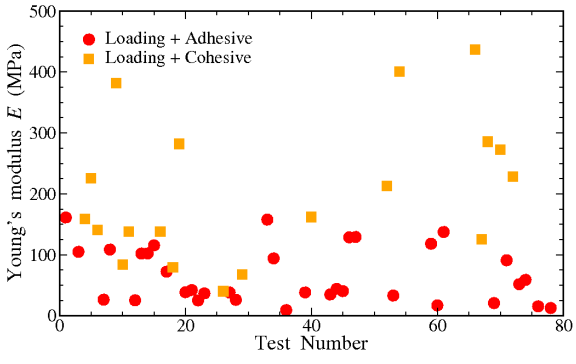

Figure 7. Young's modulus, E, associated to each neck.

For the adhesive failure, the average Young's modulus is 70 MPa, whereas for the cohesive failure, it is 200 MPa. There is a relevant scatter for this parameter, as shown in Figure 7. Besides, the difference in terms of E for the two fracture types is not as big as for σ_f. This is in line with what we expected, as the value of ice Young's modulus should be independent of the nature of the fracture occurred.

However, the values of this work are very far from the reported value for polycrystalline ice, namely 9.33 GPa [1,2,5]. This big difference may indicate that a certain ice softening process is taking place. It could simply be the inherent softness of just–solidified ice [5] or the aforementioned liquid–like layer surrounding ice particles. Both phenomena would yield a decrease of E in "fresh" ice with respect to "old" bulk ice. Nevertheless, the combination of temperature and time should avoid the effect of the liquid layer, if such effect exists.

A comment should be made regarding the parameters appearing in Equation 3. Forces and neck geometry seem correct on the basis of the fracture stress values that we have obtained. However, there is some uncertainty in the neck elongation, ΔL. Just note that to get σ_{ave} = 4 MPa with E = 10 GPa and L_{neck} = 1 mm, ΔL should be 400 nm, whereas the registered values are, at least, one order of magnitude bigger. Therefore, these values may not simply be the ice elongation, but a combination of the elongations of the neck and of some part of the machine of lower stiffness, K_{mach} (compared with ice; this is, $K_{mach} < K_{ice}$). A schematic of the system is depicted in Figure 8.

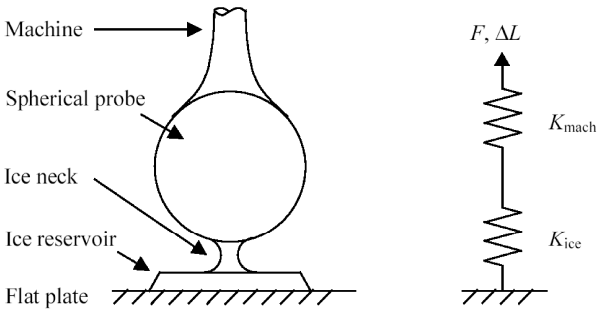

Figure 8. Schematic of the system proposed for explaining the "soft ice".

This configuration yields

$$\Delta L = \Delta L_{ice} + \Delta L_{mach} \qquad (4)$$

where the (known) value of ΔL is decomposed into two terms, one corresponding to ice and another one corresponding to the softer part of the machine. On the other hand, while the stiffness of this softer part is unknown, the stiffness of ice can be calculated as $K_{ice} = EA/L_{neck}$. As the springs depicted in Figure 8 are connected in series, the applied force is undergone by both springs. Assuming the applicability of Hooke's

law, together with Equation 4, we get

$$\frac{\Delta L}{F} = \frac{1}{K_{mach}} + \frac{1}{E}\frac{L_{neck}}{A} \qquad (5)$$

Therefore, if we plot $\Delta L/F$ *vs.* L_{neck}/A for our experiments, we can, in principle, obtain the compliance of the softer part of the machine, $1/K_{mach}$, as L_{neck}/A tends to 0, and the "real" ice Young's modulus, E, as the inverse of the slope of the linear fit given by Equation 5. Figure 9 shows the dependence of $\Delta L/F$ on L_{neck}/A, for the cohesive fractures during loading.

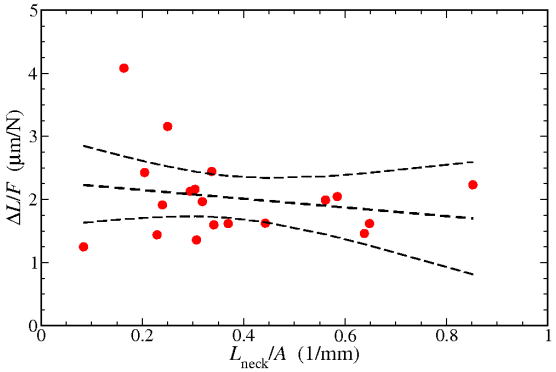

Figure 9. $\Delta L/F$ vs. L_{neck}/A plot of the necks broken during the loading step showing cohesive fracture. The linear fit is shown, as well as the 95% confidence interval for the given linear fit [12].

According to the results shown in Figure 9, the stiffness of the softer part of the machine would be $K_{mach} \approx 450$ kN/m and the value of E would be negative. However, the correlation coefficient of this linear fit is very poor (only 20%). This is: we can hardly say that a line fits our points. Anyway, if we consider the confidence interval of the fit, the value of Young's modulus can be as small as ~1 GPa, which is still one order of magnitude smaller than the real elastic modulus of polycrystalline ice. Nevertheless, note that the experimental results are somewhat concentrated around 0.3 mm^{-1} and 2 μm/N, but, at the same time, there are some values of up to 0.85 mm^{-1} and 4 μm/N. The calculation of the inverse of the slope of a new linear fit which drops out these extreme values would yield a much more accurate value of ~4 GPa, still lower than the reported values but now only two and a half times as small as those.

4. CONCLUSIONS

The mechanical behaviour of ice necks has been studied through an equivalent configuration, namely a meniscus of solidified water.

We have observed that fracture can occur prior to the loading of the samples, due to the contraction of water during solidification. Fracture can also take place during sample loading, as expected.

Independently of when fracture happens, two types of failure have been identified. The first type is an adhesive failure, in which a crack propagates between the ice meniscus and one of the attaching surfaces. The fracture stress associated to this type of failure is between 0.3 MPa and 1 MPa. The second type of failure that we have identified is the cohesive failure. In this case, the crack propagates through the middle of the samples. The fracture stress associated to this fracture type is, on average, 4 MPa. The scatter associated to these measurements is rather big. Nevertheless, these values are similar to the values reported in the bibliography. Besides, adhesive fracture and cohesive fracture have yielded different results in terms of Weibull shape parameter (1.4 *vs.* 4.3).

We have also tried to calculate the elastic modulus of ice from the necks broken during the loading step. The results are similar for adhesive failure and cohesive failure (75 MPa vs. 230 MPa, respectively). However, the obtained values of Young's modulus are, at least, one order of magnitude smaller than those reported in the literature. This has been justified by the presence of a more compliant part in the experimental set–up.

ACKNOWLEDGEMENTS

The authors would like to thank Unilever R&D Colworth (UK), for the support of this research, and to Ian Burns (Unilever R&D). A. Luque would also like to thank the Spanish Ministry of Education and Science and the European Social Fund for the funding and co–funding, respectively, of his contract (Torres Quevedo Programme).

REFERENCES

[1] Petrenko, V.F. and Whitworth, R.W., Physics of Ice, Oxford University Press, Oxford (UK), 2002.
[2] Schulson, E.M. and Duval, P., Creep and fracture of ice, Cambridge University Press, Cambridge (UK), 2009.
[3] Schulson, E.M., "The structure and mechanical behavior of ice", JOM, 51, 1999, 21–27.
[4] Mansuy, P., Contribution à l'étude du comportement viscoplastique d'un multicristal de glace: hétérogénéité de la déformation et localisation, expériences et modèles, Ph.D. thesis, University of Joseph Fourier – Grenoble I, San Martin d'Hères (France), 2001, 3–8.
[5] Petrovic, J.J., "Mechanical properties of ice and snow", J. Mat. Sci., 38, 2003, 1–6.
[6] Currier, J.H. and Schulson, E.M., "The tensile strength of ice as a function of grain size", Acta Metallurgica, 30, 1982, 1511–1514.
[7] Tromans, D. and Meech, J.A., "Fracture toughness and surface energies of covalent minerals: theoretical estimates", Minerals Eng., 17, 2004, 1–15.

[8] Kamio, Z., Matsushita, H. and Strnadel, B., "Statistical analysis of ice fracture characteristics", Eng. Fracture Mechanics, 70, 2003, 2075–2088.
[9] Fan, X., Ten, P., Clarke, C.J., Bramley, A.S. and Zhang Z., "Direct measurement of the adhesive force between ice particles by micromanipulation", Powder Technology, 131, 2003, 105–110.
[10] Hajek, J., Probability in science and engineering, Academic Press, New York (USA), 1967.
[11] Andrews, E.H. and Lockington, N.A., "The cohesive and adhesive strength of ice", J. Mat. Sci., 18, 1983, 1455–1465.
[12] Ríos, S., Métodos estadísticos, Ibérica, Madrid (Spain), 1965.

ELASTOPLASTIC CONTACT IN AN INDENTATION IMPACT TEST BY FRACTIONAL CALCULUS

M. Mateos, F. Cortés, L. Aretxabaleta

Department of Mechanical Engineering and Industrial ManufacturingMondragon Unibertsitatea, Loramendi 4, 20500, Mondragón, Spain. Phone: (+34) 943794700. Fax: (+34)943791536.
E-mail: mmateos@eps.mondragon.edu

ABSTRACT

This communication presents an elasto-viscoplastic contact model of an impact-indentation test by means of fractional calculus. The models aims at characterising this contact by a rheological model based on the superposition in series of a dashpot and a non linear spring. The dashpot gives the dissipative character and the superposition in series the permanent character of the strains. Finally, the spring gives the non linear stiffness based on Hertz theory.

The model treatment is achieved by fractional calculus, which is solved numerically using G1 method. Then, the results are compared with those obtained from experimental tests.

Finally, material properties have been obtained from the contact characterisation.

RESUMEN

En esta comunicación se presenta un modelo de contacto elasto-viscoplástico de un ensayo de impacto-indentación mediante la aplicación del cálculo fraccionario. El modelo persigue caracterizar dicho contacto mediante un modelo reológico basado en la superposición en serie de un amortiguador y un muelle no lineal. El amortiguador proporciona el carácter disipativo y la superposición en serie el carácter permanente de las deformaciones. Finalmente, el muelle proporciona la rigidez no lineal basada en la teoría de Hertz.

El tratamiento del modelo se efectúa por medio del cálculo fraccionario que se resuelve numéricamente utilizando el método G1. Posteriormente, se realiza una comparación de los resultados con los obtenidos de ensayos experimentales.

Finalmente, a partir de la caracterización del contacto se han obtenido las propiedades del material.

KEY WORDS: Fractional calculus; Hertz contact, Impact-Indentation.

1. INTRODUCTION

The use of polymeric materials has been continuously increasing in the last years within the automotive industry not only to improve fuel efficiency and crashworthiness but also for their energy dissipation capacity, possibility of recycling, design versatility and good surface quality [1]. Besides, they can be reinforced so that they increase their specific mechanical properties.

In order to design the polymeric components (material, geometry, dimensions...) in the automotive industry, the material behaviour against impact is a key point. Nevertheless, material properties (characterisation and material model) become especially important, since they depend highly on the strain rate at which they are loaded [2].

In almost all the practical situations, the parts or components are subjected to complex loads which induce a complex response in the component where non homogeneous strain and strain rate distributions prevail. This complex response can be divided into two other ones: the structural global response, in which both the material and geometry take part, and the local response, in which the material response prevails.

To fully define the local response, the use of a rheological model, based on the superposition in series of a dashpot and a non linear spring, is proposed to solve the contact problem during impact-indentation, based on Hertz theory [3, 4].

Contact problems induce non-linear equations which generally can be solved after fulfilling an arduous and complex labour.

Hertz theory is restricted to non conforming surfaces, continuous and frictionless, and to perfectly elastic solids subjected to small deformations. Contact between non conforming surfaces takes place at a point or along a line and generally, in spite of the load, contact zone dimensions are small in comparison with the solids size. Under this simplification, a local concentration of stress is originated that may be analysed regardless of the global stress distribution resulting in the solids. [6]

This paper deals with the resolution of the non-linear equations derived from the contact problem during indentation following Hertz theory by means of transforming the governing non-linear equations into linear fractional integro-differential equations.

First, a brief theoretical background is presented concerning to fractional calculus, laying emphasis on the definitions of Günwald-Letnikov and numerical treatment. Next, the experimental technique used for the impact-indentation tests is described. Then the equations resulting from the rheological model are solved after having been transformed making use of fractional calculus, obtaining a linear integro-differential fractional equation that is numerically solved. Finally, the results obtained are compared with those provided by experimental tests.

2. THEORETICAL BACKGROUND

Fractional calculus is a discipline that has historically been relegated to the theoretical mathematics, but during last decades, different applications have been attributed to this branch of mathematical analysis. [7, 8, 9, 10].

Next, two definitions of fractional derivatives are described: the ones of Riemman-Liouville and Grünwald-Letnikov.

The definition of Riemman-Liouville is generally employed for non-integer order integrals. Indeed, the α order derivative with respect t variable for a function $f(t)$, with $\alpha < 0$ and the lower integration limit being zero, is defined as

$$\mathrm{D}^{\alpha} f(t) = \frac{\mathrm{d}^{\alpha} f(t)}{\mathrm{d}t^{\alpha}} = \frac{1}{\Gamma(-\alpha)} \int_0^t (t-y)^{-\alpha-1} f(y)\,\mathrm{d}y \,, \quad (1)$$

where $\Gamma(z)$ is the gamma function of real argument z, given by

$$\Gamma(z) = \int_0^{\infty} \mathrm{e}^{-y}\, y^{z-1}\,\mathrm{d}y \,. \quad (2)$$

This function represents the generalisation of the factorial function, satisfying

$$z! = \Gamma(z+1) \,, \quad (3)$$

which coincides with the classic definition of the factorial if z is an entire number. For example, for $-1 < \alpha < 0$, the application of Eq. (1) on the function t^q yields

$$\mathrm{D}^{\alpha} t^q = \frac{\mathrm{d}^{\alpha} t^q}{\mathrm{d}t^{\alpha}} = \frac{\Gamma(q+1)}{\Gamma(q+1-\alpha)} t^{q-\alpha} \,. \quad (4)$$

This result is employed in Section 3 to transform the non-linear equations characterising the contact mechanics into linear integro-differential fractional equations.

The Grünwald-Letnikov definition of the fractional derivatives, for any real order α, arises from the backward definition of the n entire order derivative. Indeed, the first derivative is given by

$$\mathrm{D}^1 f(t) = \lim_{\Delta t \to 0} \frac{f(t) - f(t-\Delta t)}{\Delta t} \,, \quad (5)$$

the second by

$$\mathrm{D}^2 f(t) = \lim_{\Delta t \to 0} \frac{f(t) - 2f(t-\Delta t) + f(t-2\Delta t)}{(\Delta t)^2} \,, \quad (6)$$

the third by

$$\mathrm{D}^2 f(t) = \lim_{\Delta t \to 0} \frac{f(t) - 3f(t-\Delta t) + 3f(t-2\Delta t) - f(t-3\Delta t)}{(\Delta t)^3} \,, \quad (7)$$

and so on, thus the n order derivative satisfies

$$\mathrm{D}^n f(t) = \lim_{\Delta t \to 0} \left((\Delta t)^{-n} \sum_{j=0}^{N-1} (-1)^j \binom{n}{j} f(t - j\Delta t) \right) , \quad (8)$$

where:

$$N = t / \Delta t \,, \quad (9)$$

and the Newton binomial

$$\binom{n}{j} = \frac{n!}{j!(n-j)!} \,, \quad (10)$$

have been employed. If the gamma function is applied, considering that

$$(-1)^j \binom{n}{j} = \binom{j-n-1}{j} = \frac{\Gamma(j-n)}{\Gamma(-n)\Gamma(j+1)} \,, \quad (11)$$

thus Eq. (8) may be transformed into

$$\mathrm{D}^n f(t) = \lim_{\Delta t \to 0} \left((\Delta t)^{-n} \sum_{j=0}^{N-1} \frac{\Gamma(j-n)}{\Gamma(-n)\Gamma(j+1)} f(t - j\Delta t) \right). \tag{12}$$

If in this equation the n order is substituted by any real order α, the Grünwald-Letnikov definition for fractional derivatives yields

$$\mathrm{D}^\alpha f(t) = \lim_{\Delta t \to 0} \left((\Delta t)^{-\alpha} \sum_{j=0}^{N-1} \frac{\Gamma(j-\alpha)}{\Gamma(-\alpha)\Gamma(j+1)} f(t - j\Delta t) \right) \tag{13}$$

or finally,

$$\mathrm{D}^\alpha f(t) = \lim_{\Delta t \to 0} \left((\Delta t)^{-\alpha} \sum_{j=0}^{N-1} A_{j+1} f(t - j\Delta t) \right), \tag{14}$$

where the terms A_{j+1} are the so-called Grünwald-Letnikov coefficients, satisfying

$$A_{j+1} = \frac{\Gamma(j-n)}{\Gamma(-n)\Gamma(j+1)}. \tag{15}$$

In Eq. (14) it should be remarked that the fractional derivative is constructed employing all the history of the function, weighted by the Grünwald-Letnikov coefficients, putting in evidence the memory of fractional operator. To avoid the use of the gamma function in numerical applications, the following properties of the weighting coefficients may be employed:

$$A_1 = 1, \tag{16}$$

$$A_{j+1} = \frac{j - \alpha - 1}{j} A_j, \tag{17}$$

and, if $\alpha < -1$,

$$\lim_{\Delta t \to 0} A_{j+1} = 0. \tag{18}$$

This last property is known as the fading memory of fractional derivatives, implying the most recent history is more influent than the fastest.
The fractional operator can be numerically calculated by [9]:

$$\mathrm{D}^\alpha f(t) = \left(\frac{N}{t} \right)^\alpha \sum_{j=-1}^{N} w_j(\alpha)\, f\left(t - j\frac{t}{N} \right), \tag{19}$$

which is analogue to the conventional quadrature formulae, where $w_j(\alpha)$ are the weighting coefficients, depending on the derivation order. To simplify the nomenclature, Eq. (19) may be also written as

$$\mathrm{D}^\alpha f(t) = \frac{1}{(\Delta t)^\alpha} \sum_{j=-1}^{N} w_j\, f_j\,. \tag{20}$$

One of the most employed methods is the G1 one, based on the definition of Grünwald-Letnikov.

The G1 method is generally more efficient for derivation orders comprised between 0 and 1. The weighting coefficients w_j are given by

$$w_j(\alpha) = \begin{cases} 0 & \text{if } j = -1, N; \\ \dfrac{\Gamma(j-\alpha)}{\Gamma(-\alpha)\Gamma(j+1)} & \text{if } 0 \le j \le N-1; \end{cases}, \tag{21}$$

which may be also evaluated form the recurrence Eq. (17).

This numerical method will be employed in Section 4 to solve the Hertz contact problem enunciated later.

3. MATERIAL AND EXPERIMENTAL TECHNIQUE

The experimental part was presented in a previous work [10]. The material used is an injection grade isotactic Polypropylene (PP) homopolymer (SM6100K, Montell). Specimens are $4\ \mathrm{mm}$ thick and $80\ \mathrm{mm}$ diameter circular plates, and are subjected to instrumented-indentation-impact tests.

The tests are carried out in a Dartvis falling weight test machine (Ceast). A $0.7437\ \mathrm{kg}$ striker with a $12.7\ \mathrm{mm}$ diameter hemispherical dart is released from different heights. The striker hits the sample that lies on a rigid $10\ \mathrm{mm}$ thick steel surface, inducing a local indentation on the surface of the sample.

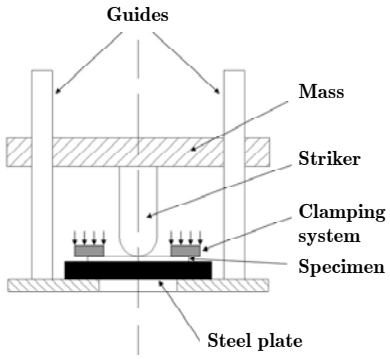

Fig. 1 Indentation-impact test configuration in a falling weight impact machine.

Up to 8 tests have been carried out in different sectors of each specimen, as the area affected by the contact strain is very small compared to the size of the whole specimen.

Tests have been carried out from $5\ \mathrm{mm}$ to $100\ \mathrm{mm}$ height, with increments of $5\ \mathrm{mm}$. Each test has been repeated 3 times to analyse reproducibility. The influence of the thickness of the specimen has also been analysed, by superposing two or three samples and comparing force-time curves.

As a result, force-time curves show a good reproducibility, even if the curves must be displaced in time to avoid the dynamical effect of the beginning of the curves i.e. due to specimen accommodation effects [5].

Experimental force-time curves show a quasi-symmetrical shape, increasing the maximum force and decreasing contact time as the impact energy increases [5].

4. RHEOLOGICAL MODEL

The response of polymeric materials subjected to impact-indentation loads may be described by the application of a rheological model based on Hertz contact theory [4, 5]. This model is based on the superposition in series of a dashpot and a non linear spring. The dashpot gives the dissipative character and the superposition in series the permanent character of the strains. Finally, the spring gives the non linear stiffness based on Hertz theory.

Figure 1. shows the rheological model of the impact-indentation test, in which m represents the striker mass, k the constant of the non linear spring and c the constant of the dashpot.

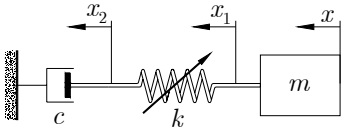

Fig. 2. Rheological model

The constant k is related to the materials' properties as follows:

$$k = \frac{4\sqrt{R}}{3}\left(\frac{1-\nu_{\mathrm{i}}^2}{E_{\mathrm{i}}} + \frac{1-\nu_{\mathrm{s}}^2}{E_{\mathrm{s}}}\right)^{-1} \qquad (22)$$

where:

R is the radius of the striker, E_{i} and E_{s} the Young modulus of the striker and specimen, respectively; ν_{i} and ν_{s} the Poisson modulus of the striker and specimen, respectively [5].

Following the model of Fig. 2, the governing equations for an impact-indentation test with initial relative velocity $\dot{x}(0) = \dot{x}_0$, which depends on the falling height of the mass h, are given by:

$$m\frac{\mathrm{d}^2 x}{\mathrm{d}t^2} = -kx_1^{3/2} = -c\frac{\mathrm{d}x_2}{\mathrm{d}t} \qquad (23)$$

Taking into account the following expression, obtained from the model:

$$x = x_1 + x_2 \qquad (24)$$

and eliminating x_2, Eq. (23) may be written as:

$$m\ddot{x} = -kx_1^{3/2} = -c\left(\dot{x} - \dot{x}_1\right) \qquad (25)$$

where the operator $(\ddot{\bullet})$ and $(\dot{\bullet})$ denote second and first derivatives with respect to time, respectively. This non-lineal differential equation may be solved, for example, by means of Runge-Kutta family algorithms.

From the solution of the α order derivative for the function t^q with respect to the variable *t* indicated in Eq. (4), taking, $q = 1$, and $\alpha = -1/2$, the term $x_1^{3/2}$ may be related with the semi-integral $\mathrm{D}^{-1/2}x_1$ by

$$\mathrm{D}^{-1/2}x_1(t) = \frac{4}{3\sqrt{\pi}}x_1^{3/2}(t)\,, \qquad (26)$$

where $\Gamma(2) = 1$ and $\Gamma(5/2) = 3\sqrt{\pi}/4$ have been taken into account.

Taking into account Eq. (26), Eq. (25) is transformed into the linear integro-differential equation

$$m\ddot{x} = -k\frac{3\sqrt{\pi}}{4}\mathrm{D}^{-1/2}x_1 = -c\left(\dot{x} - \dot{x}_1\right) \qquad (27)$$

where it should be pointed out that operator $\mathrm{D}^{(\bullet)}$ represents fractional derivative with respect to the variable x instead of t [11].

Aimed at exploring the capabilities of the fractional calculus to solve problems relative to contact mechanics, the integro-differential equations (27) are numerically solved, making use of the G1 method. To do so, an algorithm based on the central finite difference is proposed [11]. For that, uniform increments for the time Δt are considered. Hence, at the instant t^n, Eq. (27) becomes

$$m\ddot{x}^n = -k\frac{3\sqrt{\pi}}{4}\mathrm{D}^{-1/2}x_1^n = -c\left(\dot{x}^n - \dot{x}_1{}^n\right). \qquad (28)$$

The fractional operator may be discretised by Eq. (20), giving

$$m\ddot{x}^n = -\frac{3k}{4}\sqrt{\pi\,\Delta x_1}\sum_{j=0}^{n} w_j x_1^{n-j} = -c(\dot{x} - \dot{x}_1)\,, \qquad (29)$$

where, as in the previous section, it has been taken into account that G1 method has w_{-1} coefficient equal to zero. The weighting coefficients w_j are taken from Eqs. (21).

For the described case, the interval Δx_1 varies for each t_n instant, satisfying

$$\Delta x_1 = \frac{x_1^n}{n}. \tag{30}$$

Indeed, any forward displacement would be given by

$$x_1^{n-j} = (n-j)\Delta x_1, \tag{31}$$

conducing to the following equations:

$$\begin{cases} m\ddot{x}^n = -\dfrac{3}{4}k\sqrt{\pi}\left(\dfrac{x_1^n}{n}\right)^{3/2}\displaystyle\sum_{j=0}^{n} w_j\,(n-j) \\ m\ddot{x}^n = -c(\dot{x}-\dot{x}_1) \end{cases}. \tag{32}$$

This lineal differential equation may be solved by means of central finite difference method [11]. The velocity $\dot{x}^n$ and acceleration $\ddot{x}^n$ are given by

$$\dot{x}_1^n = \frac{x_1^{n+1} - x_1^{n-1}}{2\Delta t} \tag{33}$$

$$\ddot{x}^n = \frac{x^{n+1} - 2x^n + x^{n-1}}{(\Delta t)^2} \tag{34}$$

Consequently, Eqs. (32) lead finally to

$$\begin{aligned} x^{n+1} &= 2x^n - x^{n-1} - (\Delta t)^2\frac{3k}{4m}\sqrt{\pi}\left(\frac{x_1^n}{n}\right)^{3/2}\sum_{j=0}^{n} w_j(n-j) \\ x_1^{n+1} &= x_1^{n-1} + 2\Delta t\left(\frac{m}{c}\ddot{x}^n + \dot{x}^n\right) \end{aligned} \tag{35}$$

After solving the equations, k, and therefore E_s, and c may be calculated by fitting the results to the experimental ones [5]. To do so, maximum force $F_{\max}$ and restitution coefficient ε have been used.

Figure 3 represents the impact force for a drop height of a) $h = 20$ mm and b) $h = 40$ mm obtained in experimental tests and by the numerical model.

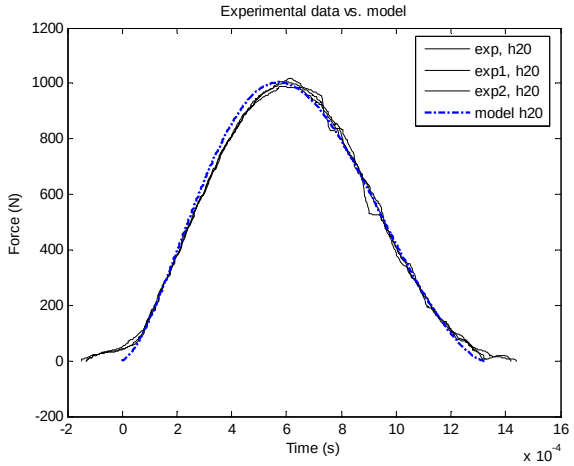

(a)

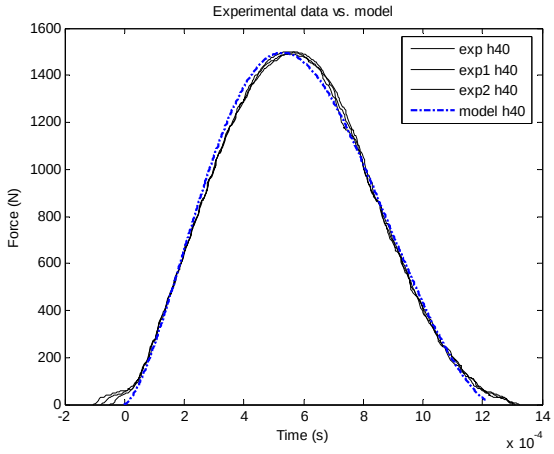

(b)

Fig. 3. Experimental impact force and the one computed by fractional calculus.

The values of $F_{\max}$, ε , k , c , and E_s, found for 2 different falling heights, $h = 20$ mm (h20 test) and $h = 40$ mm (h40 test) are shown in Table 1.

Table 1. Parameters for the rheological model.

Test	$F_{\max}$ [N]	ε	k [$\mathrm{kNm^{-3/2}}$]	c [$\mathrm{Nsm^{-1}}$]	E_s [GPa]
h20	1004	0.59	329900	6080	2.64
h40	1495	0.56	332000	6060	2.66

The elasticity moduli obtained are 2.64 GPa and 2.66 GPa for h20 and h40 tests, respectively. These values are more than twice the value obtained from impact-tensile tests (1,2 GPa) [5, 12]. Therefore, it is shown the deformation pattern dependence upon material properties.

5. CONCLUSIONS

In this communication a contact problem resulting from an impact-indentation test has been solved using fractional calculus. The proposed method consists in transforming the non-linear equation that governs the contact in a fractional integro-differential equation. The numerical solution has been carried out by means of G1 method, based on the fractional derivative definitions of Grünwald-Letnikov.

From the analysis of the results it may be stated that the elasticity modulus of PP has been obtained from the rheological model. The values obtained are more than twice the value obtained from impact-tensile tests.

Concluding, it has been proved that the fractional calculus is able to study certain mechanical contact problems. Thus more complex applications could be investigated in the future.

To better fit to experimental data, other rheological models may be used as well as new types of damping.

REFERENCES

[1] Y. Li, Z. Lin, A. Jiang, G. Chen, Experimental study of glass-fiber mat thermoplastic material impact properties and lightweight automobile body analysis, Mater. Des. 25 (2004) 579.

[2] G. Dean, B. Read, Modelling the behaviour of plastics for design under impact, Polym. Test. 20 (2001) 677.

[3] Hertz, H. *Über die Beruhrung fester elastischer Körper*. J. Reine und Angewandte Mahtematik, 92, 156-171, (1882).

[4] Sánchez-Soto, M., Gonzalo, G., Jiménez, O., Santana, O. O. y Martínez, A. B., Impacto de baja energía de un laminado epoxi-fibra de carbono, XX encuentro del Grupo Español de Fractura, Benicassim, pp. 349-354, (2003).

[5] Aretxabaleta, L., Múgica, J.I., Aurrekoetxea, J., Mateos, M., Castillo, G., Urrutibeascoa, I. y Martínez. Análisis del comportamiento a impacto-indentación de materiales poliméricos mediante el método de elementos finitos, XV encuentro del Grupo Español de Fractura, Sigüenza, pp. 305-310, (2008).

[6] Johnson, K.L. *Contact Mechanics*. Cambridge University Press (2003).

[7] Hilfer, R. *Applications of fractional calculus in physics*. World Scientific (2000).

[8] Miller, K.S. and B. Ross. *An introduction to fractional calculus and fractional differential equations*. John Wiley & sons (1993).

[9] Oldham, K.B. and J. Spanier. *The fractional calculus*. Academic Press (1974).

[10] Podlubny, I. *Fractional differential equations*. Academic Press (1999).

[11] Cortés, F., Mateos M., *Applications of fractional calculus for the impact of elastic spheres*. Symposium on Applied Fractional Calculus, Badajoz (2007).

[12] Aretxabaleta. L., *Estudio teórico-experimental del comportamiento a impacto de baja velocidad de piezas estructurales fabricadas con termoplásticos.* Tesis doctoral Mondragón Unibertsitatea, (2008).

TENSILE BEHAVIOUR OF SINGLE AND DOUBLE-STRAP REPAIRS ON ALUMINIUM STRUCTURES

A.M.G. Pinto[1], R.D.S.G. Campilho[2,3], I.R. Mendes[1], R.F. Silva[1], A.G. Magalhães[1], A.P.M. Baptista[3]

[1] Instituto Superior de Engenharia do Porto
Rua Dr. António Bernardino de Almeida, 431, 4200-072 Porto, Portugal.
E-mail: agp@isep.ipp.pt

[2] Departamento de Economia e Gestão, Universidade Lusófona do Porto,
Rua Augusto Rosa, nº 24, 4000-098 Porto, Portugal.

[3] Departamento de Engenharia Mecânica, Faculdade de Engenharia da Universidade do Porto,
Rua Dr. Roberto Frias, 4200-465 Porto, Portugal.

ABSTRACT

In this work, an experimental study was performed on the influence of plug filling, loading rate and temperature on the tensile strength of single-strap (SS) and double-strap (DS) repairs on aluminium structures. The experimental programme includes repairs with different values of overlap length (L_O=10, 20 and 30 mm), and with and without plug filling. The influence of the testing speed on the repairs strength is also addressed (considering 0.5, 5 and 25 mm/min). Accounting for the temperature effects, tests were carried out at room temperature, 50ºC and 80ºC. This will permit a comparative evaluation of the adhesive tested below and above the Glass Transition Temperature (T_g), established by the manufacturer at 67ºC. The global tendencies of the test results concerning the plug filling and overlap length analyses are interpreted from the fracture modes and typical stress distributions for bonded repairs. According to the results obtained from this work, design guidelines for repairing aluminium structures were recommended.

KEY WORDS: Epoxy adhesive, Experimental testing, Plug filling, Strap repairs.

1. INTRODUCTION

Adhesive bonding as a joining or repair method has a wide application in many industries. Repairs with bonded patches are often carried out to re-establish the stiffness at critical regions or spots of corrosion and/or fatigue cracks [1]. However, the limited understanding of the behaviour of bonded assemblies over the life of structures (including under exposure to extreme temperatures and humidity) and the lack of universal failure criteria still limits their prompt usage on industry applications, at least without a significant amount of testing [2]. SS and DS repairs are a viable option for repairing. By this technique, a hole is drilled at the weakened region to remove the damaged and cracked material, which contains sources for the premature growth of damage [3]. For the SS repairs, a circular patch is then adhesively-bonded on one of the structure faces. SS repairs are easy to execute, but the load eccentricity leads to peel peak stresses at the overlap edges [4]. These, added to the shear peak stresses developing at the same regions due to the differential straining, justify the small efficiency of SS repairs [5]. DS repairs are identical but they involve two patches, one on each face of the structure. These are more efficient than SS repairs, due to the doubling of the bonding area and suppression of the transverse deflection of the adherends [4]. Shear stresses also become more uniform as a result of smaller differential straining. A two-dimensional (2D) approximation of this geometry is often used for design [5], consisting on replacing of the hole by a gap between two separated rectangular plates. This geometry, reasonably predicting the stresses of the three-dimensional (3D) repair, is acceptable only for the optimization of geometric parameters influencing the repairs strength [6].

A few studies can be found about the effect of plug filling with adhesive the gap between the plates (2D approximation) or hole (3D repair) left by the removal of the damaged material. Campilho et al. [7] addressed this technique by the Finite Element Method (FEM) on tensile loaded 2D SS and DS repairs with carbon-epoxy adherends. The SS repairs strength slightly decreased by the use of plug filling due to plug fracture prior to failure of the adhesive layer along the overlap, due to the lateral flexure of SS repairs [4]. Conversely, plug filling highly increased the DS repairs strength (≈10% strength improvement), due to the absence of flexure of the parent structure. Soutis et al. [5] evaluated by the FEM the influence of plug filling on the compressive strength of 3D DS repairs on composite structures. The compressive strength of the repairs reached almost the undamaged strength of the laminates by filling with adhesive the open-hole of the repairs. Campilho et al. [8] addressed by the FEM and using 3D models SS and DS repairs of composite laminates under tension, compression and bending. A 1.2% strength reduction was obtained for the SS repairs with plug-filling under tension compared to the unplugged condition, due to a plug failure prior to failure along the bond length.

Published studies on the subject of adhesives technology revealed that loading rate and temperature effects largely impact on the mechanical properties of adhesives [9]. A few number of studies can be pointed out considering strain rates higher than quasi-static conditions. Some examples are the works of Zgoul and Crocombe [10] and Srivastava [11]. One of the first attempts to model the time dependent behaviour of adhesives is the work of Delale and Erdogan [12], which modelled the visco-elasticity of adhesively bonded joints using Laplace transforms. Because of the complexity of the problem, they obtained the inverse transformations numerically. Malvade et al. [13] studied adhesively bonded double-lap joints in tension for variable extension rates and temperatures. The numerical simulations took advantage of the Raghava [14] and Von Mises yield criteria coupled with nonlinear isotropic hardening to simulate damage of the adhesive.

High temperature usually leads to a strength reduction of bonded assemblies [15], due to a degradation of the adhesive properties [16] and adherend thermal mismatch, when the joined materials have different coefficients of thermal expansion [17]. However, the main factor affecting the strength of adhesive bonds under extreme temperatures is the variation of the adhesive properties [18]. Adams et al. [19] experimentally studied the performance of single-lap joints at low and room temperatures, emphasizing on the significance of adherend mismatch, shrinkage and adhesive properties on the stress state of lap joints. The work by Grant et al. [18] provides a comprehensive evaluation of the temperature effects on the strength of adhesive bonded single-lap joints under tension and bending, and also T-joints. A reduction of stiffness and strength was found increasing the test temperature.

In this work, the influence of plug filling, loading rate and temperature on the tensile strength of SS and DS repairs on aluminium structures was studied experimentally. The testing programme includes repairs with different values of L_O (10, 20 and 30 mm) and with and without plug filling. An investigation is also carried out on the influence of the testing speed on the repairs strength (0.5, 5 and 25 mm/min). Accounting for the temperature effects, tests were carried out at room temperature, 50ºC and 80ºC, allowing a comparative evaluation of the adhesive tested below and above the T_g of the adhesive, defined at 67ºC.

2. EXPERIMENTAL

2.1. Selected materials and surface preparation

The adherends and patches were cut from aluminium plates (AW6063-T6). The two-part epoxy structural adhesive Araldite® 2015 was selected for this study, characterized by a large ductility in tension and shear. The bonding surfaces of the aluminium adherends and patches were manually abraded with an 80 grit paper and then cleaned with acetone.

2.2. Geometry and dimensions of the repairs

Fig. 1 presents the repairs tested: SS repair without plug-filling (a) and with plug-filling (b), and DS repair without plug-filling (c) and with plug-filling (d). Plug-filling of the 3D repair consists on filling with adhesive the spacing left by the removal of the damaged material, whilst for the 2D repair it consists of filling the gap between the adherends. The main purpose of this modification is to increase the load transfer between the adherends [8] originally only achieved by the patches, despite the possibility of a premature plug failure for some of the SS repairs due to transverse deflection [7]. Three values of L_O were studied (10, 20 and 30 mm) comprising all the repair geometries of Fig. 1. The fixed dimensions of the repairs are outlined in Fig. 2. The influence of the testing speed and temperature on the repairs behaviour was also evaluated, considering a DS repair without plug filling and L_O=10 mm.

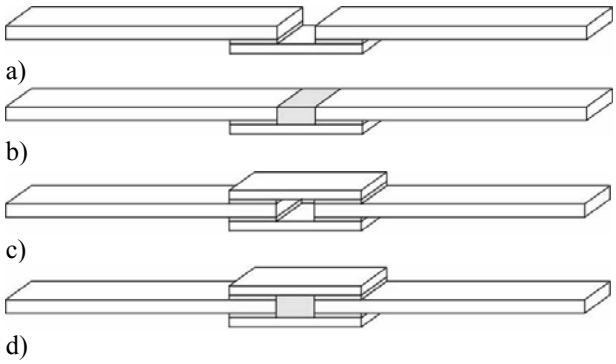

Figure 1. SS repair without (a) and with plug filling (b); DS repair without (c) and with plug filling (d).

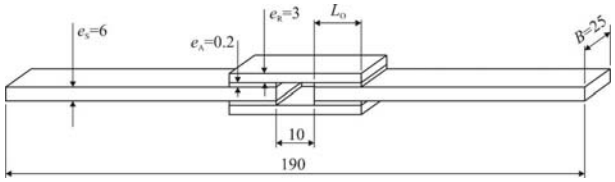

Figure 2. Nomenclature and fixed dimensions of the repairs (e_S-adherend thickness, e_A-adhesive thickness, e_R-patch thickness, L_O-overlap length, B-width).

Testing speeds of 0.5, 5 and 25 mm/min were evaluated, while test temperatures of 23ºC, 50ºC and 80ºC were considered. This range of temperatures will allow the assessment of the adhesive behaviour below and above T_g, defined at 67ºC.

2.3. Test conditions

The SS and DS repairs were tested in tension in a hydraulic testing machine (Instron® 8801) equipped with a 100kN load cell. All the repairs, except the ones tested at 50ºC and 80ºC, were tested at room

temperature. Apart from the study on the rate effects, the repairs were tested at 0.5 mm/min. Four specimens were tested for each condition.

3. RESULTS AND DISCUSSION

3.1. Strength dependence with L_O

Fig. 3 and 4 plot the P-δ curves for the SS repairs with L_O=10 mm without and with plug-filling, respectively. The progressive failure of a specimen representative of the above mentioned geometry is represented in Fig. 5 (without plug-filling) and Fig. 6 (with plug-filling), with (a) relating to the unloaded specimen, (b) to the specimen under load and (c) to fracture.

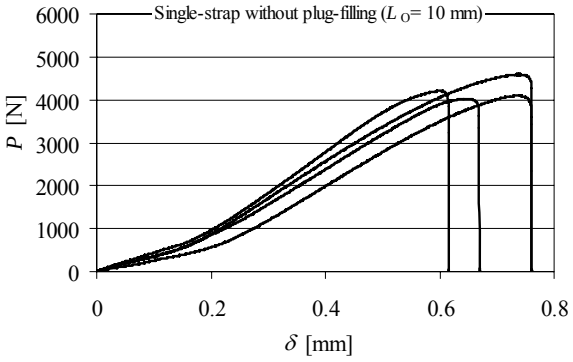

Figure 3. P-δ curves comparison for the SS repairs with L_O=10 mm (without plug-filling).

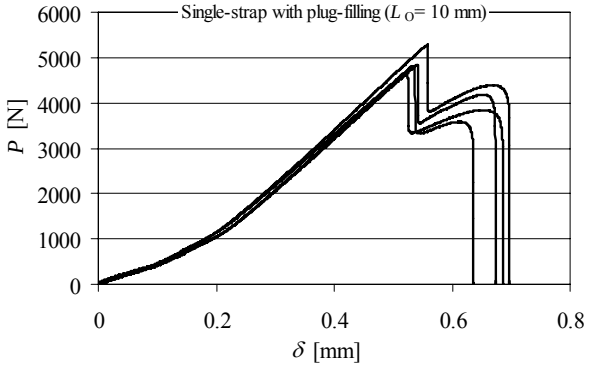

Figure 4. P-δ curves comparison for the SS repairs with L_O=10 mm (with plug-filling).

It should be emphasized at this stage that all specimens tested, except when mentioned otherwise, failed cohesively in the adhesive layer. The comparative analysis of Fig. 3 and Fig. 4 shows a major improvement on the maximum load (P_m) by using the plug. Fig. 5 and Fig. 6 show the substantial transverse deflection of the repairs, due to the asymmetry of loading that the adherends are subjected to [4]. This happening is also responsible for peel stresses peaking at the overlap edges and consequent weakening of the joints [7]. It is also visible in Fig. 6 that the plug-filled repair fails in two steps: in the first one, a cohesive fracture near one of the adherends butts occurs while the overlap is still under load. Subsequently, the repair fails at one of the overlaps. In view of this scenario, it can be concluded that the first step of failure for the plug-filled repair occurs at a higher load than P_m for the non-plugged repair, yielding a strength improvement. The subsequent drop of P is due to final failure at the overlap.

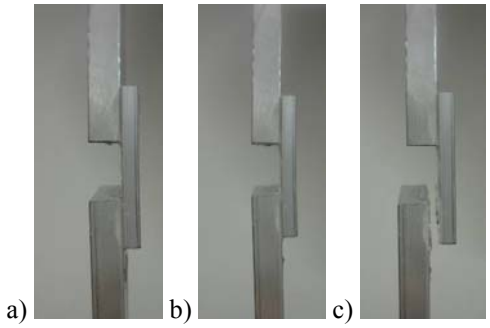

Figure 5. Failure of a SS repair with L_O=10 mm (without plug-filling).

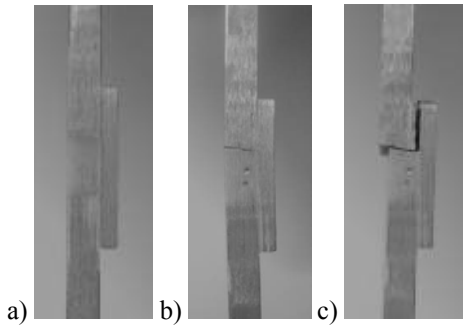

Figure 6. Failure of a SS repair with L_O=10 mm (with plug-filling).

The values of P_m and deviations for the different values of L_O are presented in Fig. 7 (SS repairs). These results show an approximate 15.6% strength improvement for the L_O=10 mm repairs by using a plug-filling. By increasing L_O, the opposite scenario took place, i.e., vertical failure near the plug prematurely to the value of P_m for the unplugged repair, yielding this modification ineffective [7]. Actually, the slight differences in Fig. 7 for L_O=20 and 30 mm are merely statistical. As a consequence of this behaviour, the positive effect of plug filling is only noticeable for sufficiently small values of L_O, since for bigger overlaps the vertical failure occurs prior to the overlap failure. It is also interesting to note a decreasing improvement of P_m with L_O, caused by increasing differential straining of the adherends with the increase of L_O, due to the larger loads sustained. In fact, whilst shear stress gradients are not important for small values of L_O, they gradually increase with this quantity, owing the increasing gradient of longitudinal strains in the adherends [4]. This is regarded in the literature as the main

justification for a strength improvement of single-lap joints or single-strap repairs with L_O at a decreasing rate, eventually leading to a strength plateau [4, 20].

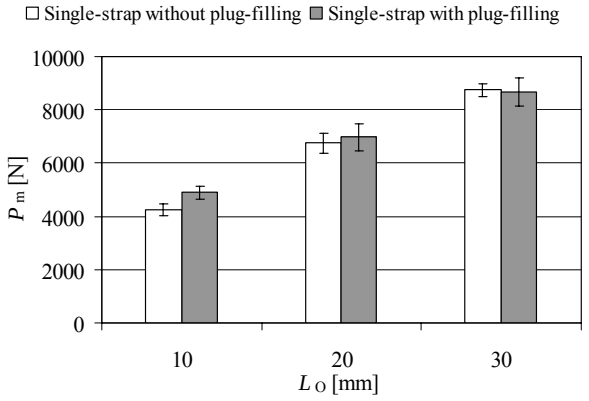

Figure 7. P_m versus L_O plot for the SS repairs (without and with plug-filling).

An equivalent analysis was performed for the DS repairs. Fig. 8 exemplifies the fracture process for both scenarios. The *P-δ* curves show the approximately linear behaviour up to failure for the repairs without and with plug filling. For the plug filled repair, this results from a simultaneous failure along the overlap and in the plug. DS repairs are under symmetric loads (Fig. 8), which eliminates the transverse flexure characteristic of SS repairs [4]. However, the patches are still under flexure, leading to peel peak stresses in the adherends [21]. Fig. 9 shows the evolution of P_m for the DS repairs with L_O. Compared to the corresponding SS values (Fig. 7), DS results show that P_m surpasses the double of the SS repairs strength, despite having twice the bonding area. This is justified by the smaller magnitude of peel and shear stresses [4]. The increase of P_m with L_O is not proportional, but is closer to being proportional than for the SS repairs, which can be explained by the reduction of differential straining effects [16]. Plug filling yields an identical absolute improvement of P_m for the three values of L_O since fracture was simultaneous in the plug and overlap. The resulting strength improvement varied between 17.1% for the L_O=10 mm repair and 4.6% for the L_O=30 mm repair.

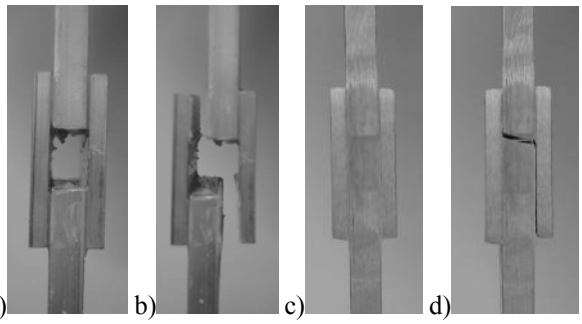

Figure 8. Failure of a DS repair with L_O=10 mm without (a and b) and with plug filling (c and d).

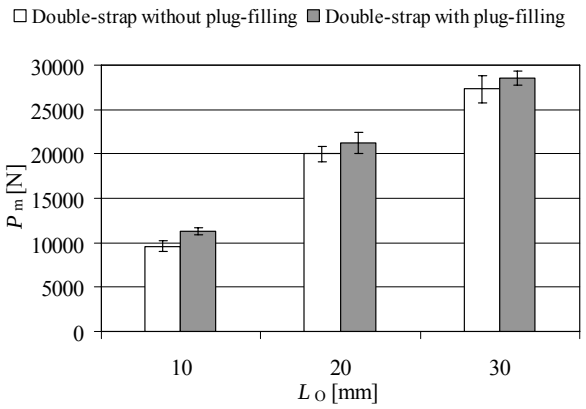

Figure 9. P_m versus L_O plot for the DS repairs (without and with plug-filling).

3.2. Strength dependence with the testing speed

Fig. 10 and Fig. 11 plot the *P-δ* curves for testing speeds of 0.5 and 25 mm/min, respectively.

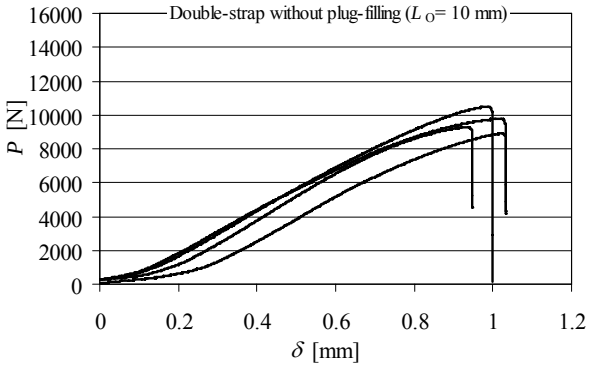

Figure 10. P-δ curves comparison for the DS repairs without plug-filling and L_O=10 mm (0.5 mm/min).

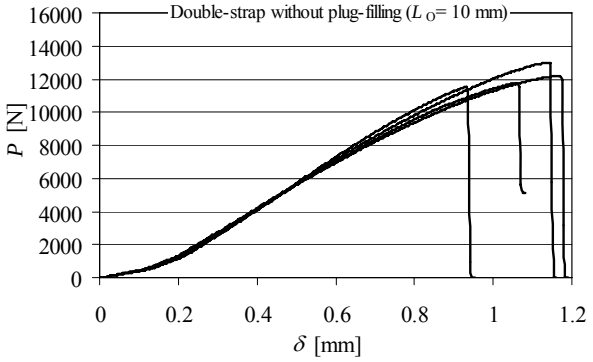

Figure 11. P-δ curves comparison for the DS repairs without plug-filling and L_O=10 mm (25 mm/min).

These figures show the difference in P_m between these two testing conditions, as P_m increases by a significant amount with testing at 25 mm/min. This is caused by the increased adhesive resistance to deformation and to molecular displacements with the increase of the testing

speed, correspondingly increasing the required load to failure [22]. Despite this fact, the stiffness, i.e., the slope of the P-δ curves is left practically unchanged.

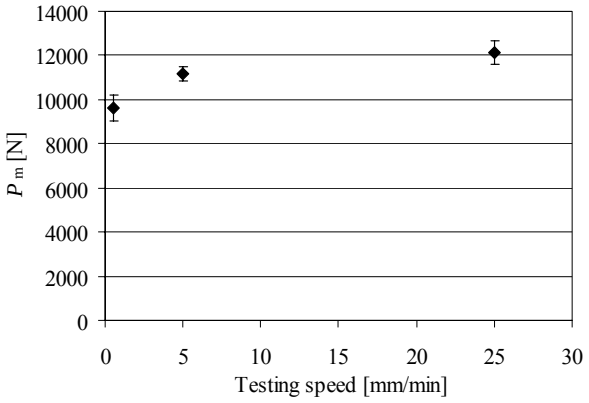

Figure 12. P_m for the DS repairs without plug-filling and L_O=10 mm as a function of the testing speed.

The average values of P_m are summarized in Fig. 12. The value of P_m increases with the testing speed, showing a bigger gradient for the smaller speeds, tending to reach a constant value for bigger testing speeds. An identical tendency was found by Zgoul and Crocombe [10], when testing a rate dependent adhesive using the single-lap joint configuration. In fact, as it is generally known, increasing the extension rate is always associated to an increase of the failure load of adhesives, accompanied by a reduction of ductility. This effect is particularly significant at high temperatures, when the adhesive becomes softened and, as a result, exhibits a higher degree of strain rate sensitivity [13].

3.3. Strength dependence with the testing temperature

The SS and DS repairs were also tested under varying operating temperatures (23ºC, 50ºC and 80ºC). Fig. 13 allows the comparison between the P-δ curves at 50ºC and 80ºC. Globally, the results showed a major strength and stiffness reduction with the increase of temperature, which was expected due to the known degradation of the adhesive properties with the temperature [16]. Actually, upon heating the adhesive, the solid polymer transforms from a rigid to a rubbery state. As a result, the molecules that are virtually frozen in position at room temperature begin to undertake rotational and translational motion. Owing to this, abrupt changes in the physical properties of the adhesive occur. It is also worth mentioning that the fracture was adhesive for all specimens tested at 50ºC and 80ºC, showing the marked degradation of the interfacial properties of the adhesive, comparing to its cohesive fracture properties. The average values of P_m for the different testing temperatures and respective variation (Fig. 14) show the expected progressive reduction of strength with the testing temperature [23].

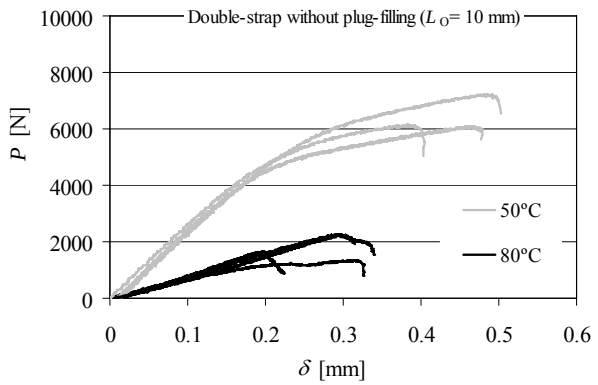

Figure 13. P-δ curves comparison for the DS repairs without plug-filling and L_O=10 mm (50ºC and 80ºC).

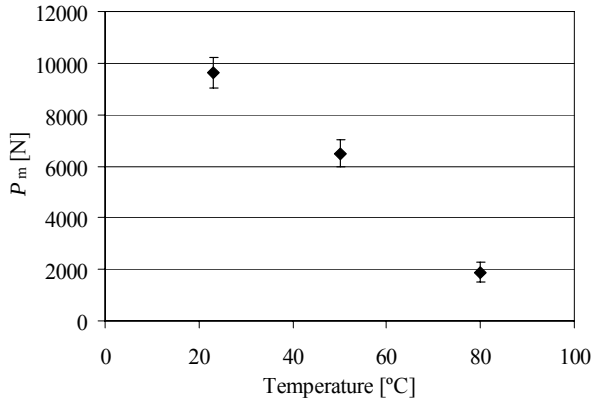

Figure 14. P_m versus L_O plot for the DS repairs without plug-filling and L_O=10 mm as a function of the temperature of testing.

4. CONCLUDING REMARKS

The influence of plug filling, loading rate and temperature on the tensile strength of single and double-strap repairs on aluminium structures was studied experimentally. Repairs were tested with and without plug filling and different values of overlap length (10, 20 and 30 mm). An investigation is also carried out on the influence of the testing speed on the repairs strength (considering 0.5, 5 and 25 mm/min). Accounting for the temperature effects, tests were carried out at room temperature, 50ºC and 80ºC, to permit a comparative evaluation of the adhesive tested below and above the Glass Transition Temperature of the adhesive (67ºC). It was globally shown that increasing the overlap length always causes a strength improvement of the repairs, but that this strength improvement is not proportional, mainly due to differential shearing effects between the adherends and patches. Plug filling of single-strap repairs is to be recommended for small overlap lengths, given that for bigger overlaps, due to the transverse deflection of single-strap repairs, the plug fails prematurely to the overlap. This caused the plug to the ineffective, since at the time of failure the plug was not contributing to the strength of the repairs. Oppositely,

due to the absence of transverse deflection, for the double-strap repairs an improvement was found for all overlap lengths evaluated. Concerning the testing speed, an increase of the maximum load was found with this quantity, more significant for the smaller testing speeds and tending to a constant value of maximum load. High temperatures gradually decreased the repairs stiffness and strength due to the degradation of the adhesive. Principles for repairing aluminium structures were established in this work, which can be extrapolated for other materials and adhesives, although with some cautions since different adherends or patches can yield variations of the stress distributions and thus the strength of the repairs. Also the varying ductility of adhesives can source some variation to the presented results.

REFERENCES

[1] Baker, A., "Bonded composite repair of fatigue-cracked primary aircraft structure", *Composites Structures*, vol. 47, pag. 431–443, 1999.

[2] de Morais, A.B., Pereira, A.B., Teixeira, J.P. and Cavaleiro, N.C., "Strength of epoxy adhesive-bonded stainless-steel joints", *International Journal of Adhesion and Adhesives*, vol. 27, pag. 679–686, 2007.

[3] Liu, X. and Wang, G., "Progressive failure analysis of bonded composite repairs", *Composite Structures*, vol. 81, pag. 331–340, 2007.

[4] Campilho, R.D.S.G., de Moura, M.F.S.F. and Domingues, J.J.M.S., "Modeling single and double lap repairs on composite materials", *Composites Science &. Technology*, vol. 65, pag. 1948–1958, 2005.

[5] Soutis, C., Duan, D.M. and Goutas, P., "Compressive behaviour of CFRP laminates repaired with adhesively bonded external patches", *Composite Structures*, vol. 45, pag. 289–301, 1999.

[6] Hu, F.Z. and Soutis, C., "Strength prediction of patch repaired CFRP laminates loaded in compression", *Composites Science & Technology*, vol. 60, pag. 1103–1114, 2000.

[7] Campilho, R.D.S.G., de Moura, M.F.S.F. and Domingues, J.J.M.S., "Numerical prediction on the tensile residual strength of repaired CFRP under different geometric changes", *International Journal of Adhesion and Adhesives*, vol. 29, pag. 195–205, 2009.

[8] Campilho, R.D.S.G., de Moura, M.F.S.F., Domingues, J.J.M.S. and Morais, J.J.L., "Computational modelling of the residual strength of repaired composite laminates using a cohesive damage model", *Journal of Adhesion and Science Technology*, vol. 22, pag. 1565–1591, 2008.

[9] Crocombe, A.D., Richardson, G. and Smith, P.A., "A Unified Approach for Predicting the Strength of Cracked and Non-Cracked Adhesive Joints", *Journal of Adhesion*, vol. 49, pag. 211–244, 1995.

[10] Zgoul, M. and Crocombe, A.D., "Numerical modelling of lap joints bonded with a rate dependent adhesive", *International Journal of Adhesion and Adhesives*, vol. 24, pag. 355–366, 2004.

[11] Srivastava, V.K., "Characterization of adhesive bonded lap joints of C/C–SiC composite and Ti–6Al–4V alloy under varying conditions", *International Journal of Adhesion and Adhesives*, vol. 23, pag. 59–67, 2003.

[12] Delale, F. and Erdogan, F., "Viscoelastic analysis of adhesive bonded joints", *Journal of Applied. Mechanics*, vol. 48, pag. 331–338, 1981.

[13] Malvade, I., Deb, A., Biswas, P. and Kumar, A., "Numerical prediction of load-displacement behaviors of adhesively bonded joints at different extension rates and temperatures", *Computational Materials Science*, vol. 44, pag. 1208–1217, 2009.

[14] Raghava, R., Caddell, R. and Yeh, G.S., "Macroscopic yield behaviour of Polymers", *Journal of Materials Science*, vol. 8, pag. 225–232, 1973.

[15] Apalak, M.K., Apalak, Z.G., Gunes, R. and Karakas, E.S., "Steady-state thermal and geometrical non-linear stress analysis of an adhesively bonded tee joint with double support", *International Journal of Adhesion and Adhesives*, vol. 23, pag. 115–130, 2003.

[16] da Silva, L.F.M. and Adams, R.D., "Joint strength predictions for adhesive joints to be used over a wide temperature range", *International Journal of Adhesion and Adhesives*, vol. 27, pag. 362–379, 2007.

[17] Adams, R.D and Mallick, V., "The Effect of Temperature on the Strength of Adhesively-Bonded Composite-Aluminium Joints", *Journal of Adhesion*, vol. 43, pag. 17–33, 1993.

[18] Grant, L.D.R., Adams, R.D. and da Silva, L.F.M., "Effect of the temperature on the strength of adhesively bonded single lap joints and T joints for the automotive industry", *International Journal of Adhesion and Adhesives*, vol. 29, pag. 535–542, 2009.

[19] Adams, R.D., Coppendale, J., Mallick, V. and Al-Hamdan, H., "The effect of temperature on the strength of adhesive joints", *International Journal of Adhesion and Adhesives*, vol. 12, pag. 185–190, 1992.

[20] Reis, P., Antunes, F. and Ferreira, J.A.M., "Influence of superposition length on mechanical resistance of single lap adhesive joints", *Composite Structures*, vol. 67, pag. 125–133, 2005.

[21] de Castro, J. and Keller, H., "Ductile double-lap joints from brittle GFRP laminates and ductile adhesives, Part I: Experimental investigation", *Composites Part B – Engineering*, vol. 39, pag. 271–281, 2008.

[22] Pocius, A.V., "Adhesion and adhesives technology, An introduction, 2nd Edition", Hanser, 2002.

[23] Harris, J.A. and Fay, P.A., "Fatigue life evaluation of structural adhesives for automotive applications", *International Journal of Adhesion and Adhesives*, vol. 12, pag. 9–18, 1992.

IMPROVED EXPERIMENTAL TECHNIQUES FOR LIFE PREDICTION UNDER THERMOMECHANICAL FATIGUE (TMF) CONDITIONS

Aitor García de la Yedra, Antonio Martín-Meizoso, Jose Luis Pedrejón

CEIT and TECNUN (University of Navarra)

Paseo de Manuel Lardizábal, 15, 20018 San Sebastián, Spain

ABSTRACT

Turbine hot section materials, superalloys, are subjected to variable loads (pressure and centrifugal) as well as variable thermal loads due to start ups and shutdowns which yields to a thermomechanical fatigue (TMF) condition. Under these conditions it is known that three kinds of degradations lead the material to fracture: creep, fatigue and oxidation, but the interaction among them is not well understood. This is why experimental techniques play an important role.

The main objective is to obtain a test-machine configuration which fulfils the corresponding ASTM standard in terms of temperature distribution, alignment, thermal and mechanical strain control, etc. This paper is focused on the former field. For that purpose some measurements were carried out with thermocouples as well as an infrared thermopraphic camera. In some cases theoretical solutions were needed (analytical and finite element method solutions) due to the fact that repetitiveness was not achieved. As a result of the different actions a configuration was obtained which allows executing thermomechanical fatigue tests.

KEY WORDS: Thermomechanical fatigue; thermal gradients; Finite Element Method

1. INTRODUCTION

TMF tests are carried out to broaden knowledge on the degradation methods of materials which suffer thermal and mechanical cyclic loads. Therefore these tests involve mechanical strain as well as thermal strain cycles applied simultaneously. The former is obtained by using a servoelectric test machine (INSTRON 8562), whereas thermal strain cycles are accomplished taking advantage of the Joule effect, instead of the usual induction heating system. The main challenge in this field is to obtain a configuration in which thermal distribution is as homogeneous as possible. It is known that heterogeneous distributions cause thermally induced additional stresses. This magnitude and temperatures have been assessed using different available tools (analytical and numerical solutions as well as experimental measurements with thermocouples and IR thermographic camera). As a result of the former action, a configuration was obtained which allows reducing previous thermal gradients and fulfilling the corresponding ASTM standard [1].

2.TEMPERATURE DISTRIBUTION MEASUREMENTS

Firstly, some experiments were accomplished to pursue the understanding of the temperature distribution along the test machine axis (axial gradients) with no mechanical strain applied. Three ribbon thermocouples (TC, N type) were used, placed one in the centre of the gauge length (12.5 mm) and the other two at the end of it, as shown in Figure 1.

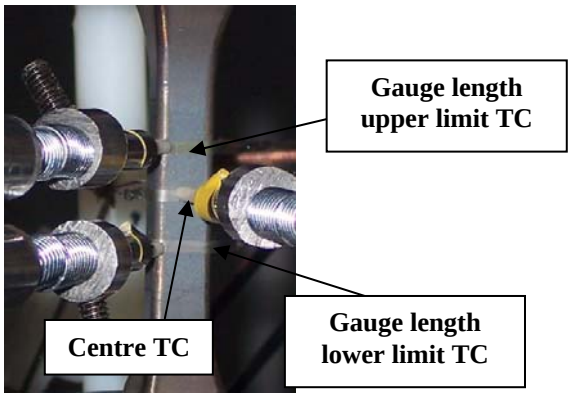

Figure 1. TC configuration

Thermal cycles range was 300ºC-950ºC with a 5ºC/s heating and cooling rates. Control temperature was carried out with central thermocouple. Test-pieces are of rectangular cross-section, 8 mm width and 5 mm thick, with corner radius of 1 mm. The material to test is stainless steel AISI 316. Although its mechanical properties differ from those of superalloys, its thermal properties turn out to be similar, if relative difference in thermal diffusivity is considered [2]. This magnitude gives an idea of the thermal inertia and the transient state, reaching the steady state more rapidly if the thermal diffusivity is higher.

Heating source (Q) is obtained thanks to the voltage drop (ΔV) when an electric current (I) passes through the test-piece.

$$Q = \Delta V\, I \quad (1)$$

At the same time, voltage drop is directly proportional to the electric resistance (R) which increases with the test-piece length (L) and decreases with its area (A).

$$\Delta V = I\, R \quad (2)$$

$$R = \rho\, L/A \quad (3)$$

This property and the test-piece geometry cause huge differences in heat source, yielding a situation where within the gauge length heat source is 50 % higher than at the ends of the test-piece. This may provoke high thermal gradients. For this reason another experiment was accomplished adding a heat source to the test machine grips by using 460 W electric resistances and surrounded by some alumina boxes as shown in Figure 2.

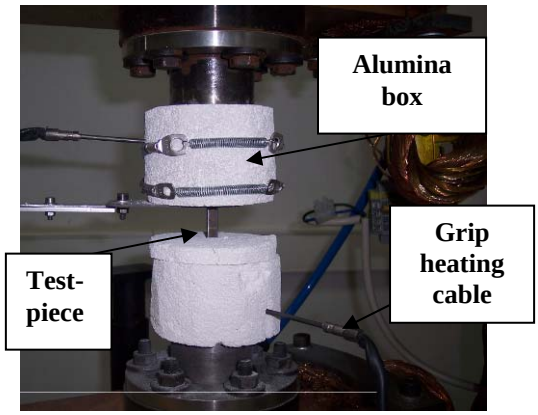

Figure 2. Grip heating method

This allowed heating those parts of the test piece where heating source was low. Besides the alumina boxes reduced heat losses, improving the efficiency of the method. The same three thermocouples, as in the previous experiments, were used placed in the same positions and some TMF thermal cycles were carried out.

Eventually, an infrared thermo graphic camera was used to contrast the results with the measurements accomplished with thermocouples due to the fact that repetitiveness in measurements was hard to achieve in some cases. As a non-contact temperature measurement method, the image obtained is a function of a material property (emissivity) which changes with temperature, surface roughness and oxidation. The strategy to avoid this drawback was to use a thermocouple at the centre of the gauge length and heat the test-piece up to the peak temperature of the TMF cycle (950ºC). If this temperature is maintained, after some time oxidation level reaches its maximum and this allows calibrating the camera with a constant emissivity value, typically 0,85. Afterwards, an image was obtained at that precise temperature for a steady state.

Measuring temperature with an IR thermography camera in a transient cycle involves a very good knowledge of emissivity value at different temperatures as well as at different oxidation states. This aspect is not covered in this paper.

Regarding radial temperature distribution, a 0.3 mm hole was drilled up to the core of one test-piece. The hole has to be small enough to not disturb the temperature distribution within the cross-section, but it also has to be large enough to fit a thermocouple (N type, Nicrosil-Nisil). However, handling of small diameter thermocouples turns out to be difficult and repetitiveness is not achieved. Some other authors have found the same difficulty when measuring radial gradients in a cross section [3]. This is why theoretical solutions were preferred.

3. THEORETICAL SOLUTIONS

3.1- Analytical solution

Heat transfer problems are governed by the following equation:

$$k\left(\frac{\delta^2 T}{\delta x^2}+\frac{\delta^2 T}{\delta y^2}+\frac{\delta^2 T}{\delta z^2}\right)+q=\rho\cdot c\cdot\frac{\delta T}{\delta t} \quad (4)$$

where k (W/m.K) is the thermal conductivity of the material, ρ (kg/m^3) the density, c (J/kg.K) specific heat, T (K) temperature and q (W/m^3) the heat source produced by the voltage drop described in equation (1).

If radial gradients are needed to assess, the partial differential equation, for a rectangular parallelepiped, may be solved assuming that no heat generation exists (TMF cooling cycle). It is also assumed that the initial temperature distribution is known and is considered homogeneous.

Equation (4) was solved using the superposition method and considering the following boundary conditions:

a) $-k\left(\frac{\delta T}{\delta x}\right)=h.[T(L,t)-T\infty]$, convection heat exchange of the outer surface on each main direction (x, y, z) ..... (5), where h=10 W/m^{2}K is the film coefficient.

b) $T(x, y, z, 0) = T_i$=1223K $\forall x, y, z$ initial homogeneous temperature distribution.....(6)

Radiation effect, which is the most damaging in terms of radial gradients, may be taken into account in

equation (5) if an equivalent film coefficient is defined. The radiation heat exchange may be rewritten as follows:

$$Q_{radiation} = \sigma \cdot \varepsilon \cdot (T^4 - T_\infty^4) \quad (7)$$

$$Q_{radiation} = \sigma \varepsilon (T + T_\infty)(T^2 + T_\infty^2)(T - T_\infty) \quad (8)$$

where σ stands for the Stefan Boltzmann constant 5.67. 10^{-8} W/m^{2}K^4, ε for the emissivity value (no units) and T_∞ for the room temperature. Equation (8) may be written in the same manner to the convection heat exchange if a radiation film coefficient is introduced ($h_r[W/m^2 \cdot K^4]$):

$$Q_{radiation} = h_r (T - T_\infty) \quad (9)$$

$$h_r = \sigma \cdot \varepsilon \cdot (T + T_\infty) \cdot (T^2 + T_\infty^2) \quad (10)$$

The above mentioned consideration was taken into account and equation (4) was solved by using a Matlab 7.5 code and an equivalent film coefficient which is a sum of convection and radiation coefficients. It was solved with 0.1 second time increments and considering property changes with temperature on each one.

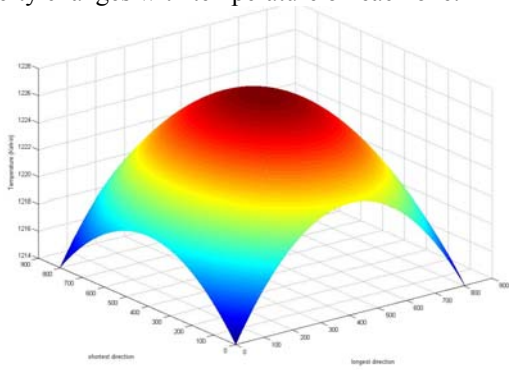

Figure 3. Analytical solution for radial gradients worst scenario in a TMF cycle

Figure 3 shows the initial and worst instant for the TMF cooling cycle. The obtained gradients were around 9ºC but after plotting the complete thermal transient a conclusion was drawn; achieved cooling rates were higher than 5ºC/s which is the value for a typical TMF test. This means that obtained thermal gradients are higher than in a real test where cooling rate is lower.

Figure 4 displays the thermal transient analysis for a two cross section spots: core, which gave the maximum temperature value and edge, which corresponds with the minimum. Besides, 5ºC/s cooling rate was plotted to compare it with the achieved curves.

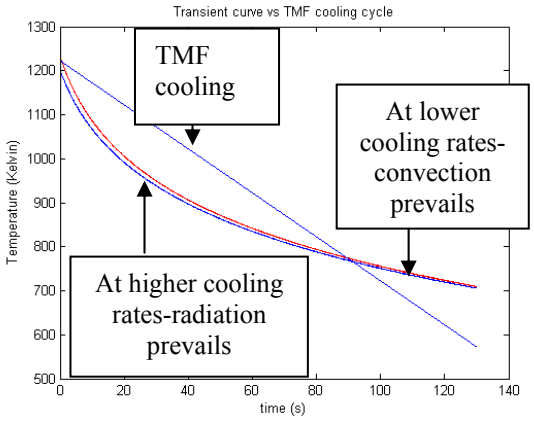

Figure 4. Transient TMF cycle for maximum (core) and minimum (edge) temperatures compared with 5ºC/s cooling rate

It was observed that if this cooling rate was needed to be followed, an input electrical current would have to pass through the test-piece during the first 90 seconds. On the other hand, when test-piece reached lower temperature values its cooling rate was very low and convection has to be forced to follow the desired ramp by blowing some cold air through some nozzles. This effect happens due to the radiation, which involves large heat exchange when temperatures are high, but it may be neglected if temperatures are sufficiently low.

Consequently, heat source due to the Joule effect should be added to equation (4) to obtain the desired ramp. Nevertheless, a coupling effect exists between Joule effect and thermal problem which makes the obtaining of the analytical transient response difficult. Therefore, numerical solutions are thought to be the best option to face the problem.

3.2- Numerical solutions

ABAQUS finite element method *(FEM)* software provides a coupled thermal-electric code suitable for solving problems such as the one introduced in this paper. Coupling arises when heat generation has to be calculated. Firstly the electrical problem has to be solved but the electric conductivity and the input current are temperature dependent. This means that they can not be known before assessing the heat source. This involves an iterative process which is solved using numerical tools.

The model simulated by FEM consists of an eight of the test-piece, due to symmetry, and the following loads and boundary conditions:

a) Input electrical current
b) 0 electric potential at the end of the test-piece.
c) Convection and radiation heat exchange with the surrounding.
d) Adiabatic surfaces, at the three planes of symmetry.

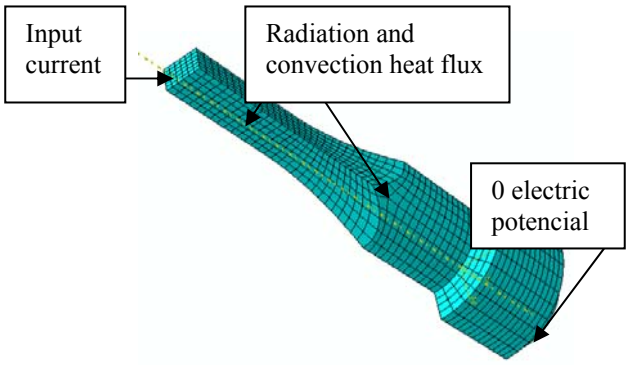

Figure 5. FEM model for the coupled thermal-electric problem

Input electrical current was measured experimentally and recorded as a function of time for a typical TMF cycle. This allows reproducing a complete transient cycle. There are some electrical and thermal properties that change with temperature and their values are needed if accuracy in the results is desired. To achieve this purpose, experimentally the test-piece was heated up to three different temperature values (350ºC, 650ºC and 950 ºC measured at the centre of the gauge length).These temperatures were maintained and the input currents were measured. Afterwards, steady state FEM analyses were carried out, for each case, trying to match theoretical results with the ones obtained experimentally by changing the thermal and electrical properties. Three were the main properties to change, thermal and electrical conductivity as well as the emissivity. The former is obtained from the data available in the bibliography [2], this means that this value change with temperature is known and therefore it was fixed in the simulations .The rest of the properties values were modified until a matching between experimental and theoretical results was obtained. As a result of the experiments the following properties were obtained for the AISI 316 stainless steel.

Table 1. AISI 316 thermal and electrical properties as a function of temperature

Temperature reached in simulations(ºC)	Thermal conductivity (W/m·K)	Electric resistivity (Ohm·m)	Emissivity
355,05	18	7,00E-07	0,7
655,25	25	8,00E-07	0,8
950,85	28	9,00E-07	0,85

Regarding convection, in the tested range, radiation heat exchange prevails over convection, as it was proved with the analytical solutions, and therefore its influence in the heat phenomena is low, unless convection is forced. However, its effect was added to the simulation with a film coefficient *(h)* equal to 10 [W/m^2.K] constant throughout the cycle, which is a typical value for natural convection.

The correct execution of the simulation generates a file with the temperature distribution for the geometry drawn and at any instant of the complete TMF cycle modelled. This file was used to carry out a static analysis to assess the induced stresses due to heterogeneous temperature distribution.

4. RESULTS

4.1 Experimental results

The results of the experiments showed that, unless further actions are taken, axial thermal gradients will exist (up to 25ºC when peak temperature is reached). It has to be noted that the corresponding standard [1] limits this value to 1% of the peak absolute temperature (Kelvin), in other words to 12.23 ºC.

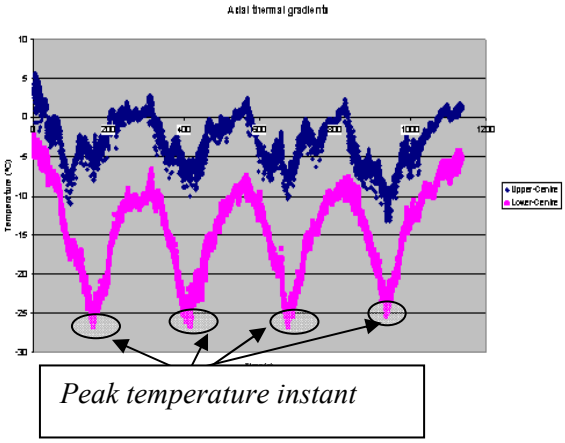

Figure 6. TMF axial gradients results for four cycles

In Figure 6 temperature measurements at the ends of the gauge length are displayed and compared to the centre thermocouple for four TMF cycles. According to the results maximum gradients happen when TMF cycle reaches its maximum temperature value, being centre thermocouple measurement much higher than those at the ends of the gauge length. It also has to be noted that the temperature at the lower gauge length limit (pink line, Figure 6) is much cooler than that at the upper gauge length limit (blue line, Figure 6) which may be attributed to the mass diffusivity effect. This means that hot air (with lower density) tends to ascend and this causes higher temperatures.

IR thermography method verifies that, even in a steady state case, axial gradients appear. Besides it helps to understand why those thermal differences occur, concluding that heat source at the end of the test-piece is low. This causes large heat flux due to conduction. An image (Figure 7) taken from that experiment clarifies what is explained here.

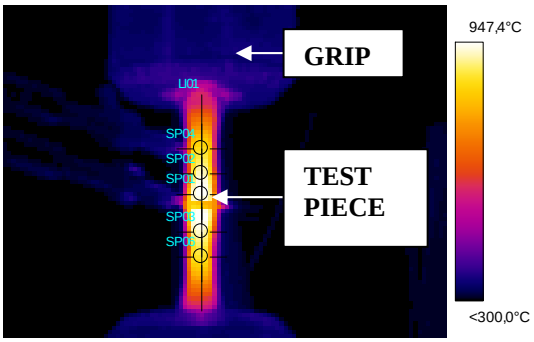

Figure 7. IR thermographic image (950ºC at the centre of the gauge length)

Figure 7 represents an instant of the test-piece and its grips when control thermocouple (centre) displays 950 ºC. Five points temperature were assessed, one placed in the centre, two close to the gauge length limit and the other two out of the gauge length. These measurements proved that within the gauge length temperature differences were around 25ºC, similar to those obtained by thermocouples, whereas those placed outside displayed differences above 100ºC. This confirms that heat flux from test-piece towards grips is huge, because of the temperature differences between them (950ºC at the former and only 300ºC at the grips).

Latest experiments (see Figure 2) with 460 W resistances for heat supplying to the grips gave excellent results as shown in ***Figure 8***:

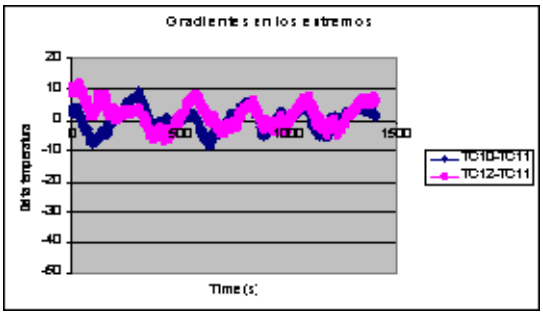

Figure 8. TMF axial gradients with grip preheating method

According to the latest results, current thermal cycles fulfil the corresponding standard [1] as they do not exceed +/-10 ºC temperature differences and the limit established is +/-12.23ºC. Unlike previous configuration, when minimum temperatures were reached, the ends of the gauge length were almost 10ºC warmer than the centre; whereas at maximum cycle temperature, the ends of the gauge length were 10ºC cooler. The reversal in thermal gradients at minimum temperatures turned out to be a good solution to avoid exceeding the established limits.

4.2 Theoretical results

Radial gradients assessment was done by matching a FEM model with experimental results as explained in section 3. As a result, a theoretical thermal transient cycle was obtained which fitted with the experimental TMF cycle.

The test-piece cross-section (quarter of it due to symmetry) was plotted, taken from the centre of the gauge length. Its temperature distribution was similar to that obtained by analytical solutions (Figure 3) with the same elliptical isothermal lines. This is shown in Figure 9.

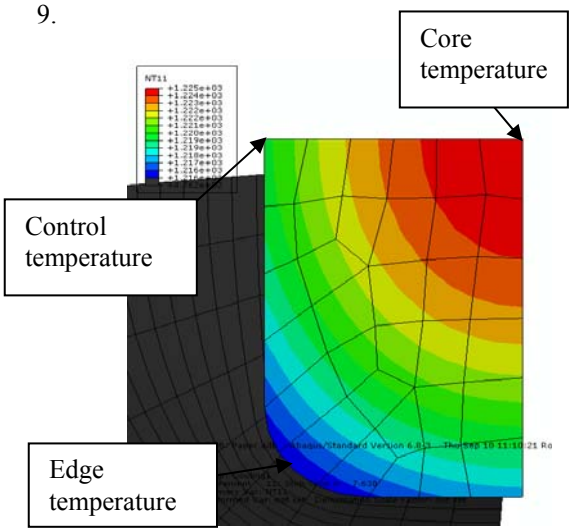

Figure 9. Maximum radial gradients in a TMF cycle

The simulation suggested that maximum radial gradients are around 9.5ºC which is distributed as follows:

a) 5ºC difference between control and core temperature.
b) -4.5 ºC difference between edge and control (Figure 9). Control temperature is the one with whom experimental TMF cycles are controlled

Although TMF standard [1] does not give a limit value for radial gradients, they have to be restricted to avoid premature failure of the test-piece. For this purpose, the static FEM analysis carried out with the temperature distribution file was studied. It was concluded that thermally induced stresses, according to von Mises criteria, may reached up to 30 MPa (lower than 5% of the stress range, $\Delta\sigma$, in a typical TMF test) within the gauge length. Besides, in the FEM thermal analysis, the effect of the grip heating was not added and therefore the assessed stresses were much higher than those in real TMF tests.

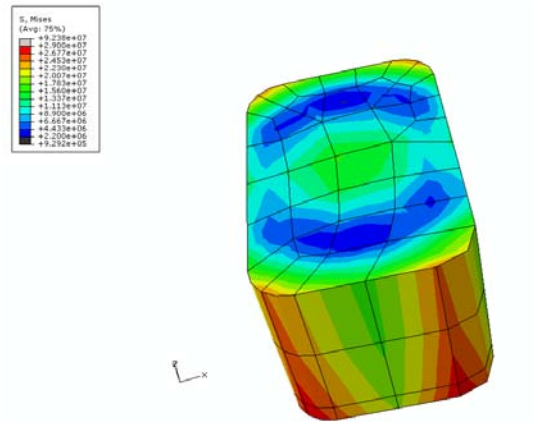

Figure 10. Thermally induced stresses according to von Mises criteria

In Figure 10 stresses caused by the temperature distribution are plotted for a whole cross section. This magnitude is higher at those locations where temperature differences are larger, such as the corners of the test-piece.

If stress tensor main components are analyzed, it may be observed that on the surface tensile stresses appear, whereas at the core the components are mainly compressive. Nevertheless, tensile values are much higher for all the cases and besides it has to be emphasized that in the fatigue phenomena cracks initiate on the surface, where induced tensile stresses are found to be maximum. Consequently the obtained temperature distribution may contribute to the crack initiation and therefore may reduce the life of the test-piece.

As expected, the stress values along the test-piece axis, in other words σ_{33} values, are observed to be most damaging due to the fact that they are originated by the axial gradients (the highest temperature differences). On the other hand, stresses caused by radial gradients, σ_{11} and σ_{22}, are considerably lower (60%). This means that cracks will tend to grow perpendicular to the direction where maximum stresses are observed, longitudinal direction.

5. CONCLUSIONS

i) Executing a non-isothermal fatigue test by Joule effect heating device may cause high axial gradients if test-piece has different area sections.

ii) A method was developed to avoid these gradients which gave excellent result, fulfilling the ASTM standard. For this purpose, heat had to be supplied to the grips.

iii) Although test-piece cross-section is small, radial gradients are produced mainly due to radiation heat exchange which is huge at peak temperature (1223 K in this case) and the high emissivity values (0.85) which increases with temperature and oxidation state.

iv) Coupled thermal-electric model developed in ABAQUS matches with experimental results and gives an excellent solution to those problems whose analytical solution is difficult.

v) Thermally induced stresses were assessed, concluding that tensile stresses prevail over compressive (mainly on the surface of the test-piece) and this may accelerate the crack initiation.

REFERENCES

[1] **ASTM E 2368-04**, "Standard Practised for Strain Controlled Thermomechanical Fatigue Testing". **American Society for Testing and Materials, ASTM, Philadelphia, USA, 2005.**

[2] **Ala-Outinen, Tiina**. "*Fire resistance of austenitic stainless steels Polarit 725 and Polarit 761"* **VTT Tiedotteita -Meddelanden Research Notes 1760. 34 p. + app. 30 p, Finland, 1996.**

[3] **T. Brendel et al**. "Temperature gradients in TMF specimens. Measurement and influence on TMF life". ***International Journal of Fatigue 30 (2008) 234-240.***

ACKNOWLEDGEMENT

Thanks are given to ITP for its financial support and materials; to the Spanish Ministry of Science and Innovation for the financial support (project MAT2008-03735/MAT) and to the Basque Government (project PI09-09).

USE OF OPTICAL TECNIQUES IN THE ASSESSEMENT OF THE DISPLACEMENT FIELD NEAR THE CRACK TIP

J. Ribeiro [1], M. Vaz [2], H. Lopes [1], F. Q. de Melo[3], J. Monteiro [4]

[1] ESTG - Instituto Politécnico de Bragança
Campus de Sta Apolónia, Apt 1134, 5301-857 Bragança
jribeiro@ipb.pt; hlopes@ipb.pt

[2] DEMec - Faculdade de Engenharia da Universidade do Porto
Rua Dr. Roberto Frias, 4200-465 Porto
gmavaz@fe.up.pt

[3] UA – Universidade de Aveiro,
Campo Universitário de Santiago, 3810-193 Aveiro
fqm@mec.ua.pt

[4] Laboratory of Optics and Experimental Mechanics
Instituto de Engenharia Mecânica e Gestão Industrial
Rua do Barroco, 174, 4465-591
jmont@fe.up.pt

ABSTRACT

A crack tip represents a highly singular stress field existing in a structural component. The evaluation of the associate strain gradient is difficult using experimental discrete methods. An efficient alternative relies on optical methods which are non contact and give continuous information about displacements fields and its derivatives when strain evaluation is necessary.
This paper describes some experimental methods to fully characterize the displacement field near a crack tip existing in flat plates. Three optical field techniques based on image analysis were used in the present work; respectively ESPI (electronic speckle pattern interferometry), MI (Moiré Interferometry), and DIC (digital image correlation). These methods present different resolutions which can be adjusted according to the expected strain gradient. While the first method depends on the laser wavelength, the second depends on the grid pitch and the last on the surface texture.

KEY WORDS: optical techniques, ESPI, Moiré Interferometry, Digital Image Correlation

1. INTRODUCTION

1.1 OPTICAL METHODS

1.1.1 ESPI

All these techniques use light to codify the surface information before and after loading to enhance displacements or strains. ESPI and MI need coherent illumination to generate the fringe patterns which characterize the object behaviour. Both set-ups have capability for in-plane displacement measurement; however, the ESPI set-up can be adapted to simultaneously measure in-plane and out-of-plane displacements. The applications of this method to fracture mechanics has been carried out in previous work were the stress intensity factor in a part through crack was measured [1]. To achieve this step the experimental setup was designed to cancel rigid body motion and coupled with accurate image processing tools, obtain the above mention displacements and rotations of the plate along the crack line. Once calculated these parameters it is followed an hybrid methodology were the compliance factors of each line spring element placed along the crack plane allow the evaluation of the consequent stress field and further assessment of the stress intensity factor.

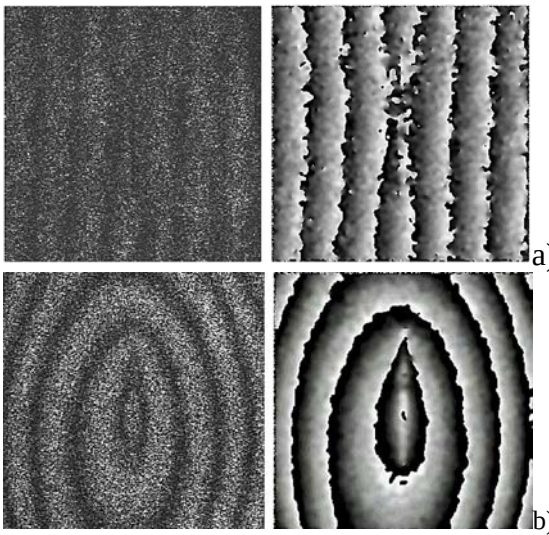

Figure 1. Fringe pattern and phase map obtained for in-plane a) and out-of-plane b) displacement measured with ESPI [1].

The problem of a part through crack is approached with precision using 3D Finite Element Techniques. However, this simulation is expensive, once it means a heavy computation effort near the singularity, were a highly refined mesh must be generated. To overcome this drawback a line spring model was proposed by Rice and Levy [2]. The model consisted in replacing the residual ligament along the part trough crack surface by a set of side edge cracked plates were each crack depth reconstructs the real crack profile, view fig. 2. Then, the structural behaviour of each side edge cracked plate of the model acts like a spring with coupled extensional displacement and crack edge rotations. Using optical techniques like ESPI it is possible to record with high precision the evolution of the conjugate crack surfaces along its length. After obtaining the mentioned displacements and rotations they can be input in the line spring equations to compute the stress intensity factor. All of these calculations are detailed in a previous work [1].

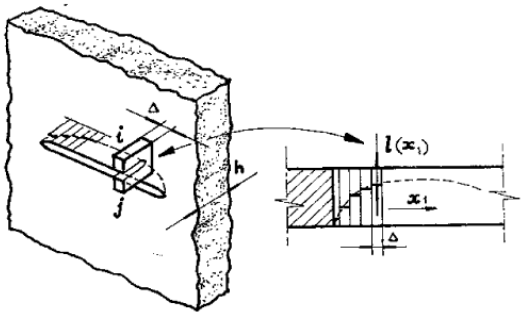

Figure 2. Line spring model replacing the structural behaviour of the remaining ligament along a part through crack [1]

1.1.2 MOIRÉ INTERFEROMETRY (MI)

Another optical method could be used to assess the displacement field near a singularity. MI relies on the superposition of two grids, being one the reference and the other following the deformation of the object surface. High frequency grids (up to 1200 lines/mm or more) are available and have to be recorded on the object surface, consisting on the object grid. The resolution depends on the grid pitch and can be adjusted to the expected displacement amplitude. This method is restricted to in-plane measurements, yet with accuracy to characterize structural singularities like a through crack [3]. As can be seen in fig. 3 the MI was used to characterize the displacements on the surface of a 3PB specimen giving results in good agreement with FEM calculation. In fig. 4 it is depicted a comparison with the numerical results obtained with FE ANSYS® [4].

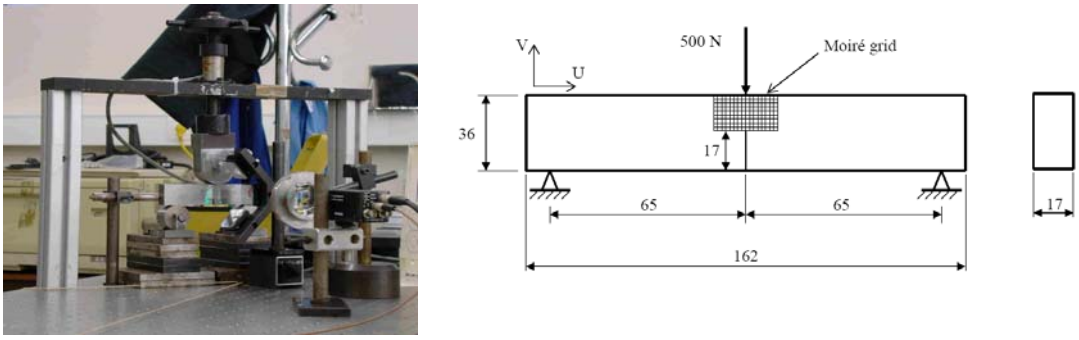

Figure *3. MI setup to obtain the 2D displacement on a 3PB test specimen*

In spite of being a very accurate tool for the experimental measurement of displacements, this is restricted to in-plane measurements which leave the line spring method incomplete for the edge crack rotations. However, the MI can be used to adjust a numerical solution and in complement, use the surface rotation obtained with the FEM. Still the MI method is fully applicable to fracture mechanics problems dealing with through cracks or side edge crack. Also in this technique image processing techniques could be involved to obtain the continuous field displacement with temporal phase shift.

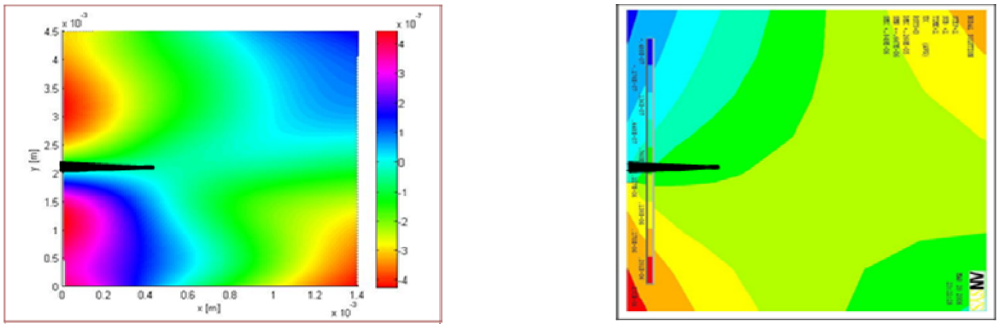

(a) (b)

Figure 4. Displacement field, in x direction, obtained with Moiré interferometry (a) and numerical results (b).

1.1.3 DIGITAL IMAGE CORRELATION (DIC)

Recently a new optical technique is being spread in the scientific community, the DIC. In this technique the object is illuminated by a non coherent light and the intensity patterns are resulting from the surface texture. These intensity patterns, which should have a random distribution, will be divided into smaller areas. Each subdivision of the picture is initially recorded and compared, by correlation, with the obtained images for different deformation states of the object. The determination of displacement and strain fields are obtained by the correlation between the random pattern of initial image (reference) and the final one (deformed) [5].

The surface texture can be natural or prepared with special painting and its size influences the accuracy of the measurement. In this particular technique the software plays an important role as the displacements are calculated from image details. This method could be used to measure 2D and 3D strain or displacement fields. Recently there are available integrated systems offering good results with easy operation. A commercial code of DIC (ARAMIS) was used to characterize in-plane displacements and strains on the surface of a 3PB specimen, similar to fig. 3. The surface preparation was done by creating a random speckle using a spray of matt black paint. The results of displacement and strain measurements are represented in fig. 5 and 6.

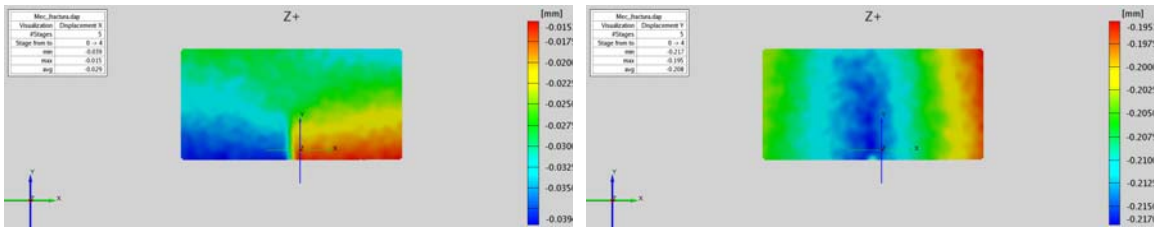

(a) (b)

Figure 5. Displacement fields obtained with Digital Image Correlation in x direction (a) and y direction (b).

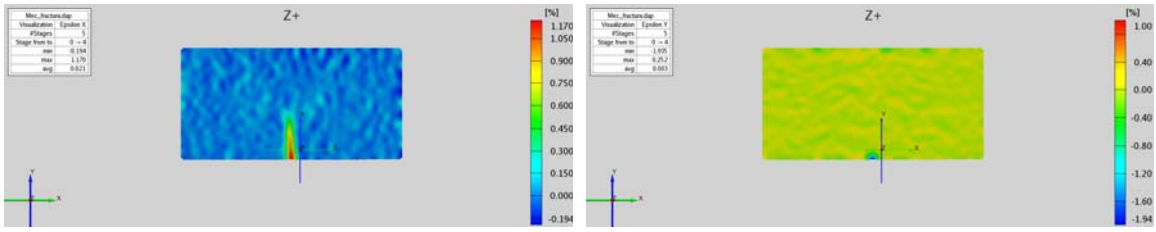

(a) (b)

Figure 6. Strain fields obtained with Digital Image Correlation in x direction (a) and y direction (b).

As can be seen in the previous figures the results obtained with DIC in spite of being discontinuous showed good accuracy and proved to be a good solution in future works. The increase of the video detectors resolution will improve this technique which is easy to use and doesn't need expensive equipment.

2. CONCLUSIONS

The procedures described appear as an interesting step in hybrid process in the evaluation of the stress intensity factor in cracked plates. The ESPI allows both in-plane and out-of-plane measurements, however it is complex, expensive and easily decorrelated; MI is less sensitive to rigid body motion and enough accurate for this application being the grid recording a difficult and longstanding task. Finally, the DIC appears to be the less expensive technique, also allows in-plane and out-of-plane measurements and the direct obtainment of strain fields, but is very demanding in the computation effort and for very high resolutions is difficult to create the speckle small enough.
All of the here presented methods can be used in fracture mechanics with good results not only in stress intensity factor assessment but also in the adjustment of numerical models for the same goal.

REFERENCES

[1] Jaime M. Monteiro, Mário A. P. Vaz, Franciso Q. Melo and J. F. Silva Gomes; "*Use of interferometric techniques for measuring the displacement field in the plane of a part-through crack existing in a plate*"; International Journal of Pressure Vessels and Piping Volume 78, Issue 4, April 2001, pg. 253-259.

[2] J. R. Rice and N. Levy, Journal of Applied Mechanics, Transctions of the ASME, 39, pg. 185-194, 1972.

[3] Ribeiro, J., Lopes, H., Monteiro, J., Vaz, M., "*Displacement Full-Field Measurement at Crack Root Using the Interferometric Moiré Technique*", 3rd International Conference on Integrity, Reliability & Failure 2009 (IRF'2009), FEUP, Porto, July 20-24, 2009.

[4] Nakasone, Y. Yoshimoto, S., and Stolarski, T. A. "*Engineering Analysis With ANSYS Software*", Edited by Elsevier, 2006, Oxford.

[5] Hu, T., Ranson, W., Sutton, M., Peters, W., "*Application of Digital Image Correlation Techniques to Experimental Mechanics*", Experimental Mechanics, nº 3, Vol. 25, pg. 232-244, 1985.

METHODOLOGY FOR IN-SITU STRESS INTENSITY FACTOR DETERMINATION ON CRACKED STRUCTURES BY DIGITAL IMAGE CORRELATION

V. Richter-Trummer[1], P.M.G.P Moreira[2], S.D. Pastrama[3], M.A.P. Vaz[1], P.M.S.T. de Castro[1]

[1] Faculdade de Engenharia da Universidade do Porto and IDMEC-Porto
Rua Dr. Roberto Frias, 4200-465 Porto, Portugal; E-mail: {valentin;gmavaz;ptcastro}@fe.up.pt

[2] Instituto de Engenharia Mecânica e Gestão Industrial, INEGI
Rua Dr. Roberto Frias, 4200-465 Porto, Portugal; E-mail: pmgpm@fe.up.pt

[3]Department of Strength of Materials, University "Politehnica" of Bucharest,
Romania, spastrama@resist.pub.ro

ABSTRACT

A methodology for in-situ stress intensity factor (SIF) determinations that can be used for the analysis of cracked structures is shown. The proposed method is demonstrated in the laboratory for the case of a central cracked plate, subjected to uniaxial tension. Three steps are used for the SIF determination. First the strain field around the crack tip is acquired using a digital image correlation based optical technique. Secondly, the stresses are calculated based on the equation from the theory of elasticity. In the third step an over determined system of equations is solved containing the stress field around the crack tip and the stress intensity facto among others.
A comparison of the obtained results was performed with results obtained using the Dual Boundary Element Method (DBEM) together with the J-Integral method for SIF determination. A good agreement can be noticed for both the stress distribution around the crack tip and for the SIF calculated based on these stresses, proving thus the ability to measure the SIF in-situ.

KEYWORDS: Fracture mechanics, in-situ stress intensity factor determination.

1. INTRODUCTION

Modern lightweight structures are often based on damage tolerance design principles, which means that the structure has to withstand the existence of cracks up to the next routine maintenance inspection or up to its defined economical end of life. The maintenance intervals have to be chosen in a way that guarantees a secure usage of the structure, which often leads to high inspection costs.
A better knowledge of the real effect of existing cracks could lead to a better planning of the maintenance operations after a crack has been found in a structure. The possibility to measure the real stress intensity factor (SIF) of a crack in-situ is therefore of high interest.
Since the ability to tolerate a substantial amount of damage is a requirement for modern lightweight structures, it has become increasingly important to develop methodologies to predict failure in fatigue damaged structures. The damage tolerant philosophy must ensure the continued safe operation of structures, which means that a structure is supposed to sustain cracks safely until it is repaired or its service life has ended. Strength assessment of structures is necessary for their in-service inspection, repair, rehabilitation, and health monitoring. The damage tolerance analysis should provide information about the effect of cracks on the strength of structures. Damage tolerance analyses can be performed using linear elastic fracture mechanics (LEFM) concepts where the stress intensity factor is a fundamental parameter. Fracture mechanics in conjunction with crack growth laws, *e.g.* Paris law [1], is widely used to analyze and predict crack growth and fracture behavior of structural components. To study crack growth and to evaluate the remaining life of a certain structural component, rigorous numerical analyses have to be performed to compute SIFs.
Structures can suffer fatigue damage throughout their service life leading to constant changes in geometry. The assumptions made during the design phase are therefore constantly changed, and numerical analyses previously performed no longer accurately show the stress distribution at critical locations. With the ability to monitor the fatigue process in-situ, non-destructive evaluation (NDE) methods are of critical importance for structural integrity evaluation and failure prevention of engineering components in service. The development of experimental techniques to obtain the SIF in real structures is therefore of high interest.

The technique presented in this work can provide a powerful experimental tool to investigate localized inhomogeneous damage and to analyze complex fatigue processes. A better fatigue-life estimation becomes feasible and reduced maintenance costs may be expected as a result.

Digital Image Correlation (DIC) is an optical analysis method that can be used for full field, non-contact 2D and 3D measurement of deformations and strains on the surface of components [2]. Longitudinal and transverse strains with any load, such as tensile, compression, bending and torsion or a combination of different loads can be monitored. The method is based on the correlation of two images acquired before and after deformation. The recorded images are analyzed and compared by a special correlation technique, which allows the determination of the surface displacements with high local resolution. In order to achieve a good correlation, the method uses a speckle pattern applied to the object surface and tracks the gray value pattern in small neighborhoods called subsets during deformation.

One of the advantages of DIC is that no physical sensor has to be installed. This type of measurement system is flexible, since it allows measuring almost any type of deformation in time and space, giving access to information about strain gradients and their variations in time. A disadvantage of this process is that it works better in laboratory under known conditions. Care has to be taken to have a clear view; fumes and similar can create noise and distorted results.

A multipoint overdeterministic method is used for SIF calculation, where experimental data collected from optical images is fitted to Muskhelishvili's equations describing the stress field around the crack tip [3]. The procedure is based on the overdeter-ministic approach, used previously in fracture mechanics for processing photoelastic data in experimental determination of SIFs [4, 5]. The values of the stresses in an unlimited number of points around the crack tip can be used in order to fit a multiterm series expansion of the stress field. A system of equations is obtained in which the coefficients of each term are the unknowns. The number of equations is equal to the number of the considered points while the number of unknowns is equal to the number of terms chosen in the series expansion, which is much lower. This overdeterministic method has the advantage of being able to use an unlimited number of data points, thus minimizing the error.

In order to evaluate the accuracy of the proposed algorithm for SIF determination, the results were compared with the numerical ones obtained using the Dual Boundary Element Method (DBEM).

1.1. The specimen

A pre-cracked MT specimen according to ASTM E647 [6] with a width of 80 mm was selected for this experiment due to its size, which is large enough for a good measurement area and small enough to maintain the fatigue loads relatively low. The specimen thickness was 4 mm and the 10 mm long initial notch was machined by spark erosion (EDM). A drawing of this specimen is shown in Figure 1.

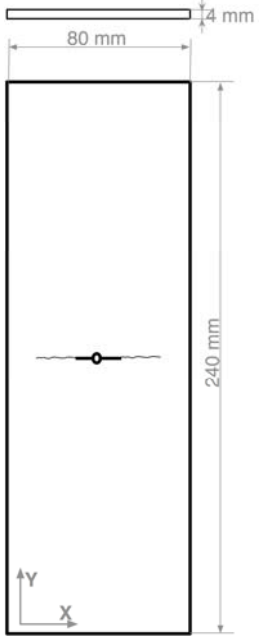

Figure 1. MT Specimen.

One advantage of this type of specimen is the fact that it has a geometry which allows the analysis of symmetric and non-symmetric cracks.

1.2. Fatigue crack growth test

80000 cycles have been performed in order to develop a fatigue crack from the initial notch. The crack half length on the monitored side was a2 = 12.31 mm, measured from the center of the crack. Table 1 shows the parameters used for fatigue loading, and Figure 2 shows a scheme of the studied crack geometry.

Table 1. Fatigue test properties

Property	Value
F_{mean}	11980 N
$F_{amplitude}$	9792 N
R-ratio	0.1
frequency	4 Hz
Number of cycles	80000

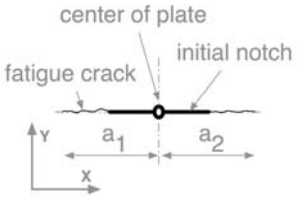

Figure 2. Scheme of the studied crack geometry.

2. Experimental SIF determination

An optical strain and deformation measurement system based on digital image correlation is used to measure the strain distribution around a fatigue crack tip. Based on the obtained measurement results, the stress intensity factor can be calculated by fitting the experimentally obtained results in the analytical stress expression near the crack tip, in the form of a series expansion with different number of terms.

The experiments have been performed in DEMEC/FEUP on a servo-hydraulic MTS 312.31 testing machine using a 250 kN load cell. Ambient temperature was 24ºC during the whole experiment. Figure 3 shows the experimental setup.

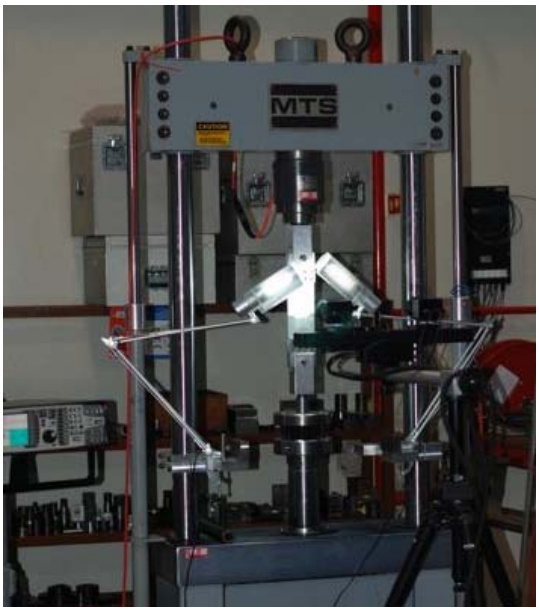

Figure 3. Experimental setup for measurement of the strain around the crack tip.

2.1. Optical strain and deformation measurement system

Only the right crack tip has been measured in this work. The aim was to demonstrate the feasibility of determining the SIF in-situ by optical means. In future works both crack tips in different loading conditions will be monitored.

For the images taken in the unloaded state, a force of only 200 N was considered, in order to allow the specimen not to stay fixed during the measurement which was performed under loadcontrol on the servohydraulic system. The loaded state was measured at the maximum load of the fatigue test, namely F_{max} = 21760 N. The crack extension was measured using a travelling optical microscope attached to a Mitutoyo digital scale with a 1/100 mm resolution.

A portable GOM (Gesellschaft für Optische Messtechnik) ARAMIS 6.0.2 workstation was used for measurement of the strain field around the crack tip. This system is based on digital image correlation, and therefore information about recognizable facets has to be given to the system.

The GOM 2M hardware was used with 50 mm focal length Schneider-Kreuznach lenses with a maximum aperture f = 2.8. Two 18 W white fluorescent lamps at 6400 K were used for illumination of the specimen surface.

The specimen is painted with a stochastic pattern necessary for the digital image correlation operation. A fine black dotted pattern is applied to the white-grounded surface for better contrast. The quality of the results proves to be high when such a prepared surface is used. Figure 4 shows the stochastic pattern applied to the specimen surface, which is used for strain calculation.

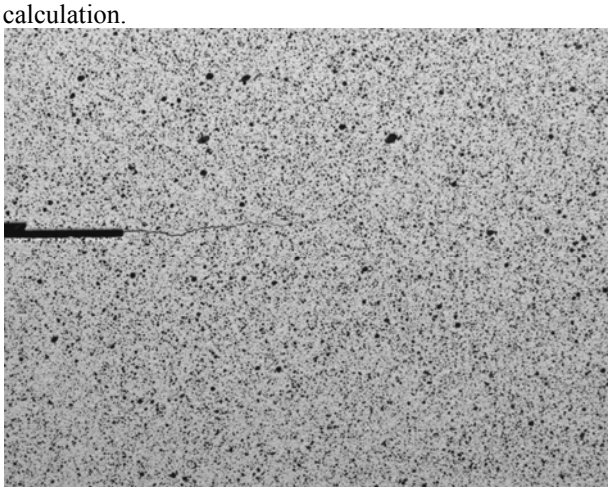

Figure 4. Stochastic pattern applied to the specimen surface for strain calculation; the crack can be recognized due to the maximum load that was applied for this image.

2.1.1. Measurement results

The painted specimen is virtually divided into facets with a size of 7×7 pixels and a facet step of 5 pixels. This means that every 5 pixels a new 7 pixel long facet starts, and overlap between facets is 2 pixels, corresponding to 29% in X and Y directions. Due to the small distance from the lenses to the specimen, an area of around 20×15 mm, corres-ponding to 324×246 facets, is measured. Strain is calculated by measuring the deformation of a facet in relation to its neighbouring facets. In order to obtain a smooth measurement, 19×19 facets where chosen for strain measurement. This is equivalent to a gauge length of about 1.21 mm in traditional measuring instruments. The validity quote was chosen to be 55%, which means that at least 55% of the 19x19 facets have to exist in order to allow the calculation of strain for a certain facet.

Figure 5 shows the obtained strain distribution around the crack tip in the direction perpendicular to the crack plane used for calculation of the SIF.

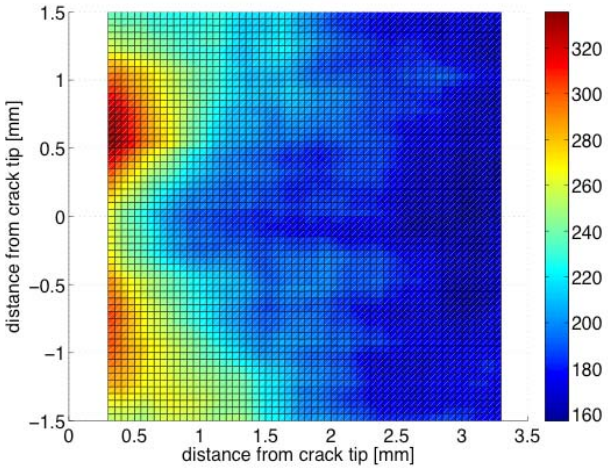

Figure 5. Smoothed strain data in Y direction; εY units are με. The crack tip is located at the centre of coordinates

2.2. Over determined SIF calculation

Knowing the stress field around the crack tip, it is possible to apply an overdeterministic SIF calculation method as was shown in [4] for example.

For the plane stress problem of a homogeneous isotropic solid, in the absence of body forces, the global field equations for the stress components in the vicinity of a straight front crack under mode I conditions can be written as shown by [7]:

$$\sigma_{xx} = \frac{K}{\sqrt{2\pi r}}\cos\frac{\theta}{2}\left(1-\sin\frac{\theta}{2}\sin\frac{3\theta}{2}\right)+\sigma_{ox}+$$
$$+\sum_{n=3}^{\infty}\left(A_n\frac{n}{2}\right)r^{\frac{n}{2}-1}\left\{\left[2+(-1)^n+\frac{n}{2}\right]\cos\left(\frac{n}{2}-1\right)\theta+\right.$$
$$\left.-\left(\frac{n}{2}-1\right)\cos\left(\frac{n}{2}-3\right)\theta\right\},$$
$$\sigma_{yy} = \frac{K}{\sqrt{2\pi r}}\cos\frac{\theta}{2}\left(1+\sin\frac{\theta}{2}\sin\frac{3\theta}{2}\right)+$$
$$+\sum_{n=3}^{\infty}\left(A_n\frac{n}{2}\right)r^{\frac{n}{2}-1}\left\{\left[2-(-1)^n-\frac{n}{2}\right]\cos\left(\frac{n}{2}-1\right)\theta+\right.$$
$$\left.+\left(\frac{n}{2}-1\right)\cos\left(\frac{n}{2}-3\right)\theta\right\},$$
$$\tau_{xy} = \frac{K}{\sqrt{2\pi r}}\sin\frac{\theta}{2}\cos\frac{\theta}{2}\cos\frac{3\theta}{2}-$$
$$-\sum_{n=3}^{\infty}\left(A_n\frac{n}{2}\right)r^{\frac{n}{2}-1}\left\{\left[(-1)^n+\frac{n}{2}\right]\sin\left(\frac{n}{2}-1\right)\theta+\right.$$
$$\left.+\left(\frac{n}{2}-1\right)\sin\left(\frac{n}{2}-3\right)\theta.\right.$$

The origin of the Cartesian (x, y) and polar (r, θ) coordinate systems is defined at the crack tip.

From the equations above, it can be verified that all three exhibit linear dependence with the coefficients K, σ_{0x}, A_3, ... , A_n. This means that a linear overdeterministic algorithm can be used to obtain these unknown coefficients, provided the values of the stresses are obtained at different points of coordinates (r, θ).

Values of the stresses obtained by optical measurement are processed with the linear overdeterministic algorithm in order to obtain the stress intensity factor. Since data may be collected in points near the crack tip, two or three terms from the series expansion would be sufficient for a good accuracy of the results. Nevertheless, seven terms were used for higher accuracy in this work.

For calculation purposes, the strain field is considered in a small quadratic area around the crack tip only, starting 0.3 mm after the crack tip and extending for 3 mm away from the tip. In this area, the strain values are read on a grid with 0.05 mm spacing, which guarantees a good degree of precision.

3. Numerical SIF determination

Linear elastic fracture mechanics (LEFM) can be used for the analysis of crack behaviour in damage tolerance. The fundamental postulate of LEFM is that the crack behaviour is determined solely by the values of the stress intensity factor, parameter which depends on the applied load and the geometry of the cracked structure.

Numerical methods should be primarily used for the stress analysis of engineering structures because of their complex geometry. When studying crack growth problems, the need for continuous re-meshing is a practical disadvantage of the finite element method (FEM).

The Boundary Element Method (BEM) is better suited for the incremental analysis of crack growth problems. An advantage of using the BEM method is the ability to easily model a great variety of cracks without the need for re-meshing of the model, as it would be necessary when using the finite element method. The main disadvantage of this method is related to difficulties of applying it to more complex structures.

The solution of general crack problems cannot be achieved with the direct application of the standard BEM, because the coincidence of the crack boundaries causes an ill-posed problem. For a pair of coincident source points on the crack boundaries, the algebraic equations relative to one of the points are identical with the algebraic equations relative to the opposite point, since the same boundary integral equation is applied at both coincident source points, with the same integration path, around the whole boundary of the problem. Among the techniques devised to overcome this difficulty, the most general are the sub-regions method and the dual boundary element method.

The DBEM introduces two independent boundary integral equations, with the displacement equation used for collocation on one of the crack surfaces and the traction equation used for collocation on the opposite crack surface. Consequently, general mixed-mode crack problems can be solved in a single-region boundary element formulation, with both crack surfaces meshed with the DBEM.
The stress intensity factor for the numerical verification is therefore calculated by the DBEM, using the J-Integral method. The code "Cracker" [8] is used for this purpose, since it has implemented a routine capable of predicting the crack growth path, which allows the validation of crack growth path predictions performed based on the optical strain measurements.

4. Comparison of numerical and experimental results

Figure 6 shows a comparison of experimental and numerical results of the strain near the crack tip for θ = 0º in front of the crack tip. An excellent agreement between the experimental and numerical result was found.

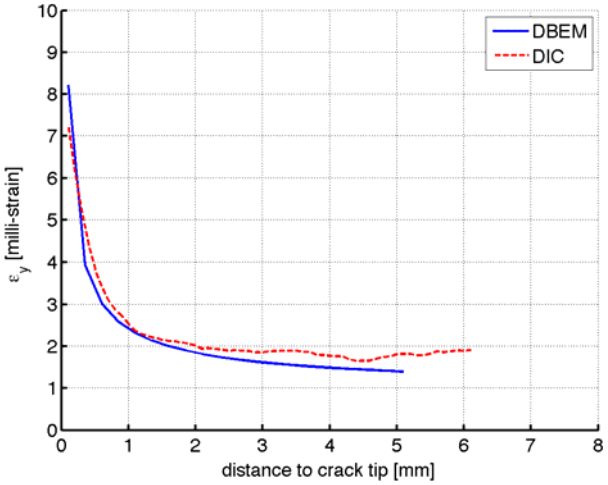

Figure 6. Strain Y comparison for numerical and experimental data.

For this case, only the stress field at the right side crack was determined experimentally and the stress intensity factor was compared to numerical results. Only mode I was considered, since the crack grows essentially perpendicularly to the loading direction. The experimental and numerical results are presented in Table 2. The numerical result was considered as reference value for the calculation of the difference parameter.

The strain field around the crack tip can be used in the present case to verify that the crack tip was correctly identified by the optical strain measurement technique. The good agreement shown in Figure 6 demonstrates the high confidence that is possible in this method. Nevertheless, the main problem found in this initial experiment was the correct determination of the crack tip in the images taken for digital image correlation.

Table 2. Comparison of the experimentally obtained SIF using DIC and the numerically determined SIF using the DBEM

a_2	DIC	DBEM	difference
SIF [MPa√mm]	475	487	2.5%

5. Discussion of the results and conclusions

As it can be seen, similar values have been obtained for the measured and calculated strain fields, which raises the confidence in the optical strain measurement system. Additionally, the experimental result for the SIF in mode I is promising, giving confidence that this technique can be applied to real life structures in order to assess their structural integrities.

Up to the moment, it is very difficult to precisely find the crack tip on the specimens, especially using digital images. This information is however fundamental for good results since the SIF strongly depends on this information. Therefore, a method has to be developed which guarantees that different operators can easily identify the crack tip.

A new procedure for processing the experimentally obtained strain values was proposed in this work. The strains measured with the GOM ARAMIS system were first converted into stresses, using the well-known equations of the theory of elasticity. Then, equations of the stress field around the crack tip, written as series development with seven terms, were used to fit the experimental data, obtaining thus an overdetermined system of equations in which the coefficients of the series expansion are the unknowns.

The overdeterministic algorithm, a numerical procedure for solving such systems, was used to solve the system and to obtain the stress intensity factor, which is the coefficient of the first term of the expansion.

The numerical calculations of the stress intensity factor using the dual boundary element method validated the methodology. A difference less than 3% was achieved, proving thus the reliability of the proposed method as long as the crack tip can be correctly detected.

Due to its flexibility, this method can be applied for in-situ fracture mechanics researches on real structures, for which a laboratory model is difficult or even impossible to conceive.

ACKNOWLEDGEMENTS
This work was partially funded by the Portuguese

Foundation for Science and Technology PhD scholarship SFRH / BD / 41061 / 2007. Dr. P. Moreira acknowledges *POPH - QREN-Tipologia 4.2* – Promotion of scientific employment funded by the ESF and MCTES.

REFERENCES

[1] P. Paris, P. Gomez, and W. Anderson, "A rational analytic theory of fatigue", The Trend in Engineering 13(1), 9-14, 1961.

[2] R.C.Gonzalez, R.E. Woods and S.L. Eddins, "Digital Image Processing Using Matlab", 1st ed., Pearson Education, Inc., 2004

[3] N.I. Muskhelishvili, "Some Basic Problems of the Mathematical Theory of Elasticity", first published in Russian, English translation P. Noordhoff, The Netherlands, 1933, 1953

[4] S.D. Pastrama, P.M.G.P. Moreira, P.M.S.T. de Castro and G. Jiga, "An overdeterministic algorithm for stress intensity factor using finite elements results", in proceedings 11th Portuguese Conference on Fracture - PCF 2008, Lisboa, Portugal, 325-332, 2008

[5] R.J. Sanford and J.W. Dally, "A General Method for Determining Mixed-Mode Stress Intensity Factors from Isochromatic Fringe Patterns", Engineering Fracture Mechanics 11(4), 621-633, 1979

[6] ASTM E647, “Standard Test Method for Measurement of Fatigue Crack Growth Rates”, ASTM International, West Conshohocken, PA, DOI: 10.1520/E0647-08, 2008

[7] C.W. Smith, A.S. Kobayashi, "Experimental Fracture Mechanics", in Handbook on Experimental Mechanics (A.S. Kobayashi, Ed.), pp.891-956, SEM, Inc., Prentice-Hall, Inc., Englewood Cliffs, NJ, 1987

[8] A. Portela, "Dual Boundary Element Analysis of Crack Growth", Computational Mechanics Publications, Southampton UK and Boston USA, 1993

AUTHORS INDEX